

Journal of Engineering and Technology for Industrial Applications



ISSN 2447-0228

October 2024

Volume 10 / No 49

Editor-in-Chief: J. C. Leite

www.itegam-jetia.org



O **ITEGAM-JETIA: Journal of Engineering and Technology for Industrial Applications** is a publication of the Galileo Institute of Technology and Education of the Amazon (ITEGAM), located in the city of Manaus since 2008. JETIA publishes original scientific articles covering all aspects of engineering. Our goal is the dissemination of research original, useful and relevant presenting new knowledge on theoretical or practical aspects of methodologies and methods used in engineering or leading to improvements in professional practice. All the conclusions presented in the articles It should be state-of-the-art and supported by current rigorous analysis and balanced assessment. Public magazine scientific and technological research articles, review articles and case studies.

JETIA will address topics from the following areas of knowledge: Mechanical Engineering, Civil Engineering, Materials and Mineralogy, Geosciences, Environment, Information and Decision Systems, Processes and Energy, Electrical and Automation, Mechatronics, Biotechnology and other Engineering related areas.

Publication Information:

ITEGAM-JETIA (ISSN 2447-0228), (online) is published by Galileo Institute of Technology and Education of the Amazon on a every two months (February, April, June, August, October and December).

Contact information:

Web page: www.itegam-jetia.org

Email: editor@itegam-jetia.org

Galileo Institute of Technology and Education of the Amazon (ITEGAM).

Joaquim Nabuco Avenue, No. 1950. Center. Manaus, Amazonas. Brazil.

Zip Code: 69020-031. Phone: (92) 3584-6145.

Copyright 2014. Galileo Institute of Technology and Education of the Amazon (ITEGAM)

The total or partial reproduction of texts related to articles is allowed, only if the source is properly cited. The concepts and opinions expressed in the articles are the sole responsibility of the authors.

Previous Notice

All statements, methods, instructions and ideas are the sole responsibility of the authors and do not necessarily represent the view of ITEGAM -JETIA. The publisher is not responsible for any damage and / or damage to the use of the contents of this journal. The concepts and opinions expressed in the articles are the sole responsibility of the authors.

Directory

Members of the ITEGAM Editorial Center - Journal of Engineering and Technology for Industrial Applications (ITEGAM-JETIA) of the Galileo Institute of Technology and Education of the Amazon (ITEGAM). Manaus-Amazonas, Brazil.

Jandecy Cabral Leite, CEO and Editorial Editor-in-Chief

Ivan Leandro Rodriguez Rico, Editorial Assistant

Alison Mendes de Brito, Information Technology Assistant

ITEGAM-JETIA. v.10, n.49. October of 2024. Manaus - Amazonas, Brazil. ISSN 2447-0228 (ONLINE)
<https://www.itegam-jetia.org>

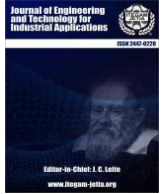
SUMMARY

- CONVOLUTIONAL NEURAL NETWORKS AND DEEP LEARNING FOR THE DETECTION OF PNEUMONIA IN X-RAY IMAGES** 6
Robinson Joel M, Manikandan G, Gokulaselvam R, Bharath R K, Praveen Kumar R, Ebenezer V
- PRECISION IN MOTION: ENHANCING AUTONOMOUS DRIVING WITH ADVANCED LANE RECOGNITION USING HIGH RESOLUTION NETWORK** 17
Santhiya P, Immanuel JohnRaja Jebadurai, Getzi Jeba Leelipushpam Paulraj, Ebenezer V, Kiruba Karan S
- AN ONLINE INCREMENTAL ADAPTATION MECHANISM TO SUBDUE THE EFFECT OF DRIFT IN STREAMING DATA** 23
Ushashree P, R B V Subramanyam
- EXPLORING THE MECHANICAL PROPERTIES AND WATER ABSORPTION BEHAVIOR OF KERATIN FIBER-REINFORCED EPOXY COMPOSITES: INSIGHTS INTO SUSTAINABLE MANUFACTURING** 31
Deepak Kachhot, Rishi Dewangan, Motilal Rinawa, Umesh Kumar Dwivedi
- A BLOCKCHAIN-BASED DIGITAL EDUCATIONAL CERTIFICATE VERIFICATION SYSTEM** 40
Tolulope Ifeyemi, Ajibola Oluwafemi Oyedeji, Fiyinfoluwa Adebisi
- LOAD FLOW, SHORT CIRCUIT AND MOTOR STARTING STUDIES IN ELECTRICAL POWER SUBSTATIONS.** 47
Mohan Muniappan
- THE EVALUATION OF THE BLENDED LEARNING IMPLEMENTED AT AL-AHGAF UNIVERSITY, YEMEN: A STUDENTS' PERSPECTIVE** 59
Hamzah Alaidaros, Omer Salim Bakahakam, Asma Abdulrhman
- IMPACT OF GRAIN BOUNDARIES ON THE ELECTRICAL CHARACTERISTICS AND BREAKDOWN BEHAVIOR OF POLYCRYSTALLINE SILICON PIN DIODES: A SIMULATION STUDY** 64
Abdelaziz Rabehi, Abdelmalek Douara, Elbar Mohamed, Roumaissa Zenzen, Mohamed Amrani
- PRECISION CROP PREDICTION USING IOT-ENABLED SOIL SENSORS AND MACHINE LEARNING** 70
Binson V A, Sania Thomas, Manju G, Syam Kishor K S
- ADVANCED DUAL-LOOP CONTROL ARCHITECTURE FOR SUPERIOR PMSM PERFORMANCE UTILIZING FINITE-CONTROL-SET MODEL PREDICTIVE CONTROL AND EXPONENTIAL REACHING LAW SLIDING MODE CONTROL** 76
Djaloul Karboua, Youcef Chouiha, Ben Ouadeh Douara, Ibrahim Farouk Bouguenna, Said Benkaihou, Belgacem Toul
- ENHANCING MECHANICAL AND CORROSION PROPERTIES OF BRASS COMPOSITES WITH CARBONIZED COCONUT SHELL ASH** 85
Mathew Olurotimi Adeoti, Tamba Jamiru, Taoreed Adesola Adegbola
- A COMPREHENSIVE REVIEW ON APPLICATION OF AI ALGORITHMS FOR GRID CONNECTED SOLAR PHOTOVOLTAIC SYSTEMS** 92
Jahnavi W V, Chandra Sekhar J N
- IMPACT OF NITROGEN INCORPORATION ON BAND GAP BOWING IN ZINC-BLENDE $GAAs_{1-x}N_x$: A FIRST-PRINCIPLES STUDY** 101
oukli mimouna, Ghلام Karima, Seyf Eddine Bechekir

<i>A COMPARISON BETWEEN A CONVENTIONAL AND AUGMENTED RAIL GUN LAUNCHER'S PERFORMANCE.</i>	109
<i>Mohamed Hichem Lahrech, Ahmed Chaouki Lahrech, Abdelkader Bouhlal</i>	
<i>SOLVING THE UNIT COMMITMENT PROBLEM OF 10-GENERATORS SET BY PSO WITH DIFFERENT SPINNING-RESERVE VALUES OBTAINED FROM HOUR-HOUR LOAD DEMAND INCREASING</i>	116
<i>Ali Sadeq Alsowaidi, Seyed Mahmoud Modaresi</i>	
<i>ASSESSMENT OF CEMENT CONTENT IN CURED CONCRETE BY CHEMICAL STUDY OF MATERIALS SCIENCE AND SUSTAINABLE MANUFACTURING TECHNOLOGY</i>	122
<i>Mohankumar Namdeorao Bajad</i>	
<i>HYDRAULIC PERSPECTIVE FOR FLOW OVER PARABOLIC WEIR AND UNDER PARABOLIC GATE</i>	128
<i>Ihsan Abdulkareem Abdulhussein; Rafi Mohammed Qasim, Ayad Abdulkhaliq Yahya</i>	
<i>THE DETERMINANTS OF PERFORMANCE OF NEWSPAPERS INDUSTRY: A MEDIATING EFFECT OF COMPETITIVE ADVANTAGE</i>	134
<i>Deus Nichodemus Shatta</i>	
<i>INFLUENCE OF THE LUBRICANT TEMPERATURE OF SPLASHED LUBRICATED WORM GEARBOX ON CHURNING POWER LOSSES</i>	143
<i>Hardik G Chothani, D.J. Marsonia, N.N. Jadedda, S.H. Zala</i>	
<i>INTERFERENCE REDUCTION SCHEME FOR FEMTOCELL ULTRA-DENSE-NETWORK: CONCEPT AND RESEARCH CHALLENGES</i>	150
<i>Gbenga Victor Adekogba, Adedeji, K.B., Olasoji, Y.O</i>	
<i>UPQC-S, A FRONTLINE DEPLOYABLE POWER LINE SOLUTION FOR HOLISTIC POWER QUALITY ENHANCEMENT</i>	165
<i>Sajid MohmedIqbal Patel, Mohammedirfan Iqbal Siddiqui, Dhaval R Patel</i>	
<i>DYNAMIC AND HYDRAULIC PERFORMANCE OF A PERIPHERAL PUMP IMPELLER MADE OF PINEAPPLE FIBER REINFORCED BIOCOMPOSITE MATERIAL</i>	177
<i>Sergio Andres Gomez Suarez, Alfonso santos Jaimes, Edwin Cordoba Tuta</i>	
<i>ENHANCING PERFORMANCE OF PERMANENT MAGNET SYNCHRONOUS MOTOR DRIVES THROUGH HYBRID FEEDBACK LINEARIZATION AND SLIDING MODE CONTROL</i>	184
<i>Djaloul Karboua, Toufik Mebkhouta, Youcef Chouiha, Abdelkader Azzeddine Bengharbi, Ben ouadeh Douara, Belgacem Toulal</i>	
<i>THE MACHINE LEARNING FOR PREDICTING GAS TURBINE PERFORMANCE IN NAVAL VESSELS</i>	193
<i>Laib Lakhdar, Toufik Tayeb Naas</i>	
<i>CONTROL-WAVE: GESTURE CONTROL GLOVE</i>	200
<i>Yogita Deepak Mane, Dr. Neeta Patil, Akshay Agrawal</i>	
<i>ACOUSTICAL NOISE MITIGATION IN SLIP ANGLE CONTROLLED DTC OF OPEN-END WINDING INDUCTION MOTOR DRIVE USING AISPWM BASED TRIPLE RANDOMIZATION SCHEME FOR EV APPLICATION</i>	208
<i>Ganesh Challa, Dr. M. Damodar Reddy</i>	
<i>ANALYSIS OF FUEL CELL POWERED EV CHARGING STATION</i>	217
<i>Pavan Kumar Reddy Bondu, Vyza Usha Reddy, Dr.</i>	



-
- THE IMPACT OF NANO ADDITIVES IN CORN OIL BIODIESEL USED IN COMBUSTION ENGINES ON THE ENVIRONMENT: AN EXPERIMENTAL APPROACH*** **222**
Raviteja Surakasi, K Ch Sekhar, M Jayakrishna, Rapaka Jagadeesh, D Bhanuchandra Rao, Ivan Leandro Rodriguez Rico
- THE PREDICTING ACADEMIC PERFORMANCE IN UNIVERSITY STUDENTS USING MACHINE LEARNING*** **228**
Ernesto Bolaños-Rodríguez, Cristina Flores-Amador, Asdrúbal López-Chau, Alonso Ernesto Solis-Galindo, Antonio Zárate-Rosas
- APPLYING PROPORTIONAL–INTEGRAL–DERIVATIVE CONTROLLERS ON WIRED NETWORK TCP'S QUEUE TO SOLVE ITS INCOMPATIBILITY WITH THE WIRELESS AD-HOC NETWORK*** **234**
Yaser Ali Enaya, Abdulamir Abdullah Karim, Dr. Mohammed Qasim Sulttan, Salam Waley Shneen
- PROCESS IMAGES-BASED CONTROLLER FUZZY-PI TO CONTROL EFFICIENCY IN ELECTRIC DRIVES*** **239**
Luis D Rojas Puron, Idania Aguilera Fernández, Luis M Rojas Aguilera, Joao E Neto



RESEARCH ARTICLE







OPEN ACCESS

CONVOLUTIONAL NEURAL NETWORKS AND DEEP LEARNING FOR THE DETECTION OF PNEUMONIA IN X-RAY IMAGES

Robinson Joel M¹, Manikandan G², Gokulaselvam R³, Bharath R K⁴, Praveen Kumar R⁵, Ebenezer V⁶

^{1,2,3,4,5}Department of Information Technology, Kings Engineering College, Chennai, India.

⁶Assistant Professor, Division of Computer Science and Engineering, Karunya Institute of Technology and Sciences, Coimbatore, India.

¹<http://orcid.org/0000-0002-3030-8431>  ²<http://orcid.org/0000-0002-4323-8231> , ³<http://orcid.org/0009-0000-6502-0226> 
⁴<http://orcid.org/0009-0002-7456-4506>  ⁵<http://orcid.org/0009-0007-3903-9431> , ⁶<http://orcid.org/0000-0002-0801-6915> 

Email: joelnazareth@gmail.com, mani4876@gmail.com, gokulaselvamravindran@gmail.com, bharnish888@gmail.com, praveenkumarethinam@gmail.com, ebenezer@karunya.edu

ARTICLE INFO

Article History

Received: December 13th, 2023

Revised: September 06th, 2024

Accepted: September 06th, 2024

Published: Month 30th, 2024

Keywords:

X-Ray,
Artificial Intelligence,
Radiologist,
Data accessibility,
Accuracy.

ABSTRACT

Artificial intelligence has been used in a variety of industries during the course of its growth, especially over the past decade as a result of the enormous rise in data accessibility. Its main objective is to assist people in making judgements that are more reliable, quick, and accurate. The usage of machine learning and artificial intelligence in the medical profession is growing. This is especially true for medical fields that employ a variety of biological picture kinds and where diagnostic procedures rely on collecting and analysing a substantial amount of digital data. Machine learning-based evaluation of medical photos enhances reporting uniformity and accuracy. In order to help decision-makers make the most accurate diagnosis, this study promotes the use of machine learning algorithms to evaluate chest X-ray images. With the aid of the CNN (Convolutional Neural Network) algorithm, the process will "learn" based on previously collected X-ray data from both healthy and sick patients (the training set). This research provides an approach to photo interpretation based on deep learning. This technique will reduce radiologists' burden because of its accuracy of more than 91% and nearly immediate findings, especially for those who must analyse an extensive amount of patient pictures.



Copyright ©2024 by authors and Galileo Institute of Technology and Education of the Amazon (ITEGAM). This work is licensed under the Creative Commons Attribution International License (CC BY 4.0).

I. INTRODUCTION

Pneumonia is an inflammatory disease that affects the air sacs in either or both of the lungs. It can be brought on by a variety of infectious agents, including organisms such as bacteria, viruses, fungi, as well as certain chemicals. Pneumonia can range in severity from mild to severe, and it can have negative effects, especially in vulnerable populations including young children of all ages, the elderly, and people with weakened immune systems. Typically, a combination of physical exams, chest X-rays, lab testing, and perhaps sputum cultures are used to diagnose pneumonia.

Even though artificial intelligence (AI) [1] was acknowledged as a field of study at the start of the twentieth century, scientific communities did not look into it in depth for a very long time due to its poor applicability. Due to the rise of processing power and the accumulation of enormous amounts of data over the past 20 years, AI has attracted interest from the

educational and industry sectors. Throughout the several "Seasons of AI" that AI underwent during its development, there were various stages. The period spanning from the start of the 20th century to the present, which is sometimes described as the "AI Winter," used to be the most well known season of AI. This fact is one of the main reasons why AI at this point could not develop fast.

Pneumonia [2], a viral lung disease, primarily affects the pulmonary capillaries and prevents oxygen from entering the bloodstream. Coughing, pain in the chest, a high body temperature, and breathing difficulties are typical symptoms. Most typically, pneumonia is brought on by bacterial, viral, or autoimmune conditions. Blood tests and chest X-rays are used to identify inflammation. The corona virus (Covid-19) [3], whose patients are at a higher risk of developing pneumonia, is relevant in terms of test accuracy and decoding speed at this time. The current significant increase in patients need a rapid and accurate solution for interpreting the X-rays. A Deep Learning-based technique for picture decoding is demonstrated in this paper. Since it yields

findings almost immediately and with a precision level of over 90%, this technology will be used to reduce the burden of radiologists whom must evaluate a huge number of patient images. With the aid of the CNN (Convolutional Neural Network) algorithm [4], the process will "learn" based on previously collected X-ray data from both healthy and sick patients (the training set).

To tackle the issue, you must create a deep network. The initial objective of the network's depth is the chance that the picture reflects a confirmed case of pneumonia. The range of the likelihood ranges from 0 to 1, with 1 denoting a specific instance of pneumonia. The test picture set, which is entirely different from the training set, will be used to assess performance. A probability of error of no more than ten percent, or an accuracy rate of more than 90%, will be regarded as good achievement.

Construct the PRECISION and the RECALL [5] effectiveness graph for the network you choose, with each point on the graph generated for an alternative threshold level) in proportion to the likelihood the network produced (to choose a positive example, such as pneumonia. The threshold for each value will be in increments of 0.5 from 1.0 to 9.0. Mark the SCORE-F scores [5] that are going to be determined based on each pair of PRECISION-RECALL numbers on the diagram as well. What criteria yielded the greatest SCORE-F value? Try some of the following modifications to increase accuracy and effectiveness for the internet connection you chose: Introduction of one layer as per your option; the decision must be supported. Incorporation of two additional layers as per your option; the choice that you make must be supported.

Examine five modifications to the total amount of kernels used for convolution (no extra layers) and/or the depth of the current layers. The decision must be supported. Use the following training methods to assess the network's performance. Examine how the EPOCHS [6] and APPROACHING number RATES affect the algorithm: SGD algorithm, including both MOMENTUM and MOMENTUM, as options NESTEROV [7]. Algorithm ADAM [8], RMSPROP algorithm [9]. Analyse the impact of the following modifications with dropout in the event there is a layer, see what happens if its likelihood DROPOUT's [10] parameter is changed.

II RELATED WORK

Radiographs [11], usually referred to as X-ray pictures, are an important diagnostic tool in the medical industry and several other industries. They are made by exposing a body or an item to X-rays and then recording the radiation that results on a specialised detector or film. An electromagnetic radiation with a greater energy than visible light is an x-ray. When X-rays travel through an item, solid tissues like bones absorb them while less dense tissues like muscles and organs disperse them. An image that resembles a shadow is produced when a detector on the opposite side of the item records the fluctuating X-ray exposure levels.

The initial step before building a model is often preprocessing the input data. The images were uploaded as grayscale for the purpose of the study after being scaled down from their original RGB colour space to 200x200 pixels. The pixel intensity levels were then normalised by dividing the pixel values by 255. In this way, the pixels in the image are represented by floating point integers between 0 and 1, rather than utilising integer numbers from 0 to 255. This should positively affect CNN's performance.

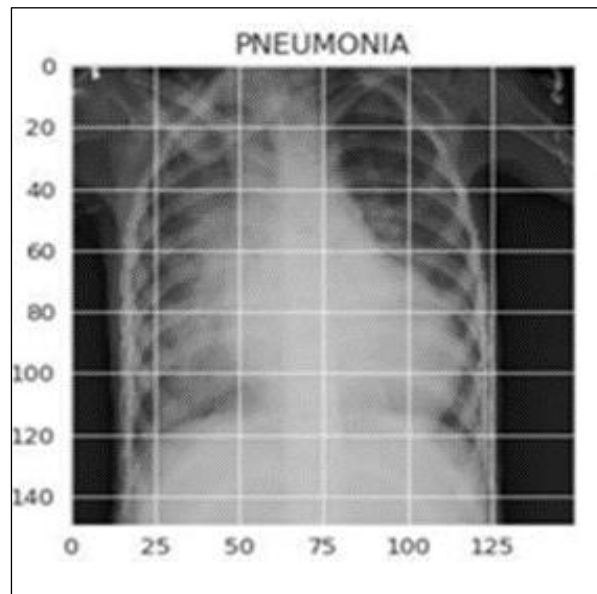


Figure 1: A chest X-ray labeled as pneumonia.
Source: Authors, (2024).

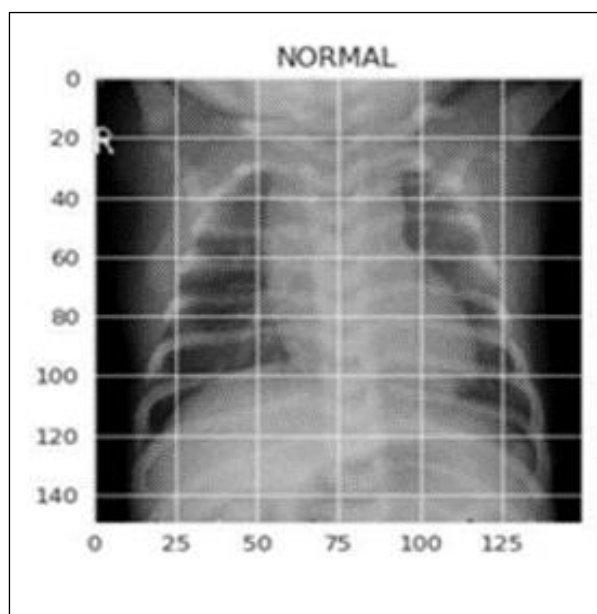


Figure 2: A chest X-ray labeled as normal.
Source: Authors, (2024).

An artificial neural network called a convolutional neural network (CNN or ConvNet) is specialised for processing and analysing visual input, such as pictures and movies. Many computer vision applications, such as image classification, object identification, picture segmentation, and others, have seen significant success with CNNs. They are especially successful at tasks requiring sequential feature extraction because they are modelled after the structure and operation of the visual system in humans.

The foundational units of CNNs are convolutional layers. They compute the number of dots at each place by scanning over the input picture with convolutional filters, commonly called as kernels. The network can recognise characteristics like borders, materials, and patterns thanks to this action. Activation functions, such as ReLU, are frequently added after convolutional layers to add non-linearity. The geographic dimensions of the map of features created by convolutional layers are decreased by pooling layers, also known as subsampling or down-sampling layers. By doing so, computation is reduced and the network is strengthened

against changes in input. Max-pooling and average-pooling are two common pooling techniques.

The applications like Numpy, one of the python lass Pandas, the another class is Keras, the platform is Jupyter Notebook, to map the chart matplotlib used, and seaborn were extensively utilised in this example. The model was trained and evaluated locally using a PC equipped with an processor AMD Ryzen 5 with the speed of 3600 CPU, and RAM memory space of 16GB of 3200MHz speed RAM. The model has to be trained for up to 90 minutes. The photos were categorised using a machine learning technique based on CNN. The CNN is an instance of deep learning neural networks. The most popular applications for CNNs in picture classification and identification mark a substantial development in these domains. Input and output are just a couple of the layers that make them up, with hidden layers placed in between.

Convolutional neural networks (CNNs) and deep learning are two fields where the term "Conv2D" is frequently used. It speaks about a particular kind of layer that neural networks employ to interpret two-dimensional input, such as photographs. A neural network's Conv2D layer convolutionally processes the input data using a series of adaptive filters or kernels. These filters "convolve" or glide across the information that is entered to create feature maps that draw attention to key patterns or characteristics. A Conv2D layer produces a collection of feature maps, which are then utilised as inputs by different layers in the network's architecture.

Rectified Linear Unit, or ReLU, is a popular function of activation in artificial neural networks, particularly deep learning models. It is used to add non-linearity to the model by applying it to the final result of a single neuron or a layer of a neural network. The following is a definition of the ReLU activation function, which is $\max(0, x) = f(x)$. In the above formula, "x" stands for the function's input and "f(x)" for the output. The ReLU procedure is straightforward yet efficient. The value "x" is returned in its original form if the input is affirmative ($f(x) = x$). It returns zero if the input value "x" is negative or 0 ($f(x) = 0$).

ReLU is highly computational since it just uses the max function and simple mathematical operations; it doesn't need exponential functions or other sophisticated calculations. ReLU enables neural networks to describe complicated, nonlinear connections in data by introducing nonlinearity into the network. For deep learning models to be successful, this is essential. The network may become sparse as a result of ReLU. Only a portion of neurons are active at any given moment since negative values are assigned to zero, which might help with capacity for modelling and training efficiency.

Convolutional neural networks (CNNs) frequently employ the MaxPool2D layer for the processing of images and other 2D input. It is mostly employed to down-sample or subsample an input tensor, so lowering its geographic dimensions while preserving crucial data. Max pooling is a type of layer of pooling that chooses the highest value from a collection of values inside a predetermined area of the tensor that was input.

Flattening as shown in the figure is a frequently used procedure in a variety of programming tasks, particularly when working with layered data, tree structures, or processing information. You may streamline data structures and have easier access to elements for analysis or change. A crucial stage in CNN, we shall employ it when flat output is desired. The Classifier layer, which sits above the classification layer, is where we will attempt to convert a matrix with two dimensions towards vector values.

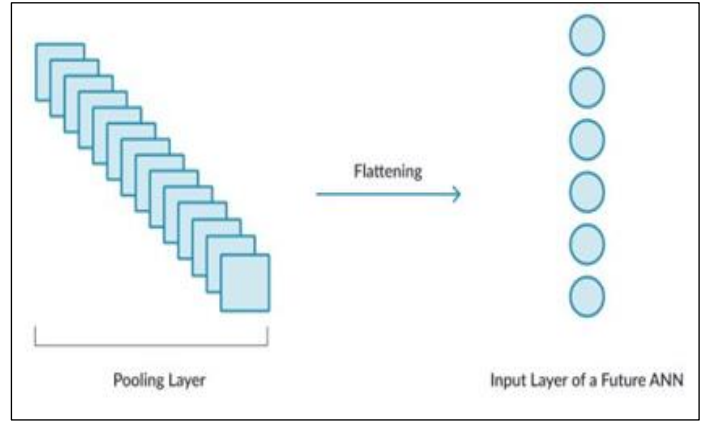


Figure 3: Layer Architecture.
Source: Authors, (2024).

A layer as shown in the figure is said to be dense if each of the neurons in the topmost layer obtains input from every neuron in the layer below it. The most prevalent layer in models was shown to be the thick layer. The layer multiplies a product by a matrix in the background, having the matrix contents acting as verifiable weights. The layer's function is to really modify the vector dimension because the layer's origin is a vector (Figure 3).

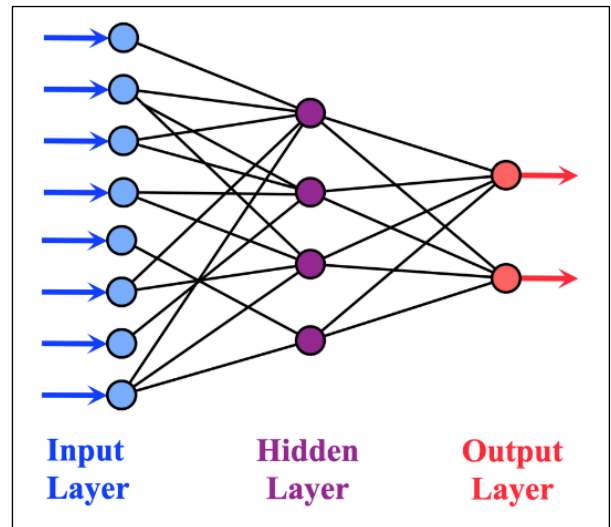


Figure 4: A shallow neural network with a Dense layer.
Source: Authors, (2024).

Sets the number of pictures in the control set, for example, as well as the size of the representative group used for training. The number of epochs (which partition the collection into groupings according to the number of epochs when compared to various sample groups) that we train using a particular sample group. Loss Function: A loss function is a mathematical formula that converts the values of any number of parameters into a precise Figure 4 that reflects the "cost" of a certain occurrence. This feature is used to do optimisation with the goal of minimising output.

III RESULTS AND DISCUSSION

In this study, 5,863 genuine X-rays of pneumonia victims as well as healthy individuals were found in an archive downloaded from the Kaggle website. Three folders are used to organise the photographs in the database. During the learning process, the set of training images is a collection of samples (labelled pictures) that is used to alter parameters, such as weights. Validation - The validation set, a different set used for control throughout the

training process, allows for increasing the hyperparameters (such as training rate) that are often not changed during training, hence enhancing the categorization level of the pictures. There are 8 photographs in the series without pneumonia and 8 images with pneumonia.

The set of test images is a collection of untagged pictures used to evaluate the performance of the network by putting it to the test after training. In summary, the operating principle is: The system is first trained (Train). The system is currently learning how to recognise photos using a variety of criteria and weights. The testing step comes next. We are now checking each image individually without tags. Finally, we contrast the verification control set, which

truly evaluates the degree of learning success in the learnt parameters. Through here, we arrive at a specific accuracy, expressed in percent (Accuracy).

The Recall-Precision graph, whose points are produced for various threshold levels in proportion to the likelihood the network generates for selecting a personal example, describes the performance of the fundamental model. Table 1 shows that the greatest average harmonic (F1 -Score) is 0.8556825 and that it happens for a threshold for probability level of 0.4, meaning that the best performance will be obtained if designate that all samples where the likelihood is beneficial (positive for pneumonia) will be beyond 0.4 as shown in Figure 5.

Table 1: Description of the performance of the Recall-Precision.

Threshold	Recall	Precision	F-Score:
0.1	0.9688	0.65207	0.7794947
0.15	0.9585	0.69556	0.8061705
0.2	0.9449	0.73047	0.8240016
0.25	0.9303	0.76085	0.8370907
0.3	0.9150	0.78751	0.8465588
0.35	0.8995	0.81027	0.8525626
0.4	0.8844	0.82872	0.8556825
0.45	0.8650	0.8453	0.8550874
0.5	0.8471	0.86024	0.8536374
0.55	0.8250	0.88944	0.8498365
0.6	0.8007	0.90215	0.842791
0.65	0.7735	0.91522	0.8329102
0.7	0.74410	0.92686	0.8208399
0.75	0.70428	0.92683	0.8003814
0.8	0.65540	0.9368	0.7712586
0.85	0.5896971	0.9494	0.7275372
0.9	0.4970978	0.9642	0.7560144

Source: Authors, (2024).

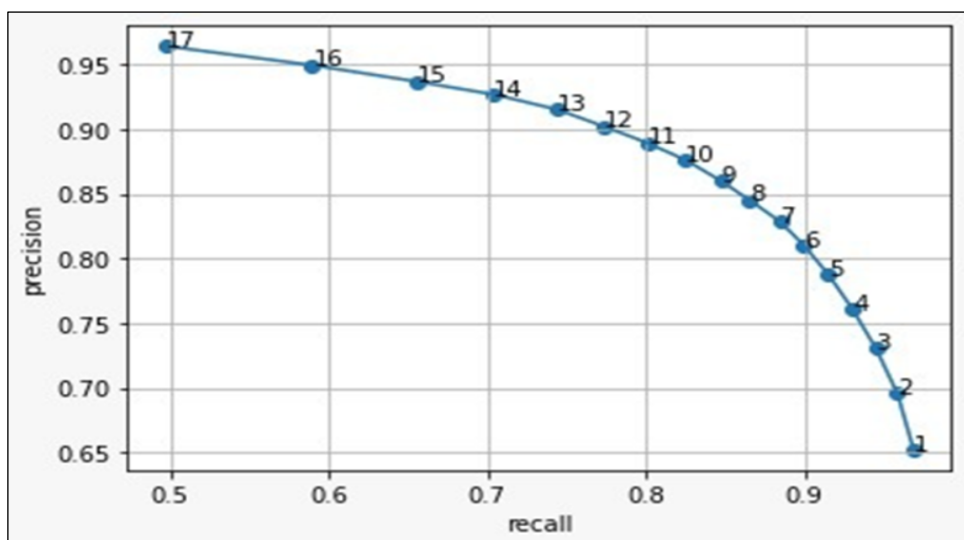


Figure 5: Recall-Precision graph.

Source: Authors, (2024).

Table 2: Result for the different kernel, for Conf2D, and for Max pool.

Methods followed as	Loss of the model	Accuracy
depth of convolution = 32	0.27854	0.9087
depth of convolution =64	0.269219	0.879
depth of convolution =128	0.4191	0.8349
addition of two 32 layers	0.2069	0.9199
addition of two 64 layers	0.268848	0.9006
one layer of 32 and one of 64	0.369782	0.8638
one layer of 64 and 128 Layer	0.30123	0.891
reducing the kernels of the convolution to (2X2)	0.2755	0.891
reducing the kernels of the convolution to (4X4)	0.2527	0.9119
Reducing dense layer to 32	0.28824	0.9103
Layers depth are doubled	0.28439	0.9151
Increasing kernels on each layer	0.48511	0.8349

Source: Authors, (2024).

Table 3: Result for the different kernel, for Conf2D, and for Max pool.

Methods followed as	recall	precision	Accuracy in %
depth of convolution = 32	0.82	0.8245	90.87%
depth of convolution =64	0.8295	0.834	87.98%
depth of convolution =128	0.807	0.8155	83.49%
addition of two 32 layers	0.7991	0.809	91.99%
addition of two 64 layers	0.8014	0.8103	90.06%
one layer of 32 and one of 64	0.8042	0.8135	86.38%
one layer of 64 and 128 Layer	0.8065	0.8157	89.10%
reducing the kernels of the convolution to (2X2)	0.7731	0.7936	89.10%
reducing the kernels of the convolution to (4X4)	0.7889	0.8016	91.19%
Reducing dense layer to 32	0.813	0.8261	91.03%
Layers depth are doubled	0.7903	0.8094	91.51%
Increasing kernels on each layer	0.777	0.7963	83.499

Source: Authors, (2024).

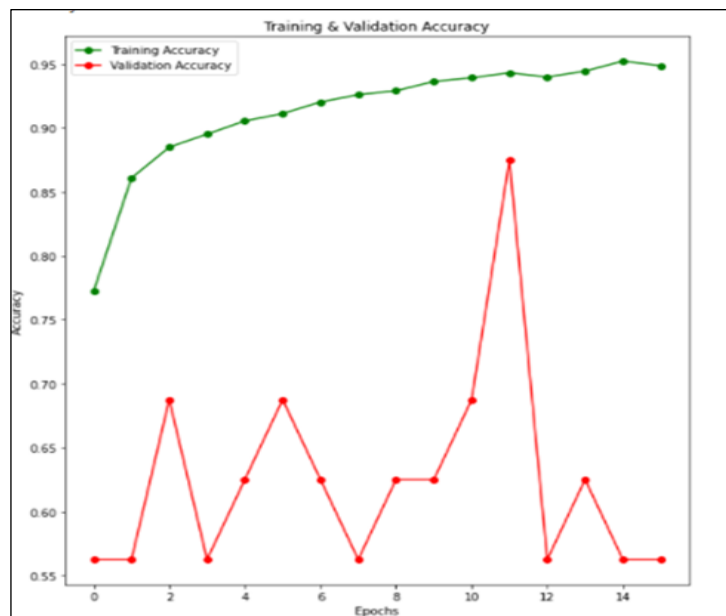


Figure 6a: Training and Testing validation accuracy and its loss against epochs.

Source: Authors, (2024).

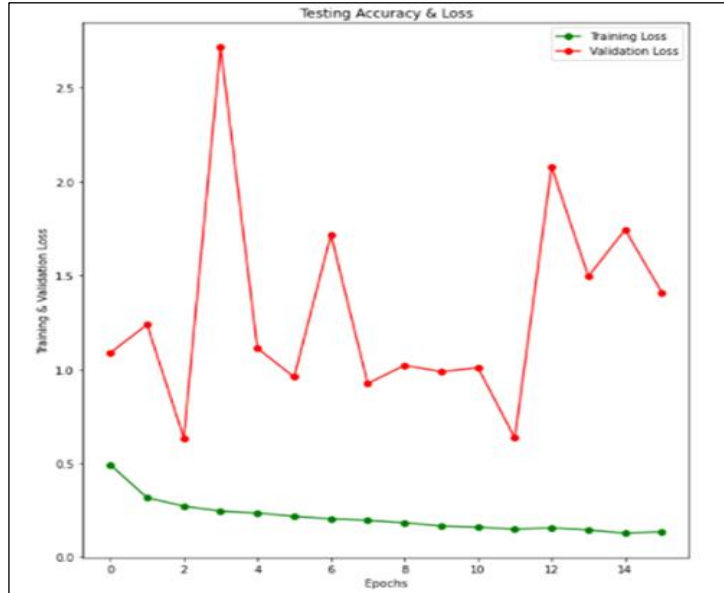


Figure 6b: Training and Testing validation accuracy and its loss against epochs. Source: Authors, (2024).

The above figure 6a and Figure 6b also Table 2 and Table 3 shows the accuracy chart that there is a decline in the 12th repetition and a regularity beginning with the 10th iteration. It is evident from the decrease in the graph that some oscillations cause the learning rate lowering mechanism to become active. In any

event, the system's accuracy stays at about 90%. Lets employ this strategy after coming to the ultimate judgement that extending the convolution to depth 32 produced the highest accuracy enhancement of 90.8%.

Table 4: Stochastic Gradient Descent with Different Learning Rates and Epochs.

SGD	Loss of the model	accuracy
SGD learning rate=0.05, Epochs num=8	0.4024	0.8574
SGD Learning rate=0.001 Epochs=16	0.7018	0.625
SGD Learning rate=0.0001 Epochs =32	0.6805	0.625
SGD+Momentum=0.4 +Nesterov=True	0.4117	0.8766
learning rate=0.0001 epochs=16	0.6697	0.625
SGD+Momentum=0.8 +Nesterov=True		
learning rate = 0.05 epochs=8	0.4052	0.7965
learning rate = 0.05 epochs= 16	0.6961	0.625

Source: Authors, (2024).

Table5: Stochastic Gradient Descent with Different Learning Rates and Epochs.

SGD	recall	precision	Accuracy in %
SGD learning rate=0.05, Epochs num=8	0.5814	0.7194	85.74%
SGD Learning rate=0.001 Epochs=16	0.2579	0.1436	62.50%
SGD Learning rate=0.0001 Epochs =32	0.5006	0.1452	62.50%
SGD+Momentum=0.4 +Nesterov=True	0.6306	0.7383	87.66%
learning rate=0.0001 epochs=16	0.4505	0.1474	62.50%
SGD+Momentum=0.8 +Nesterov=True			
learning rate = 0.05 epochs=8	0.5356	0.6973	79.65%
learning rate = 0.05 epochs= 16	0.268	0.1466	62.50%

Source: Authors, (2024).

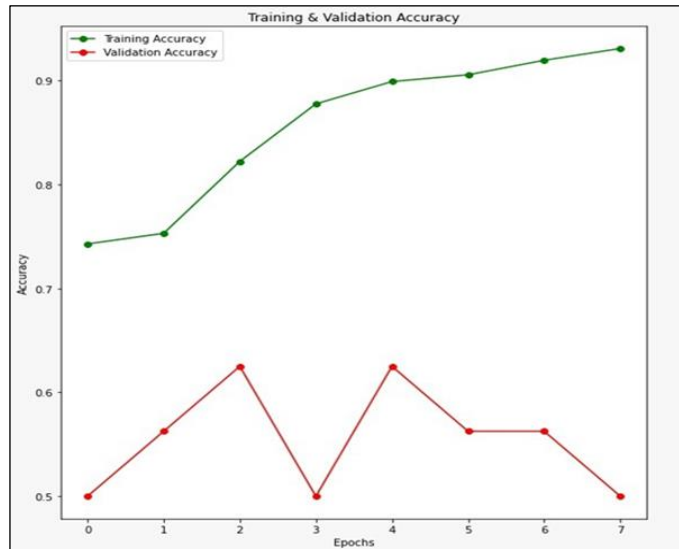


Figure 7a: Training and Testing validation accuracy and its loss against epochs.
Source: Authors, (2024).

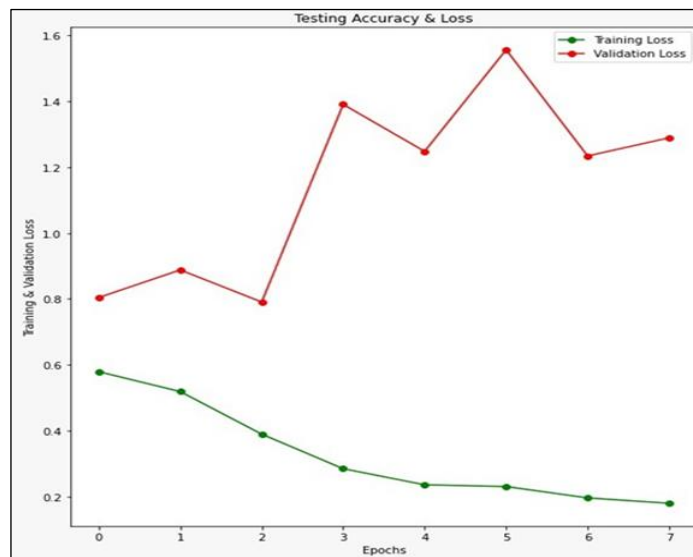


Figure 7b: Training and Testing validation accuracy and its loss against epochs.
Source: Authors, (2024).

s shown in the Figure 7a and Figure 7b also Table 4 and Table 5, the optimizer (SGD) clearly produces results below the 90% accuracy threshold, we will not be using it. We will not be using this optimizer given that it is clear that we were not able to achieve the 90% accuracy level with Nesterov and this strategy (SGD + Momentum).

When deep neural networks with several layers are being trained or when various model parameters have varying scales, Root Mean Squared Propagation noted as RMSProp is very helpful. When compared to approaches that use fixed learning rates, such stochastic gradient descent (SGD), it facilitates the individual adaptation of learning processes for each parameters vary resulting in more rapid convergence and greater performance.

Table 6: Root Mean Squared Propagation with different Learning Rate and different epochs.

RMSProp	Loss of the model	accuracy
learning rate=0.0001 epochs =8	0.6955	0.625
learning rate=0.0001 epochs =16	0.5228	0.8317
learning rate=0.001 epochs=16	0.3556	0.9054
learning rate=0.001 epochs=8	0.3095	0.891
learning rate=0.001 epochs=32	0.3874	0.9006

Source: Authors, (2024).

Table 7: Root Mean Squared Propagation with different Learning Rate and different epochs .

RMSProp	Recall	Precision	Accuracy in %
learning rate=0.0001 epochs =8	0.2272	0.2684	62.50%
learning rate=0.0001 epochs =16	0.6938	0.7694	83.17%
learning rate=0.001 epochs=16	0.8099	0.8389	90.54%
learning rate=0.001 epochs=8	0.7277	0.7822	89.10%
learning rate=0.001 epochs=32	0.8508	0.871	90.06%

Source: Authors, (2024).

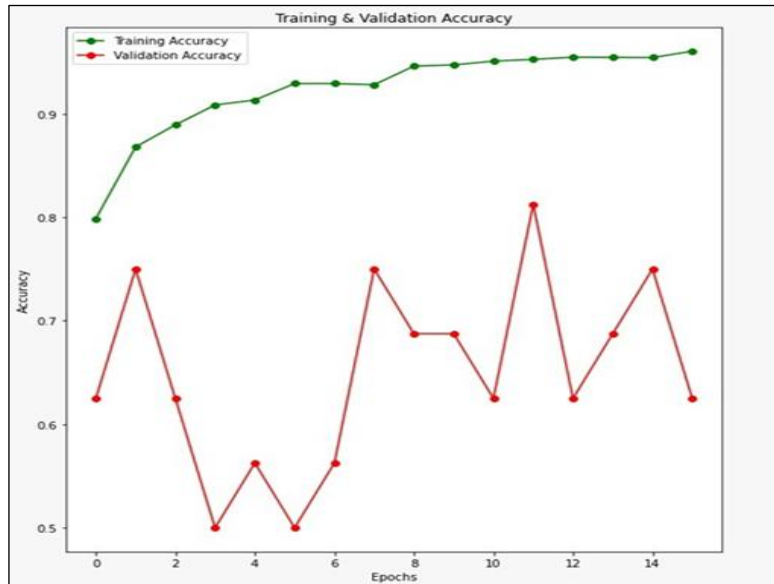


Figure 8a: Training and Testing validation accuracy and its loss against epochs
Source: Authors, (2024).

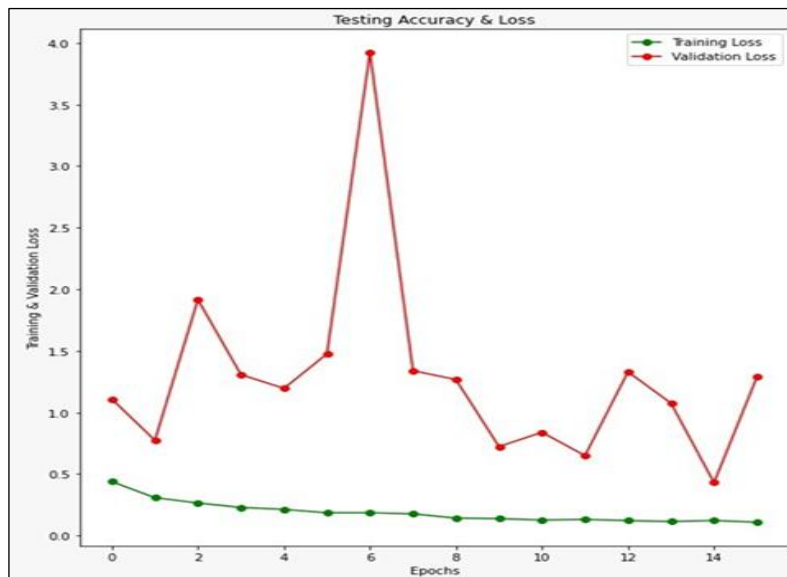


Figure 8b: Training and Testing validation accuracy and its loss against epochs
Source: Authors, (2024).

As shown in the Table 6 and Table 7 also Figure 8a and Figure 8b, different learning rates and different epochs are applied on the dataset. In machine learning and optimisation, "Root Mean Squared Propagation" does not constitute an often used word or algorithm. You could have meant "Root Mean Square Propagation," which might have been a potential misspelling or

variant of the widely used optimisation process known as "RMSprop." As shown in the Figure 9 and Figure 10, the Recall and Precision with different Learning Rates and different epochs are measured and accuracy of the model also measured.

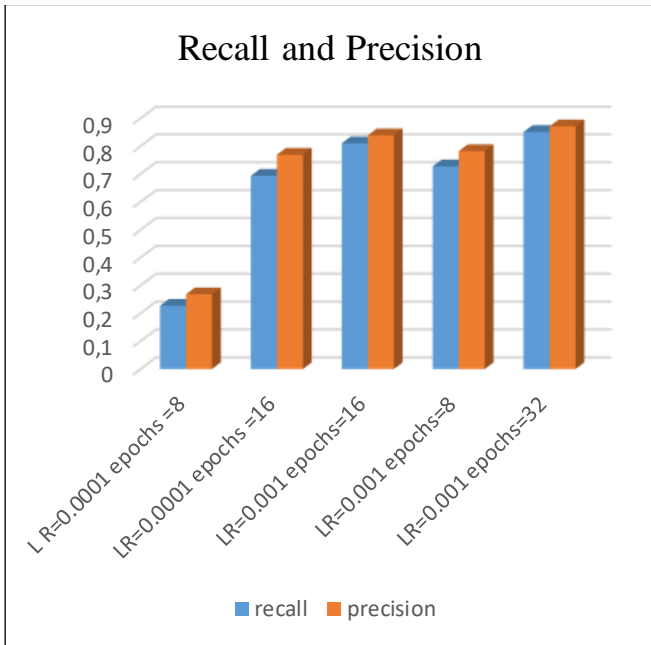


Figure9: RMSP Recall and Precision with different Learning Rates and different epochs.
Source: Authors, (2024).

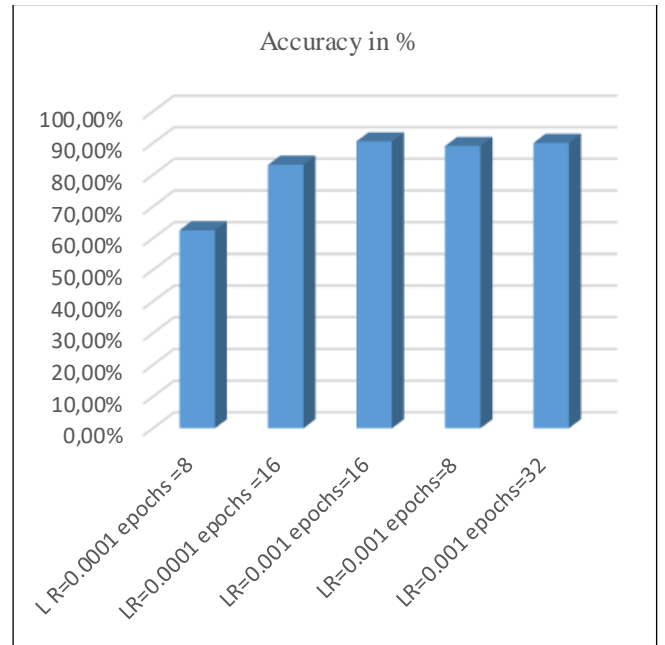


Figure 10: RMSP Accuracy with different Learning Rates and different epochs.
Source: Authors, (2024).

The chance of training a specific node in a layer is the default meaning of the dropout hyperparameter, where 1.0 denotes no dropout and 0.0 denotes no outputs from the layer. Around 0.5

and 0.8 is an acceptable range for dropout within a layer that is hidden. The dropout rate for input layers is higher, typically 0.8. From the equation 1 and 2 we can find out the dropout algorithm.

$$z_i^{(t+1)} = w_i^{(t+1)}y^t + b_i^{(t+1)} \quad (1)$$

$$y_i^{(t+1)} = f(z_i^{(t+1)}) \quad (2)$$

Table 8: Value generated for different dropout rate.

Dropout	Loss of the model	accuracy
dropout=0.1	0.2978	0.9038
dropout=0.2	0.3578	0.9022
Dropout =0.3	0.3332	0.8942
Dropout =0.4	0.3126	0.9135

Source: Authors, (2024).

Table 9: Value generated for different dropout rate.

Dropout	recall	precision	Accuracy in %
dropout=0.1	0.77	0.8215	90.38%
dropout=0.2	0.786	0.832	90.22%
Dropout =0.3	0.7776	0.8315	89.42%
Dropout =0.4	0.7416	0.8137	91.35%

Source: Authors, (2024).

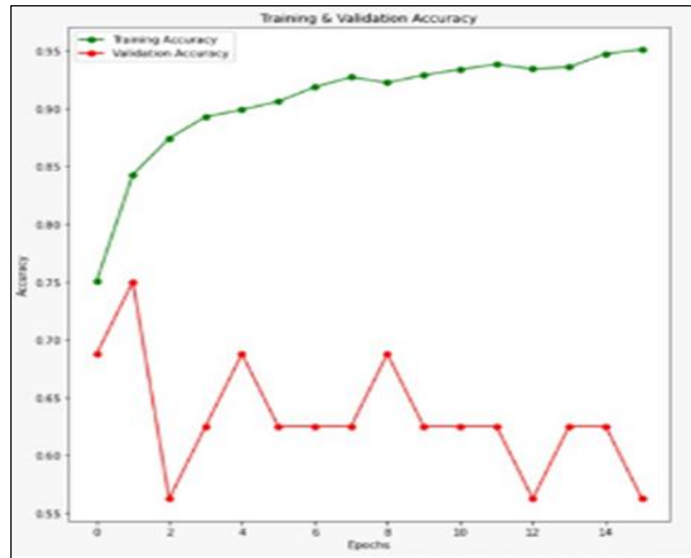


Figure 11a: Training and Testing validation accuracy and its loss against epochs. Source: Authors, (2024).

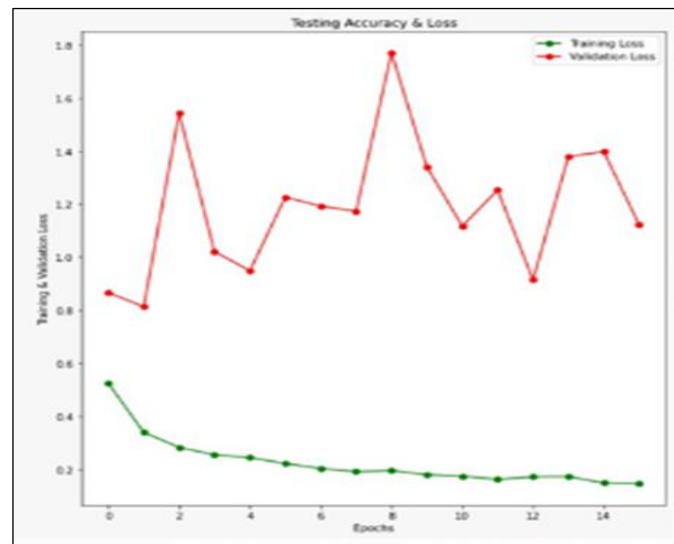


Figure 11b: Training and Testing validation accuracy and its loss against epochs. Source: Authors, (2024).

Figure 8a & Figure 8b, Figure 9a & Figure 9b, Figure 10a & Figure 10b, and Figure 11a & Figure 11b shows the Training and Testing validation accuracy and its loss against epochs. Dropout is a regularisation approach in machine learning as shown in Table 8 and Table 9 that keeps neural networks from overfitting. When a machine learning algorithm learns the set used for training too thoroughly—including the noise and outliers—it is said to be overfitting, and this results in poor generalisation on fresh, untried data.

A method called "dropout" is intended to deal with this problem. It involves randomly "dropping out" (that is, setting to zero) a certain percentage of the components (neurons) in an artificial neural network during development. During every training iteration, a randomised fraction of neurons is selected to be deactivated or "dropped out". These neurons that have fallen out have zero output. This altered data is used to train the neural network.

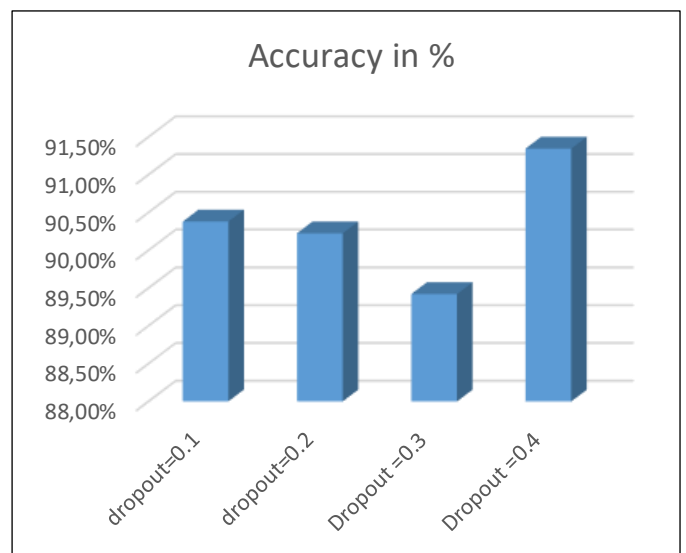


Figure 12: Accuracy with different Learning Rates and different epochs using Dropout. Source: Authors, (2024).

Accuracy with different Learning Rates and different epochs using dropout is shown in Figure 12.

IV. CONCLUSION

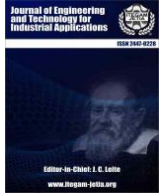
Throughout the development of artificial intelligence, many different businesses have employed it, particularly in the last ten years due to the tremendous increase in data accessibility. Its fundamental goal is to help individuals make decisions that are more trustworthy, rapid, and accurate. Artificial intelligence and machine learning are increasingly being used in the medical field. This is particularly relevant for medical professions where diagnostic processes depend on gathering and interpreting substantial amounts of digital data and which use a range of biological image types. The examination of medical images using machine learning improves the accuracy and consistency of reporting. This study encourages the application of machine learning algorithms to assess chest X-ray pictures in order to aid decision-makers in making the most precise diagnosis. The procedure will "learn" based on previously athered X-ray information on both normal and sick patients (the training set), using the CNN (Convolutional Neural Network) algorithm. Thus work offers a deep learning-based method for interpreting photos. Because of this technique's over 91% accuracy and almost instantaneous results, radiologists will have less work to do—especially those who have to analyse a large number of patient images.

V. REFERENCES

- [1] H. Wang, Y. Liu, Z. Han and J. Wu, "Extension of media literacy from the perspective of artificial intelligence and implementation strategies of artificial intelligence courses in junior high schools," *2020 International Conference on Artificial Intelligence and Education (ICAIE)*, Tianjin, China, 2020, pp. 63-66, doi: 10.1109/ICAIE50891.2020.00022.
- [2] A. Serener and S. Serte, "Deep learning for mycoplasma pneumonia discrimination from pneumonias like COVID-19," *2020 4th International Symposium on Multidisciplinary Studies and Innovative Technologies (ISMSIT)*, Istanbul, Turkey, 2020, pp. 1-5, doi: 10.1109/ISMSIT50672.2020.9254561.
- [3] S. Kurahashi, "Estimating Effectiveness of Preventing Measures for 2019 Novel Coronavirus Diseases (COVID-19)," *2020 9th International Congress on Advanced Applied Informatics (IIAI-AAI)*, Kitakyushu, Japan, 2020, pp. 487-492, doi: 10.1109/IIAI-AAI50415.2020.00103.
- [4] R. Xin, J. Zhang and Y. Shao, "Complex network classification with convolutional neural network," in *Tsinghua Science and Technology*, vol. 25, no. 4, pp. 447-457, Aug. 2020, doi: 10.26599/TST.2019.9010055.
- [5] S. A. Khan and Z. Ali Rana, "Evaluating Performance of Software Defect Prediction Models Using Area Under Precision-Recall Curve (AUC-PR)," *2019 2nd International Conference on Advancements in Computational Sciences (ICACS)*, Lahore, Pakistan, 2019, pp. 1-6, doi: 10.23919/ICACS.2019.8689135.
- [6] N. Adiga, D. Govind and S. R. Mahadeva Prasanna, "Significance of epoch identification accuracy for prosody modification," *2014 International Conference on Signal Processing and Communications (SPCOM)*, Bangalore, India, 2014, pp. 1-6, doi: 10.1109/SPCOM.2014.6984007.
- [7] P. Gu, S. Tian and Y. Chen, "Iterative Learning Control Based on Nesterov Accelerated Gradient Method," in *IEEE Access*, vol. 7, pp. 115836-115842, 2019, doi: 10.1109/ACCESS.2019.2936044.
- [8] S. Peng, W. Li, D. Guo and H. Peng, "Efficiency optimization control of interior permanent magnet synchronous motor based on Adam algorithm," *2023 International Symposium on Signals, Circuits and Systems (ISSCS)*, Iasi, Romania, 2023, pp. 1-4, doi: 10.1109/ISSCS58449.2023.10190871.
- [9] M. A. Labbaf Khaniki, M. Behzad Hadi and M. Manthouri, "Feedback Error Learning Controller based on RMSprop and Salp Swarm Algorithm for Automatic Voltage Regulator System," *2020 10th International Conference on Computer and Knowledge Engineering (ICCKE)*, Mashhad, Iran, 2020, pp. 425-430, doi: 10.1109/ICCKE50421.2020.9303718.
- [10] N. Bacanin, E. Tuba, T. Bezdan, I. Strumberger, R. Jovanovic and M. Tuba, "Dropout Probability Estimation in Convolutional Neural Networks by the Enhanced Bat Algorithm," *2020 International Joint Conference on Neural Networks (IJCNN)*, Glasgow, UK, 2020, pp. 1-7, doi: 10.1109/IJCNN48605.2020.9206864.
- [11] O. Nomir and M. Abdel-Mottaleb, "Hierarchical Dental X-Ray Radiographs Matching," *2006 International Conference on Image Processing*, Atlanta, GA, USA, 2006, pp. 2677-2680, doi: 10.1109/ICIP.2006.313061.
- [12] K. Qing and R. Zhang, "An Efficient ConvNet for Text-based CAPTCHA Recognition," *2022 International Symposium on Intelligent Signal Processing and Communication Systems (ISPACS)*, Penang, Malaysia, 2022, pp. 1-4, doi: 10.1109/ISPACS57703.2022.10082852.
- [13] J. Si, S. L. Harris and E. Yfantis, "A Dynamic ReLU on Neural Network," *2018 IEEE 13th Dallas Circuits and Systems Conference (DCAS)*, Dallas, TX, USA, 2018, pp. 1-6, doi: 10.1109/DCAS.2018.8620116.
- [14] G. Lin, A. Milan, C. Shen and I. Reid, "RefineNet: Multi-path Refinement Networks for High-Resolution Semantic Segmentation," *2017 IEEE Conference on Computer Vision and Pattern Recognition (CVPR)*, Honolulu, HI, USA, 2017, pp. 5168-5177, doi: 10.1109/CVPR.2017.549.
- [15] R. V. Kumar Reddy, B. Srinivasa Rao and K. P. Raju, "Handwritten Hindi Digits Recognition Using Convolutional Neural Network with RMSprop Optimization," *2018 Second International Conference on Intelligent Computing and Control Systems (ICICCS)*, Madurai, India, 2018, pp. 45-51, doi: 10.1109/ICCONS.2018.8662969.



ISSN ONLINE: 2447-0228



RESEARCH ARTICLE

OPEN ACCESS

PRECISION IN MOTION ENHANCING AUTONOMOUS DRIVING WITH ADVANCED LANE RECOGNITION USING HIGH RESOLUTION NETWORK

P.Santhiya¹, Immanuel JohnRaja Jebadurai², Getzi Jeba Leelipushpam Paulraj³
V.Ebenezer⁴, S. Kiruba Karan⁵

^{1,2,3,4,5}School of Computer Science and Technology, India.
Karunya Institute of Technology and Sciences, Coimbatore, Tamilnadu, India.

¹ <http://orcid.org/0000-0002-4653-023X> ² <http://orcid.org/0000-0002-8548-3333> ³ <http://orcid.org/0000-0002-7270-6796>
⁴ <http://orcid.org/0000-0002-0801-6926> ⁵ <http://orcid.org/0009-0006-0995-2876>

Email: pvsanthiya89@gmail.com, immanueljohnraja@gmail.com, getzi@karunya.edu, ebenezer@karunya.edu, kirubakarandev19@gmail.com

ARTICLE INFO

Article History

Received: January 23th, 2024
Revised: September 18th, 2024
Accepted: September 18th, 2024
Published: September 04th, 2024

Keywords:

Autonomous cars,
Lane detection,
Deep learning,
Semantic Segmentation,
HR-Net architecture

ABSTRACT

Autonomous cars are revolutionizing transportation by navigating roadways without human intervention using digital technology and artificial intelligence. However, reliable lane recognition is a big barrier in this endeavor. Lane identification is a complex topic that presents significant challenges to computer vision and machine learning systems. Accurate lane line detection can be challenging due to real-world driving conditions, resulting in negatively impacts steering angle prediction. In response to this difficulty, our research proposes a novel strategy to improving lane detection and steering control accuracy. To recognize lanes with better precision, we use computer vision techniques, namely semantic segmentation. Semantic segmentation allows the vehicle's internal artificial intelligence system to classify each pixel in an image as belonging to a given object class, such as road lanes. The precise lane detection required for secure and dependable navigation is addressed by this suggested methodology, which addresses a crucial part of autonomous driving technology. In this paper we have improved the accuracy and robustness of autonomous vehicles, preparing them to face the difficulties of real-world road conditions, by using HR-Net architecture.



Copyright ©2024 by authors and Galileo Institute of Technology and Education of the Amazon (ITEGAM). This work is licensed under the Creative Commons Attribution International License (CC BY 4.0).

I. INTRODUCTION

An autonomous vehicle is a vehicle that travels without human inputs using a mix of sensors, cameras, radar and artificial intelligence. Autonomous vehicles are in-charge of observing their environment, keeping an eye on critical systems and exercising control, including steering, lane monitoring etc. It can maneuver itself maintaining its lane, dodging hazards in a swift and smooth manner. A pivotal role of autonomous vehicles is lane detection, which employs computer vision to identify lane markings. However, due to the dynamic road conditions that can be experienced while driving, lane detection becomes a difficult task. As a human driver it is hard to remain in the correct lane for an extended period. Humans are prone to tiredness, sleepiness, inattention, and driver fatigue. Besides that, using smartphones, entertainment and navigation system can interrupt the driver and

jeopardize the safety. Therefore, the cost of road accidents to society are significant both in terms of harm to people and financial loss.

For [1] Increase in safety and reducing road accidents, saving lives of people are one of great interest in the context of Advanced Driver Assistance Systems. However, the complex and challenging structure of roads and vehicles needs to be detected for the safety of the people and the autonomous vehicles. There are several factors that affect lane detection in real time, for example [2] the lane markings are detected mainly based on basic gradient changes due to real-time limitations which leads to slow processing speed. Autonomous vehicles have a variety of methods for detecting lanes. According to [3], to recognize lane markings on the road, color thresholding is used, which involves filtering out pixels with values below a certain threshold. However, this technique can also identify other white areas that are not lanes,

therefore it might not completely fix the issue. [4], Regardless of many approaches have been put out to increase precision while expediting speed, various hindrances, including lane markings variations, lighting fluctuations, and shadowy conditions, demands the development of robust detection system. In lane-detection, model-based and learning-based approaches are the two most used approaches. Model based methods afford rapid computation speeds, while learning-based methods extend robustness amidst complexity.

According to [5] Lane detection minimizes the possibility of accidents caused by lane departure by assisting in maintaining the car in its selected lane. Additionally, it aids in the detection of roadblocks and other cars, enabling the car to react appropriately to prevent crashes. Highly accurate lane marking identification is possible with lane detection algorithms, which facilitates vehicle navigation [4]. This is especially helpful when there is low visibility or other obstructions that prevent the driver from seeing the lane lines. According to [5] Comparing Lane detecting algorithms to other sensor technologies like lidar and radar, they are comparatively less expensive. As a result of this, they are a desirable choice for makers of autonomous vehicles trying to cut expenses.

According to [6] Manufacturer adoption of lane detecting algorithms is facilitated by their easy integration with current ADAS systems. This is very helpful for adding ADAS capability to older vehicles. Overall, lane detection is an essential technology for autonomous vehicles, providing a number of benefits that raise the standard for accuracy, cost-efficiency, and safety. Lane detection should become even more dependable and robust in the future as researchers continue to create novel algorithms and sensor technologies.

This paper [4] discusses over a number of lane detection techniques, such as using ridge detectors to identify road lanes in aerial photos. The study emphasizes the difficulties in lane recognition and the growing need for more reliable and precise algorithms. An algorithm for lane recognition that can manage intricate road conditions and dynamic surroundings is presented in paper [7]. The program tracks and detects lane markings in real-time using a combination of edge detection, Hough transform, and Kalman filter. Although, the proposed algorithm's imperfections such as its susceptibility to noise and occlusion, which may impair its effectiveness in practical situations, are not covered in the paper.

HR-Net stands out by its capacity to concurrently record high-resolution data at several scales. HR-Net retains fine-grained information in contrast to conventional methods that down sample the input image, enabling a more thorough comprehension of the scene. This capacity to extract features at many resolutions comes in handy in situations where lane markings are indistinct or dispersed. We incorporate HR-Net into the lane detection procedure in our trials. We make use of a large dataset with challenging circumstances like urban environments, highways, and inclement weather. By using HR-Net's benefits in managing even the tiniest aspects, the installation has been modified to enhance efficiency.

Our research results demonstrate how effective HR-Net can be with lane detection tasks. Even in scenarios in which conventional techniques might struggle, the model performs exceptionally well at precisely drawing lanes and predicting the steering angle of the vehicle. HR-Net consistently outperforms other lane detection algorithms in comparison analyses conducted against a variety of datasets.

II. THEORETICAL REFERENCE

II.1 HIGH RESOLUTION NETWORK

The HRModule is responsible for processing features concurrently at various resolutions. Let's define X for the input tensor and X_i for the i -th branch. This represents the output of each branch at a distinct resolution. The following is a representation of the operations:

$$X_i = f_i(X), \quad i = 1, 2, \dots, n \quad (1)$$

Where the function corresponding to the i -th branch applies is denoted by f_i . Typically, activation functions, normalization, and convolutional layers are used in this function.

II.2 STAGED AGGREGATION

Connecting features across different resolutions is the ultimate objective of staged aggregation. When X_i is the result of the X_i -th branch and A_i represents the aggregated characteristics at the X_i -th stage, the aggregation can be expressed as follows:

$$A_i = g_i(X_1, X_2, \dots, X_i), \quad (2)$$

where $F_{g_i} = f_{i^*}$ is a function which incorporates features from $F_{1 \times 1}$ to $F_{i \times 1}$. The network can benefit from context learned at coarser resolutions in addition to high-resolution details according to this aggregation process.

II.3 TASK SPECIFIC HEAD

The final stage involves a task-specific head for the particular application (lane detection, for instance). Let Y represent the output predictions and H as the features following the staged aggregation. The head for the task at hand can be shown as:

$$Y = h(H), \quad (3)$$

where h is a specific to the task function that might involve activation functions, completely linked layers, and maybe other actions customized for the application.

II.3 LOSS FUNCTION FOR TRAINING

A loss function termed L is used to figure out the extent to which the model's predictions deviate from the ground truth during training. Usually, the criteria for the work specify the loss. For instance, the mean squared error (MSE) loss is frequently selected for lane detection:

$$L = NI \sum_{i=1}^N (Y_i - Y_i^g)^2, \quad (4)$$

where N is the number of samples, Y_i is the predicted output, and Y_i^g is the ground truth.

III. MATERIALS AND METHODS

Implementing a high-resolution network is one method of lane detection. High spatial resolution image processing is a feature of this kind of network that is critical for identifying minute details like lane markers due to the fact that high resolution networks can learn complicated properties from the input images, they usually contain several layers and many parameters. Pre-processing the input image is the initial stage in incorporating a high-resolution

network for lane detection. This entails enhancing the features—such as edges and colour gradients—that are relevant for lane detection through the application of various filters and transformations. After that, the network receives the pre-processed image and uses a number of convolutional layers to process it. An array of probability maps demonstrating the probability of each pixel being a lane marker are the network's output. The actual lane boundaries are subsequently extracted via postprocessing from these probability maps. This entails using a variety of methods to eliminate noise and outliers and smooth the borders.

The potential of a high-resolution network to handle a variety of road and lighting situations is one benefit when employing it for lane detection. The network may be trained to recognize lane markings in a variety of lighting scenarios, including direct sunshine and dimly lit environments. Additionally, it is capable of handling various road surfaces like gravel, concrete, and asphalt. The capability of a high-resolution network to detect many lanes at once is another benefit. This is crucial when driving on multilane roads since you have to stay in your own lane and keep vehicles out of the surrounding lanes. One of the most significant features of autonomous driving systems is steering angle prediction; this function can be made more accurate by utilizing a high-resolution network such as HRNet.

In conclusion, a high-resolution network for lane detection is a potent method for autonomous driving. It can recognize numerous lanes at once and handle a wide range of road and lighting situations. High resolution networks are probably going to become more crucial as autonomous driving technology develops in order to guarantee safe and effective driving.

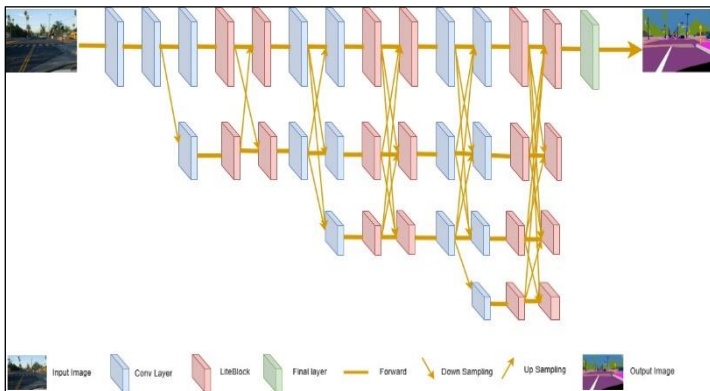


Figure 1: HRNet Architecture.
Source: Authors, (2024).

A detailed illustration of the HRNet architecture is provided in Figure 1, providing a clear understanding of its composition and design. This figure shows the more complex aspects of HRNet's network architecture and provides an illustration of how it handles the segmentation task. Figure 1 provides a visual aid that enhances understanding while making simpler to understand HRNet's functioning in the context of segmentation activities by outlining the essential elements.

IV. RELATED WORKS

Safety is the main objective of every road lane detection system. Lane detection techniques have been proposed in a number of literary works. The real-time lane recognition approach that the authors of this work devised in [8] has an accuracy of 88% and can identify lane signs on the highway in near-real time. However, under different lane detecting settings, these methods exhibit poor

accuracy [9]. Only 80% of the time could lane borders be accurately identified utilizing the RANSAC-based boundary detection technique that the authors of [10] presented. The authors of the paper [11] said that their suggested model had an accuracy of 88%. Numerous obstacles must be overcome, including perspective distortions, generalization, lane structure variability, and the detection of both lane boundaries. The potential of the model to predict the lane effectively is essential in the very promising subject of lane identification. The algorithm used in [12] has a major drawback when it comes to addressing false positive and false negative rates in lane detecting. While false negatives can lead to lane markings being missed, false positives can result in unnecessary alerts or incorrect decisions. The management of edge conditions, like fading intermittent lane markings, which are critical to the system's dependability, is not covered by the authors in [13].

Real-Time Lane Detection Networks for Autonomous Driving: A real-time lane detection technique called LaneNet has been developed [14]; however, its accuracy is limited to 86%. In contrast, the UNet model achieved 90% accuracy, while Segnet obtained 89% accuracy when compared to U-Net [15] and SegNet [16]. The purpose of the paper [17] is to conduct picture segmentation without requiring detailed pixel-level annotation by presenting a weakly supervised semantic segmentation technique. Depending on how well-made and efficient the procedure is, the created pseudo-labels by picture masking may or may not be accurate. The segmentation performance of the model may be lowered by noisy or inadequate pseudo-labels produced by poorly masked areas. The multi-layer deep convolutional neural network used in the research [17] is called the VGG11 encoder, and it can capture features at different scales and degrees of abstraction. The model is able to comprehend both high-level semantic context and low-level features thanks to its hierarchical representation, which makes the segmentation model more reliable and accurate. TerausNet may be applied to a variety of photo segmentation challenges due to its adaptability and flexibility. Semantic segmentation and object recognition are two medical imaging applications where the U-Net design has proven to be effective. Squeeze U-SegNet is utilized for brain MRI segmentation utilizing the techniques described in paper [15]. This model might be affected by variations in MRI data, such as different imaging protocols, scanning equipment, or patient demographics.

Deep neural networks have been employed by the paper's author [18] to detect lanes in continuous driving scenes. While lane detection in complicated road scenarios like crossings, construction zones, or busy urban surroundings can be naturally more difficult, the algorithm utilized is intended to be robust under harsh conditions and has limited generalization to unexpected and extreme scenarios. In these circumstances, the model's performance can be jeopardized. Sensing Image Semantic Segmentation is achieved by a number of alternative techniques, including pseudo-labelling in [16]. The drawback of this approach is that it may cause the model to become unduly confident in its predictions during training, even when those forecasts turn out to be inaccurate. This problem could lead to poor generalization and make it difficult for the model to adapt to novel or complex settings. TerausNet and Attention-Aware RCNN have been combined to bring the strengths of both architectures, resulting in enhanced accuracy for brain tumor segmentation and classification. The authors of paper [19] used this combination to segment and

classify brain tumors in MRI images. By helping the model focus on important regions, the attention processes reduce false positives and improve accuracy. The authors of the paper [20] used a technique by using front-view images to ensure improvements in the accuracy and operating speed. DSUNet-PP from the paper [21] performs more effectively than UNet-PP. In lateral error tests carried out in a real car on a real road, DSUNet-PP performs better than a modified UNet. These findings demonstrate the effectiveness and efficiency of DSUNet for autonomous driving's lane detection and path prediction. The authors of paper [22] used image augmentation and the identification of driving lanes on motorways, we employ a CNN. Edge extraction and line detection are typically the initial steps in the lane detection procedure. Prior to lane detection, a CNN can be used to improve the input images by eliminating objects and noise that do not have effect on the edge detection outcome. However, a large dataset and a significant amount of processing power are needed to train traditional CNNs. The study in [23] proposes a real-time lane detection method that takes advantage of deep learning capabilities by using a lightweight convolutional neural network model as a feature extractor. The generated model is trained using a dataset of 16×64 pixel-sized image patches, and to facilitate quick inference, a non-overlapping sliding window technique is used. Subsequently, a polynomial is fitted to the clustered predictions in order to model the lane borders.

IV. RESULTS AND DISCUSSIONS

IV.1 DATASETS

TuSimple dataset [24] and Udacity dataset has been used to analyze the suggested technique. TuSimple dataset contains 6,408 road pictures of resolution 1280 x 720 resolution. Udacity dataset contains custom images of a custom track which is used to predict the steering angle. The dataset was gathered in a variety of daytime hours and traffic situations during fair to moderate weather. There are 34,680 photos in the dataset for testing and 88,880 for training. Context-based annotations are included with curved splined. Additionally, this dataset records the state of the roads under many circumstances, including normal, congested, night, shadow and arrow.

IV.2 PERFORMANCE ANALYSIS

The ratio of correctly classified instances to the total number of instances, as indicated by formula (5), is the measure of accuracy. The terms that are related include:

$$Accuracy = \frac{True\ Positive + True\ Negative}{True\ Positive + False\ Positive + False\ Negative + True\ Negative} \quad (5)$$

Several instances of true-positives (TP) represent situations in which actual events are accurately predicted to be true. True-Negatives (TN): In circumstances in which real false cases are precisely called false.

False-Positives (FP): Whenever true cases are mistakenly anticipated to be false based on real false cases.

Instances when true instances are inaccurately predicted as false are known as False-Negatives (FN).

The experiments were carried out using Python libraries like NumPy, Keras, TensorFlow, Flask, Socketio, and OpenCV on a

local computer and Google Colaboratory. The following are the specifications of the local machine:

- 11th generation Intel Core i7 processor,
- 16GB RAM,
- 1TB SSD,
- Nvidia GeForce RTX 3060 graphics card

To achieve solid and trustworthy findings, the model was run through twenty rounds of execution

IV.3 RESULTS

The implementation of HRNet architecture in the research's lane detection and steering angle prediction showed outstanding results, with a remarkable accuracy of 93.2%. Compared with various architectures, this performs more effectively: UNet recorded an accuracy of 84.3%, while ResNet34 achieved 85.3% on TuSimple Dataset. The foundation for HRNet's improved accuracy is that it can extract more complex lane features and, in return, predict steering angles with greater precision due to the fact it can record high-resolution spatial information at various scales. The results of this study demonstrate the effectiveness of HRNet in lane detection and steering angle prediction tasks, highlighting its potential to enhance autonomous vehicle performance and safety through reliable and accurate environmental perception. Table.1 tabulates the performance analysis of the HRNet with two other deep neural architectures such as UNet and ResNet34.

Table 1: Performance of architectures on TuSimple dataset.

Model	Accuracy	FP	FN
Unet	84.30%	0.09	0.09
ResNet34	85.30%	0.1	0.12
HRNet	93.20%	0.1	0.11

Source: Authors, (2024).

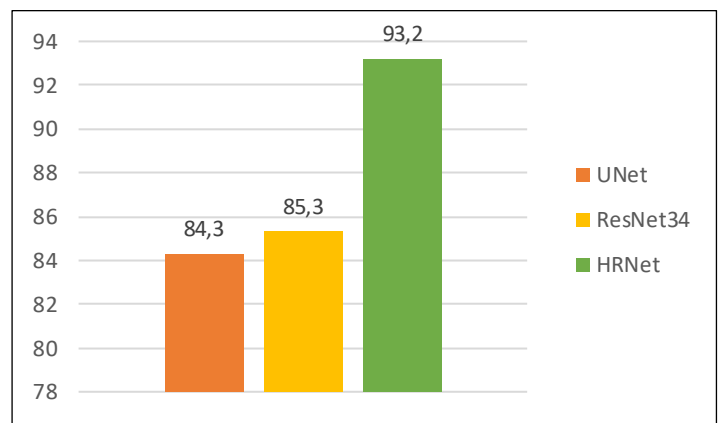


Figure 2: Performance results of deep neural architectures on TuSimple dataset.

Source: Authors, (2024).

The provided images in Figure 3 gives visual evidence of the model's ability to identify lanes. These images, which were captured using the steering angle prediction and lane recognition system in place, clearly demonstrate the ability of the model to recognize and define lane boundaries. The lanes stand out clearly, demonstrating how well the HRNet design captures fine-grained spatial features. The 93.2% accuracy rate of the model's successful lane detection in these images not only validates its accuracy but also highlights its practicality in real-world situations. The model's capacity to improve environmental perception-a crucial component

in the development of sophisticated driver-assistance systems and autonomous vehicles is strongly illustrated by these visual results.

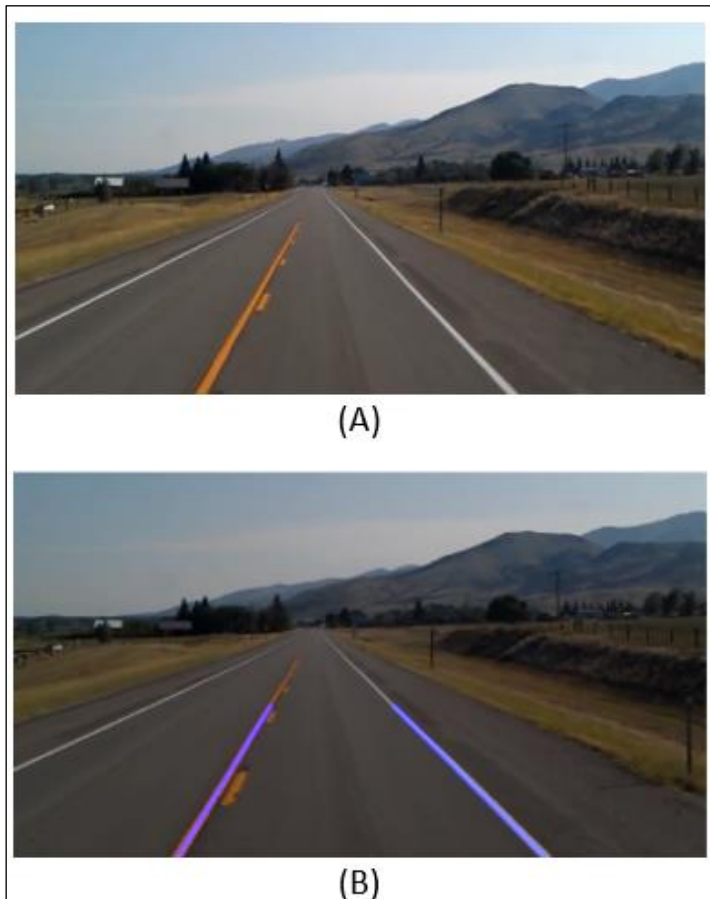


Figure 3: (a) Shows the road image (b) denotes the model detecting the lane.

Source: Authors, (2024).

V. CONCLUSION

In conclusion, the development of autonomous vehicles, driven by advancements in computer vision, artificial intelligence, and sensor technologies, demonstrates a revolutionary change in the transportation industry. Lane detection is vital for the secure and efficient functioning of self-driving vehicles since it helps keep lanes in order, avoid impediments, and improve navigation in general. However, sophisticated lane detecting systems are required as a result of the difficulties caused by changing lighting circumstances, dynamic road conditions, and the requirement for real-time processing. The computational speed and robustness of traditional lane detection approaches, such as color thresholding and simple gradient modifications, are constrained. These issues are addressed with the emergence of high-resolution networks, such as HR-Net, which capture fine details and make it feasible to recognize various lanes in a variety of situations. With its task-specific heads and staged aggregation, the HR-Net architecture offers a flexible framework for lane detection, especially in situations where other methods might not be as successful.

VI. AUTHOR'S CONTRIBUTION

Conceptualization: P.Santhiya and S. Kiruba Karan.

Methodology: P.Santhiya and S. Kiruba Karan.

Investigation: P.Santhiya, Getzi Jeba Leelipushpam Paulraj and S. Kiruba Karan.

Discussion of results: P.Santhiya, Getzi Jeba Leelipushpam Paulraj, Ebenezer, S.Kiruba Karan.

Writing – Original Draft: Ebenezer.

Writing – Review and Editing: Ebenezer.

Resources: Immanuel JohnRaja Jebadurai.

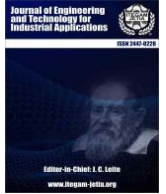
Supervision: Immanuel JohnRaja Jebadurai.

Approval of the final text: Immanuel JohnRaja Jebadurai.

VII. REFERENCES

- [1] A. A. Assidiq, O. O. Khalifa, M. R. Islam and S. Khan, "Real time lane detection for autonomous vehicles," 2008 International Conference on Computer and Communication Engineering, Kuala Lumpur, Malaysia, 2008, pp. 82-88, doi: 10.1109/ICCCE.2008.4580573.
- [2] Z. Kim, "Robust Lane Detection and Tracking in Challenging Scenarios," in IEEE Transactions on Intelligent Transportation Systems, vol. 9, no. 1, pp. 16-26, March 2008, doi: 10.1109/TITS.2007.908582.
- [3] Aminuddin, Nur & Mat Ibrahim, Masrullizam & Mohd Ali, Nursabillah & Radzi, Syafeeza & Bin Mohd Saad, Wira Hidayat & Darsono, Abdul. (2017). A NEW APPROACH TO HIGHWAY LANE DETECTION BY USING HOUGH TRANSFORM TECHNIQUE. Journal of Information and Communication Technology. 16. 10.32890/jict2017.16.2.8231.
- [4] Waykole S, Shiwakoti N, Stasinopoulos P. Review on Lane Detection and Tracking Algorithms of Advanced Driver Assistance System. Sustainability. 2021; 13(20):11417. <https://doi.org/10.3390/su132011417>.
- [5] Weiyu Hao, Review on lane detection and related methods, Cognitive Robotics, Volume, 2023, Pages 135-141, ISSN 2667-2413, <https://doi.org/10.1016/j.cogr.2023.05.004>.
- [6] N. J. Zakaria, M. I. Shapiai, R. A. Ghani, M. N. M. Yassin, M. Z. Ibrahim and N. Wahid, "Lane Detection in Autonomous Vehicles: A Systematic Review," in IEEE Access, vol. 11, pp. 3729-3765, 2023, doi: 10.1109/ACCESS.2023.3234442.
- [7] Wu Z, Qiu K, Yuan T, Chen H. A method to keep autonomous vehicles steadily drive based on lane detection. International Journal of Advanced Robotic Systems. 2021;18(2). doi:10.1177/17298814211002974.
- [8] Cao J, Song C, Song S, Xiao F, Peng S. Lane Detection Algorithm for Intelligent Vehicles in Complex Road Conditions and Dynamic Environments. Sensors (Basel). 2019 Jul 18;19(14):3166. doi: 10.3390/s19143166. PMID: 31323875; PMCID: PMC6679325.
- [9] T. T. Duong, C. C. Pham, T. H. -P. Tran, T. P. Nguyen and J. W. Jeon, "Near real-time ego-lane detection in highway and urban streets," 2016 IEEE International Conference on Consumer Electronics Asia (ICCE-Asia), Seoul, Korea (South), 2016, pp. 1-4, doi: 10.1109/ICCE-Asia.2016.7804748.
- [10] Kim, Y., Hwang, Y. (2019), "A lane detection method based on deep learning with RGB photos". IEEE Access 7, pages 118160–118173.
- [11] Z. Kim, "Robust Lane Detection and Tracking in Challenging Scenarios," in IEEE Transactions on Intelligent Transportation Systems, vol. 9, no. 1, pp. 16-26, March 2008, doi: 10.1109/TITS.2007.908582.
- [12] Wang, Y., Teoh, E.K. and Shen, D., 2004. "Lane detection and tracking using B-Snake. Image and Vision computing", 22(4), pp.269-280.
- [13] Erkan Oğuz, Ayhan Küçükmanisa, Ramazan Duvar, Oğuzhan Urhan, "A deep learning based fast lane detection approach," Chaos, Solitons & Fractals, Volume 155, 2022, 111722, ISSN 0960-0779, <https://doi.org/10.1016/j.chaos.2021.111722>.
- [14] Z. Teng, J. -H. Kim and D. -J. Kang, "Real-time lane detection by using multiple cues," ICCAS 2010, Gyeonggi-do, Korea (South), 2010, pp. 2334-2337, doi: 10.1109/ICCAS.2010.5669923
- [15] Wang, Z., Ren, W. and Qiu, Q., 2018. "Lanenet: Real-time lane detection networks for autonomous driving". arXiv preprint arXiv:1807.01726.
- [16] Dayananda, C., Choi, J.Y. and Lee, B., 2022. "A Squeeze U-SegNet Architecture Based on Residual Convolution for Brain MRI Segmentation". IEEE Access, 10, pp.52804-52817

- [17] Wang, J., HQ Ding, C., Chen, S., He, C. and Luo, B., 2020. "Semi-supervised remote sensing image semantic segmentation via consistency regularization and average update of pseudo-label". *Remote Sensing*, 12(21), p.3603
- [18] Vladimirov, I.; Shvets, A. "TerausNet: U-Net with VGG11 Encoder Pre-Trained on Imagenet for Image Segmentation". arXiv 2018, arXiv:1801.05746.
- [19] Q. Zou, H. Jiang, Q. Dai, Y. Yue, L. Chen, and Q. Wang, "Robust lane detection from continuous driving scenes using deep neural networks," *IEEE Trans. Veh. Technol.*, vol. 69, no. 1, pp. 41–54, 2020, doi: 10.1109/TVT.2019.2949603
- [20] Kaushik, P. and Ratan, R., 2021. Combining TerausNet and Attention Aware Faster RCNN For Brain Tumor Segmentation And Classification In MRI Images. *NVEO-NATURAL VOLATILES & ESSENTIAL OILS Journal* NVEO, pp.3957-3988
- [21] Baek, SW., Kim, MJ., Suddamalla, U. et al. Real-Time Lane Detection Based on Deep Learning. *J. Electr. Eng. Technol.* 17, 655–664 (2022). <https://doi.org/10.1007/s42835-021-00902-6>
- [22] Lee, DH., Liu, JL. End-to-end deep learning of lane detection and path prediction for real-time autonomous driving. *SIViP* 17, 199–205 (2023). <https://doi.org/10.1007/s11760-022-02222-2>
- [23] Jihun Kim, Jonghong Kim, Gil-Jin Jang, Minho Lee, Fast learning method for convolutional neural networks using extreme learning machine and its application to lane detection, *Neural Networks*, Volume 87, 2017, Pages 109-121, ISSN 0893-6080, <https://doi.org/10.1016/j.neunet.2016.12.002>.
- [24] T. Getahun, A. Karimodini and P. Mudalige, "A Deep Learning Approach for Lane Detection," 2021 IEEE International Intelligent Transportation Systems Conference (ITSC), Indianapolis, IN, USA, 2021, pp. 1527-1532, doi: 10.1109/ITSC48978.2021.9564965.
- [25] S. Shirke and R. Udayakumar, "Lane datasets for lane detection," *Proc. 2019 IEEE Int. Conf. Commun. Signal Process. ICCSP 2019*, no. April, pp. 792–796, 2019, doi: 10.1109/ICCSP.2019.8698065.



RESEARCH ARTICLE

OPEN ACCESS

AN ONLINE INCREMENTAL ADAPTATION MECHANISM TO SUBDUE THE EFFECT OF DRIFT IN STREAMING DATA

Ushashree P¹, R B V Subramanyam²

¹ Department of Computer Science and Engineering, National Institute of Technology, Warangal, India

² Professor, Department of Computer Science and Engineering, National Institute of Technology, Warangal, India.

¹ <http://orcid.org/0000-0001-5154-9632> , ² <http://orcid.org/0009-0005-8907-198> 

Email: up720075@student.nitw.ac.in , rbvs66@nitw.ac.in

ARTICLE INFO

Article History

Received: May 24th, 2024

Revised: September 06th, 2024

Accepted: September 16th, 2024

Published: September 04th, 2024

Keywords:

Adaptive learning,
Concept drift,
Model retraining,
Online learning,
Streaming data.

ABSTRACT

Concept drift detection and adaptation is one of the crucial components of a resilient machine learning pipeline in production. The Adaboost is an ensemble approach that incorporates incremental learning, that is widely used for concept drift adaptation in streaming data. It is generally combined with other methods such as ARF classifiers and Bagging Classifiers. This study presents a collection of online incremental learning algorithms for streaming data to adjust machine learning categorization when there is concept drift. Better results are obtained on the Australian power dataset, demonstrating the efficacy of our approach in comparison to the current benchmark.



Copyright ©2024 by authors and Galileo Institute of Technology and Education of the Amazon (ITEGAM). This work is licensed under the Creative Commons Attribution International License (CC BY 4.0).

I. INTRODUCTION

Concept drift in machine learning system, is a statistical property of the models where the target variable distribution which the machine learning model tries to predict changes over time, thereby making the model's effectiveness limited or severely impacted. The predictions from such models become less accurate with time. Almost all machine learning models face this challenge in production and thus it's a usual part and parcel of a machine learning lifecycle. It is also probably the most common reason why ML model needs to be refreshed and retrained periodically. Concept drift arises because usually the incoming data distribution changes over time and thus it drifts away from the historical data that was used during training, it may so happen that the relationships and correlations among features may also change. Thus, a shift in the distribution $P(y|X)$, where y is the real target label and X is the input feature vector, could be used to characterize the phenomenon of concept drift.

Concept drift can further be understood with an example. Suppose a classification model is trained to detect any unusual network access request to a server in the field of cyber security. When this model was trained, 1,000 requests a minute was an

extremely large number of requests that could indicate a malicious attack. But later due to business expansion or marketing campaign, the website became very popular and now receiving 1000s of request is no big deal. Thus, an update to the model is required to take into account the change in data distribution and then only it can perform at an optimal level. Detecting concept drift as soon as possible is essential for maintaining models' performance in production.

To understand concept drift, it is essential to understand the data drift and model decay. The shift in the distribution of data over time is known as data drift. Concept drift can have many types based on its pattern.

Depending on the pattern, drifts can be divided into several types:

Gradual Concept Drift is the most prevalent kind of concept drift that can happen as a result of change in nature of business, launch of new line of business, tools or data collection approaches or deprecating legacy systems and schema with new ones. Such drifts are hard to notice as its impact is only visible after a long-time gap unless the systems are specially trained to notice small changes in the dataset every now and then.

Recurring Concept Drift occurs due to seasonal change in business processes. But not always such changes can be picked up

by a time series model even when seasonality is considered during model building. Customer churn, new competitors, market fluctuation etc. can cause this kind of drift.

Instantaneous Concept Drift are caused by abrupt events that could be outliers for example COVID-19 pandemic impacted all businesses and models were tuned to consider the new reality. When the performance of the model such as accuracy, F1 -Score, R squared etc. starts deteriorating as time is passing, it is called model decay. When it goes down below a threshold, the model needs to be re-trained on a re-labeled dataset. Model decay occurs for one of the following reasons.

Covariate Shift: when a shift occurs in the independent feature variables.

Prior Probability Shift: when shift occurs in the dependent target variable.

Concept Drift: when shift occurs in the relationship itself between the independent feature vector and the dependent target variable.

A novel approach to handle the issue of concept drift in machine learning system is proposed in this paper which demonstrates the superior performance over concept drift detection on benchmark dataset. The developed method is a unique ensemble of incremental learning algorithms to adapt concept drift in streaming data applications. The obtained result surpasses the current best result on the Australian Electricity dataset, which is commonly used as the benchmark dataset for studying the concept drift problem in literature.

The paper is segmented into the subsequent sections. Section II provides an overview of the different tasks that were performed towards identification and handling of concept drift, Section III describes the dataset used in this study and focus on our methodology and algorithms to handle concept drift, Section IV shows result and comparison with current benchmarks and finally Section V provides a conclusion.

II. THEORETICAL REFERENCE

In this section, a comprehensive review on the various work done in concept drift detection as well as adaptation is provided along with the summary of advantages and disadvantages for each method implemented.

For [1] provides a comprehensive survey on concept drift, its types, detection and adaption. It describes the problem of drift specifically in the machine learning environment and its challenges, especially classification of streaming data. The authors argue how in classification problems, a variation in the concept or distribution of dataset over any time period is defined as concept drift and how the performance of such models degrade even in stationary data. They thus point out that handling this problem is more challenging in data streams particularly. They begin with categorization of current streaming data classification algorithms along with benchmark results and their capability to solve the issue of concept drift. They also provide a comparison of various tools available. They further list down the benchmark datasets and performance metrics used in literature. It therefore serves a roadmap for any new researcher working in the domain of concept drift for streaming data classification.

Accurate Concept Drift Detection Method (ACDDM) is a new framework proposed by [2] for concept drift detection. Abilities to identify conceptual deviations in changing data streams. The status of the previously calculated error rate was initially evaluated by calculating a term called Hoeffding's inequality. It measures the probability of error. If the current error

of the learner base differs from the calculated error of the Hoeffding inequality, concept drift can occur in many cases, leading to its occurrence. However, this method only detects drift without adaptation.

According to [3] discuss an Incremental learning framework that helps it to learn the correct classification for the future/further unseen data points from the historic streaming data. In this paper, the authors proposed a well-known idea of an ensemble learning method based on incremental learning to handle both class imbalance and concept drift too. Their work focuses only on the concept drift as class imbalance is not of much interest to them. They handle concept drift by a dynamic cost-sensitive weighting scheme which helps the classifier weight each datapoint according to their classification model's performance and sensitivity. Authors apply the proposed method on Australia's electricity pricing to predict if the price will go up or down compared to that of another city Victorias in a given 24-hour time period. The authors argue that their method beat the current benchmark on the given dataset.

Machine learning algorithms [4] are used to extract knowledge from real-time data, which is typically stored in a static database and processed in batches. They handle the changing patterns of data. Additionally, the ideas may alter as time passes. In the streaming environment, these elements should be given priority. According to [5] argues that previous methods quoted so far for concept drift detection first detect the time and positions of the drift occurrence and then only tries to adapt it by modelling the change in distribution of the data. They mention that such an approach is unlikely to work when underlying factors for change are predictable, thereby making the model miss any future concept drift trend of the streaming data. Authors say that such cases have not been fully explored in previous works which they have included in their novel method called DDG-DA1. The authors contend that the novel approach can efficiently and methodically predict the source of data distribution and enhance the efficacy of models that are susceptible to concept drift. They made it possible by first training a predictor which can estimate the future data distribution, then once the data distribution is estimated they generate a training sample and train a new model on the generated data. They test their methods on real world datasets such as electricity data or stock price data. Electricity load data and solar irradiance data are common and obtain benchmark result on all these.

For [6] handles real world data and existing concept drift. The major focus is on decision-based problems in real world environment. It mainly deals with the problem of the concept drift, specifically about the time, type and pattern of the drift in a non-stationary environment. According to [7] present a comprehensive survey that classifies different concept drift detectors based on their main features, drawbacks, and benefits. They concluded by proposing areas for further investigation, difficulties encountered in research, and the direction of future studies.

Provides a tool for quantitative measurement and description of concept drift by computing marginal distributions of variables. Such quantitative drift analysis techniques lay the foundation of communicating the drift in terms of Bayesian and marginal probabilities. Authors provide their results on three benchmark datasets and thus demonstrate the effectiveness of quantitative drift measurement techniques on real-world learning tasks [8]. [9] Handles concept drift by relying on computation and analysis of the empirical loss of online learning systems or algorithms. Their method is developed based on obtaining statistical parameters from data distribution of loss by shuffling and

re utilizing the data several times through resampling. Additionally, they provide a theoretical guarantee for the designed procedure—an upper bound—based on the performance and stability of the underlying learning algorithms. According to the results of their experiments, their method performed well even in the presence of gaussian noise and had very high recall and precision values [9].

Provides a detailed survey on adaptive learning process for supervised learning. Authors first create a well-defined category of existing strategies implemented for concept drift detection and adaptation, then they provide an overview of the most well-known and popular techniques as well as algorithms. They also discuss the evaluation strategy for such adaptive algorithms under the presence of concept drift and present several illustrative examples and applications. Their survey covers the different facets of concept drift along with types, algorithms examples, applications, advantages, and disadvantages in an integrative way to reflect on the existing work done in this direction [10].

Most research work in [11-13] has the limitations of data streams—such as their infinite length, concept change, concept evolution, and concept recurrence—are the focus of most research endeavors. Concept drift detectors are used in many different applications, such as churn prediction for mobile companies and theft detection in the energy distribution system. Despite this, these algorithms are unreliable when handling dirty data.

According to [14] proposed a novel approach titled Optimum-path Forest classifier which is used for handling concept drift based on the decision of the OPF classifiers committee. For [15] experimentally assesses the prequential methodology by examining its three commonly employed ways for updating the prediction model: Basic Window, Sliding Window, and Fading Factors. The main objective is to determine the most precise variant for experimentally evaluating prior results in situations when idea drifts occur. The focus is mostly on the accuracy observed within the entire data flow.

For [16] discussed the performance of detection and introduced an algorithm that integrates both False positive rate and the error rate. It is called Drift Detection Method with False Positive rate for multi-label classification (DDM-FP-M). It initially calculates false positive rate and then interlaced with the Drift Detection method. Method integrates the disagreement measure, a diversity measure commonly used in static learning, with the Page-Hinkley test to detect drifts in streaming scenarios [17]. Through the analysis of both artificial and real-life situations [18] have seen that each data stream may necessitate a distinct measurement function in order to detect changes in concepts, Considering the particular features of the respective application field.

The online sequential extreme learning machines method is validated using two synthetic case studies that involve various types of idea drift. For [19] method is applied to two publicly available real-world datasets. According to [20] discussed an ensemble methodology to identify a collection of highly reliable predictions using clustering algorithms and classifier predictions. Then they used the Kullback-Leibler (KL) divergence method to quantify the disparities in distribution between consecutive segments, with the aim of identifying any changes in the underlying notion. Assessed the effectiveness of single-variable change detection methods. These techniques are applied to ensembles, in which every member scans a certain feature in the input space of an unsupervised problem detecting changes. An extensive evaluation of the ensemble combinations was given [21].

III. MATERIALS AND METHODS

III.1 DATASET

The Electricity dataset [22] used in this study was obtained from the Australia's New South Wales Electricity Market. The dataset consists of 45,312 records and 10 attributes. The target variable in this dataset represents the price change of electricity compared to the moving average of its demand over the previous 24-hour period. The dataset exhibits a significant complexity and has been extensively studied in the literature, with numerous benchmark results given. Consequently, this dataset is an ideal choice for implementing novel concept drift models, including our own.

The variables of this dataset are nswdemand, nswprice, vicdemand, vicprice, and transfer price. It gives the electricity demand and price for Victoria and New South Wales, two Australian states. There is a measurement of the power transferred between these two states. The transfer price change as compared to a moving average of the electricity demand during the preceding 24 hours is shown by the target label. The datapoints are generated at an interval of 30 minutes. The raw values are normalized after data collection in the interval of [0,1]. Two columns namely ID and date are dropped as those are not helpful towards our goal and therefore, 8 attributes are left in the training and test datasets.

III.2 PREPROCESSING

Standard data preprocessing steps are implemented to measure the quality of data. There are no missing values, and all numeric columns are already scaled in the range of [0,1]. Correlation among all variables is computed to determine whether there is a strong correlation between them. The correlation plot is shown in Figure 1.

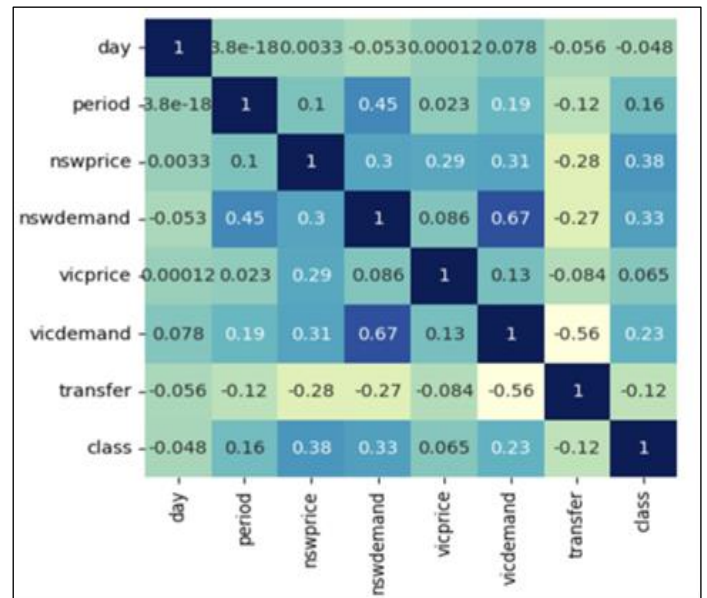


Figure 1: Correlation among variables in electricity dataset. Source: Authors, (2024).

Feature engineering is implemented to compute new derived features from the original 8 features of this dataset. Polynomial feature selection with degree 2 and 3 are done to generate 55 and 120 features respectively. During the modelling phase, different versions of models are trained with original

features as well as derived feature sets of 55 and 120 and results are compared. The dataset is also described in Table 1.

Table 1: Dimensions of the electricity dataset.

	Dataset shape	Training set shape	Test set shape
Original features	(45312,8)	(31718,8)	(13594,8)
derived features (Degree 2)	(45312,55)	(31718,55)	(13594,55)
derived features (Degree 3)	(45312,120)	(31718,120)	(13594,120)

Source: Authors, (2024).

III. 3 MODELS

There are multiple ways to handle concept drift in machine learning systems. For batch processing, models can be retrained with new instances and relabeled target variable, when concept drift is observed. For streaming data, incremental learning is usually the most preferred solution. The ideal solution for handling concept drift is thus to quickly adapt to concept drift. As most real-life production level machine learning applications run on streaming data, online learning to handle concept drift is ideal and the same has been explored by various work done so far. Our work develops a unique mixture of online learning algorithms which beats the current best obtained result on Austrian electricity dataset for concept drift adaption. Concept drift can be formally described as follows.

When two-time instances t and $t + 1$ experience concept drift, it is described as

$$X: P_t(X, y) \neq P_{t+1}(X, y) \quad (1)$$

In Eq.1 P_t denotes the joint probability distribution of data at time t and P_{t+1} denotes the distribution at time $t+1$. Concept drift has occurred if the two distributions are not equal.

In the realm of Bayesian Probability [2], the classification of data point is done using the class label posterior probabilities, where each class y 's posterior probability can be expressed in terms of X as in Eq.2

$$P(y|X) = P(y) P(X|y) / P(X) \quad (2)$$

where $P(y)$ is the known prior probability of the class y , $P(X|y)$ is the marginal probability of X given class y and

$$P(X) = \sum_{i=1}^n P(y)P(X|y) \quad (3)$$

Bayesian theory shows that the concept drifts can have two types:

Real concept drift: This kind of drift indicates a shift in the model's performance. i.e change in the class labels posterior probabilities.

Virtual drift: This kind of drift refers to a shift in the underlying distribution of the features while the performance of the model remains unchanged. i.e., without changing the conditional probability, the $P(X)$ input probability distribution changes.

III.3.1 Incremental Learning

Incremental learning is an approach where each data point is sent successively to train the machine learning model. It is the standard approach for streaming data where the entire batch of data cannot be used in one shot for training, so model is made to learn in an incremental fashion with model weights getting updated as and when new data samples arrive for training. At any given time, step t , the historical data can be described as:

$$XH = (X_1, X_2, X_3 \dots X_t) \quad (4)$$

So, for next instance $t+1$, to predict a label y_{t+1} using data till X_{t+1} a learner L_t is trained using either all the data points or a sample from the given data XH then the learner L_t is used to predict the label for the data point X_{t+1} . The identical procedure is recurred for the next data point where predicted y_{t+1} from the classification model is used as input along with X_{t+1} . So, X_{t+1} and Y_{t+1} becomes a part of historical data. Figure 2 shows a pictorial representation of incremental learning. The incremental learning algorithms explored and adapted in this work are described here:

Adaboost classifier [23] is a boosting ensemble method also popular for batch modelling. In case of AdaBoost, when a new observation arrives, the model learns from it k times. Initially weights are randomly initialized and updated based on misclassification error. The value of k is calculated from a Poisson distribution of model parameters. The parameters or weights are updated when the weak learners fit on the data successively. AdaBoost classifiers are known to perform well in case of concept drift under streaming data due to its nature of learning the weights from misclassification from individual data points. It also handles biasness which is a common pattern in incremental learning.

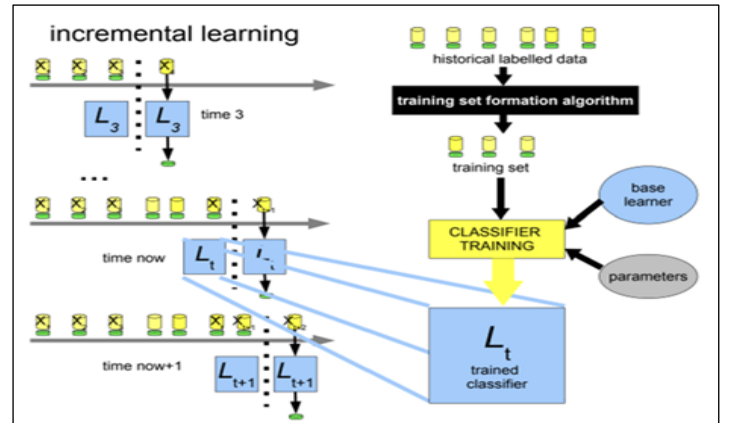


Figure 2: Incremental Learning process.

Source: [24].

Leveraging Bagging [25] is a bagging technique to handle high variance in incoming data streams. It is an improvement over the classic Oza Bagging classification model. The performance of bagging is leveraged or improved by increasing its sampling frequency or the resampling rate. It also uses a Poisson probability distribution mechanism to arrive at the re-sampling process. A higher weight value of the Poisson distribution considers the high variance in training data and thus different range of weights are updated accordingly to accurately classify the data samples.

The ADWIN algorithm is used by Leveraging Bagging techniques to manage concept drift. It keeps track of each classifier's performance within the ensemble and replaces underperforming classifiers with new dummy classifiers when

concept drift is identified. In the next stage, the dummy classifier's weights are changed once more. Recent efforts have achieved state-of-the-art performance on numerous standard data sets by leveraging bagging classifiers, as detailed in the results section.

Logistic regression [26] is a classical method for batch learning as well as online learning. This also supports learning with mini batches of data. For many ensemble methods in incremental learning such as Leveraging bagging classifier or AdaBoost classifier, it is used as a base learner. The working principle remains the same even for the case of single instance learning mechanism. Adaptive Random Forest classifier [27] is another very important method for incremental learning. It is popular for its ability to induct variance with replacement, and randomly selecting feature subset based on entropy of splits of nodes and its ability to do drift detection for base trees.

Adaptive random forest work on the principle of training background trees when a drift detection warning is generated, and it replaces the active tree in case warning escalates to a drift i.e. trees are generated on the fly when drift is observed and thus model is updated with new trees which learns from the pattern of data points which caused the drift. Thus, it adapts the drift detection mechanism. ADWIN Bagging [28] another bagging method based on Oza bagging classification model. ADWIN can be used as drift detector as well as drift adaptation methods. Once a concept drift is observed, the worst classifier of the ensemble which is calculated using the error estimated by ADWIN optimizer is replaced with a new classifier which learns the weight to handle the drift.

Hoeffding trees [29] are a class of tree-based models for incremental learning which has different flavors for different use cases. For example: Hoeffding Any Time Tree (HATT), vanilla Hoeffding Tree, EFDT etc. Each variant has its own advantages and disadvantages. Some are slower, others are faster but less accurate and so on. These methods work by splitting re-evaluation based on node purity and provides a theoretical upper bound for converges. Such methods continually revisit the nodes of the trees and update its internal structure. It handles non-stationarity better than many incremental learning algorithms.

III.3.2 Ensemble Online Learning

The multiple combinations of methods described in the above section are implemented with different parameters to train an online learning algorithm. More than 15 combinations are trained with either different feature sets or model parameter sets and then those are compared with each other and the available literature on best performing models.

The schematic diagram of the best performing ensemble is shown in Figure 3. It shows a model pipeline consisting of three different classifiers namely AdaBoost classifier, Leveraging bagging classifier and logistic regression. The data is also scaled in the range (0,1) before model training using a standard scaler. The number of classifiers within the boosting ensemble is 3. Random seed is set as well so that the model results can be reproduced. In comparison to other algorithms, the execution time of the developed solution is also much better with 192 seconds whereas some of the other classifiers such as ARF classifier takes as much as 1800 seconds with up to 10 internal boosting classifiers.

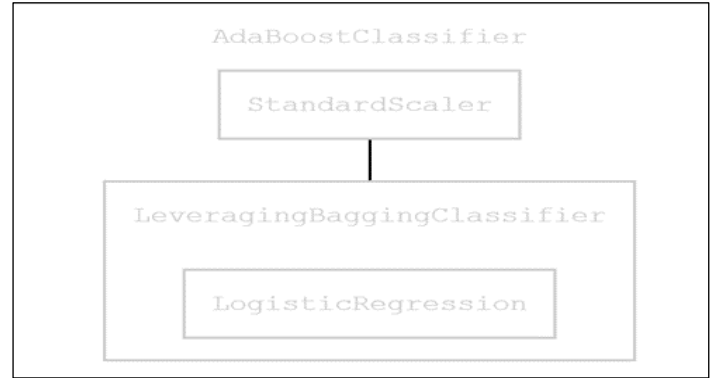


Figure 3: The best performing ensemble of incremental methods.

Source: Authors, (2024).

Pseudocode for AdaBoost Optimized:

Input: Define the training data set T1 for classifier, Number of basic supervised classifiers M and streaming incremental dataset D

Output: Class values for each sample of Testing set T2

BEGIN

01: Create the first ensemble leveraging bagging classifier model on the training data set T1 by Bagging

02: t=0

03: Repeat:

04: t=t+1

05: Fetch the new incoming sample from incremental set Di

06: Classify the sample Di by base classifier logistic regression on the previous ensemble model

07: Update parameters of each leveraging classifier

08: Calculate error to find the classifier performing below threshold by base classifier

09: if the sum of error < 0.5

10: Store the label of Di

11: A new base classifier to be trained on the labeled Di

12: Bagging tree to be pruned, and the new classifier to be added to the ensemble bagging model to replace the worst-performing one

13: Assign the new classifier a weight based on misclassification error

14: else

15: pass

16: End if condition

17: Update the Leveraging bagging ensemble model parameters to the Ada-boost classifier

18: continue until the end of the data stream from D.

19. end for loop

20. END

III.3.3 Training Process

The model process is shown in Figure 4. The original dataset is used for model training as well as derived features generated using polynomial feature engineering. Multiple different models are trained, results of which are shown in result section. Accuracy, Recall, Precision and F1-score are used to measure the performance of trained models. Effective data processing steps such as NA removal, duplicate checking, scaling,

normalization, outlier detection and train test split are performed before model training.

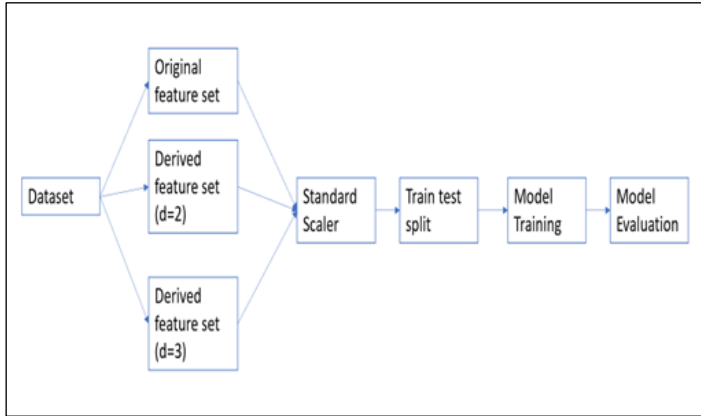


Figure 4: Training process for concept drift adaptation. Source: Authors, (2024).

IV. RESULTS AND DISCUSSIONS

Model experiments and results are documented in this section. Table 2 shows the various methods implemented on the electricity dataset and the result obtained on the same. Model column provides the name of the algorithm, description column provides the information on model parameters and accuracy and f1-score is shown in third and fourth column. The result is sorted on increasing order of f1-score. The very last row of the table shows the best model. The precision and recall values are not shown for the sake of brevity but the same can be understood from the f1-score values. For the best model, precision 89.14% is and recall is 87.97%. the best model is a combination of AdaBoost classifier used with the pipeline of leveraging bagging classifier and logistic regression with number of models as 3. It provides an accuracy of 90.32% and f1-score of 88.55%. The developed algorithm is named AdaBoost Optimized as highlighted in Table 2 with a star mark.

Table 2: Model Comparison

Model	Description	Accuracy (%)	F1-Score (%)
ADWIN Bagging Classifier	Number of models: 3	67.31	53.69
ADWIN Boosting Classifier	Number of models: 3	68.06	58.8
Hoeffding Tree Classifier	Default parameters	74.02	65.24
Extremely Fast Decision			
Tree Classifier	Default parameters	74.28	65.58
ARF Classifier	Hyper parameter updated	75.6	67.73
FFM Classifier	Nfactors 10, intercept=.5,	75.12	67.87
AMF Classifier	Default parameters	76.03	68.34
Leveraging Bagging Classifier	ARF Classifier as base, No. of models: 7	75.25	68.45
AdaBoost Classifier	Number of models: 5	75.52	68.6
AdaBoost Classifier	Hoeffding Adaptive Tree Classifier as base	74.67	68.95
ARF Classifier	Leaf_prediction=mc, Number of models: 3	76.74	70.02
AdaBoost Classifier	ARF Classifier as base, No, of models:5	79.58	75.34
AdaBoost Classifier	ARF Classifier as base, No. of models: 10	80.22	76.25
Ada Boost Classifier*	Leveraging Bagging Classifier and Logistic Regression as base.	90.32	88.55

Source: Authors, (2024).

Model results on derived features with degree 2 and 3. From Table 3, it is evident that increasing number of features is not helping the model. When the same ARF classifier is trained using original set of features, result is slightly better with accuracy of 76.74% and f1-score of 70.02% in comparison to derived features of 75.31% as accuracy and 67.67% as f1-score.

Table 3: Models on derived features.

Model	Derived features degree	Accuracy	F1-Score
ARF Classifier	D=2	73.79	64.09
ARF Classifier	D=3	75.31	67.67

Source: Authors, (2024).

The result obtained is compared with the result obtained by other researchers on the same dataset as shown in Table 4. The best results obtained so far are DDG-DA [5], DDM [2] and leveraging bagging classifier [30] with the accuracy of 84.98%, 85.41% and 88.12% respectively. In comparison to above, AdaBoost Optimized obtains an accuracy of 90.32% which is several steps ahead. The developed model has a better f1-score as well, which shows that the model is quite stable even with class imbalance.

Table 4: Model Performance Comparison.

	Accuracy (%)	F1-Score (%)
DDG-DA [5]	84.98	
DDM [2]	85.41	
Leveraging Bagging classifier [30]	88.12	86.45
AdaBoost Optimized	90.32	88.55

Source: Authors, (2024).

In order to further show the advantage of online learning, A classification model is trained using batch learning on the same data and the compare the result with online learning. A number of classification models are trained, but only the best performing model is shown in Table 5. Random forest model performs the best with an accuracy of 84.07% and F1-score as 80.62 % which is much lower compared to the online algorithm AdaBoost Optimized.

Table 5: Batch learning vs online learning.

	Model Name	Accuracy	F1-Score
Batch	Random Forest	84.07	80.62
Online	AdaBoost Optimized	90.32	88.55

Source: Authors, (2024).

V. CONCLUSIONS

Concept drift is a prevalent issue observed in operational Machine Learning models. It is critical to incorporate into the ML pipeline the tools and techniques required to detect and address concept drift; failure to do so will result in a gradual degradation of model performance, and results from it will not be useful. Incorporating some basic steps in ML production pipeline can help in detecting potential errors early and help keep models updated and relevant. Methods developed in this paper do a great job handling concept drift. It can further be improved for unstructured data scenarios.

VI. AUTHOR'S CONTRIBUTION

Conceptualization: Ushashree P.

Methodology: Ushashree P.

Investigation: Ushashree P.

Discussion of results: Ushashree P, R B V Subramanyam

Writing – Original Draft: Ushashree P.

Writing – Review and Editing: Ushashree P

Supervision: R B V Subramanyam

Approval of the final text: Ushashree P

VII. ACKNOWLEDGMENTS

I would like to express my sincere gratitude to Professor R B V Subramanyam for his constant guidance and support. I would also like to thank my friends and colleagues for their valuable input and suggestions. I am also grateful to my parents without their support nothing would have been possible.

VIII. REFERENCES

[1] Mehta, S. (2017). Concept drift in streaming data classification: algorithms, platforms and issues. *Procedia computer science*, 122, 804-811.

[2] Yan, M. M. W. (2020). Accurate detecting concept drift in evolving data streams. *ICT Express*, 6(4), 332-338.

[3] Ng, W. W., Zhang, J., Lai, C. S., Pedrycz, W., Lai, L. L., & Wang, X. (2018). Cost-sensitive weighting and imbalance-reversed bagging for streaming imbalanced and concept drifting in electricity pricing classification. *IEEE Transactions on Industrial Informatics*, 15(3), 1588-1597.

[4] Ramírez-Gallego, S., Krawczyk, B., García, S., Woźniak, M., & Herrera, F. (2017). A survey on data preprocessing for data stream mining: Current status and future directions. *Neurocomputing*, 239, 39-57.

[5] Li, W., Yang, X., Liu, W., Xia, Y., & Bian, J. (2022, June). DDG-DA: Data Distribution Generation for Predictable Concept Drift Adaptation. In *Proceedings of the AAAI Conference on Artificial Intelligence* (Vol. 36, No. 4, pp. 4092-4100).

[6] Lu, J., Liu, A., Song, Y., & Zhang, G. (2020). Data-driven decision support under concept drift in streamed big data. *Complex & intelligent systems*, 6(1), 157-163.

[7] Agrahari, S., & Singh, A. K. (2022). Concept drift detection in data stream mining: A literature review. *Journal of King Saud University-Computer and Information Sciences*, 34(10), 9523-9540.

[8] Webb, G. I., Lee, L. K., Petitjean, F., & Goethals, B. (2017). Understanding concept drift. *arXiv preprint arXiv:1704.00362*.

[9] Harel, M., Mannor, S., El-Yaniv, R., & Crammer, K. (2014, June). Concept drift detection through resampling. In *International conference on machine learning* (pp. 1009-1017). PMLR.

[10] Gama, J., Žliobaitė, I., Bifet, A., Pechenizkiy, M., & Bouchachia, A. (2014). A survey on concept drift adaptation. *ACM computing surveys (CSUR)*, 46(4), 1-37.

[11] Wang, S., Schlobach, S., & Klein, M. (2011). Concept drift and how to identify it. *Journal of Web Semantics*, 9(3), 247-265.

[12] Faria, E. R., Gonçalves, I. J., de Carvalho, A. C., & Gama, J. (2016). Novelty detection in data streams. *Artificial Intelligence Review*, 45, 235-269.

[13] Masud, M. M., Al-Khateeb, T. M., Khan, L., Aggarwal, C., Gao, J., Han, J., & Thurasingham, B. (2011, December). Detecting recurring and novel classes in concept-drifting data streams. In *2011 IEEE 11th International Conference on Data Mining* (pp. 1176-1181). IEEE.

[14] Iwashita, A. S., de Albuquerque, V. H. C., & Papa, J. P. (2019). Learning concept drift with ensembles of optimum-path forest-based classifiers. *Future Generation Computer Systems*, 95, 198-211.

[15] Hidalgo, J. I. G., Maciel, B. I., & Barros, R. S. (2019). Experimenting with prequential variations for data stream learning evaluation. *Computational Intelligence*, 35(4), 670-692.

[16] Wang, P., Jin, N., & Fehring, G. (2020, August). Concept drift detection with false positive rate for multi-label classification in iot data stream. In *2020 International Conference on UK-China Emerging Technologies (UCET)* (pp. 1-4). IEEE.

[17] Mahdi, O. A., Pardede, E., Ali, N., & Cao, J. (2020). Diversity measure as a new drift detection method in data streaming. *Knowledge-Based Systems*, 191, 105227.

[18] de Mello, R. F., Vaz, Y., Grossi, C. H., & Bifet, A. (2019). On learning guarantees to unsupervised concept drift detection on data streams. *Expert Systems with Applications*, 117, 90-102.

[19] Yang, Z., Al-Dahidi, S., Baraldi, P., Zio, E., & Montelatici, L. (2019). A novel concept drift detection method for incremental learning in nonstationary environments. *IEEE transactions on neural networks and learning systems*, 31(1), 309-320.

[20] Khezri, S., Tanha, J., Ahmadi, A., & Sharifi, A. (2020). STDS: self-training data streams for mining limited labeled data in non-stationary environment. *Applied Intelligence*, 50, 1448-1467.

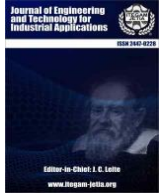
[21] Faithfull, W. J., Rodríguez, J. J., & Kuncheva, L. I. (2019). Combining univariate approaches for ensemble change detection in multivariate data. *Information Fusion*, 45, 202-214.

[22] Harries, M., & Wales, N. S. (1999). Splice-2 comparative evaluation: Electricity pricing.

[23] Žliobaitė, I. (2010). Learning under concept drift: an overview. *arXiv preprint arXiv:1010.4784*.

[24] Oza, N. C., & Russell, S. J. (2001, January). Online bagging and boosting. In *International Workshop on Artificial Intelligence and Statistics* (pp. 229-236). PMLR.

- [25] Bifet, A., Holmes, G., & Pfahringer, B. (2010). Leveraging bagging for evolving data streams. In *Machine Learning and Knowledge Discovery in Databases: European Conference, ECML PKDD 2010, Barcelona, Spain, September 20-24, 2010, Proceedings, Part I* 21 (pp. 135-150). Springer Berlin Heidelberg.
- [26] LaValley, M. P. (2008). Logistic regression. *Circulation*, 117(18), 2395-2399.
- [27] Gomes, H. M., Bifet, A., Read, J., Barddal, J. P., Enembreck, F., Pfahringer, B., ... & Abdesslem, T. (2017). Adaptive random forests for evolving data stream classification. *Machine Learning*, 106, 1469-1495.
- [28] Bifet, A., Holmes, G., Pfahringer, B., Kirkby, R., & Gavalda, R. (2009, June). New ensemble methods for evolving data streams. In *Proceedings of the 15th ACM SIGKDD international conference on Knowledge discovery and data mining* (pp. 139-148).
- [29] Manapragada, C., Webb, G. I., & Salehi, M. (2018, July). Extremely fast decision tree. In *Proceedings of the 24th ACM SIGKDD International Conference on Knowledge Discovery & Data Mining* (pp. 1953-1962).
- [30] Zliobaite, I. (2013). How good is the electricity benchmark for evaluating concept drift adaptation. arXiv preprint arXiv:1301.3524.



RESEARCH ARTICLE

OPEN ACCESS

EXPLORING THE MECHANICAL PROPERTIES AND WATER ABSORPTION BEHAVIOR OF KERATIN FIBER-REINFORCED EPOXY COMPOSITES: INSIGHTS INTO SUSTAINABLE MANUFACTURING

Kachhot Deepak^{1*}, Dewangan Rishi², Rinawa Motilal³, Dwivedi Umesh Kumar⁴

^{1,2}Department of Mechanical Engineering, Amity University Rajasthan, Jaipur, India

³Department of Mechanical Engineering, Govt. Engineering College Jhalawar, Jhalawar, India

⁴Department of Applied Science, Amity University Rajasthan, Jaipur, India

¹<https://orcid.org/0000-0001-6329-2619> , ²<http://orcid.org/0000-0002-1973-6726> , ³<http://orcid.org/0000-0001-7561-2270> , ⁴<http://orcid.org/0000-0002-8990-2275>

E-mail: ^{1*}deepakkachhot27@gmail.com, ²rdewangan@jpr.amity.edu, ³motilal.rinawa@gmail.com, ⁴ukdwivedi@jpr.amity.edu

ARTICLE INFO

Article History

Received: June 04th, 2024

Received: September 06th, 2024

Accepted: September 06th, 2024

Published: September 04th, 2024

Keywords:

Keratin fiber,
epoxy composites,
mechanical properties,
water absorption behavior,
density values.

ABSTRACT

This study investigates the mechanical properties and the water absorption behavior of Keratin fiber-reinforced epoxy composites. The Keratin fibers were used as reinforcement with epoxy. Samples were prepared using the Hand lay-up method, having different amounts of reinforcement. The samples were characterized for their mechanical behavior as per ASTM standards. The tensile strength peaks found at 30wt% declined thereafter due to weakened interfacial bonding. Enhanced tensile moduli observed with fiber loading peaked at 30wt%. Flexural strength and modulus raised to 30wt%. Izod impact strength increased consistently with higher percentages, reaching a maximum of 40wt%. Density values closely matched with theoretical values, with epoxy composites demonstrating lower densities. The positive aspect is found that even after 40 days, only 4.04% of water was absorbed by the composite containing 40wt% fiber which shows the hydrophobic nature of the composite. Certainly, the thickness swelling behavior is notably adequate, owing to the low water absorption characteristics exhibited by fiber composite. This research highlights the significance of Keratin fibers composite in the field of automobile, shed manufacturing, and Marine products manufacturing industry.



Copyright ©2024 by authors and Galileo Institute of Technology and Education of the Amazon (ITEGAM). This work is licensed under the Creative Commons Attribution International License (CC BY 4.0).

I. INTRODUCTION

Since few decades, lot of research are going on to find out the new class of materials and their applications. In 19th century, synthetic plastic was used to manufacture the parts for automobile, aircraft, wind turbine and so on. Due to the low strength of plastic, it is found that, its parts are not able to transmit the full load, this limitation increased the scientists focus on to do the research on fiber-based composite to enhance the load transmitting capacity of plastic. Synthetic fibers show good mechanical strength due to this glass fiber and Carbon fibers are the most used synthetic fiber for reinforcement materials and still used in various applications like in automobile, aero-plane, ship manufacturing industries etc. Although synthetic fibers show good properties results but due to non-biodegradable properties and health hazards, it creates ecological problems. Due to this reason, there is a need to find the

new alternative fibers which can not only substitute of existing one but also it should be easily available, cost effective, bio-degradable and should have high specific property [1]. This research was focused on finding the appropriate natural fiber, matrix agent and adhesive property enhancement techniques through which desired mechanical strength can be achieved, which can be used for various industrial applications.

Generally natural fibers are categorized into three divisions: plant based, animal/human based, and minerals based. Plant based fibers are extracted from leaves, fruits, stems or seeds of the plants, animal/human-based fibers are like hairs, wool, feather, silk etc. and asbestos, graphite, glass fibers etc. are categorized under the mineral fibers [2], [3]. Due to their less cost, low density, minimal health hazards, less pollution, eco-friendly and bio-degradable nature, if a new composite is developed through reinforcement, it would not only be beneficial for

environmental concern but also would be economical [4]. These advantages are sufficient to lead the research on the natural fiber-based polymer composite and increase the commercial utilization of these in different industries. The property of natural fiber depends on their physical nature, age of the plant, chemical composition of the fiber and some other additives like wax, ash present in it etc. [5].

The utilization of waste materials to augment or enhance the characteristics of polymer composites has garnered considerable research interest worldwide in recent decades[2], [6], [7]. Hair is known for its elasticity, smoothness, strength, and softness, attributes primarily attributed to its cortex keratin. The long chains of cortex keratin are compressed to create a regular structure that is both strong and flexible. This inherent flexibility is a key factor in enhancing the flexibility of the composite material. Hair can be used as a fiber reinforcing material in composites due to its high tensile strength, non-degradable material, abundantly available and hair is obtainable at a very low cost as a waste material [2].

Keratin, a significant by-product of pig farming, finds various applications in industries such as chemicals, pharmaceuticals, dyes, and biodiesel production.[8]. Recycled Keratin may have promising opportunity to enhance the mechanical properties and durability of polymer composites while simultaneously addressing environmental concerns within the global pork industry. From the study it is found that the Mechanical Property of the Natural fiber reinforced Polymer composite depends on Fiber selection, Matrix selection, Interface strength, Fiber dispersion, Manufacturing Method, Porosity and Fiber orientation.[9].

According to [8] have explored the potential of Keratin fibers as reinforcement in polymer composites, leveraging their widespread availability, cost-effectiveness, and potential to mitigate environmental footprints. Methods for manufacturing composites vary widely depending on the materials involved and the desired properties of the final product. Several common manufacturing methods include Hand Lay-Up, Spray-Up, Vacuum Bagging, Pultrusion, Compression Molding, Filament Winding, Injection Molding, Additive Manufacturing (3D Printing) [1],[2], [10],[11].

From the study it is found that chemical alteration of natural fibers enhances the adhesion between the matrix and natural fibers through chemical reactions. Numerous studies have investigated the impact of chemical treatment on natural fibers [12-14]. The distinct hydrophilic nature of natural fibers contrasts with the hydrophobic nature of matrices, resulting in weak bonding at the interfaces of natural fiber composites. Chemical treatment alters the inherent hydrophilic behavior of fibers, thereby improving adhesion properties between the matrix and fibers [15], [16]. Various chemical treatment methods have been explored, including alkaline treatment, silane treatment, acetylation, benzoylation, peroxide treatment, malleated coupling agents, sodium chlorite treatment, acrylonitrile grafting, isocyanate treatment, stearic acid treatment, permanganate treatment, triazine treatment, oleoyl chloride treatment, and fungal treatments.

II. MATERIALS AND METHODS

II.1 MATERIALS

Keratin fiber i.e. Pig hair procured from local pig farmers at Achrol, Jaipur, Rajasthan, India. The fiber was examined under a light microscope, pig fibers exhibit three distinct regions [17]. These regions include the outermost thin cuticle (measured 0.28 to

0.32 mm), the central medulla (measured 0.36 to 0.39 mm), and a thick cortex (measured 0.40 to 0.46mm) situated between the cuticle and the medulla. The fibers obtained in the lengths ranged from 75 to 100mm. Here Chopped fibers(4-5mm) were used for reinforcement [18]. Keratin Fiber was used as reinforcement and the matrix was Epoxy and Hardner in fabrication of natural fiber composite. To enhance fiber bonding characteristics, a NaOH solution was used for fiber treatment. The density of used Pig hair was 1.6 g/cm³. Physical properties of Pig hair are mentioned in Table 1.

Table 1: Physical properties of Pig Hair.

Keratin Properties	Value
Tensile strength (cN tex ⁻¹)	14.05
Young's modulus (Gpa)	6.39
Maximum load at rupture(N)	9.2–13.8
Extensibility	31.53%
Average Mid-Section diameter (mm)	0.16
Average Length (mm)	35.7
Aspect Ratio	249
Water Absorption (%)	95
Surface Roughness (µm)	0.104
Density of Keratin (g/cm ³)	1.59– 1.88

Source: [19], [20].

Epoxy demonstrates good mechanical Properties, here Epoxy (LY556) and hardener (HY-951) were employed as matrix material. Physical properties of Epoxy resin are listed in Table 2.

Table 2: Physical properties of Epoxy resin.

Epoxy Resin Property	Value
Density, g/cm ³	1.1-1.4
Tensile Strength, Mpa	35-100
Impact Strength J/cm	0.3
Elongation, %	1-6
Compressive Strength, Mpa	100-200
Elastic Modulus, Gpa	3-6
Cure Shrinkage, %	1-2
Water Absorption, (24 Hrs at 20°C)	0.1-0.4

Source: [21].

Before started the development of composites, Keratin fibers underwent a thorough cleaning process. These were washed with distilled water and detergent, then sun-dried for one week to eliminate impurities. Subsequently, the fibers underwent chemical treatment to enhance wettability and improve interfacial bonding between the fibers and the matrix.

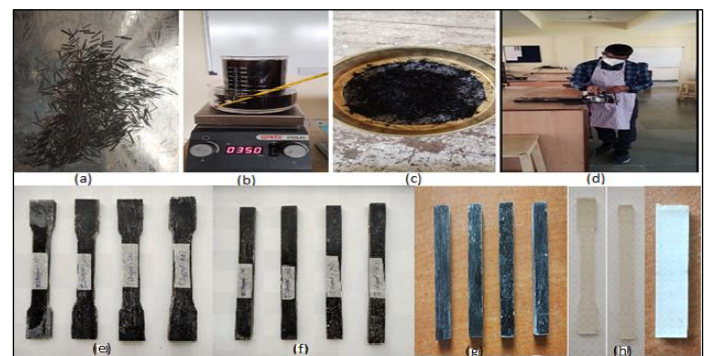


Figure 1: Preparation of Treated Chopped Keratin fiber reinforced Epoxy Composite (a) Chopped Keratin Fiber (b) Treatment with 0.25M NaOH (c) Drying process (d)Cutting samples as per ASTM standards (e) Tensile Test Samples (g) Flexural Test Samples € Impact Test Samples and (h) Control Samples.

Source: Authors, (2024).

The chemical treatment involved immersing the fibers in a 0.25 M NaOH solution in a water bath maintained at 60°C for one hour. Afterward, the fibers were rinsed multiple times with distilled water to remove any residual NaOH solution adhering to the fiber surface and then dried in an oven at 60°C for one hour.[22],[23].

II.2 FABRICATION METHOD OF COMPOSITE

Before starting fabrication, the quantities of fibers and resin needed for composite creation were calculated based on the selected weight fraction and fiber composition. The fiber weight percentage(wt%) ranged from 10wt% to 40wt%, while the epoxy resin varied from 90wt% to 60wt%. Molds were prepared using plywood, silicone rubber, and lamination sheets. To facilitate the easy removal of the specimen, a wax layer was evenly applied to the entire surface of the molding box. Additionally, a releasing agent comprising polyvinyl acetate was also applied to both the upper and lower surfaces of the molding box before initiating the molding process. A dwell time of 30 minutes was taken to dry before proceeding the fabrication process. A solution of epoxy resin and hardener with weight ratio of 10:1 was prepared. Chopped fibers were randomly sprinkled onto the first layer of epoxy matrix. The remaining mix was poured onto the mold, followed by uniform distribution of fibers. The mold was then closed with another lamination sheet and plywood and cured under a 20 kg load for 24 hours before demolding. Composite sheets (300 mm × 150 mm) were fabricated with a laminate thickness of 5 mm, by utilizing the hand layup method in four different wt% of fiber loading as mentioned in Table 3.

Table 3: Weight percentage of fibers and resin for composite creation.

Sample Name	NaOH Treated Keratin	Composition
TCPH10	Treated Chopped Keratin Fiber	10wt% TCPH+90wt % Epoxy Resin
TCPH20	Treated Chopped Keratin Fiber	20wt% TCPH+80wt % Epoxy Resin
TCPH30	Treated Chopped Keratin Fiber	30wt% TCPH+70wt % Epoxy Resin
TCPH40	Treated Chopped Keratin Fiber	40wt% TCPH+60wt % Epoxy Resin

Source: Authors, (2024).

II.3 TESTING AND CHARACTERIZATION OF COMPOSITE

To investigate the mechanical properties of polymer composites Tensile Test, Flexural Test, Impact Test, Water Absorption Test and Density Analysis were conducted after cutting the samples as per the ASTM standards as shown in Figure 1, The following methods were used to determine the values of various tests.

II.3.1 Tensile test

Tensile testing was performed using a computerized universal testing machine with a crosshead speed of 1 mm per minute, measuring a gauge length of 50 mm. The composite sample specimens were prepared according to the standards outlined in ASTM D638 for evaluating tensile strength [24]. The specimens were then securely positioned within the grips of the universal testing machine for the duration of the test. Tensile strength is calculated using the following formula.

$$\rho = \frac{\text{Load (N)}}{\text{Original Cross Section Area (mm}^2\text{)}} \text{ N/mm}^2 \quad (1)$$

Tensile Modulus was calculated using the following formula.

$$\rho_m = \frac{\text{Stress}}{\text{Strain}} \quad (2)$$

Here $\text{Stress} = \frac{\text{Maximum Load}}{\text{Cross section Area of Specimen}}$ and $\text{Strain} = \frac{\Delta L}{L}$, $\Delta L = \text{Change in length(Displacement)}$ and $L = \text{Gauge length (mm)}$

II.3.2 Flexural Strength

The flexural strength of a material demonstrates its resistance to deformation caused by bending forces. To evaluate this property, a flexural test was conducted using the 3-point bending setup in accordance with the ASTM D790 standard[25]. During the test, a load was applied at the midpoint of the beam until the specimen fractured. The load at the breaking point and the dimensions of the sample were utilized to compute the flexural strength of the composite using the following formula.

$$\rho_f = \frac{3FL}{2wt^2} \quad (3)$$

where $\sigma_f = \text{Flexural strength (N/mm}^2\text{)}$, $F = \text{Load (N)}$, $L = \text{length or span (mm)}$, $w = \text{width (mm)}$ and $t = \text{thickness respectively}$ Flexural Modulus of the composite was calculated using the following formula.

$$E = \frac{L^3F}{4dwt^3} \quad (4)$$

Here $L = \text{Span length(mm)}$, $F = \text{Load(N/mm}^2\text{)}$, $d = \text{Displacement(mm)}$, w & $t = \text{width and thickness of composite(mm)}$.

2.3.3 Impact test

The impact test assesses a material's capacity to withstand or absorb impact or shock loading, typically by quantifying the energy absorbed during fracture. The Izod impact test was performed on the specimen in accordance with the ASTM D256 standard at room temperature.

$$\text{Impact Strength} = \frac{\text{Energy Absorbed (J)}}{\text{Area of Composite (mm}^2\text{)}} \quad (5)$$

II.3.4 Relative Density analysis

The density of a composite material is influenced by both the polymer matrix and the reinforcing fibers. Density analysis involves understanding the interplay between matrix and reinforcing fibers. These materials continue to revolutionize industries by providing lightweight, strong, and versatile solutions. To calculate the density of a polymer composite, we need to consider the densities of its individual components (resin, fibers, core, etc.).

Measured Density:

The measured density (ρ_e) of the samples was determined following the guidelines outlined in ASTM D1895.

Density was calculated using the subsequent formula, utilizing the average data obtained from three replicate samples.

The formula for density is- Density $\rho_e = \frac{M_c}{V_c}$

Where, M_c = represents the mass of the composites measured using an analytical balance (Gram), V_c = indicates the volume of the composites derived from their dimensions (length*width*thickness) measured using a digital caliper[26]

Theoretical Density

To calculate the theoretical density of the composite material, the following equation is used. It expresses the density of the composite material in terms of the volume fractions of its constituents, formulated as:

$$\rho_c = \rho_f V_f + \rho_m V_m$$

Here

ρ_c = Density of Composite, ρ_f = Density of Fiber, ρ_m = Density of Matrix, V_f = Volume fraction of Fiber and V_m = Volume fraction of Fiber

The equation for calculating the volume fraction of voids is as follows: According to [27].

$$V_f = \frac{\rho_c - \rho_e}{\rho_e} \quad (6)$$

II.3.5 Water Absorption and Thickness Swelling Examination

Water Absorption test was accomplished according to ASTM D570 standard. All the composite samples were dipped in distilled water and their weight was measured at regular intervals of time up to saturation point at room temperature. The ratio of increase in mass of the specimen to the initial mass is given as the percentage moisture absorption [28].

Mathematically, it was calculated using the following equation.

$$\% \text{ Absorption} = \frac{W_t - W_d}{W_d} \times 100 \quad (7)$$

Where, W_t = Wet Weight and W_d = Dry Weight

Thickness Swelling measures the change in thickness of the composite material after it has been soaked in distilled water. It provides insights into how much the material expands or swells due to water absorption. The measurement of the composite's thickness swelling was performed using a micrometer with a minimum resolution of 0.01 mm. To determine the Thickness Swell (TS) of the sample, the following equation was utilized [29].

$$TS(\%) = \frac{\delta_f - \delta_i}{\delta_i} \times 100 \quad (8)$$

where δ_i and δ_f are the initial and final thickness of the composite specimen after immersion in the distilled water.

IV. RESULTS AND DISCUSSIONS

IV.1 RELATIVE DENSITY ANALYSIS

Theoretical density was calculated as discussed in 2.3.4. The experimental values of density closely aligned with theoretical values. The average value of density for each composite is

illustrated in Tables 4. The findings revealed that epoxy composites containing fibers at 10wt%, 20wt%, 30wt% and 40wt% exhibit slightly lower densities than the theoretical values. This variance may be attributed to the presence of voids content within the composites[26].

The composites were fabricated via the hand layup process, despite the use of rollers to mitigate voids, some air particles become trapped. This occurrence may leads to the formation of weaker sections within the composite.

Table 4: Theoretical vs Experimental Density of Composite.

Sample Name	Theoretical Density of Composite ρ (g/cm ³)	Average Experimental Density of Composite ρ (g/cm ³)	Fraction of voids (%)
TCPH10	1.17	1.15	1.2%
TCPH20	1.18	1.16	1.3%
TCPH30	1.20	1.17	1.7%
TCPH40	1.21	1.19	1.9%

Source: Authors, (2024).

IV.2 TENSILE BEHAVIOR ANALYSIS

Tensile strength and Tensile Modulus of epoxy-based composites reinforced with Keratin fiber are illustrated in Table 5. The findings revealed that up to 30wt% the tensile strength was increased, and peaking was found at 30wt% as shown in figure 2. Beyond this threshold, however, further increments lead to a decline in tensile strength. The peak value recorded stands at 35.24 MPa for composites containing 30wt% Keratin Fiber and 70wt% Epoxy.

Table 5: Tensile strength and Tensile Modulus of epoxy-based composites reinforced with Keratin Fiber.

Sample	Ultimate Tensile Strength (MPa)	Average Ultimate Tensile Strength (MPa)	Tensile Modulus (MPa)	Average Tensile Modulus (MPa)
TCPH10	1	20.04	1155.74	1227.32
	2	20.62	1227.67	
	3	22.81	1298.56	
TCPH20	1	30.15	1216.42	1270.01
	2	30.97	1258.85	
	3	31.88	1334.77	
TCPH30	1	34.68	1385.12	1416.42
	2	35.93	1472.63	
	3	35.12	1391.52	
TCPH40	1	21.44	1342.14	1411.72
	2	23.25	1490.28	
	3	22.87	1402.74	

Source: Authors, (2024).

Strength is predominantly governed by the interfacial adhesion between the fiber and the matrix. Notably, at 40wt% Keratin Fiber content, the interfacial bonding weakens due to resin material inadequacy. This deficiency prevents proper resin penetration, leading to potential delamination between Keratin Fiber layers.

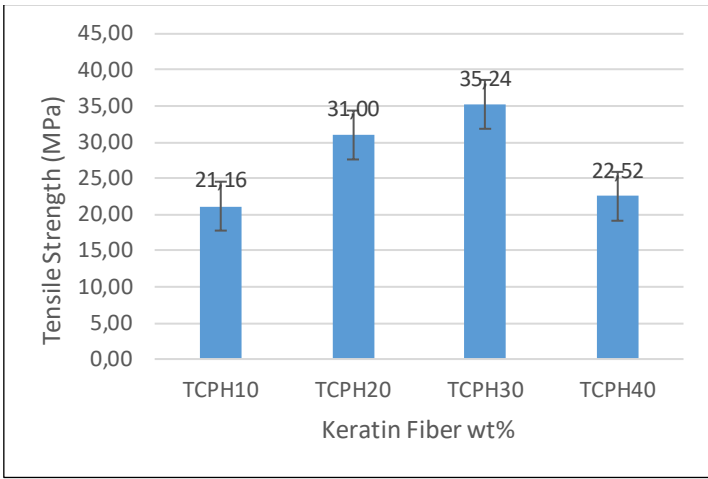


Figure 2: Tensile Strength: Chopped Keratin Fiber Reinforced Epoxy.
Source: Authors, (2024).

Figure 3 illustrates the tensile moduli, reflecting the stiffness of the developed composites under tensile loads. Notably, the moduli exhibited significant enhancement within the range of 10-40wt% fiber reinforcement, reaching an optimum value at 40wt%. The apparent decline in tensile modulus observed in the 40wt% fiber reinforced composites may be attributed to fiber agglomeration and the less amount of matrix present over the region that deteriorates the binding between fibers. Occasional fiber agglomeration, stemming from experimental imperfections that hinder fiber dispersion, can lead to these defects. Since optimal fiber dispersion is known to facilitate good interfacial bonding and minimize voids by ensuring complete fiber encapsulation by the matrix, fiber agglomeration tends to exacerbate these issues. Notably, the 30wt% fiber reinforced composite exhibited the highest tensile modulus of 1416.42 MPa.

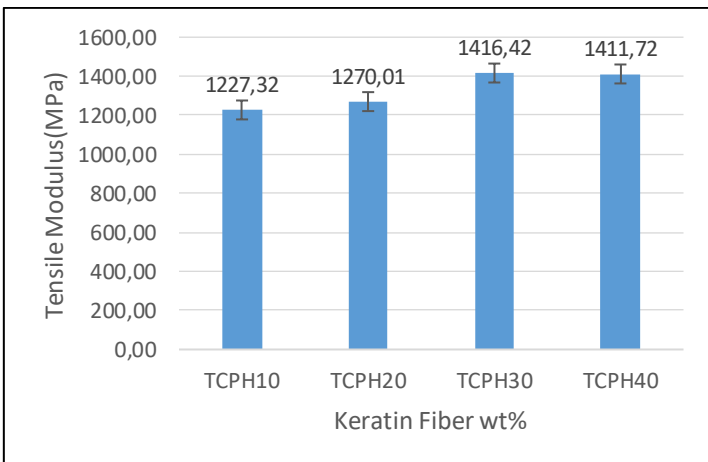


Figure 3: Tensile Modulus: Chopped Keratin Fiber Reinforced Epoxy.
Source: Authors, (2024).

IV.3 FLEXURAL STRENGTH ANALYSIS

The flexural strength and Flexural Modulus results for both neat epoxy and KeratinFiber-reinforcedepoxy composites are depicted in Table 6. Neat epoxy exhibits a flexural strength of 101.29 MPa. The inclusion of Keratin Fiber up at 30% by weight increase in flexural strength.

Table 6: Flexural strength and Flexural Modulus of epoxy-based composites reinforced with Keratin Fiber.

Sample	Ultimate Flexural Strength (MPa)	Average Ultimate Flexural Strength (MPa)	Flexural Modulus (MPa)	Average Flexural Modulus (MPa)
TCPH10	1	46.83	1991.29	2029.51
	2	47.37	2010.44	
	3	47.88	2086.81	
TCPH20	1	56.05	3109.18	3193.73
	2	56.62	3198.47	
	3	57.24	3273.54	
TCPH30	1	75.42	3956.41	3889.61
	2	74.31	3820.90	
	3	74.68	3891.53	
TCPH40	1	62.83	3688.25	3623.84
	2	62.16	3614.87	
	3	61.29	3568.41	

Source: Authors, (2024).

Notably, the composite comprising 30% Keratin Fiber demonstrates the highest flexural strength recorded at 74.80 MPa among all laminated compositions tested. However, the 40% Keratin Fiber threshold in reinforced epoxy composites leads to a decline in flexural strength, a reduction in flexural strength is attributed to resin material deficiency resulting in inadequate interfacial bonding between the hair mat and epoxy. Under load application, specimens experience delamination on the bottom side opposite to the applied load.

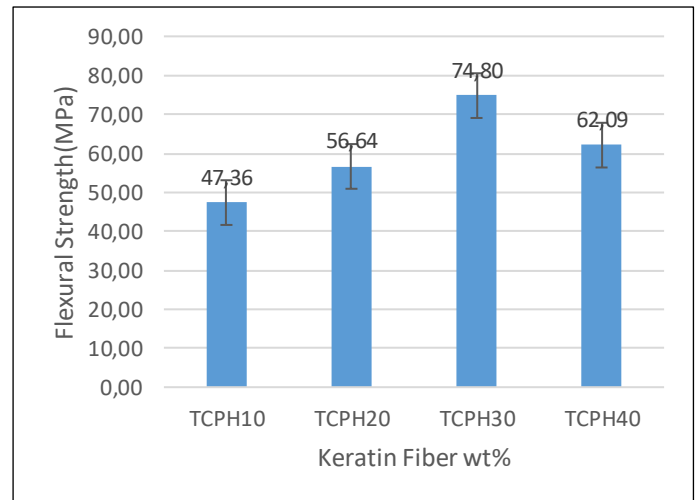


Figure 4: Flexural Strength: Chopped Keratin Fiber Reinforced Epoxy.
Source: Authors, (2024).

Figure 5 depicts the flexural modulus of both the developed composites. The trend observed in Figure 4, most of the developed composites exhibit improved flexural. This reflects that with increasing fiber contents Tensile modulus increased. This could be attributed to the uniform load distribution within the fibers as the fiber content increases to bear the load more efficiently. This observation aligns with the findings in Figure 5. Notably, the composite with a 30wt% fiber content demonstrated the highest flexural modulus at 3889.61 MPa, followed by the 20wt% Keratin fiber reinforced composite at 3193.73 MPa. These results indicate well-dispersed fibers with enhanced interaction with the matrix, thereby improving the fiber-matrix interfacial adhesion and

directly increasing the flexural modulus. Such enhancement may not be as pronounced with lower fiber weight fractions.

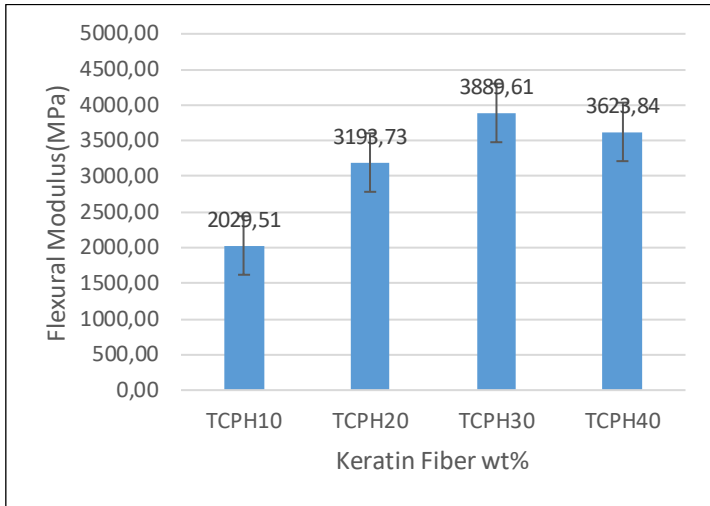


Figure 5: Flexural Modulus: Chopped Keratin Fiber Reinforced Epoxy. Source: Authors, (2024).

Overall, the trend suggests that flexural moduli tend to rise with increasing fiber content, highlighting the preference for higher weight fractions in the development of Keratin fiber reinforced epoxy composites to achieve superior flexural strength and stiffness.

IV.4 IMPACT ENERGY ANALYSIS

Experimental evaluation was conducted on Izod impact strength of Epoxy and Keratin Fiber-reinforced epoxy composites depicted in Table 7. The results revealed a clear trend: impact strength increases with the rise in weight percentage of Keratin Fiber up to 40wt%, as illustrated in Figures 7, respectively.

Table 7: Impact Energy absorbed by epoxy-based composites reinforced with Keratin Fiber.

	Sample	Impact Energy(J/mm ²)	Average Impact Energy(J/mm ²)
TCPH10	1	4.16	4.14
	2	4.13	
	3	4.12	
TCPH20	1	5.02	4.99
	2	4.97	
	3	4.99	
TCPH30	1	7.7	7.77
	2	7.76	
	3	7.84	
TCPH40	1	9.84	9.87
	2	9.91	
	3	9.87	

Source: Authors, (2024).

Notably, for composites containing 40wt% Keratin Fiber and 60wt% epoxy, the maximum impact energy required for specimen fracture in the Izod tests were recorded at 9.87 J/mm², respectively. Previous studies have similarly illustrated such events through examinations of impact energy in Polymer Matrix Composites [30].

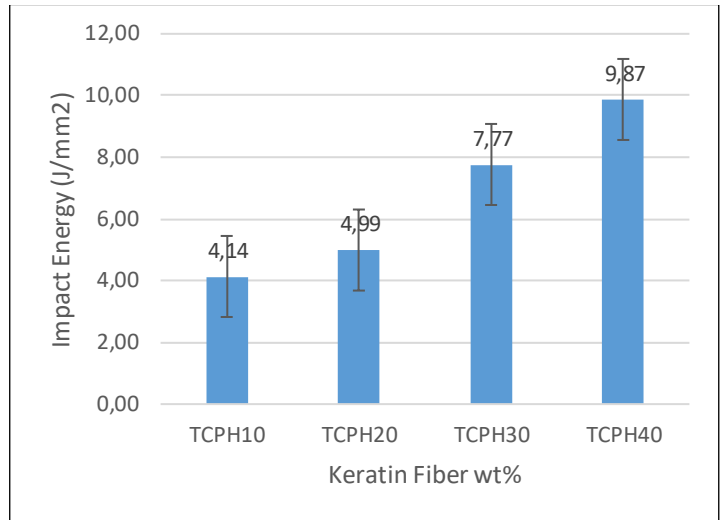


Figure 6: Impact Variation: Treated Chopped Keratin Fiber Reinforced Epoxy and Control. Source: Authors, (2024).

The increase in impact strength with the rise in weight percentage of Keratin Fiber up to 40wt% can be attributed to the reinforcement effect provided by the incorporation of Keratin fibers into the material matrix. As the weight percentage of Keratin Fiber increases, more fibers are dispersed throughout the matrix, effectively reinforcing it and enhancing its mechanical properties, including impact strength. Beyond 40wt%, however, there may be diminishing returns or other factors coming into play that limit further improvements in impact strength.

IV.5 WATER ABSORPTION AND THICKNESS SWELLING EXAMINATION

The outcomes from doing water absorption tests on the treated Keratin fiber reinforced composites are illustrated in Table 8. It is well-established that natural fibers exhibit high hydrophilicity, meaning that a higher fiber content leads to greater moisture absorption, as confirmed by the increasing moisture absorption trend depicted in Fig. 8 as fiber fraction increases.

Table 8: Percentage of Water Absorbed by Composite.

Sample Name	Day 0	Day 1	Day 2	Day 3	Day 10	Day 20	Day 30	Day 40
TCPH 10	0.00 %	0.27 %	0.49 %	0.71 %	1.15 %	1.32 %	1.32 %	1.37 %
TCPH 20	0.00 %	0.51 %	0.92 %	1.16 %	1.62 %	1.94 %	2.03 %	2.08 %
TCPH 30	0.00 %	0.82 %	1.23 %	1.59 %	2.28 %	2.87 %	3.14 %	3.28 %
TCPH 40	0.00 %	0.91 %	1.32 %	1.68 %	2.45 %	3.17 %	3.63 %	4.04 %

Source: Authors, (2024).

Initially, the higher moisture absorption rate was observed within the 24 hours. It can be attributed to chemical treatment which alters the hair's structure, potentially increasing its porosity and allowing it to absorb water more readily. After around 20 days, the rate of water absorption starts to stabilize as the hair reaches a saturation point where it can no longer absorb significant amounts of additional water.

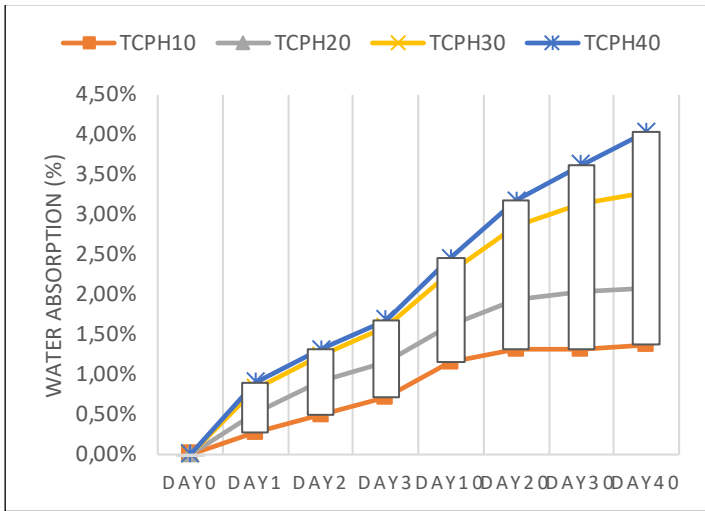


Figure 7: Water absorption: Treated Chopped Keratin fiber reinforced composites. Source: Authors, (2024).

On the contrary, the reduced size of the fiber fraction and subsequent enhanced dispersion facilitate superior encasement of the fibers within the matrix. This significantly diminishes the rate at which water permeates into the fibers, ultimately enhancing the resistance to absorption. Conversely, as elucidated earlier, the composite reinforced with 40wt% treated Keratin fiber exhibited the lowest resistance to water absorption and displayed the highest hydrophilicity among all the composite samples. Here the good thing is that even after 40 days only 1.37% water absorbed by 10wt% Keratin fiber composite and maximum water absorption was also good as 4.04% by 40wt% Keratin fiber composite. Due to its less water absorption behavior of the Keratin fiber, its thickness swelling behaviors was also found quite sufficient as illustrated in Table 9.

Table 9: Percentage of thickness swelling due to water absorption by Composite.

Sample Name	Day1	Day2	Day3	Day1 0	Day2 0	Day3 0	Day4 0
TCPH10	0.49 %	0.68 %	0.88 %	1.36 %	1.56 %	1.56 %	1.56 %
TCPH20	0.58 %	0.78 %	0.97 %	1.75 %	1.95 %	1.95 %	1.95 %
TCPH30	0.60 %	1.00 %	1.20 %	2.00 %	2.20 %	2.20 %	2.20 %
TCPH40	0.80 %	1.29 %	1.49 %	2.39 %	2.69 %	3.59 %	3.69 %

Source: Authors, (2024).

The 40wt% Keratin Fiber composites gave higher values of thickness swelling, followed by pure epoxy as depicted in Figure 9. The higher values of thickness swelling for composites can be attributed to water absorption, causing the fibers and epoxy matrix to expand. However, over time, water can also penetrate between the fibers and the epoxy matrix, leading to saturation [29].

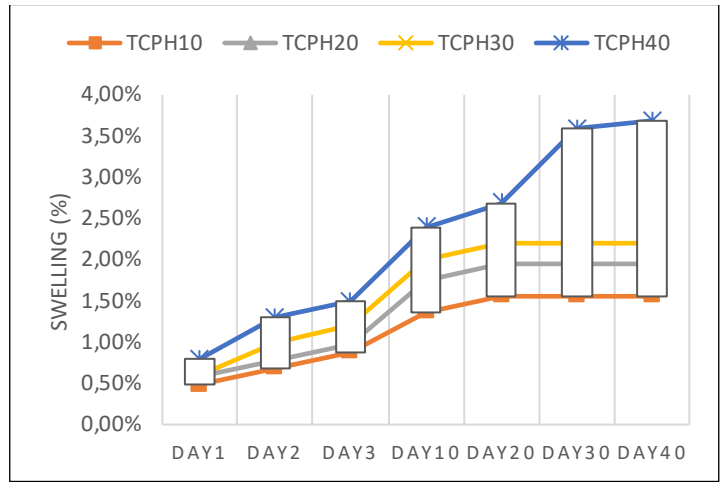


Figure 8: Swelling behavior: Treated Chopped Keratin fiber reinforced composites. Source: Authors, (2024).

IV.6 SCANNING ELECTRON MICROSCOPY (SEM) IMAGE ANALYSIS

In this context, Scanning Electron Microscopy (SEM) is employed to examine different facets of surface morphology within composites. This includes analyzing fiber-matrix bonding, identifying voids, microcracks, observing crack propagation, and assessing fiber agglomeration. SEM image reveals the observations in Treated chopped Keratin fiber composites highlight a strong attachment between fibers and matrix, suggesting superior interfacial bonding depicted in Figure 10. This enhanced bonding enhances adhesion between fiber surface and matrix, consequently improving the mechanical properties of treated chopped fiber-reinforced composites.



Figure 9: SEM: Bonding between the Treated Chopped Keratin Fiber with epoxy polymer. Source: Authors, (2024).

V. CONCLUSIONS

The study investigates the tensile, flexural, and impact strengths of epoxy composites reinforced with Keratin fiber. Due to weaker interfacial bonding, tensile strength declined after reaching its peak of 35.24 MPa at 30 weight percent fiber content. Even with the sporadic fiber aggregation, the tensile modulus improved as well, reaching 1416.42 MPa at 30% weight percentage. At 30wt%, flexural strength rose to 74.80 MPa; however, because of insufficient resin bonding, a drop occurred with a larger fiber content. At 30wt%, the flexural modulus peaked at 3889.61 MPa. The impact energy of composites with 40wt% Keratin Fiber was found to be the greatest, measuring 9.87 J/mm².

Impact strength increased steadily as Keratin Fiber content increased, reaching a peak at 40wt%. Tests on water absorption revealed a direct correlation between moisture uptake and fiber content, which stabilized after 20 days. Although 40wt% Keratin Fiber composites had the most hydrophilicity but still managed water absorption and swelling, higher fiber content composites showed superior resistance to absorption.

Density measurements revealed that voids caused minor departures from theoretical values; Keratin Fiber composites had densities that were lower than expected. The composites showed notable improvements in mechanical performance and hydrophobic qualities, which qualified them for use in maritime, construction, and automotive applications.

IX. AUTHOR'S CONTRIBUTION

Conceptualization: Umesh Kumar Dwivedi

Methodology: Deeap Kachhot, Umesh Kumar Dwivedi

Investigation: Deeap Kachhot

Discussion of results: Moti Lal Rinawa

Writing –Original Draft: Deeap Kachhot, Rishi Dewangan

Writing –Review and Editing: Deeap Kachhot, Rishi Dewangan, Moti Lal Rinawa, Umesh Kumar Dwivedi

Resources: Kachhot Deepak, Dewangan Rishi, Rinawa Motilal, Dwivedi Umesh Kumar

Supervision: Rishi Dewangan, Moti Lal Rinawa, Umesh Kumar Dwivedi

Approval of the final text: Kachhot Deepak, Dewangan Rishi, Rinawa Motilal, Dwivedi Umesh Kumar

X. REFERENCES

- [1] K. Mohan Kumar, V. Naik, V. Kaup, S. Waddar, N. Santhosh, and H. V. Harish, "Nontraditional Natural Filler-Based Biocomposites for Sustainable Structures," *Advances in Polymer Technology*, vol. 2023, 2023, doi: 10.1155/2023/8838766.
- [2] S. K. Ramamoorthy, M. Skrifvars, and A. Persson, "A review of natural fibers used in biocomposites: Plant, animal and regenerated cellulose fibers," *Polymer Reviews*, vol. 55, no. 1. Taylor and Francis Inc., pp. 107–162, Jan. 02, 2015. doi: 10.1080/15583724.2014.971124.
- [3] B. Vijaya Ramnath et al., "Evaluation of mechanical properties of abaca-jute-glass fibre reinforced epoxy composite," *Mater Des*, vol. 51, pp. 357–366, 2013, doi: 10.1016/j.matdes.2013.03.102.
- [4] J. J. Andrew and H. N. Dhakal, "Sustainable biobased composites for advanced applications: recent trends and future opportunities – A critical review," *Composites Part C: Open Access*, vol. 7. Elsevier B.V., Mar. 01, 2022. doi: 10.1016/j.jcomc.2021.100220.
- [5] T. A. Nguyen and T. H. Nguyen, "Banana Fiber-Reinforced Epoxy Composites: Mechanical Properties and Fire Retardancy," *International Journal of Chemical Engineering*, vol. 2021, 2021, doi: 10.1155/2021/1973644.
- [6] A. Verma and V. K. Singh, "Human Hair: A Biodegradable Composite Fiber – A Review," *Int J Waste Resour*, vol. 6, no. 2, 2016, doi: 10.4172/2252-5211.1000206.
- [7] S. Maiti, M. R. Islam, M. A. Uddin, S. Afroj, S. J. Eichhorn, and N. Karim, "Sustainable Fiber-Reinforced Composites: A Review," *Advanced Sustainable Systems*, vol. 6, no. 11. John Wiley and Sons Inc, Nov. 01, 2022. doi: 10.1002/adsu.202200258.
- [8] N. H. Mohan, L. K. Nayak, M. K. Tamuli, and A. Das, "Pig hair fibre utilization in India: Present status and future perspectives," *Indian Journal of Animal Sciences*, vol. 84, no. 2. pp. 99–102, Feb. 2014. doi: 10.56093/ijans.v84i2.37808.
- [9] K. L. Pickering, M. G. A. Efendy, and T. M. Le, "A review of recent developments in natural fibre composites and their mechanical performance," *Composites Part A: Applied Science and Manufacturing*, vol. 83. Elsevier Ltd, pp. 98–112, Apr. 01, 2016. doi: 10.1016/j.compositesa.2015.08.038.
- [10] S. Vigneshwaran et al., "Recent advancement in the natural fiber polymer composites: A comprehensive review," *Journal of Cleaner Production*, vol. 277. Elsevier Ltd, Dec. 20, 2020. doi: 10.1016/j.jclepro.2020.124109.
- [11] S. Palanisamy, K. Vijayananth, T. M. Murugesan, M. Palaniappan, and C. Santulli, "The Prospects of Natural Fiber Composites: A Brief Review," *International Journal of Lightweight Materials and Manufacture*, Jan. 2024, doi: 10.1016/j.ijlmm.2024.01.003.
- [12] J. S. S. Neto, R. A. A. Lima, D. K. K. Cavalcanti, J. P. B. Souza, R. A. A. Aguiar, and M. D. Banea, "Effect of chemical treatment on the thermal properties of hybrid natural fiber-reinforced composites," *J Appl Polym Sci*, vol. 136, no. 10, Mar. 2019, doi: 10.1002/app.47154.
- [13] N. Karthi, K. Kumaresan, S. Sathish, S. Gokulkumar, L. Prabhu, and N. Vigneshkumar, "An overview: Natural fiber reinforced hybrid composites, chemical treatments and application areas," in *Materials Today: Proceedings*, Elsevier Ltd, 2019, pp. 2828–2834. doi: 10.1016/j.matpr.2020.01.011.
- [14] B. Koohestani, A. K. Darban, P. Mokhtari, E. Yilmaz, and E. Darezereshki, "Comparison of different natural fiber treatments: a literature review," *International Journal of Environmental Science and Technology*, vol. 16, no. 1. Center for Environmental and Energy Research and Studies, pp. 629–642, Jan. 29, 2019. doi: 10.1007/s13762-018-1890-9.
- [15] S. O. Amiandamhen, M. Meincken, and L. Tyhoda, "Natural Fibre Modification and Its Influence on Fibre-matrix Interfacial Properties in Biocomposite Materials," *Fibers and Polymers*, vol. 21, no. 4. Korean Fiber Society, pp. 677–689, Apr. 01, 2020. doi: 10.1007/s12221-020-9362-5.
- [16] A. Gholampour and T. Ozbakkaloglu, "A review of natural fiber composites: properties, modification and processing techniques, characterization, applications," *Journal of Materials Science*, vol. 55, no. 3. Springer New York LLC, pp. 829–892, Jan. 01, 2020. doi: 10.1007/s10853-019-03990-y.
- [17] S. L. Koch, M. D. Shriver, and N. G. Jablonski, "Variation in Human Hair Ultrastructure among Three Biogeographic Populations," 2018. [Online]. Available: <https://www.elsevier.com/open-access/userlicense/1.0/>
- [18] M. J. Raghu and G. Goud, "Tribological Properties of Calotropis Procera Natural Fiber Reinforced Hybrid Epoxy Composites," *Applied Mechanics and Materials*, vol. 895, pp. 45–51, Nov. 2019, doi: 10.4028/www.scientific.net/amm.895.45.
- [19] G. Araya-Letelier, J. Concha-Riedel, F. C. Antico, C. Valdés, and G. Cáceres, "Influence of natural fiber dosage and length on adobe mixes damage-mechanical behavior," *Constr Build Mater*, vol. 174, pp. 645–655, Jun. 2018, doi: 10.1016/j.conbuildmat.2018.04.151.
- [20] N. H. Mohan et al., "Tensile properties of hair fibres obtained from different breeds of pigs," *Biosyst Eng*, vol. 119, pp. 35–43, Mar. 2014, doi: 10.1016/j.biosystemseng.2014.01.003.
- [21] S. Suthar and Dr. D. Kumar, "Fabrication and Depiction of Reinforced Human Hair Polymer Matrix Composites," *Int J Res Appl Sci Eng Technol*, vol. 10, no. 2, pp. 1370–1386, Feb. 2022, doi: 10.22214/ijraset.2022.40541.
- [22] I. O. Oladele, J. L. Olajide, and A. S. Ogunbadejo, "The Influence of Chemical Treatment on the Mechanical Behaviour of Animal Fibre-Reinforced High Density Polyethylene Composites," *American Journal of Engineering Research*, p. 2015, [Online]. Available: www.ajer.org
- [23] R. U. Arinze, E. Oramah, E. C. Chukwuma, N. H. Okoye, and P. U. Chris-Okafor, "Mechanical impact evaluation of natural fibres with LDPE plastic composites: Waste management in perspective," *Current Research in Green and Sustainable Chemistry*, vol. 5, Jan. 2022, doi: 10.1016/j.crgsc.2022.100344.
- [24] K. Selvakumar and O. Meenakshisundaram, "Mechanical and dynamic mechanical analysis of jute and human hair-reinforced polymer composites," *Polym Compos*, vol. 40, no. 3, pp. 1132–1141, Mar. 2019, doi: 10.1002/pc.24818.
- [25] S. Sathish, K. Kumaresan, L. Prabhu, S. Gokulkumar, S. Dinesh, and N. Karthi, "Experimental Testing on Mechanical Properties of Various Natural Fibers Reinforced Epoxy Hybrid Composites," *Indian J Sci Technol*, vol. 11, no. 25, pp. 1–6, Jul. 2018, doi: 10.17485/ijst/2018/v11i25/122231.
- [26] T. Azhary, Kusmono, M. W. Wildan, and Herianto, "Mechanical, morphological, and thermal characteristics of epoxy/glass fiber/cellulose nanofiber

hybrid composites,” *Polym Test*, vol. 110, Jun. 2022, doi: 10.1016/j.polymertesting.2022.107560.

[27] B. P. Nanda and A. Satapathy, “Processing and characterization of epoxy composites reinforced with short human hair,” in *IOP Conference Series: Materials Science and Engineering*, Institute of Physics Publishing, Mar. 2017. doi: 10.1088/1757-899X/178/1/012012.

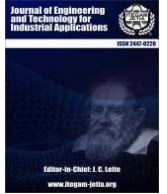
[28] Z. Kamble and B. K. Behera, “Mechanical properties and water absorption characteristics of composites reinforced with cotton fibres recovered from textile waste,” *J Eng Fiber Fabr*, vol. 15, 2020, doi: 10.1177/1558925020901530.

[29] T. Bera, N. Mohanta, V. Prakash, S. Pradhan, and S. K. Acharya, “Moisture absorption and thickness swelling behaviour of luffa fibre/epoxy composite,” *Journal of Reinforced Plastics and Composites*, vol. 38, no. 19–20, pp. 923–937, Oct. 2019, doi: 10.1177/0731684419856703.

[30] K. Selvakumar and O. Meenakshisundaram, “Mechanical and dynamic mechanical analysis of jute and human hair-reinforced polymer composites,” *Polym Compos*, vol. 40, no. 3, pp. 1132–1141, Mar. 2019, doi: 10.1002/pc.24818.



ISSN ONLINE: 2447-0228



RESEARCH ARTICLE

OPEN ACCESS

A BLOCKCHAIN-BASED DIGITAL EDUCATIONAL CERTIFICATE VERIFICATION SYSTEM

Tolulope Ifeyemi¹, Ajibola Oyedeji² and Fiyinfoluwa Adebisi³

^{1, 2, 3} Department of Computer Engineering, Olabisi Onabanjo University, Ago-Iwoye, Nigeria

¹ <http://orcid.org/0009-0002-1057-6460>, ² <http://orcid.org/0000-0002-0180-492X>, ³ <http://orcid.org/0009-0001-5494-5216>

Email: toluwalopeifeyemi@gmail.com, oyedeji.ajibola@oouagoiwoye.edu.ng, adebiyifiyinfoluwa8@gmail.com

ARTICLE INFO

Article History

Received: June 09th, 2024

Revised: September 14th, 2024

Accepted: September 14th, 2024

Published: September 04th, 2024

Keywords:

Certificate Verification,
Blockchain,

Celo,
User Experience.

ABSTRACT

The reliance on paper-based educational certificates and the lack of a robust and tamper-proof system for verifying academic credentials in the Nigerian education system make them vulnerable to forgery and alterations. The situation poses challenges in guaranteeing the legitimacy of such qualifications, and a need arises for a secure system to verify academic credentials. The proposed solution is a blockchain-based digital certificate verification system (BCVS) that utilizes the Celo blockchain as the underlying blockchain platform to store each digital certificate hash and meta-data, which is unique, secure, and permanently recorded on the blockchain. The system also includes a QR code feature to verify the certificate's authenticity instantly. Ten users evaluated the system, and the average scores are as follows: the user interface had 78%, the application database security scored 66%, the blockchain data security achieved 82%, the revocation mechanism achieved a score of 67%, and the maintainability achieved a score of 46%. While the system is designed to cater to university requirements and can revoke certificates if needed, it represents an advancement in certificate verification, thereby simplifying the process and improving the overall experience for everyone involved, with the potential to be scaled and customized for other universities, institutions, and use cases.



Copyright ©2024 by authors and Galileo Institute of Technology and Education of the Amazon (ITEGAM). This work is licensed under the Creative Commons Attribution International License (CC BY 4.0).

I. INTRODUCTION

The issue of certificate forgery is widespread in most developing countries, and the reliance on paper-based certificates makes them vulnerable to fraud, forgery, and unauthorized alterations [1]. There needs to be a robust and tamper-proof system for verifying academic credentials in the Nigerian education system to address certificate forgery. In the education system, there is a need for a secure method to verify academic credentials to combat certificate forgery. This poses challenges in guaranteeing the legitimacy and reliability of qualifications [2-4].

With the rapid development and deployment of information technology, developing solutions for diverse problems across various domains has become pertinent [5]. Blockchain technology (BT) is an emerging technology that has significant benefits across various application areas such as cross-border payments, identity management, real estate management, and supply chain [6], [7]. Blockchain provides an immutable electronic certification system, making it considerably more challenging for

individuals to manipulate academic credentials [1]. BT is witnessing a broad research focus and adoption in various countries across different domains [8-10].

Using blockchain technology to uphold the integrity of certificates from forgery and make verification processes efficient is a reliable approach [11]. Using distributed ledger technology allows for transactions without the need for intermediaries. It functions as a system that guarantees tamper-proof and immutable transaction records, making it an ideal option for certificate verification systems [12]. This project aims to design, implement, and evaluate a user-friendly, secure, and scalable blockchain-based digital certificate verification system (BCVS) leveraging blockchain technology to revolutionize how certificates are generated and verified.

Several review studies highlight key contributions, challenges, and future focus of blockchain-based systems for academic certificate verification [2],[4]. The papers show that blockchain has the potential to manage the certificate verification process securely. Additional benefits lie in cost, ease of making

decisions, customer attraction, and potential for exponential growth of businesses [13], [14]. Research developed a blockchain-based model for transcripts in Saudi Arabia in a bid to achieve digital transformation in the educational sector [15]. The Ministry of Education Transcript Verification blockchain (Saudi Arabia) (MOETVBC) framework proposed a novel hyper ledger fabric blockchain using distributed and decentralized ledgers across global P2P Network nodes. The system uses smart contracts to provide a secure method for the verification of students' certificates and degrees.

A prototype model based on the security features of BT and cloud storage to verify and validate educational credentials is presented [1]. The digital assets pass through a temporary storage phase where a unique certificate's distinct identifier is generated through a hashing algorithm. Further, a cryptographic encryption technique has been added to improve system security [1]. A Smart contract, Certi, was developed for storing certificates based on Ethereum, which provides a platform for potential employers or admission teams to authenticate stored certificates [11].

Similarly, Verificate is a system that leverages blockchain technology to store and authenticate certificates submitted securely and assures students of the secure storage of the certificate [16]. The system achieves its goal using distributed systems like IPFS and Ethereum. Verificate proves to be successful in preventing document counterfeiting [16]. Furthermore, a blockchain-based

verification system utilizes technology for certificate verification, employing an authentication scheme for owners and storing students' time and space information as blocks on the blockchain to achieve a secure and tamper-proof digital asset [17].

While there are undeniable benefits, it is essential to acknowledge that several challenges still need to be overcome to successfully implement blockchain-based systems to their full potential [7]. Blockchain-based verification systems have been widely adopted in several fields to ensure the integrity and credibility of certificates; however, these potentials have seen limited application in Africa and Nigeria, specifically in the educational system where certificates are issued [13].

The aim of this project is the development of a blockchain-based certificate verification system for digital certificates. In addition, the proposed solution will be able to issue digital certificates for the subscribed institution, with a case study of Olabisi Onabanjo University, Ago-Iwoye, Nigeria.

II THEORETICAL REFERENCE

The following sections describe requirement gathering, system design, implementation, testing, and deployment stages taken for the completion of the system using a modified waterfall model, as shown in Figure 1 [18].

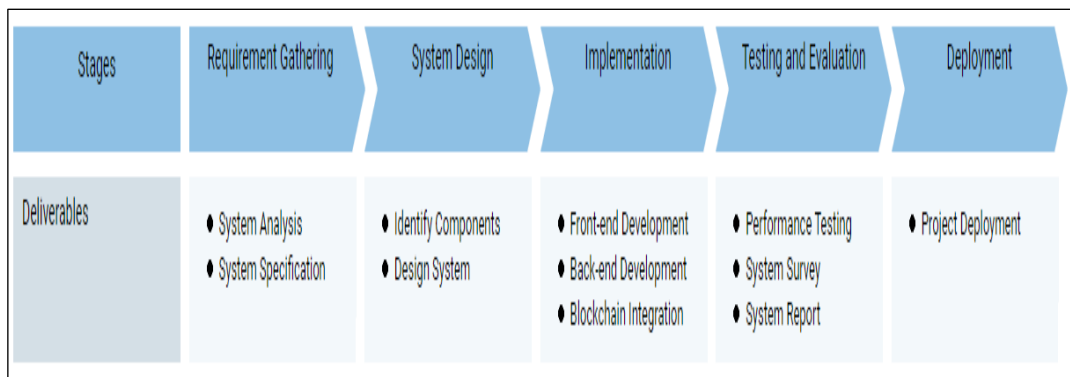


Figure 1: Project Methodology.

Source: Authors, (2024).

II.1 REQUIREMENT GATHERING

The major functional requirements of the system are presented as follows;

- i. The creation of a record of the certificate by the issuer of a certificate on the blockchain.
- ii. The certificate would be securely signed using the issuer's key.
- iii. Publication of the signed certificate on the blockchain.
- iv. Individuals who wish to verify the authenticity of a given certificate can utilize this solution.

II.1.1 ISSUING APPLICATION

The key functionalities and components of the Issuing Application include:

1. **User Authentication:** This feature ensures secure access to the Application. It verifies the identity of all users before granting them access.
2. **Administration Dashboard:** This interface allows administrators to effectively manage data, user privileges, and other administrative tasks.

3. **Certificate Auditing:** This function enables the review and verification of certificates to ensure their validity and integrity.
 - i. **Certificate Viewing:** The Application provides several viewing options for different certificate states:
 - ii. **Signed and Published Certificates:** This feature allows users to view certificates that have been signed and are currently active.
 - iii. **Revoked Certificates:** This feature allows users to view revoked certificates.
4. **Certificate Revocation:** This critical function allows the application system admin to revoke certificates when necessary, rendering the certificate status invalid.

II.1.2 VERIFICATION APPLICATION

The verification applications are responsible for checking the authenticity and integrity of the certificates issued before. It can be verified using two methods with steps as follows:

1. **Using the file upload method:**
 - i. The user uploads the digital copy of the certificate in PDF format.

- ii. The system calculates the hash value of the uploaded digital file.
- iii. The client sends a request to the API endpoint.
- iv. Then, an interaction with the blockchain to fetch the required data for verification
- v. The system applies the verification logic to compare the calculated hash value with the retrieved hash value from the blockchain to ensure data integrity.
- vi. The system checks the database to confirm if the calculated hash value exists and extracts other required information.

2. Using the certificate ID method:

- i. The user enters the Certificate ID.
- ii. The client sends a request to the API endpoint.
- iii. Then, an interaction with the blockchain to fetch the required data for verification
- iv. The system applies the verification logic to compare the certificate ID with the retrieved certificate ID from the blockchain to ensure data integrity.
- v. Check the database to confirm the existence of the certificate ID value.

II.2 SYSTEM DESIGN

During this phase, the focus is on developing the system design for the blockchain-based certificate verification system, including the architecture and the need to identify the components required for the system, including the blockchain type, the technology stack, and several other tools. As shown in Figure 2, the system briefly consists of five components in the system architecture overview: verification application, issuing Application, the Celo Blockchain, and MongoDB Database.

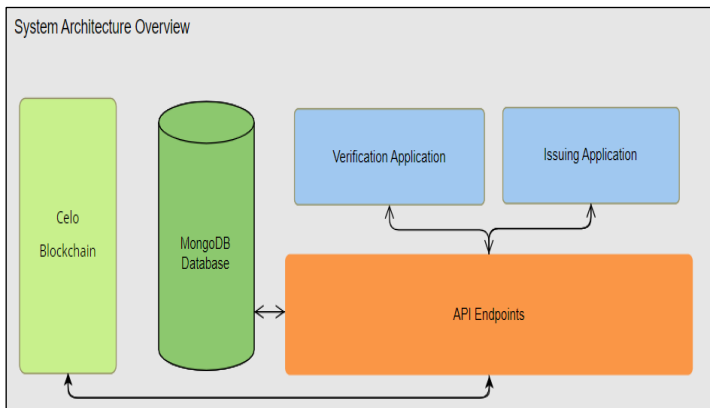


Figure 2: System Architecture Overview.
Source: Authors, (2024).

The blockchain serves as a component of trust for a distributed database. These data include the generated hash from all the certificates issued and more.

II.2.1 Celo Blockchain and Technology Selection

The blockchain acts as the infrastructure of trust for saving authentication and other metadata using a distributed database. Typically, these data include the generated hashed data from all the certificates issued. The Celo blockchain is suitable for developing a digital certificate verification system due to its carbon-negative status, cost-effectiveness, and energy-efficient proof-of-stake consensus mechanism tokenized carbon credits that enable composable ecological assets. The Celo blockchain also has a

native accounting unit, the cryptocurrency CELO, which is used to implement cryptocurrencies or tokens as contracts. Moreover, the Celo blockchain serves a purpose as both the primary currency and an ERC 20 compatible token on the Celo blockchain. These characteristics position the Celo blockchain as an option for establishing a certificate authentication system [19], [20]. The Celo network means that even wallet users with high latency, low bandwidth, or high-cost data tariffs can use Celo. Celo removes the need to check every header before a received header can be trusted.

II.2.2 Mongodb

The MongoDB is employed as the database since it successfully manages JSON-based data, which provides more storage for other metadata. MongoDB is a NoSQL database used to manage JSON-based data structures [21]. It provides storage for other related metadata of the certificate on the system. This metadata can include various information related to the certificates, such as the issuer's details, the recipient's details, the date of issue, and more, providing a comprehensive and efficient database solution for the blockchain-based certificate verification system.

II.2.3 Verification Application

The verification application checks the authenticity and integrity of the digital certificates initially generated and issued by the Issuing Application. This is achieved through two primary methods: the file upload method and the certificate ID method.

In the file upload method, the user uploads the digital copy, which is the certificate's PDF file. The system then calculates the hash value for the digital copy, which serves as a unique identifier for the certificate. The client then requests the blockchain, interacting with the blockchain API to fetch the transaction message associated with the certificate. The logic of the verification process involves comparing this transaction message with the verification data. This includes verifying the hash value on the certificate to ensure there has been no tampering and confirming if the hash value is present in the database.

The certificate ID method follows a similar process. The user enters the Certificate Issue Code, and the client requests the blockchain. The blockchain API is again used to fetch the transaction message. The verification logic involves checking the hash value on the certificate to avoid tampering and confirming if the hash value is both in the database and on the blockchain.

These methods support the primary function of the verification application, which is to check the authenticity and integrity of the digital certificates that have been initially generated and issued. By fetching the transaction message through an API endpoint and comparing it with the verification data, the Application ensures that each certificate is valid and trustworthy. This robust verification process contributes to the overall reliability and security of the certificate system.

II.2.4 Issuing Application

The issuing application is responsible for the main business logic of issuing and signing the certificate. It serves as the backbone of the certificate verification system in handling critical tasks of generating and issuing, thereby ensuring the system's integrity, reliability, and security. There is a dedicated interface for system administrators. It allows them to manage various aspects of the system and audit the certificates by viewing various types of certificates, including issued and revoked certificates. This ensures transparency and accountability in the certificate issuance process.

It also has the revoking certificate functionality, which allows for the invalidation of certificates when necessary, which could be due to a variety of reasons such as expiration, errors, fraudulent activities, or institution disciplinary measures.

II.2.5 Api Endpoints

The role of the API endpoints is pivotal and crucial because they serve as the communication gateway between the frontend, backend, and blockchain system, as illustrated in Figure 3. The stored metadata can be retrieved through specific API endpoints. These endpoints are designed to handle requests from

the front end of this system, fetch the requested data from the MongoDB database, and return it in a structured format. This process ensures that all relevant information about an issued certificate is readily available and can be accessed efficiently.

Leveraging the power of MongoDB for metadata storage and retrieval helps enhance the system's robustness. It keeps the blockchain less cluttered, as only the essential certificate data is stored, while MongoDB handles the rest. This design choice contributes to the scalability and performance of the system, ensuring it remains fast and responsive even as the number of issued certificates grows.

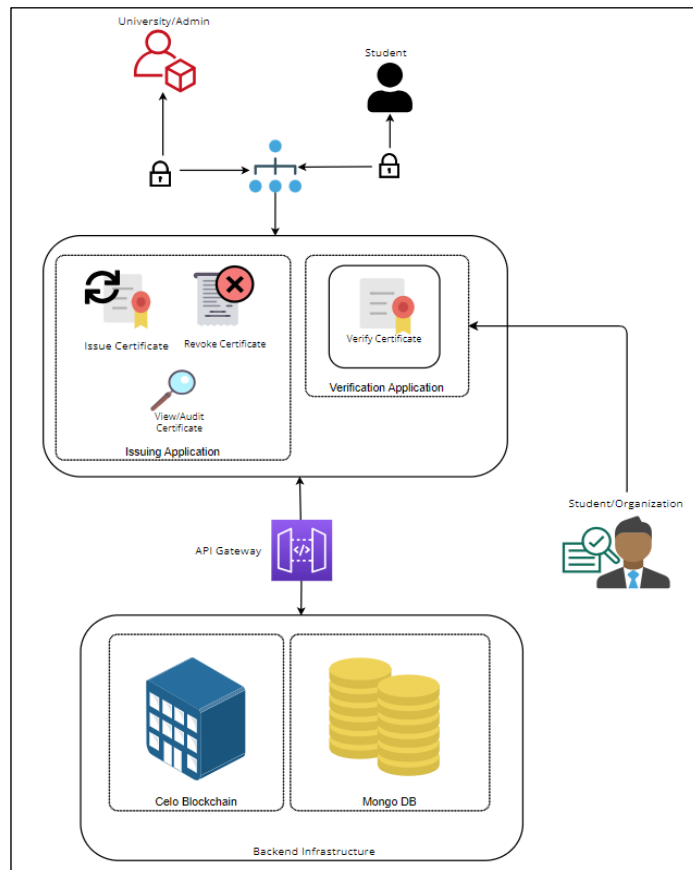


Figure 3: Illustration of the system architecture design.
Source: Authors, (2024).

II.2.5 DEPLOYMENTS

The deployment phase involves transitioning our blockchain-based certificate verification system from a development setting into a real-world operational environment. The backend logic provides the ability to write and read certificate meta-data and interact with the local database (MongoDB). The system's backend, built on NodeJS for the server configuration and API endpoints, was deployed on Render. The front end, constructed using React, is being deployed on Vercel and is available at <https://bcvs.vercel.app>. Furthermore, a provisioned Celo account loaded with Celo cryptocurrency allows transactions and store records on the Celo blockchain to be executed seamlessly.

III. RESULTS AND DISCUSSION

The BCVS has been implemented with a user-friendly interface, as shown in Figure 4, depicting the landing page with login options for students and administrators.

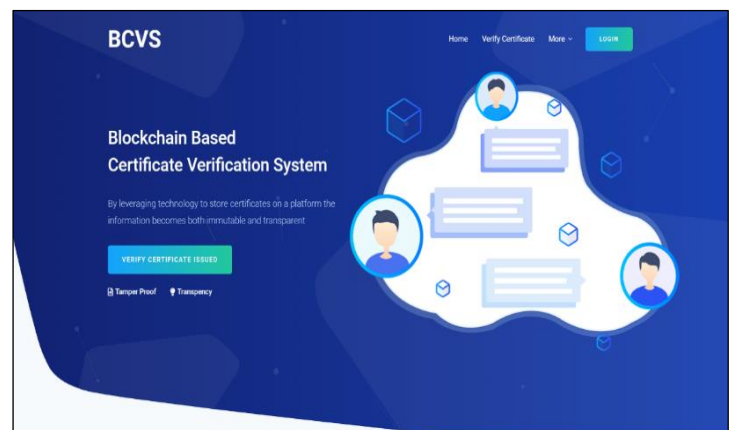


Figure 4: BCVS Landing Page.
Source: Authors, (2024).

III.1 DIGITAL CERTIFICATE ISSUING

The admin issues the digital certificate by correctly entering the candidate's details in the form in Figure 5. After clicking the Submit button, a preview of the submitted form details is prompted for confirmation. The digital certificate is created when action is taken, followed by the certificate hash value and certificate ID stored on the Celo Blockchain public ledger. Figure 6 is a sample of the generated certificate. An essential feature of this certificate is including a QR code, which serves the purpose of verification.

Figure 5: Certificate Issuing Form.
Source: Authors, (2024).



Figure 6: A Generated Digital Certificate.
Source: Authors, (2024).

III.2 DIGITAL CERTIFICATE ISSUING

An organization or legal entity requiring verification of an issued certification can either upload a PDF file of the issued digital certificate or use the certificate ID, as shown in Figures 7 and 8, respectively. Figure 9 is the result of the verification, showing the valid status of the certificate.

Figure 7: Verification with file upload.
Source: Authors, (2024).

Figure 8: Verification with a certificate ID.
Source: Authors, (2024).

Figure 9: A Verified Digital Certificate.
Source: Authors, (2024).

III.3 CELO BLOCKCHAIN TRANSACTION

The Celo Blockchain Transaction system serves as the foundation for the certificate verification system. Each transaction can represent actions like issuing, verifying, or revoking a certificate. Important information included in these transactions usually consists of the certificate's identifier, the issuer's details, the recipient's information, and the timestamp. In Figure 10, the transactions on the blockchain provide transparency and traceability. This ensures that every transaction is permanently recorded and easily auditable by any participant in the network. The transparency offered by this system helps establish trust among users and dramatically reduces the risks associated with fraud and unauthorized modifications.

Transaction Hash	Method	Block	Age	From	To	Value
0x0f00916a299924e2...	Transfer	2134020	17 hrs 40 mins ago	0x2E0466e8a82094...	0x2f0c517ec276c3f1...	0.001 CELO
0x4b2073752a054870...	Transfer	2134031	17 hrs 51 mins ago	0x2E0466e8a82094...	0x2f0c517ec276c3f1...	0.001 CELO
0x637a7a85073954c...	Transfer	2133269	1 day 11 hrs ago	0x2E0466e8a82094...	0x2f0c517ec276c3f1...	0.001 CELO
0x11c44687964c8112...	Transfer	2133071	1 day 19 hrs ago	0x2E0466e8a82094...	0x2f0c517ec276c3f1...	0.001 CELO
0x18995f7903110a...	Transfer	2132079	1 day 19 hrs ago	0x2E0466e8a82094...	0x2f0c517ec276c3f1...	0.001 CELO

Figure 10: Transactions on Celo by the System.
Source: Authors, (2024).

III.4 EVALUATION RESULT

Ten users (A-J) tested the BCVS to determine the system's performance and acceptability. The system was scored on a scale of 0 – 10, with 0 being the worst and 10 being the best, based on the criteria presented in Table 1. The user interface achieved a score of 78%, the certificate data security by the application database achieved a score of 66%, the blockchain data security achieved an accuracy of 82%, the revocation mechanism achieved a score of 67%, and the maintainability achieved a score of 46%.

Table 1 System Evaluation Result

User	User Interface	Certificate Data	Blockchain Data Security	Revocation mechanism	Maintainability
A	8	6	8	7	5
B	9	6	8	6	6
C	7	7	9	7	4
D	7	7	8	7	5
E	8	6	7	6	5
F	8	8	8	8	4
G	8	6	8	6	5
H	9	7	9	7	3
I	7	6	9	6	4
J	7	7	8	7	4
Average Rating	0.78	0.66	0.82	0.67	0.45
Percentage	78%	66%	82%	67%	45%

Source: Authors, (2024).

The SWOT (strengths, weaknesses, opportunities, and threats) analysis of the BCVS is presented in Figure 11 below.

STRENGTHS	OPPORTUNITIES
<ul style="list-style-type: none"> The utilization of blockchain guarantees that every certificate is unique, secure and permanent. This greatly helps to minimize the chances of certificate forgery. The system simplifies the procedure of issuing and verifying certificates. The inclusion of QR code further helps improve accessibility. 	<ul style="list-style-type: none"> The current design is tailored for Olabisi Onabanjo University certification. However, there is an opportunity for adoption by other organizations. Opportunity for integration with existing document verification systems in use by other institutions.
WEAKNESSES	THREATS
<ul style="list-style-type: none"> BCVS is currently limited for verification of certificates from OOU generated from the system. The security and functionality of the system is dependent on the blockchain platform used. Maintenance of the system requires specialized knowledge of web3 technologies, which could serve as a barrier for administrators and developers in charge. 	<ul style="list-style-type: none"> Adoption of the BCVS may face resistance from institutions due to the technicality of blockchain systems, and reluctance to change from already existing processes. Rapid advancements in technology could require new integrations to the system or else could potentially make the system obsolete. Changes in regulation or policies related to data privacy and blockchain technology could impact the operation or viability of the system.

Figure 11: SWOT Analysis.

Source: Authors, (2024).

The BCVS focuses on certificate verification. It only inherently supports other documents if incorporated into the code base. The system's security fundamentally depends on the underlying blockchain platform, the hosting provider, and the database used for metadata storage. Therefore, any vulnerabilities or potential breaches in these areas could compromise the system's integrity.

IV. CONCLUSION

This project aims to develop an efficient and scalable certificate verification system for Olabisi Onabanjo University that can issue and verify certificates through the Celo blockchain platform. The system is designed to cater to university

requirements and can revoke certificates. It represents an advancement in certificate verification, simplifying the process and improving the overall experience for everyone involved. The user evaluation result revealed an acceptance with a recommendation for regular maintenance.

The user's recommendations to improve BCVS include strengthening security measures, integrating additional document verification, and improving the user experience. As blockchain technology continues to advance, there are possibilities to improve the system's abilities and expand its usage to many other universities and industries besides Nigeria and Africa's education sector.

V. AUTHOR'S CONTRIBUTIONS

Conceptualization: Tolulope Ifeyemi, Ajibola Oyedeji and Fiyinfoluwa Adebisi

Methodology: Tolulope Ifeyemi, Ajibola Oyedeji and Fiyinfoluwa Adebisi

Investigation: Tolulope Ifeyemi, Ajibola Oyedeji and Fiyinfoluwa Adebisi

Discussion of results: Tolulope Ifeyemi, Ajibola Oyedeji and Fiyinfoluwa Adebisi

Writing: Tolulope Ifeyemi, Ajibola Oyedeji and Fiyinfoluwa Adebisi

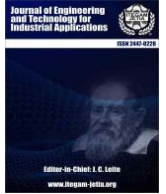
Supervision: Tolulope Ifeyemi, Ajibola Oyedeji and Fiyinfoluwa Adebisi

Approval of the final text: Tolulope Ifeyemi, Ajibola Oyedeji and Fiyinfoluwa Adebisi

VI. REFERENCES

- [1] S. I. Mouno, T. Rahman, A. M. Raatul, and N. afees Mansoor, "Blockchain-Enhanced Academic Certificate Verification: A Decentralized and Trustworthy Framework," in *2024 International Conference on Advances in Computing, Communication, Electrical, and Smart Systems (iCACCESS)*, Mar. 2024, pp. 1–5, doi: 10.1109/iCACCESS61735.2024.10499524.
- [2] A. Rustemi, F. Dalipi, V. Atanasovski, and A. Risteski, "A Systematic Literature Review on Blockchain-Based Systems for Academic Certificate Verification," *IEEE Access*, vol. 11, 2023, doi: 10.1109/ACCESS.2023.3289598.
- [3] O. S. Saleh, O. Ghazali, and M. E. Rana, "Blockchain based framework for educational certificates verification," *Journal of Critical Reviews*, vol. 7, no. 3, 2020, doi: 10.31838/jcr.07.03.13.
- [4] S. Pathak, V. Gupta, N. Malsa, A. Ghosh, and R. N. Shaw, "Blockchain-Based Academic Certificate Verification System—A Review," 2022, pp. 527–539.
- [5] A. O. Oyedeji, O. Folorunsho, O. R. Abolade, and N. I. Eighbiremonlen, "Development of a web-based system for matching losers and finders of personal items," *Mindanao J. Sci. Technol.*, vol. 19, no. 1, pp. 293–306, 2021, doi: 10.61310/mndjsteect.1006.21.
- [6] L. Zhang, L. Ci, Y. Wu, and B. Wiwatanapataphee, "The real estate time-stamping and registration system based on Ethereum blockchain," *Blockchain Res. Appl.*, vol. 5, no. 1, p. 100175, Mar. 2024, doi: 10.1016/j.bcr.2023.100175.
- [7] G. Habib, S. Sharma, S. Ibrahim, I. Ahmad, S. Qureshi, and M. Ishfaq, "Blockchain Technology: Benefits, Challenges, Applications, and Integration of Blockchain Technology with Cloud Computing," *Futur. Internet*, vol. 14, no. 11, p. 341, Nov. 2022, doi: 10.3390/fi14110341.
- [8] A. Al Hussain, M. A. Emon, T. A. Tanna, R. I. Emon, and M. M. H. Onik, "A Systematic Literature Review of Blockchain Technology Adoption in Bangladesh," *Ann. Emerg. Technol. Comput.*, vol. 6, no. 1, pp. 1–30, Jan. 2022, doi: 10.33166/AETIC.2022.01.001.
- [9] T. Ahram, A. Sargolzaei, S. Sargolzaei, J. Daniels, and B. Amaba, "Blockchain technology innovations," in *2017 IEEE Technology & Engineering Management Conference (TEMSCON)*, Jun. 2017, pp. 137–141, doi: 10.1109/TEMSCON.2017.7998367.

- [10] S. H. Ammous, "Blockchain Technology: What is it Good for?," *SSRN Electron. J.*, 2016, doi: 10.2139/ssrn.2832751.
- [11] N. Malsa, V. Vyas, J. Gautam, A. Ghosh, and R. N. Shaw, "CERTbchain: A Step by Step Approach Towards Building A Blockchain based Distributed Appliaction for Certificate Verification System," in *2021 IEEE 6th International Conference on Computing, Communication and Automation (ICCCA)*, Dec. 2021, pp. 800–806, doi: 10.1109/ICCCA52192.2021.9666311.
- [12] Y. C. Elloh Adja, B. Hammi, A. Serhrouchni, and S. Zeadally, "A blockchain-based certificate revocation management and status verification system," *Comput. Secur.*, vol. 104, p. 102209, May 2021, doi: 10.1016/j.cose.2021.102209.
- [13] S. Pu and J. S. L. Lam, "The benefits of blockchain for digital certificates: A multiple case study analysis," *Technol. Soc.*, vol. 72, 2023, doi: 10.1016/j.techsoc.2022.102176.
- [14] F. Casino, T. K. Dasaklis, and C. Patsakis, "A systematic literature review of blockchain-based applications: Current status, classification and open issues," *Telemat. Informatics*, vol. 36, pp. 55–81, Mar. 2019, doi: 10.1016/j.tele.2018.11.006.
- [15] S. Alangari, S. M. Alshahrani, N. A. Khan, A. A. Alghamdi, J. Almalki, and W. Al Shehri, "Developing a blockchain-based digitally secured model for the educational sector in Saudi Arabia toward digital transformation," *PeerJ Comput. Sci.*, vol. 8, 2022, doi: 10.7717/PEERJ-CS.1120.
- [16] T. Thakare, T. Phatak, G. Wadhani, T. Karotra, and R. L. Priya, "Verifyate – Transforming Certificate Verification Using Blockchain Technology," *Signals Commun. Technol.*, vol. Part F2283, pp. 211–220, 2024, doi: 10.1007/978-3-031-49593-9_12.
- [17] K. Kumutha and S. Jaya lakshmi, "The Impact of the Blockchain on Academic Certificate Verification System-Review," *EAI Endorsed Trans. Energy Web*, p. 169426, Jul. 2018, doi: 10.4108/eai.29-4-2021.169426.
- [18] A. O. Oyedeji, M. O. Osifeko, O. Folorunsho, O. R. Abolade, and O. O. Ade-Ikuesan, "Design and Implementation of a Medical Diagnostic Expert System," *J. Eng. Sci.*, vol. 10, no. 2, pp. 103–109, 2019, [Online]. Available: <https://www2.kuet.ac.bd/JES/>.
- [19] cLabs, "Celo: A Multi-Asset Cryptographic Protocol for Decentralized Social Payments," 2018.
- [20] H. Rawhouser *et al.*, "Scaling, blockchain technology, and entrepreneurial opportunities in developing countries," *J. Bus. Ventur. Insights*, vol. 18, p. e00325, Nov. 2022, doi: 10.1016/j.jbvi.2022.e00325.
- [21] K. Chodorow, "MongoDB: The Definitive Guide: Powerful and Scalable Data Storage," p. 432, 2013, [Online]. Available: https://books.google.co.uk/books?hl=en&lr=&id=uGUKiNkKRJ0C&oi=fnd&pg=PP1&dq=MongoDB&ots=h9mwLfcRAf&sig=JyYXcMiVgJ4rLC_FUvKE10fgwpA.



RESEARCH ARTICLE

OPEN ACCESS

LOAD FLOW, SHORT CIRCUIT AND MOTOR STARTING STUDIES IN ELECTRICAL POWER SUBSTATIONS

Mohan Muniappan.

Lead Engineer, GE Renewable Energy, Dresden, Germany.

<http://orcid.org/0000-0001-8209-5610>

Email: mohanbe.m@gmail.com

ARTICLE INFO

Article History

Received: June 16th, 2024

Revised: September 05th, 2024

Accepted: September 05, 2024

Published: September 04, 2024

Keywords:

Power System Studies,
Power Flow,
Short Circuit Faults,
Motor Starting,
Switching Transients.

ABSTRACT

Power system studies are essential for the proper planning and design of electrical power substations. This paper presents the load flow, short circuit, and motor starting studies for 33/6.6/0.44 kV electrical power substation. In this paper, the load flow study calculates the active power, reactive power, and bus voltage at various locations of the substation under various operating conditions and configurations. The short circuit study evaluates the transient performance of the substation under various fault conditions such as phase-to-ground fault and three-phase-to-ground fault cases. The motor starting studies analyze the transient performance of the substation while switching the induction motors. The modeling of 33/6.6/0.44 kV electrical power substation and simulation case studies are performed in PSCAD/EMTDC software. The simulation results show the steady state and transient performance of the substation under such scenarios.



Copyright ©2024 by authors and Galileo Institute of Technology and Education of the Amazon (ITEGAM). This work is licensed under the Creative Commons Attribution International License (CC BY 4.0).

I. INTRODUCTION

Power system studies are very important for the design of electrical power substations which can be done during the planning stage. The power system simulation platform provides the opportunity to analyze the performance of the electrical power substations under steady state and transient situations by performing a variety of power system studies.

Reference [1] has presented the load flow study of a 132 kV substation in Punjab State Transmission Corporation Limited (PSTCL). The short circuit study of the 400 kV soja substation is presented in [2]. The load flow & short circuit study of the 110/20 kV substation in Romania is presented in [3-5]. The short circuit study of the Brazilian power distribution system is presented in [6]. The load flow study of the 138/69 kV substation is presented in [7]. The load flow analysis of the 132/11 kV substation in Pakistan is presented in [8]. Reference [9] has presented the load flow and short circuit study of a 220/63/30 kV substation in Algeria which is managed by the Sonelgaz group's transmission network management company (GRTE). Reference [10] has presented the load flow and short circuit study of the 132/33/11 kV substation in West Bengal which is owned by West Bengal State Electricity Transmission Corporation Limited (WBSETCL). The

short circuit study of the 33/11 kV Alomara substation is presented in [11]. The comparative load flow study of the 400/230 kV substation in Bangladesh is presented in [12]. The load flow and short circuit study of the electrical power distribution system in Iraq is presented in [13]. Reference [14] has presented the load flow study of a 66 kV substation in Trivandrum which is managed by Kerala State Electricity Board Limited (KSEB). The short circuit study of the 132/33 kV substation in Nigeria is presented in [15]. The load flow and short circuit study of the 132/33 kV Mawlai Nongkwar Substation is presented in [16]. The motor starting study for the substation and power plant is presented in [17-22].

In this paper, the power system studies such as load flow, short circuit, and motor starting studies are performed by considering the case study of 33/6.6/0.44 kV electrical power substation. These studies are performed in PSCAD/EMTDC software considering different operating scenarios and then the PSCAD result data are processed in MATLAB software. This paper is more related to the consulting business on power system studies which may be helpful for many power system consultants and engineers to refer to these studies.

This paper is organized as follows. Section 1 presents the importance and considerations for the load flow, short circuit, and motor starting studies. Section 2 presents the modeling of the

electrical power substation considered for the case study. Section 3 presents the simulation cases, results, and analysis for the load flow, short circuit, and motor starting studies. Finally, Section 4 concludes with the important observations.

II. POWER SYSTEM STUDIES

In this section, the following power system studies are explained.

- Load flow studies.
- Short circuit studies.
- Motor starting studies.

II.1. LOAD FLOW STUDIES

Load flow is commonly referred to as power flow and it is one of the most common studies to assess the steady-state performance of the electrical power substation under various operating conditions and configurations. The objective of load flow studies is to determine the voltage, current, active, and reactive power flow, power factor, voltage drop, and losses for all the buses of the system.

Load flow studies are very important for the following requirements [23], [24]:

- Power system planning, design, and operation. It can be used to determine the optimum size of the equipment in the system.
- To determine the steady state performance under different loading conditions (start-up, minimum, normal, and maximum), and various operating configurations (generator/transmission line/load outages, tie-breaker closed, etc).
- Load flow studies are the initial condition for short circuit, transient stability, harmonic, protection coordination, and motor starting studies.
- To identify the requirement of capacitive or inductive VAR support to maintain the voltage within acceptable limits.
- To determine the transformer and load tap settings and voltage set points for the generator exciter/regulator.

The following study scenarios can be considered for the load flow studies [24]. However, it may vary depending on the configuration of the electrical power substation.

- Power generation sources can be in and out of service.
- The minimum and maximum loading conditions.
- The capacitor banks can be in and out of service.
- The outage of transformers can be considered.
- The load flow study can consider the following criteria while the engineer performs the study [23]:
- Voltage levels can be maintained as per the standard.
- The power flow of the transmission lines and transformers can be within the thermal limits.
- The reactive power limits of the generator can be maintained as per the capability curves.

II.2. SHORT CIRCUIT STUDIES

The short circuit is an abnormal connection of relatively low impedance between two points of different potentials. Hence, an overcurrent (i.e., short circuit current) will flow into the system which can damage the power system equipment. Short circuit faults can occur in the electrical power substations due to loose connection, insulation failure, aging of insulation, voltage or mechanical stress applied to the equipment, lightning strikes, wind storms, presence

of animals such as birds. The short circuit studies can be used to determine the transient behavior of the electrical power substation under short circuit or fault conditions. This study helps to determine the total fault current and fault current contribution sources such as power grids, generators, and motors.

The main purpose of short circuit studies is given below [23], [25], [26]:

- To determine the maximum possible fault current which helps to determine the protective device interrupting capability.
- To design the equipment rating of new systems such as bus bars, transformers, cables, and protective devices.
- To verify the acceptable equipment rating of existing systems.
- To calculate the incident energy for arc flash studies.

The short circuit contribution mainly depends on the operating level of generations and loads, system impedance, operating configuration of electrical power substation, and transient behavior of power system components. The study scenarios for short circuit studies can be the minimum and maximum short circuit contributions and operating configurations of electrical power substations.

II.3. MOTOR STARTING STUDIES

Improper motor starting can damage the motor, create disturbance to the locally connected loads and buses, power quality issues, and service interruptions. Therefore, motor starting studies are recommended before installation. The objective of motor starting studies is to check whether the motor can be started successfully under various operating conditions. Motor starting studies are required if the motor horsepower rating exceeds 30% of the base kVA rating of the supplying transformer or 10% to 15% of the generator kVA rating if there is no transformer.

The main purpose of motor starting studies are to verify that [23], [27]:

- The motor can be started within the acceptable voltage drop and it will not affect other loads.
- The motor can be started within the acceptable start-up time.
- The speed-torque and thermal characteristics of the motor are evaluated correctly.
- The motor feeders are properly sized.
- The protection device for the motor is set properly such that the motor will not trip during start-up.
- Identifying the type and size of the starter/drive to start the motor.

The study scenario for the motor starting studies can be the minimum and maximum voltage support sources from the electrical power substation.

III. ELECTRICAL POWER SUBSTATION MODEL

The electrical power substation model considered for the case study is shown in Figure 1 and it is modeled in PSCAD/EMTDC software. In this model, the 33 kV AC network is connected to the 16 MVA, 33/6.6 kV transformers through cables and then it is connected to the 6.6 kV bus. The 6.6 kV bus is connected to the induction motor loads & capacitor banks. Also, it is connected to the 0.44 kV bus through 2 MVA, 6.6 kV/0.44 kV transformers & cables. Then, the 0.44 kV bus is connected to the lumped RL loads.

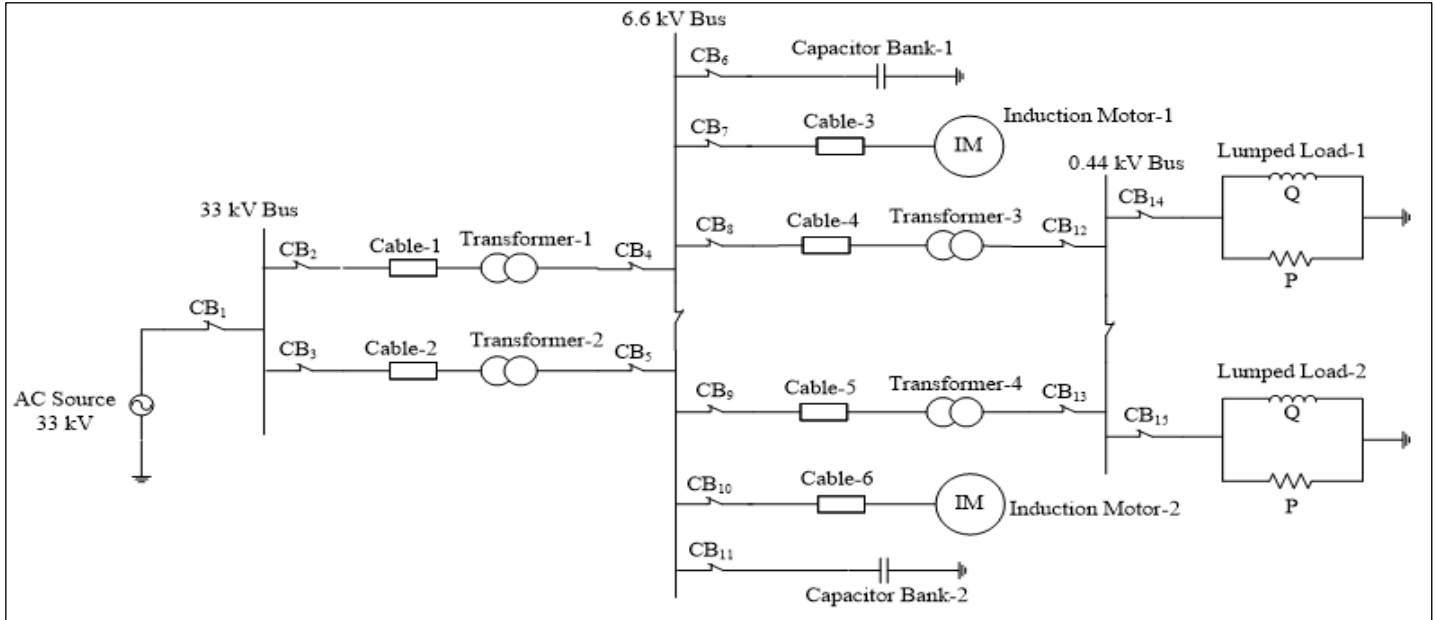


Figure 1: Electrical Power Substation Model. iFluids Engineering. Source: Author, (2024).

III.1. AC NETWORK & POWER TRANSFORMER MODEL

The AC network model is represented as an AC source with an equivalent short circuit MVA. The AC network impedance is represented by the impedance with an equivalent X/R ratio. The AC network parameters are listed in Table 1. The two transformers with different ratings are connected at the 33 kV and 6.6 kV buses. The transformer parameters are listed in Table 2.

Table 1: AC Network Parameters.

System Parameters	Value
Short circuit MVA	817.93 MVA
System voltage	33 kV
Source impedance (Z = R+jX)	Z = 1.69+j12.1 Ω R = 1.69 Ω & L = 38.5 mH
X/R ratio	7.147
Frequency	50 Hz

Source: Author, (2024).

Table 2: Transformers Parameters.

System Parameters	Transformer-1	Transformer-2
Rated MVA	16 MVA	2 MVA
Rated voltage	33/6.6 kV	6.6/0.44 kV
Impedance	6.4 %	6.25 %
Winding type	Δ/Y	Δ/Y
Frequency	50 Hz	50 Hz

Source: Author, (2024).

III.2. AC CABLE MODEL

The two cables are connected between the 33 kV bus and transformers. Also, the four cables are connected between 6.6 kV bus and 2 MVA transformers, and 3000 kW induction motor loads. Since all the cables are very short distance by length, the cable is represented by the equivalent impedance (i.e., resistance and reactance). The cable parameters are listed in Table 3.

Table 3: AC Cable Parameters.

System Parameters	Value
Equivalent impedance for Cable 1 & 2	0.1756+j0.2826 Ω
Equivalent impedance for Cable 3	0.0215+j0.0171 Ω
Equivalent impedance for Cable 4	0.0025+j0.0019 Ω
Equivalent impedance for Cable 5	0.003+j0.0023 Ω
Equivalent impedance for Cable 6	0.0235+j0.0187 Ω

Source: Author, (2024).

III.3. LOAD MODEL

The two types of loads such as induction motor loads and lumped RL loads are connected to the study substation. The induction motor loads are connected to the 6.6 kV bus. The lumped RL loads are connected to the 0.44 kV bus.

III.3.1. Induction Motor Loads

The motor loads are modeled as a squirrel cage induction motor with a rating of 3000 kW, 6.6 kV. In this motor model, the machine is set to be torque input (control) mode with slip and initial speed set to zero. The mechanical load characteristics greatly influence the starting response of the motor. The mechanical torque is directly proportional to the square of the speed. This equation is modeled and given as input to the mechanical torque of the motor. The induction motor parameters are listed in Table 4.

III.3.2. Lumped RL Loads

The lumped loads are modeled as passive loads such as resistive (R) and inductive (L) loads. The lumped loads are connected to the 0.44 kV bus. The lumped RL load parameters are listed in Table 5.

III.4. CAPACITOR BANKS MODEL

The two capacitor banks (i.e., capacitor bank-1 & capacitor bank-2) are connected at the 6.6 kV bus and the rating of the capacitor banks are 250 kVAR. The capacitor bank parameters are listed in Table 6.

Table 4: Induction Motor Parameters.

System Parameters	Value
Rated power	3000 kW
Rated voltage	6.6 kV
Frequency	50 Hz
Power factor at rated load in per unit	0.9
Efficiency at rated load in per unit	0.955
Starting current	7.1 per unit
Starting torque/Full load torque	2.9 per unit
Maximum torque/Full load torque	2.8 per unit
Number of poles	2
Moment of inertia (J)	76.3 kJ/m ²
Slip at full load	0.0083 per unit

Source: Author, (2024).

Table 5: Lumped Load Parameters.

System Parameters	Lumped Load-1	Lumped Load-2
Active Power & Reactive Power	287.3 kW 220.9 kVAR	154.4 kW 139.8 kVAR
Frequency	50 Hz	50 Hz
Rated voltage	415 V	415 V

Source: Author, (2024).

Table 6: Capacitor Banks Parameters.

System Parameters	Value
Reactive power rating	$Q_c = V^2/X_c = 250 \text{ kVAR}$
Capacitor value	$C = Q_c/\omega V^2 = 18.2 \mu\text{F}$
Rated voltage	6.6 kV
Frequency	50 Hz

Source: Author, (2024).

IV. SIMULATION STUDIES

In this section, the simulation analysis for the load flow, short circuit, and motor starting studies under various operating conditions are presented.

IV.1. LOAD FLOW ANALYSIS

The load flow analysis is performed for the following cases:

- Normal Operation: Maximum Loading Conditions
- Minimum Loading Conditions: Outage of Induction Motor Loads
- Outage of Transformers

IV.1.1. Normal Operation: Maximum Loading Conditions

In this case, the load flow analysis is performed for the maximum loading conditions (i.e., with all the transformers and loads). The simulation analysis is performed for two cases such as without and with capacitor banks connected at 6.6. kV bus.

Case-1: Without Capacitor Banks at 6.6. kV Bus: In Case-1, the induction motors and lumped loads are loaded at the maximum level and the two capacitor banks are removed from the 6.6 kV bus. The active power, reactive power, bus voltage, and power factor measured at various locations of the substation are shown in Table

7. From the simulation results, it can be observed that the AC voltage at 6.6 kV bus is reduced to 6.56 kV and the AC voltage at 0.44 kV bus is also reduced due to the maximum loading of the induction motors.

Case-2: Capacitor Banks Connected at 6.6. kV Bus: In Case-2, the induction motors and lumped loads are loaded at the maximum level and the two capacitor banks are connected to the 6.6 kV bus. The active power, reactive power, bus voltage, and power factor measured at various locations of the substation are shown in Table 7. From the simulation results, it can be observed that the AC voltage at the 6.6 kV bus is reduced to 6.56 kV and the AC voltage at 0.44 kV bus is also reduced due to the maximum loading of the induction motors. The active power and power factor measured at the CB₆ and CB₁₁ are equivalent to zero because these branches are connected to the capacitor banks. The power factor measured at 33 kV bus is improved due to the capacitor banks connected to the substation.

IV.1.2. Minimum Loading Conditions: Outage of Induction Motor Loads

In this case, the load flow analysis is performed for the minimum loading conditions such as the outage of two induction motor loads. The lumped loads are connected to the 0.44 kV bus. The simulation analysis is performed for two cases such as without and with capacitor banks connected at 6.6. kV bus.

Case-1: Without Capacitor Banks at 6.6. kV Bus: In Case-1, the two induction motor loads and capacitor banks are removed from the 6.6 kV bus. The active power, reactive power, bus voltage, and power factor measured at various locations of the substation are shown in Table 8. From the simulation results, it can be observed that the AC voltage at the 6.6 kV and 0.44 kV bus are improved due to the removal of induction motor loads. Also, the measurements at CB₇ and CB₁₀ are not mentioned in Table 8 due to the outage of induction motor loads.

Case-2: Capacitor Banks Connected at 6.6. kV Bus: In Case-2, the induction motor loads are removed from the 6.6 kV bus and the capacitor banks are connected to the 6.6. kV bus. The active power, reactive power, bus voltage, and power factor measured at various locations of the substation are shown in Table 8. From the simulation results, it can be observed that the AC voltage at the 6.6 kV and 0.44 kV buses are improved when compared to Case-1 due to the capacitor banks. The measurements at CB₇ and CB₁₀ are not mentioned due to the removal of induction motor loads. The active power and power factor measured at the CB₆ and CB₁₁ are equivalent to zero because these branches are connected to the capacitor banks. Also, the power factor measured at 33 kV bus is improved.

IV.1.3. Outage of Transformers

In this case, the load flow analysis is performed for the outage of two transformers such as transformer-2 and transformer-4. The simulation analysis is performed for two cases such as without and with capacitor banks connected at 6.6. kV bus.

Case-1: Without Capacitor Banks at 6.6. kV Bus: In Case-1, the two transformers (i.e., transformer-2 and transformer-4) and capacitor banks are removed from the substation. The active power, reactive power, bus voltage, and power factor measured at various locations of the substation are shown in Table 9. From the simulation results, it can be noticed that the AC voltage at the 6.6 kV and 0.44 kV buses are reduced due to the induction motor loads.

Also, the measurements at CB₃, CB₅, CB₉ and CB₁₃ are not mentioned due to the outage of transformers.

Table 7: Load Flow Results for Maximum Loading Conditions.

Measurement Locations in Figure 1	Bus Voltage (kV)		Active Power (MW)		Reactive Power (MVAR)		Power Factor	
	Without capacitor banks	With capacitor banks	Without capacitor banks	With capacitor banks	Without capacitor banks	With capacitor banks	Without capacitor banks	With capacitor banks
CB ₁	33	33	6.602	6.584	3.055	2.619	0.9	0.93
CB ₂	33	33	3.301	3.292	1.527	1.309	0.9	0.93
CB ₃	33	33	3.301	3.292	1.528	1.309	0.9	0.93
CB ₄	6.554	6.56	3.303	3.294	1.304	1.089	0.93	0.94
CB ₅	6.554	6.56	3.303	3.294	1.305	1.089	0.93	0.94
CB ₆	-	6.56	-	-	-	0.2461	-	-
CB ₇	6.554	6.56	3.008	2.998	1.089	1.119	0.94	0.94
CB ₈	6.554	6.56	0.2877	0.2882	0.1955	0.1958	0.82	0.82
CB ₉	6.554	6.56	0.3025	0.3031	0.2359	0.2363	0.79	0.79
CB ₁₀	6.554	6.56	3.008	2.999	1.089	1.119	0.94	0.94
CB ₁₁	-	6.56	-	-	-	0.2461	-	-
CB ₁₂	0.4344	0.4348	0.2883	0.2888	0.1711	0.1715	0.85	0.85
CB ₁₃	0.4338	0.4342	0.3031	0.3037	0.2107	0.2111	0.82	0.82
CB ₁₄	0.4311	0.4315	0.222	0.2224	0.149	0.1493	0.83	0.83
CB ₁₅	0.4303	0.4307	0.3628	0.3634	0.2328	0.2333	0.84	0.84

Source: Author, (2024).

Table 8: Load Flow Results for Outage of Induction Motor Loads.

Measurement Locations in Figure 1	Bus Voltage (kV)		Active Power (MW)		Reactive Power (MVAR)		Power Factor	
	Without capacitor banks	With capacitor banks	Without capacitor banks	With capacitor banks	Without capacitor banks	With capacitor banks	Without capacitor banks	With capacitor banks
CB ₁	33	33	0.5857	0.587	0.775	0.2776	0.62	0.91
CB ₂	33	33	0.2931	0.2937	0.3874	0.1387	0.62	0.91
CB ₃	33	33	0.2926	0.2932	0.3876	0.1389	0.62	0.91
CB ₄	6.591	6.598	0.2987	0.2993	0.218	0.03045	0.8	0.99
CB ₅	6.591	6.598	0.2981	0.2988	0.2183	0.03021	0.8	0.99
CB ₆	-	6.598	-	-	-	0.2489	-	-
CB ₈	6.591	6.598	0.2909	0.2915	0.1977	0.1981	0.82	0.82
CB ₉	6.591	6.598	0.3059	0.3066	0.2385	0.239	0.79	0.79
CB ₁₁	-	6.598	-	-	-	0.2489	-	-
CB ₁₂	0.4368	0.4373	0.2916	0.2922	0.1731	0.1734	0.85	0.85
CB ₁₃	0.4363	0.4367	0.3066	0.3072	0.2131	0.2135	0.82	0.82
CB ₁₄	0.4335	0.4339	0.2245	0.225	0.1507	0.151	0.83	0.83
CB ₁₅	0.4327	0.4332	0.3639	0.3676	0.2355	0.236	0.84	0.84

Source: Author, (2024).

Table 10: Load Flow Results for Outage of Transformers.

Measurement Locations in Figure 1	Bus Voltage (kV)		Active Power (MW)		Reactive Power (MVAR)		Power Factor	
	Without capacitor banks	With capacitor banks	Without capacitor banks	With capacitor banks	Without capacitor banks	With capacitor banks	Without capacitor banks	With capacitor banks
CB ₁	33	33	6.593	6.596	2.951	2.459	0.91	0.93
CB ₂	33	33	6.593	6.596	2.951	2.459	0.91	0.93
CB ₄	6.51	6.524	6.584	6.588	2.565	2.083	0.93	0.95
CB ₆	-	6.524	-	-	-	0.2434	-	-
CB ₇	6.51	6.524	3.006	3.006	1.083	1.085	0.94	0.94
CB ₈	6.51	6.524	0.5714	0.5738	0.3979	0.3996	0.82	0.82
CB ₁₀	6.508	6.521	3.006	3.007	1.083	1.085	0.94	0.94
CB ₁₁	-	6.521	-	-	-	0.2432	-	-
CB ₁₂	0.4286	0.4295	0.572	0.5744	0.3623	0.3639	0.84	0.84
CB ₁₄	0.422	0.4229	0.2127	0.2136	0.1428	0.1434	0.83	0.83
CB ₁₅	0.4179	0.4187	0.342	0.3435	0.2196	0.2205	0.84	0.84

Source: Author, (2024).

Case-2: Capacitor Banks Connected at 6.6 kV Bus: In Case-2, the transformers (i.e., transformer-2 and transformer-4) are removed from the substation and the capacitor banks are connected to the 6.6 kV bus. The active power, reactive power, voltage, and power factor measured at various locations of the substation are shown in Table 9. From the simulation results, it can be noticed that the AC voltage at the 6.6 kV and 0.44 kV buses are improved when compared to Case-1 due to the capacitor banks. The measurements at CB₃, CB₅, CB₉ and CB₁₃ are not mentioned due to the outage of transformers. The active power and power factor measured at the CB₆ and CB₁₁ are equivalent to zero because these branches are connected to the capacitor banks. Also, the power factor measured at 33 kV bus is improved.

IV.2. SHORT CIRCUIT ANALYSIS

For the short circuit analysis, the maximum short circuit contributions are considered since it is the worst-case scenario. The simulation cases are given below:

- Three-Phase-to-Ground Fault
 - Three-Phase-to-Ground Fault and Breaker Trip
- Phase to Ground Fault
 - Single Phase-to-Ground Fault and Breaker Trip

IV.2.1. Three-Phase to Ground Fault

For this case study, the presence of transformers, loads such as induction motors and lumped loads, and capacitor banks are considered. The three-phase-to-ground fault is applied at 2 sec in between CB₈ and cable-4. After the fault, the circuit breakers CB₈ and CB₁₂ are opened at 2.1 sec. The fault resistance is 0.01 Ω. The response measured at 6.6 kV bus CB₈ location is shown in Figure 2.

From the simulation results, it can be observed that the peak value of the phase voltage (V_{AC}) is reduced from 5.35 kV to 0.85 kV during fault (i.e., 2 to 2.1 sec). The peak value of phase voltage is increased to 12 kV at 2.1 sec due to the switching operation of the circuit breaker and capacitor banks. The peak value of phase current (I_{AC}) is increased up to 84 kA at the first cycle and the steady state peak phase current is around 55 kA during fault. The active power (P) is increased up to 129 MW at the first spike and then the steady state oscillation around 71 MW during fault. The reactive power (Q) is varied up to 147 MVAR during the breaker trip. The reactive power is ramped down and reached the steady state value at 2.14 sec. The active power is increased to the abnormal value due to the increment of the fault current.

The response measured at the 33 kV bus CB₁ location is shown in Figure 3. From the simulation results, it can be observed that the AC voltage (V_{AC}) measured at the 33 kV bus CB₁ location is not affected due to the fault on 6.6 kV bus. The peak value of phase current (I_{AC}) is increased up to 16.58 kA at the first cycle and the steady state peak phase current is around 11.2 kA during fault. The active power (P) is increased up to 269 MW at the first spike and then the steady state oscillation around 105 MW during fault. The reactive power (Q) is increased up to 505 MVAR and then the steady state oscillation around 443 MVAR during fault. The reactive power is reached the steady state value at 2.13 sec. The active and reactive power is increased to the abnormal value due to the increment of the fault current.

Under the 3-phase-to-ground fault, the transient response of the substation is almost the same for without and with capacitor banks cases. Therefore, this paper has presented only the response of the substation with capacitor banks under the 3-phase-to-ground fault condition.

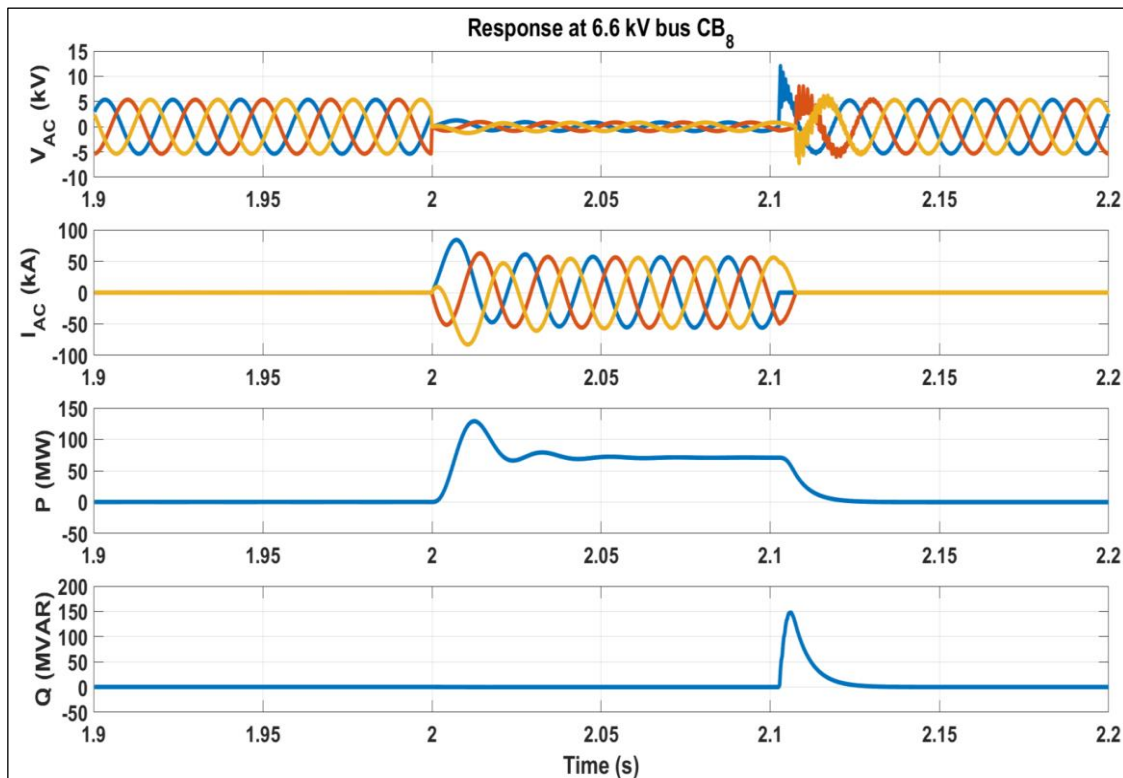


Figure 2: Response at 6.6 kV bus CB₈ location due to 3-phase-to-ground fault. Source: Author, (2024).

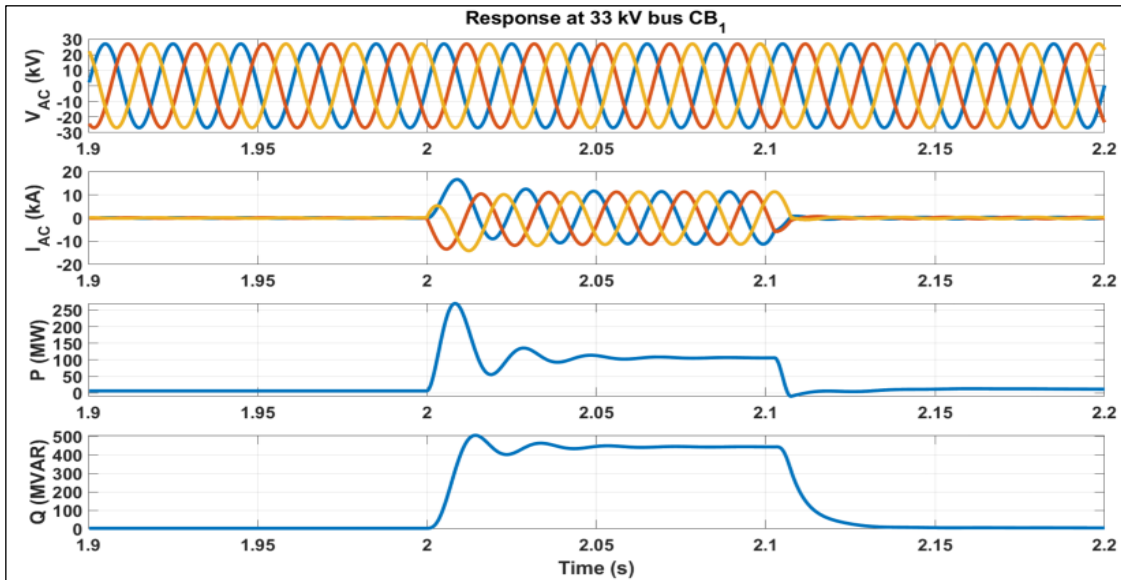


Figure 3: Response at 33 kV bus CB₁ location due to 3-phase-to-ground fault. Source: Author, (2024).

IV.2.2. Single Phase to Ground Fault

For this case study, the presence of transformers, loads such as induction motors and lumped loads, and capacitor banks are considered. Phase A to ground fault is applied at 2 sec in between CB₈ and cable-4. After the fault, the circuit breakers CB₈ and CB₁₂ are opened at 2.1 sec. The fault resistance is 1 Ω.

The response measured at the 6.6 kV bus CB₈ location is shown in Figure 4. From the simulation results it can be observed that the peak value of phase voltage (V_{AC}) is reduced from 5.35 kV to 0.94 kV during fault (i.e., 2 to 2.1 sec). At the same time, the voltage on the other 2 healthy phases is increased higher than the rated value (i.e., temporary overvoltage). The peak value of phase B voltage is increased to 8.35 kV and the peak value of phase C voltage is increased to 8.58 kV. The peak value of phase current (I_{AC}) is increased up to 1.1 kA at the first cycle and the steady state peak phase current is around 0.978 kA during fault. The active power (P) is increased up to 0.87 MW and the reactive power (Q)

is increased up to 0.9 MVAR during fault. The active and reactive power is reached the steady state value at 2.136 sec.

The response measured at the 33 kV bus CB₁ location is shown in Figure 5. From the simulation results, it can be observed that the AC voltage (V_{AC}) measured at the 33 kV bus CB₁ location is not affected due to fault on the 6.6 kV bus. The peak value of phase A current (I_{AC}) is increased to 0.24 kA and the peak value of phase B current is also increased to 0.27 kA during fault. The active power (P) is increased up to 9.85 MW and the reactive power (Q) is increased up to 3 MVAR during fault. The active and reactive power is reached the steady state value around 2.125 sec.

Under the single-phase to ground fault condition, the transient response of the substation is almost the same for without and with capacitor banks cases. Therefore, this paper has presented only the response of the substation with capacitor banks under the 1-phase to ground fault condition.

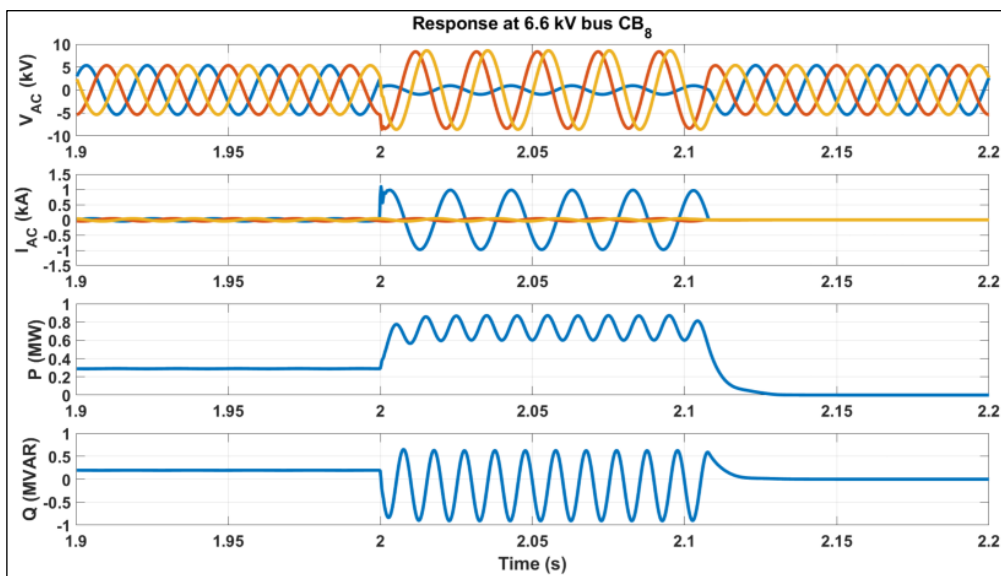


Figure 4: Response at 6.6 kV bus CB₈ location due to phase A to ground fault. Source: Author, (2024).

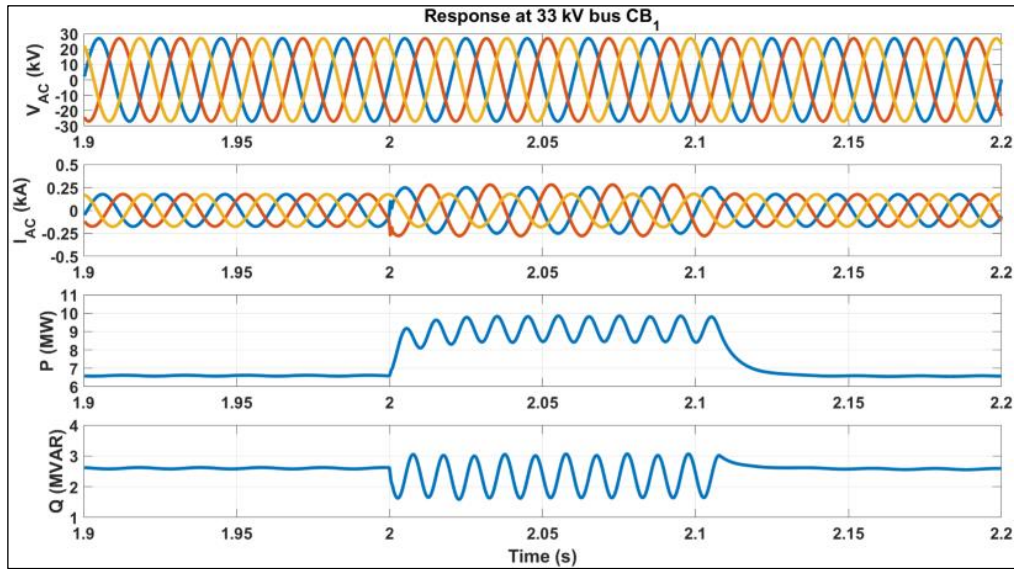


Figure 5: Response at 33 kV bus CB₁ location due to phase A to ground fault.
Source: Author, (2024).

IV.3. MOTOR STARTING ANALYSIS

For the motor starting analysis, the response of the substation is analyzed under the starting of one and two induction motor loads. The simulation cases are given below:

- Starting of induction motor 1
- Starting of induction motors 1 and 2

IV.3.1. Starting of Induction Motor-1

In this case, the performance of the substation is analyzed under the starting operation of induction motor-1 (CB₇ branch). For this study, the presence of AC source, transformers, transmission lines, and lumped loads are considered. Also, the capacitor bank-1 at branch CB₆ is connected to the substation. The induction motor-2 at branch CB₁₀ and the capacitor bank-2 at branch CB₁₁ are removed from the substation. The induction motor-1 is started at 1 sec by closing the circuit breaker CB₇. The response of the substation due to the start-up of induction motor-1 is shown in Figure 6.

Figure 6 (a) shows the response measured at the 6.6 kV bus CB₇ location. During motor start-up, the line-to-line RMS voltage (V_{rms}) is reduced from 6.6 kV to 6.3 kV and the RMS current (I_{rms}) is increased to 2.08 kA. The active power (P) measured at CB₇ is increased to 13.16 MW and the reactive power (Q) is varied to 19.53 MVAR. The line-to-line RMS voltage, RMS current, active and reactive power are recovered back to the steady state value at around 2.25 sec.

Figure 6 (b) shows the response of induction motor-1 during start-up. The electrical torque (T_e) is increased up to 5.8 per unit with an oscillatory transient. The mechanical torque (T_m) and speed (ω) are increased in a ramp manner and reached the steady state at around 2.25 sec.

Figure 6 (c) shows the response measured at the 33 kV bus CB₁ location. The line-to-line RMS voltage (V_{rms}) at the 33 kV bus is not affected due to the motor start-up at the 6.6 kV bus. But the RMS current is increased to 0.428 kA, the active power (P) is increased to 13.98 MW, and the reactive power (Q) is increased to 21.12 MVAR. Therefore, the AC current, active and reactive power at 33 kV bus has been affected significantly due to induction motor-1 starting at 6.6 kV bus.

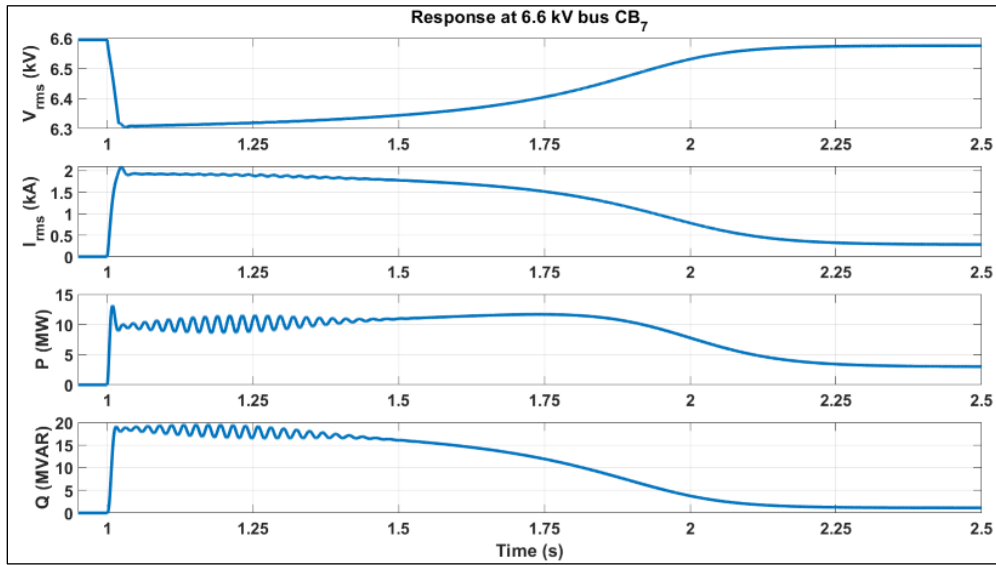
IV.3.2. Starting of Induction Motor 1 and 2

In this case, the performance of the substation is analyzed during the starting operation of induction motor-1 (CB₇ branch) and induction motor-2 (CB₁₀ branch). For this study, the presence of AC source, transformers, transmission lines, lumped loads, and capacitor banks are considered. Also, the capacitor bank-1 at branch CB₆ and capacitor bank-2 at branch CB₁₁ are connected to the substation. The induction motor-1 and induction motor-2 are started at 1 sec by closing the circuit breakers CB₇ and CB₁₀. The response of the substation due to the start-up of induction motor load-1 and induction motor load-2 is shown in Figure 7.

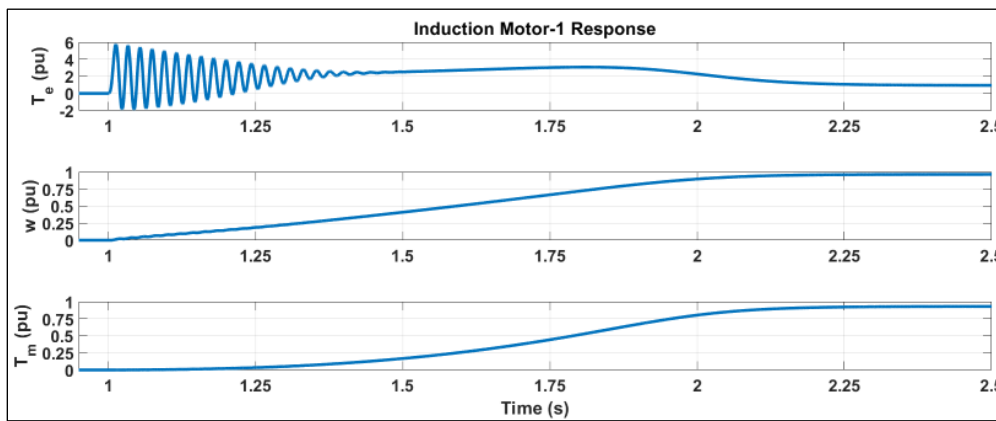
Figure 7 (a) & (c) shows the response measured at the 6.6 kV bus CB₇ & CB₁₀ location. During motors 1 & 2 start-up, the line-to-line RMS voltage (V_{rms}) is reduced from 6.6 kV to 6.044 kV and the RMS current (I_{rms}) is increased to 2.003 kA. The active power (P) is increased to 12.37 MW, and the reactive power (Q) is varied to 17.99 MVAR. The line-to-line RMS voltage, RMS current, active and reactive power are recovered back to the steady state value at around 2.4 sec. Figure 7 (b) & (d) shows the response of the induction motors 1 & 2 during start-up. The electrical torque (T_e) is increased up to 5.41 per unit with an oscillatory transient. The mechanical torque (T_m) and the speed (ω) are increased in a ramp manner and reached the steady state at around 2.25 sec. Also, the transient response measured at 6.6 kV bus CB₇ and CB₁₀ are almost the same.

Figure 7 (e) shows the response at the 33 kV bus CB₁ location. The line-to-line RMS voltage (V_{rms}) at the 33 kV bus is not affected due to the motors 1 & 2 start-up at the 6.6 kV bus. But the RMS current is increased to 0.8 kA, the active power (P) is increased to 26.18 MW, and the reactive power (Q) is varied to 40.16 MVAR. Therefore, the AC current, active and reactive power at 33 kV bus has been affected significantly due to motors 1 & 2 starting at 6.6 kV bus.

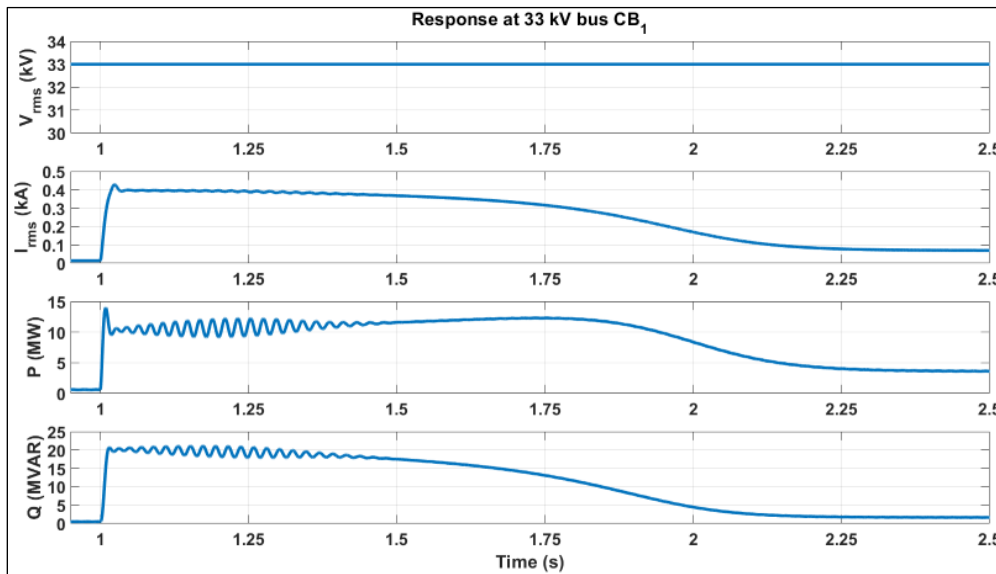
If the two induction motors are started at different times, the transient response (i.e., AC current, active and reactive power) at 33 kV bus is similar to the previous case shown in Figure 6. If the two motors are started at the same time, then the transient response at 33 kV bus is increased twice when compared to the previous case.



(a)



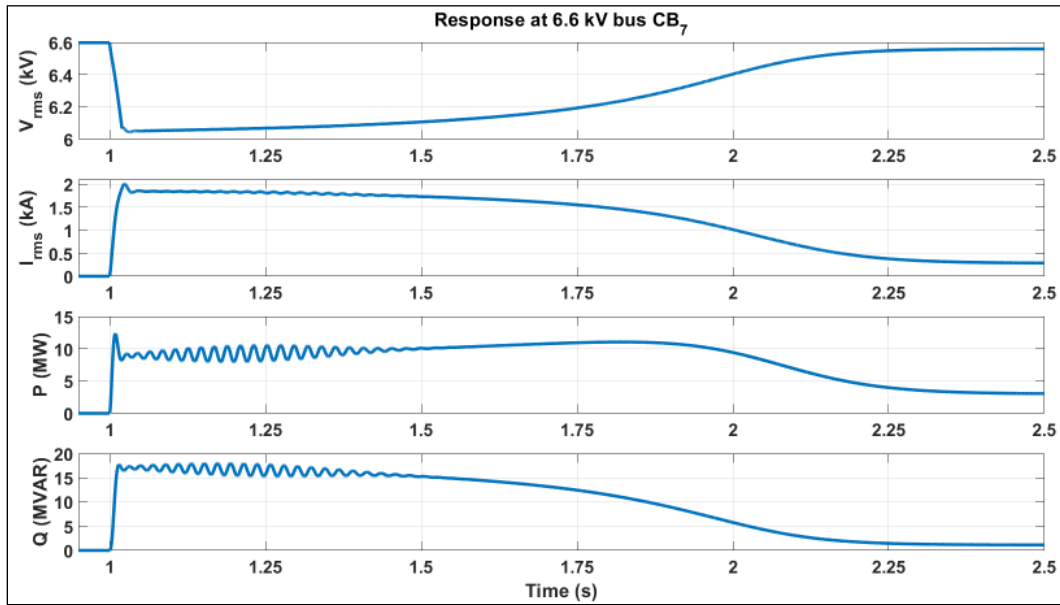
(b)



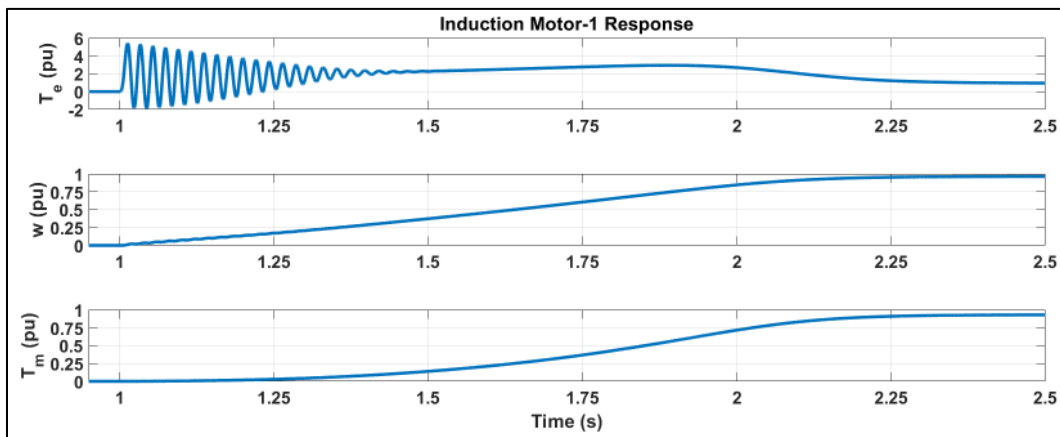
(c)

Figure 6: Response of substation during induction motor-1 start-up. (a) Response at 6.6 kV bus CB₇ location, (b) Induction motor-1 response, (c) Response at 33 kV CB₁ location.

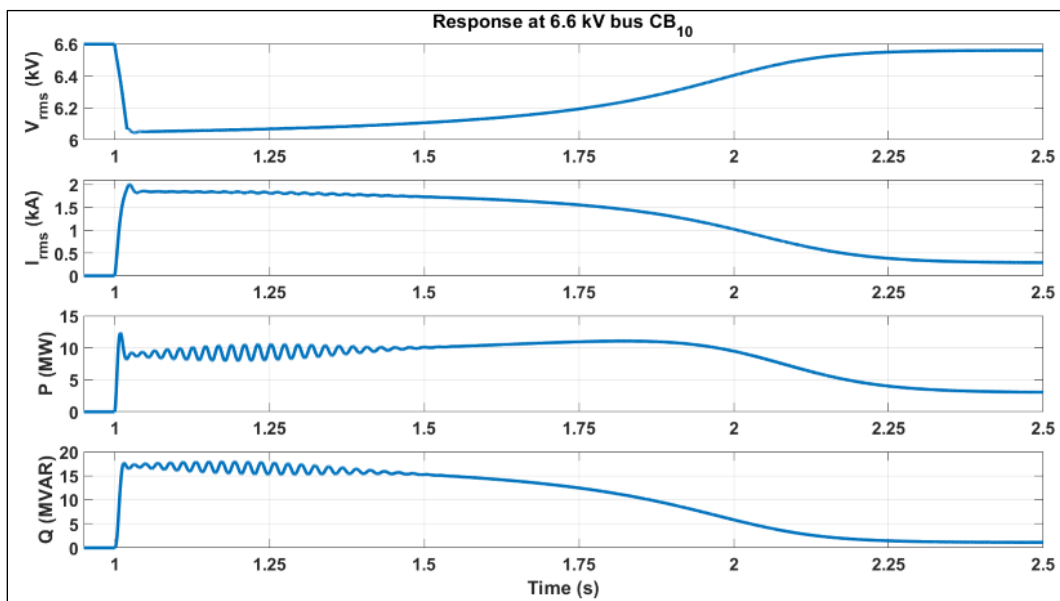
Source: Author, (2024).



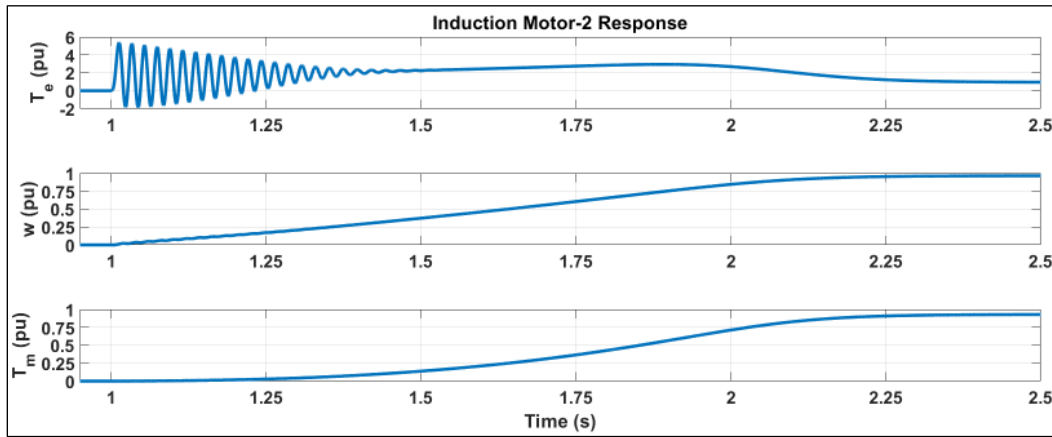
(a)



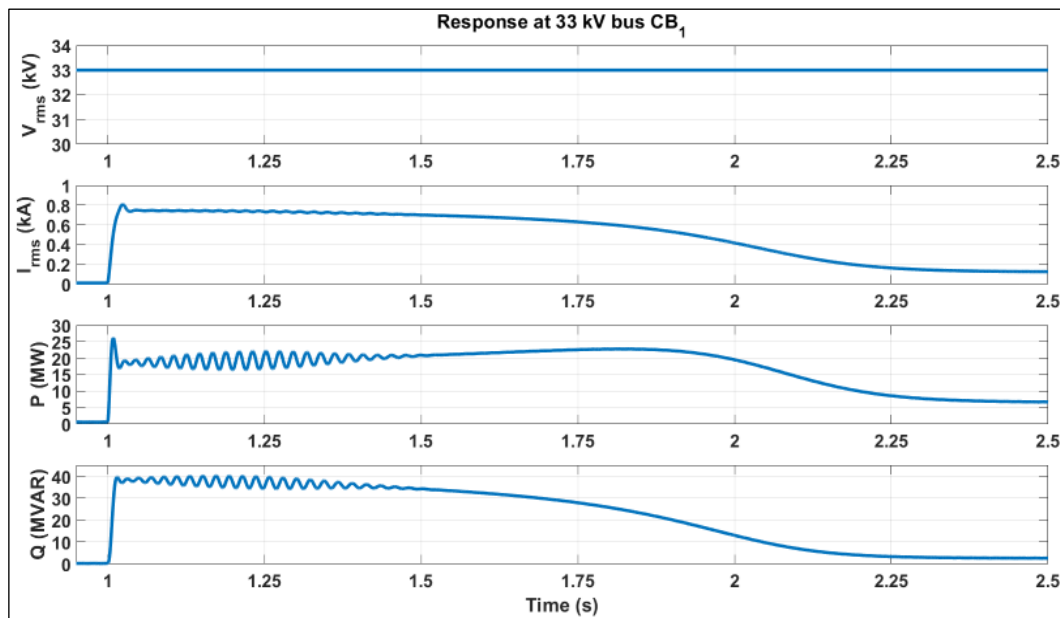
(b)



(c)



(d)



(e)

Figure 7: Response of substation during induction motors 1 & 2 start-up. (a) Response at 6.6 kV Bus CB₇ location, (b) Induction motor-1 response, (c) Response at 6.6 kV Bus CB₁₀ location, (d) Induction motor-2 response, (e) Response at 33 kV CB₁ location. Source: Author, (2024).

V. CONCLUSIONS

In this paper, the load flow, short circuit, and motor starting studies for the 33/6.6/0.44 kV electrical power substation are presented. The observations from those studies are given below:

- The load flow analysis is performed for the maximum and minimum loading and transformer outage conditions considering both without and with capacitor banks. From the simulation results, it can be observed that the AC voltage at 6.6 kV and 0.44 kV buses are reduced due to the induction motors and lumped loads. Also, the power factor at the 33 kV terminal is improved due to the presence of capacitor banks at the 6.6 kV bus.
- The short circuit analysis is performed for the three-phase-to-ground fault and single-phase-to-ground fault cases. From the results, it can be noticed that the fault current, active power, and reactive power at 33 kV and 6.6 kV bus are increased to the abnormal value during three-phase-to-ground fault. The single-phase-to-ground fault has produced temporary overvoltage on the other two healthy phases. However, the single phase-to-ground fault has less

impact on the transient response of the fault current, active power, and reactive power.

- The motor starting analysis is performed for the starting of single and double induction motor load cases. From the results, it can be observed that the starting of the induction motor load has a significant impact on the transient response of the AC current, electrical torque, active power, and reactive power at 6.6 kV and 33 kV bus. Also, the transient response of AC current, active power, and reactive power at 33 kV bus has been doubled when the two induction motors are started at the same time.

VI. AUTHOR'S CONTRIBUTION

Conceptualization: Mohan Muniappan.

Methodology: Mohan Muniappan.

Investigation: Mohan Muniappan.

Discussion of results: Mohan Muniappan.

Writing – Original Draft. Mohan Muniappan.

Writing – Review and Editing: Mohan Muniappan.

Resources: Mohan Muniappan.

Supervision: Mohan Muniappan.

Approval of the final text: Mohan Muniappan.

VII. ACKNOWLEDGMENTS

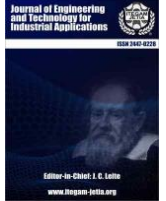
The author would like to thank iFluids Engineering for providing the data.

VIII. REFERENCES

- [1] Kapahi, R. (2013). Load flow analysis of 132 KV substation using ETAP software. *International Journal of Scientific & Engineering Research*, 4 (2), 5.
- [2] Rathod, V. J., & Patel, G. R. (2013). Short circuit analysis on 400 kV sub-station soja. *International Journal of Engineering Research and Development e-ISSN*, 62-67.
- [3] Micu, D. D., Braicu, S. F., Czumbil, L., & Stet, D. (2016, September). Load flow and short-circuit analysis in a Romanian 110/20 kV retrofitted substation. In 2016 51st International Universities Power Engineering Conference (UPEC) (pp. 1-6). IEEE.
- [4] Czumbil, L., Braicu, S. F., Micu, D. D., Stet, D., & Ceclan, A. (2017, June). Analysis of load flow and short-circuit issues in a retrofitted 110/20 kV Romanian substation. In 2017 14th International Conference on Engineering of Modern Electric Systems (EMES) (pp. 13-16). IEEE.
- [5] Braicu, S. F., Czumbil, L., Micu, D. D., Stet, D., Ceclan, A., Simion, E., & Nourri, H. (2017, June). Load flow analysis in a 110/20 kV Romanian substation. In 2017 International Conference on Modern Power Systems (MPS) (pp. 1-4). IEEE.
- [6] Ramos, M. J. S., Bernardon, D. P., Comassetto, L., Resener, M., & Daza, E. B. (2012, September). Analysis of short-circuit asymmetrical currents in power distribution systems. In 2012 47th International Universities Power Engineering Conference (UPEC) (pp. 1-6). IEEE.
- [7] Abadia Gomez, V. (2019). Load Flow Analysis of 138/69kV Substation Using Electrical Transient & Analysis Program (ETAP).
- [8] Siddique, A., Yonghai, X. U., Aslam, W., Hanan, M., Azhar, A., & Munir, H. M. (2019, May). Load flow analysis of 132/11 kV grid station Bahawalpur region Pakistan and its voltage improvement through FACTS devices using ETAP. In 2019 IEEE Innovative Smart Grid Technologies-Asia (ISGT Asia) (pp. 922-927). IEEE.
- [9] Zeggai, A., & Benhamida, F. (2019, February). Power flow and Short circuit of 220 kV Substation using ETAP. In 2019 Algerian Large Electrical Network Conference (CAGRE) (pp. 1-6). IEEE.
- [10] Pal, S., & Biswas, P. (2019, November). Real Time Short Circuit Fault Analysis of a Sub-Station by Soft Computing. In 2nd International Conference on Non-Conventional Energy: Nanotechnology & Nanomaterials for Energy & Environment (ICNNEE).
- [11] Mohammed, Y. A. Y. (2020). Short-circuit fault level calculation on 33/11 KV substation by using ETAP simulator according to the IEC 60909 standard.
- [12] Khan, R., Newaz, A. I., Haque, M. F., & Nafis, N. Q. A. (2020). Comparative load flow analysis of a 400/230 KV grid substation in Bangladesh (Brac University).
- [13] Al-bayaty, H., Kider, M. S., Jasim, O. N., & Shakor, A. (2022). Electrical distribution grid of Kirkuk City: A case study of load flow and short circuit valuation using ETAP. *Periodicals of Engineering and Natural Sciences*, 10(3), 311-322.
- [14] Baby, K., & Sreekumar, K. L. (2017). Load flow analysis of 66 kv substation using Etap software. *International Research Journal of Engineering and Technology (IRJET)*, 4(02).
- [15] Agbontaen, F. O., & Idiagi, N. S. (2022). Short Circuit Analysis of a Nigerian 132/33 kV Injection Substation. *Advances in Engineering Design Technology*, 4(1).
- [16] D. Blah, C. Manar, and P. K. Dhal, "Study of Short Circuit and Load Flow Analysis of 132/33 KV Mawlai Nongkwar Substation", *IJRAMT*, vol. 3, no. 6, pp. 99-103, Jun. 2022.
- [17] Shilling, S. R. (1995). DYNAMIC MOTOR STARTING ANALYSIS FOR A 5500HP SHIPPING PUMP ON AN OFFSHORE PLATFORM.
- [18] Managuli, R. A. (1996). Motor starting with shunt capacitors: An alternate approach to voltage dip control. University of Nevada, Las Vegas.
- [19] Chakrasali, R. L., Sheelavant, V. R., & Nagaraja, H. N. (2011). A Novel method of Starting Induction Motor-A Comparative Study. *International Journal of Power Electronics and Drive Systems*, 1(1), 41.
- [20] Matanov, N. (2019, June). Study of the impact of induction motors starting on the supply voltage. In 2019 16th Conference on Electrical Machines, Drives and Power Systems (ELMA) (pp. 1-5). IEEE.
- [21] Latt, A. Z. (2019). Three Phase Induction Motor Starting Analysis Using ETAP. *International Journal of Latest Technology in Engineering, Management & Applied Science (IJLTEMAS)*, 8(IV).
- [22] Mahmood, F. M., & Hashjin, M. R. (2022). Starting Analysis of Squirrel Cage Induction Motors 1000 kW by Variable Frequency Drive in Power System Case study: Tabriz Pump station.
- [23] IEEE Industry Applications Society. Power Systems Engineering Committee. (1990). IEEE Recommended Practice for Industrial and Commercial Power Systems Analysis: Approved May 31, 1990, IEEE Standards Board: Approved October 26, 1990, American National Standards Institute. IEEE.
- [24] "IEEE Recommended Practice for Conducting Load-Flow Studies and Analysis of Industrial and Commercial Power Systems," in IEEE Std 3002.2-2018, vol., no., pp.1-73, 12 Nov. 2018.
- [25] "IEEE Recommended Practice for Conducting Short-Circuit Studies and Analysis of Industrial and Commercial Power Systems," in IEEE Std 3002.3-2018, vol., no., pp.1-184, 29 March 2019.
- [26] "Short-circuit currents in three-phase a.c. systems," IEC 60909, 2016.
- [27] "IEEE Recommended Practice for Conducting Motor-Starting Studies and Analysis of Industrial and Commercial Power Systems," in IEEE Std 3002.7-2018, vol., no., pp.1-107, 26 April 2019.



ISSN ONLINE: 2447-0228



RESEARCH ARTICLE

OPEN ACCESS

THE EVALUATION OF THE BLENDED LEARNING IMPLEMENTED AT AL-AHGAFF UNIVERSITY, YEMEN: A STUDENTS' PERSPECTIVE

Hamzah Alaidaros¹, Omer Salim Bakahakam² and Asma Abdulrhman³

^{1, 2, 3} Faculty of Computer Science and Engineering, Al-Ahgaff University, Mukalla, Hadramaout, Yemen.

¹ <http://orcid.org/0000-0001-7464-6419> , ² <http://orcid.org/0009-0005-6683-9322> , ³ <http://orcid.org/0009-0003-4487-6637> 

Email: hamzah@ahgaff.edu, omerbhkm0@gmail.com, asma.shekh@ahgaff.edu

ARTICLE INFO

Article History

Received: June 27th, 2024

Revised: September 12th, 2024

Accepted: September 12th, 2024

Published: September 04th, 2024

Keywords:

Aprendizagem combinada,
perspectiva dos alunos,
Universidade Al-Ahgaff,
Iêmen.

ABSTRACT

Abstract—Numerous universities worldwide have implemented the blended learning as students prefer other complementary approaches of content delivery. Recently, blended learning has become the most popular educational approach that universities apply due to the involvement of information communication technology (ICT). This study aims to evaluate the blended learning implemented at Al-Ahgaff University, Yemen from the students' perspective. A survey questionnaire was used to collect data from 28 students who involved in the blended learning, while thematic analysis technique was employed for data analysis. The students' perspective has measured in terms of getting benefits from the blending learning, their motivation towards the blending learning, their acceptance for the environment of the blending learning, and the advantages and disadvantages of the blending learning. The evaluation results reveal that blended learning method is a modern approach for learning that assists in activating the discussion between lecturer and students, and in improving their abilities and skills in research. Nevertheless, the majority of students confirm that the blended learning environment is not suitable due to external reasons. The electricity and Internet disconnection have a negatively impact on implementing the blended learning.



Copyright ©2024 by authors and Galileo Institute of Technology and Education of the Amazon (ITEGAM). This work is licensed under the Creative Commons Attribution International License (CC BY 4.0).

I. INTRODUCTION

It must define the problem and importance of the research carried out, it presents a (not very extensive) review of the literature on the subject of the article, including the authors' contributions to the state of the art. If you use abbreviations or acronyms, first write the words that identify them and then, in parentheses, the acronym. This set also establishes the research question, the objectives of the work and hypothesis, if necessary, the importance and limitations of the study.

There are different learning approaches that can effectively influence the learning process and present the learning content for various students [1]. For many decades, the traditional teaching approach was the main way for course delivering in universities [2]. However, the advancement of information communication technology (ICT) has recently impacted universities students to prefer other complementary approaches of content delivery [3]. Accordingly, blended learning has become the alternative approach

of complementing conventional face to face learning and online learning [2]. In this regard, Ali, et al. [4] confirmed that blended learning has become the most popular educational approach that universities apply to teaching and learning due to the involvement of ICT.

The blended learning is defined as the new approach of teaching and learning that combines the classroom learning with the online learning platform [2]. It is the alternative learning approach that incorporates the advantages of online learning and face-to-face learning to support educational differentiation [5]. In addition, Kacetla and Semradovaa [1] defined the blended learning as the term that is employed in teaching and learning process with a combination of numerous activities such as face-to-face instruction and live e-learning. Oweis [6] stated that the blended learning combines both direct and indirect approaches of online learning that usually involves the internet and intranet, whilst indirect learning conducted concurrently within traditional classes. In addition, the blended learning integrates different learning

methods with various teaching methods, objectives, environments, and resources [5],[7].

Several publications have confirmed that blended learning has many benefits. For instance, it can offer flexibility and efficiency [4], as well as make the teaching and learning process more interactive [3]. In addition, it can increase students' knowledge and skills [8] and academic performance [5]. Other studies suggest that blended learning is a solution to classroom insufficiency [4], and it can solve the problems of traditional and online learning [9]. Musawi and Ammar [8] stated that blended learning utilizes appropriate ICTs to combine times and modes of learning and integrate the best aspects of face-to-face and online interactions, while indicated that blended learning can provide individual learning opportunities for both students and lecturers [4].

According to [8] stated that implementing the blended learning in universities worldwide has proven successful. In addition [5] reported that the blended learning has been applied in numerous courses, for example, nursing, mathematics business, and English learning. However, [10] confirm that it is important to explore the students' perspective on the blended learning. In this context, the blended learning has been implemented in the Faculty of Computer Science and Engineering, Al-Ahgaff University, Yemen [11]. Al-Ahgaff University is a none profit university established in 1994, and it has started adopting the online learning during the Covid-19 pandemic [12].

Lately, several studies have been carried out to examine the students' perspective on the blended learning implemented in different universities, such as University of Bisha [2], Muni University [4], and South East European University [13]. These studies motivated the current study to explore the students' perspective of Al-Ahgaff university on the blended learning. Therefore, this study aims to evaluate the blended learning implemented at Al-Ahgaff University. In particular, it examines their perception on the learning method, benefits, and environment suitability. Then, it focuses on identifying the advantages and disadvantages of the blending learning from their perspective.

The contents of the remaining sections are organized as follows. Section II reviews the literature and highlights the related works. Section III describes the research method employed in achieving the study objective. Section IV presents and discusses the study results. Section V concludes the findings and suggests some remarks for forthcoming work.

II. RELATED WORK

The enumerations of citations in the body of the article must be sequenced in the order in which they appear, according to the example shown below.

Recently, blended learning has attracted the attention of university teachers and students over the world. Therefore, numerous studies have been conducted to review and examine the effectiveness of the blended learning implemented in different universities.

According to [5] conducted a systematic review to evaluate the effects of blended learning in physical education among university students. The study discussed the problems with traditional physical education and the advantages of the blended learning model over traditional instructional methods. A focus was directed to the effects of blended learning on motor skills, satisfaction, learning interests, and learning attitudes. The results demonstrated that blended learning effectively improves students'

physical performance, and significantly improves students' academic performance, satisfaction, and interest in learning.

For [2] carried out a study to find out the effect of blended learning on students' performance and satisfaction in South East European University. A structured questionnaire was used to gather data from 319 students. The results of the analysis show that blended learning has an impact on both students' performance and students' satisfaction. The course management and interaction have a positive significant effect on students' satisfaction and performance, with the latter having a stronger effect on both satisfaction and performance outcomes from blended learning. Finally, the study shows that there is a correlation in on hand between blended learning and students' improved performance, and on the other hand a positive correlation between satisfaction and performance.

According to [3] carried out a study aimed to investigate the effect of using Google Classroom's on blended learning on English ability of university students at STMIK-AMIK Riau in Pekanbaru-Riau, Indonesia. A quasi-experimental design was employed, and experimental and control group were conducted with 68 students. Quantitative data were collected through an instrument consists of multiple-choice questions. Pre-test and post-test were used to measure the students' English ability before and after conducting the treatments in both groups. The study results indicated that blended learning through Google Classroom improves students' English ability. However, the study claimed to conduct further studies in using of Google Classroom on different domains.

According to [4] conducted study that analyzed the strengths, weaknesses, opportunities and threats (SWOT) of blended learning in the Public Universities of Uganda, in a case study of Muni University. A questionnaire was employed with 25 lecturers and 189 students and the data collected were analyzed using SPSS. This paper provides a baseline study to help government and public universities that would like to implement or newly incorporate blended learning to identify strengths, weaknesses, opportunities and threats associated with the blended learning approach. As a result, the study provided a baseline to help government and public universities that would like to implement or newly incorporate blended learning. The study recommended that for a successful implementation of blended learning, steady power supply should be provided, internet accessibility should be improved. In addition, the university should provide blended learning training for both students and lecturers. Finally, policies, rules and standards pertaining to blended learning should be enacted for both the government and university.

For [8] conducted a study aimed to examine the effect of different blending levels of traditional and e-learning delivery on academic achievement and students' attitudes towards blended learning at Sultan Qaboos University, Oman. Three educational programs based on blended learning were designed to be delivered to students attending the "introduction to educational technology" course, whereby each program differs in its blending proportion between traditional and online learning. The study focused on determining the most suitable blending ratio between the two delivery formats for this course, and comparing the effectiveness of the three blending levels to the traditional instruction in terms of developing students' academic achievement and their attitudes towards using blended learning. The results indicated a statistically significant difference at the level of <0.05 between the mean scores of all the experimental groups and the three control groups in the post academic achievement test. However, the study recommended using a blended learning strategy with all blending ratios in teaching and developing different learning variables.

[10] conducted a study investigated the perceptions and obstacles faced by EFL learners in the implementation of blended learning in an abnormal learning system. In the study, a semi-structured open-ended questionnaire and semi-structured interviews were conducted with 48 undergraduate EFL students from University of Tadulako, Indonesia. The participants perceived that learning through blended learning needs more experiences in utilizing online learning mode and requires more study times to make them get used to the internet. Some learners perceived the implementation of blended learning as easier, helpful, flexible, and fun. However, the learners reported that they face different problems on the implementation of blended learning, such as unclear online instruction, poor internet connectivity, and delay to respond questions on the online learning classes.

A survey study conducted by [13] to examine students' perceptions and satisfaction towards the three components of a blended learning environment: multimedia learning materials, assessment, and interactive activities in the College of Arts & Sciences, Al-Namas, the University of Bisha, Saudi Arabia. Quantitative data was collected in the form of 12 Likert items in which 22 Saudi students are asked to evaluate their learning experiences. The researcher's observation was used to decode, and explain the responses of the participants qualitatively. The result revealed that learners prefer illustrated text materials to video, plain text and audio materials, flexible assessments to non-flexible assessment, and blended communication tools like WhatsApp, blogging, wikis, collaborative activities, and discussion forum.

According to [14] conducted to explore the students' perspective and to investigate the effects on the grammar performance of EFL students when using blended learning at Irbid National University, Jordan. A quasi-experimental design was employed, whereby 28 students involved in pre and post tested, and divided into two groups. Only 13 students were in a blended learning group and they completed structured interviews; however, the remaining 15 were in a control group. The study result revealed that the post test results of the students in the blended learning group were higher than the post test results of the students in the control group. It confirmed that blended learning improved the students' digital skills as well as provided them with flexibility and easy access to learning materials, and attracted their attention. The blended learning also encouraged the interactions between the students themselves and their teachers.

Overall, it is clear that several evaluation studies have been carried out to examine the students' perspective on the blended learning implemented in different universities. Particularly, the blended learning has been evaluated in the University of Bisha, Saudi Arabia [2], Pekanbaru, Riau, Indonesia [3], Muni University, Uganda [4], Sultan Qaboos University, Oman [8], University of Tadulako, Indonesia [10], South East European University, North Macedonia [13], and Irbid National University, Jordan [14]. Therefore, the current study aims to evaluate the blended learning implemented at Al-Ahgaff University, Yemen.

III. METHODOLOGY

The study uses a mixed-method design of research to investigate the perspective of students who have participated in the blended learning implemented at Al-Ahgaff University on the academic year 2022-2023. It mainly focuses on examining the student's perception through answering the following research questions (RQs):

- RQ1: To what extent students got benefits from the blending learning approach?

- RQ2: To what extent students were motivated towards the blending learning approach?
- RQ3: To what extent the environment of the blending learning was suitable and appropriate?
- RQ4: What are the advantages and disadvantages of the blending learning from student's perspective?

A survey questionnaire was used to collect data from Al-Ahgaff University students who involved in the blended learning. The survey questionnaire is a useful and powerful technique that is used for data collection to measure opinions and perceptions [15]. The survey questions were adopted from the related work, such as [2],[3],[8],[10],[13], and [14], while the survey instrument was validated by three experts from the relevant area, as argued by [16]. The survey instrument consisted of six sections. Section 1 is for obtaining the participants demographic information. Sections 2 to 5 are for answering the identified RQs, while section 6 is for getting the participants comments and suggestions. Sections 2 to 4 have different questions in which the students are asked to respond. They have a Likert scale survey with 3-scale points: 'Agree,' 'Neither Agree nor Disagree,' and 'Disagree.' They choose the option as per their learning experiences and preferences during the classes. The 3-scale points is selected as it is the most widely used approach to scale the responses in survey research. It is simple for the students to decide if they like or dislike, it minimizes their confusions, and it is easy to measure.

In this study, data were collected on 9-10 October 2023 with the promise that the collected data would be kept confidential and only be used for research purposes. However, to analyze the collected data, the researchers applied thematic analysis by Clarke and Braun [17], which describes an iterative process of going from messy data to a map of the most critical themes in the data. The process of thematic analysis is familiarizing the researcher with the data, generating initial codes, searching for themes, reviewing themes, defining and naming themes, and producing the report. Results and discussion are detailed provided in the next section.

IV. RESULTS AND DISCUSSIONS

The empirical findings of this study are structured into six sections start by presenting the participants demographic information, then provide answers to the four research questions, and followed by student's comments and suggestions as analyzed below.

IV.1 STUDENTS' DEMOGRAPHIC INFORMATION

This study was conducted in the department of Information Technology (IT) at the Faculty of Computer Science and Engineering, Al-Ahgaff University, in Yemen in the academic year 2022-2023. Twenty-eight (28) students (64% males and 36% females) were undergraduates between the age group of 19 to 22 years. Participants were enrolled in Fundamentals of Information Technology, a course in IT Bachelor's program. The semester consisted of 16 weeks in which the course had three credit hours a week. Participants took face-to-face classroom an hour and a half a week, while taking an online class on the other hour and a half.

IV.2 STUDENTS' DEMOGRAPHIC INFORMATION

Around 90% of the participants emphasized that lessons become difficult and unclear during implementing the blended learning. In addition, 82% of the participants acknowledged that they prefer traditional learning, and they do not effectively learn

during the blended learning. Overall, 75% of the participants indicated that they did not get benefits of the blended learning.

However, 61% of the participants emphasized that blended learning makes the lecturer focus on particular lessons and pre-identified points. Moreover, two-thirds (65%) think that the success of blended learning is related with the type of subject, in which 68% confirmed that blended learning do not help students getting satisfied marks in comparing with other subjects' marks that are taught with traditional approach. Furthermore, only 22% of the participants agreed that blended learning helps in acquiring new knowledge and skills, while 56% of them were disagreed and the remaining (22%) indicated that they are "neither agree nor disagree". Besides, 43% of the participants agreed that blended learning reduces the time of learning comparing with the traditional approach, whilst 50% of them were disagreed and the remaining (7%) indicated that they are "Neither agree nor disagree".

IV.3 STUDENTS' MOTIVATION TOWARDS BLENDED LEARNING METHOD

Only 14% of the participants agreed, and same percentage are don know, that blended learning provides satisfaction similar to the traditional learning although the majority of students were disagreed. Additionally, 82% of the participants affirmed that blended learning does not support different teaching methodologies, such as lecture, discussion, focus groups. However, 79% of the participants indicated that blended learning is impossible to be implemented in practical classes of the information technology (IT) program.

Although 64% of the participants acknowledged that lecturer has paid care on student's differences during performing classes in the blended learning; however, two-thirds of them emphasized that lecturer did not make them like the blended learning. Therefore, 57% stated that they did not give more interest for classes of the blended learning. They confirmed that blended learning does not support self-study and grant the confidence. Nevertheless, only 26% claimed that blended learning provides motivation for learning and make it interesting comparing to the traditional approach, whilst 15% are "Neither agree nor disagree" and the remaining (59%) were disagreed on that claim.

IV.4 SUITABILITY OF LEARNING ENVIRONMENT WHEN APPLYING BLENDED LEARNING METHOD

Initially, 58% of the participants affirmed that the existing environment for implementing the blended learning was not suitable as it does not help students to focus on the lecturer explanation. In this context, 57% acknowledged that necessary tools and software for conducting classes within blended learning were not available. On the other hand, 79% of the participants affirmed that preparing the environment for blended learning classes consumes too much time, whereby 90% of them confirmed that external reasons, for example electricity and Internet disconnection, have a negatively impact on implementing the blended learning.

Regarding to the used approach, 71% of the participants acknowledged that using of Intranet (without Internet) at the beginning of the semester was not suitable for implementing the blended learning classes. Nonetheless, 61% of them affirmed that using commercial software, such as Zoom, at the middle of semester, was better. In addition, 71% of the participants affirmed that the absence of lecturer in one of the two classes helps students on careless, whereby half of the participants (50%) acknowledged

that they can use the microphone for discussion and interaction with lecturer who is in the other classroom.

IV.5 STUDENTS' PERSPECTIVE ON ADVANTAGES AND DISADVANTAGES OF BLENDED LEARNING METHOD

This subsection presents students' perspective on advantages and disadvantages of blended learning method.

For the advantages, some students stated that blended learning method helps in distance learning, and it improves self-study concept. They also considered that recorded video classes are the most advantage of the blended learning method. Some students indicated that using the blended learning method has benefits for the lecturers and students. It reduces the lecturer effort and assists students to focus on the classes. Besides, some students affirmed that blended learning method has helped them in activating the discussion between them, and following their lessons consequently. It also aided them in improving their abilities and skills in research. They confirmed that blended learning method is a modern approach for learning, it might be applied to the none core subjects.

For the disadvantages, around 70% of students stated that lecturer in the blended learning focuses only on the students who are in the classroom. Thus, a big and notable careless for students who are sit on the other classrooms. This leads to less interaction with those students and would generate none active students whom do not care to their lessons. In addition, 40% indicated that the disconnection of the electricity and Internet are the key disadvantages of employing the blended learning method. A group of students acknowledge that blended learning needs a lot of time to review lessons comparing to the traditional learning. Additionally, some students added: "the technical issues in addition to the disconnection of the electricity and Internet lead to loss much time of the class. This is a clear sign indicates that the environment is not suitable for implementing the blended learning." Moreover, other students wrote: "the blended learning has difficulty impacts understanding lessons, and to some extent, there is no interaction and discussion between lecturer and students."

IV.6 STUDENTS' COMMENTS AND SUGGESTIONS

This section presents the students' comments and suggestions. A student wrote: "blended learning method should be applied with theoretical subjects nor practical classes". Another student also suggested applying the blended learning method at most with one subject per semester conditionally with a theoretical subject. However, a student suggested that blended learning might be implemented via recorded video classes and then show it for students in the classroom. Besides, two students wrote: "the class room for blended learning should be well prepared. Also, it is better to use Zoom instead of Intranet". Further, some students claimed to find a way to allow students to ask questions during the class or provide them a specific time for their questions at the end of the class.

V. CONCLUSIONS

This paper presented and discussed the evaluation results of the blended learning implemented at Al-Ahgaff University, Yemen. In the current study, 28 students from the Faculty of Computer Science and Engineering, who involved in the blended learning, have participated to express their opinion and perspective.

Students' perceptions were collected by using a survey questionnaire, while thematic analysis technique was employed for data analysis.

The findings of the current study confirm that blended learning method is a modern approach for learning that assists in activating the discussion between lecturer and students. In addition, blended learning makes the lecturer focus on particular lessons and pre-identified points. Moreover, it can improve the research abilities and skills of students. However, the majority of students acknowledged that they prefer traditional learning as they did not get benefits from the blended learning. Furthermore, they affirmed that the blended learning environment is not suitable due to external reasons. For instance, electricity and Internet disconnection have a negatively impact on implementing the blended learning.

Future work will focus on evaluate the blended learning implemented at Al-Ahgaff University from the lecturer's and technicians' perspective through conducting interviews with them. The interview is the suitable method to explore such in-depth sensitive topics on human behavior and social interactions.

VI. AUTHOR'S CONTRIBUTION

Conceptualization: Hamzah Alaidaros, Omer Salim Bakahakam, and Asma Abdulrhman.

Methodology: Hamzah Alaidaros, Omer Salim Bakahakam, and Asma Abdulrhman.

Investigation: Hamzah Alaidaros, Omer Salim Bakahakam, and Asma Abdulrhman.

Discussion of results: Hamzah Alaidaros, Omer Salim Bakahakam, and Asma Abdulrhman.

Writing – Original Draft: Hamzah Alaidaros, Omer Salim Bakahakam, and Asma Abdulrhman

Writing – Review and Editing: Hamzah Alaidaros, Omer Salim Bakahakam, and Asma Abdulrhman.

Resources: Hamzah Alaidaros, Omer Salim Bakahakam, and Asma Abdulrhman .

Supervision: Hamzah Alaidaros, Omer Salim Bakahakam, and Asma Abdulrhman.

Approval of the final text: Hamzah Alaidaros, Omer Salim Bakahakam, and Asma Abdulrhman.

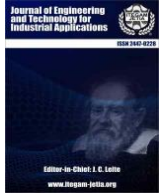
VII. ACKNOWLEDGMENTS

The authors wish to thank Al-Ahgaff University for funding this study. A great thank goes to all students who shared their opinions, views, and valuable suggestions.

VIII. REFERENCES

- [1] J. Kacetla and I. Semradovaa, "Reflection on blended learning and e-learning – case study," *Procedia Computer Science*, vol. 176 pp. 1322-1327, 2020.
- [2] J. Zeqiri, V. Kareva, and S. Alija, "The Impact of Blended Learning on Students' Performance and Satisfaction in South East European University," presented at the ENTRENOVA Croatia, 2020.
- [3] L. A. D. Warman, "The Effect of Google Classroom in Blended Learning on University Students' English Ability," *J-SHMIC : Journal of English for Academic*, vol. 8, pp. 12-23, 2021.
- [4] G. Ali, B. A. Buruga, and T. Habibu, "SWOT Analysis of Blended Learning in Public Universities of Uganda: A Case Study of Muni University," *Multisiplinary Scientifiv Journal*, vol. 2, pp. 410-429, 2019.
- [5] C. Wang, R. D. O. Dev, K. G. Soh, N. J. M. Nasiruddin, and Y. Wang, "Effects of Blended Learning in Physical Education among University Students: A Systematic Review," *Educational Science*, vol. 12, pp. 1-15, 2022.

- [6] T. I. Oweis, "Effects of Using a Blended Learning Method on Students' Achievement and Motivation to Learn English in Jordan: A Pilot Case Study.," *Education research international*, vol. 2018, p. 7425924, 2018.
- [7] N. Megahed and A. Hassan, "A Blended Learning Strategy: Reimagining the Post-Covid-19 Architectural Education.," *Archnet-IJAR: International Journal of Architectural Research*, vol. 16, pp. 184-202, 2021.
- [8] A. S. A. Musawi and M. E. Ammar, "The Effect of Different Blending Levels of Traditional and E-Learning Delivery on Academic Achievement and Students' Attitudes towards Blended Learning at Sultan Qaboos University," *TOJET: The Turkish Online Journal of Educational Technology*, vol. 20, pp. 127-139, 2021.
- [9] S. K. Halverson L, Huyett S, Henrie C, Graham C "Blended Learning Research in Higher Education and K-12 Settings," in *Learning, Design, and Technology*, B. L. M. Spector, M. Childress, Ed., ed: Springer International Publishing, 2017, pp. 1-30.
- [10] G. N. Manurung, K. Manurung, S. R. Mertosono, and A. Kamaruddin, "Perceptions of EFL Learners in the Implementation of Blended Learning Post-natural Disaster at a University in Indonesia," *Theory and Practice in Language Studies*, vol. 10, pp. 959-968, 2020.
- [11] Al-Ahgaff University. (08 Feb 2024). *Al-Ahgaff University-Home Page*. Available: <http://ahgaff.edu/>
- [12] H. Alaidaros, A. Kherd, and H. A. Al-Aidroos, "Students' Perception of Online Learning during Covid-19 Pandemic at Al-Ahgaff University, Yemen: A Survey," presented at the International Conference of Modren Trends in ICT Industry (MTICTI), Sana'a, Yemen, 2021.
- [13] A. Anas, "Perceptions of Saudi Students to Blended Learning Environments at the University of Bisha, Saudi Arabia," *Arab World English Journal (AWEJ)*, vol. 6, pp. 261-277, 2020.
- [14] K. B. A. Al Bataineh, A. E. A. A. Banikalef, and A. Albashtawi, "The effect of blended learning on EFL students' grammar performance and attitudes: an investigation of Moodle.," *Arab World English Journal (AWEJ)*, vol. 10, p. 324-334, 2019.
- [15] H. Alaidaros, M. Omar, and R. Romli, "A Review on the Methods of Evaluating the New Approaches Proposed in the Agile Context," *International Journal of Computer and Information Technology (IJCIT)*, vol. 10, pp. 5-10, 2021.
- [16] D. B. McCoach, Gable, R. K., & Madura, J.P., *Instrument development in the affective domain*, 3rd ed. New York: Springer, 2013.
- [17] V. Clarke and V. Braun, "Thematic analysis," in *Encyclopedia of critical psychology*, ed: Springer, 2014, pp. 1947-1952.



RESEARCH ARTICLE

OPEN ACCESS

IMPACT OF GRAIN BOUNDARIES ON THE ELECTRICAL CHARACTERISTICS AND BREAKDOWN BEHAVIOR OF POLYCRYSTALLINE SILICON PIN DIODES: A SIMULATION STUDY

Abdelaziz Rabehi¹, Abdelmalek Douara², Mohamed Elbar³, Roumaissa Zenzen⁴ and Mohamed Amrani⁵

¹ Telecommunications and Smart Systems Laboratory, Faculty of Science and Technology, University of Djelfa, Algeria.

² Laboratoire de Micro-électronique Appliquée. Université Djillali Liabès de Sidi Bel Abbés, BP 89, 22000, Sidi Bel Abbés, Algeria

³ Faculty of Science and Technology, Tissemsilt University, Algeria.

⁴ Applied automation and industrial diagnostic Laboratory (LAADI), Faculty of Science and Technology, University of Djelfa, Algeria.

⁵ LMT Laboratory, Faculty of Sciences and Technology, University of Jijel, Jijel, Algeria.

¹<http://orcid.org/0000-0001-8684-4754> ²<http://orcid.org/0000-0001-8684-4754> ³<http://orcid.org/0000-0002-2636-946> ⁴<http://orcid.org/0009-0007-8921-9947> ⁵<http://orcid.org/0009-0003-2863-908>

Email: abdelaziz.rabehi@univ-djelfa.dz, m.elbar@univ-djelfa.dz, abdelmalekreal@gmail.com, zenzen-roumaissa@hotmail.com, amranimedba@yahoo.fr.

ARTICLE INFO

Article History

Received: July 11th, 2024

Revised: September 18th, 2024

Accepted: September 18th, 2024

Published: September 04th, 2024

Keywords:

PIN,
avalanche,
breakdown voltages,
impact ionization.

ABSTRACT

In this paper, we present a comprehensive two-dimensional simulation program designed to model the intricate electrical characteristics of reverse-biased lateral polysilicon PIN diodes. Our methodology involves the numerical resolution of a system of partial differential equations, specifically Poisson's equation and the continuity equations for both electrons and holes, incorporating the significant effects of impact ionization. By employing this simulation approach, we are able to accurately derive the current-voltage (I-V) characteristics of the reverse-biased structure, including detailed analyses of breakdown phenomena. The geometrical model employed in our study assumes that the polysilicon layer is composed of a sequence of crystallites with well-defined mean grain sizes. These crystallites are separated by lateral grain boundaries that run parallel to the metallurgical junction, influencing the overall electrical behavior of the diode. Our simulation results provide critical insights into the impact of these grain boundaries on the diode's performance, highlighting the role of trapping centers and their effect on the electric field distribution and carrier dynamics within the device. Furthermore, this study discusses the implications of our findings for the design and optimization of polysilicon-based electronic components, suggesting potential improvements in device fabrication and performance. The comprehensive analysis presented in this paper not only enhances the understanding of polysilicon PIN diodes but also contributes to the broader field of semiconductor device engineering.



Copyright ©2024 by authors and Galileo Institute of Technology and Education of the Amazon (ITEGAM). This work is licensed under the Creative Commons Attribution International License (CC BY 4.0).

I. INTRODUCTION

Polycrystalline silicon, commonly referred to as polysilicon or PC-Si, has become an integral material in the integrated circuit industry due to its versatile electrical properties [1-3], which can vary significantly. This material's application spans various electronic components, including thin-film transistors (TFTs), photovoltaic cells, PN junction diodes, and both PIN and Schottky diodes [4-6]. Polysilicon is composed of numerous small silicon

crystals, known as crystallites, which are typically about a tenth of a micron in size and exhibit the same crystalline structure as single-crystal silicon [7], [8].

The unique structure of polycrystalline silicon can be attributed to its composition of monocrystalline grains of different orientations [9], [10]. These grains are separated by highly disordered, narrow regions known as grain boundaries, which are typically only a few angstroms wide and are rich in defects [11-13]. These grain boundaries play a crucial role in determining the

electrical properties of polysilicon [14], [15]. The deep energy states within these boundaries can trap free carriers, significantly influencing the material's conductivity and behavior in electronic devices [16-18].

The significance of polysilicon in semiconductor technology was first highlighted by Seto in 1975 [19], who proposed a one-dimensional analytical model to describe the electrical properties of polycrystalline silicon films [20]. This model underscored the impact of grain boundaries on the material's electrical characteristics [21], particularly in terms of carrier trapping and mobility reduction [22-24]. Subsequent research has expanded on Seto's foundational work, exploring the complex interactions between crystallites and grain boundaries, and their implications for device performance.

As polysilicon continues to be a material of choice in the fabrication of advanced electronic components, understanding its properties and behavior under various conditions remains critical. This paper focuses on a two-dimensional simulation study of the electric characteristics of reverse-biased lateral polysilicon PIN diodes. By numerically solving the system of partial differential equations, including Poisson's equation and the continuity equations for both electrons and holes, we aim to elucidate the current-voltage (I-V) characteristics of these diodes, particularly considering the effects of impact ionization and breakdown phenomena.

This study's insights are expected to contribute significantly to the design and optimization of polysilicon-based electronic components, enhancing their performance and reliability in various applications.

II. PHYSICAL MODEL

The physical model that provides the IV characteristics is typically based on solving a system of differential equations. Solar cells, like all semiconductor devices, are modelled using five basic equations: Poisson's equation, the continuity equations for both electrons and holes, and the two transport equations, which are collectively described by the drift-diffusion model [25].

$$\left\{ \begin{array}{l} \frac{\partial^2 \varphi}{\partial x^2} + \frac{\partial^2 \varphi}{\partial y^2} = \frac{q}{\epsilon} (-p + n - \Sigma p_T + \Sigma n_T - N_D^+ + N_A^-) \\ -\frac{1}{q} \left(\frac{\partial^2 j_h}{\partial x^2} + \frac{\partial^2 j_h}{\partial y^2} \right) = r_h - g_h \\ \frac{1}{q} \left(\frac{\partial^2 j_e}{\partial x^2} + \frac{\partial^2 j_e}{\partial y^2} \right) = r_e - g_e \\ j_{nx} = -q n \mu_n \frac{\partial \varphi}{\partial x} + q D_n \frac{\partial n}{\partial x} \\ j_{ny} = -q n \mu_n \frac{\partial \varphi}{\partial y} + q D_n \frac{\partial n}{\partial y} \end{array} \right. \quad (1)$$

The advantage of this model is that it accounts for the effects of trapping centers, which significantly influence the behavior of semiconductor devices [26]. To solve these equations, the discretization method employed is the finite difference method, and the Scharfetter-Gummel approximation is used to enhance the accuracy of the numerical solution [27].

III. NUMERICAL SOLUTION

Solving the system of equations that describe the behavior of a semiconductor device is challenging due to the large number of unknown variables. To make the problem more manageable, we simplify it to a system with three unknowns: the electrostatic potential (φ), and the electron (n) and hole (p) concentrations. These equations are highly nonlinear because of the exponential terms present in the expressions for n and p .

Among the numerical methods available for solving differential equations, we employ the finite difference method. In

this approach, after discretizing the study domain, we replace the differential equations with difference equations. This process transforms the continuous problem into a discrete one that can be solved using numerical techniques.

To solve the resulting system, we use the algorithm developed by Gummel [28]. This algorithm iteratively solves the three equations of the system by updating each unknown in turn. Each equation is solved based on estimated values for the other two unknowns. After solving one equation, the corrected value of the unknown is used in the subsequent equations. This iterative process is repeated until the solutions for all three equations converge, ensuring an accurate and stable solution for the system.

This method's iterative nature allows for handling the nonlinearities in the equations effectively, providing a robust framework for analyzing the IV characteristics of semiconductor devices.

IV. GEOMETRIC AND PHYSICAL MODEL A PIN DIODE BASED ON POLYCRYSTALLINE SILICON

The geometric and physical model of the PIN diode based on polycrystalline silicon is fundamental to understanding its electrical characteristics. The PIN diode structure consists of three distinct zones along the X axis: the P+ region, the intrinsic (I) region, and the N region. The dimensions of these regions are detailed in Table 1 below.

Table 1: Dimensions of the PIN Diode.

Zone	Dimension
P+	100
I	200-800 nm
N	700 nm
First joint grain (Lg1)	100 nm
Crystallite size (Lg)	160 nm

Source: Authors, (2024).

The geometric model assumes that the polysilicon layer comprises a series of crystallites with defined mean grain sizes. These crystallites are separated by lateral grain boundaries, which are parallel to the metallurgical junction (see Figure .1).

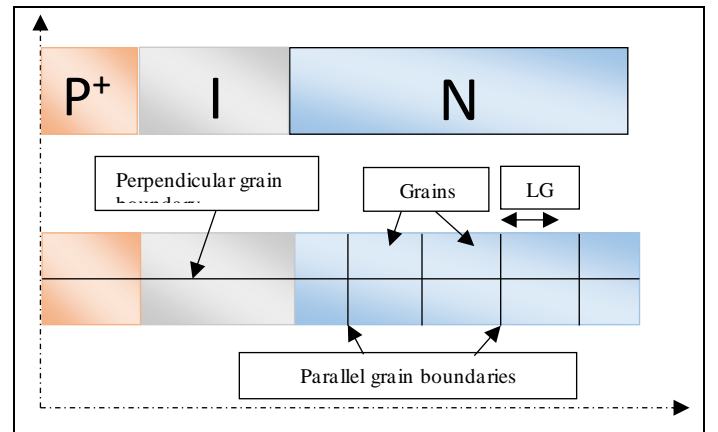


Figure 1: Geometric model of a PIN diode based on polycrystalline silicon.

Source: Authors, (2024).

In this model, the grain boundaries play a significant role in the electrical properties of the diode. These boundaries are populated with traps, both acceptor and donor types, with a surface density denoted as NTA and NTD, respectively. These traps are assumed to be monoenergetic and are located exclusively within the grain boundaries, which are set at a thickness of 1 nm. The traps

can be amorphous, with energy levels ETA and ETD positioned symmetrically in the middle of the bandgap.

The ionization rate of these states follows the classical Shockley-Read-Hall (SRH) formalism, which is critical for understanding the recombination and generation processes within the diode. The SRH model describes the ionization rates for donor-type and acceptor-type traps as follows:

For the discrete density of states of ionized donor-type traps:

$$N_{TD}^+ = N_{TD} \frac{C_p \cdot p + C_n \cdot N_C \exp\left(\frac{E_{TD} - E_C}{kT}\right)}{C_n \left(n + N_C \exp\left(\frac{E_{TD} - E_C}{kT}\right) \right) + C_p \left(p + N_V \exp\left(\frac{E_V - E_{TD}}{kT}\right) \right)} \quad (2)$$

$$N_{TA}^- = N_{TA} \frac{C_n \cdot n + C_p \cdot N_V \exp\left(\frac{E_V - E_{TA}}{kT}\right)}{C_n \left(n + N_C \exp\left(\frac{E_{TA} - E_C}{kT}\right) \right) + C_p \left(p + N_V \exp\left(\frac{E_V - E_{TA}}{kT}\right) \right)} \quad (3)$$

Where:

N+TD: the density of states discrete traps ionized donor-type.
 N-TA: the density of states discrete traps ionized acceptor-type.
 Cn and Cp are the coefficients of capture and emission of electrons and holes and NTA, NTD, respectively, the total density of states discrete donor and acceptor traps located at ETA and ETD.

The traps at the grain boundaries significantly influence the electrostatic potential and carrier concentrations within the diode, affecting the overall device performance, particularly under reverse bias conditions. Understanding these interactions is essential for optimizing the design and functionality of polycrystalline silicon PIN diodes.

V. ENERGY BAND STRUCTURES

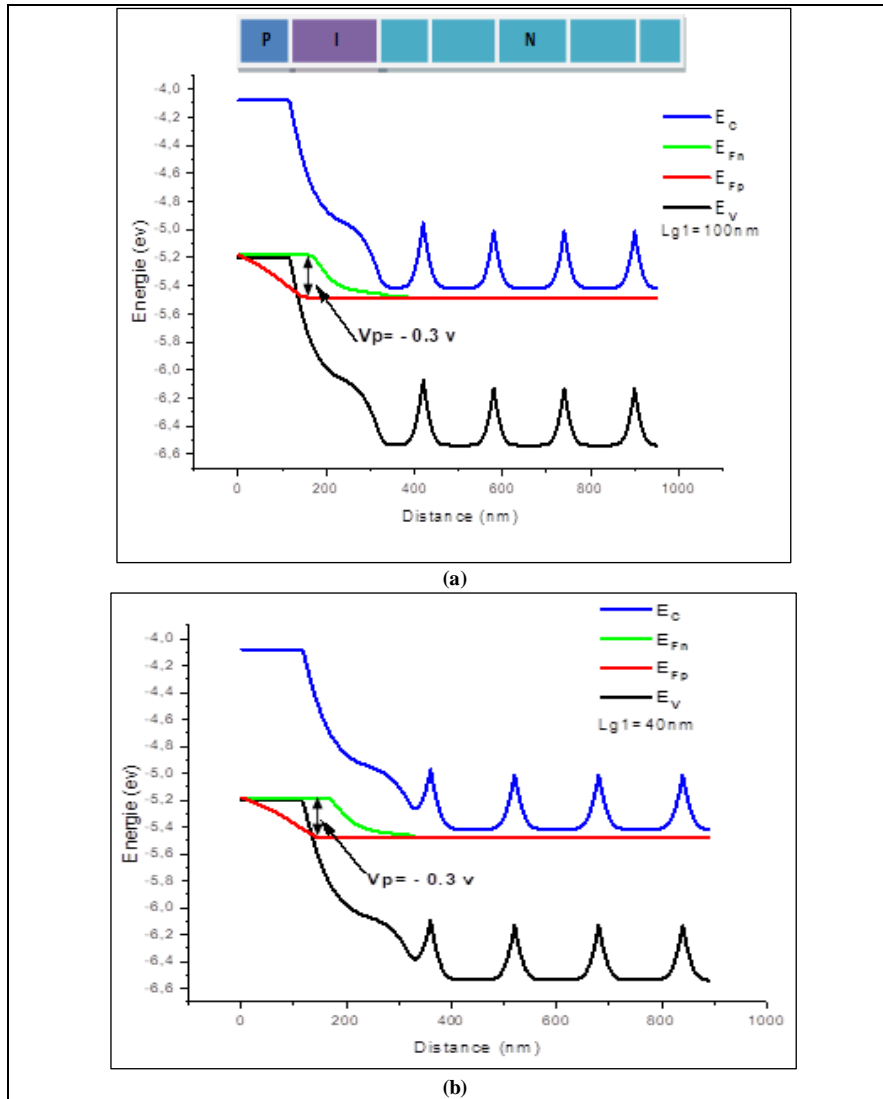


Figure 2: Energy band structures of a polycrystal PIN diode polarized in inverse, with Na=5.1018 cm⁻³, Nd= 5.1017 cm⁻³, NT=3.1012 cm⁻³, Li=200nm, Vp=-0.3.

Source: Authors, (2024).

Like all devices based on polycrystalline silicon, the energy band structures of a polycrystal PIN diode show the crucial role played by the grain boundaries. These boundaries, particularly the first joint parallel grain, block the electrostatic potential and

prevent the space charge zone from expanding into the volume of the layer. This blocking effect creates a potential barrier that can only be overcome when a certain reverse voltage is applied. At this point, the first grain boundary's blocking potential is released, and

the subsequent parallel grain boundaries take over the blocking function.

Figure .2a illustrates the energy band structure with a crystallite size $L_g=100$ nm. The potential barriers created by the grain boundaries are evident, showing how these boundaries impede the flow of carriers, particularly under reverse bias conditions.

Figure .2b depicts the energy band structure with a reduced crystallite size $L_g1=40$. The smaller grain size results in a higher density of grain boundaries, which further influence the distribution of the electrostatic potential across the device.

These figures highlight the significant role of grain boundaries in shaping the electrical characteristics of polycrystalline silicon PIN diodes. The grain boundaries not only trap free carriers but also create potential barriers that affect the movement of charge carriers, particularly under reverse bias conditions. This understanding is critical for designing more efficient and reliable polycrystalline silicon-based electronic components.

VI. TWO-DIMENSIONAL DISTRIBUTION OF ELECTROSTATIC POTENTIAL

The distribution of electrostatic potential (ϕ), electron concentration (n), and hole concentration (p) in a PIN diode based on polycrystalline silicon is obtained by solving a two-dimensional system composed of Poisson's equation and the continuity equations for electrons and holes. The parameters for this simulation include $N_a=5.10^{18} \text{ cm}^{-3}$, $N_d= 5.10^{17} \text{ cm}^{-3}$, $N_T=3.10^{12} \text{ cm}^{-2}$, $L_g=160\text{nm}$, $L_g1=100\text{nm}$, $L_i=200\text{nm}$, $V_p=-0.3$.

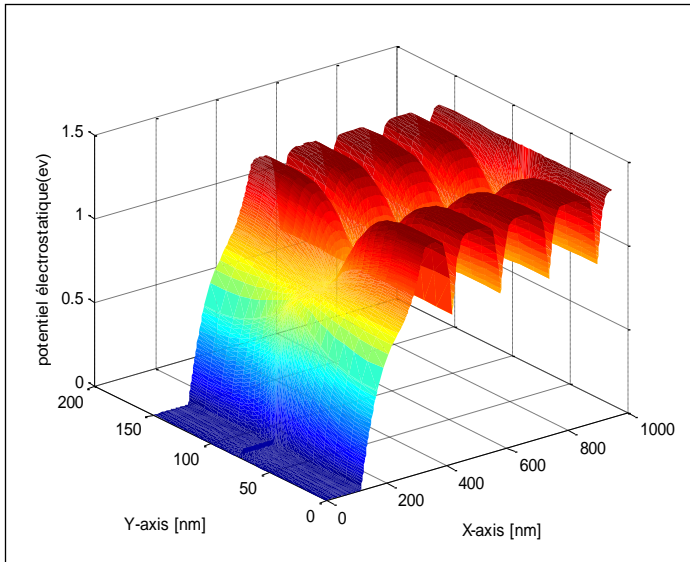


Figure 3: Distribution of the electrostatic potential. Source: Authors, (2024).

The variation of the electrostatic potential shown in Figure 3 indicates that in the highly doped P+ region, the potential perpendicular to the grain boundary has a negligible effect, characterized by a low intergranular barrier height. Conversely, in the less doped N region, the barrier height due to the metallurgical junction is proportional to the reverse voltage V_p . Near the metallurgical junction, the intergranular barrier height does not depend on the applied field and reaches its maximum at the intersection of grain boundaries. The potential barriers created by these grain boundaries form deserted areas on both sides, limiting the passage of free carriers from one crystallite to another.

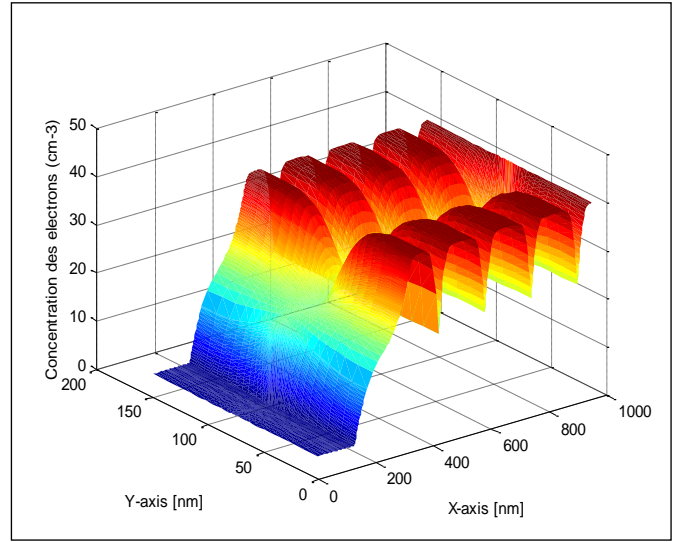


Figure 4: Semi-logarithmic concentration distribution of electron Source: Authors, (2024).

Using Figure 4, which represents the distribution of free electrons $n(x,y)$ in the device, we observe that the majority of electrons in the N region are trapped due to the high density of acceptor traps in the grain boundaries ($N_T=3.10^{12} \text{ cm}^{-2}$). Consequently, a significant concentration of electrons compared to the dopant ($N_d=5.10^{17} \text{ cm}^{-3}$) is observed, indicating that the crystallites are partially depleted of free carriers.

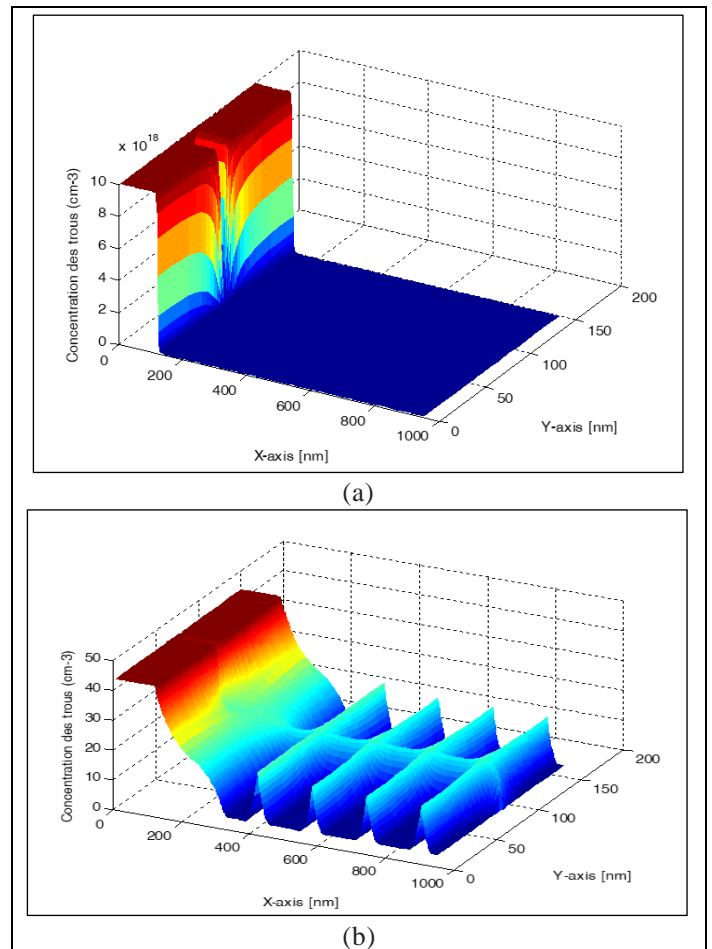


Figure 5: The concentration of holes, linear distribution (a), semi-logarithmic (b). Source: Authors, (2024).

Figure .5 illustrates the concentration distribution of holes in the device. In the P+ region, electrons are minority carriers, making their concentration negligible compared to that of the dopant. Similarly, holes, which are minority carriers in the N region, become the majority carriers in the P+ region. This transition is depicted in both the linear and semi-logarithmic plots, showing how carrier concentrations vary across different regions of the diode.

VII. INFLUENCE OF GRAIN JOINTS ON REVERSE CURRENT

The variation of current as a function of the reverse voltage (VP) between polycrystalline silicon and monocrystalline PIN diodes is depicted in Figure 6. The parameters for this analysis include ($N_A=5.1019 \text{ cm}^{-3}$, $N_D = 5.1017 \text{ cm}^{-3}$, $N_T = 3.1012 \text{ cm}^{-2}$, $L_g=160 \text{ nm}$, $L_{g1}=100 \text{ nm}$).

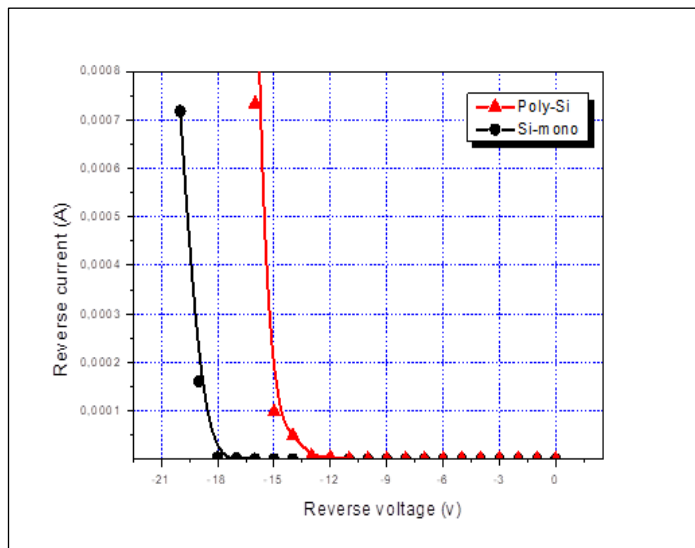


Figure 6: Current-voltage characteristic in the polycrystalline and monocrystalline PIN diode.

Source: Authors, (2024).

The graph shows a clear distinction between the breakdown voltages of the two types of diodes. The polycrystalline silicon PIN diode exhibits a breakdown voltage of approximately 12V, whereas the monocrystalline silicon PIN diode shows a higher breakdown voltage of around 18V. This significant difference indicates that the avalanche breakdown occurs more rapidly in the polycrystalline diode compared to the monocrystalline one.

This behavior can be attributed to the presence of grain boundaries in the polycrystalline material, which contain trap states that reduce the breakdown voltage. The grain boundaries trap free carriers, creating a larger space charge region compared to the metallurgical junction alone. For impact ionization to occur, a high electric field and a sufficient space charge region are necessary to accelerate carriers, thereby generating electron-hole pairs through impact ionization. These newly generated pairs further accelerate, creating more pairs and leading to the avalanche phenomenon.

The difference in breakdown behavior between the polycrystalline and monocrystalline diodes is primarily due to the presence of grain boundaries in the polycrystalline film. These boundaries facilitate the trapping of carriers, thus lowering the breakdown voltage and accelerating the avalanche breakdown process.

VIII. CONCLUSION

This study has provided a comprehensive simulation and analysis of the electrical characteristics of reverse-biased lateral polysilicon PIN diodes, with a particular focus on the effects of grain boundaries and impact ionization. By numerically solving the system of partial differential equations, including Poisson's equation and the continuity equations for electrons and holes, we obtained detailed current-voltage (I-V) characteristics of these diodes.

Our findings reveal a significant difference in the breakdown voltages between polycrystalline and monocrystalline silicon PIN diodes, with the former exhibiting a lower breakdown voltage of 12V compared to 18V for the latter. This difference is primarily due to the presence of grain boundaries in the polycrystalline material, which contain deep energy states that trap free carriers, thereby reducing the breakdown voltage and accelerating the avalanche breakdown process.

The grain boundaries in polycrystalline silicon play a critical role in shaping the diode's electrical behavior. These boundaries create potential barriers that impede carrier movement and contribute to a larger space charge region, which is essential for the onset of impact ionization. The presence of traps at these boundaries facilitates carrier trapping and recombination, further influencing the breakdown characteristics.

The results of this study have important implications for the design and optimization of polysilicon-based electronic components. Understanding the impact of grain boundaries on the electrical properties of polycrystalline silicon diodes can lead to better control of device performance and reliability. For instance, strategies to minimize the adverse effects of grain boundaries, such as improving crystallite size uniformity or optimizing doping levels, could enhance device efficiency and durability.

Moreover, the insights gained from this simulation study can be applied to a broader range of semiconductor devices that utilize polycrystalline materials, including photovoltaic cells and thin-film transistors. Future work could involve experimental validation of the simulation results, as well as the exploration of alternative materials and structures that may offer improved performance characteristics.

In conclusion, this study underscores the critical importance of grain boundaries in determining the electrical characteristics of polycrystalline silicon PIN diodes. By providing a detailed understanding of these effects, we contribute to the advancement of semiconductor technology and the development of more efficient and reliable electronic devices.

IX. AUTHOR'S CONTRIBUTION

Conceptualization: Abdelaziz Rabehi, Abdelmalek Douara, Mohamed Elbar.

Methodology: Abdelaziz Rabehi, Abdelmalek Douara, Mohamed Elbar.

Investigation: Abdelaziz Rabehi, Abdelmalek Douara, Mohamed Elbar, Roumaissa Zenzen and Mohamed Amrani.

Discussion of results: Abdelaziz Rabehi, Abdelmalek Douara, Mohamed ELBAR, Roumaissa Zenzen and Mohamed Amrani.

Writing – Original Draft: Abdelaziz Rabehi, Mohamed Elbar.

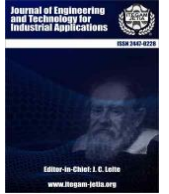
Writing – Review and Editing: Abdelaziz Rabehi, Abdelmalek Douara, Mohamed Elbar.

Supervision: Abdelaziz Rabehi, Abdelmalek Douara, Mohamed Elbar, Roumaissa Zenzen and Mohamed Amrani.

Approval of the final text: Abdelaziz Rabehi, Abdelmalek Douara, Mohamed Elbar, Roumaissa Zenzen and Mohamed Amrani.

VIII. REFERENCES

- [1] Kamins T.I. Electrical Properties of Polycrystalline-Silicon Thin Films for VLSI. MRS Proceedings. 1986; 71:261. doi:10.1557/PROC-71-261.
- [2] Seto, John YW. "The electrical properties of polycrystalline silicon films." Journal of Applied Physics 46.12 (1975): 5247-5254.
- [3] Kamins, Ted. Polycrystalline silicon for integrated circuits and displays. Springer Science & Business Media, 2012.
- [4] RABEHI, Abdelaziz, Mawloud GUERMOUI, and Redouane MIHOUB. "Direct and diffuse solar radiation components estimation based on RBF model: Case study." Leonardo Electronic Journal of Practices and Technologies 31 (2017): 93-110.
- [5] Yu, C.; Xu, S.; Yao, J.; Han, S. Recent Advances in and New Perspectives on Crystalline Silicon Solar Cells with Carrier-Selective Passivation Contacts. Crystals 2018, 8,430
- [6] Rabehi, A., Akkal, B., Amrani, M. et al. Current–Voltage, Capacitance–Voltage–Temperature, and DLTS Studies of Ni₆H–SiC Schottky Diode. Semiconductors 55, 446–454 (2021). <https://doi.org/10.1134/S1063782621040138>.
- [7] Goel, Saurav, et al. "Nanoindentation of polysilicon and single crystal silicon: Molecular dynamics simulation and experimental validation." Journal of physics D: applied physics 47.27 (2014): 275304.
- [8] Rabehi, Abdelaziz, et al. "Accurate parameter estimation of Au/GaN/GaAs schottky diode model using grey wolf optimization." Revista Mexicana de Física 70.2 Mar-Apr (2024): 021004-1.
- [9] Trempa, Matthias, et al. "Grain boundaries in multicrystalline silicon." Handbook of Photovoltaic Silicon (2019): 589-636.
- [10] Quirk, J., et al. "Grain boundaries in polycrystalline materials for energy applications: First principles modeling and electron microscopy." Applied Physics Reviews 11.1 (2024).
- [11] Zhao, Mo, et al. "Structures and energies of $\Sigma 3$ asymmetric tilt grain boundaries in silicon." Journal of Materials Research 36.10 (2021): 2025-2036.
- [12] Younsi, Ahmed Memdouh, et al. "Ab-initio study on structural, magnetic, electronic and optical properties of SrCo_{1-x}A_xO₃ (A= Fe or Cr, x= 0.125 and 0.25)." Modern Physics Letters B 38.09 (2024): 2450055.
- [13] Zhu, Qi, et al. "Inclination-governed deformation of dislocation-type grain boundaries." Journal of Materials Research 36 (2021): 1306-1315.
- [14] Ghosh, Amal K., Charles Fishman, and Tom Feng. "Theory of the electrical and photovoltaic properties of polycrystalline silicon." Journal of Applied Physics 51.1 (1980): 446-454
- [15] Ziane, Abderrezzaq, et al. "Frequency dependent capacitance and conductance–voltage characteristics of nitride GaAs Schottky diode." Semiconductors 55 (2021): 51-55
- [16] Magramene, Alima, et al. "Passivation of grain boundary electronic activity in polycrystalline silicon thin films by heat treatment and hydrogenation." The International Journal of Advanced Manufacturing Technology 128.9-10 (2023): 4331-4337
- [17] Jin, Handong, et al. "It's a trap! On the nature of localised states and charge trapping in lead halide perovskites." Materials Horizons 7.2 (2020): 397-410
- [18] Douara, Abdelmalek, Abdelaziz Rabehi, and Mostefa Hamdani. "Effect of Geometrical and Physical parameters of AlGaN/GaN HEMT on the electrical characteristics with AlN spacer layer." International Journal of Advanced Studies in Computers, Science and Engineering 11.12 (2022): 1-9.
- [19] Kamins, T. I. "Electrical Properties of Polycrystalline-Silicon Thin Films for VLSI." MRS Online Proceedings Library (OPL) 71 (1986): 261.
- [20] Quirk, J., et al. "Grain boundaries in polycrystalline materials for energy applications: First principles modeling and electron microscopy." Applied Physics Reviews 11.1 (2024).
- [21] Vahidi, H.; Syed, K.; Guo, H.; Wang, X.; Wardini, J.L.; Martinez, J.; Bowman, W.J. A Review of Grain Boundary and Heterointerface Characterization in Polycrystalline Oxides by (Scanning) Transmission Electron Microscopy. Crystals 2021, 11, 878. <https://doi.org/10.3390/cryst11080878>.
- [22] Nabil, B., et al. "Fabrication and characteristics of Hg/n-bulk GaN schottky diode." Leonardo Journal of Sciences 26 (2015): 113-123.
- [23] Vahidi, H.; Syed, K.; Guo, H.; Wang, X.; Wardini, J.L.; Martinez, J.; Bowman, W.J. A Review of Grain Boundary and Heterointerface Characterization in Polycrystalline Oxides by (Scanning) Transmission Electron Microscopy. Crystals 2021, 11, 878. <https://doi.org/10.3390/cryst11080878>
- [24] Bolognesi, Alessandro, et al. "Effects of grain boundaries, field-dependent mobility, and interface trap states on the electrical characteristics of pentacene TFT." IEEE Transactions on electron devices 51.12 (2004): 1997-2003
- [25] Slimani, A. : Développement Du Logiciel Sim 3D Pour La Résolution Numérique à Trois Dimension De l'Equation de Poisson Et Les Deux Equations De Continuité journal of Scientific Research N° 0 vol. 2 (2010)
- [26] Kerkhoven, T. On the Scharfetter-Gummel Box-Method simulation of semiconductor devices and processes Vol. 5 Edited by S. Selberherr (1993)
- [27] Gummel H.K: A self-consistent iterative scheme for one-dimensional steady state transistor calculations IEEE Trans. Electron Devices 11, 455–465 (1964)
- [28] M. Amrani « Modalisation mono et bidimensionnelle des caractéristique C-V et I-V d'une jonction PN réalisée à base de silicium polycristallin ».Thèse de docteur d'état, 1999-2000



PRECISION CROP PREDICTION USING IOT-ENABLED SOIL SENSORS AND MACHINE LEARNING

Syam Kishor K S¹, Manju G², Sania Thomas³ and Binson V A⁴

¹Department of Physics, Government College, Ambalapuzha, Kerala, India

²Department of Computer Science, Government College, Ambalapuzha, Kerala, India

³ Department of Computer Science and Engineering, Saintgits College of Engineering, Kottayam, Kerala, India

⁴Department of Electronics Engineering, Saintgits College of Engineering, Kottayam, Kerala, India

¹<http://orcid.org/0009-0000-1226-2137> , ²<http://orcid.org/0009-0004-3580-881> , ³<http://orcid.org/0000-0002-2625-63> , ⁴<http://orcid.org/0000-0003-1964-287> ,

Email: syamkishorks@gmail.com, manjualoshious@gmail.com, sania.thomas@saintgits.org, binson.va@saintgits.org

ARTICLE INFO

Article History

Received: July 23th, 2024

Received: September 17th, 2024

Accepted: September 17th, 2024

Published: October 04th, 2024

Keywords:

XGBoost,
Soil nutrients,
Smart farming,
Crop prediction,
Machine learning.

ABSTRACT

This paper introduces a cutting-edge approach for crop prediction that harnesses IoT-enabled soil sensors and machine learning models, specifically targeting cardamom, black pepper, and coffee in Idukki District, Kerala, India. The study aims to bridge the gap between soil nutrient analysis and precision agriculture by integrating a JXCT 7-in-1 soil sensor with Arduino UNO. This sensor provides accurate real-time measurements of soil moisture, temperature, pH, electrical conductivity, nitrogen, phosphorus, and potassium levels, which are critical for assessing soil health and suitability. The dataset used comprises 300 soil samples for cardamom, 320 for black pepper, and 300 for coffee, providing a robust foundation for analysis. Data from these sensors were processed using XGBoost and AdaBoost algorithms. Among the models, XGBoost achieved the highest accuracy of 91.2% and an AUC of 0.93, while AdaBoost also demonstrated strong performance with an AUC of 0.91. The results confirm the effectiveness of the system in providing precise crop suitability predictions and supporting farmers in making informed decisions based on comprehensive soil data. This approach not only improves crop yields and promotes sustainable farming practices but also shows potential for broader application in different regions and crops. Future research could expand the dataset and incorporate additional IoT devices to enhance the system's accuracy and agricultural impact.



Copyright ©2024 by authors and Galileo Institute of Technology and Education of the Amazon (ITEGAM). This work is licensed under the Creative Commons Attribution International License (CC BY 4.0).

I. INTRODUCTION

Agriculture is a cornerstone of the Indian economy, contributing significantly to the country's GDP and employing a substantial portion of its population. With over 50% of the workforce engaged in agricultural activities, the sector is pivotal for the nation's socio-economic development. Traditional farming practices, however, face numerous challenges such as unpredictable weather patterns, pest infestations, and soil degradation [1]. These issues can lead to reduced crop yields and economic instability for farmers, highlighting the need for innovative solutions to sustain agricultural productivity. To address these issues and enhance productivity, the concept of smart farming has emerged. Smart farming leverages advanced technologies like the Internet of Things (IoT), data analytics, and machine learning

to optimize agricultural practices, reduce waste, and increase crop yields. IoT devices, such as soil sensors and weather stations, provide real-time data on environmental conditions, allowing farmers to monitor their fields with precision. Data analytics can then interpret this data to offer actionable insights on irrigation scheduling, fertilization, and pest control. Machine learning models further enhance smart farming by predicting crop suitability, detecting disease outbreaks, and forecasting weather patterns. By integrating these technologies into agriculture, farmers can make informed decisions, leading to sustainable and efficient farming methods [2-4].

Kerala, located in the southwestern part of India, is known for its diverse agricultural landscape. The state's Idukki district, particularly the Kumily Panchayat, is renowned for the cultivation of high-value crops like cardamom, black pepper (pepper), and

coffee. Over 80% of the people living in this area are farmers. These crops not only contribute significantly to the local economy but also hold an essential place in the global spice market [5]. However, the productivity of these crops is highly dependent on soil health, which necessitates thorough soil analysis. Soil nutrient content, including potassium, phosphorus, and nitrogen, along with other parameters like temperature, pH, moisture content, and electrical conductivity, play a crucial role in determining crop suitability and yield [6]. Therefore, regular and precise soil analysis is vital for ensuring the optimal growth and productivity of cardamom, pepper, and coffee in this region.

The advent of IoT-enabled crop prediction systems has revolutionized traditional agricultural practices by integrating soil analysis with advanced technology [3]. IoT-enabled soil sensors provide real-time data on various soil parameters, enabling farmers to monitor soil health continuously. In sustainable and smart farming continuous monitoring of soil parameters are mandatory. This data-driven approach allows for timely interventions, such as the application of fertilizers or water, based on the specific needs of the soil and crop [7],[8]. The benefits of using IoT in agriculture are manifold, including improved resource management, reduced environmental impact, and enhanced crop yields. By continuously monitoring soil conditions and predicting crop suitability, IoT-enabled systems help farmers make informed decisions, ultimately leading to more sustainable and efficient farming practices. For improved crop production and sustainability, soil fertility analysis and cultivation based on that analysis are essential.

Machine learning further enhances the capabilities of smart farming systems by analyzing the data collected from IoT-enabled sensors to predict crop outcomes. Machine learning models can process vast amounts of data to identify patterns and correlations that may not be apparent through traditional analysis [2], [8]. In the context of agriculture, these models can predict the most suitable crops for specific soil conditions, forecast crop yields, and recommend optimal farming practices. By leveraging historical data and real-time inputs, machine learning models provide actionable insights that help farmers optimize their operations. The integration of machine learning with IoT-enabled sensors thus represents a significant advancement in the field of precision agriculture, enabling a more data-driven approach to farming. Supervised and unsupervised machine learning algorithms are extensively used for smart farming [9-13]. Pudumalar et al. developed a precision agriculture model using machine learning algorithms to aid farmers on small, open farms in predicting suitable crops [14]. Their ensemble recommendation system employs decision trees, CHAID (Chi Squared Automatic Interaction Detection), K-Nearest Neighbors, and Naive Bayes, utilizing a majority voting technique for high accuracy and efficiency. Kalimuthu et al. created a machine learning-based IoT system for crop prediction based on climatic conditions, helping farmers select cost-effective crops [15]. Rao et al. conducted a comparative study of KNN, decision tree, and random forest models to determine the best-suited crop for specific lands, finding the random forest classifier with entropy and gini criteria achieved the highest accuracy at 99.3%, while KNN had the lowest at 97% [16]. Elbasi et al. used supervised machine learning for smart farming, enhancing crop production and minimizing waste with an IoT-enabled system providing insights on planting, irrigation, and harvesting [12]. Their research evaluated fifteen algorithms and introduced a new enhanced algorithm, finding that the Bayes Net algorithm had a classification accuracy of 99.59%, while Naive Bayes Classifier and Hoeffding Tree reached 99.4%.

In this study, we focus on developing a crop prediction system for different soil types based on soil nutrient analysis. Using IoT-enabled soil sensors, we measured essential soil parameters such as potassium, phosphorus, nitrogen content, temperature, pH, moisture content, and electrical conductivity. The study focuses on cardamom, pepper, and coffee, as these are the major crops cultivated in the study area. We utilized machine learning models to predict the most suitable crops for the soil under measurement. This research aims to demonstrate the potential of combining IoT technology with machine learning to enhance agricultural productivity and sustainability in the region.

II. MATERIALS AND METHODS

In this study, we developed a crop prediction system for different soil types based on soil nutrient analysis, focusing on the cultivation of cardamom, pepper, and coffee in the Kumily Panchayat of Idukki District, Kerala, India. We employed IoT-enabled soil sensors to collect real-time data on essential soil parameters and used machine learning algorithms to predict the most suitable crops for the analyzed soil. This section details the methodologies used for sample collection, hardware integration, and the classification process employing machine learning models.

II.1 SAMPLE COLLECTION

The study was conducted in the Kumily Panchayat of Idukki District, Kerala, India, a region renowned for its cultivation of cardamom, pepper, and coffee. These crops are vital to the local economy, and soil health plays a crucial role in determining their yield and quality. To gather comprehensive data for nutrient analysis and crop prediction, extensive soil sampling was undertaken. The crops under study are shown in Figure 1. The sampling locations were carefully chosen to represent the diverse agricultural zones within the Panchayat, ensuring that the soil samples reflected the variability in soil properties across different fields. These zones included high-altitude areas primarily used for coffee and cardamom cultivation and lower-altitude regions where pepper is predominantly grown.

For cardamom fields, samples were collected from various elevations within the plantations to account for micro-environmental variations affecting soil properties. A total of 300 samples were taken from various cardamom fields, at depths ranging from 0 to 30 cm, the typical rooting zone for cardamom plants. This approach ensured a comprehensive understanding of the soil conditions specific to cardamom cultivation. In pepper fields, samples were collected from both the base of the vines and the inter-vine spaces. A total of 320 samples were taken from various pepper fields, providing a thorough understanding of the soil conditions influencing pepper growth and capturing variations that could affect nutrient availability and plant health. For coffee fields, given the extensive root system of coffee plants, soil samples were collected from a slightly deeper profile, up to 50 cm depth. A total of 300 samples were taken from various coffee fields, ensuring the capture of nutrient availability within the entire root zone, which is critical for the healthy growth of coffee plants.

Each soil sample was collected using a soil auger to ensure consistency. The samples were placed in sterile, labeled bags and transported to the laboratory for analysis using sensors. Care was taken to avoid contamination between samples, and all tools were sterilized between uses. In total, 920 samples were collected: 300 from cardamom fields, 320 from pepper fields, and 300 from coffee fields.

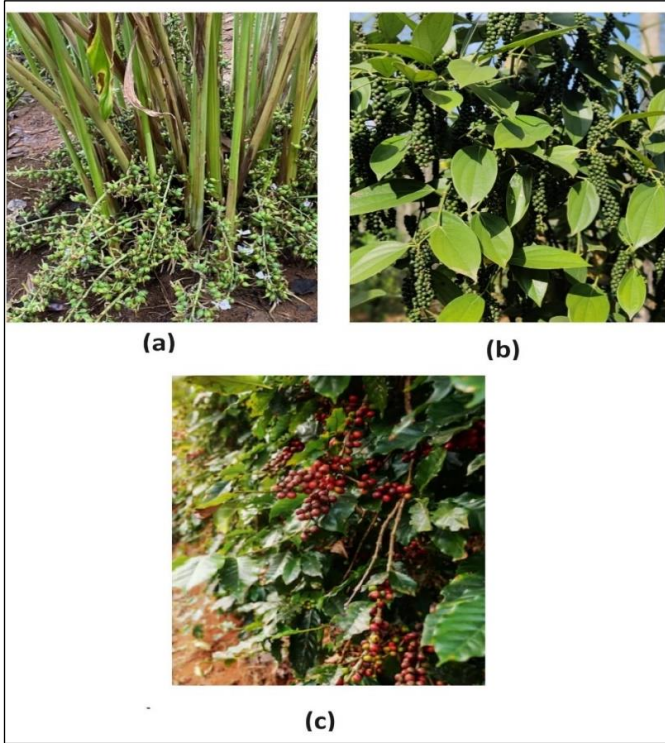


Figure 1: Crops under study (a) cardamom (b) black pepper (c) coffee.

Source: Authors, (2024).

The primary soil parameters measured included potassium (K), phosphorus (P), nitrogen (N) content, temperature, pH, moisture content, and electrical conductivity. These parameters were chosen due to their critical roles in plant growth and soil health. The detailed analysis of these parameters provided the necessary data for training and validating the machine learning models used in this study. Each sample's nutrient profile was then used to predict the suitability of the soil for cultivating cardamom, pepper, or coffee using advanced machine learning techniques.

II.2 HARDWARE DETAILS

The core of our hardware setup was the JXCT 7-in-1 soil sensor, an advanced IoT-enabled device capable of measuring multiple soil parameters simultaneously. This is shown in Figure 2.



Figure 2: 7 in 1 Soil Sensor.

Source: Authors, (2024).

This sensor is designed to provide accurate real-time data on soil moisture, temperature, pH, electrical conductivity, nitrogen,

phosphorus, and potassium levels. The JXCT 7-in-1 soil sensor is particularly suitable for agricultural applications due to its robustness, precision, and ease of integration with microcontroller platforms like Arduino.

The JXCT 7-in-1 soil sensor features high-precision probes that penetrate the soil to measure the desired parameters. It uses electrochemical sensors to detect nutrient levels and capacitive sensors for moisture content. The sensor outputs data in a digital format, making it compatible with various microcontroller interfaces. The integration of the JXCT 7-in-1 soil sensor with the Arduino UNO was a critical aspect of our hardware setup. This is shown in figure 3. The JXCT 7-in-1 soil sensor, known for its ability to measure multiple soil parameters with high precision, was connected to the Arduino UNO to facilitate real-time data acquisition. To begin, the sensor's V_{CC} (power) pin was connected to the 5V pin on the Arduino, while the GND (ground) pin was connected to the GND pin on the Arduino. The sensor's data output pins, typically labeled as TX and RX, were connected to the appropriate digital input pins on the Arduino to enable seamless communication between the sensor and the microcontroller.

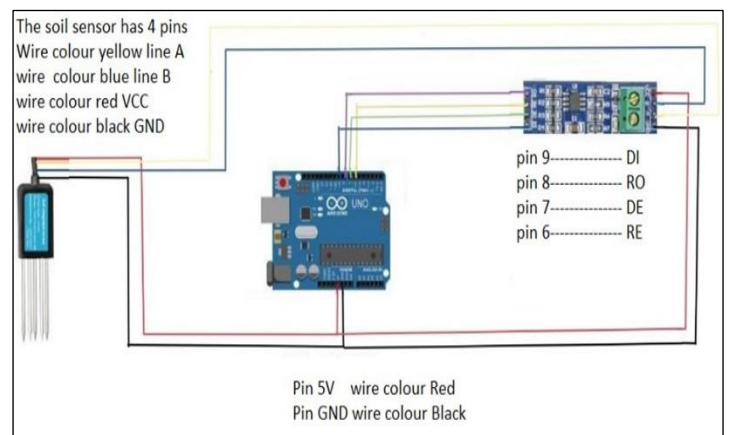


Figure 3: Sensor interfacing with Arduino UNO.

Source: Authors, (2024).

We developed a custom Arduino sketch to read the sensor data and transmit it for further analysis. This sketch utilized the Arduino SoftwareSerial library to manage the serial communication with the sensor. The program was designed to read data from the sensor at regular intervals, process the information, and store it in a structured format suitable for machine learning applications. To facilitate real-time monitoring and remote data access, the Arduino UNO was integrated with the JXCT 7-in-1 soil sensor. This setup enabled continuous monitoring of soil conditions and provided a robust foundation for our crop prediction system. By leveraging the capabilities of the JXCT 7-in-1 soil sensor and the Arduino UNO, we were able to collect precise, real-time soil data critical for accurate crop suitability analysis.

II.3 CLASSIFICATION

The core objective of our study was to predict the most suitable crops (cardamom, pepper, and coffee) for the soil samples based on the measured parameters. To achieve this, we employed machine learning techniques, specifically using the XGBoost and AdaBoost algorithms. These algorithms were chosen for their robustness, accuracy, and efficiency in handling complex, non-linear relationships within the data. The ensemble learning methods have shown great performances in sensor-based systems across various fields, including healthcare, agriculture, and automation [17-20]. In agricultural systems, particularly those

utilizing data and images, these algorithms have demonstrated excellent results [21]. By combining the strengths of multiple algorithms, ensemble learning methods enhance predictive accuracy and robustness. In agriculture, these methods can analyze soil data, weather patterns, and crop images to provide precise recommendations for crop management, pest control, and irrigation scheduling. This approach improves crop yields and sustainability and optimizes resource usage and reduces environmental impact [22],[23].

The dataset used for training and testing the machine learning models consisted of comprehensive soil parameter measurements (independent variables) and corresponding crop suitability classifications (dependent variable). The soil parameters included potassium content, phosphorus content, nitrogen content, soil temperature, pH level, moisture content, and electrical conductivity, which are critical indicators of soil health and fertility. The crop suitability labels were determined based on historical crop yield data and expert agronomic advice, categorizing each sample as suitable for cardamom, pepper, or coffee. This labeling process involved analyzing past crop performance in conjunction with expert insights to ensure accurate and reliable suitability classifications.

XGBoost is an advanced implementation of the gradient boosting algorithm that optimizes performance and efficiency. It builds an ensemble of decision trees sequentially, where each tree corrects the errors of its predecessor. Key hyperparameters for XGBoost include the learning rate, maximum depth of trees, and the number of trees [24]. These parameters were optimized using cross-validation techniques to prevent overfitting and ensure generalizability. AdaBoost is another ensemble learning technique that combines the predictions of multiple weak classifiers to create a strong classifier [25]. In our case, decision trees with limited depth were used as the weak classifiers. AdaBoost assigns higher weights to misclassified instances in each iteration, forcing the model to focus on difficult cases. The primary hyperparameters for AdaBoost include the number of weak classifiers and the learning rate, which were also fine-tuned through cross-validation.

The performance of the trained models was evaluated using standard metrics such as accuracy, precision, recall, and f1-score. Additionally, we used confusion matrices to analyze the classification results and identify areas of improvement. The model with the best performance metrics was selected for deployment.

III. RESULTS AND DISCUSSIONS

In this study, we employed cross-validation methods to evaluate the performance of our machine learning models, specifically XGBoost and AdaBoost, in predicting the suitability of soil for cardamom, pepper, and coffee cultivation. Cross-validation is a robust statistical method that involves partitioning the dataset into subsets, training the model on some subsets, and validating it on others to ensure the model's reliability and generalizability. We used three different cross-validation techniques: 3-fold, 5-fold, and 10-fold. In 3-fold cross-validation method the dataset was divided into three equal parts. In each iteration, two parts were used for training, and one part was used for validation. This process was repeated three times, with each part serving as the validation set once. In 5-fold method, the dataset was divided into five equal parts. In each iteration, four parts were used for training, and one part was used for validation. This process was repeated five times, with each part serving as the validation set once. 10-fold cross-validation divides dataset into ten equal parts. In each iteration, nine parts were used for training, and one part was used for

validation. This process was repeated ten times, with each part serving as the validation set once.

The performance of the models was evaluated using four key metrics: accuracy, precision, recall, and F1-score. These metrics provide a comprehensive understanding of the models' performance. Accuracy is the ratio of correctly predicted instances to the total instances. Precision is the ratio of correctly predicted positive observations to the total predicted positives. Recall is the ratio of correctly predicted positive observations to the all observations in actual class. F1-Score represents the weighted average of precision and recall [26-28]. The results of the cross-validation for both XGBoost and AdaBoost models are summarized in Tables 1 and 2.

Table 1: XGBoost Model Performance.

Cross-Validation	Accuracy	Precision	Recall	F1-score
3-Fold	85.7	87.3	83.4	85.2
5-Fold	88.9	90.2	86.7	88.4
10-Fold	91.2	94.3	89.5	95.0

Source: Authors, (2024).

Table 2: AdaBoost Model Performance.

Cross-Validation	Accuracy	Precision	Recall	F1-score
3-Fold	82.4	84.0	80.1	82.0
5-Fold	86.3	88.1	84.7	86.4
10-Fold	88.5	89.7	86.2	87.8

Source: Authors, (2024).

The superior performance of the XGBoost model can be attributed to its ability to handle complex, non-linear relationships in the data and its effectiveness in preventing overfitting. XGBoost, being an ensemble learning method, builds multiple decision trees sequentially, with each tree correcting the errors of its predecessor. This approach allows the model to learn intricate patterns in the soil data, which is crucial for accurate crop prediction.

Accuracy: The XGBoost model achieved a high accuracy of 91.2% with 10-fold cross-validation, indicating that it correctly predicted the suitability of soil for cardamom, pepper, and coffee in most instances. This high accuracy demonstrates the model's reliability and potential for practical application in precision agriculture.

Precision and Recall: The precision of 94.3% signifies that the model has a low rate of false positives, meaning it rarely predicts a crop as suitable when it is not. The recall of 89.5% indicates that the model successfully identifies most of the actual suitable crops, with few false negatives. The balance between precision and recall, reflected in the high F1-score of 95.0%, highlights the model's robustness and its ability to provide actionable insights for farmers.

Comparison with AdaBoost: While the AdaBoost model also performed well, its accuracy, precision, recall, and F1-score were consistently lower than those of the XGBoost model. This difference can be attributed to AdaBoost's sensitivity to noisy data and outliers, which can impact its performance. In contrast, XGBoost's regularization techniques help mitigate the effects of such data irregularities, enhancing its predictive power.

The results clearly indicate that the XGBoost model outperformed the AdaBoost model across all cross-validation methods. The best performance was achieved using the 10-fold cross-validation method with XGBoost, yielding an accuracy of 91.2%, precision of 94.3%, recall of 89.5%, and an F1-score of 95.0%. The confusion matrix of XGBoost that has given best results in the prediction is shown in Figure 4.

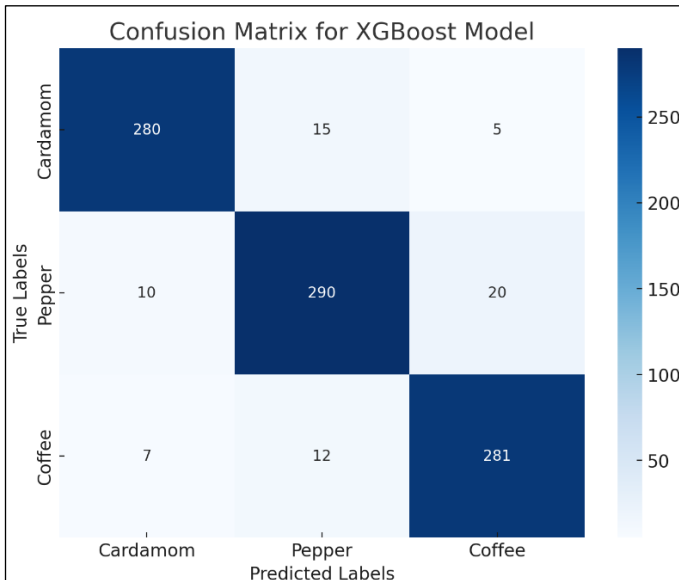


Figure 4: Confusion matrix XGBoost. Source: Authors, (2024).

The confusion matrix for the XGBoost shown in the Figures 4, provide a comprehensive breakdown of the models' predictions for the three crops: cardamom, pepper, and coffee. The confusion matrix is a crucial tool in evaluating the performance of classification models by comparing the actual target values with the predicted values.

For the XGBoost model, the confusion matrix reveals that out of 300 actual instances of soil for cardamom, 280 were correctly identified as soil for cardamom, while 15 were incorrectly classified as soil for pepper, and 5 were misclassified as soil for coffee. This high number of correct predictions (280) against a relatively low number of incorrect predictions (20) demonstrates the model's effectiveness in identifying cardamom. For soil suitable for pepper, out of 320 actual instances, 290 were correctly classified, but 10 were mistakenly predicted as soil for cardamom and 20 as soil for coffee. Although the number of correct predictions remains high (290), the errors indicate slight confusion between soil for pepper and the other crops, particularly soil for coffee. This might be due to overlapping soil nutrient profiles between these crops, which the model had to navigate. Similarly, for soil suitable for coffee, the confusion matrix shows that out of 300 instances, 281 were accurately predicted as soil for coffee. However, there were 7 instances where soil for coffee was incorrectly identified as soil for cardamom and 12 as soil for pepper. Despite these errors, the majority of predictions for coffee were correct, highlighting the model's proficiency in distinguishing coffee from the other two crops.

These detailed breakdowns for each crop category allow us to thoroughly understand the model's strengths and weaknesses in making predictions. The high number of true positives across all categories highlights the model's robust overall performance. However, the presence of false positives and false negatives underscores areas where the model could be further refined. Specifically, the errors in prediction suggest a need for fine-tuning to better distinguish between pepper and coffee, which appear to have some similarities in their soil nutrient profiles as captured by the sensor data. These similarities could be leading to misclassifications, indicating that the model might benefit from additional training data or enhanced feature engineering to improve its discriminative power. By addressing these issues, we can increase the model's accuracy and reliability, ensuring more precise

crop suitability predictions and better support for farmers in making informed decisions.

The ROC (Receiver Operating Characteristic) curve is a valuable tool for assessing the performance of a classification model by illustrating the trade-off between the true positive rate (sensitivity) and the false positive rate (1-specificity) across various threshold settings. In this analysis, the ROC curves were evaluated using a 10-fold cross-validation method to ensure robust and reliable performance metrics. The ROC curve of XGBoost and AdaBoost for the crop prediction is shown in Figure 5.

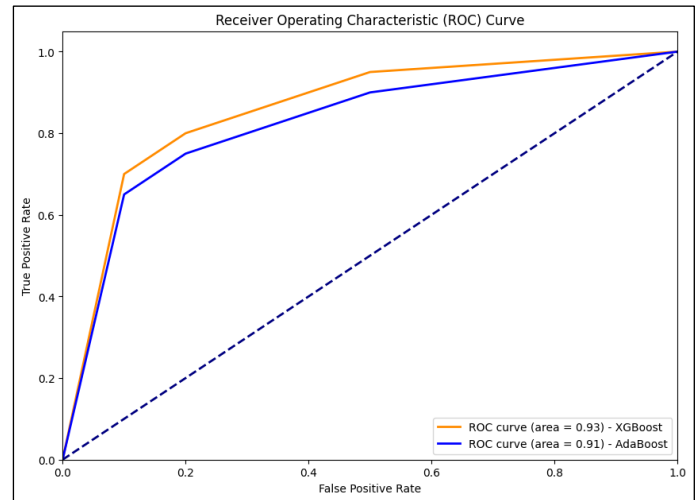


Figure 5: ROC curve of XGBoost and AdaBoost. Source: Authors, (2024).

For the XGBoost model, the ROC curve achieved an impressive AUC (Area Under the Curve) of 0.93. This high AUC value indicates that XGBoost excels in distinguishing between the different crop classes, demonstrating a strong capability to correctly classify instances while minimizing false positives. The ROC curve for XGBoost is notably close to the top left corner of the plot, reflecting its high accuracy and effectiveness in predicting crop types based on soil nutrient data. In comparison, the AdaBoost model yielded an AUC of 0.91. Although slightly lower than XGBoost, this AUC still represents strong performance. The ROC curve for AdaBoost, while also showing good discriminative ability, reveals a marginally higher rate of false positives compared to XGBoost. This suggests that while AdaBoost performs well, it is less precise in separating the crop classes than XGBoost. The ROC curve analysis reinforces the findings from the confusion matrix and performance metrics, highlighting that the XGBoost model, with its superior AUC, is more effective for crop prediction in this context. The use of a 10-fold cross-validation method has provided a robust evaluation of model performance, confirming the reliability and accuracy of XGBoost in precision agriculture applications.

IV. CONCLUSIONS

This study introduces an innovative crop prediction system utilizing IoT-enabled soil sensors and advanced machine learning to assess soil suitability for cardamom, pepper, and coffee in Idukki District, Kerala, India. By integrating a JXCT 7-in-1 soil sensor with an Arduino UNO, the system precisely measures key soil parameters such as potassium, phosphorus, nitrogen, temperature, pH, moisture content, and electrical conductivity. These inputs are processed through XGBoost and AdaBoost algorithms, with the XGBoost model achieving the highest accuracy of 91.2% in 10-fold cross-validation, and an AUC of 0.93, reflecting its strong

predictive capability. AdaBoost also performed well with an AUC of 0.91. The findings demonstrate the effectiveness of combining IoT technology with machine learning for precision farming, enabling farmers to make data-driven decisions for improved crop yields and sustainable practices. The study's approach is adaptable to other regions and crops, highlighting its potential for broad agricultural application. Future research could expand the dataset and refine models, integrating additional IoT devices to further enhance farm management and productivity.

V. AUTHOR'S CONTRIBUTION

Conceptualization: Syam Kishor K S, Manju G, Sania Thomas and Binson V A.

Methodology: Syam Kishor K S, Manju G, Sania Thomas and Binson V A.

Investigation: Syam Kishor K S, Manju G, Sania Thomas and Binson V A.

Discussion of results: Syam Kishor K S, Manju G, Sania Thomas and Binson V A.

Writing – Original Draft: Syam Kishor K S, Manju G, Sania Thomas and Binson V A.

Writing – Review and Editing: Syam Kishor K S, Manju G, Sania Thomas and Binson V A.

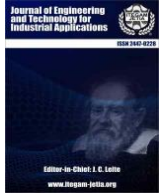
Resources: Syam Kishor K S, Manju G, Sania Thomas and Binson V A.

Supervision: Syam Kishor K S, Manju G, Sania Thomas and Binson V A.

Approval of the final text: Syam Kishor K S, Manju G, Sania Thomas and Binson V A.

VI. REFERENCES

- [1] A. Suruliandi, G. Mariammal and S.P. Raja, "Crop prediction based on soil and environmental characteristics using feature selection techniques", *Mathematical and Computer Modelling of Dynamical Systems*, vol. 27, no. 1, pp. 117140, Jan 2021.
- [2] G.K. Jha, P. Ranjan, M. Gaur, S Priya, S Terence and J. Immaculate, "A Machine Learning Approach to Recommend Suitable Crops and Fertilizers for Agriculture", *Recommender System with Machine Learning and Artificial Intelligence: Practical Tools and Applications in Medical Agricultural and Other Industries*, pp. 89-99, Jun 2020.
- [3] G. Balakrishna and N.R. Moparthy, "Study report on Indian agriculture with IoT", *International Journal of Electrical and Computer Engineering*, vol. 10, no. 3, pp. 2322, 2020.
- [4] Badri N M and Vanadana K, "Crop recommendation system using machine learning." *ITEGAM-JETIA*. vol.10, no.48, pp. 63-68, July 2024.
- [5] Sethi A, Lin CY, Madhavan I, Davis M, Alexander P, Eddleston M, and Chang SS. "Impact of regional bans of highly hazardous pesticides on agricultural yields: the case of Kerala", *Agri.Food Sec.* vol. 11, pp. 1-3, Dec 2022.
- [6] Manju G, Thomas S and V A Binson, "Enhancing agricultural productivity: predicting crop yields from soil properties with machine learning", *Afr J Biol Sci.* vol. 6, pp. 394-403, June 2024.
- [7] Sadia Afrin, Abu Talha Khan, Mahrin Mahia, Rahbar Ahsan, Mahbubur Rahman Mishal, Ahmed Wasit, et al., "Analysis of Soil Properties and Climatic Data to Predict Crop Yields and Cluster Different Agricultural Regions of Bangladesh", *IEEE International Conference on Computer and Information Science*, 2018.
- [8] X. E. Pantazi, D. Moshou, T. Alexandridis, R. L. Whetton and A. M. Mouazen, "Wheat yield prediction using machine learning and advanced sensing techniques", *Computers and Electronics in Agriculture*, vol. 121, pp. 57-65, Aug 2016.
- [9] V A Binson, George MM, Sibichan MA, Raj M, and Prasad K. "Freshness Evaluation of Beef using MOS Based E-Nose", *In 2023 International Conference on Intelligent Data Communication Technologies and Internet of Things (IDCIoT)* (pp. 792-797). IEEE, Jan 2023.
- [10] N. Gandhi, L. J. Armstrong, O. Petkar and A. K. Tripathy, "Rice crop yield prediction in India using support vector machines", *In 2016 13th International Joint Conference on Computer Science and Software Engineering (JCSSE)*, pp. 1-5, July 2016.
- [11] Thomas S and Thomas J, "Non-destructive silkworm pupa gender classification with X-ray images using ensemble learning", *Artif Intell Agri.* vol. 6, pp. 100-10, Jan 2022.
- [12] E. Elbasi, C. Zaki, A. E. Topcu, W. Abdelbaki, A. I. Zreikat, E. Cina, et al., "Crop prediction model using machine learning algorithms", *Applied Sciences*, vol. 13, no. 16, pp. 9288, 2023.
- [13] Thomas S and Thomas J, "Nondestructive and cost-effective silkworm, *Bombyx mori* (Lepidoptera: Bombycidae) cocoon sex classification using machine learning", *Int J Trop Insect Sci.* vol. 44, pp. 1125–1137, Mar 2024.
- [14] S. Pudumalar, E. Ramanujam, R. H. Rajashree, C. Kavya, T. Kiruthika and J. Nisha, "Crop recommendation system for precision agriculture", *Eighth International Conference on Advanced Computing (ICoAC)*, pp. 32-36, 2017.
- [15] M. Kalimuthu, P. Vaishnavi and M. Kishore, "Crop Prediction using Machine Learning", *2020 Third International Conference on Smart Systems and Inventive Technology (ICSSIT)*, pp. 926-932, 2020.
- [16] Rao M S, Arushi S, NV Subba Reddy and Dinesh U Acharya, "Crop prediction using machine learning", *In Journal of Physics: Conference Series*, vol. 2161, pp. 012033, 2022.
- [17] V. A. Binson, M. Subramoniam, Youhan Sunny and Luke Mathew, "Prediction of pulmonary diseases with electronic nose using SVM and XGBoost", *IEEE Sens J*, Aug 2021.
- [18] J. Babber, P. Malik, V. Mittal and K. C. Purohit, "Analyzing Supervised Learning Algorithms for Crop Prediction and Soil Quality", *2022 6th International Conference on Computing Methodologies and Communication (ICCMC)*, pp. 969-973, 2022.
- [19] Y. Shendryk, R. Davy and P. Thorburn, "Integrating satellite imagery and environmental data to predict field-level cane and sugar yields in Australia using machine learning", *Field Crops Research*, vol. 260, pp. 107984, Jan. 2021.
- [20] Paithane P M, "Random forest algorithm use for crop recommendation." *ITEGAM-JETIA*, vol. 9, no. 43, pp. 34-41, Oct 2023.
- [21] Thomas S and Thomas J, "An optimized method for mulberry silkworm, *Bombyx mori* (Bombycidae: Lepidoptera) sex classification using TLBPSGA-RFEXGBoost", *Bio open*. vol. 13, no. 7, 060468, July 2024.
- [22] H. K. Adli et al., "Recent Advancements and Challenges of AIoT Application in Smart Agriculture: A Review", *Sensors*, vol. 23, no. 7, pp. 3752, Apr. 2023.
- [23] J. Jung, M. Maeda, A. Chang, M. Bhandari, A. Ashapure and J. Landivar-Bowles, "The potential of remote sensing and artificial intelligence as tools to improve the resilience of agriculture production systems", *Curr. Opin. Biotechnol.*, vol. 70, pp. 15-22, Aug. 2021.
- [24] T Chen and C. Guestrin, "Xgboost: A scalable tree boosting system[C]", *Proceedings of the 22nd acm sigkdd international conference on knowledge discovery and data mining*, pp. 785-794, 2016.
- [25] T. Hastie, S. Rosset, J. Zhu and H. Zou, "Multi-class AdaBoost", *Statistics And Its Interface*, vol. 2, no. 3, pp. 349-360, 2009.
- [26] Z. Zhai, J. F. Martínez, V. Beltran and N. L. Martínez, "Decision support systems for agriculture 4.0: Survey and challenges", *Comput. Electron. Agric.*, vol. 170, pp. 105256, Mar. 2020.
- [27] S. Y. Chaganti, P. Ainapur, M. Singh and S. Oktaviana, "Prediction Based Smart Farming", *In 2019 2nd International Conference of Computer and Informatics Engineering (IC2IE)*, pp. 204-209, Sep 2019.
- [28] S. Maya Gopal and R. Bhargavi, "Performance evaluation of best feature subsets for crop yield prediction using machine learning algorithms", *Appl. Artif. Intell.* vol. 33, pp. 621–642, June 2019.



RESEARCH ARTICLE

OPEN ACCESS

ADVANCED DUAL-LOOP CONTROL ARCHITECTURE FOR SUPERIOR PMSM PERFORMANCE UTILIZING FINITE-CONTROL-SET MODEL PREDICTIVE CONTROL AND EXPONENTIAL REACHING LAW SLIDING MODE CONTROL

Djaloul Karboua¹, Youcef Chouiha², Ben Ouadeh Douara³, Ibrahim Farouk Bouguenna⁴, Said Benkaihoul⁵ and Belgacem Toual⁶

^{1, 6} dept. Electrical Engineering–LASER Lab, Djelfa University Djelfa, Algeria.

^{2,3,5} dept. Electrical Engineering–LAADI Lab, Djelfa University Djelfa, Algeria.

⁴ Institute for Electrical Engineering University of Mascara Mascara, Algeria.

¹ <http://orcid.org/0000-0003-0155-9925> ² <http://orcid.org/0000-0001-9055-8953> ³ <http://orcid.org/0000-0002-0548-5300> ,

⁴ <http://orcid.org/0000-0001-8631-8172> ⁵ <http://orcid.org/0000-0002-8824-9761> ⁶ <http://orcid.org/0000-0001-6900-9920> ,

Email: djaloul.karboua@univ-djelfa.dz , y.chouiha@univ-djelfa.dz , b.douara@univ-djelfa.dz , i.bouguenna@univ-mascara.dz , saidbenkaihoul@gmail.com , Toualb@gmail.com

ARTICLE INFO

Article History

Received: July 26th, 2024

Received: September 18th, 2024

Accepted: September 18th, 2024

Published: September 27th, 2024

Keywords:

PMSM,
Dual-Loop Control,
Robust technique,
ERL-SMC,
FCS-MPC.

ABSTRACT

This article contributes to the field by providing a comprehensive dual-loop control solution that addresses the limitations of individual control techniques and offers a robust and efficient framework for advanced PMSM control. In the current loop, FCS-MPC is employed to predict the future behavior of the motor currents and select the optimal control action from a finite set of possible inputs. This method ensures minimal current ripple, improved transient response, and efficient handling of the non-linearities and constraints inherent in PMSM operation. The predictive nature of FCS-MPC allows for real-time optimization, enhancing the overall efficiency of the current regulation. For the speed loop, the ERL-SMC is designed to provide robust control against parameter variations and external disturbances. The exponential reaching law ensures a faster and smoother reaching phase, reducing chattering and improving the steady-state performance. By incorporating an ERL, the sliding mode controller can swiftly bring the system states to the sliding surface and maintain them, thus achieving high accuracy in speed tracking and robust performance under various operating conditions. The combination of FCS-MPC and ERL-SMC harnesses the predictive capabilities and optimization of the former with the robustness and disturbance rejection of the latter. This hybrid control strategy is evaluated through extensive simulations in MATLAB/Simulink. The simulation results demonstrate significant improvements in dynamic response, tracking accuracy, reduced overshoot, and enhanced disturbance rejection. Additionally, the proposed approach shows superior performance in handling sudden load changes and parameter uncertainties, confirming its potential for high-performance PMSM drive applications.



Copyright ©2024 by authors and Galileo Institute of Technology and Education of the Amazon (ITEGAM). This work is licensed under the Creative Commons Attribution International License (CC BY 4.0).

I. INTRODUCTION

Permanent Magnet Synchronous Motors (PMSMs) have become a cornerstone in various industrial applications due to their high efficiency, power density, and excellent performance characteristics. These motors are particularly valued in applications demanding precise speed and position control, such as robotics,

electric vehicles, and aerospace technologies. To fully exploit the advantages of PMSMs, vector control strategies are crucial for effective management of the current and speed loops [1-4].

Field Oriented Control (FOC) is one of the most widely used methods for controlling PMSMs. FOC decouples the torque and flux components, allowing independent control of the motor's d-axis and q-axis currents. However, despite its popularity, FOC

suffers from several limitations. The implementation of FOC requires precise tuning of PI controllers and accurate knowledge of motor parameters, making it complex and challenging in practical scenarios. Additionally, FOC is highly sensitive to parameter variations, which can degrade control accuracy and stability. The method also tends to have a slower dynamic response compared to more advanced control techniques. Another conventional method is Direct Torque Control (DTC), which directly controls the motor's torque and flux without the need for coordinate transformation. DTC offers faster dynamic response but comes with its own set of drawbacks. It often results in significant torque and flux ripple, leading to increased acoustic noise and mechanical stress. Furthermore, the nonconstant switching frequency in DTC complicates the design of power electronic converters, and like FOC, DTC's performance is sensitive to motor parameter variations [5-8]. Sliding Mode Control (SMC) is known for its robustness against parameter variations and external disturbances. Classical SMC ensures that the system states reach and remain on a predefined sliding surface. However, the main issue with classical SMC is chattering, which refers to high frequency oscillations caused by the discontinuous control action. Chattering can cause wear and tear in mechanical components and increase energy losses. Additionally, designing an effective sliding surface and reaching law in classical SMC requires careful tuning, which can be complex and application-specific [9-12].

Exponential Reaching Law-based Sliding Mode Control (ERL-SMC) addresses some of the shortcomings of classical SMC. By modifying the reaching law, ERL-SMC aims to reduce chattering and improve control performance. The exponential reaching law provides a continuous control action during the reaching phase, significantly reducing chattering. This approach also enhances robustness against disturbances and parameter variations and offers better steady-state accuracy and dynamic response compared to classical SMC. It also provides maintaining high-speed tracking accuracy and enhancing system stability under varying operating conditions [13], [14].

FiniteControl-Set Model Predictive Control (FCS-MPC) is a cutting-edge control strategy that has gained significant attention in recent years due to its ability to handle complex control problems with a high degree of precision. Unlike traditional control methods that rely on continuous control signals, FCS-MPC operates by predicting the future behavior of the system over a finite time horizon and selecting the optimal control action from a discrete set of possible inputs. This approach enables FCS-MPC to effectively manage non-linearities and system constraints, providing enhanced control performance. The predictive nature of FCS-MPC allows for the anticipation of future states, leading to improved transient responses and reduced steady-state errors. Furthermore, FCS-MPC's ability to minimize current ripple and optimize power efficiency makes it particularly suitable for applications in Permanent Magnet Synchronous Motor (PMSM) drives, where precision and efficiency are paramount. By continuously updating the control inputs based on real-time system feedback, FCS-MPC ensures that the control objectives are met with minimal deviation, thereby offering a robust and adaptive control solution for modern electrical drive systems [15-17]. To overcome the limitations of these conventional control methods, this paper proposes a dual-loop control strategy for PMSM drives. This strategy integrates FiniteControl-Set Model Predictive Control (FCS-MPC) for the current loop with Exponential Reaching Law-based Sliding Mode Control (ERL-SMC) for the speed loop. By combining FCS-MPC for the current loop and ERL-SMC for the speed loop, the proposed dualloop control strategy aims to harness the predictive capabilities

and optimization of FCS-MPC with the robustness and disturbance rejection of ERL-SMC. This hybrid approach is validated through extensive simulations in MATLAB/Simulink, demonstrating significant improvements in dynamic response, tracking accuracy, and overall system robustness compared to conventional control method based on ERL-SMC. This study provides a comprehensive dual-loop control solution that addresses the limitations of individual control techniques and offers a robust and efficient framework for advanced PMSM control. The structure of this paper is organized as follows: Section 2 focuses on constructing a comprehensive model of the Permanent Magnet Synchronous Motor (PMSM) system. In Section 3, we detail the design of the Exponential Reaching Law Sliding Mode Controller (ERL-SMC) specifically for the PMSM speed loop, emphasizing its robustness and performance improvements. Section 4 is dedicated to the design of the Finite Control Set Model Predictive Control (FCS-MPC) for the PMSM current loop, highlighting its predictive capabilities and control accuracy. Following the control design sections, Section 5 presents the simulation setup and results, providing a thorough discussion on the effectiveness and efficiency of the proposed control strategies. Finally, Section 6 concludes the paper and summarizing the key findings.

II. CONSTRUCTING A MODEL OF THE PMSM SYSTEM

Before implementing any control strategy, it is imperative to transform the three-phase Permanent Magnet Synchronous Motor (PMSM) system into a two- phase representation using the Park transformation. The adoption of a d-q rotor reference frame significantly simplifies the derived equations, expediting the numerical calculations essential for computational simulations. This simplification not only accelerates the computational process but also ensures the constancy of resultant variables during steady-state operation, thereby facilitating subsequent computations and streamlining the design of the control system. Moreover, the d-q model within the rotor reference frame is widely recognized and favored in current literature due to its simplicity and applicability. Assumptions within this model include a cage-free rotor, sinusoidal back-EMF, negligible saturation, and minimal eddy current and hysteresis losses [18], [19]. Additionally, to utilize the nonlinear model effectively, the PMSM system is described by Equation 1, where the state variables comprise the stator speed, direct current, and quadrature current [20], [21].

$$\begin{cases} \frac{di_d}{dt} = \frac{1}{L_d} \cdot (u_d - R_s \cdot i_d + L_q \cdot \omega_r \cdot i_q) \\ \frac{di_q}{dt} = \frac{1}{L_q} \cdot (u_q - R_s \cdot i_q - L_d \cdot \omega_r \cdot i_d - \omega_r \cdot \Phi_f) \\ \frac{d\omega_r}{dt} = \frac{3 \cdot p^2}{2 \cdot J} \cdot (\Phi_f \cdot i_q + (L_q - L_d) i_d i_q - \frac{F}{J} \cdot \omega_r - \frac{p}{J} \cdot T_l) \\ \frac{d\theta_r}{dt} = \omega_r \end{cases} \quad (1)$$

i_d, i_q are d-q axis equivalent stator currents ; u_d, u_q are d-q axis equivalent stator voltages ; θ_r, ω_r are rotor position and rotor speed ; p is number of pole pairs ; R_s is per phase stator resistance; L_d, L_q are d-q axis equivalent stator inductance ; T_e, T_l are electromagnetic and load torques ; J is moment of inertia of the rotor ; F is friction constant of the rotor and Φ_f is rotor magnetic flux linking the stator.

III. DESIGNING THE ERL-SMC FOR THE PMSM SPEED LOOP

Sliding mode control primarily aims to establish a switching surface that adheres to principles of existence, convergence, and stability. This involves adjusting the system's structure to guide the state trajectory towards this surface. Systems with adaptable structures undergo changes during operation. Sliding mode control typically operates in two modes: convergence towards the surface and subsequent sliding along it. Once the system reaches the switching surface, it follows a dynamic described by the sliding mode, asymptotically moving towards the equilibrium point within a finite time frame. The synthesis of sliding mode control methodically addresses performance and stability concerns. Implementation of this control entails three key steps: selecting the sliding surface, defining sliding conditions, and calculating the SMC law. The general formula for sliding surfaces is designed as follows [22-25]:

$$S(x, t) = \left(\frac{d}{dt} + \lambda \right)^{n-1} e(t) \quad (2)$$

Where λ is a positive number chosen by the designer (a parameter that fixes the dynamic of the error in sliding mode), n is system order, $S(x, t)$ is the sliding surface and $e(t)$ is tracking error. Once the sliding surface is established, the system trajectory is directed towards the origin, eventually reaching it asymptotically, as dictated by the sliding condition described in the following equation [26]:

$$\frac{1}{2} \frac{d}{dt} S^2 \leq \eta |S| \quad (3)$$

Where $\eta > 0$ Following the establishment of the sliding surface and adherence to the sliding condition, the control law is determined through a two-phase approach. Firstly, the sliding phase is enacted to ensure the system remains on the sliding surface, achieved by designing an equivalent term where $S(x, t) = 0$ and $\dot{S}(x, t) = 0$. Subsequently, the approach phase is initiated to meet the sliding condition, accomplished by formulating a switching law where $S(x, t) \neq 0$ and $\dot{S}(x, t) = 0$. The specific design of the SMC control law unfolds as [27]:

$$u = u_{eq} + u_s \quad (4)$$

Using the exponential approach law, one can reduce the occurrence of rapid oscillations in the control signal while preserving the dynamic performance of the sliding mode arrival process through careful adjustment of parameters k_1 and k_2 . However, if k_2 is set too high, it may result in undesirable chattering. To overcome this problem the ERL-SMC has been improved using the Pseudo-sliding mode based on continuous approximation [14], [28]. Similarly, within this context, the speed tracking error and the sliding surface can be expressed as follows:

$$\begin{cases} e_\omega = \omega_r^{ref} - \omega_r \\ S_\omega = \omega_r^{ref} - \omega_r \end{cases} \quad (5)$$

With reference to the sliding phase outlined earlier, the equivalent term takes on the following expression:

$$i_{q-eq}^{ref} = \frac{2 \cdot J}{3 \cdot p^2 \cdot \Phi_f} \cdot \left(\dot{\omega}_r^{ref} + \frac{F}{J} \omega_r + \frac{p}{J} \cdot T_l \right) \quad (6)$$

Given the preceding approach phase, the switching term based on ERL-SMC and Pseudo-sliding mode is delineated as follows:

$$u_s = k_1 \cdot \text{tgh}(S_\omega) + k_2 \cdot S_\omega \quad (7)$$

Where S is sliding surface of SMC and k_1, k_2 , are the gains used to regulate the ERL based on Pseudo sliding mode controller. The control law for the PMSM's speed loop, based on the ERL-SMC, can be formulated using the equivalent and switching terms as follows:

$$i_q^{ref} = i_{q-eq}^{ref} + i_{q-s}^{ref} \quad (8)$$

IV. DESIGNING OF THE FCS-MPC FOR THE PMSM CURRENT LOOP

Predictive control is a control strategy that relies on a dynamic mathematical model of the system to forecast future behavior. It optimizes control inputs over a specified time horizon by considering system dynamics, constraints, and desired objectives. The controller updates its predictions and optimizations in real time, adapting to changes and disturbances to achieve optimal performance. This method is widely used in complex systems requiring precise and adaptive control, such as industrial processes, robotics, and energy systems. Key features of this type of controller include selecting the best actions by minimizing a cost function and using a system model to predict future variable behavior over a set time horizon. A summary of the Model Predictive Control (MPC) operating principle is illustrated in Figure 1. Using the system model and the available measurements up to time k , future state values are projected until a predetermined horizon at time $k + N$. By minimizing the cost function, the optimal sequence of actions is determined, and the first action in this sequence is implemented. This procedure is repeated at each sampling instant, incorporating the most recent data. The prediction model used is a discrete-time model, expressed in the following state space form [16], [17].

$$\begin{cases} x(k+1) = A \cdot x(k) + B \cdot u(k) \\ y(k) = C \cdot x(k) + D \cdot u(k) \end{cases} \quad (9)$$

A cost function that reflects the desired system behavior must be defined. This function takes into account future states, control actions, and reference values.

$$J = f(x(k), u(k), \dots, u(k+N)) \quad (10)$$

The objective of the MPC optimization problem is to minimize the cost function J over a specified time horizon N , while considering constraints and the system model. This process results in a series of N optimal control actions, but only the first action in the sequence is implemented by the controller. At each sampling instant, new measured data is used to resolve the optimization problem, generating a new set of optimal control actions each time. This approach is known as receding horizon control [17].

$$u(k) = [1 \ 0 \ \dots \ 0] \arg \min_u J \quad (11)$$

stator current of the PMSM. The maximum current for the quadrature axis (q) and the direct axis (d) is indicated by i_{max} . The future reference currents $i_d^*[k + 1]$ and $i_q^*[k + 1]$ are estimated using Lagrange extrapolation based on prior sampling points [k], [k1], and [k2], as detailed in [16].

$$i_{dq}^*[k + 1] = 3i_{dq}^*[k] - 3i_{dq}^*[k - 1] + i_{dq}^*[k - 2] \quad (16)$$

V. SIMULATION, RESULTS AND DISCUSSION

To demonstrate the effectiveness of the dual-loop control studied in this paper for the PMSM, a simulation model was built in Matlab/Simulink, as shown in Figure 3 for the ERLSMC with FCS-MPC. These controls are applied to the speed and current loops of the PMSM. To validate the dual-loop control, various scenarios are presented to prove its effectiveness. The selection of design parameters was based on a thorough analysis of PMSM performance using several criteria: stability, performance characteristics, robustness, cost function, and energy minimization. The PMSM parameters used in this work are listed in Table 2.

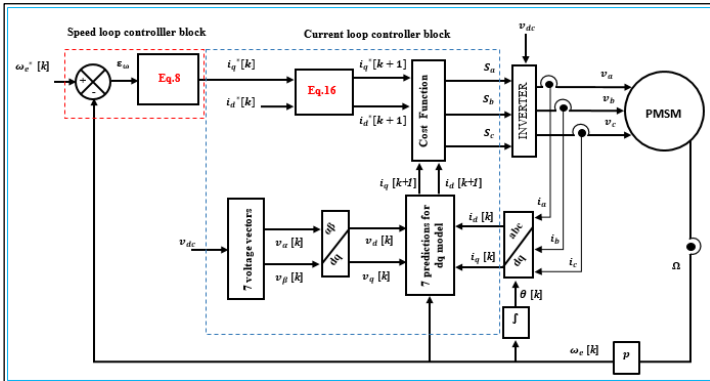


Figure 3: Scheme of PMSM controller based on a novel dual-loop control design. Source: Authors, (2024).

Table 2: Parameters of the PMSM drive.

PMSM's parameters		
$R_s = 0.6 \Omega$	$L_d = 1.4 \cdot 10^{-3} H$	$L_q = 2.8 \cdot 10^{-3} H$
$F = 1.4 \cdot 10^{-3} M.m.s^{-1}$	$\Phi_f = 12 \cdot 10^{-2} Wb$	$J = 1.1 \cdot 10^{-3} kg.m^2$
$v_{dc} = 100V$		$p = 4$

Source: Authors, (2024).

In the first scenario, the PMSM operates in a stable state with the speed stabilized at a medium level (600 rpm) and a load torque of 5 N·m applied. This scenario showcases the performance of speed, torque, and the direct and quadratic currents. Additionally, a comparison is made between the classical PMSM drive design based on the ERL-SMC and the novel PMSM drive design based on the dual-loop control. As shown in Figure 4, the speed performance indicates that the novel design based on the dualloop control outperforms the classical design based on the ERLSMC in terms of rise time (Tr) and steady-state error (SSE). The rise time for the novel design is approximately 6 ms, whereas the classical design has a rise time of approximately 12 ms. The steady-state error for the novel design is around 0.006%, compared to 0.05% for the classical design. Moreover, the novel design is stabilized with minimal chattering, while the classical design suffers from significant chattering. Specifically, the chattering for

the novel design is between +0.055 and -0.035, while for the classical design, it is between +0.15 and -0.85.

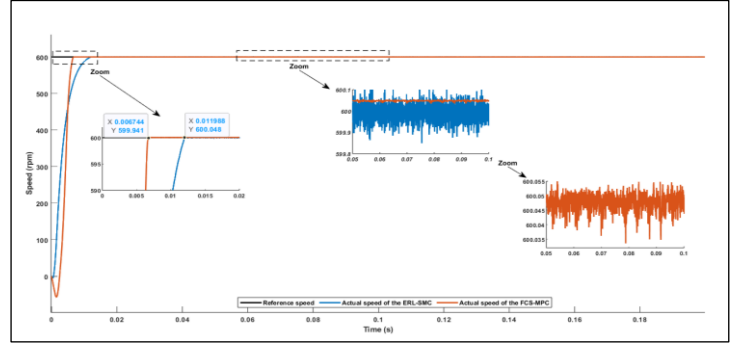


Figure 4: PMSM speed performance under the first scenario. Source: Authors, (2024).

Regarding the electromagnetic torque performance illustrated in Figure 5, the novel design significantly minimizes torque ripple compared to the traditional ERL-SMC design, which experiences substantial torque ripple. The torque ripple in the novel FCSMPC design ranges between +0.15 and -0.15, while the ERLSMC design exhibits a torque ripple range between +0.55 and -0.5. Moreover, Figure 6 highlights the superior performance of the novel design in terms of direct and quadratic current control. The tolerance band for the direct current in the novel control design is notably narrower than that of the ERL-SMC. Specifically, the tolerance band for the direct current in the novel control design is between +0.15 and -0.15, whereas for the ERL-SMC, it is between +0.5 and -0.5. These estimates are similarly applicable to the quadratic current.

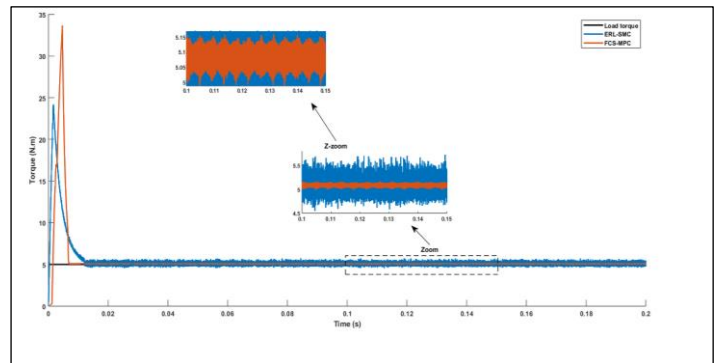


Figure 5: PMSM electromagnetic torque performance under the first scenario. Source: Authors, (2024).

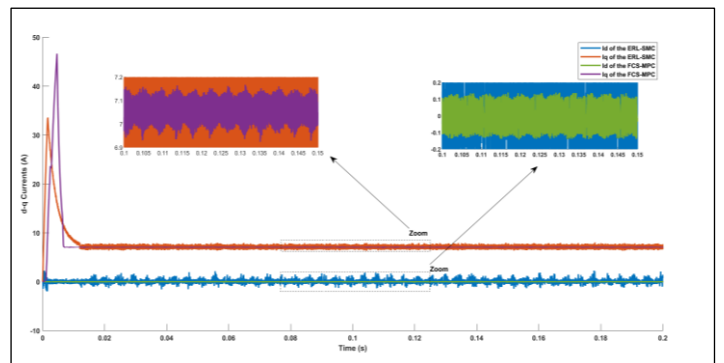


Figure 6: PMSM d-q currents performance under the first scenario. Source: Authors, (2024).

The second scenario is presented to demonstrate the robustness of the novel control design under external disturbances. Various load torque values (1 N.m, 2 N.m, 5 N.m, and 3 N.m) were applied at different time instances, as shown in Figure 8. Under these conditions, the novel control design exhibits superior speed performance compared to the classical ERA-SMC design. Although the rise time remains consistent with the first scenario for both controls, overshoots and undershoots occur during changes in load torque. The overshoot/undershoot rate in the novel control design is limited to 0.6%, which is significantly lower than that of the classical control design, as illustrated in Figure 7. Regarding electromagnetic torque performance, depicted in Figure 8, the novel control design outperforms the classical control design with substantially lower steady-state error and reduced chattering. Additionally, Figure 9 shows that the novel control design maintains excellent performance in terms of direct and quadratic currents. This results in high-quality electrical power, reduced noise, lower losses, and improved stability under external disturbances.

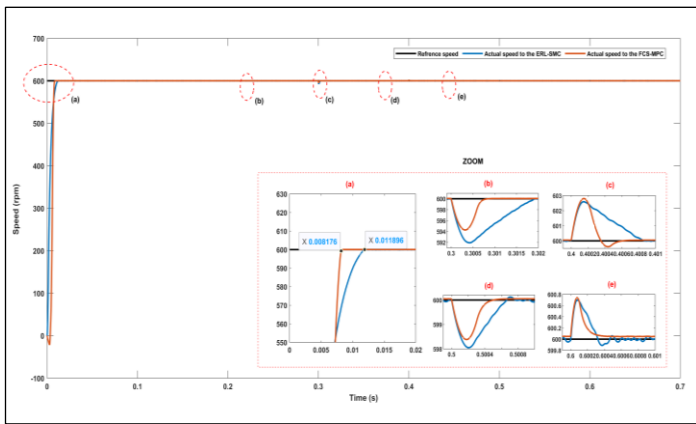


Figure 7: PMSM speed performance under the second scenario. Source: Authors, (2024).

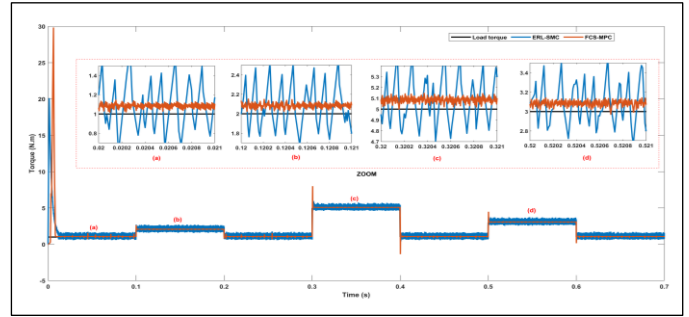


Figure 8: PMSM electromagnetic torque performance under the second scenario. Source: Authors, (2024).

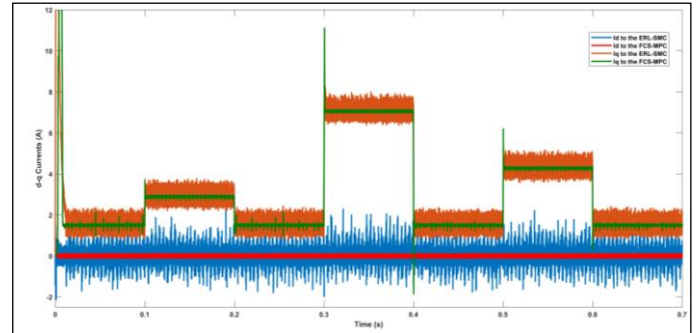


Figure 9: PMSM d-q currents performance under the second scenario. Source: Authors, (2024).

The three-phase current performance is significantly enhanced with the novel control design, which effectively minimizes current oscillations and maintains stability within a consistent tolerance band during load torque variations, as demonstrated in Figure 10. In contrast, the classical control design exhibits inferior performance for the three-phase current, characterized by a wider tolerance band and reduced stability during load torque changes. Detailed information regarding the current performance of both control designs is provided in Figures 10 and 11. This scenario examines the robustness of the novel control design under parameter uncertainties.

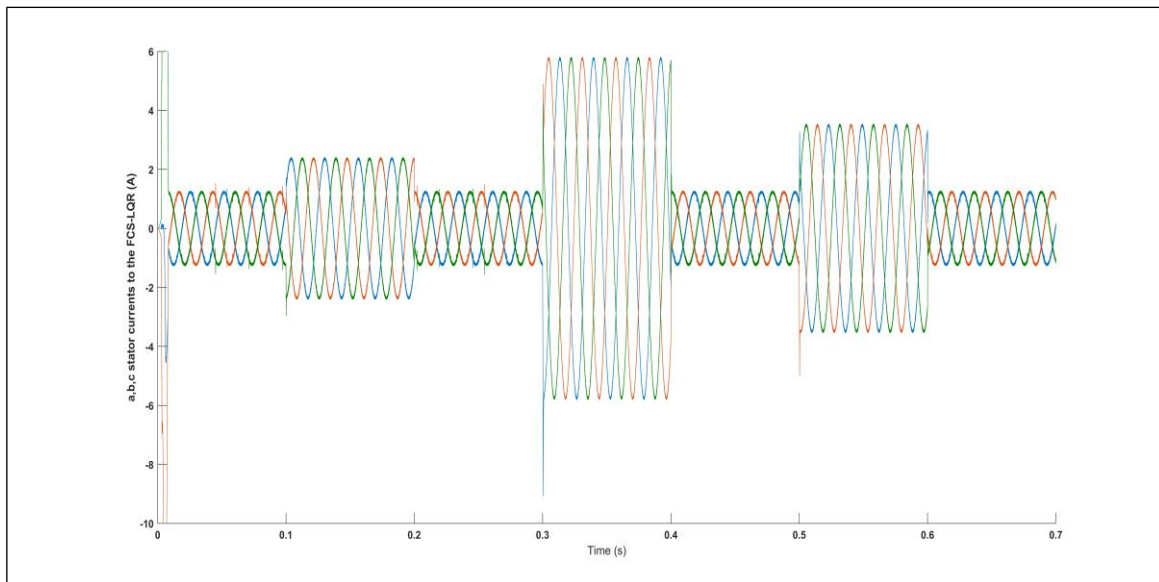


Figure 10: PMSM a,b,c currents performance based on the novel control design under the second scenario. Source: Authors, (2024).

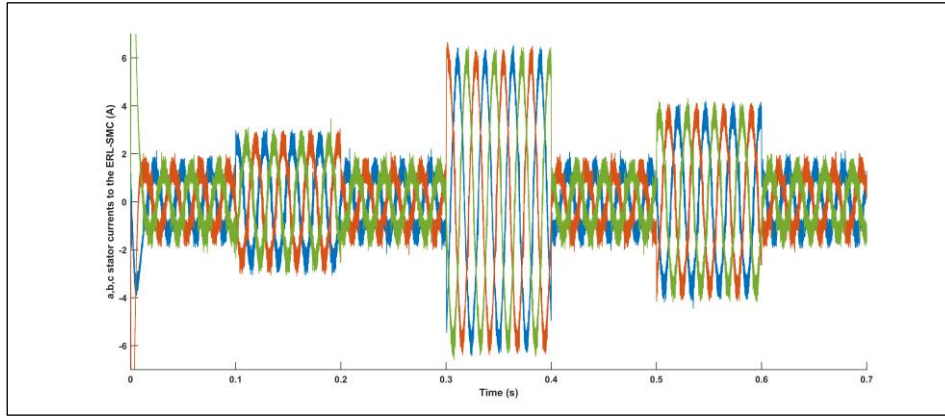


Figure 11: PMSM a,b,c currents performance based on the classical control design under the second scenario. Source: Authors, (2024).

The variations in PMSM parameters, including resistance, direct and quadratic inductances, and inertia, were studied at increasing rates. Figure 12 illustrates this scenario, showing changes at 0%, 50%, 100%, 150%, and 200% with a medium speed of 600 rpm. Additionally, the novel control performs well in terms of the uncertainty rate (UR) for the change in rise time across the different percentages of PMSM parameter changes, with the UR estimated at 0.004096 seconds. Furthermore, the novel control design exhibits a very small steady-state error. The steady-state error percentage between the reference speed and the 200% uncertainty level is estimated at 0.025%, between the reference speed and the 0% uncertainty level at 0.008%, and between the 0% and 200% uncertainty levels at 0.01.

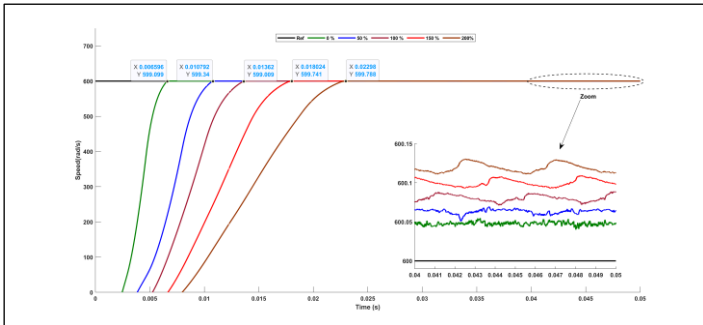


Figure 12: PMSM speed performance under the uncertainties scenario. Source: Authors, (2024).

The final scenario tests the speed performance of the PMSM using the novel control design at high speed levels. This novel control design is compared to the classical ERL-SMC-based control design. This scenario is particularly challenging because the PMSM operates across vastly different speed ranges, with each range representing a distinct operational state and large changes in rotational speed between states. Under this scenario, the durability of the studied controls is evaluated. Figure 13 illustrates the high performance of the PMSM, where the speed varies between low (50 rpm), medium (375 rpm), and high (1000 rpm). This analysis explores the performance characteristics and phenomena that might impede the PMSM’s performance, as well as the control design’s flexibility in adapting to changes in speed levels from one state to another.

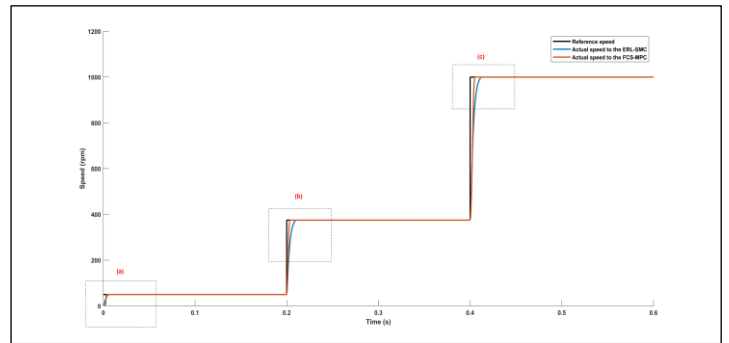


Figure 13: PMSM speed performance under the speed levels changes. Source: Authors, (2024).

To determine which technique performs better, we will analyze each speed level individually. Figure 14 focuses on region (a) from Figure 13, showcasing the speed performance of the PMSM at a low speed of 50 rpm, with a comparative study of the mentioned techniques. According to Figure 14 and Table 3, the novel control design outperforms the classical ERL-SMCbased control design in terms of performance characteristics and durability. The novel control design achieves the smallest steady-state error, estimated at 0.02%, as well as the smallest rise time, estimated at 3.2ms

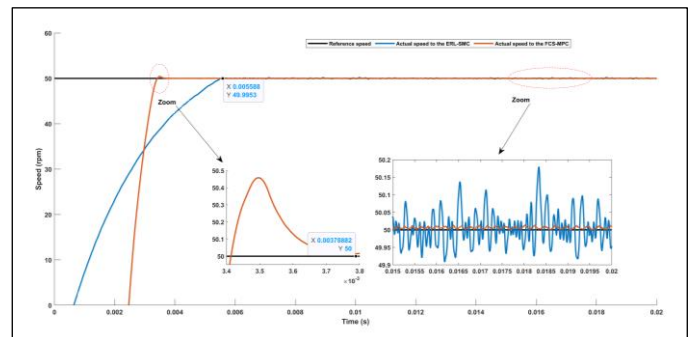


Figure 14: PMSM speed performance under the low speed level. Source: Authors, (2024).

The second level involves transitioning to medium speed and evaluating the PMSM speed as it moves from slow to medium operation. Figure 15 and Table 3 focus on region (b) from Figure 13, highlighting the PMSM’s performance at a medium speed of 375 rpm. At this level, the novel control design excels in speed performance characteristics compared to the classical control design. The rise time during application is estimated at 3.5 ms, the steady-state error is 0.007%, and stability is optimal with the novel

control design. These results indicate that the novel control design is highly suitable for medium speed, particularly when transitioning from low to medium speed.

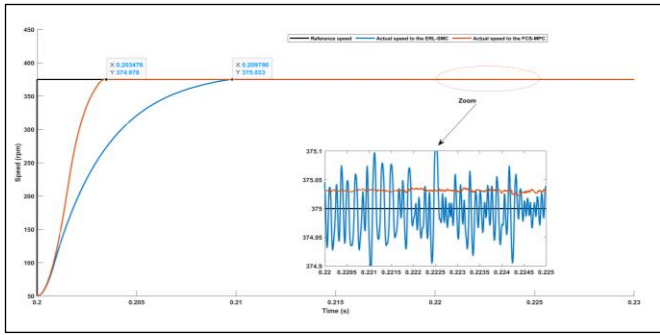


Figure 15: PMSM speed performance under the medium speed level.

Source: Authors, (2024).

Figure 16 and Table 3 highlight region (c) from Figure 13, illustrating the transition to the third level, representing the highest performance speed of 1000 rpm. Despite this abrupt change from medium to high speed, the novel control design demonstrates superior durability and performance characteristics for the PMSM compared to the classical ERL-SMC control design. A detailed analysis of performance characteristics, based on Figures 13, 14, 15, 16, and Table 3, reveals that the average rise time for the novel control design is estimated at 4 ms, while the classical control design is 9.2 ms. The average uncertainties in speed performance are estimated at 0.8 ms for the novel control design and 3.3 ms for the classical control design. Thus, the novel control design outperforms the classical control design in most speed performance characteristics.

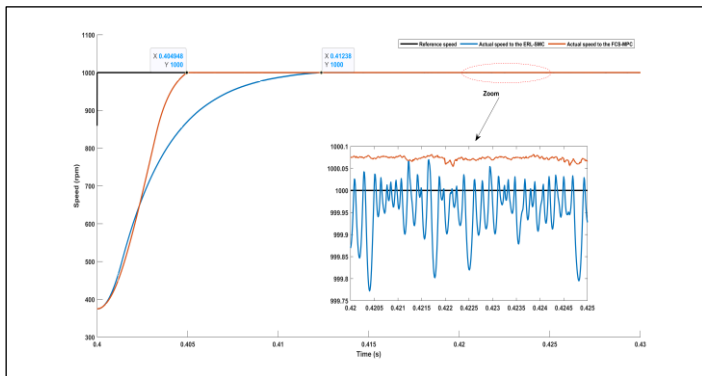


Figure 16: PMSM speed performance under the high speed level.

Source: Authors, (2024).

Table 3: Performance characteristics comparison under variation of speed levels between the novel control design (ncd) and the classical control design based on (CCD) ERL-SMC.

Performance Characteristics	NCD	CCD
Rise Time (ms)		
Low speed	3.789	5.588
Medium speed	3.5	9.8
High speed	4.9	12.2
Steady-state error (%)		
Low speed	0.04	0.4
Medium speed	0.01	0.03
High speed	0.008	0.02
Performance Stability	Medium stable	Little stability

Source: Authors, (2024).

VI. CONCLUSIONS

This paper presents a novel dual-loop control strategy for enhancing PMSM performance, utilizing Finite Control Set Model Predictive Control (FCS-MPC) for the current loop and Exponential Reaching Law Sliding Mode Control (ERL-SMC) for the speed loop. The innovative control design has demonstrated superior performance under various conditions, including uncertainties, disturbances, and changes in speed levels. The FCS-MPC method effectively predicts future motor current behavior and selects optimal control actions, resulting in minimal current ripple, improved transient response, and efficient handling of the non-linearities and constraints inherent in PMSM operation. Concurrently, the ERL-SMC provides robust control against parameter variations and external disturbances, ensuring accurate speed tracking and reduced chattering. Extensive simulations in MATLAB/Simulink confirm that the novel dual-loop control design significantly outperforms the classical ERL-SMC-based control design. It exhibits excellent characteristics in terms of dynamic response, tracking accuracy, reduced overshoot, and enhanced disturbance rejection. The novel control approach also shows exceptional capability in managing sudden load changes and parameter uncertainties, further validating its potential for high-performance PMSM drive applications. Overall, this study contributes a robust and efficient dual-loop control framework that leverages the strengths of both FCS-MPC and ERL-SMC, offering a substantial improvement over traditional control methods and advancing the field of PMSM control systems.

VII. AUTHOR'S CONTRIBUTION

Conceptualization: Djaloul Karboua, Youcef Chouiha, Ben ouadeh Douara, Ibrahim Farouk Bouguenna, Said Benkaihou and Belgacem Toul.

Methodology: Djaloul Karboua, Youcef Chouiha, Ben ouadeh Douara, Ibrahim Farouk Bouguenna, Said Benkaihou and Belgacem Toul.

Investigation: Djaloul Karboua, Youcef Chouiha, Ben ouadeh Douara, Ibrahim Farouk Bouguenna, Said Benkaihou and Belgacem Toul.

Discussion of results: Djaloul Karboua, Youcef Chouiha, Ben ouadeh Douara, Ibrahim Farouk Bouguenna, Said Benkaihou and Belgacem Toul.

Writing – Original Draft: Djaloul Karboua, Youcef Chouiha, Ben ouadeh Douara, Ibrahim Farouk Bouguenna, Said Benkaihou and Belgacem Toul.

Writing – Review and Editing: Djaloul Karboua, Youcef Chouiha, Ben ouadeh Douara, Ibrahim Farouk Bouguenna, Said Benkaihou and Belgacem Toul.

Resources: Djaloul Karboua, Youcef Chouiha, Ben ouadeh Douara, Ibrahim Farouk Bouguenna, Said Benkaihou and Belgacem Toul.

Supervision: Djaloul Karboua, Youcef Chouiha, Ben ouadeh Douara, Ibrahim Farouk Bouguenna, Said Benkaihou and Belgacem Toul.

Approval of the final text: Djaloul Karboua, Youcef Chouiha, Ben ouadeh Douara, Ibrahim Farouk Bouguenna, Said Benkaihou and Belgacem Toul.

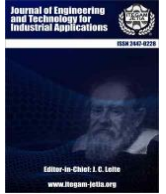
VIII. REFERENCES

[1] D. Fu, X. Zhao, and H. Yuan, "High-precision motion control method for permanent magnet linear synchronous motor", *IEICE Electronics Express*, vol. 18, no. 9, pp. 20210097–20210097, 2021. <https://doi.org/10.1587/elex.18.20210097>

- [2] B. K. Bose, "Power electronics and motion control-technology status and recent trends", *IEEE Transactions on Industry Applications*, vol. 29, no. 5, pp. 902–909, 1993. <https://doi.org/10.1109/28.245713>
- [3] Y. Pan, X. Liu, Y. Zhu, B. Liu, and Z. Li, "Feedforward decoupling control of interior permanent magnet synchronous motor with genetic algorithm parameter identification", *Progress In Electro magnetics Research M*, vol. 102, pp. 117–126, 2021. <https://doi.org/10.2528/PIERM21032903>
- [4] W. Li, "Application of pmsm control in electric vehicle", *Internal Combustion Engine & Parts*, vol. 298, no. 22, pp. 51–52, 2019.
- [5] J.-W. Jung, V. Q. Leu, T. D. Do, E.-K. Kim, and H. H. Choi, "Adaptive pid speed control design for permanent magnet synchronous motor drives", *IEEE Transactions on Power Electronics*, vol. 30, no. 2, pp. 900–908, 2014. <https://doi.org/10.1109/TPEL.2014.2311462>
- [6] J. Hu, J. Zou, F. Xu, Y. Li, and Y. Fu, "An improved pmsm rotor position sensor based on linear hall sensors", *IEEE Transactions on Magnetics*, vol. 48, no. 11, pp. 3591–3594, 2012. <https://doi.org/10.1109/TMAG.2012.2202279>
- [7] W. Liu, S. Chen, and H. Huang, "Adaptive nonsingular fast terminal sliding mode control for permanent magnet synchronous motor based on disturbance observer", *IEEE Access*, vol. 7, pp. 153791–153798, 2019. <https://doi.org/10.1109/ACCESS.2019.2948945>
- [8] X. Zhang, L. Sun, K. Zhao, and L. Sun, "Nonlinear speed control for pmsm system using sliding-mode control and disturbance compensation techniques", *IEEE transactions on power electronics*, vol. 28, no. 3, pp. 1358–1365, 2012. <https://doi.org/10.1109/TPEL.2012.2206610>
- [9] K. Mei and S. Ding, "Second-order sliding mode controller design subject to an upper-triangular structure", *IEEE Transactions on Systems, Man, and Cybernetics: Systems*, vol. 51, no. 1, pp. 497–507, 2018. <https://doi.org/10.1109/TSMC.2018.2875267>
- [10] Y. Shtessel, M. Taleb, and F. Plestan, "A novel adaptive-gain super-twisting sliding mode controller: Methodology and application", *Automatica*, vol. 48, no. 5, pp. 759–769, 2012. <https://doi.org/10.1016/j.automatica.2012.02.024>
- [11] Z. Zhou, B. Zhang, and D. Mao, "Robust sliding mode control of pmsm based on rapid nonlinear tracking differentiator and disturbance observer", *Sensors*, vol. 18, no. 4, p. 1031, 2018. <https://doi.org/10.3390/s18041031>
- [12] C. Xie, J. Wu, Z. Guo, Y. Wang, and J. Liu, "Sensorless control of vehicle-mounted pmsm based on improved sliding mode observer", in *Journal of Physics: Conference Series*, vol. 2030, no. 1. IOP Publishing, 2021, p. 012004. <https://doi.org/10.1088/1742-6596/2030/1/012004>
- [13] D. Karboua, B. Toual, A. Kouzou, B. O. Douara, T. Mebkhoua, and A. N. Bendenidina, "High-order super-twisting based terminal sliding mode control applied on three phases permanent synchronous machine", *Periodica Polytechnica Electrical Engineering and Computer Science*, vol. 67, no. 1, pp. 40–50, 2023. <https://doi.org/10.3311/PPEc.21026>
- [14] D. Karboua, B. Toual, B. O. Douara, T. Mebkhoua, M. L. Benaissa, and Y. Chouiha, "Expansion switching law based sliding mode applied on a three-phase permanent magnet synchronous machine", in *2022 2nd International Conference on Advanced Electrical Engineering (ICAEE)*. IEEE, 2022, pp. 1–6. <https://doi.org/10.1109/ICAEE53772.2022.9961993>
- [15] I. F. Bouguenna, A. Tahour, R. Kennel, and M. Abdelrahem, "Multiple-vector model predictive control with fuzzy logic for pmsm electric drive systems", *Energies*, vol. 14, no. 6, p. 1727, 2021. <https://doi.org/10.3390/en14061727>
- [16] J. Rodriguez and P. Cortes, "Predictive control of power converters and electrical drives", *John Wiley & Sons*, 2012. <https://doi.org/10.1002/9781119941446>
- [17] J. A. Andersson, J. Gillis, G. Horn, J. B. Rawlings, and M. Diehl, "Casadi: a software framework for nonlinear optimization and optimal control", *Mathematical Programming Computation*, vol. 11, pp. 1–36, 2019. <https://doi.org/10.1007/s12532-018-0139-4>
- [18] P. Pillay and R. Krishnan, "Modeling of permanent magnet motor drives," *IEEE Transactions on industrial electronics*, vol. 35, no. 4, pp. 537–541, 1988. <https://doi.org/10.1109/41.9176>
- [19] T. P. Kumar and P. Samyuktha, "Vector control drive of permanent magnet synchronous motor using resolver sensor", *International Journal of Computer Science Engineering (IJCSSE)*, vol. 2, no. 04, 2013.
- [20] M. Nicola, C.-I. Nicola, and D. Selis, "Improvement of pmsm sensorless control based on synergetic and sliding mode controllers using a reinforcement learning deep deterministic policy gradient agent", *Energies*, vol. 15, no. 6, p. 2208, 2022. <https://doi.org/10.3390/en15062208>
- [21] R. Abdessemed, "Modélisation et simulation des machines électriques: électrotechnique", *Ellipses*, 2011.
- [22] W. Perruquetti and J. P. Barbot, "Sliding mode control in engineering", *Marcel Dekker New York*, 2002, vol. 11. <https://doi.org/10.1201/9780203910856>
- [23] W. Gao, Y. Wang, and A. Homaifa, "Discrete-time variable structure control systems," *IEEE transactions on Industrial Electronics*, vol. 42, no. 2, pp. 117–122, 1995. <https://doi.org/10.1109/41.370376>
- [24] D. Karboua, T. Belgacem, Z. H. Khan, C. Labiod, and I. K. Ibraheem, "Toward an optimal twisting-sliding mode control of a three-phase pmsm for electric vehicles", *Advances in Mechanical Engineering*, vol. 15, no. 9, p. 16878132231198664, 2023. <https://doi.org/10.1177/16878132231198664>
- [25] J. Guldner and V. Utkin, "The chattering problem in sliding mode systems", in *Proc. 14th Int. Symp. of Mathematical Theory of Networks and Systems (MTNS)*, 2000.
- [26] J.-J. E. Slotine, W. Li et al., "Applied nonlinear control", *Prentice hall Englewood Cliffs, NJ*, 1991, vol. 199, no. 1.
- [27] K. Djaloul, T. Belgacem, I. Atif, C. Youcef, M. Toufik, and D. B. Ouadeh, "High order sliding mode control based on a new terminal strategy applied on the speed permanent magnet synchronous machine", in *2023 XIX International Scientific Technical Conference Alternating Current Electric Drives (ACED)*. IEEE, 2023, pp. 1–6. <https://doi.org/10.1109/ACED57798.2023.10143468>
- [28] Y.-G. Huangfu, "Research of nonlinear system high order sliding mode control and its applications for pmsm", *Ph.D. dissertation, Northwestern Polytechnical University (China)*, 2010.
- [29] X. Gao, M. Abdelrahem, C. M. Hackl, Z. Zhang, and R. Kennel, "Direct predictive speed control with a sliding manifold term for pmsm drives", *IEEE Journal of Emerging and Selected Topics in Power Electronics*, vol. 8, no. 2, pp. 1258–1267, 2019. <https://doi.org/10.1109/JESTPE.2019.2923285>
- [30] M. Abdelrahem, C. Hackl, R. Kennel, and J. Rodriguez, "Sensorless predictive speed control of permanent-magnet synchronous generators in wind turbine applications", in *PCIM Europe 2019; International Exhibition and Conference for Power Electronics, Intelligent Motion, Renewable Energy and Energy Management*. VDE, 2019, pp. 1–8.
- [31] Y. Zhang, D. Xu, J. Liu, S. Gao, and W. Xu, "Performance improvement of model-predictive current control of permanent magnet synchronous motor drives", *IEEE Transactions on Industry Applications*, vol. 53, no. 4, pp. 3683–3695, 2017. <https://doi.org/10.1109/TIA.2017.2690998>



ISSN ONLINE: 2447-0228



RESEARCH ARTICLE

OPEN ACCESS

ENHANCING MECHANICAL AND CORROSION PROPERTIES OF BRASS COMPOSITES WITH CARBONIZED COCONUT SHELL ASH

Mathew Olurotimi Adeoti¹, Prof. Tamba Jamiru² and Taoreed Adesola Adegbola³

^{1, 2, 3} Department of Mechanical and Mechatronics Engineering, Tshwane University of Technology, Pretoria, South Africa.

¹<http://orcid.org/0009-0006-9308-0936> ²<http://orcid.org/0000-0002-9492-1921> ³<http://orcid.org/0000-0002-6881-72>

Email: ¹AdeotiMO@tut.ac.za, ²JamiruT@tut.ac.za, ³AdesolaAT@tut.ac.za

ARTICLE INFO

Article History

Received: August 06th, 2024

Received: September 19th, 2024

Accepted: September 19th, 2024

Published: October 04th, 2024

Keywords:

Brass,
Composite,
Coconut shell,
Mechanical properties,
Corrosion,
Hardness test.

ABSTRACT

This study investigates the mechanical properties and corrosion behavior of brass (Cu-Zn alloy) reinforced with carbonized coconut shell ash (CSA) composites. The coconut shells were obtained, sun-dried, crushed, carbonized at 500 °C and sieved. The resulting CSA was then incorporated into molten brass scrap, which was first preheated to 950°C. For reproducibility purposes, several samples were prepared with varying CSA weight fraction (0wt%, 5wt%, 10wt%, and 15wt%). The samples were characterized by using metallurgical microscopes to assess their microstructure and homogeneity. The mechanical properties, including: ultimate tensile strength (UTS), hardness, impact energy, and compressive strength, were evaluated. The corrosion analysis was carried out by attaching the respective samples to a holder in the electrolytic streams of the acid and chloride solution in the constructed sand slurry pot using potentiodynamic polarization. X-ray fluorescence was used to determine the elemental composition of the brass scraps. The results indicated that increased CSA content improved UTS, hardness, and compressive strength. However, a reduction in impact energy was observed. The sample with 15wt% weight fraction of CSA, exhibited the highest UTS (326.32 N/mm²), hardness (281.67 HRB), and compressive strength (198.3 MPa). Nevertheless, sample A with 0wt% weight fraction of CSA, showed the highest impact energy (35.59 J). Corrosion rates varied, with sample A showing the moderate rate of corrosion resistance, sample B is prone to high rate of corrosion, sample C has the poorest corrosion resistance, while sample D exhibited the best overall corrosion resistance. This study demonstrates that CSA reinforcement enhances the mechanical properties of brass composites, making them suitable for various engineering applications.



Copyright ©2024 by authors and Galileo Institute of Technology and Education of the Amazon (ITEGAM). This work is licensed under the Creative Commons Attribution International License (CC BY 4.0).

I. INTRODUCTION

Brass (Cu-Zu) alloy is a formidable material for aerospace, valves, channels, and automobile applications due to their excellent corrosion resistance, low-friction coefficient, non-magnetism, forgeability, machinability, tensile strength, and hardness [1]. In categories, brass is useful where high corrosion resistance is needed, moderate mechanical strength is required, and electrical/thermal conductivity is desired [2]. Factors, such as: weight percentage of copper in brass alloy, and process temperature, determine the brass alloy type and applications area. For instance, bronze, gold, color brass alloys can be obtained, by 10:90; 15:85; and 38:62 zinc and copper weight ratios [3]. Based on structure, brass has been divided into alpha (α) and alpha-beta

($\alpha + \beta$) brass. There are also leaded brasses. Leaded brass is a brass alloy, which contains a small proportion of lead for the purpose of easy machining while maintaining the corrosion and mechanical properties integrity of the brass alloy [4]. Of course, lead is an environmental pollutant, and when it is leached in drinking water via plumbing systems, it becomes harmful substance, leading to the cause of neurological disorder and threat to pregnancy [5].

To enhance the mechanical properties of brass alloy and also reduce the negative impact of lead in brass, literature has reported alternative alloying elements [6]. For example, the addition of small amounts of elements, such as: aluminum, manganese, or silicon in brass, can improve the strength, corrosion resistance, and durability of brass without relying on lead. Casting

infiltration, diffusion bonding, spark plasma sintering, and extrusion are examples metal matrix composite of production methods [7]. Metal matrix composites have metal as the matrix and other material (e.g., non-metals) as the reinforcement. They possess excellent mechanical strength, low density, lightweight, conductivity, hardness, stiffness, wear, and abrasion resistance [8], [9]. The ultimate characteristics of a metal matrix composite (MMC) are influenced by several key factors, such as: the specific alloying elements used in the matrix, the choice of reinforcement materials, and the synthesis technique employed. The method of synthesis—whether it be casting, powder metallurgy, or another technique—plays a crucial role in determining the uniformity, bonding quality, and overall performance of the composite. Ceramic compounds, such as: silicon-carbides, aluminum-oxides, and carbon allotropes, have been used to reinforce metals, such as: aluminum, magnesium, copper, and alloys [10]. Despite the plethora of advantages of metal matrix composite with nonmetallic materials (e.g., ceramic, silicon nitride, graphite), high processing cost, low wettability of ceramic-nanoparticles, non-uniform dispersion, and availability problems, are disadvantaged to metal matrix composites with nonmetallic materials [11].

Therefore, this study is concerned with metal matrix composite having agro-waste as reinforcement. Processed agro-waste into powder form has the reinforcing potential for metal matrix mechanical properties. Examples of the commonly used agro-waste for metal matrix composite, include: coconut shell, groundnut shell, rice husk, palm kernel shell, maize stalk ash, breadfruit, seed hull-ash, aloe vera, bean pod ash, cow-horn, and bagasse ash. Owing to the natural benefits of organic waste, such as: environmental benignity, availability, easy processing, low cost, and low weight, their use as reinforcing material for the synthesis of brass matrix, is promising [12]. In the study presented by [13], waste rice husk ash was used as a reinforcing material for aluminum alloy. The aluminum alloy was obtained from car scrap. The scrap aluminum alloy was first melted in a muffle furnace of graphite crucible. The rice husk ash was preheated at a temperature of about 300 °C to form good wettability with the aluminum matrix. The mixture of the metal and the waste organic material was obtained at a temperature of ~680 °C and stirred at 200 rpm for 5 minutes. The fabricated metal matrix composite in the presence of alumina catalyst as secondary reinforcing agent, has excellent hardness, ductility, compressive, and tensile strengths properties. In another study [14], groundnut shell ash and hemp fiber ash have been used to reinforce aluminum to produce metal matrix composite. According to, [15], carried out an experimentation on aluminum and agro-waste composite. In the study, fly ash and aloe vera were engaged to reinforce aluminum matrix and the results showed aluminum matrix composite possessing significant improved mechanical properties.

It is therefore envisaged in this study that agro-waste can be beneficial as a significant reinforcement for brass alloy. In this study, due to the easy availability, low cost, low density, and environmental benignity of coconut shell ash (CSA), it is chosen as the reinforcing material for brass alloy. The study focuses on the characterization of the brass alloy/coconut shell ash composite. Therefore, the investigation carried out in this study principally involved the mechanical characterization of brass scraps reinforced with carbonized-CSA

II. MATERIALS AND METHOD

The major raw materials used in this study, are brass scraps and Coconut shell. The equipment used includes a sieve shaker 1.18mm, Crusher, metallurgical microscope model number,

NJF-120A, disc grinder, sensitive weighing machine, charcoal-fired crucible furnace, ladle, Vernier caliper, lathe machine, meter rule, crucible pot, Mansoto Tensometer, Izod impact testing machine, computer-controlled hardness testing machine and energy dispersion XRF machine.

II.1 THE REINFORCING COCONUT SHELL ASH

The coconut shells used in this work were obtained from Ilorin, Nigeria. Thereafter, the shells were cleaned and sun-dried. To obtain the power form of the coconut shells, the dried shells were subjected to crushing and grinding processes. The powdered shells were packed in a crucible pot and carbonized in the furnace at the temperature of 500 °C to form a CSA. The carbonized CSA was cooled and sieved by using 1.18 mm mesh. Figure 1 shows the coconut shell, crushed coconut shell and coconut shell powder, respectively.



Figure 1: The reinforcing coconut shell organic waste (a) uncrushed (b) crushed, and (c) powder.

Source: Authors, (2024).

II.2 THE METAL MATRIX

The enumerations of citations in the body of the article must be sequenced in the order in which they appear, according to the example shown below.

II.3 THE BRASS ALLOY/CSA METAL MATRIX COMPOSITE

The homogenous mixture of the carbonized-CSA and the molten metal was obtained by continuous stirring. The composite of the metal matrix/CSA in molten form, was afterward poured into a mould cavity and allowed to solidify. The fabricated brass alloy/CSA composite was machined by using the lathe machine. For repeatability purposes, various samples were prepared by varying the volume fraction of the matrix and reinforcing materials. Table 1 shows the composition of the fabricated metal matrix/CSA composites.

Table 1: Sample preparation of the developed composites

Samples	Brass (%)	CSA (%)
A	100	0
B	95	5
C	90	10
D	85	15

Source: Authors, (2024).

II.4 CHARACTERIZATION

II.4.1 the Mechanical Properties of Brass Alloy/CSA Composites

The mechanical properties characterizations were carried out according to ASTM E18-19, ASTM E8, and ASTM A370. The hardness test was performed on a standard computerized Vickers Hardness Testing Machine, Model MV1-PC with a load of 0.3kgf, max/min limit of 500/300HV. The tensile test was carried out on a standard method by using the Monsanto Tensometer, type W Serial No. 9875. The samples were gripped in the chucks of the Tensometer and load was applied with the aid of load handle until the samples fracture. The impact test was carried out by using Izod Impact Testing Machine with V-notches of depth of 0.5mm. Scanning electron microscope (SEM) model SIRIUS50/3.8 (ASPEX 3020) was used to examine the morphology of the samples. The corrosion analysis was carried out by attaching the respective samples to a holder in the electrolytic streams of the acid and chloride solution in the constructed sand slurry pot by using potentiodynamic polarization at a revolution of 960 rev./min for 120 minutes in each case. The slurry was prepared by adding sand in the proportion of 10 g per 10 litres of tap water. The surfaces of the samples were prepared by polishing with emery papers of 60D, 320D, 600C, 800C 100C and 1200C, respectively. This was done to eliminate scaling, surface contaminants, and oxide film on the metal surface. Followed by the elimination of scaling, surface contaminants, and oxides film from the metal surface is the de-greasing of the samples with acetone to remove grease, dirt, or dust in order to avoid error in experimentation, and subsequent corrosion rate measurement. The de-greased surface was thereafter air-dried prior to immersion; and their initial weights were obtained by using weigh balance. All the experiments were repeated in triplicate to ensure good reproducibility of the results. The elemental composition analysis of the scrap brass was obtained by using X-ray fluorescent analyzer (XRF, model: minipal 4 No. DY 1055) [16].

III RESULTS AND DISCUSSION

Table 2 shows the various elements of the scrap brass with their percentage weight in the metal composition. The major elements are copper (56.81%) and zinc (37.4%). The metal scrap can be classified as Alpha (α) brass.

Table 2: Elemental composition of scrap brass.

Elements	Wt(%)
Si	0.70
Ca	0.51
Ca	56.81
Zn	32.04
Ti	0.02
Mn	0.04
As	0.28
Nb	0.30
Fe	1.00
Sb	0.80
Ni	1.50
Pb	6.00

Source: Authors, (2024).

The micrograph presented in Figure 2 for samples B, C, and D shows that the carbonized coconut shell ash is evenly distributed as reinforcement within the brass matrix. Homogeneity was achieved through continuous stirring of the carbonized-CSA with varied compositions into the brass matrix, as evidenced by the

absence of agglomeration or segregation of the carbonized CSA in each of the samples. The microstructure also reveals that the brass matrix and carbonized-CSA are interfacially bonded. This result is consistent with literature [9],[17],[18].

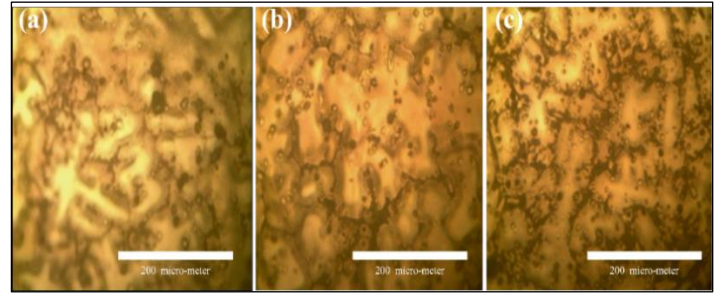


Figure 2: SEM micrograph for: (a) sample B (b) sample C, and (c) sample D.

Source: Authors, (2024).

Figure 3 illustrates the variation in ultimate tensile strength among the fabricated samples. It is evident from Figure 3 that Sample D exhibits the highest tensile strength at 326.32 N/mm². This result indicates that the tensile strength of the brass alloy increases with a higher volume fraction of the reinforcing carbonized coconut ash (CAS). Following Sample D, the tensile strengths of the samples decrease in the order of Sample C, Sample B, and Sample A. The observed trend of increasing tensile strength from Sample A to Sample D suggests an enhancement in the tensile properties, likely due to variations in their composition and the effective diffusion of the carbonized CAS within the matrix. Consequently, the formation of stronger bonds and intermolecular attractions in the resulting composite is most pronounced in the metal alloy containing the highest proportion of the agro-waste filler.

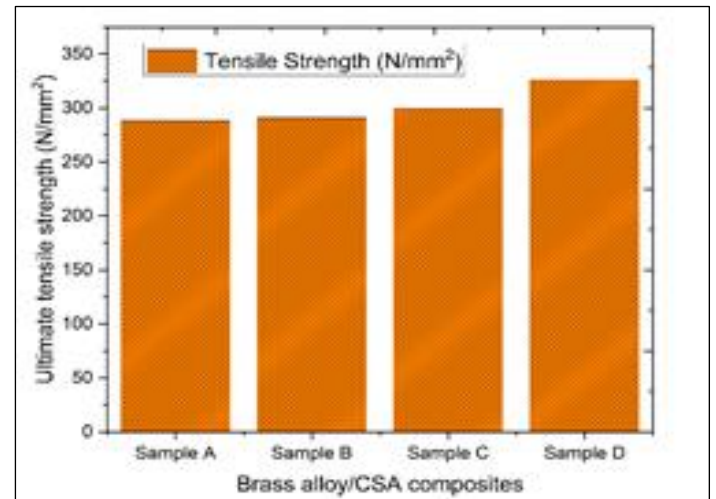


Figure 3: Variation of ultimate tensile strength of brass reinforced carbonized CSA samples.

Source: Authors, (2024).

The brass matrix composite, as presented in Figure 4, shows a significant enhancement with the addition of carbonized-CSA reinforcement. The hardness values exhibit a clear upward trend from Sample A to Sample D. Specifically, Sample D achieves the highest hardness value of 281.67 HRB. This increase in hardness indicates that Sample D is the most resistant to indentation and deformation among the tested samples. Higher hardness values typically correlate with enhanced material strength and reduced ductility, suggesting that Sample D possesses superior mechanical properties compared to the other samples. The

proportional increase in hardness values from Sample A to Sample D highlights the beneficial impact of increasing the volume fraction of carbonized-CSA reinforcement within the brass matrix. As the proportion of CSA increases, the composite material becomes more resistant to wear and deformation, contributing to its overall durability and robustness. The underlying reason for this improvement can be attributed to the effective dispersion and bonding of the carbonized-CSA within the brass matrix. The CSA particles act as reinforcement, impeding dislocation motion and enhancing the material's load-bearing capacity. This leads to a more rigid and structurally sound composite, capable of withstanding higher stress without undergoing significant deformation. Furthermore, the consistent increase in hardness values suggests a possible enhancement in the structural integrity of the material. This observation aligns with previous findings reported by sources [9],[19], which indicate that the addition of carbonized CSA reinforcement can significantly improve the mechanical properties of metal matrix composites.

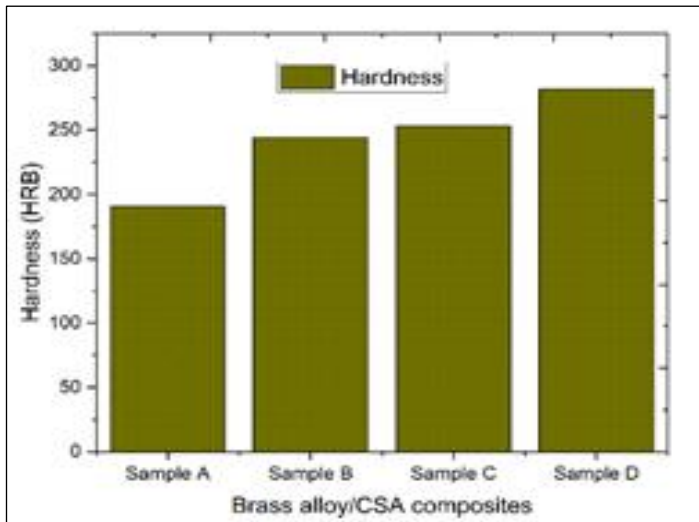


Figure 4: Variation of hardness of brass reinforced carbonized-CSA composites. Source: Authors, (2024).

The compression strength results depicted in Figure 5 show that the addition of carbonized-CAS as reinforcement significantly improves the strength of brass matrix materials. The compressive strength increases from Sample A to Sample D, with Sample D exhibiting the highest compressive strength at 198.3 MPa. This indicates that Sample D is the most resistant to compressive forces, which is consistent with its higher ultimate tensile strength and hardness values. The trend suggests that the modifications made to each successive sample have enhanced their ability to withstand compressive loads. This result is in line with findings reported by [20]. Moreover, the correlation between the compressive strength, ultimate tensile strength, and hardness values further validates the reinforcing capability of CSA. As compressive strength is a critical parameter for materials subjected to heavy loads, the enhanced values indicate that the brass matrix composite with CSA reinforcement is more durable and capable of sustaining higher loads without collapsing or deforming. This enhancement is particularly beneficial for applications in structural components, automotive parts, and other areas where materials are regularly exposed to significant compressive forces.

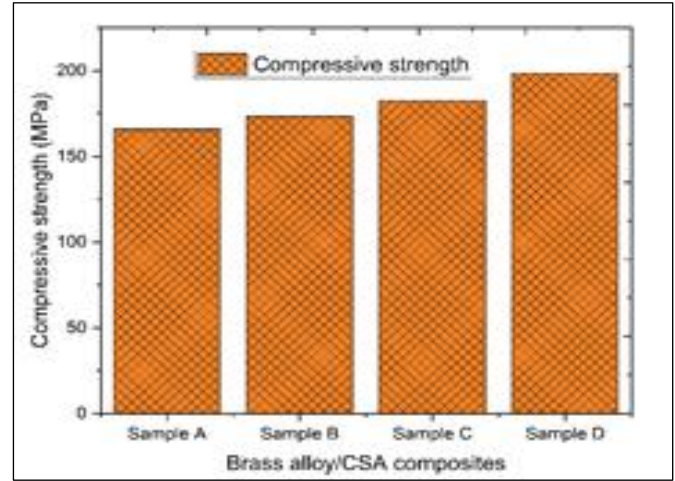


Figure 5. Variation of Compressive strength of brass reinforced carbonized CSA composites. Source: Authors, (2024).

On the contrary, Figure 6 illustrates the decrease in impact energies of the brass metal composite with an increasing volume fraction of carbonized coconut shell ash (CSA) addition. Impact energy decreases from Sample A to Sample D, with Sample A exhibiting the highest impact energy at 35.59 J. This suggests that Sample A can absorb more energy before fracturing, indicating better toughness compared to the other samples. This reduction in impact energy, coupled with the increase in hardness and ultimate tensile strength (UTS), indicates a trade-off between toughness, compressive strength, and ultimate tensile strength. Essentially, this result shows the possibility that materials fabricated with excellent hardness and tensile strength may possess low impact energy (or, impact toughness). This result is in agreement with the study conducted by [21]. Furthermore, the elongation as shown in Figure 7 also decreases as the carbonized-CSA volume fraction increases. However, sample B showed a higher elongation than the other samples. This inconsistency in the elongation trend may be as a result of measurement error. This result agree with literature [22].

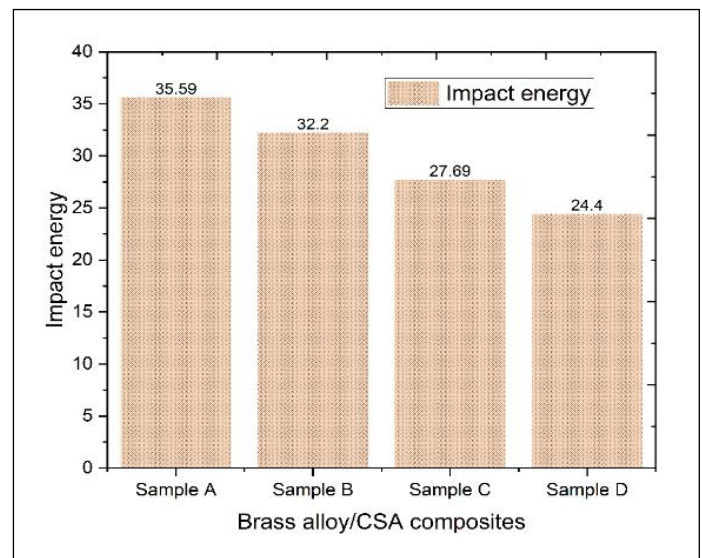


Figure 6: Variation of Impact energy of brass reinforced carbonized-CSA composites. Source: Authors, (2024).

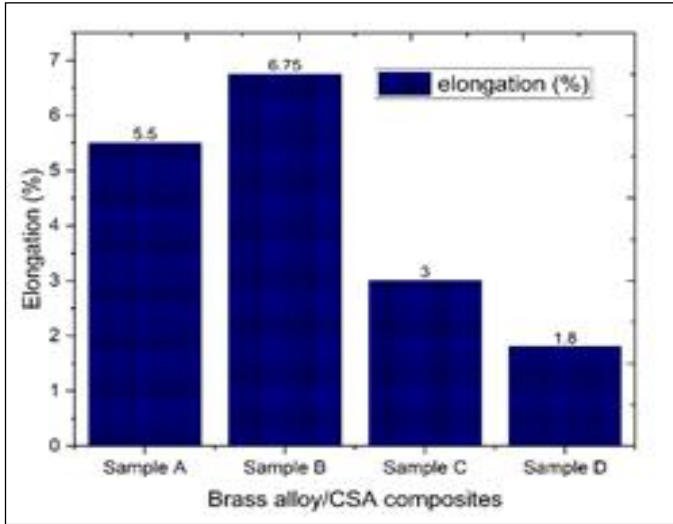


Figure 7: Variation of elongation of brass reinforced carbonized-CSA composites.

Source: Authors, (2024).

III.1 THE CORROSION PROPERTIES OF BRASS ALLOY/CSA COMPOSITES

The corrosion analysis was carried out by attaching each of the respective samples to a holder in the electrolytic streams of acid and chloride solution in the constructed sand slurry pot by using potentiodynamic polarization method. The potentiodynamic polarization curves of the samples are shown in Figure 8. The corrosion potential (E_{Corr}), corrosion current density (I_{Corr}), tafel slopes (β_c and β_a) values, are measured. The results showed diverse variation in corrosion potential and the corrosion current densities of the samples. The corrosion current density and corrosion potential of the brass alloy are: $-4.433 \mu A/cm^2$ and $301.20 mV$.

The brass alloy/CSA composite containing 5wt% (Sample B), showed a $-218.75 mV$, corrosion potential and $4.911 \mu A/cm^2$ corrosion current density. Even though the corrosion potential of the composite of sample B is more positive than sample A,

however, its high corrosion current density compared sample A, depicted a high corrosion rate. Moreover, sample C showed the worst corrosion performance with the highest corrosion potential and corrosion current density ($534 mV$ and $6.396 \mu A/cm^2$). Nevertheless, sample D exhibits the lowest corrosion current density and moderate corrosion potential ($327.40 mV$ and $3.494 \mu A/cm^2$). Furthermore, the improvement in the corrosion resistance of the metal matrix is also observed from the anodic and cathodic values measured from the Tafel curves. As shown in Table 3, sample D has the least negative cathodic value compared to other samples. This least negative cathodic and moderate anodic values, corroborate the corrosion current density and corrosion potential values previously presented. The general observation from the corrosion results is that the corrosion rate of the composites increases as the content of carbonized-CSA increases to 10% volume fraction. However, further addition of the carbonized-CSA, led to the reduction in the rate of corrosion, as evident in sample D. This result agrees with literature [23, 24].

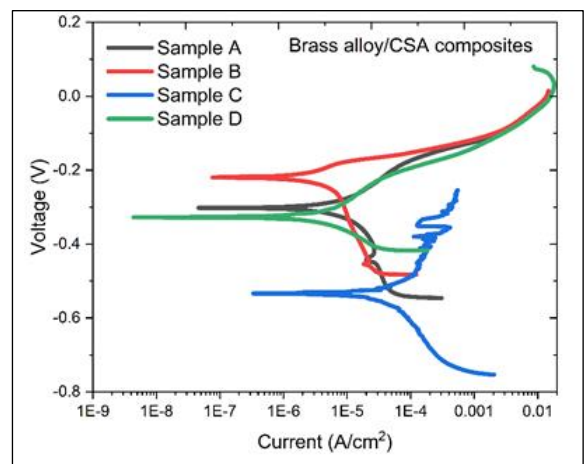


Figure 8: Potentiodynamic polarization curves of the fabricated brass alloy/CSA composites.

Source: Authors, (2024).

Table 3: Brass alloy/CSA composites corrosion analysis parameters.

Sample	Corrosion potential (mV)	Corrosion current density ($\mu A/cm^2$)	Anodic value (mV/dec)	Cathodic value (mV/dec)	Remarks
A	-301.20 This is a moderate corrosion potential, since the value is more positive than the corrosion potential of samples C and D.	4.433 The low corrosion current density of this sample, when compared to sample B and C, shows a moderate corrosion resistance.	0.0987 This is a moderate rate of oxidation reaction.	-0.1173 The cathodic value indicates moderate rate of reduction.	Moderate corrosion resistance
B	-218.75 When compared to other samples, this corrosion potential shows the best electrochemical stability and probably, a more resistant to corrosion.	4.911 This is a high corrosion current density, indicating a higher corrosion rate than sample A.	0.0321 This is the lowest anodic value, indicating a slower rate of metal dissolution.	-0.3858 This is the highest negative cathodic values, indicating a high corrosion current density.	Prone to corrosion due to high corrosion current and cathodic value
C	-534.00 This is the most negative corrosion potential; therefore, the sample probably has the poorest corrosion resistance.	6.396 This is the highest corrosion current density, indicating that this sample is more subjective to corrosion.	0.2647 The highest anodic value, indicating a rapid rate of oxidation or metal dissolution.	-0.2317 Relatively moderate rate of reduction.	Poor resistance to corrosion
D	-327.40 This is a moderate corrosion potential; however, it is more negative than sample A and B.	3.494 This sample exhibits the lowest corrosion current density, indicating the best overall corrosion resistance among the samples.	0.1178 Relatively moderate rate of oxidation or metal dissolution.	-0.0912 The least negative cathodic value. This value indicates the slowest rate of reduction and excellent corrosion resistance	Overall best resistance to corrosion. This is due to the balance between anodic and cathodic reaction. In addition, the sample has the lowest corrosion current density and moderate corrosion potential.

Source: Authors, (2024).

IV CONCLUSION

Carbonized coconut shell ash (CSA) has been used to enhance the mechanical properties and corrosion resistance of brass. The experimental investigation has demonstrated significant enhancements in mechanical properties with increasing CSA content. An addition of CSA significantly increased the UTS of the composites, with Sample D (15% CSA) exhibiting the highest UTS of 326.32 N/mm². This suggests improved resistance to tensile stress due to the strong interfacial bonding between the brass matrix and CSA. Hardness of the composites increased with CSA content, with Sample D achieving the highest hardness value of 281.67 HRB. This indicates enhanced resistance to deformation and indentation. Compressive strength also improved with higher CSA content, with Sample D showing the highest compressive strength of 198.3 MPa. This reinforces the material's capability to withstand compressive loads. The impact energy decreased with increasing CSA content, with Sample A (0% CSA) having the highest impact energy of 35.59 J. This trade-off suggests a reduction in toughness with increased hardness and tensile strength. Corrosion tests revealed that sample A had a moderate rate corrosion resistance, sample B is prone to high rate of corrosion, sample C has the poorest corrosion resistance, while sample D exhibited the best overall corrosion resistance.

Declaration of competing interests: The authors have no competing interest to declare that are relevant to the content of this article.

Acknowledgements: The authors acknowledge the contributions of Dr. Folorunsho Oladipo of Electrical Engineering Department, TUT and financial support from Tshwane University of Technology (TUT), Pretoria, South Africa, without which this work would not have been published.

Data Availability:

'The raw/processed Data required to produce these findings cannot be shared at this time due to technical and time limitations'.

V. AUTHOR'S CONTRIBUTION

Conceptualization: Mathew Olurotimi Adeoti, Prof. Tamba Jamiru and Taoreed Adesola Adegbola.

Methodology: Mathew Olurotimi Adeoti, Prof. Tamba Jamiru and Taoreed Adesola Adegbola.

Investigation: Mathew Olurotimi Adeoti, Prof. Tamba Jamiru and Taoreed Adesola Adegbola.

Discussion of results: Mathew Olurotimi Adeoti, Prof. Tamba Jamiru and Taoreed Adesola Adegbola.

Writing – Original Draft: Mathew Olurotimi Adeoti, Prof. Tamba Jamiru and Taoreed Adesola Adegbola.

Writing – Review and Editing: Mathew Olurotimi Adeoti, Prof. Tamba Jamiru and Taoreed Adesola Adegbola.

Resources: Mathew Olurotimi Adeoti, Prof. Tamba Jamiru and Taoreed Adesola Adegbola.

Supervision: Mathew Olurotimi Adeoti, Prof. Tamba Jamiru and Taoreed Adesola Adegbola.

Approval of the final text: Mathew Olurotimi Adeoti, Prof. Tamba Jamiru and Taoreed Adesola Adegbola.

VI REFERENCES

[1] S. Selvamani, K. Rajan, M. Samykano, R. Kumar, K. Kadirgama, and R. Mohan, "Investigation of tensile properties of PLA–brass composite using FDM," *Progress in Additive Manufacturing*, vol. 7, no. 5, pp. 839-851, 2022.

[2] J. Johansson, "Towards Sustainable Manufacturing of Brass Components: Characterisation, Machinability and Solid-State Recycling of Lead-Free Brass," 2022.

[3] H. Y. Atay, G. Uslu, Y. Kahmaz, and Ö. Atay, "Investigations of microstructure and mechanical properties of brass alloys produced by sand casting method at different casting temperatures," in *IOP conference series: materials science and engineering*, 2020, vol. 726, no. 1: IOP Publishing, p. 012018.

[4] P. Stavroulakis, A. I. Toufatzis, G. A. Pantazopoulos, and A. S. Paipetis, "Machinable leaded and eco-friendly brass alloys for high performance manufacturing processes: A critical review," *Metals*, vol. 12, no. 2, p. 246, 2022.

[5] T. Zhu, W. Li, J. C. M. Kwok, K. W. Siu, L. Yin, and A. H. W. Ngan, "Metallurgical pathways of lead leaching from brass," *npj Materials Degradation*, vol. 7, no. 1, p. 69, 2023.

[6] M. A. Alam, H. Ya, A. Ahmad, M. Yusuf, M. Azeem, and F. Masood, "Influence of aluminum addition on the mechanical properties of brass/Al composites fabricated by stir casting," *Materials Today: Proceedings*, vol. 48, pp. 811-814, 2022.

[7] A. Kumar, O. Vichare, K. Debnath, and M. Paswan, "Fabrication methods of metal matrix composites (MMCs)," *Materials Today: Proceedings*, vol. 46, pp. 6840-6846, 2021.

[8] L. Singh, B. Singh, and K. K. Saxena, "Manufacturing techniques for metal matrix composites (MMC): an overview," *Advances in Materials and Processing Technologies*, vol. 6, no. 2, pp. 441-457, 2020.

[9] M.O Adeoti, M.S Abolarin, K. Olaiya, and B. Bongfa, "Comparison of the mechanical properties of sand and gravity die cast aluminium scraps," *Int. J. Engg. Res. & Sci. & Tech.*, vol. 4, pp. 37-43, 2015.

[10] R. Casati and M. Vedani, "Metal matrix composites reinforced by nanoparticles—a review," *Metals*, vol. 4, no. 1, pp. 65-83, 2014.

[11] P. Pawar, R. Wabale, and A. Utpat, "A comprehensive study of aluminum based metal matrix composites: challenges and opportunities," *Materials Today: Proceedings*, vol. 5, no. 11, pp. 23937-23944, 2018.

[12] O. O. Joseph and K. O. Babaremu, "Agricultural waste as a reinforcement particulate for aluminum metal matrix composite (AMMCs): a review," *Fibers*, vol. 7, no. 4, p. 33, 2019.

[13] S. P. Dwivedi, P. Sharma, and A. Saxena, "Utilization of waste spent alumina catalyst and agro-waste rice husk ash as reinforcement materials with scrap aluminium alloy wheel matrix," *Proceedings of the Institution of Mechanical Engineers, Part E: Journal of Process Mechanical Engineering*, vol. 234, no. 6, pp. 543-552, 2020.

[14] M. Palanivendhan and J. Chandradass, "Experimental investigation on mechanical and wear behavior of agro waste ash based metal matrix composite," *Materials Today: Proceedings*, vol. 45, pp. 6580-6589, 2021.

[15] C. H. Gireesh, K. D. Prasad, K. Ramji, and P. Vinay, "Mechanical characterization of aluminium metal matrix composite reinforced with aloe vera powder," *Materials Today: Proceedings*, vol. 5, no. 2, pp. 3289-3297, 2018.

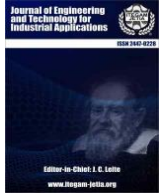
[16] K. Olaiya, M.O Adeoti, I. Adigun, R. Saheed, U. Eboeime, and L. Jimoh, "Comparative study of the mechanical properties of sandcast and die-cast aluminium for engineering applications," *International Journal of Scientific & Engineering Research*, vol. 10, no. 8, 2019.

[17] J. Gu, R. Li, S. Chen, Y. Zhang, S. Chen, and H. Gu, "Microstructure and wear behavior of laser clad Ni45+ high-carbon ferrochrome composite coatings," *Materials*, vol. 13, no. 7, p. 1611, 2020.

[18] B. Aramide, T. Jamiru, S. Pityana, R. Sadiku, and P. Popoola, "Scanning Speed Effect on the Microstructure, Hardness, Wear, and Corrosion Performance of VC-Cr 3 C 2 Reinforced Laser Claddings on Steel Baseplate for Tillage Application," *Transactions of the Indian Institute of Metals*, vol. 75, no. 8, pp. 2149-2157, 2022.

[19] V. Aigbodion, S. Hassan, S. Olajide, O. Agunsoye, A. Abdulrahman, and G. Okafor, "The use of rice husk ash as an aggregate for foundry sand mould production," in *Proceedings of the 25th NMS Conference, Nigeria*, 2008, pp. 16-22.

- [20] V. S. Prasad and A.S. Rao, "Electroslag melting for recycling scrap of valuable metals and alloys," *Recycling of Metals and Engineered Materials*, pp. 503-516, 2000.
- [21] Q. Wang *et al.*, "Effect of heat treatment on tensile properties, impact toughness and plane-strain fracture toughness of sand-cast Mg-6Gd-3Y-0.5 Zr magnesium alloy," *Materials Science and Engineering: A*, vol. 705, pp. 402-410, 2017.
- [22] C. Jawalkar, A. S. Verma, and N. Suri, "Fabrication of aluminium metal matrix composites with particulate reinforcement: a review," *Materials Today: Proceedings*, vol. 4, no. 2, pp. 2927-2936, 2017.
- [23] Y. Say, O. Guler, and B. Dikici, "Carbon nanotube (CNT) reinforced magnesium matrix composites: The effect of CNT ratio on their mechanical properties and corrosion resistance," *Materials Science and Engineering: A*, vol. 798, p. 139636, 2020.
- [24] K. Munir, C. Wen, and Y. Li, "Graphene nanoplatelets-reinforced magnesium metal matrix nanocomposites with superior mechanical and corrosion performance for biomedical applications," *Journal of Magnesium and Alloys*, vol. 8, no. 1, pp. 269-290, 2020.



RESEARCH ARTICLE

OPEN ACCESS

A COMPREHENSIVE REVIEW ON APPLICATION OF AI ALGORITHMS FOR GRID CONNECTED SOLAR PHOTOVOLTAIC SYSTEMS

W.V. Jahnvi¹, J. N. Chandra Sekhar²

^{1,2} Dept. Of EEE, Sri Venkateswara University College of Engineering – Tirupati, India.

¹ <http://orcid.org/0009-0005-5889-5868> , ² <http://orcid.org/0000-0003-2767-2467>

Email: wvjahnvi@gmail.com, chandrashkar.jn@svuniversity.edu.in

ARTICLE INFO

Article History

Received: August 12th, 2024

Revised: September 19th, 2024

Accepted: September 19th, 2024

Published: September 27th, 2024

Keywords:

Artificial Intelligence,
Photovoltaic system,
PID controller,
Optimization Techniques,
Machine Learning.

ABSTRACT

The preponderance significant renewable energy is solar energy and corporations and governments are investing more in it every year. The most significant issues with PV systems are resolved with Artificial Intelligence (AI). Due to increased processing power, tools, and data collection, artificial intelligence (AI) is becoming more and more prevalent in diverse photovoltaic (PV) system applications. It has been discovered that the methodologies now in use for designing, forecasting, control and maintenance aspects for the solar Photovoltaic business provide findings that are somewhat erroneous. Additionally, applying AI to complete these activities has increased in accuracy and precision and is currently a very intriguing issue. Similar to this, proportional-integral-derivative controllers have unparalleled acceptance and reputation in control systems. PID tuning is still an important area of study, due to its simple structures, robustness to model errors, and easy operations, PID controllers are widely employed in engineering practices. In this context, this paper aims to review the accord among artificial intelligence (AI) applications for photovoltaic (PV) systems and Tuning of PID controllers. This Review paper analyses the appropriate application of AI for designing, maintenance and control of Grid-connected solar Photovoltaic systems as well as advanced control strategies and control algorithms for Tuning PID controller.



Copyright ©2024 by authors and Galileo Institute of Technology and Education of the Amazon (ITEGAM). This work is licensed under the Creative Commons Attribution International License (CC BY 4.0).

I. INTRODUCTION

The ability to employ Artificial Intelligence for research has been expanded tremendous rise of digital data and processing power, due to advancements in AI and ML algorithms. [1] gives the importance of AI which exposed to a much greater urgency in the face of familiar difficulties. The growing accessibility of knowledge, in peculiar threatens the specification and self-determination of b people and country. Artificial intelligence (AI) research is aimed at creating such a computer and expanding our knowledge of intelligence. [2] gives review of artificial intelligence algorithms. Overall, AI tools and approaches are inventive, practical, and beneficial. If these were the only criteria used to assess AI's progress, it would be regarded as one of the most accomplished technical domains. Human mental abilities, on the other hand, are immensely complex and have proven to be extraordinarily difficult to imitate.

Fossil fuel consumption has caused a number of eco-friendly issues, such as the greenhouse effect and global warming. As a result, there is now a greater need for renewable energy sources. Solar photovoltaic (PV) technology is quickly expanding its role in the electrical generation industry. Concerns concerning the synchronization method are brought up by the recent interest in solar Photovoltaic integration into the grid. The modest stand-alone system has been successfully replaced by a grid connected PV system in ongoing research. [3] Investigators progressive efforts have turned the modest stand-alone PV system into a grid-connected. Figure 1 below shows the example of the PV system. The primary goal is to synchronize the utility of PV system to send actual electricity to meet load needs.

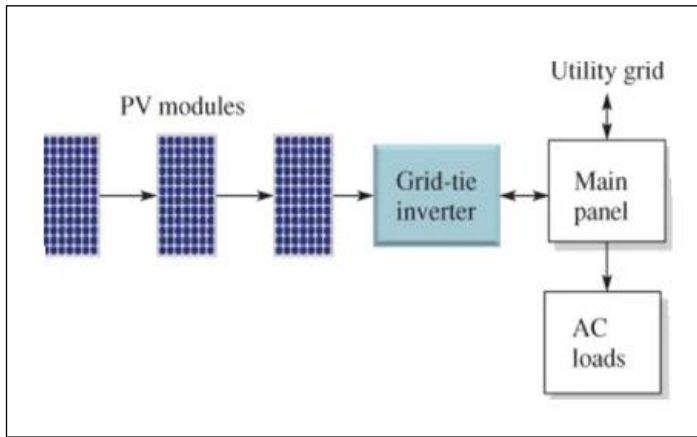


Figure 1: Structure of grid-tied PVs.
Source: Authors, (2024).

Photovoltaic systems are grid-connected satisfy the voltage and frequency standards stated in the IEEE standard for integrating dispersed energy resources with power systems. By giving systems, a set of intricate instructions to follow, it trains them to think, reason, and make judgements much as people do. Both businesses and individuals utilize the technique often in their daily operations. Additionally, it has been determined that the use of AI in the digitalization of power systems has a huge potential to help with enhancing stability, dependability, dynamic reaction, and other crucial developments for the power system network [4]. The qualities of design considerations, forecasting, converter control and maintenance are heavily studied in the literature out of the specified fields of AI use. The components of cybersecurity are evolving and were thought to be the upcoming trends for AI applications in solar energy systems. The development of AI to support the system learning process for enhancing efficiency and lowering reaction time has advanced due to the data availability in the operation of power systems.

In [5] Describes integration of a photovoltaic system utilizing a Marx multilevel inverter under various ecological situations. The P&O MPPT technique is to transition the pulse from the PV panel to the Boost Converter, and grid integration was accomplished utilizing PLL with a closed loop control strategy using the Phase Disposition method. PI parameters pioneered the controller design methodology. [6] A unique grid-connected photovoltaic control mechanism has been developed using boost converter and an L filter. The control objectives are to track the maximum power point of the PV panel, balance the power exchange by regulating the DC link voltage and ensure a unity power factor in the grid.

Proportional Integral Derivative controllers are used significantly and recognized for development control in today's industry due to aspects such as their simplicity, high efficiency and reliability. Tuning of PID control parameter has been a topic of present study. Reduced settling time and low overshoot in the steady state response are the main goals of PID control settings. Ziegler and Nichols (1942) established the first PID controller parameter tuning rules, and numerous further tuning rules were proposed afterwards. [7] investigated the performance of PID while taking the coupling impact of LFC and AVR into account, first utilizing the traditional controller (Z-N) approach to enhance the performance and then applying advanced intelligence techniques to produce more accurate results. Error is the difference in computation between the process value (PV) arriving from the field measurement sensor and the desired process trajectory or setpoint, set by the operator or by sophisticated process control logic. The

controller output moves the final control element and has been computed in accordance with the present and previous error values in order to minimize error. The most efficient control action depends on the PID parameters' ideal values in the PID control algorithm. [8] About 90% of control system applications uses PID controllers.

Various tuning approaches are described in this review study, and observation of existing algorithms tuning method responsiveness is examined. Many methods for adjusting and producing optimized gain factors have been utilized in the past, including the Ziegler-Nichols technique, particle swarm optimization, genetic algorithm and artificial neural network.

Subsequent part of this article is prepared as: Section II explains about AI Frame work for grid connected PV system. Section III gives AI applications in design, forecasting, control and maintenance of PV system. Section IV investigates the modelling of PID controller Tuning. Section V classify the AI algorithms for PID controller tuning. Section VI finally a conclusion is given.

II. AI FRAME WORK FOR GRID CONNECTED PHOTOVOLTAIC SYSTEM

Artificial Intelligence utilizes a variety of approaches to study power system challenges such as architecture, control, monitor, forecast and security. [9] literature divides artificial intelligence into five categories: optimization, data analysis, categorization, regression and clustering. Intelligent PV plants are built in [10], with linear programming-based optimization for scaling PV, energy storage systems and model predictive control. Same optimization technique is used for the designing the storage system as well as operation of the entire IPV power plant to achieve exclusive sizing and control.

Furthermore, with increased access to power system operational data, AI implementation has increased significantly, as has accuracy. In this case, the data collected is used to allow AI-enabled learning methodologies for spotting different difficulties and irregularities in system and suitable action within the time frame is specified. [11] uses irradiance forecasting with LSTM network to estimate the day profile for PV system operation. This information enables the developers to determine the performance of the PV in calculating the lowest, middle and high-power outputs. [12] A data driven strategy for detection of false data injection in system control. According to findings, procedure may be carried out online with the help of reinforcement learning methodologies. AI approaches are used practically scientific sector and business to improve services or solve issues that traditional methods cannot address [13]. We look at how artificial intelligence is being used in the PV industry.

PV systems encounter a variety of issues during installation and operation, because modules are sensitive to unstable climatic conditions. [14] provides a study of the challenges encountered in PV plants; also, module maintenance is critical to ensure maximum production and increase security of the installations. Figure 2 explains about the frame work and also describes about the applications of AI for grid connected solar PV in power systems. Optimization needs expert, decision making and heuristic search approaches for design, forecasting and control. Whereas classification, Regression and Clustering needs learning algorithms for maintenance, control and forecasting.

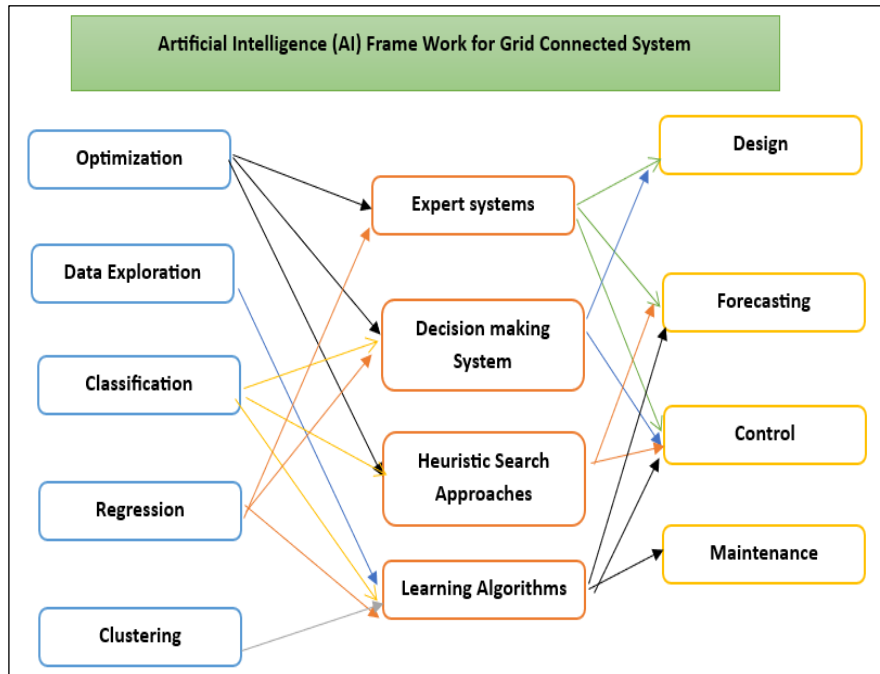


Figure 2: AI frame work for grid connected system.
Source: Authors, (2024).

Renewable energy (RE) supplies have attained peak performance in meeting contemporary energy demands. Among the numerous RE resources, photovoltaic is regarded as sustainable energy. [15] A Re-lift Luo converter is used single-phase grid-integrated solar PV system using chicken swarm optimization method. As PV output is periodic, the converter output varies as well and kept constant by using proportional-integral based closed loop control using optimized CS algorithm and normalized output then sent into grid through voltage source inverter. Furthermore, complexity of the power module construction and the complicated working circumstances for a solar photovoltaic (PV) inverter may damage the dependability of these modules, lowering the functional efficiency of the total grid-connected PV systems [16]. These limits are thought to have a significant influence on the safety and failure cost of GCPIs.

Linearization of a power flow (PF) model is a significant method for simplification and acceleration of power system management, operation, and optimization calculations. [17] Traditional model-based techniques generate linearized PF models by approximating the methodical Power Flow model based on the physical properties of power system. This [18] offers a novel neural network (NN) structure based on gradient descent least squares regression controlling integration of grid to solar PV systems to improve the quality of power. In this case, a neuron structure with single layer is employed to extract the fundamental component from load current. The GDLSR-based NN structure reduces harmonic components, DC offsets and distortions from nonlinear current during FC extraction, hence enhancing power quality in both normal and abnormal grid conditions. The dominance of renewable energy sources with power electronics-interfaced solar photovoltaic systems in recent years has caused grid frequency instability. [19] research offers a new machine learning based virtual inertia synthetization. Artificial intelligence approaches have been widely employed in the previous decade for MPPT in solar power systems under partial shading conditions. [20] A comprehensive fuzzy logic based maximum power tracking controller has been constructed and results demonstrating quick

convergence to MPP and low variation in extremely and effectively under specified atmospheric circumstances.

III. AI APPLICATIONS FOR GRID CONNECTED PHOTOVOLTAIC SYSTEM

It is a branch of computer science engineering that concentrates on developing advanced computers, gadgets and systems. [21] characterized a system's capacity to appropriately absorb external information, acquire knowledge, utilize techniques to achieve specific objectives. [22] AI is essentially provision for intelligent that can process information and make judgements in the same manner that humans consider. It is used to make machines intelligent so that they can accomplish complicated tasks effectively.

In [23] investigations-based AI focus on the designing and size of solar photovoltaic, regarded as essential aspects. Solar radiation modelling, prediction, and forecasting is one such extensive use. According to the research released, the Artificial Neural Network is commonly employed approach among the several strategies offered in solar energy literature. [24] Many studies have used Back Propagation Neural Network to forecast solar irradiance, energy, water heating system, daily ambient temperature and maximum power. [25] Artificial Neural Fuzzy Integrated Systems was used to estimate PV power supply, clearness index, radiation prediction and SCPP performance. In certain cases, a mix of methodologies is used to provide the best outcomes in forecasts, estimates and forecasting. [26] Various AI approaches were employed by the writers. The most widely utilized approaches in solar energy were ANN BPNN, ANFIS, and GA. According to the conclusions of this research, these strategies are commonly employed in many types of solar forecasts. ANN stood out as the most effective of these strategies and has distinct benefits in terms of computation speed, accuracy, and generalization capabilities over other modelling approaches. Figure 3 depicts AI applications.

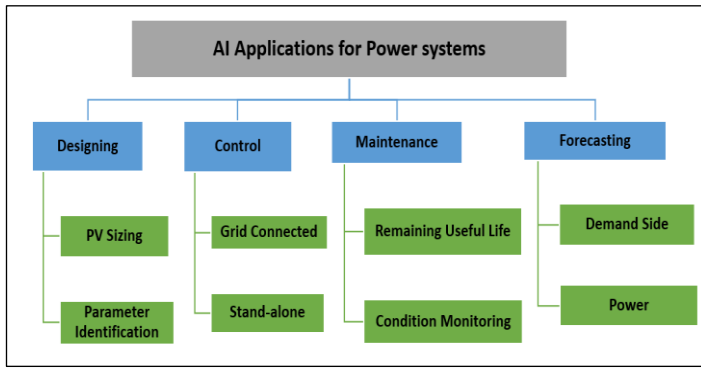


Figure 3: Applications of Artificial Intelligence in Power systems. Source: Authors, (2024).

III. 1. APPLICATION OF AI FOR DESIGNING

Artificial intelligence techniques are becoming more helpful alternatives than traditional methodologies. It plays a major role in power system designing which involves photovoltaic systems sizing and parameter identification.

Accurate size of a PV solar system is critical for ensuring the quality and stability of power supply, maximizing the economic lifecycle redeem. The major purpose is to provide overview of AI methods for sizing photovoltaic systems, such as stand-alone, grid-connected, and hybrid systems. [27] demonstrates AI's promise as a design tool for optimal PV arrangement. Furthermore, advantage employing AI-based sizing of PV systems delivers effective optimization, particularly in remote places where meteorological data is not always accessible. In this [28] artificial neural network and genetic algorithm are proposed to identify the appropriate size of PV systems, particularly in remote places. The GA-ANN technique has been proved useful for modelling the optimal size coefficient SAPV systems. The advantage of this method is to estimate the PV-array area and battery useable volume using merely geographical coordinates for any place. Generalized regression neural network is utilized in [29]. To adjust the coefficients and assess the possibility of load loss in standalone systems. The created model produces coordination coefficients with a MAE of 0.6%, while the simulation produced a load loss probability of 0.5%.

Parameter identification is critical not just for PV system modelling and simulation, but also for problem detection. The two-parameter identification are single diode and double diode model. Photovoltaic module parameter extraction is recognized as vital issue evaluating the PV energy systems performance. In this [30] the demand for supply-based Optimization Algorithm is used to extract the PV models' specifications. Because of its simplicity of implementation and great optimization capabilities, it is commonly employed to address complex nonlinear problems. In mathematical PV module models, the Triple-Diode Model is widely used. Thus, SDOA regarded as a competitive optimizer in comparison to other strategies documented in current methodologies. The genetic algorithm technique is utilized in [31] double diode solar cell model identification. Suggested method estimates currents and shunt resistance by using diode voltages as a function of temperature. The findings indicate the best experimental I-V curve with high convergence. In this [32], two strong AI approaches, Adaptive Neuro-Fuzzy Inference System and Artificial Neural Network are used to calculate the parameters in differential equations of dynamic systems. Extraction of unknown values of solar cell models are important for PV system performance. [33] demonstrates how to extract parameters from solar cell models

using the symbiotic organisms search efficient metaheuristic method. SOS was stimulated by interaction of symbiotic methods used to improve overall determination in the ecosystem. Advantages such free tuning algorithm for specific parameters, having better balance among investigation and maltreatment.

III. 2. APPLICATION OF AI FOR CONVERTER CONTROL

Based on method of operation, power electronic converter control categorized as Grid connected control and Standalone control

Grid connected Controllers are used to manage the power and frequency on inverter's AC side and decrease harmonics in system. An inverter control algorithm is used to handle the switches. However, AI greatly improves controller performance as well as inverter reaction time to transient faults. A unique cascaded H-bridge inverter with FL control method for PV applications has been suggested in [34]. Its performance meets the requirement for flexible electric power generation while also reducing the impact of disturbances produced by cloud darkening or fluctuations. Because of flexibility, suggested system may be enhanced by increasing the number of tiers, lowering THD even further. An adaptive neuro-fuzzy model using multilevel inverter photovoltaic system was suggested in [35]. The suggested controller's objective is to eliminate the need for an ideal PWM switching. Variations in output of H-bridge cascaded MLI are rigorously prohibited by the suggested technique. The ANFIS has a grid voltage input, a difference voltage, and a control voltage output goal in this technique. The ANFIS sets the rules and has been carefully calibrated using these parameters.

In Standalone control after the DGs are unplugged from the grid, they must continue to run and meet the demand. Distribution grids should address the load-supply balance while simultaneously managing the output in this mode of operation. [36] Traditionally, the inverter's stand-alone mode was examined through SVPWM. Researchers all around the world are concerned about and working to improve the efficiency of distribution generation (DG) inverters. An inverter control mechanism is being developed to alleviate the issue. When operating in grid connected inverters have voltage control and harmonics difficulties. This [37] presents a control technique for DGs that operate in both the conditions. The inverter's GC operation is accomplished through the CC mode, and SA control includes a VC loop capable of overcoming limitations associated with load shedding.

III. 3. APPLICATION OF AI FOR MAINTENANCE

AI may assist to save money and resources by optimizing maintenance schedules, minimizing waste and extending the life of equipment.

Photovoltaic systems have originated as significant renewable energy sources. when PV energy grows, it is critical to investigate defects and degradation of PV systems in order to improve the stability and performance in electrical systems. [38] A fault distribution technique is developed to ensure accurate and early failure detection in PV systems. Batteries play an important part in grid connected PV systems and must give the needed performance. Various diagnostics and prognostics for battery health monitoring, have been investigated. For battery issues, AI-based diagnostic approaches have been investigated. [39] develops a Bayesian regression for remaining useful life estimation in batteries. To calculate the RUL for batteries, electrochemical process method is combined with a statistical model. Furthermore,

relevance vector machine technique is being investigated for analyzing battery health. An adaptive Gaussian mixture model-based battery health monitoring system is proposed.

Condition Investigation in Grid connected systems are generally subjected to demanding and complicated operating conditions. They may experience a variety of fault occurrences, both at the component and system levels. Grid connected PV system safety and dependability are critical to ensuring the system's efficient functioning. Monitoring the state of PV modules is critical for improving power conversion efficiency. Delamination, discoloration, cell fracture, short circuit, glass crack and other problems can occur in PV panels. For defect diagnosis in PV panels, [40] use random forest approaches. The output of voltage and current under various temperature circumstances is acceptable. In [41], a failure diagnostic technique for PV panels is created using probabilistic neural network and radial basis networks. This diagnostic method has been found to be less susceptible to outliers and to have excellent generalization accuracy.

III. 4. APPLICATION OF AI FOR FORECASTING

As the number of Grid connected photovoltaic systems increased in recent years, having accurate projections for electricity generation supplied into the grid has become increasingly crucial. The primary reason for the rise is a reduction in investment expenses. Forecasting methodologies have been widely used by

market participants. An overview of energy market systems and the corresponding forecasting needs for intermittent renewable energy sources.

The majority of the research has been on demand side projections rather than distributed energy resource outputs [42], Load projections have been utilized in a number of studies to improve system functioning. [43] provides a study of sun irradiance forecasting strategies utilizing four distinct supervised machine learning and deep learning algorithms. The comparison of the various approaches revealed that the ANN algorithm produces effective performance compared to other methods.

Accurate estimates of PV system output power can help to revealing critical information to control the energy grid more effectively, allowing grid operators to handle rapid fluctuations in power in the grid. A study of solar power forecasting in [44] evaluates several methodologies and approaches to increase prediction model accuracy and minimize uncertainty. According to the review, ANN often employed with ML approaches in prediction of solar power conditions and with a large number of input variables. support vector machines techniques employ supervised modelling methods with input factors such as global horizontal irradiance and other performance specifications. [45] ANN and ensemble techniques are used to forecast power output. Table 1 below gives the summary of the AI methods used for grid-tied Photo voltaic systems.

Table 1: Summary of AI Application techniques for Grid Connected PV systems.

Applications	Method	Algorithm	Advantage	Reference
Designing	PV Sizing	GA-ANN	Efficiently predicts input data	27,28,29
	Parameter Identification	ANN	High accuracy	32,33
Control	Grid connected	AI	Capability to manage multi-inverter grid-connected DG	34,35
	Standalone	Fuzzy	Reliable in Control of System	37
Maintenance	RUL	RVM	Robust and high accuracy	38,39
	Condition Monitoring	RF	Achieve better performance and accuracy	40
Forecasting	Demand	ANN, ML, DL	Efficiently handles the nonlinear data	43
	Power	ANN	High precision and quick response	45

Source: Authors, (2024).

IV. MODELLING OF PROPORTIONAL INTEGRAL AND DERIVATIVE CONTROLLER

This controller has significant role in utility systems due to its serenity of implementation and efficacy of performance in electrical power systems. Most of the industrial applications PID controllers are employed. These controllers date back to the governor design of the 1890s. As per the survey in 1989, 90% of process industries employ them. PIDs are universally used in industry due to simplicity and ease of online re-tuning. For PID tuning, numerous strategies have been used, with the Ziegler Nichols technique being one of the first [46]. Figure 4 below shows Schematic diagram of PID.

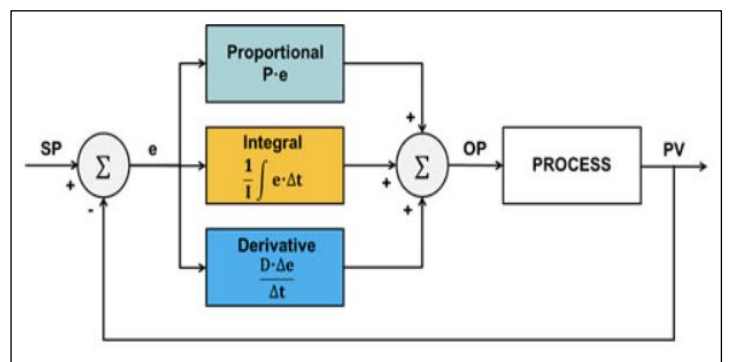


Figure 4: PID controller Schematic representation.

Source: Authors, (2024).

PID controllers use computational models to self-tune or auto-tune. PID controller self-tuning effectively modify the parameters in modelling computational process and comparing the

outputs to check the deviations, in which case the PID settings are reset to obtain the desired response. For tuning of proportional-integral-derivative controller a three-tank system using a mixed optimization approach is presented [47] to acquire optimal controller settings, the unit step response of integral-square-error is reduced.

V. CLASSIFICATION OF PID CONTROLLERS TUNING

An overview of tuning approaches is shown in Figure 5.

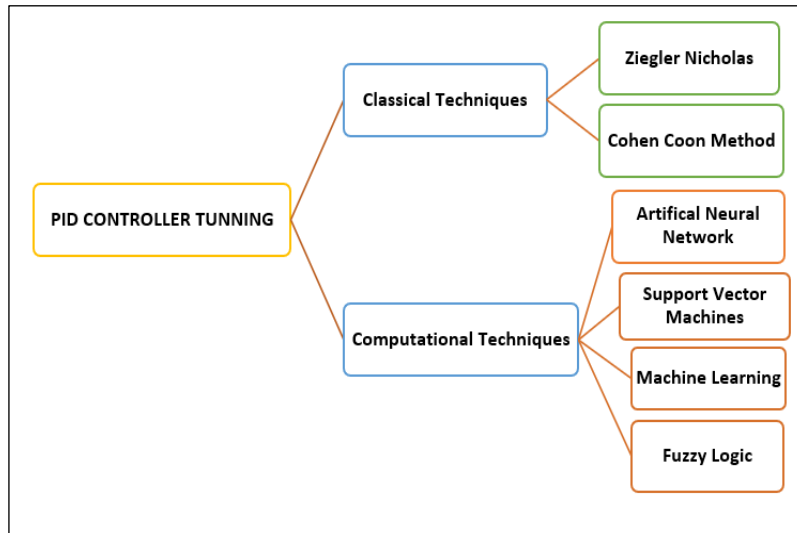


Figure 5: Classification of PID Controller Tunning.
Source: Authors, (2024).

V.1. CLASSICAL TECHNIQUES

Conventional systems estimate the system model to develop controller settings based on these assumptions. The feedback of the systems is measured in order to determine their progress.

V.1.1. Ziegler Nichols Method

The two scientists in 1942 introduced most fundamentally recognized and widely used tuning procedure [48]. Ziegler and Nichols have presented two techniques. PID controllers for spindle motor systems were tuned using the first technique. [49]. The second way is based on previous experience with certain frequencies. The goal is to base the controller settings on the frequencies that are most important for stability. The first strategy, devised by Ziegler and Nichols, is based on certain controller assumptions. Hence controller is destructive, resulting in uncontrolled oscillations.

V.1.2. Cohen Coon Method

In [50] FOLPD model is used to specify PID controller parameters. The fundamental structure requirement is the rejection of load perturbations. Cohen Coon approach produces similar findings to the Ziegler Nichols method.

V.2. COMPUTATIONAL TECHNIQUES

The various intelligent optimization techniques for PID controller tuning are discussed below.

V.2.1. ARTIFICIAL NEURAL NETWORKS

Computations and mathematics are used to replicate human-brain processes in the model. Many of the recent achievements are in the field of artificial intelligence research, such as image and speech recognition, robotics and the use of ANNs. Figure 6 shows the ANN based PID tuning. Though ANN model

is used for highly nonlinear systems. In [51] neural network control design was specified with inherent drawbacks of ANN theory, in determination of neurons and layers.

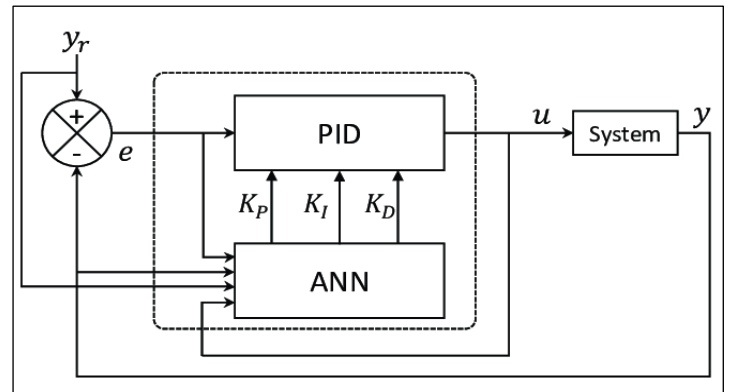


Figure 6: Architecture of ANN based PID
Source: Authors, (2024).

V.2.2. Support Vector Machine

Be concise PID control techniques are commonly used in the majority of chemical processes. However, tuning PID parameters is a critical issue as they have significant impact on adherence of the control system [52]. Support Vector Machine is a set of supervised learning techniques used for classification and regression. layman's words, SVM training algorithm predicts whether a new example belongs in one of two categories given a set of labelled data. In more technical terms, an SVM generates a hyperplane in a high dimension space, which is utilized for classification and regression.

V.2.3. Fuzzy Logic

It is the relationships between control engineering and artificial intelligence. The FLC augments the standard PID by adjusting controller's settings on-line in response to changes in

signal error and error. When compared to the solo Fuzzy, the PID Controller performs well. In the Fuzzy Controller elementary rules are made; whereas in PID Controller based Fuzzy, manifold rules are established for all three Controllers and exhibits improvements quicker, as shown in Figure 7.

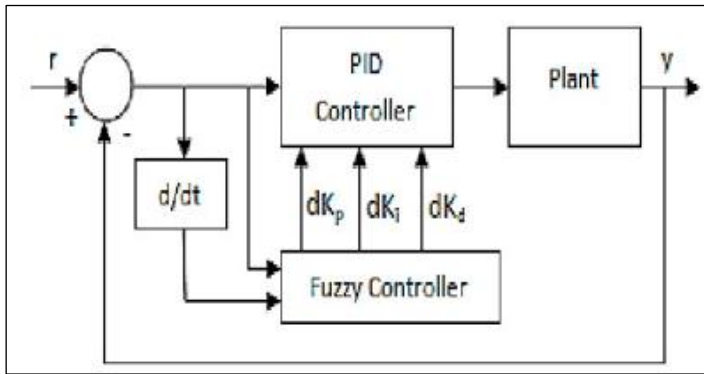


Figure 7: Architecture of Fuzzy based PID.
Source: Authors, (2024).

The rules determined by the system are managed and experienced [53]. Designing integral rule bases may be challenging. As a result, this is an ideal design and additional configurations in which a PI- fuzzy controller and PD-fuzzy controller work together to create a PID- controller.

V.2.3. Machine Learning

Due to its Accuracy and Precision, these algorithms are extensively used industrial control system. However, adjusting PID parameters are not easy, and various approaches have been published in the literature. The purpose [54] study is to demonstrate a machine learning strategy combining gradient descent with multivariate regression and the normal equation as shown in fig 8. As an example, the first order cruise control system is employed, and the results demonstrate effective progress towards autonomous adjustment of PID data using trained data.

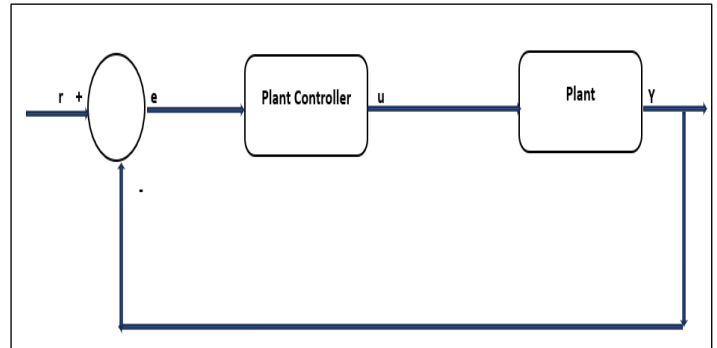


Figure 8: Machine Learning based PID.
Source: Authors, (2024).

Advantages and Disadvantages of all the PID controller Tuning Techniques are given in Table 2 below

Table 2: Summarized Strengths and Weakness of PID Controller Techniques.

Technique	Strengths	Weakness
Ziegler Nichols	Proven and Online Method	Very Aggressive
Cohen Coon	Good process and Offline Method	Good for first order process
Artificial Neural Network	Convergence to Precise Model	Take More Time for Execution
Support vector Machine	Efficient Design Simple control	Low Accuracy
Fuzzy Logic	Simple control structure	Simple Fuzzy Information
Machine Learning	Robustness	Requires data for calculation

Source: Authors, (2024).

VI. CONCLUSION

The First Part of the study undertaken in this work leads to the conclusion that there are several research articles published utilizing different AI algorithms to diverse goals in the combination of solar Grid Connected System. The most often used AI approaches for the Grid Connected Photovoltaic Systems are in Designing, Converter Control, Maintenance and Forecasting have been discussed in brief along with its advantages and applications. Similarly, the second part of the research examined a wide range of strategies for PID tuning. Following a brief overview of the approach, there was an accomplishment in tuning and self-tuning of the controllers applying various control techniques. Applications of these controllers will be encouraged more as computer technology and smart machines advance. As a result, more research into PID algorithms is required. Thus, this article

gives a brief description AI application for Grid Connected Photovoltaic systems and PID Controller tuning.

VII. AUTHOR'S CONTRIBUTION

Conceptualization: W.V.Jahnavi, J.N.Chandra Sekhar.
Methodology: J.N.Chandra Sekhar.
Investigation: W.V.Jahnavi, J.N.Chandra Sekhar.
Discussion of results: W.V.Jahnavi.
Writing – Original Draft: W.V.Jahnavi, J.N.Chandra Sekhar.
Writing – Review and Editing: W.V.Jahnavi.
Resources: W.V.Jahnavi, J.N.Chandra Sekhar.
Supervision: J.N.Chandra Sekhar.
Approval of the final text: J.N.Chandra Sekhar.

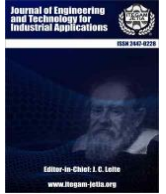
VIII. REFERENCES

- [1] Bryson, JJ 2019, The Past Decade and Future of AI's Impact on Society. in Towards a New Enlightenment? A Transcendent Decade. vol. 11, Turner, Madrid.
- [2] Jameela Ali Akrimi, et al "Review of Artificial Intelligence" International Journal of Science and Research (IJSR), India Online ISSN: 2319-7064, Volume 2 Issue 2, February 2013.
- [3] Pragya Gawhade, Amit Ojha "Recent advances in synchronization techniques for grid-tied PV system: A review" Energy Reports 7 (2021) 6581–6599.
- [4] Zhao, S.; Blaabjerg, F.; Wang, H. An Overview of Artificial Intelligence Applications for Power Electronics. IEEE Trans. Power Electron. 2021, 36, 4633–4658, doi:10.1109/tpe.2020.3024914.
- [5] L. M. Krishna, J. N. Chandra Sekhar, M. Naresh, P. Samuel "Performance Analysis of Grid Integrated Photo-Voltaic Systems Using Marx Multilevel Inverter In Different Environmental Conditions" U.P.B. Sci. Bull., Series C, Vol. 80, Iss. 2, 2018 Issn 2286-3540.
- [6] Youssef Mchaouar et al, "Advanced sensorless nonlinear control strategy for grid connected photovoltaic systems via the two-time scale singular perturbation technique" International Journal of Power Electronics, 2023 Vol.17 No.2, pp.129 – 165, doi: 10.1504/IJPELEC.2023.128864
- [7] Ghassan Abdullah Salman, Assama Sahib Jafar, Ammar Issa Ismael "Application of artificial intelligence techniques for LFC and AVR systems using PID controller" International Journal of Power Electronics and Drive System (IJPEDS) Vol. 10, No. 3, Sep 2019, pp. 1694~1704
- [8] M. Prabhat Dev, Sidharth Jain, Harish Kumar, B. N. Tripathi and S. A. Khan "Various Tuning and Optimization Techniques Employed in PID Controller: A Review" Smart Innovation, Systems and Technologies ISBN 978-981-15-2646-6 ISBN 978-981-15-2647-3 (eBook). doi: <https://doi.org/10.1007/978-981-15-2647-3>
- [9] Kurukuru, V.S.B.; Haque, A.; Khan, M.A.; Sahoo, S.; Malik, A.; Blaabjerg, F. "A Review on Artificial Intelligence Applications for Grid-Connected Solar Photovoltaic Systems". Energies 2021, 14, 4690. <https://doi.org/10.3390/en14154690>.
- [10] Saez-de-Ibarra, A.; Milo, A.; Gaztanaga, H.; Debusschere, V.; Bacha, S. Co-Optimization of Storage System Sizing and Control Strategy for Intelligent Photovoltaic Power Plants Market Integration. IEEE Trans. Sustain. Energy 2016, 7, 1749–1761, doi:10.1109/tste.2016.2555704.
- [11] Liu, C.-H.; Gu, J.-C.; Yang, M.-T. "A Simplified LSTM Neural Networks for One Day-Ahead Solar Power Forecasting". IEEE Access 2021, 9, 17174–17195, doi:10.1109/access.2021.3053638.
- [12] Wang, Z.; Chen, Y.; Liu, F.; Xia, Y.; Zhang, X. "Power System Security Under False Data Injection Attacks with Exploitation and Exploration Based on Reinforcement Learning". IEEE Access 2018, 6, 48785–48796, doi:10.1109/access.2018.2856520.
- [13] Pallathadka, H.; Ramirez-Asis, E.H.; Loli-Poma, T.P.; Kaliyaperumal, K.; Ventayen, R.J.M.; Naved, M. "Applications of artificial intelligence in business management, e-commerce and finance. Mater. Today Proc. 2021, in press.
- [14] Alshahrani, A.; Omer, S.; Su, Y.; Mohamed, E.; Alotaibi, S. "The technical challenges facing the integration of small-scale and large-scale PV systems into the grid: A critical review". Electronics 2019, 8, 1443.
- [15] Elango Kannan, Maheswari Avudaiappan, Saravanan Kaliyaperumal, Suresh Muthusamy, Santhiya Pandiyan, Hitesh Panchal, Kannan Manickam & Chandrasekar Shanmugam (2023) A novel single phase grid connected solar photovoltaic system for state of charge estimation using recurrent neural networks, Energy Sources, Part A: Recovery, Utilization, and Environmental Effects, 45:1, 841-859, DOI: 10.1080/15567036.2023.2172097
- [16] Haque, A.; Bharath, K.V.S.; Khan, M.A.; Khan, I.; Jaffery, Z.A. Fault diagnosis of Photovoltaic Modules. Energy Sci. Eng. 2019,7, 622–644, doi:10.1002/ese3.255.
- [17] Liu, Y.; Zhang, N.; Wang, Y.; Yang, J.; Kang, C. Data-Driven Power Flow Linearization: A Regression Approach. IEEE Trans. Smart Grid 2019, 10, 2569–2580, doi:10.1109/tsg.2018.2805169.
- [18] Kumar, N.; Singh, B.; Panigrahi, B.K. Framework of Gradient Descent Least Squares Regression-Based NN Structure for Power Quality Improvement in PV-Integrated Low-Voltage Weak Grid System. IEEE Trans. Ind. Electron. 2019, 66, 9724–9733, doi:10.1109/tie.2018.2886765.1
- [19] Kah Yung Yap, Charles R. Sarimuthu, And Joanne Mun-Yee Lim "Grid Integration of Solar Photovoltaic System Using Machine Learning-Based Virtual Inertia Synthesis in Synchronverter" IEEE Access 20 march 2020. Doi:10.1109/ACCESS.2020.2980187.
- [20] J. N. Chandrasekhar, S. Rakesh "Photovoltaic Array Maximum Power Point Tracking Using Fuzzy Control Method" International Journal of Engineering Research & Technology (IJERT) Vol. 2 Issue 7, July – 2013, ISSN: 2278-0181
- [21] Kolbjornsrud, V., Amico, R., & Thomas, R. J. (2016). The promise of artificial intelligence.
- [22] Michalski, R.S., Carbonell, J.G., Mitchell, T.M. (1984). Machine learning: An artificial intelligence approach. Berlin: Springer-Verlag.
- [23] Mellit, A., & Pavan, A. M. (2010). A 24-h forecast of solar irradiance using artificial neural network: Application for performance prediction of a grid-connected PV plant at Trieste, Italy. Solar Energy, 84(5), 807–821.
- [24] Mellita A, Kalogirou SA. Artificial intelligence techniques for photovoltaic applications: a review. Prog Energy Combust Sci 2008;34(5):574–632.
- [25] Mellit, A., & Kalogirou, S. A. (2011). ANFIS-based modelling for photovoltaic power supply system: A case study. Renewable energy, 36(1), 250–258.
- [26] Jeffrey T. Delloso, Eleonor C. Palconit "Artificial Intelligence (AI) in Renewable Energy Systems: A Condensed Review of its Applications and Techniques" September 2021 DOI: 10.1109/EEEIC/ICPSEurope51590.2021.9584587.
- [27] Mellit, A.; Kalogirou, S.; Hontoria, L.; Shaari, S. Artificial intelligence techniques for sizing photovoltaic systems: A review. Renew. Sustain. Energy Rev. 2009, 13, 406–419, doi: 10.1016/j.rser.2008.01.006.
- [28] Mellit, A. Sizing of a stand-alone photovoltaic system based on neural networks and genetic algorithms: Application for remote areas. Istanbul Univ. J. Electr. Electron. Eng. 2007, 7, 459–469.
- [29] Khatib, T.; Elmenreich, W. An Improved Method for Sizing Standalone Photovoltaic Systems Using Generalized Regression Neural Network. Int. J. Photoenergy 2014, 2014, 1–8, doi:10.1155/2014/748142.
- [30] Abdullah M. Shaheen, Ragab A. El-Sehemy, Guojiang Xiong, Ehab Elattar, Ahmed R. Ginidi "Parameter identification of solar photovoltaic cell and module models via supply demand optimizer" Ain Shams Engineering Journal 13 (2022) 101705.
- [31] Petcuț, F.M.; Leonida-Dragomir, T. Solar cell parameter identification using genetic algorithms. Control. Eng. Appl. Inform. 2010, 12, 30–37.
- [32] Vatankhah, R.; Ghanatian, M. Artificial neural networks and adaptive neuro-fuzzy inference systems for parameter identification of dynamic systems. J. Intell. Fuzzy Syst. 2020, 39, 6145–6155, doi:10.3233/JIFS-189085.
- [33] Xiong, G.; Zhang, J.; Yuan, X.; Shi, D.; He, Y. Application of Symbiotic Organisms Search Algorithm for Parameter Extraction of Solar Cell Models. Appl. Sci. 2018, 8, 2155, doi:10.3390/app8112155.
- [34] Cecati, C.; Ciancetta, F.; Siano, P. A Multilevel Inverter for Photovoltaic Systems with Fuzzy Logic Control. IEEE Trans. Ind. Electron. 2010, 57, 4115–4125, doi:10.1109/tie.2010.2044119.
- [35] Karuppusamy, P.; Natarajan, A.M.; Vijeyakumar, K.N. An Adaptive Neuro-Fuzzy Model to Multilevel Inverter for Grid Connected Photovoltaic System. J. Circuits Syst. Comput. 2015, 24, 1550066, doi:10.1142/s0218126615500668.
- [36] Khan, J.F.; Bhuiyan, S.M.; Rahman, K.M.; Murphy, G.V. Space vector PWM for a two-phase VSI. Int. J. Electr. Power Energy Syst. 2013, 51, 265–277, doi:10.1016/j.ijepes.2013.02.029.
- [37] Khan, M.A.; Haque, A.; Kurukuru, V.S.B.; Wang, H.; Blaabjerg, F. Standalone operation of Distributed Generation Systems with Improved Harmonic Elimination Scheme. IEEE J. Emerg. Sel. Top. Power Electron. 2021, doi:10.1109/jestpe.2021.3084737.

- [38] Kurukuru, V.S.B.; Blaabjerg, F.; Khan, M.A.; Haque, A. A Novel Fault Classification Approach for Photovoltaic Systems. *Energies* 2020, 13, 308, doi:10.3390/en13020308.
- [39] Yu, J. Health Degradation Detection and Monitoring of Lithium-Ion Battery Based on Adaptive Learning Method. *IEEE Trans.Instrum. Meas.* 2013, 63, 1709–1721, doi:10.1109/tim.2013.2293234.
- [40] Chen, Z.; Han, F.; Wu, L.; Yu, J.; Cheng, S.; Lin, P.; Chen, H. Random forest based intelligent fault diagnosis for PV arrays using array voltage and string currents. *Energy Convers. Manag.* 2018, 178, 250–264, doi:10.1016/j.enconman.2018.10.040.
- [41] Akram, M.N.; Lotfifard, S. Modeling and Health Monitoring of DC Side of Photovoltaic Array. *IEEE Trans. Sustain. Energy* 2015, 6, 1245–1253, doi:10.1109/tste.2015.2425791.
- [42] Khan, M.A.; Mishra, S.; Harish, V.S.K.V. Grid connected energy efficient building with roof top SPV. In *Proceedings of the 2017 Recent Developments in Control, Automation & Power Engineering (RDCAPE)*; Institute of Electrical and Electronics Engineers (IEEE), Noida, India 26–27 October 2017; pp. 120–124.
- [43] Ağbulut, Ümit; Gürel, A.E.; Biçen, Y. Prediction of daily global solar radiation using different machine learning algorithms: Evaluation and comparison. *Renew. Sustain. Energy Rev.* 2021, 135, 110114, doi:10.1016/j.rser.2020.110114.
- [44] Nespoli, A.; Ogliari, E.; Leva, S.; Pavan, A.M.; Mellit, A.; Lughì, V.; Dolara, A. Day-Ahead Photovoltaic Forecasting: A Comparison of the Most Effective Techniques. *Energies* 2019, 12, 1621, doi:10.3390/en12091621.
- [45] Omar, M.; Dolara, A.; Magistrati, G.; Mussetta, M.; Ogliari, E.; Viola, F. Day-ahead forecasting for photovoltaic power using artificial neural networks ensembles. In *Proceedings of the 2016 IEEE International Conference on Renewable Energy Research and Applications (ICRERA)*; Institute of Electrical and Electronics Engineers (IEEE), Birmingham, UK, 20–23 November 2016; pp. 1152–1157.
- [46] Hari Om Bansal, Rajamayoor Sharma, P. R. Shreeraman “PID Controller Tuning Techniques: A Review” *Journal of Control Engineering and Technology (JCET)*, 17 May 2017.
- [47] V.P. Singh; N. Patnana; S.P. Singh “ PID controller tuning using hybrid optimisation technique based on Box’s evolutionary optimisation and teacher-learner-based-optimisation” *International Journal of Computer Aided Engineering and Technology*, 2020 Vol.13 No.1/2, pp.258 – 270. doi: 10.1504/IJCAET.2020.108124
- [48] Åström, K.J., Hägglund, T., 2004. Revisiting the Ziegler–Nichols step response method for PID control. *J. Process Control* 14, 635–650.
- [49] C. S. Soh, C. Bi and K. C. Chua, “Direct PID Tuning For Spindle Motor Systems,” *Asia-Pacific Magnetic Recording Conference*, Singapore, pp. 1-2, Nov-Dec.2006.
- [50] G. H. Cohen, and G. A. Coon, “Theoretical considerations of retarded control,” *Transactions of ASME*, vol. 75, pp. 827-834, 1953.
- [51] DOLEŽEL, Petr, MAREŠ, Jan, “Self-tuning PID Control using Genetic Algorithm and Artificial Neural Networks,” *ASR 2009 Instruments and Control*, pp. 33- 39, 2009.
- [52] K. Takao, Y. Toru and H. Takao, “A Design of PID Controllers with a Switching Structure by a Support Vector Machine,” *International Joint Conference on Neural Networks*, pp. 4684 – 4689, 2006.
- [53] Devendra Somwanshi, Mahesh Bundele ,Gaurav Kumar , Gajal Parasha “Comparison of Fuzzy-PID and PID Controller for Speed Control of DC Motor using LabVIEW” *Procedia Computer Science* 152 (2019) 252–260.
- [54] Andrew Zulu “Towards Explicit PID Control Tuning using Machine Learning” *IEEE Africon 2017 Proceedings*.



ISSN ONLINE: 2447-0228



RESEARCH ARTICLE OPEN ACCESS

IMPACT OF NITROGEN INCORPORATION ON BAND GAP BOWING IN ZINC-BLENDE $\text{GaAs}_{1-x}\text{N}_x$ A FIRST-PRINCIPLES STUDY

Mimouna Oukli¹, Ghلام Karima², Seyf Eddine Bechekir³

^{1,2}Applied Materials Laboratory (A.M.L), Faculty of Electrical Engineering, Djillali Liabes University of Sidi Bel Abbas, Sidi Bel Abbas, Algeria.

³Laboratory of Intelligent control And Electrical Power System (ICEPS), Djillali Liabes University of Sidi Bel-Abbès, Sidi Bel-Abbès, Algeria

¹<http://orcid.org/0000-0002-4871-6919> ²<http://orcid.org/0000-0001-8276-0609> ³<http://orcid.org/0000-0002-6143-7>

Email: mounaoukli@yahoo.fr, ouklimouna22@gamil.com, seyfeddine.electrotechnique@gmail.com

ARTICLE INFO

Article History

Received: August 14th, 2024

Revised: September 06th, 2024

Accepted: September 06th, 2024

Published: October 04th, 2024

Keywords:

Ab-initio calculations,

Nitrides,

Structural properties,

Bowing parameter.

ABSTRACT

This study, utilizing full-potential linear muffin-tin orbital (FPLMTO) calculations within density functional theory (DFT), delved into the structural properties of zinc-blende $\text{GaAs}_{1-x}\text{N}_x$ alloys. By varying the nitrogen concentration ($x = (0.125, 0.083, \text{ and } 0.063)$), we observed deviations from Vegard's law for lattice parameters and nonlinear behavior of the bulk modulus. The band gap bowing was primarily attributed to volume deformation effects, as elucidated by the Ferhat approach. Our findings demonstrate that the electronic and structural properties of $\text{GaAs}_{1-x}\text{N}_x$ are strongly influenced by the nitrogen concentration. These variations present exciting opportunities for bandgap engineering and the design of wide-bandgap optoelectronic devices.



Copyright ©2024 by authors and Galileo Institute of Technology and Education of the Amazon (ITEGAM). This work is licensed under the Creative Commons Attribution International License (CC BY 4.0).

I. INTRODUCTION

Dilute nitride alloys, such as $\text{GaAs}_{1-x}\text{N}_x$ and $\text{GaSb}_{1-x}\text{N}_x$, have emerged as promising materials for infrared optoelectronic devices, particularly for telecommunications applications including solar cells [1], long-wavelength light-emitters ($1.3 \mu\text{m}$ – $1.55 \mu\text{m}$), and tunable photodetectors [2-7]. These alloys offer unique properties, notably a significant reduction in their bandgap energy, rendering them highly attractive for various applications [8, 9]. This band gap reduction is primarily attributed to the incorporation of a small amount of nitrogen [10] (typically less than 5%) into III-V compounds [11-14]. This phenomenon, known as "bowing," is linked to the strong curvature of the relationship between alloy composition and bandgap energy that has been experimentally observed for some dilute nitrides such as GaPN [1],[15], InPN [16] and GaAsN [17]. The "bowing factor," a key characteristic of these materials, is influenced by factors such as the electronegativity and atomic radius of nitrogen compared to those of arsenic [18].

While the band gap of a typical mixed compound exhibits a linear relationship with composition, as described by Vegard's law, certain materials, like GaNAs, GaInNAs, and GaNP, deviate significantly from this behavior, exhibiting a large band gap

bowing with a bowing coefficient as large as 20 eV [19]. This anomalous decrease in band gap, often termed "large band gap bowing," has been extensively studied using theoretical and computational methods [20-31]. To gain a deeper understanding of the factors influencing this bowing effect, theoretical and computational methods have been extensively employed. However, the underlying mechanisms remain elusive.

To explore the underlying causes of this bowing phenomenon, measurements and calculations on semiconductor alloys indicate that the band gap energy deviates from the linear behavior given by Vegard's law [32], termed 'large band gap bowing'. The magnitude of the bowing factor varies significantly among different alloys and its physical origins are not fully understood. Our phenomenological model aims to elucidate these factors by investigating the structural properties of III-V ternary alloys containing nitrogen in zinc blend structure. To better understand the physical origins of the large dispersion and composition-dependent bowing in $\text{A}_{1-x}\text{B}_x\text{C}$ alloys, we have used our recently developed phenomenological model Ferhat [33], which has been shown to account successfully for the optical band gap bowing of III-V semiconductor alloys.

This study investigates the impact of nitrogen incorporation on the gap bowing behavior of zinc-blende GaAs_{1-x}

xN_x alloys. We will further explore the influence of nitrogen incorporation on this phenomenon. Full-potential linear muffin-tin orbital (FPLMTO) calculations within density functional theory (DFT) will be employed to systematically study these alloys over a range of compositions.

The paper is organized as follows. The method is briefly commented in Section 2. Results are discussed in Section 3. Finally, in section 4 we summarize the main conclusions of this work

II. COMPUTATIONAL DETAILS

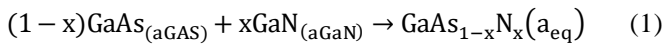
This study employed the extended FPLMTO (PLW) method [34],[35] for its calculations. This method, capable of handling all types of structures, including open ones, describes the electron exchange-correlation energy using the local density approximation (LDA) [36] and the [37] parameterization. The computations were performed using the lmtART computer code [38-40], which expands the potential within the non-overlapping muffin-tin sphere in spherical harmonics and the s , p , and d basis functions in plane waves in the interstitial regions. Convergence of the calculations was achieved when the total energy reached an accuracy of 10^{-4} Ry.

For the binary compounds under investigation, a cubic unit cell containing four atoms was considered. Each lattice site is occupied by two atoms: a gallium (Ga) atom located at the origin $(0, 0, 0)a_0$, and a nitrogen (N) or arsenic (As) atom positioned at $(1/4, 1/4, 1/4)a_0$ in the zincblende structure (where a_0 is the lattice parameter for both binary compounds).

Tetragonal unit cells of 16, 24, and 32 atoms were used for ternary systems with $x=0.125$, $x=0.083$, and $x=0.063$, respectively. A primitive cell was used for binary systems.

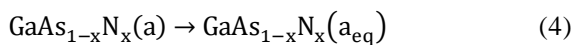
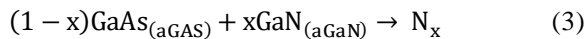
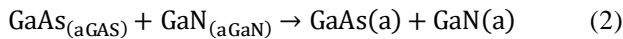
The optical bandgap bowing (b) in a binary alloy system was analyzed by decomposing it into three contributions [32],[39]: volume deformation (VD), charge exchange (CE), and structural relaxation (SR). The VD term represents the response of binary compounds to pressure changes, the CE term relates to charge transfer at $a = a(x)$, and the SR term describes the change in the bandgap during relaxation.

For a given average concentration of x , the ternary alloy exhibits the following reaction:



Where a_{GaAs} and a_{GaN} are the equilibrium lattice parameters of the parent materials GaAs and GaN, respectively, the equilibrium lattice parameter of the ternary alloy $\text{GaAs}_{1-x}\text{N}_x$ varies with x .

Equation (1) can be decomposed into three steps:



The first step quantifies the impact of volume deformation on the bowing parameter by analyzing the relative response of GaN and GaAs to hydrostatic pressure. This is followed by considering the charge transfer between GaN and GaAs, and

finally, the relaxation of the alloy's bonds. The overall bowing parameter is determined by summing up these three contributions.

These terms were calculated for various concentrations ($x=0.125$, $x=0.083$, and $x=0.063$) to determine the total bowing effect at the direct energy gap E_{Γ} . The construction of total bowing is:

$$b = b_{VD} + b_{CE} + b_{SR} \quad (5)$$

Ferhat and Bechstedt proposed a model for the bandgap bowing parameter in the ternary $\text{GaAs}_{1-x}\text{N}_x$ alloy [40]. This model posits that the bowing parameter is composed of three distinct contributions, each dependent on the nitrogen concentration (x), which was investigated for $x = 0.125$, 0.083 , and 0.063 in this study. These contributions are defined by specific mathematical relationships [2, 3]

$$b_{VD} = \frac{E_{\text{GaAs}}(a_{\text{GaAs}}) - E_{\text{GaAs}}(a)}{1-x} + \frac{E_{\text{GaN}}(a_{\text{GaN}}) - E_{\text{GaN}}(a)}{x} \quad (6)$$

$$b_{CE} = \frac{E_{\text{GaAs}}(a)}{1-x} + \frac{E_{\text{GaN}}(a)}{x} - \frac{E_{\text{Ga}_{1-x}\text{N}_x}(a_{\text{eq}})}{x(1-x)} \quad (7)$$

$$b_{SR} = \frac{E_{\text{GaAs}_{1-x}\text{N}_x}(a) - E_{\text{GaAs}_{1-x}\text{N}_x}(a_{\text{eq}})}{x(1-x)} \quad (8)$$

Where the equilibrium lattice constants of GaAs and GaN are represented by a_{GaAs} and a_{GaN} respectively, and the equilibrium lattice constant of the alloy with the average composition x is represented by a_{eq} . The energy gaps of the binary compounds GaAs and GaN are represented by E_{GaAs} and E_{GaN} respectively, and the energy gap of the alloy $\text{GaAs}_{1-x}\text{N}_x$ for $x=0.125$, 0.083 and 0.063 is represented by $E(\text{GaAs}_{1-x}\text{N}_x)$.

III. RESULTS AND DISCUSSIONS

In this section, we investigate the electronic properties of the parent binary compounds GaN and GaAs, as well as their ternary alloys, by computing their band structures using our calculated lattice parameters.

The total energy of each binary compound and the ternary GaAsN , as a function of volume, is depicted in Figures 1 through 5. These plots visualize how the total energy of the systems changes when their volume is altered.

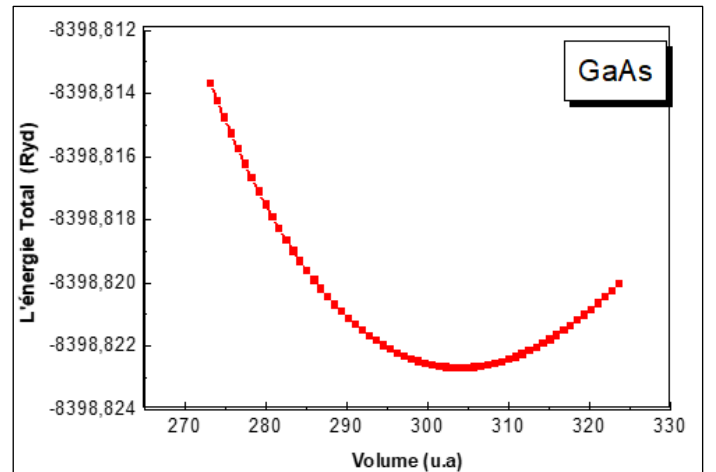


Figure 1: Total energy per molecule as a function of volume for GaAs using LDA calculation.

Source: Authors, (2024).

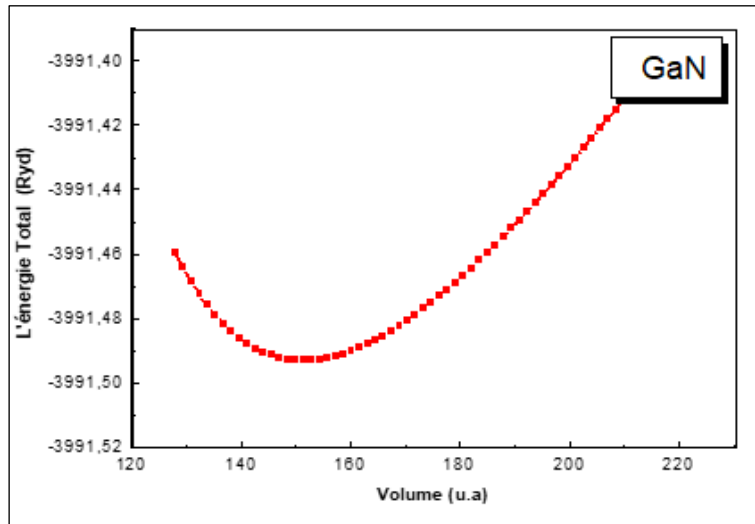


Figure 2: Total energy per molecule as a function of volume for GaN using LDA calculation. Source: Authors, (2024).

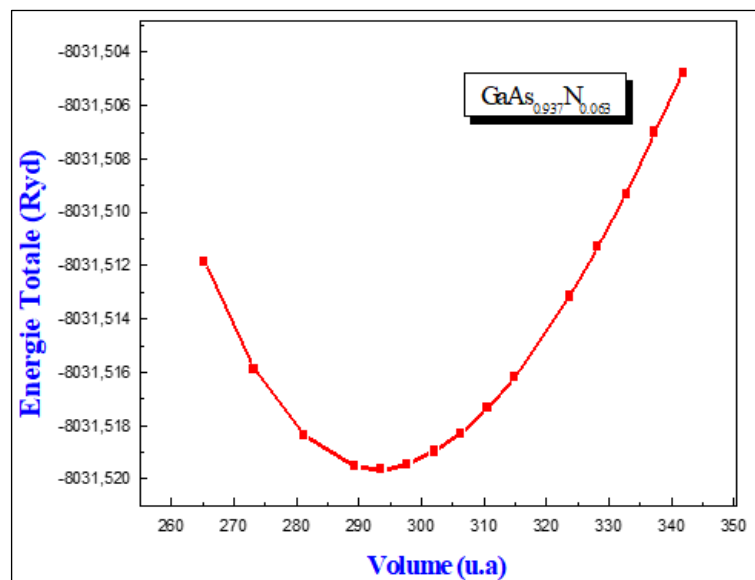


Figure 3: Total energy per molecule as a function of volume for $\text{GaAs}_{1-x}\text{N}_x$ ($x=0.063$) using LDA calculation. Source: Authors, (2024).

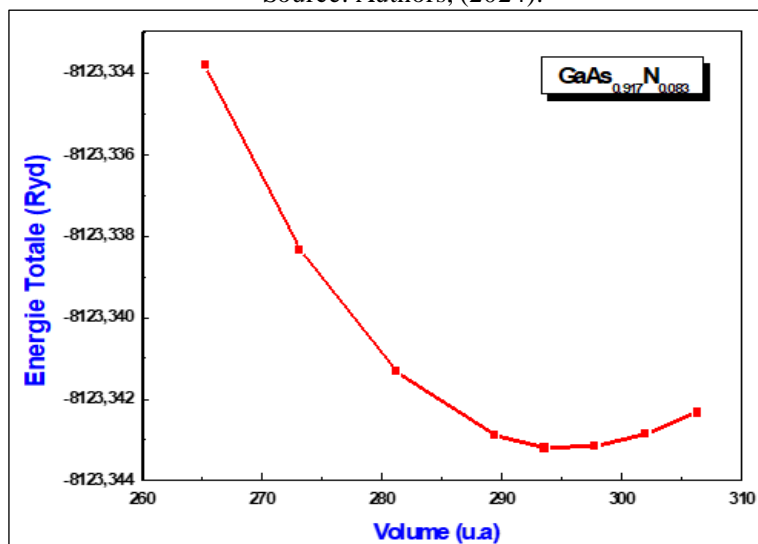


Figure 4: Total energy per molecule as a function of volume for $\text{GaAs}_{1-x}\text{N}_x$ ($x=0.083$) using LDA calculation. Source: Authors, (2024).

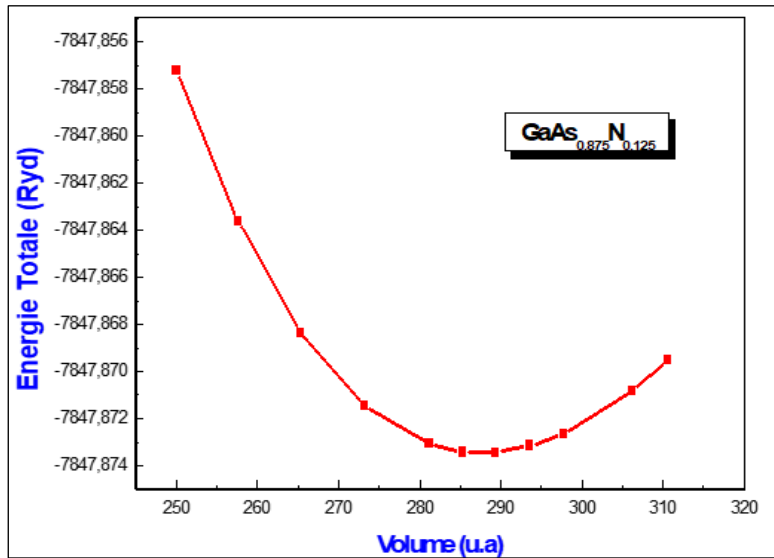


Figure 5: Total energy per molecule as a function of volume for GaAs_{1-x}N_x(x=0.125) using LDA calculation. Source: Authors, (2024).

To determine the equation of state, we fit our DFT total energy calculations, E(V), to the Murnaghan equation of state [41].

$$E(V) = E_0 + \frac{B}{B(B-1)} \left[V \left(\frac{V_0}{V} \right)^{B_0} - V_0 \right] + \frac{B_0}{B_0} (V - V_0) \quad (9)$$

Where E₀ is the energy at equilibrium volume V₀, B₀ is the bulk modulus, and B' is its pressure derivative. By minimizing the total energy with respect to volume, we obtained the equilibrium lattice constant, bulk modulus, and its derivative for both binary and ternary compounds. These results are summarized in and Table I.

Table 1: The structural parameters of the investigated compounds. V₀ is the equilibrium volume per unit formula (V₀= a₀³/4 for binary, V₀= (c₀/a₀). a₀³/4 for the tetragonal ternaries), a₀ represents the lattice constant for the binaries and ternaries, B is the bulk modulus and B' is its pressure derivative.

	V ₀ (Å ³)	a ₀ (Å ³)	c ₀ /a ₀	B (GPa)	B'
x=0		5.646		68.699	4.765
Exp	44.989	5.653[17]	1	75.50[46]	
Theoretical studies		5.664[39] 5.666[40]		69.71[41], 69.60[40], 76.47[12]	4.28 [12]
x=1		4.480		192.564	4.963
Exp		4.50 [41], [42] [44]	1	190.932 [43], 206.9[42]	
Theoretical studies	22.476	4.46[43] [45] 4.48[46] 4.50[8], [45] 4.56[39], 4.55[47]		189.488[8]	5.30[47] 4.46[8]
x=0.125	42.600	5.544	2	73.701	4.556
x=0.083	43.342	5.576	3	71.788	4.798
x=0.063	43.716	5.592	4	71.935	4.789

a Ref [17], b Ref [12], c Ref [8], d Ref [39], e Ref [40], f Ref [41], g Ref [42], h Ref [43], i Ref [46], k Ref [47]. Source: Authors, (2024).

Our calculated equilibrium lattice parameters for GaN and GaAs are 4.480 Å and 5.646 Å, respectively, exhibiting deviations of only 0.69% and 0.75% from the experimental values of 4.511 Å and 5.6535 Å [12], [48]. The computed bulk modulus for zinc-blende GaAs and GaN is in good agreement with

experimental data and previous theoretical studies [12]. Notably, GaN demonstrates a lower compressibility compared to GaAs.

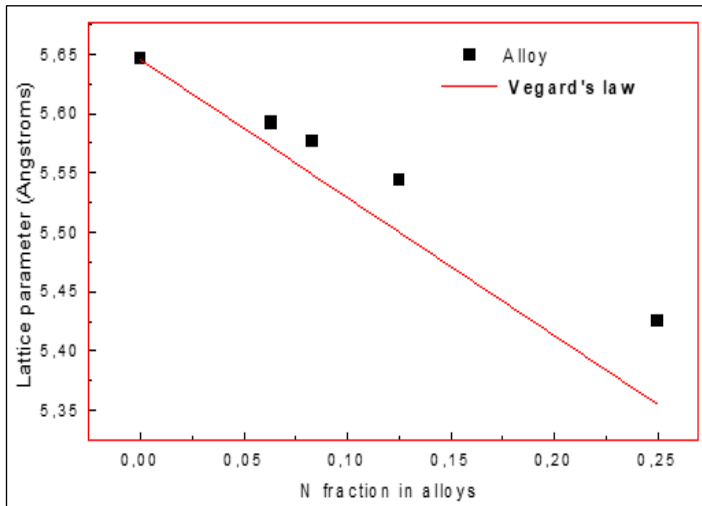


Figure 6: Lattice constant versus nitrogen concentration x in $\text{GaAs}_{1-x}\text{N}_x$.
Source: Authors, (2024).

For a given nitrogen concentration, the ternary alloys exhibit nearly identical equilibrium lattice parameters, displaying a linear variation (Figure 6).

However, a significant positive deviation from Vegard's law is observed for $\text{GaAs}_{1-x}\text{N}_x$, with an upward bowing parameter of -0.385 \AA determined through polynomial fitting. This deviation is primarily attributed to the substantial size mismatch and lattice constant disparity between GaAs and GaN [31].

The bulk modulus of $\text{GaAs}_{1-x}\text{N}_x$ deviates notably from a linear concentration dependence, exhibiting a downward bowing of 45.82 GPa . This disparity results in a considerable deviation in rigidity for all systems studied. Notably, an increase in nitrogen concentration within $\text{GaAs}_{1-x}\text{N}_x$ correlates with a lattice parameter decrease and a bulk modulus increase, consistent with general trends observed in other III-V semiconductors and alloys [12], [49].

We began by calculating the band structures of the binary compounds GaAs and GaN. Both materials exhibited direct band gaps, with the valence band maximum (VBM) and conduction band minimum (CBM) located at the Γ point in the Brillouin zone. A comparison of our calculated bandgaps (0.206 eV for GaAs and 1.916 eV for GaN) with experimental values (1.52 eV for GaAs and 3.20 eV for GaN [12,49,50]) reveals an underestimation. However, given the focus of this study on qualitative trends rather than quantitative accuracy, this discrepancy does not significantly impact our conclusions.

Subsequently, we calculated the band structures for the ternary alloy $\text{GaAs}_{1-x}\text{N}_x$ and plotted the resulting gap variations (Figure. 7). A critical consideration when studying ternary alloys is the choice of unit cell. The unit cell employed in our calculations is a supercell, not a primitive cell. Consequently, the calculated band gaps may not always correspond to the true fundamental band gaps, which are typically obtained from calculations using primitive cells. This discrepancy arises from the zone folding effect inherent to supercell calculations.

Normally, if one of the binary constituents has an indirect band gap, the supercell of the ternary alloy might exhibit a spurious direct bandgap due to zone folding. However, in the present case, both GaAs and GaN possess direct band gaps at the Γ point. Therefore, zone folding is not expected to alter the fundamental gap nature of the ternary alloy.

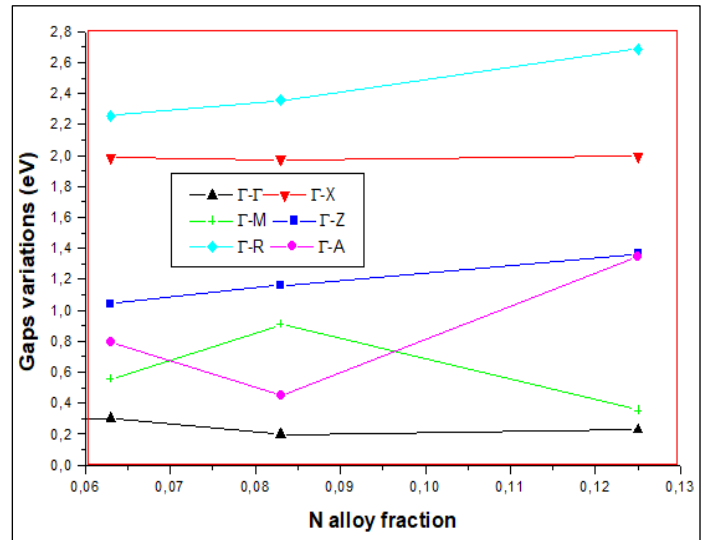


Figure 7: Gaps variation with the N fraction in the alloys.
Source: Authors, (2024).

For selected nitrogen concentrations ($x = 0.0625, 0.083,$ and 0.125) within the dilute nitride regime, our calculations indicate direct bandgaps located at the Γ point (Fig. 8, 9 and 10). However, as the nitrogen content increases from $\text{GaAs}_{0.937}\text{N}_{0.063}$ to $\text{GaAs}_{0.875}\text{N}_{0.125}$, a nonlinear variation in the Γ - Γ gap is observed. This behavior is similar to that reported for dilute nitride GaAsN alloys. Interestingly, the Γ -M and Γ -A gaps also exhibit nonlinear trends, with the Γ -M gap increasing while the Γ -A gap decreases. This complex behavior is likely attributed to zone folding effects, as the quantum states at these high-symmetry points are linear combinations of states from different high-symmetry points in the reciprocal lattice of the primitive cell.

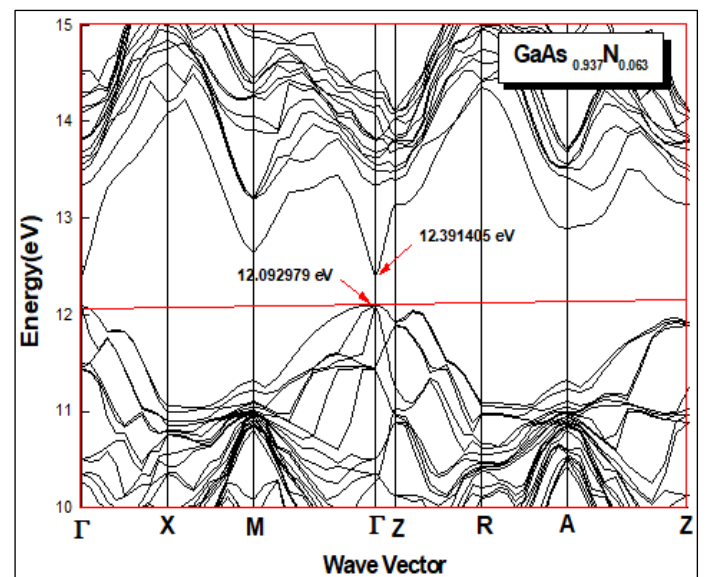


Figure 8: The band structure of the strained bulk $\text{GaAs}_{0.937}\text{N}_{0.063}$ alloy at a lattice parameter of a ($x=0.063$).
Source: Authors, (2024).

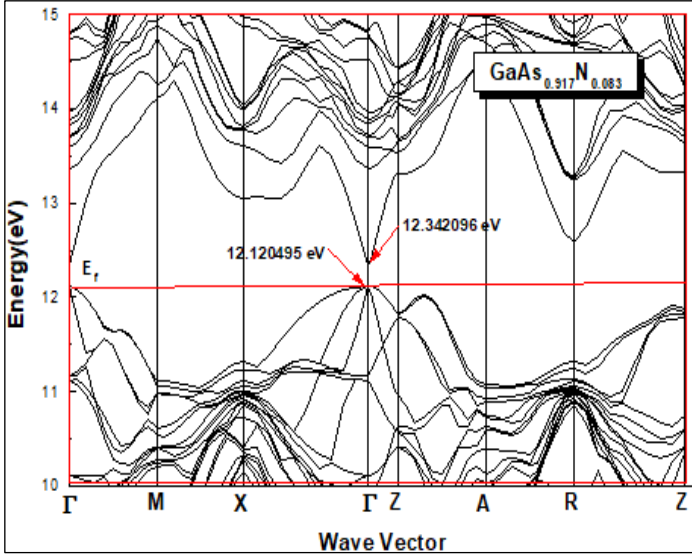


Figure 9: The band structure of the strained bulk $\text{GaAs}_{0.917}\text{N}_{0.083}$ alloy at a lattice parameter of $a(x=0.0873)$.
Source: Authors, (2024).

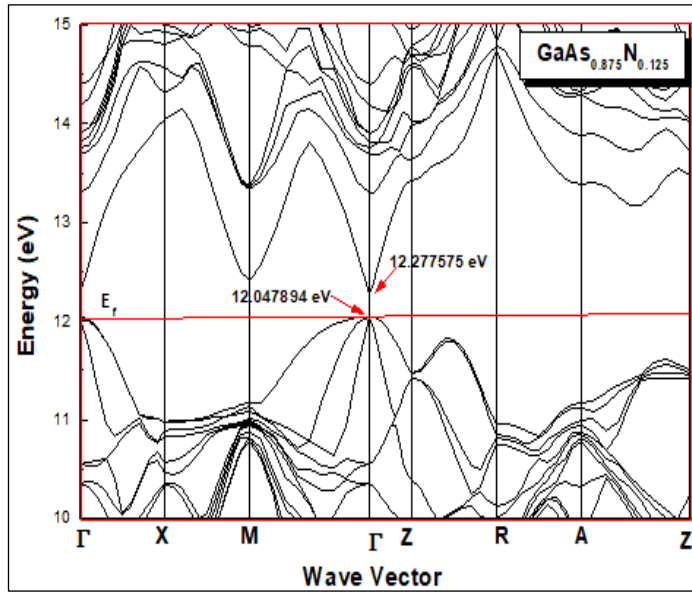


Figure 10: The band structure of the strained bulk $\text{GaAs}_{0.875}\text{N}_{0.125}$ alloy at a lattice parameter of $a(x=0.125)$.
Source: Authors, (2024).

The ternary $\text{GaAs}_{1-x}\text{N}_x$ alloys exhibit a direct bandgap character with both the valence band maximum (VBM) and conduction band minimum (CBM) located at the Γ point in the Brillouin zone. A notable trend is the increase in bandgap energy with increasing nitrogen content (x). However, this variation is nonlinear, indicating a more complex relationship between composition and bandgap than a simple linear interpolation.

Table 2 summarizes the calculated bandgaps for the various samples. Our results indicate a strong dependence of the bandgap on nitrogen atom distribution within the supercell, highlighting the significant influence of nitrogen incorporation on the conduction band structure. Even small nitrogen concentrations (a few percent) can dramatically affect the electronic properties of GaAs.

Table 2: The gap energies (in eV) between the upper VB and the lower CB of the zinc blende (ZB) of all the present binary and ternaries.

	$x=0$	$x=1$	$x=0.063$	$x=0.125$	$x=0.083$
$\Gamma-\Gamma$	0,239	1,916	0,298	0,229	0,221
$\Gamma-X$	1,918	4,717	1,987	1,993	1,999
$\Gamma-M$	2,642	6,606	0,555	0,354	0,933
$\Gamma-Z$	-----	-----	1,043	1,365	1,186
$\Gamma-R$	0,828	4,874	2,259	2,688	2,380
$\Gamma-A$	-----	-----	0,794	1,345	0,472

Source: Authors, (2024).

Our calculations reveal a pronounced sensitivity of the calculated band gaps to the spatial distribution of nitrogen atoms within the supercell. This observation underscores the critical role of nitrogen incorporation in modifying the conduction band structure. Even a modest nitrogen content of a few percent in GaAs can significantly perturb the electronic properties of the material. This sensitivity arises from the formation of localized electronic states associated with nitrogen atoms, which act as perturbations to the host GaAs lattice. These localized states can introduce new energy levels within the band gap, leading to band gap narrowing and altering the overall electronic structure. Consequently, the precise arrangement of nitrogen atoms within the supercell has a substantial impact on the resulting band gap, highlighting the importance of considering configurational disorder effects in theoretical modeling of these materials.

According to the model proposed by Van Vechten and Bergstresser [51], the electronegativity difference between constituent atoms is a critical factor influencing the degree of disorder within an alloy system, which in turn affects the bandgap. In the case of $\text{GaAs}_{1-x}\text{N}_x$, the varying electronegativity between Ga, As, and N atoms results in different degrees of disorder for different alloy compositions. This disorder contributes to the nonlinear behavior of the bandgap.

To quantify the impact of disorder on the bandgap, we introduced the total curvature parameter (b) for the $\Gamma-\Gamma$ transition. Our calculations summarized in the table 3 yielded values of 12.52 eV, 18.56 eV, and 24.66 eV for $\text{GaAs}_{0.875}\text{N}_{0.125}$, $\text{GaAs}_{0.917}\text{N}_{0.083}$, and $\text{GaAs}_{0.937}\text{N}_{0.063}$, respectively. These values suggest a significant increase in disorder with decreasing nitrogen content.

Another crucial factor affecting the bandgap is volume deformation (VD). Our calculations indicate that the contribution of VD to the total energy gap curvature parameter is substantial, especially for the $\text{GaAs}_{0.937}\text{N}_{0.063}$ alloy. This implies that the lattice expansion due to the incorporation of larger nitrogen atoms plays a dominant role in modifying the bandgap for this particular composition.

Table 3: Calculated bowing parameters b for $\text{GaAs}_{1-x}\text{N}_x$ alloys. The contributions due to volume deformation (b_{VD}), electronegativities (b_{CE}), and structural relaxations (b_{SR}) are also listed. All values are in eV.

Composition x	$x=0.125$	$x=0.083$	$x=0.063$
b_{VD}	14.585	22.609	30.044
b_{CE}	-2.195	-4.210	-5.447
b_{SR}	0.134	0.165	0.061
b	12.525	18.564	24.662

Source: Authors, (2024).

The significant role of volume deformation (VD) in contributing to the band gap bowing parameter is directly linked to the substantial lattice mismatch between the constituent binary compounds GaAs and GaN. In many alloy systems, the VD term is closely correlated with the overall volume of the unit cell, as represented by the lattice parameter (a). Consequently, the pronounced VD bowing parameter observed in $\text{GaAs}_{1-x}\text{N}_x$ can be attributed to the considerable difference in lattice constants between GaAs and GaN.

It is important to note that while charge exchange (ECB) can also influence bandgap bowing, its contribution is significantly smaller than that of VD in this system. This disparity is consistent with the relatively low ionicity of the constituent elements.

Structural relaxation (b_{SR}), which accounts for atomic displacements from ideal lattice positions, is found to have a minimal impact on bandgap bowing in $\text{GaAs}_{1-x}\text{N}_x$ due to the limited lattice mismatch between the two binary compounds. This study primarily focused on nitrogen concentrations above 7%. A comprehensive understanding of the bandgap bowing behavior at lower nitrogen levels would require further investigation.

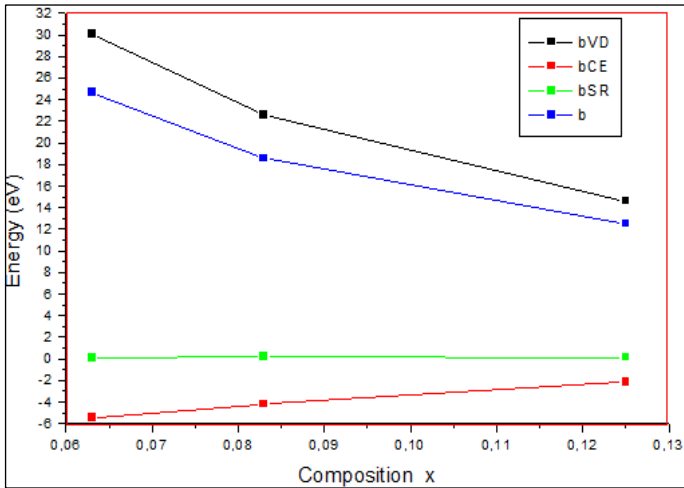


Figure 11: Curvature parameter variation b and the three contributions b_{VD} , b_{CE} , and b_{SR} considering concentration x . Source: Authors, (2024).

IV. CONCLUSIONS

This study employed ab-initio FPLMTO calculations to investigate the structural properties of cubic and tetragonal $\text{Ga}(\text{As},\text{N})$ alloys, focusing on the critical role of interstitial regions, to clarify the mechanism of the large band gap bowing of the dilute nitride semiconductors, we calculated band edge energies of $\text{GaAs}_{1-x}\text{N}_x$.

Our findings indicate a complex interplay between volume deformation (VD), charge transfer (CE), and structural relaxation (SR) in determining the bandgap bowing behavior of these alloys.

For the majority of compositions studied, VD emerges as the dominant factor influencing bandgap bowing, with CE playing a comparatively minor role. Structural relaxation effects (SR) were found to be relatively weak in these systems. Collectively, VD and SR, constituting the structural component, primarily govern the overall bandgap bowing.

It is important to note that the present investigation focused on nitrogen concentrations exceeding 7%. A comprehensive understanding of bandgap bowing across the entire composition range would require further studies.

These results provide valuable insights into the fundamental mechanisms underlying bandgap bowing in $\text{GaAs}_{1-x}\text{N}_x$ alloys, contributing to the development of more accurate theoretical models and facilitating the design of optoelectronic devices based on these materials.

V. ACKNOWLEDGMENTS

One of the authors, O. M thanks the S.Y.Savrasov for Mindlab software freely available. This work has been supported by Applied Materials Laboratory (A.M.L).

V. AUTHOR'S CONTRIBUTION

Conceptualization: Mimouna Oukli, Ghلام Karima, SeyfeddineBechekir

Methodology: Mimouna Oukli, Ghلام Karima, SeyfeddineBechekir

Investigation: Mimouna Oukli, Ghلام Karima, SeyfeddineBechekir

Discussion of results: Mimouna Oukli, Ghلام Karima, SeyfeddineBechekir

Writing – Original Draft: Mimouna Oukli, Ghلام Karima, SeyfeddineBechekir

Writing – Review and Editing: Mimouna Oukli, Ghلام Karima, SeyfeddineBechekir

Resources: Mimouna Oukli, Ghلام Karima, SeyfeddineBechekir

Supervision: Mimouna Oukli, Ghلام Karima, SeyfeddineBechekir

Approval of the final text: Mimouna Oukli, Ghلام Karima, SeyfeddineBechekir

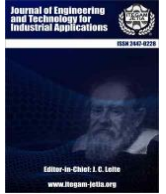
VI. REFERENCES

- [1] Paola Prete , Nico Lovergine, Progress in Crystal Growth and Characterization of Materials, Volume 66, Issue 4, November 2020, 100510,
- [2] Z. Zaaboub, F. Hassen, H. Maaref, Solid State Communications. 314-315 (2020) 113913.
- [3] Jian V. Lia, Man Hoi Wongb, Thin Solid Films 758 (2022) 139422. Volume 758, 30 September2022, 139422.
- [4]Takashi Tsukasakia, Naoki Mochidaa , Miki Fujitab , Toshiki Makimotoa, , Physica B: Condensed Matter, Volume 625, 15 January 2022, 413482.
- [5] Arpad Kosaa,, LubicaStuchlikovaa , Ladislav Harmathaa , Jaroslav Kovaca , Beata Scianab ,Wojciech Dawidowskib , Marek Tlaczalab, Materials Science in Semiconductor Processing, Volume 74, February 2018, Pages 313-318,
- [6] Justin C. Goodrich, Damir Borovac, Chee-Keong tan & Nelson tansu, Scientific RepoRts | (2019) 9:5128.

- [7] Wadi Bachir Bouiadjraa, Abdelkader Saidanea, Abdelkader Mostefaa Mohamed Heninib, M. Shafib, Superlattices and Microstructures, Volume 71, July 2014, Pages 225-237.
- [8] Francesco Biccari, Alice Boschetti, Giorgio Pettinari, Federico La China, Massimo Gurioli, Francesca Intonti, Anna Vinattieri, MayankShekhar Sharma, Mario Capizzi, Advanced Material, Volume 30, Issue 21, May 24, 2018,1705450.
- [9] S Gagui, H meradji, S Ghemid, Y Megdoud, B ZAIDI, B Ulhaq, R Ahmed, B Hadjoudja, B Chouial, Bull. Mater. Sci. (2023) 46:63
- [10] S gagui, S Ghemid, H Meradji, B Zaidi, BakhtiarUlhaq, R Ahmed, B Hadjoudja, B Chouial and S A Tahir, Pramana, J. Phys. (2023) 97:145.
- [11] M. Lahoual, A. Gueddim, N. Bouarissa, Transactions on Electrical and Electronic Materials (2019) 20:344–349.
- [12] Eßer et al. Appl. Phys. Lett. 107, 062103 (2015).
- [13] Yibo Wang, Yan Liu, Genquan Han, Hongjuan Wang, Chunfu Zhang, Jincheng Zhang, Yue Hao, Superlattices and Microstructures, Volume 106, June 2017, Pages 139-146.
- [14] I. Vurgaftman, J.R. Meyer, J. Appl. Phys. 94, 3675 (2003).
- [15] A. Gueddim, R. Zerdoum, N. Bouarissa, J. Phys. Chem. Solids 67(8), 1618–1622 (2004).
- [16] K.M. Yu, W. Walukiewicz, J. Wu, J.W. Beeman, J.W. Ager, E.E. Haller, W. Shan, H.P. Xin, C.W. Tu, Synthesis of III–Nx–V1-x thin films by N ion implantation. Appl. Phys. Lett. 78, 1077 (2001).
- [17] S. Ben Bouzid, F. Bousbih, R. Chtourou, J.C. Harmand, P. Voisin, Effect of nitrogen in the electronic structure of GaAsN and GaInAs(N) compounds grown by molecular beam epitaxy. Mater. Sci. Eng. B 112, 64 (2004).
- [18] F. Hassena, Z. Zaabouba, M. Bouhlela, M. Naffoutia, H. Maarefa, N.M. Garni, Thin Solid Films, Volume 594, Part A, 2 November 2015, Pages 168-171.
- [19] X.Z. Chen, D.H. Zhang, Y.J. Jin, J.H. Li, J.H. Teng, N. Yakovlev, Journal of Crystal Growth, 362 (2013) 197–201.
- [20] Chuan-Zhen Zhao, Na-Na Li, Tong Wei, Chun-Xiao Tang, Ke-Qing Lu, Appl. Phys. Lett. 100 (2012) 142112.
- [21] W. Shan, W. Walukiewicz, J.W. Ager III, E.E. Haller, J.F. Geisz, D.J. Friedman, J.M. Olson, S.R. Kurtz, Phys. Rev. Lett. 82 (1999) 1221.
- [22] J. Wu, W. Walukiewicz, K.M. Yu, J.W. Ager III, E.E. Haller, Y.G. Hong, H.P. Xin, C.W. Tu, Phys. Rev. B 65 (2002) 241303.
- [23] A. Lindsay, E.P. O'Reilly, Phys. Rev. Lett. 93 (2004) 196402.
- [24] E.P. O'Reilly, A. Lindsay, S. Tomic, M. Kamal-Saadi, Semicond. Sci. Technol. 17(2002) 870.
- [25] W.J. Fan, M.F. Li, T.C. Chong, J.B. Xia, J. Appl. Phys. 79 (1996) 188.
- [26] L. Bellaïche, S.-H. Wei, A. Zunger, Appl. Phys. Lett. 70 (1997).
- [27] L. Bellaïche, S.-H. Wei, A. Zunger, Phys. Rev. B 54 (1996) 17568.
- [28] Kurt A. Mader, A. Zunger, Phys. Rev. B 50 (1994) 17393.
- [29] P.R.C. Kent, A. Zunger, Phys. Rev. B 64 (2001) 115208.
- [30] V. Timoshevskii, M. Côté, G. Gilbert, R. Leonelli, S. Turcotte, J.-N. Beaudry, P. Desjardins, S. Larouche, L. Martinu, R.A. Masut, Phys. Rev. B 74 (2006) 165120.
- [31] C.-K. Tan, J. Zhang, X.-H. Li, G. Liu, B.O. Tayo, N. Tansu, J. Display Technol. 9 (2013) 272L.
- [32] S. T. Murphy, A. Chroneos, C. Jiang, U. Schwingenschlögl, R. W. Grimes, PHYSICAL REVIEW B 82, 073201 2010.
- [33] M. Ferhat, Phys. Status Solidi b 241 (2004) R38.
- [34] S.Y. Savrasov, Phys Rev B 54, 16470 (1996).
- [35] <http://www.physics.ucdavis.edu/~mindlab/>
- [36] <http://www.fkf.mpg.de/andersen/>
- [37] P. Hohenberg, W. Kohn, Phys. Rev. 136, B864 (1964).
- [38] Perdew J P and Wang Y Phys. Rev. B 45, 13244 (1992).
- [39] J.E. Bernard, A. Zunger, Phys. Rev. B 36 (1987) 3199.
- [40] M. Ferhat, F. Bechstedt, Phys. Rev. B 65 (2002) 075213.
- [41] F.D. Mumaghan, Proc. Natl. Acad. Sci. USA. 30, 5390 (1944).
- [42] M.J. Espitia R et al. / Journal of Magnetism and Magnetic Materials 451 (2018) 295–299.
- [43] L.I. Karaouzène et al. / Optik 168 (2018) 287–295
- [44] M. Issam Ziane, et al., Mater. Sci. Semicond. Process. 16 (2013) 1138,
- [45] M. Abu-Jafar, A.I. Al-Sharif, A. Qteish, Solid State Commun. 116 (2000) 389,
- [46] S. Adachi, J. Appl. Phys. 61 (1987) 4869.
- [47] H. Baaziz, Z. Charifi, A.H. Reshak, B. Hamad, Y. Al-Douri, Appl. Phys. A 106 (2012) 687.
- [48] S. Saib, N. Bouarissa b, Solid-State Electronics 50 (2006) 763–768
- [49] K. Beladjal, A. Kadri, K. Zitouni, K. Mimouni - Superlattices and Microstructures, Vol. 155, (2021), pp 106901.
- [50] M. Briki et al., Superlattices and Microstructures 45 (2009) 80_90
- [51] J. A. Van Vechten and T. K. Bergstresser, Phys. Rev. B 1, 3351 (1971)



ISSN ONLINE: 2447-0228



RESEARCH ARTICLE

OPEN ACCESS

A COMPARISON BETWEEN A CONVENTIONAL AND AUGMENTED RAIL GUN LAUNCHER'S PERFORMANCE

Mohamed Hichem Lahrech¹, Ahmed Chaouki Lahrech² and Abdelkader Bouhlal³

^{1,2} Faculty of Technology, Ziane Achour University of Djelfa, Algeria

³ Electrical Engineering Department. Nuclear Research Center of Birine. Djelfa, Algeria.

¹ <http://orcid.org/0009-0002-5602-387X> ² <http://orcid.org/0000-0001-9738-364X> ³ <http://orcid.org/0009-0000-7000-11>

Email : ¹ mh.lahrach@univ-djelfa.dz, ² ahmed.lahrech@univ-djelfa.dz, ³ aek.bouhlal@gmail.com

ARTICLE INFO

Article History

Received: August 19th, 2024

Received: September 16th, 2024

Accepted: September 16th, 2024

Published: October 04th, 2024

Keywords:

Laplace force,

Electromagnetic Launcher,

Inductance mutual coupling,

Plasma effect,

High speed Projectile.

ABSTRACT

An electromagnetic launcher is a device that uses the interaction between the magnetic fields produced by electrical currents to accelerate a projectile. Such an accelerator constitutes an alternative to the launchers propelled by chemical reactions and offers the advantage of being able to obtain very high speeds. The aim of this paper is to compare the performances of the Conventional Rail Gun (CRG) and the Augmented Rail Gun (ARG). This last is presented in the form of a launcher (CRG) reinforced by a second pair of rails, The prototype proposed is of small gauge (60 cm in length and 15 mm in diameter). The launcher's power supply is comprised of condensers' benches, which supply current to two distinct circuits: the inner circuit connects to the projectile, while the outer circuit generates an additional magnetic field. The maximum current of the inner circuit is worth 200 kA, and that of the external circuit is equal to 300 kA. The launcher makes it possible to accelerate projectiles with one or several bridges of current; the projectile mass lies between 2.0 g and 20 g.



Copyright ©2024 by authors and Galileo Institute of Technology and Education of the Amazon (ITEGAM). This work is licensed under the Creative Commons Attribution International License (CC BY 4.0).

I. INTRODUCTION

Electromagnetic launch technology is a unique form of electric propulsion that can transform electrical energy into kinetic energy. The current pulses generate an electromotive force that propels emission components, such as aircraft, missiles, satellites, rockets, and other objects, along conductive tracks at a high speed [1]. Over the past ten years, there has been extensive research and development focused on the augmented electromagnetic railgun [2-5]. Electromagnetic rail launchers are part of the electric launcher family, the simple concept involves placing a projectile between two rails connected to an electrical energy source. The current generates a magnetic field that interacts with the projectile's current. This interaction generates a Laplace force that is responsible for the projectile's movement [6-9]. In conventional electromagnetic launchers, a substantial electrical current must flow through the rails and armature in order to generate a strong electromagnetic force capable of propelling the projectile at high speed. As a result of magnetic flux diffusion, the electrical current becomes focused on the back of the armature [10], leading to a concentration of high current and the subsequent generation of heat

due to the Joule effect and friction. Subsequently, they have the ability to undergo a transformation into plasma contacts. To maintain optimal efficiency, it is crucial to prevent such a transition, as it leads to a rise in the resistance of the current bridge, thereby reducing the launcher's performance. Furthermore, it significantly erodes the rails and reduces the launcher's lifespan. One alternative method to enhance muzzle velocity is by using magnetic field augmentation. This technique increases the magnetic flux in the bore, resulting in a higher accelerating force on the armature without the need to increase the current being used. Several augmentation methods, such as series-augmented and parallel-augmented, have been thoroughly studied [2],[11] and [12]. It is therefore important to limit the current intensity of the bridges without reducing the propulsive force. This can be achieved by applying an external field to the projectile's current bridges [4].

For a projectile with a current bridge (P) in an augmented launcher (Figure 1), the magnetic coenergy of the circuit is equal to:

$$W_C = \frac{1}{2}L_R I_R^2 + \frac{1}{2}L_P I_R^2 + \frac{1}{2}L_A I_A^2 + \frac{1}{2}L_P I_A^2 + M_{R A} I_A \quad (1)$$

The force acting on the current bridge is determined by the virtual work method:

$$F_P = \frac{\partial W_C}{\partial x} = \frac{1}{2} \frac{\partial L_R}{\partial x} I_R^2 + \frac{\partial M}{\partial x} I_R I_A \quad (2)$$

The inductances of the external circuit, L_2 and L_p , do not vary when the projectile moves. Their partial derivative with respect to the position of the projectile is therefore zero. Let us introduce the following notations: $L'_R = \frac{\partial L_R}{\partial x}$, $M' = \frac{\partial M}{\partial x}$. The electromagnetic force on the bridge, and therefore on the projectile, is then written as:

$$F_P = \frac{1}{2} L'_R I_R^2 + M' I_R I_A \quad (3)$$

$$F_P = \frac{1}{2} (L'_R + 2M' \frac{I_A}{I_R}) I_R^2 \quad (4)$$

We can deduce the force due to the nth current

1) In the case of parallel augmentation:

$$F_{P,n(parallel)} = \frac{1}{2} (L'_R + 2M'_{RA} \frac{I_A}{I_R} + 2M'_{R3} \frac{I_3}{I_R} + \dots + 2M'_{Rn} \frac{I_n}{I_R}) I_R^2 \quad (5)$$

$$F_{P,n(parallel)} = \frac{1}{2} (L'_R + 2M'_{RA} \frac{I_A}{I_R} + \sum_{i=3}^n 2M'_{Ri} \frac{I_i}{I_R}) I_R^2 \quad (6)$$

2) In the case of series augmentation $I_A = I_R = I_n$ the force is written:

$$F_{P,n(serie)} = \frac{1}{2} (L'_R + 2M'_{RA} + 2M'_{R3} + \dots + 2M'_{Rn}) I_R^2 \quad (7)$$

$$F_{P,n(serie)} = \frac{1}{2} (L'_R + 2M'_{RA} + \sum_{i=3}^n 2M'_{Ri}) I_R^2 \quad (8)$$

3) In the case of the conventional launcher:

The mutual inductance M' is zero, the force then becomes:

$$F_P = \frac{1}{2} L'_R I_R^2 \quad (9)$$

II. BEHAVIOR ANALYSIS OF THE LAUNCHER OPERATING IN CRG AND ARG MODES

After modeling the CRG and ARG launchers and establishing the propulsion force equations (3) and (9). The following terms will be calculated analytically:

- L'_R : gradient of the self-inductance of the rails of the internal circuit, $\mu\text{H}/\text{m}$.
- M' : gradient of the mutual inductance of the internal and external circuits, $\mu\text{H}/\text{m}$.

The launcher can be represented by an equivalent electrical circuit in Figure 3. Such a representation will make it possible to describe the evolution of the different currents circulating in the launcher (Figure 4).

In order to carry out the simulation work with the "Circuit Maker" software, it is necessary to determine the different

electrical parameters of the equivalent circuit (Table 1). The objective of the simulation is to study the behavior of the launcher based on the dynamics of the projectile [6], [7]. The designed launcher can operate in CRG mode by powering only the inner rails and also in ARG mode by exciting the outer and inner rails simultaneously.

Table 1: Electrical parameters of the launcher operating in CRG and ARG modes.

Parameter	Value
Resistance of the inner rails and the projectile Rx1	0.05mΩ
Resistance of the outer rails Rx2	0.002 mΩ
Inductance of the inner rails Lx	0.5 μH
Inductance of the outer rails Lx1	1.76 μH
Connection resistance Rc and Rc1	8 mΩ
Connection inductance Lc and Lc1	1.6 μH
Storage inductance Ls	0.2μH
Wiring resistance Ri and Ri1	0.8 mΩ
Wiring inductance Li and Li1	1.6 μH
Power source for the external circuit	Capacitor bank of 0.5mf under a voltage of 8 kV.
Energy source for the internal circuit	Capacitor bank of 0.5mf under a voltage of 7 kV.

Source: Authors, (2024).

The flowchart (Figure 2) represents the different steps of the simulation to obtain the speed shape as a function of the projectile displacement; the weight of the projectile is fixed at 20 g:

1) Fixing the geometry: the outer circuit is identical to the inner circuit; the length is fixed at 60 cm.

2) Calculation of electrical parameters: the parameters are presented in the following table after the analytical calculation [7]. The parameters M' and L'_R of equation (10) are also calculated analytically: $M' = 0,156\mu\text{H}/\text{m}$, $L'_R = 0,5\mu\text{H}/\text{m}$

3) Composition of the equivalent electrical circuits of the launcher: the electrical circuit of the outer rails is identical to the inner circuit; the only values that change are the resistances and inductances of the outer rails. The augmented rail launcher is presented as two electrically independent circuits but magnetically coupled by the mutual M' via the inner and outer rails. The launcher is represented by two equivalent circuits formed by resistances and inductances. In other words, the equivalent circuit corresponding to the inner rails is only that of the launcher operating in CRG mode. The circuit of the augmented rail launcher is shown in Figure 3.

4) Evolution of the currents in the inner and outer rails of the launcher. The equivalent diagram of the launcher will then allow us to represent the evolution of the currents in the inner and outer rails (Figure 4). After determining these currents, we calculate the thrust force of the projectile (Figure 5) it should be noted that a thrust force of the order of 40 kN is obtained for a current of 300 kA flowing in the inner circuit and 330 kA in the outer circuit.

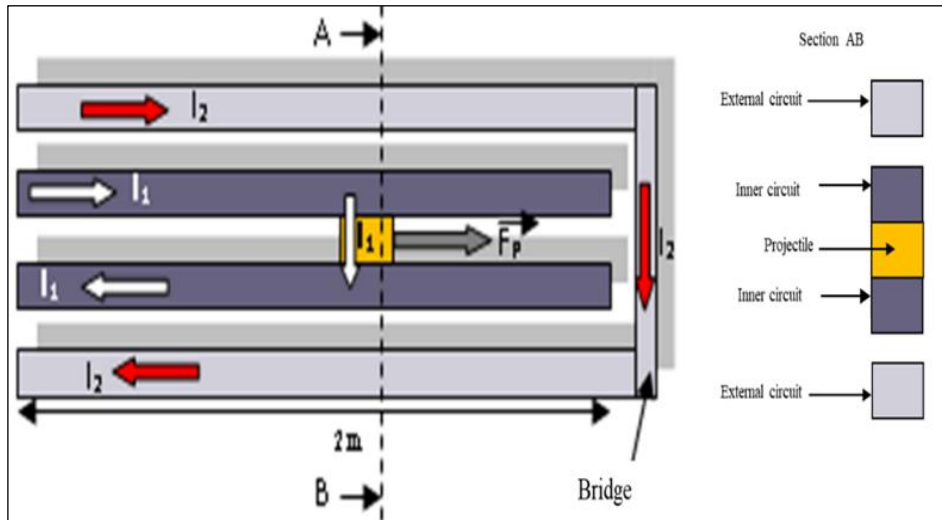


Figure 1: The projectile with a current bridge in the augmented launcher. Source: Authors, (2024).

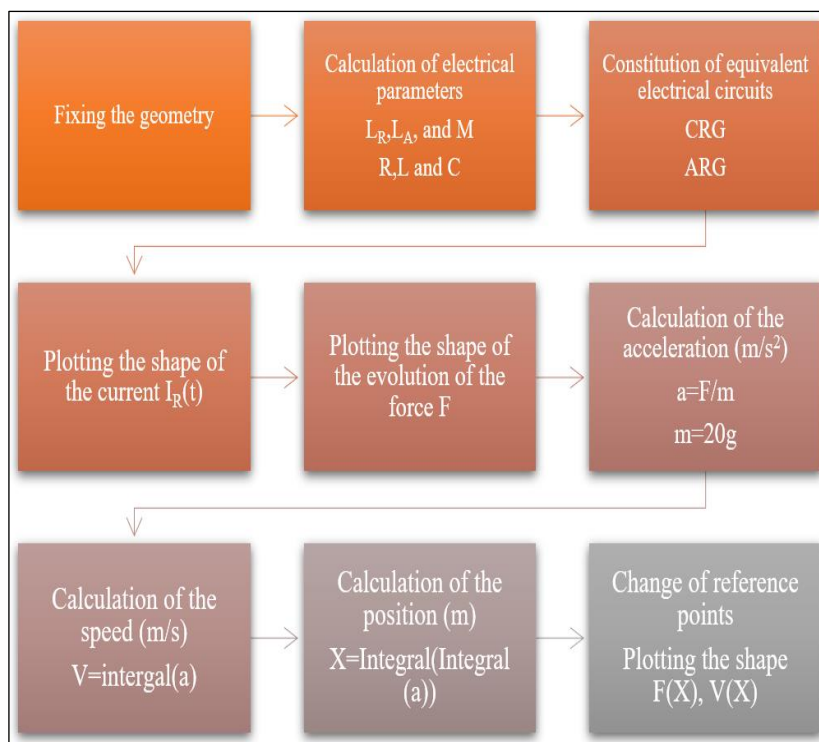


Figure 2: Simulation flowchart. Source: Authors, (2024).

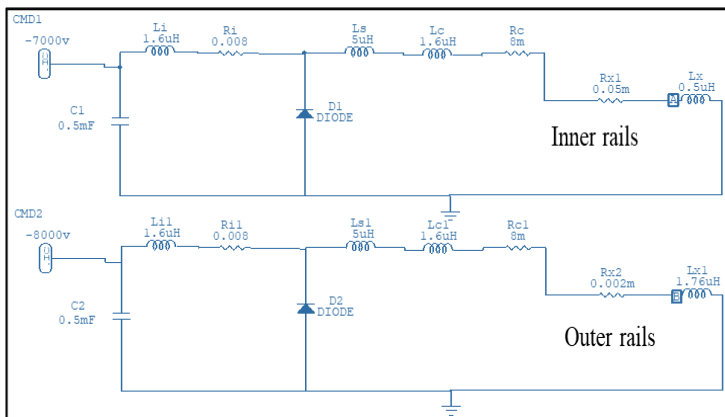


Figure 3: The equivalent electrical circuit of the launcher operating in ARG and CRG modes. Source: Authors, (2024).

III. DYNAMICS OF THE LAUNCHER PROJECTILE OPERATING IN CRG AND ARG MODES

The determination of the instantaneous currents $I_1(t)$ and $I_2(t)$ in Figure 4 would allow us to calculate and represent the acceleration, speed, and evolution of the force over time.

- 1) Acceleration of the projectile as a function of time: With a projectile of mass equal to 20 g, the acceleration reaches a value of $2.0 \times (10^6) \text{ m/s}^2$. (Figure 6)
- 2) Projectile velocity as a function of time:

The evolution of the velocity is deduced from the acceleration, and we note values of the order of 1.01 km/s. (Figure 7)

3) The ELM force and speed as a function of displacement:

In the Figure 8, we have also plotted the evolution of the force of the launcher operating in CRG mode in order to be able to make a comparison.

It is clear from the curves in Figures 8 and 9 that the maximum propulsion force is greater in the case of the launcher operating in ARG mode has a greater maximum propulsion force. The contribution of the outer rails is therefore notable through the electromagnetic mutual M between the two pairs of rails. The R_F ratio between the forces is of the order of 1.6:

$$R_F = \frac{F_{ARG}}{F_{CRG}} \quad (10)$$

The comparison of the performances of the two types of launchers shows that a clear improvement of more than 60% is observed. The architecture of the launcher with two pairs of rails proves to be a very practical solution for the propulsion of projectiles at high speeds. This architecture is more convincing with a better choice of the ratio between the currents circulating in the inner and outer rails.

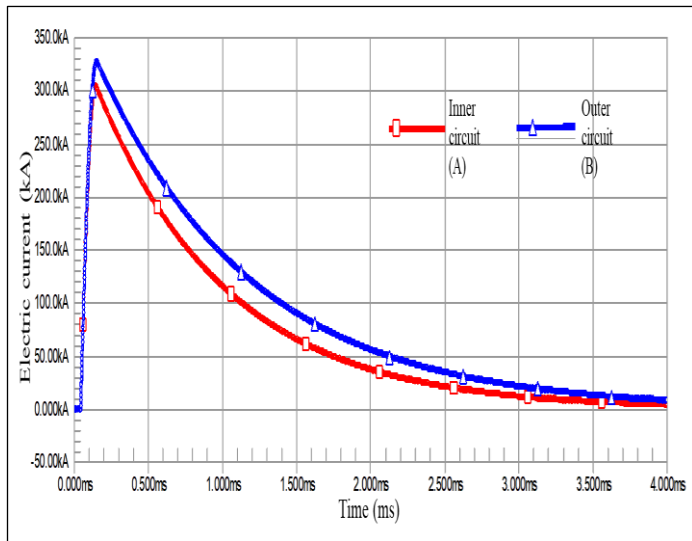


Figure 4: The simulated currents at points (A) and (B), (A: inner rails) and (B: outer rails). Source: Authors, (2024).

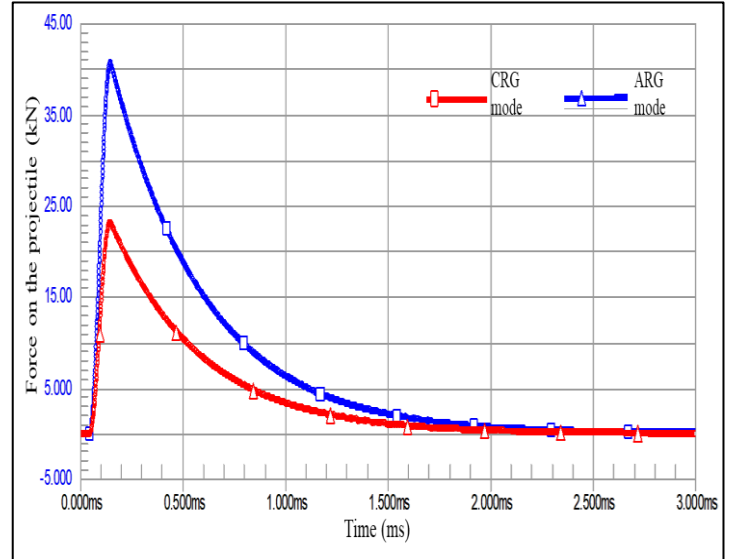


Figure 5: Comparison between forces on the projectile (kN) as a function of time (ms). (CRG and ARG modes). Source: Authors, (2024).

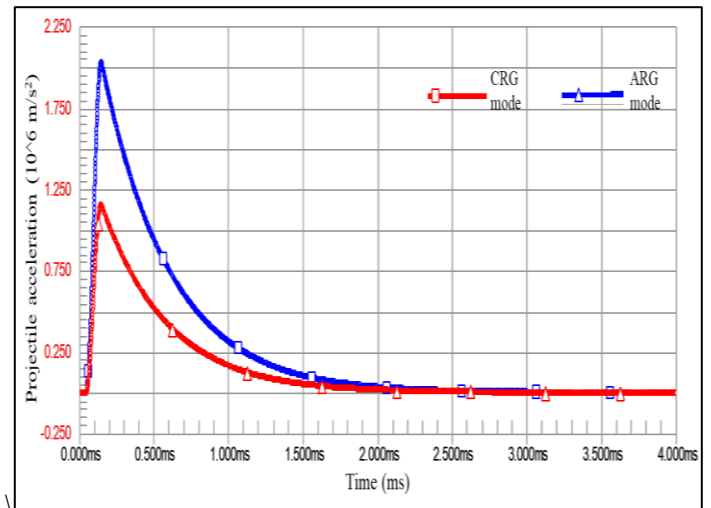


Figure 6: Comparison between projectile accelerations (10^6 m/s^2) as a function of time (ms). (CRG and ARG modes). Source: Authors, (2024).

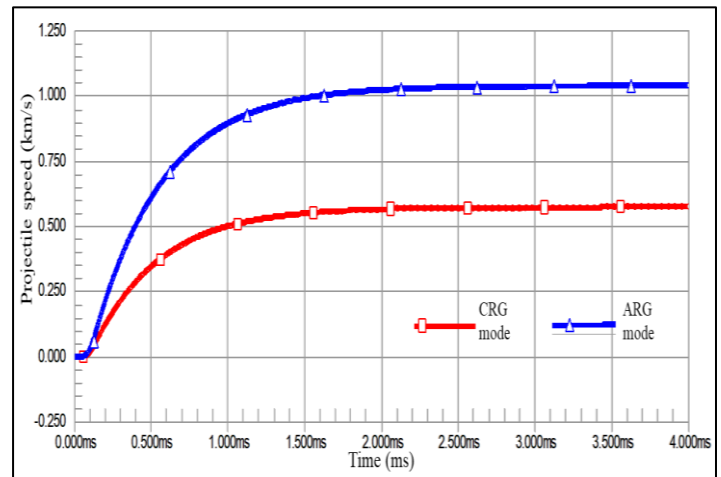


Figure 7: Comparison between the projectile speeds (km/s) as a function of time (ms) (CRG and ARG modes). Source: Authors, (2024).

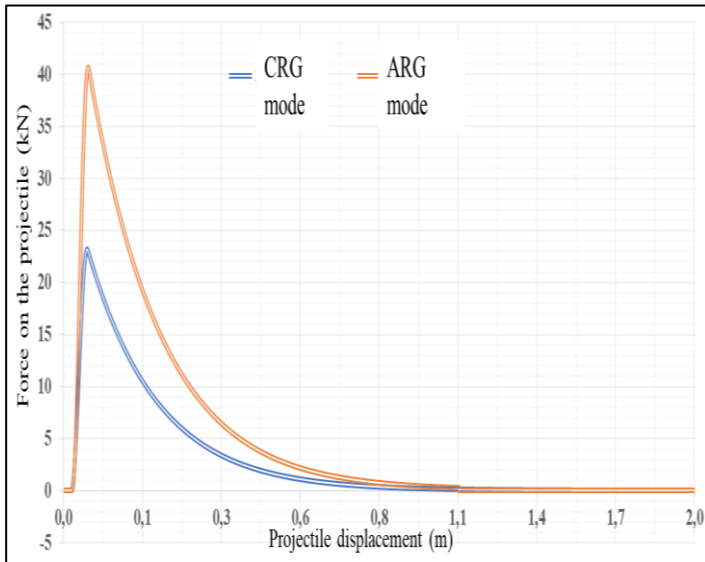


Figure 8: Comparison between the ELM forces of CRG and ARG as a function of the projectile displacement along the length of the rails in meters.

Source: Authors, (2024).

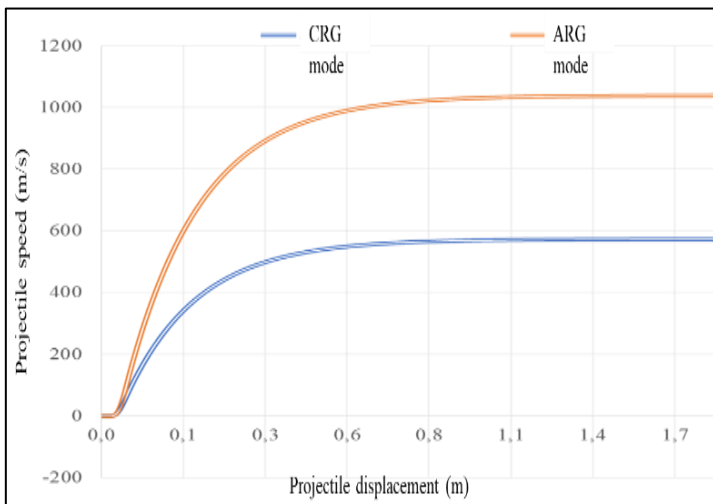


Figure 9: Comparison between the projectile speeds as a function of its displacement along the rails (CRG and ARG modes).

Source: Authors, (2024).

IV. PROTOTYPE PRODUCTION

After the analytical study carried out previously, a prototype was produced with rounded section rails. With such a shape, the propulsion force is greater compared to that obtained with rectangular section rails. Indeed, the results obtained by the researchers at the Saint Louis Institute have shown that the inductance gradient responsible for the force is better in the case where the rails have a rounded shape [6].

This launcher has two pair of rails with a rounded shape on the inside and outside (Figure 10), with dimensions represented in Table 2:

Table 2: dimensions of inner and outer rails.

	Length (cm)	Radius (cm)	Opening angle	Thickness (mm)
Inner rails	60	0.75	75°	3
Outer rails	60	1.5	75°	3

Source: Authors, (2024).

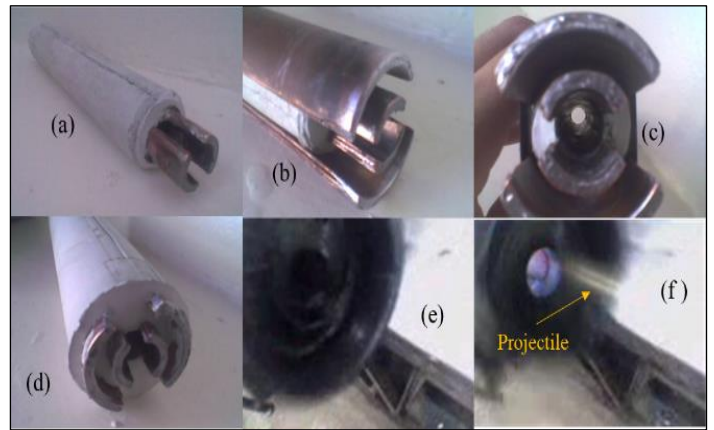


Fig 10: Augmented rail launcher prototype, (a) a pair of rounded shape copper for inner rails placed in a ceramic mold (CRG mode), (b) additional pair of rounded shape copper for outer rails superposed on inner rails (ARG mode), (c) cross-sectional view of launcher, (d) two pairs of rails placed in a ceramic mold (ARG mode), (e) the launcher Muzzle before the launch, (f) the launcher muzzle after the launch of the projectile.

Source: Authors, (2024).

In Figure 11, the four rails of the launcher must have connection terminals in the form of connecting cables, allowing different connections, of the series or parallel type. To this end, the two output ends (mouths) of the two outer rails are linked, and the ends of the two inner rails appear as free electrical terminals.



Figure 11: Augmented Rail Launcher Wiring.

Source: Authors, (2024).

The first test was unsuccessful, which was predictable because of the heating of the electrical contact parts between the projectile (Figure 12a) and the inner rails. This heating occurs mainly during the short duration (pulse) of the electrical supply (Figure 12b),[13]. We recommend techniques to address this phenomenon effectively. It is useful to mention a judicious technique for reducing the concentrations of high current densities in the multifilament contact regions. The projectile is equipped with contacts in the form of a brush [1], [6].

For our part, we have opted for a solution that consists of using a system that will propel the projectile at the same time as the electrical pulse supplying the rails. This assistance system is in the form of a breech comprising a spring and a piston in a cylindrical jacket (Figure 13). Following the pre-accelerator assembly, we recorded 12/16 successful shots; Figure 14 illustrates the projectile's exit through the launcher's muzzle.

We recorded an average speed of 507 m/s for CRG mode and 800 m/s for ARG mode with Dopplerradar. We noticed a speed increase of 57%, which is very close to the theoretical value.

Unfortunately, the enormous friction of the projectile on the rails and the excessive heat from the plasma prevented us from achieving speeds near the theoretical value. All of these phenomena reduce the launcher's performance. After all these results, we can deduce the efficiency of the launcher, which is equal to 80%.

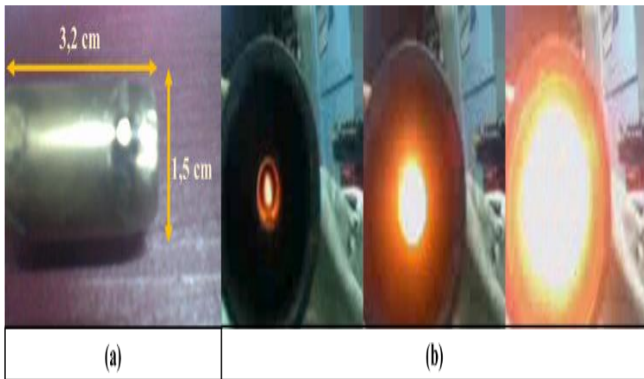


Figure 12: Projectile of the augmented rail launcher: (a) dimensions of the projectile, (b) the heating of the electrical contact parts between the projectile and the inner rails.
Source: Authors, (2024).



Figure 13: Final assembly of the augmented rail launcher.
Source: Authors, (2024).

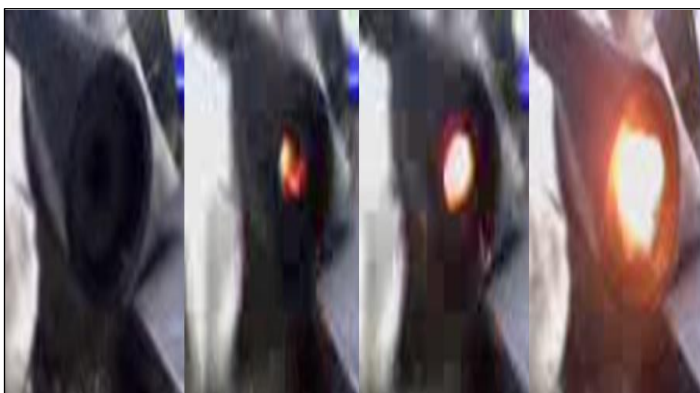


Figure 14: Firing sequences with the augmented rail launcher.
Source: Authors, (2024).

V. CONCLUSION

Despite the lack of electrical energy used, we adopted a pre-accelerator in order to avoid the problem of welding the projectile. The simulation calculation and experimental results shows that the increase in rails allows for a 60% increase in propulsion force. Certainly, the increase in rails presents itself as a

solution to improve the propulsion of the projectile while also remedying the heating problems caused by high current concentrations.

We believe that through our humble work, we have contributed to the opening of the field of study of the rail launcher, where several works can be considered on the improvement of performance by the simultaneous association of solutions relating to the increase and arrangement of the rails, their power supply, and the adaptation of technologies.

VI. AUTHOR'S CONTRIBUTION

Conceptualization: Mohamed Hichem Lahrech, Ahmed Chaouki Lahrech and Abdelkader Bouhlal.

Methodology: Mohamed Hichem Lahrech and Abdelkader Bouhlal.

Investigation: Mohamed Hichem Lahrech, Ahmed Chaouki Lahrech and Abdelkader Bouhlal.

Discussion of results: Mohamed Hichem Lahrech, Ahmed Chaouki Lahrech and Abdelkader Bouhlal.

Writing – Original Draft: Mohamed Hichem Lahrech and Ahmed Chaouki Lahrech

Writing – Review and Editing: Mohamed Hichem Lahrech and Ahmed Chaouki LAHRECH

Resources: Mohamed Hichem Lahrech, Ahmed Chaouki Lahrech and Abdelkader Bouhlal.

Supervision: Mohamed Hichem Lahrech, Ahmed Chaouki Lahrech and Abdelkader Bouhlal.

Approval of the final text: Mohamed Hichem Lahrech and Ahmed Chaouki Lahrech.

VIII. REFERENCES

- [1] V. Vertelis, G. Vincent, M. Schneider, S. Balevičius, V. Stankevič, et N. Žurauskienė, « Magnetic Field Expulsion From a Conducting Projectile in a Pulsed Serial Augmented Railgun », *IEEE Transactions on Plasma Science*, vol. 48, n° 3, p. 727-732, mars 2020, doi: 10.1109/TPS.2020.2970764.
- [2] T. G. Engel, « The High-Efficiency Mode of Electromagnetic Launcher Operation », *IEEE Transactions on Plasma Science*, vol. 48, n° 4, p. 1106-1110, avr. 2020, doi: 10.1109/TPS.2020.2978202.
- [3] Q. Lin et B. Li, « Field-Circuit Coupled Analysis of a Series-Augmented Electromagnetic Railgun », *IEEE Transactions on Plasma Science*, vol. 48, n° 6, p. 2287-2293, juin 2020, doi: 10.1109/TPS.2020.2991160.
- [4] C. Li et al., « Simulations on Saddle Armature With Concave Arc Surface in Small Caliber Railgun », *IEEE Transactions on Plasma Science*, vol. 47, n° 5, p. 2347-2353, mai 2019, doi: 10.1109/TPS.2019.2894165.
- [5] M. B. Heydari, M. Asgari, et A. Keshtkar, « A Novel Structure of Augmented Railgun Using Multilayer Magnets and Sabots », *IEEE Transactions on Plasma Science*, vol. 47, n° 7, p. 3320-3326, juill. 2019, doi: 10.1109/TPS.2019.2921222.
- [6] J. Gallant et P. Lehmann, « Experiments with brush projectiles in a parallel augmented railgun », *IEEE Transactions on Magnetics*, vol. 41, n° 1, p. 188-193, janv. 2005, doi: 10.1109/TMAG.2004.838988.
- [7] M. Coffo et J. Gallant, « Modelling of a Parallel Augmented Railgun with Pspice Validation of the Model and Optimization of the Augmenting Circuit », in *2007 IEEE 34th International Conference on Plasma Science (ICOPS)*, juin 2007, p. 1020-1020. doi: 10.1109/PPPS.2007.4346326.
- [8] P. Lehmann, H. Peter, F. Jamet, et V. Wegner, « Some remarks concerning the optimization of a railgun system », *IEEE Transactions on Magnetics*, vol. 31, n° 1, p. 546-551, janv. 1995, doi: 10.1109/20.364635.
- [9] P. D. Aalto et F. Y. Yee, « Plated armature contacts for solid armature electromagnetic railgun launchers », *IEEE Transactions on Magnetics*, vol. 31, n° 1, p. 667-672, janv. 1995, doi: 10.1109/20.364614.

[10] X. Fu, D. Zhang, W. Yuan, et P. Yan, « Design and Analysis of the 270-kJ PPS for Augmented Railgun », *IEEE Transactions on Plasma Science*, vol. 45, n° 7, p. 1496-1502, juill. 2017, doi: 10.1109/TPS.2017.2705839.

[11] T. G. Engel, J. M. Neri, et M. J. Veracka, « Characterization of the Velocity Skin Effect in the Surface Layer of a Railgun Sliding Contact », *IEEE Transactions on Magnetics*, vol. 44, n° 7, p. 1837-1844, juill. 2008, doi: 10.1109/TMAG.2008.922310.

[12] H. Kashii, M. Yamada, et T. Shikura, « Pre-accelerator design by estimation of erosion », *IEEE Transactions on Magnetics*, vol. 27, n° 1, p. 56-60, janv. 1991, doi: 10.1109/20.100993.

[13] J. Gallant, T. Vancaeyzeele, B. Lauwens, B. Wild, F. Alouahabi, et M. Schneider, « Design Considerations for an Electromagnetic Railgun Firing Intelligent Bursts to Be Used Against Antiship Missiles », *IEEE Transactions on Plasma Science*, vol. 43, n° 5, p. 1179-1184, mai 2015, doi: 10.1109/TPS.2015.2416774.



ISSN ONLINE: 2447-0228



RESEARCH ARTICLE
ACCESS

OPEN

SOLVING THE UNIT COMMITMENT PROBLEM OF 10-GENERATORS SET BY PSO WITH DIFFERENT SPINNING-RESERVE VALUES OBTAINED FROM HOUR-HOUR LOAD DEMAND INCREASING

Ali Sadeq Alsowaidi¹ and Seyed Mahmoud Modaresi²

^{1, 2} Department of Electrical Engineering, South Tehran Branch, Islamic Azad University, Tehran, Iran.

¹ <http://orcid.org/0009-0005-3572-2438> , ² <http://orcid.org/0000-0003-1020-155> 

Email: alialsowaidi1603@gmail.com, dr.modares@yahoo.com

ARTICLE INFO

Article History

Received: August 21th, 2024

Revised: September 17th, 2024

Accepted: September 19th, 2024

Published: September 27th, 2024

Keywords:

Unit Commitment Problem,
Particle Swarm Optimization,
Power System Operation,
Spinning-Reserve Constraints,
Generation Cost.

ABSTRACT

Regarding energy efficiency, the unit contract problem (UCP) is significant. It need to be seen as the assurance of occasions and energy commodities in which the generator offers the most value in addition to having a large amount of energy storage. In this study, we offer a novel approach to solve the UCP issue for a 10-generator test system with variable prices depending on hourly variations in power demand, utilizing particle swarm optimization (PSO). The objective is to keep energy levels sufficient to fulfill demand while reducing the total cost of producing power. Initially, a collection of objects that may hold the key to solving UCP are generated via the suggested PSO technique. Their dedications to the project and the power they create have an impact on everyone's health because of the mobility restriction. Using a combination of their own and other objects' histories, objects may discover the best solution for UCP via the iterative adjustments in speed and location made by the PSO algorithm. This strategy might boost generator economy and efficiency while also resolving the UCP issue. A number of scenarios with various storage factors should be taken into account in order to assess the PSO method's efficacy. The results demonstrate that the cost-confidence ratio is regarded as equal and that the algorithm may converge to the ideal or nearly optimal solution. The efficiency of alternative optimization techniques and the suggested PSO approach are compared using comparative analysis. The findings demonstrate that PSO is more cost-effective than earlier research in identifying the effects of rising storage prices on power consumption between 50 and 100 MW.



Copyright ©2024 by authors and Galileo Institute of Technology and Education of the Amazon (ITEGAM). This work is licensed under the Creative Commons Attribution International License (CC BY 4.0).

I. INTRODUCTION

In order to fulfill energy demand while lowering overall production costs, generators must cooperate effectively for the electric power system to function efficiently. This issue is resolved by the Contract issue (UCP), which works out the optimal generator scheduling strategy, taking into account their obligations (on/off) and the locations where they can reliably provide power. The intricate issue of UCP has a direct bearing on energy planning. However, these approaches struggle to handle the scenario's complexity and the problem's complexity, particularly when it comes to the requirements of the fans and

other challenges, which is a unique circumstance. They often resolve challenging optimization issues. The Particle Swarm Optimization (PSO) algorithm is one of the PSO algorithms; it is inspired by the behavior of swarms of fish or birds. PSO provides an effective approach to a wide range of optimization issues, including electrical system-related ones. Repurposing garbage is the new way of solving this issue. The goal is to lower the overall cost of manufacturing while still adhering to the spinning specifications in order to boost productivity and dependability. The strategy aims to address issues with energy efficiency while addressing the drawbacks of conventional methods and offering

workable, efficient alternatives. Numerous research studies have looked at PSO's potential for power optimization and have shown that it may be used to handle a wide range of energy production-related issues, such as budgetary allocation, energy efficiency, and energy management. By taking into account the impact of valves, Lee et al. [1] used PSO to address the transmission issue. The results demonstrated the superiority of this strategy over others. [2] Used PSO to effectively resolve multi-objective issues that take into account both environmental and economic goals at the same time. The results demonstrate that PSO is capable of resolving competing goals and offering many Pareto-optimal options. In a different research, Hu et al. [3] used PSOs to reduce power loss and provide consistent power, hence controlling voltage and power loss in power distribution.

Additionally, PSO advancements have spawned a number of variations and hybrid strategies. Kennedy and Eberhart's objective [4] was to apply the idea of adaptive inertia to PSO; this weight accelerated the concept's convergence and preserved equilibrium between exploration and exploitation. Furthermore, combining PSO with other optimization techniques has shown promising results. For example, Wang et al. suggested a hybrid PSO-GA method. [5] They combine the local search capability of GA with the global search capability of PSO to achieve the most efficient produced power distribution. Regarding the Unit Commitment Issue, PSO has a track record of successful investigations. For the sake of this example, Liu's team [6] used PSO to solve the UCP while accounting for the maximum rate restriction and the spinning time limits; they were able to achieve the best generator scheduling and improved system reliability. In a similar vein, Chen et al. [7] used a novel PSO method to solve the UCP with a valve-like property, and this technique showed that it could provide nearly optimum solutions.

Previous studies have shown that PSO can handle the Unit Commitment Issue for a test system consisting of ten generators with varying values for the spin reserve. The development and use of a modified PSO algorithm that takes into consideration the UCP's reserve storage needs is the paper's unique contribution. The algorithm's effectiveness is ascertained by carrying out in-depth trials and comparing the outcomes with those of other widely used optimization techniques.

II. LITERATURE REVIEW

The unit commitment issue is to determine the power settings of committed units that have to abide by the regulations of both the producing unit and the system, as well as the states (on/off) of power generating units for each time slot. Minimizing the total operating cost within the given time range is the aim of the UC problem. As a result, the total of the fuel and equipment starting costs for the generating units becomes the goal function. The UC issue has the following mathematical explanation: Reduce TC, which may be found by:

$$\sum_{i=1}^N \sum_{t=1}^T [I_i(t)F_i(P_{T_i}(t)) + S_i(t)(1 - I_i(t - 1))I_i(t)] \quad (1)$$

the fuel cost of unit i at time t is provided by $F_i(P_{T_i}(t))$, where N is the number of generators, T is the total scheduling hours, $P_{T_i}(t)$ is the power production of unit i at time t , and $I_i(t)$ is the ON/OFF state of unit i at time t (ON ndOFF=0).

$$F_i(P_{T_i}(t)) = a_i + b_i P_{T_i}(t) + c_i P_{T_i}(t)^2 \quad (2)$$

where a_i , b , and c stand for unit I 's fuel cost coefficients.

(t) At time t , what is the initial investment needed for unit I , as mentioned?

$$S_i(t) = \begin{cases} S_{hi} & \text{if } T_{i,off}(t) \leq T_{i,Down} + T_{i,cold} \\ S_{ci} & \text{if } T_{i,off}(t) > T_{i,Down} + T_{i,cold} \end{cases} \quad (3)$$

Where is the hot starting price? T_{iDown} is the least amount of time spent down, T_{iCold} is the cold start time of unit i , S_{ci} is the cold starting cost, and t is the continuous length of time off of unit i at time t .

1) System real power balance

$$\sum_{i=1}^N I_i(t)P_{T_i}(t) = P_i(t) \quad (4)$$

The system power demand at time t is represented by $P_t(t)$.

2) System spinning reserve requirement

When the power grid sends a signal, the reserve version of the generator, known as Spinning Reserve, is prepared to start generating. This may happen in a matter of minutes. The service description fits the profile of most thermal generating assets (coal plant, for example), which need several hours to "warm up" and start producing. Consequently, this process pays generators that are set to spin reserve to use fuel in a "hot standby," spinning, and ready to swiftly align and create.

$$\sum_{i=1}^N I_i(t)P_{T_i}^{max} \geq P_i(t) + P_R(t) \quad (5)$$

The system spinning reserve at time t is denoted by $P_R(t)$.

3) Generation unit's limits

$$P_{T_i}^{min}(t) \leq P_{T_i}(t) \leq P_{T_i}^{max} \quad (6)$$

where the lowest and maximum production limits of unit I at time t are, respectively, represented by $n(t)$ and $P_{max}(t)$.

4) Minimum up/down times

$$\begin{aligned} (T_{i,on}(t - 1) - T_{i,Up})(I_i(t - 1) - I_i(t)) &\geq 0 \\ (T_{i,off}(t - 1) - T_{i,Down})(I_i(t - 1) - I_i(t)) &\geq 0 \end{aligned} \quad (7)$$

(t) represents unit i 's continually on time.

5) Ramp up and ramp down rates:

$$P_{T_i}(t) - P_{T_i}(t - 1) \leq UR_i \quad (8)$$

$$P_{T_i}(t - 1) - P_{T_i}(t) \leq DR_i$$

where UR_i and DR_i , respectively, stand for the ramp up and ramp down rates of unit I .

III PSO-BASED METHODOLOGY

Kennedy and Eberhart developed the particle swarm optimization method [8], [9], a heuristic optimization technique that is based on social psychology. It has been noted that PSO works well with problems that have high dimensionality, numerous optima, differentiability threshold, or nonlinear. Evolution has shown that it is efficient. Compared to other optimization techniques, it offers a number of advantages, including being easy to use and potentially producing a high-quality solution with a steady tendency to converge.

Other evolutionary computational techniques modify the individual by using evolutionary operators. Nevertheless, PSO does not have an evolutionary mechanism for this. Rather, every entity in PSO swoops around, seeking a location that is dynamically modified according to its own flight history as well as the histories of its partners. Each person is seen as a volumeless sphere inside a d-dimensional exploratory space. Each particle keeps track of where it is in the space of issues; this is linked to its greatest level of achievement to yet. The term "pbest" refers to this figure. The total value and location of the largest gain made by any particle in the population to date is another advantageous feature of the particle swarm optimizer's global version. The gbest is the name given to this area. Particle swarm optimization is the idea of changing the velocity of each particle at each iteration to achieve its maximum and most advantageous positions. The item's velocity is enhanced by a random term that uses a random number generator to accelerate the object in the direction of its best and largest locations. In d-dimensional space, the *i*th particle, for instance, is represented by the formula $x=(x_{i1},x_{i2},\dots,x_{id})$. The documentation for the *i*th particle's former location is $best=(pbest_{i1},pbest_{i2},\dots,pbest_{id})$. The gbest is the indicator of the biggest particle in each population. For particle *i*, the frequency of position change (velocity) is expressed as $v = v=(v_{i1},v_{i2},\dots,v_{id})$. The current velocity and the distance from pbest_{*i*} to gbest_{*d*} may be used to calculate the changed velocity and location of each individual particle, as shown by the following formula:

$$v_{i,d}^{k+1} = wv_{i,d}^k + c_1 \times rand_1 \times (pbest_{i,d}^k - x_{i,d}^k) + c_2 \times \quad (9)$$

$$rand_2 \times (gbest_d^k - x_{i,d}^k)$$

$$x_{i,d}^{k+1} = x_{i,d}^k + v_{i,d}^{k+1} \quad (10)$$

In this case, *w* is the inertia weight factor, *C*₁ and *C*₂ are the acceleration constants, *rand*₁ and *rand*₂ are the uniform random numbers between 0 and 1, *x*_{*k*} is the current position of individual *i* at iteration *k*, *pbest* is the particle best of individual *i*, and *gbest* is the generation best of the group $k, v_d^{min} \leq v_{i,d}^k \leq v_d^{max}$ is the velocity of individual *i* at iteration *k*.

The option *vmax* determines the extent to which areas close to the goal location and close to the current position are taken into account in the aforementioned procedures. Particles will struggle to pass through the advantageous solutions if *v^{max}* is

too low. Particles won't have enough time to explore outside of the local solutions if *v^{max}* is too high. In the past, *v^{max}* was usually set at 10–20% of the range of variation on each dimension when using PSO. The weight of the random term that pushes each particle in the direction of their greatest and most advantageous locations is called the constant *C*₁. Before being reattached, the particles may travel great distances from their intended destinations when *C*₁ and *C*₂ have low values. On the other hand, high values cause a quick movement in the direction of or away from the targeted places. Because of this, the acceleration *C*₁ and *C*₂ values were often chosen to be in the range of 2.0 based on prior information. Equation (11) guarantees a proportionate balance between local and global exploration and exploitation for a range of inertia-related weights. According to the initial plan, *w* would gradually decline at a pace of 0.9 to 0.4. Generally, the following formula is used to calculate the inertia weight.

$$w = w_{max} - \frac{w_{max} - w_{min}}{Iter_{max}} \times Iter \quad (11)$$

The maximum iteration number (generations) is represented by *Iter_{max}*, the current iteration number is *Iter*, and the maximum and lowest values of inertia weight are represented by *w_{max}* and *w_{min}*, respectively.

IV. SIMULATION

For the purposes of this paper, we assume that power reserve value should be proportional and enough to cover load demand increasing in range between 50 to 100 MW should be added over load demand, since 50 MW is the lowest increase in load demand (as we can notice in table-1-: increasing from hour 1 to hour 2 and hour4 to hour5) and 100MW is the highest increasing value (as in increasing from hour2 to hour3 and hour5 to hour6):

Table 1: The typical daily load requirement in hours.

Hour	Load (MW)	Hour	Load (MW)	Hour	Load (MW)
1	700	9	1300	17	1000
2	750	10	1400	18	1100
3	850	11	1450	19	1200
4	950	12	1500	20	1400
5	1000	13	1400	21	1300
6	1100	14	1300	22	1100
7	1150	15	1200	23	900
8	1200	16	1050	24	800

Source: Authors, (2024).

This increasing in load demand will force the operator to respond effectively in two aspects, first: use ready spinning reserve to cover increasing in load demand and second, support spinning reserve for next hours.

For better planning, we will use PSO to solve UCP of 10Gen set regarding 6 different values of spinning reserve in range between 50-100MW (50, 60, 70, 80, 90 and 100) MW, figure -1- show the load demand and red-shaded area represent spinning-reserve range between 50-100 MW.

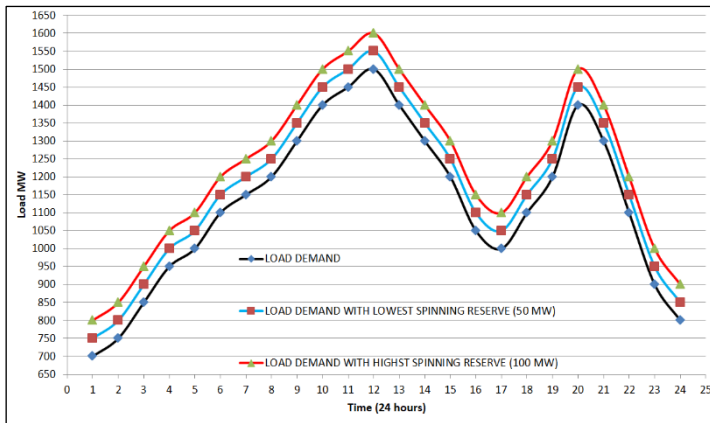


Figure 1: 24 hours load demand and spinning reserve range between 50-100 MW.
Source: Authors, (2024).

A particle's orientation may be altered by altering one of its coordinates using the binary PSO technique. On the other

hand, a large number of optimizations exist in the other direction, varying in quality across levels and factors. The approach is only the change in the chance that a coordinate has a binary value (0 or 1) in the binary form of PSO [10]. Therefore, substituting equation (12) for equation (10) is the key difference between the binary PSO and the primary PSO.

$$\text{if } (rand < S(v_{i,d}^{k+1})) \{ \\ x_{i,d}^{k+1} = 1$$

Else {

$$x_{i,d}^{k+1} = 1 \tag{12}$$

where $S(v)$ is a sigmoid function that restricts the range of transformation to $[0,1]$, and $rand$ is a random integer selected from a uniform distribution that is limited to $[0,1]$.

$$S(v) = \frac{1}{1+e^{-v}} \tag{13}$$

The discrete variant preserves v_{max} , thus $|v_{i,d}^{k+1}| < v_{max}$. This only reduces the final possibility that the bit x_{id} will take on a binary value. More flexibility will be possible with a smaller v_{max} [11]. See [10] for further details on binary PSO.

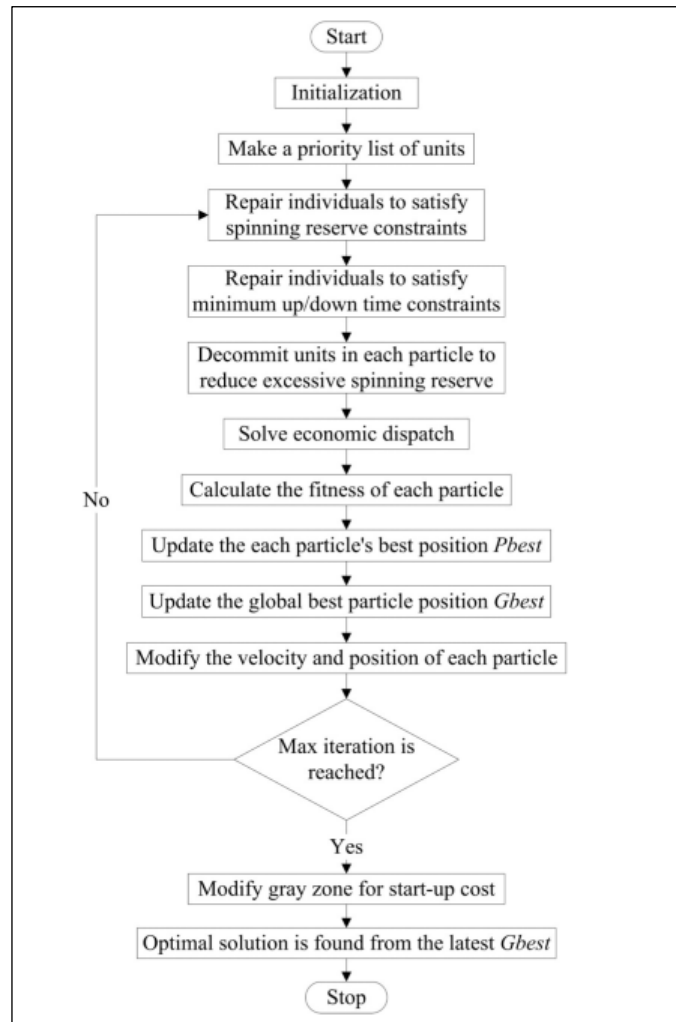


Figure 2: Binary Particle Swarm optimization for the UC problem.
Source: Authors, (2024).

A test bench with 10 units and a 24-hour timetable makes up the 10-unit system. Table (2) displays the necessary generator and data for this challenge.

Table 2: Data of the 10-Unit System.

Parameters	Unit 1	Unit 2	Unit 3	Unit 4	Unit 5
Pmax(MW)	455	455	130	130	162
Pmin(MW)	150	150	20	20	25
a(\$/hr)	1000	970	700	680	450
b(\$/MWhr)	16.19	17.26	16.60	16.50	19.70
c(\$/MW2hr) x 10 ⁻⁴	4.8	3.1	20	21.1	39.8
Min up time(hr)	8	8	5	5	6
Min down time(hr)	8	8	5	5	6
Hot start-up cost(\$)	4500	5000	550	560	900
Cold start-up cost (\$)	9000	10000	1100	1120	1800
Cold start-up hrs(hr)	5	5	4	4	4
Initial status(hr)	8	8	-5	-5	-6
Parameters	Unit 6	Unit 7	Unit 8	Unit 9	Unit 10
Pmax(MW)	80	85	55	55	55
Pmin(MW)	20	25	10	10	10
a(\$/hr)	370	480	660	665	670
b(\$/MWhr)	22.26	27.74	25.92	27.27	27.79
c(\$/MW2hr) x 10 ⁻⁴	71.2	7.9	41.3	22.2	17.3
Min up time(hr)	3	3	1	1	1
Min down time(hr)	3	3	1	1	1
Hot start-up cost(\$)	170	260	30	30	30
Cold start-up cost (\$)	340	520	60	60	60
Cold start-up hrs(hr)	2	2	0	0	0
Initial status(hr)	-3	-3	-1	-1	-1

Source: Authors, (2024).

Results show feasible operation control on increasing pattern within economical frame and so far safe and reliable operation as in table 3:

Table 3: Six different values of spinning reserve with total operation cost at each case.

Spinning Reserve MW	Total Operation cost
50	557046.535860194
60	558043.128870206
70	558337.564043407
80	558902.236240183
90	559655.047590170
100	560968.143280082

Source: Authors, (2024).

Also, we can notice in Figure-3- an impressive behavior of total cost increasing in spinning reserve range of 60MW to

70MW which is increase in production cost get slighter comparing to increasing of total cost in range of 70, 80, 90 and 100MW.

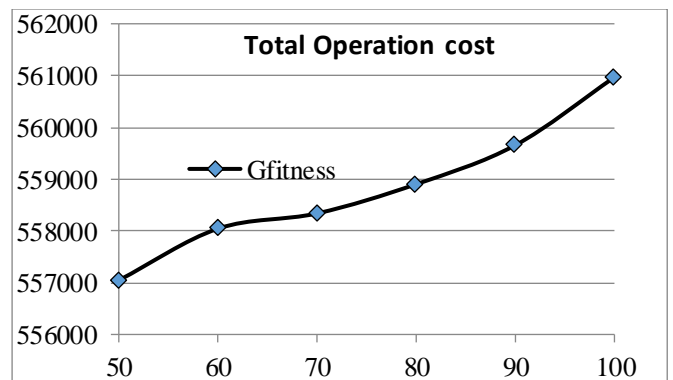


Figure 3: Total cost of units in 6 cases along with different spinning reserves values.

Source: Authors, (2024).

V. CONCLUSIONS

Simulation of PSO for 10 Generators set system using MATLAB in 6 cases represents 6 different values of spinning reserve base on load demand hour to hour minimum and maximum increasing values show magnificent results and wide reduction in cost of operation comparing with results obtained from earlier researches [11], [10].

VI. AUTHOR'S CONTRIBUTION

Conceptualization: Ali Sadeq Alsowaidi and Seyed Mahmoud Modaresi.

Methodology: Ali Sadeq Alsowaidi and Seyed Mahmoud Modaresi.

Investigation: Ali Sadeq Alsowaidi and Seyed Mahmoud Modaresi.

Discussion of results: Ali Sadeq Alsowaidi and Seyed Mahmoud Modaresi.

Writing – Original Draft: Ali Sadeq Alsowaidi and Seyed Mahmoud Modaresi.

Writing – Review and Editing: Ali Sadeq Alsowaidi and Seyed Mahmoud Modaresi.

Resources: Ali Sadeq Alsowaidi and Seyed Mahmoud Modaresi.

Supervision: Ali Sadeq Alsowaidi and Seyed Mahmoud Modaresi.

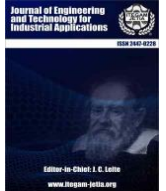
Approval of the final text: Ali Sadeq Alsowaidi and Seyed Mahmoud Modaresi.

VIII. REFERENCES

- [1] Ying Wang, Jianzhong Zhou, Youlin Lu, Hui Qin, Yongqiang Wang, "Chaotic self-adaptive particle swarm optimization algorithm for dynamic economic dispatch problem with valve-point effects," *Expert Systems with Applications*, vol. 38, no. 11, pp. 14231-14237, 2011. DOI: 10.1016/j.eswa.2011.03.053.
- [2] J. Hazra and A. K. Sinha, "A multi-objective optimal power flow using particle swarm optimization," *EUROPEAN TRANSACTIONS ON ELECTRICAL POWER*, vol. 21, pp. 1028–1045, 2011. DOI: 10.1002/etep.494.
- [3] Kuang Honghai, Su Fuqing, Chang Yurui, Wang Kai, He Zhiyi, "Reactive power optimization for distribution network system with wind power based on improved multi-objective particle swarm optimization algorithm," *Electric Power Systems Research*, vol. 213, 2022, 108731. DOI: 10.1016/j.epr.2022.108731.
- [4] J. Kennedy and R. Eberhart, "Particle swarm optimization," in *Proceedings of ICNN'95 - International Conference on Neural Networks*, Perth, WA, Australia, 1995, pp. 1942-1948, vol. 4. DOI: 10.1109/ICNN.1995.488968.
- [5] David Voss, James Underwood, Jason Kerth, David K. Bellman, Kevin Pykkonen, Kenneth M. Bryden, "Chapter 9 - Path to commercialization," in *Thermal, Mechanical, and Hybrid Chemical Energy Storage Systems*, Klaus Brun, Timothy Allison, Richard Dennis, Eds., Academic Press, 2021, pp. 513-568.
- [6] Ahmadi, A., Venayagamoorthy, G.K., Sharma, R., "Performance of a smart microgrid with battery energy storage system's size and state of charge," in *Proceedings of CIASG 2014*, 2015, pp. 1–7. DOI: 10.1109/CIASG.2014.7127250.
- [7] Ahmed, S., Ghosh, K.K., Mirjalili, S., Sarkar, R., "AIEOU: Automata-based improved equilibrium optimizer with U-shaped transfer function for feature selection," *Knowledge-Based Systems*, vol. 228, 107283, 2021. DOI: 10.1016/j.knosys.2021.107283.
- [8] M. Clerc and J. Kennedy, "The particle swarm: Explosion stability and convergence in a multi-dimensional complex space," *IEEE Transactions on Evolutionary Computation*, vol. 6, no. 1, pp. 58-73, 2002. DOI: 10.1109/TEVC.2001.943278.
- [9] Akan, Yurdusev Yakup and J. Michael Herrmann, "Stability, Entropy and Performance in PSO," *Proceedings of the Companion Conference on Genetic and Evolutionary Computation*, pp. 1864-1875, 2023.
- [10] L. G. Zwe, "Discrete particle swarm optimization algorithm for unit commitment," in *IEEE Power Engineering Society General Meeting*, 2003, pp. 418-424.
- [11] T. Logenthiran and D. Srinivasan, "Particle Swarm Optimization for unit commitment problem," in *2010 IEEE 11th International Conference on Probabilistic Methods Applied to Power Systems*, Singapore, 2010, pp. 642-647. DOI: 10.1109/PMAPS.2010.5528899.



ISSN ONLINE: 2447-0228



RESEARCH ARTICLE

OPEN ACCESS

ASSESSMENT OF CEMENT CONTENT IN CURED CONCRETE BY CHEMICAL STUDY OF MATERIALS SCIENCE AND SUSTAINABLE MANUFACTURING TECHNOLOGY

Mohankumar N. Bajad

DoCE, STES's SCOE, Pune, Maharashtra - India

<http://orcid.org/0000-0003-1056-0178>

Email: mnbajad@rediffmail.com

ARTICLE INFO

Article History

Received: November 14th, 2023

Revised: October 01th, 2024

Accepted: October 02th, 2024

Published: October 31th, 2024

Keywords:

California, hardened concrete, titration, X-ray diffraction.

ABSTRACT

An effort was made in this investigation to determine the cement content in cured concrete. A test procedure used to determine calcium oxide which further leads to the assessment of cement in concrete that has been hardened was applied to the laboratory test. The content of cement of three different concrete samples that have been hardened of known proportions was precisely determined by applying the simplified California Test 403 procedure. The California Test 403 method originally used in order to determine the calcium oxide concentration in hardened concrete has been simplified by modifying several steps. The test results are verified by parameter determination of the composition in concrete by X-ray diffraction (XRD) using the JCP (Joint Committee of powder diffraction standards file) database. Good agreement between the results obtained by the titration and analytical methods of the instrument and the actual results is observed.



Copyright ©2024 by authors and Galileo Institute of Technology and Education of the Amazon (ITEGAM). This work is licensed under the Creative Commons Attribution International License (CC BY 4.0).

I. INTRODUCTION

Concrete is a heterogeneous composite construction product obtained by mixing and hardening components such as cement, aggregates and water. The performance of concrete depends on the quality of the components, their proportions, their location and the contact conditions. Cement plays an important role in binding the ingredients together and creating concrete that is hard, strong and cohesive with age. There are several types of cement, in which Portland cement is commonly used in general civil construction [1]. Portland cement is manufactured from the same rocks, ores, and minerals that make up concrete aggregates. Furthermore, no Portland cement component is sufficiently consistent from one cement maker to the next. Therefore, testing concrete is the current practice that includes other mineral admixtures such as fly ash, silica fume, etc. in a rather complex mixture. It is difficult to determine the percentage of cement in hardened concrete due to the lack of a perfect procedure for determining the proportions of concrete. In addition, the use of organic admixtures in concrete as admixtures in concrete has made it more difficult to determine the actual proportions of materials in the concrete in the solid state after bridge construction/collapse. However, the difference in composition (element) between cement

and aggregate is one of the correct choices for determining cement in hardened concrete. As a result, chemical examination of hardened concrete can reveal a plethora of information regarding the mix's composition and potential degradation reasons. Documentation on the chemical analysis of hardened concrete is rarely available. ASTM C108 [2] and BS 1881[3] describe a similarly brief procedure for figuring out how much cement is in hardened concrete. All chemical analysis procedures are based on the chemical analysis of hydraulic cement (ASTM C114-11b) [4]. California Test 403 is a chemical analytical procedure commonly used to determine the proportions of components in concrete. The ASTM approach involves chemically detecting the amount of dissolved silica and calcium oxide in a sample and then indirectly computing the percentage of cement by assuming or establishing from the original cement's analysis. The initial amounts of silica and calcium oxide in cement were determined (ASTM C1084-10). This approach produces reliable findings, especially if initial cement and aggregate samples are available, but it is time intensive and cannot be used on concrete with aggregates that develop considerable amounts of silica and calcium oxide under test circumstances. Hime briefly described several chemical analytical procedures commonly used to evaluate the cement content in

hardened concrete [5]. Basically, all chemical analysis procedures are based on the chemical composition of cement. The calcium oxide content, the soluble silica content, the sulfate content, and the chloride content are the less enumerable determinations of cement content. Covault and Poovey employed neutron activation studies to determine cement content [6]. By adding the radioactivity and determining the cement content from the cement content VB count rate curve, the volume of cement in a radioactive concrete trial was determined. This technique, however, necessitates the use of costly irradiation and counting equipment. Furthermore, it cannot be used with calcium-containing aggregates. Iddings and his colleagues studied the feasibility of several analysts for enabling nuclear techniques, stable tracer analysis, measurement of natural radioactivity, and copper dilution. taste in the determination of cement in concrete [7]. Neutron activation analysis was shown to be quick once again, albeit it was impeded by inaccuracies caused by variables typical in concrete structures. It also necessitates an expensive installation. Other techniques are either uneconomical or only practical under ideal conditions. It should also be mentioned that when employing radioisotopes, personnel safety must be assured against any radiation dangers [8].

The analysis will incur an additional cost as a result of this requirement. Kossivas devised a method for calculating the cement content of a concrete sample using its sulphate concentration [9]. This method necessitates the knowledge of the cement's sulphate content as well as the fact that all sulphates are obtained from the cement. The usage of aggregates containing excessive levels of sulphates can lead to serious problems. In addition, the overall characterization of the aggregates in terms of their suitability for use in final construction was determined by petrographic analysis as well as by X-ray diffraction (XRD) [10],[11]. The petrographic analysis confirms the composition of the original aggregate which helps to fill in the gaps to infer the test results. Therefore, petrographic analysis can still be one of the useful methods for the assessment and characterization of concrete. In this study, an attempt was made to find out how much cement is in hardened concrete samples of known proportions, in order to compare the results and find the accuracy.

The XRD technique is a flexible, non-destructive method for revealing detailed information on the chemical composition and crystal structure of natural and artificial materials. The chemical test procedure suggested in this article is a simplified version of the California 03 test. Here, the procedure was developed as a result of various practical problems raised during the process. tested according to California 03 test. Concrete with iron content exceeding traceable limits can be easily analysed with this simplified procedure.

II. ANALYTICAL PROCEDURE

Accurate concrete analysis requires good procedure and a qualified analyst with good knowledge of the composition and properties of cement and concrete. Sometimes avoidance or tolerance is not possible and then the analyst must then disclose not just the findings of his investigation, but also the direction and size of the mistake connected with that outcome. Hardened concrete is mainly a mixture of cement and aggregates. Here mainly discussed the procedure for determining the ratio of cement in concrete [12]. The cement content of a hardened concrete sample is commonly calculated by assuming that all of the calcium or acid-soluble silica

in the concrete sample comes from port-land cement components [13]. Although the percentages of calcium oxide and silicon dioxide in Portland cement vary by grade and by cement maker, the cement is expected to have between 63.5 and 21% dissolved silica (SiO_2). In most cases, an error of less than 5% in the computation of Portland cement will result [14]. If the aggregate contains limestone or dolomite, the calcium content of Portland cement will be incorrectly high when tested. Because most aggregates' silicon components are insoluble, soluble silica is commonly used as a substitute. Because most aggregate silicon components are insoluble, soluble silica is often regarded as a reliable approach for determining cement concentration [15].

In general, aggregates without limestone components are preferred for concrete use. The California 03 test procedure used to analyse hardened concrete for calcium oxide content is discussed here.

III. METHODOLOGY AND INVESTIGATIONS

III.1 CALIFORNIA TEST 403 TO DETERMINE THE CALCIUM OXIDE CONTENT

Step by step procedures for California Test 403 method are shown in Figure 1.

III.2 PROPERTIES OF TEST SPECIMEN

The chemical composition of the cement sample used for the concrete is shown in Table 1. Three different hardened concrete samples of known proportions were collected. The cement used to prepare the concrete samples for this study contained 43.50% CaO as mentioned in the manufacturer's report. Descriptions of concrete core samples, namely A, B, C, which are approximately four times larger in diameter than the maximum aggregate size used in the preparation of concrete, are presented in Table 2 [16].

III.3 TEST PREPARATION

Air-dried concrete cores are weighed and stored in water for 24 hrs, then dried at 110°C for another 24 hrs. The sample is ignited at 550 °C to remove absorbed moisture. The concrete sample is then ground into dust. However, not all particles are completely crushed when sprayed. The milled sample is therefore sieved through 4 .75 mm aperture and the percentage pass is determined as shown in Table 3. Then, approximately 100 grams of finer particles are sieved through 40 or 420 micrometre sieves. 2 grams of sample passed through a 420-micron sieve was then used for the determination of calcium oxide. The procedure to be applied to find out how much calcium oxide there is. The process for determining calcium oxide in concrete is outlined in the next section.

III.4 TEST PROCEDURE ADOPTED

The different steps applied to perform the analytical procedure are shown in the following diagram Figure 2. Several steps of the California Test 403 procedure for the determination of calcium oxide in concrete have been modified and applied to the analysis of concrete samples.



Figure 1: California Test 403 Procedure.
Source: Authors, (2023).

Table 1: Oxide compositions of Portland cement.

Compositions	Contents in %
CaO	43.48
SiO ₂	16.95
IR	15.52
LOI	1.61
MgO	1.65
SO ₃	2.72
Fly Ash	17.98

Source: Authors, (2024).

Table 2: Ingredient of the hardened concrete samples.

Sample	Cement (%)	Sand (%)	Aggregate (%)	Water (%)
A	18.00	22.32	51.41	8.27
B	17.25	22.81	51.62	8.30
C	18.80	21.77	51.14	8.27

Source: Authors, (2024).

Table 3: Particle size analysis of concrete samples.

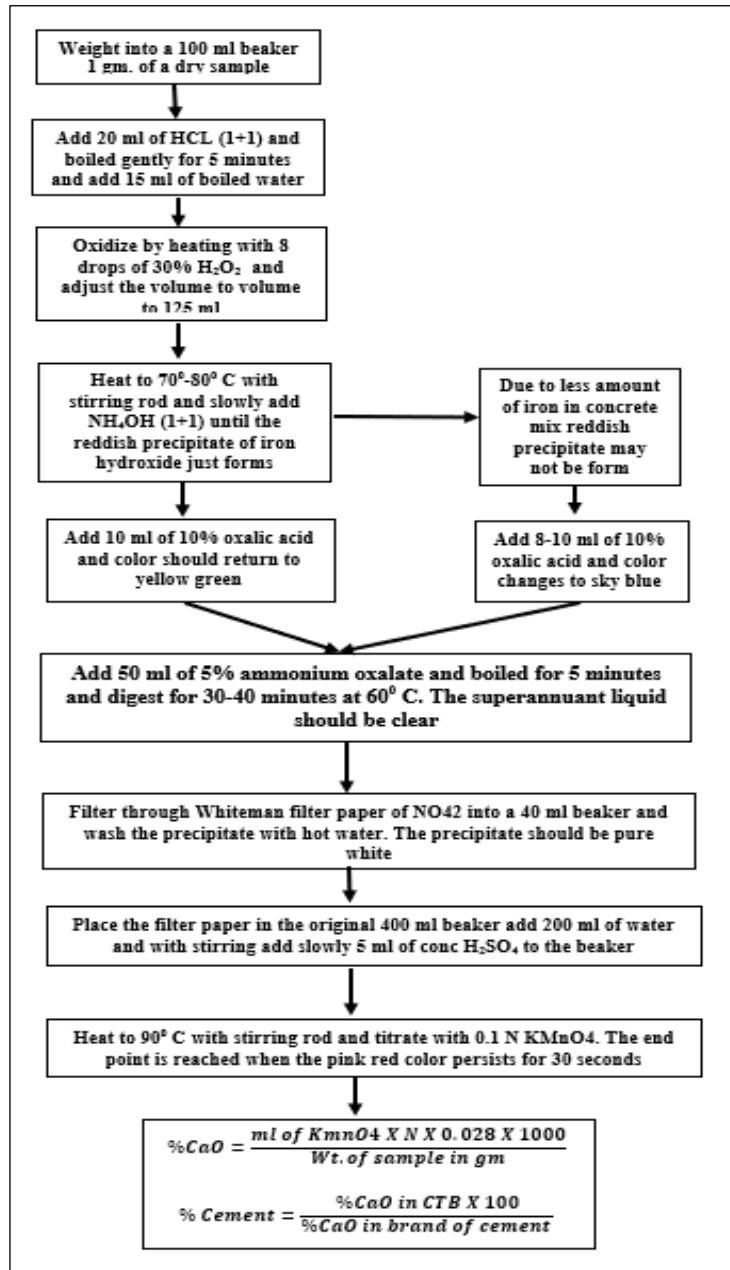
Particulars	A	B	C
Amount of passing through 4.75mm sieve (kg)	2.852	3.413	2.396
Amount of retained in 4.75mm sieve (kg)	4.658	5.824	3.892
Percentage of passing through 4.75mm sieve (%)	37.47	36.96	38.10

Source: Authors, (2024).

III.5 ANALYSIS OF CONCRETE SAMPLES

The three samples mentioned in Table 2 were originally tested to analyse the application of the California Test 403 procedure and some steps were changed as necessary. Step 3 of the California 403 trial was found to be ineffective with all samples included in their starting formulation. However, the addition of iron crystals in the samples resulted in a slightly reddish colour, ensuring that the iron composition was traceable in the sample to aid the test step. Therefore, the modified step 4, as shown in Figure 1 was considered for all samples to perform further experiments. The analytical results obtained by the adopted procedure shown in Figure 2 is shown in Table 4. The calcium oxide content of each sample was initially determined for powder passing 4.75 mm and extrapolated. for subsequent full concrete samples.

Figure 2: Flow of the adopted chemical procedure.



Source: Authors, (2024).

Table 4: Chemical analysis of concrete samples.

Particulars	A	B	C
KmnO ₄ required for titration (ml)	71	72	74
Percentage of CaO (%) (sample passes through 4.75 mm sieve)	20.15	20.00	20.71
For whole concrete CaO (%)	7.56	7.34	7.90
Cement (%)	17.36	16.88	18.14

Source: Authors, (2024).

III.6 XRD INSPECTION

X-ray diffraction is a widely accepted instrumental procedure used to offer extensive information on natural and artificial materials' chemical makeup and crystal structure. There are many cases where researchers have explored XRD methods for qualitative and quantitative analysis of cement systems and have proven to be popular and reliable [10,17]. Concrete powder samples were prepared for XRD analysis and spectroscopic

analysis was performed by X-ray diffraction [Model: D8 Advance; Brand: Bruker, Germany] using the JCP 2:00 database and the chemical compositions were evaluated as shown in Table 5. The XRD model describes the chemical compositions and one of them is shown in Figure 3.

Table 5: Chemical analysis of overall concrete samples.

Sample	Calcium oxide content (%)			Error (%)	
	True	Evaluated	XRD	True Vs Evaluated	True Vs XRD
A	7.82	7.56	8.55	-3.59	+9.08
B	7.50	7.35	8.17	-2.20	+8.67
C	8.16	7.90	8.93	-3.44	+9.19

Source: Authors, (2024).

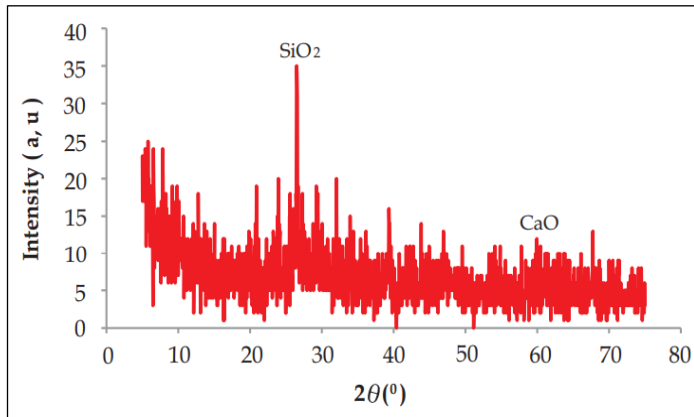


Figure 3: XRD plot of 4.75 mm size passing sample C.
Source: Authors, (2024).

IV. DEBATE AND ARGUMENT

The assessed calcium oxide content in each concrete sample was compared with the actual percentage of calcium oxide in the respective concrete samples and was found to be in good agreement. In addition, the calcium oxide content in each concrete sample observed by XRD analysis is also close to the estimated estimate. Therefore, the adopted simplified California 403 test can be established as one of the most accurate methods for evaluating cement in concrete samples.

V. CONCLUSIONS

The overall quality of hardened concrete depends mainly on the quality of its components. Calcium in cement has the main task of binding concrete components together and forming heterogeneous concrete slabs. It is clear that the presence of different elements of the individual components leads to the heterogeneity of the hardened concrete and increases the complexity of the mixture. Therefore, it is quite difficult to separate the individual components/components from the hardened concrete. In addition, it is not possible to determine the percentage of cement in concrete that has been hardened by conventional procedures. The chemical test procedure is quite precisely applied to concrete manufactured with calcium-free aggregates. The analyses and experiments in this paper lead to the following findings.

- a) The California 403 test is one of the most accurate procedures for determining calcium oxide in hardened concrete with traceable amounts of elemental iron and calcium-free aggregates;
- b) In normal concrete, mortar (cement and fine aggregate) accounts for about 40% of the total weight of concrete. So, in the case of concrete with calcium-free aggregates, aggregates larger than 4.75mm can be filtered and grout can be used for chemical analysis;
- c) Step 3 of the California 403 Test does not give positive results if less than trace iron oxide is present. Instead, steps 4 and 5 of the adopted chemical analysis procedures can be useful for determining the exact calcium oxide and cement percentage in concrete that has been hardened, and;
- d) The method applied provides an exact amount of calcium oxide as well as the cement percentage in the concrete with a variation of 10%.

VII.6 AUTHORS' CONTRIBUTIONS

Conceptualization: Mohankumar N. Bajad.
Methodology: Mohankumar N. Bajad.
Investigation: Mohankumar N. Bajad
Discussion of results: Mohankumar N. Bajad.
Writing – Original Draft: Mohankumar N. Bajad.
Writing – Review and Editing: Mohankumar N. Bajad.
Resources: Mohankumar N. Bajad.
Supervision: Mohankumar N. Bajad.
Approval of the final text: Mohankumar N. Bajad.

VIII. ACKNOWLEDGEMENTS

The author would like to thank the authorities of S. T. E. S. Pune for their enthusiastic support. Valuable comments, efforts and timely help from everyone in a particular discipline are greatly appreciated. A thank you to all the authors whose publications have provided us with directional information over time. The cooperation and help received from the scientific and technical staff of the Laboratory of Advanced Materials and Library in the preparation of this paper is greatly appreciated.

IX. REFERENCES

- [1] S. Wilkie, "Thomas Dyerb challenges in the analysis of historic concrete: Understanding the limitations of techniques, the variability of the material and the importance of representative samples," *Int. J. Archit. Herit.*, 2020. <https://doi.org/10.1080/15583058.2020.1749728>
- [2] "Standard test method for Portland-cement content of hardened hydraulic-cement concrete," *ASTM Proc.*, pp. C1084-C1010.
- [3] *Testing Concrete. Methods for Analysis of Hardened Concrete*, p. BS1881-124:1988.
- [4] "Standard test methods for chemical analysis of hydraulic cement," *ASTM Proc. C*, pp. 114-11b.
- [5] H. G. William, "'Chemical Methods of Analysis of Concrete', handbook of analytical techniques in concrete," *Sci. Technol.*, pp. 105-126, 2006.
- [6] D. O. Covault and C. E. Poovey, "Use of neutron activation to determine cement content of Portland cement concrete," *HRB Bulletin 340*. Available at: <https://onlinepubs.trb.org/Onlinepubs/hrbulletin/340/340-001.pdf>. Washington, DC: Highway Research Board, pp. 1-29, 1962. <https://onlinepubs.trb.org/Onlinepubs/hrbulletin/340/340-001.pdf>
- [7] F. A. Iddings et al., "Nuclear techniques for cement determination," *Highway Res. Rec. 268*. Washington, DC: Highway Research Board, pp. 118-130, 1969.
- [8] J. Lee and Taegyu Lee, "Influences of chemical composition and fineness on the development of concrete strength by curing conditions," *Materials (Basel)*, vol. 12, no. 24, p. 4061, 2019. <https://doi.org/10.3390/ma12244061>
- [9] K. G. Kossivas, 'Cement Content Determination in Hardened Concrete,' *Rock Processing Chemical Research Seminar*. Chicago: W. R. Grace and Company, 1969.
- [10] "Methods of test for aggregates for concrete: Petrographic examination," *Indian Standard*. New Delhi: Bureau of Indian Standards, vol. 2386, no. VIII, 1963.
- [11] K. Chatterjee, "'X-ray diffraction', handbook of analytical techniques in concrete," *Sci. Technol.*, pp. 275-332, 2006.
- [12] H. S. Wong et al., "Microscopy techniques for determining water-cement (w/c) ratio in hardened concrete: A round-robin assessment," *Mater. Struct.*, vol. 53, p. 25, 2020. <https://doi.org/10.1617/s11527-020-1458-2>
- [13] B. W. Jo et al., "Strength and Durability Assessment of Portland Cement Mortars Formulated from Hydrogen-Rich Water," 2017. <https://doi.org/10.1155/2017/2526130>

[14] Department of Transportation et al., "California," Method Test. Cem. Treated Base Concr. Calcium Oxide, 1989.

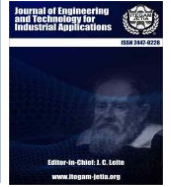
[15] K. M. J. Pierre et al., "Chemical analysis of the parameters determining the quality of a case of cement from cement sold on the Mbuji-Mayi markets," Open Access Libr. J., vol. 8, pp. 1-8, 2021. DOI: 10.4236/oalib.1106966

[16] "Method of test for strength of concrete," Indian Standard. New Delhi: Bureau of Indian Standards, vol. 516, p. 4, 1959.

[17] J. Hulimka and M. Kałuza, "Basic chemical tests of concrete during the assessment of structure suitability—Discussion on selected industrial structures," Appl. Sci., vol. 10, no. 1, p. 358, 2020. <https://doi.org/10.3390/app10010358>



ISSN ONLINE: 2447-0228

RESEARCH ARTICLE
ACCESS

OPEN

HYDRAULIC PERSPECTIVE FOR FLOW OVER PARABOLIC WEIR AND UNDER PARABOLIC GATE

Ihsan A. Abdulhussein¹, Rafi M. Qasim², Ayad A. Yahya³

¹ Prof. Dr., Basrah Engineering Technical College, Southern Technical University, Al-Zubayer Street, Basrah, Iraq.

² Assist. Prof., Basrah Engineering Technical College, Southern Technical University, Al-Zubayer Street, Basrah, Iraq.

³ Lecturer Dr., Technical Institute of Basrah, Southern Technical University, Al-Zubayer Street, Basrah, Iraq.

¹ <http://orcid.org/0000-0002-0281-0870> ² <http://orcid.org/0000-0002-1882-0766> ³ <http://orcid.org/0000-0002-6264-94>

Email: *drengihssan@stu.edu.iq, rafi.mohammed@stu.edu.iq, ayad.alyousof@stu.edu.iq

ARTICLE INFO

Article History

Received: December 22th, 2023

Revised: October 15th, 2024

Accepted: October 15th, 2024

Published: October 31th, 2024

Keywords:

flume flow,
hydraulic structure,
gate,
weir.

ABSTRACT

The weir-gate structure is a very important discharge structure. Thus, understanding the hydraulic features of this structure is necessary. The water flow over the weir and under the gate was investigated experimentally. Both the weir and gate have a parabolic shape; therefore, this paper aims to understand the appropriateness of using a non-regular shape in the hydraulic features of the discharge structure. The following variables and parameters are adopted in this study: actual discharge, water depth above the weir crest, vertical distance between the weir and gate, cross-sectional area of flow that crosses the weir and gate, downstream water depth, discharge coefficient, Froude number, and Reynolds number. It is found that all these hydraulic variables and parameters depend mainly on the water flow velocity, water flow depth, and flow area that cross the weir and gate, respectively. As well, the variation in the results trend will be attributed to overlapping between weir flow velocity and gate flow velocity. The use of a weir and gate with a parabolic shape produces a slight alteration in some hydraulic features, and this can be considered one benefit of using a non-regular shape for the discharge structure. The conflict between water flow velocity and water flow depth will be reflected directly in the Froude number and Reynolds number.



Copyright ©2024 by authors and Galileo Institute of Technology and Education of the Amazon (ITEGAM). This work is licensed under the Creative Commons Attribution International License (CC BY 4.0).

I. INTRODUCTION

A weir-gate structure is referred to as a hydraulic irrigation structure that operates in order to achieve many functions, such as flow measurement, diverting the flow direction, controlling the flow depth, removing floating material by weir, and removing deposit material by gate. Therefore, this structure faces many challenges during its serviceability life, so it is very important to realize the hydraulic characteristics and geometrical dimensions of this structure in order to avoid any variation in the supply flow rate and water depth in any irrigation system during the operational period. Several papers dealt with this subject, so we selected some of these papers to give a simple review of this irrigation structure. [1] experimentally assessed the impact of oblique angles and cylinder diameter on the composite cylindrical weir-gate structure. To achieve this objective, sixteen models of composite discharge structures are tested in the flume. Four oblique angles are adopted in this study; for any angle, four

diameters are used. From the results they found, the ratio of diameter to height and the ratio of length to height are inversely proportional to the flow rate; also, the flow rate will increase with increases in the diameter and decrease with decreases in the oblique angle. [2] conducted many experiments in order to build an equation to predict the real discharge, which is passed through the composite weir-gate structure. In this work, uniform and non-uniform shapes for gates and weirs are used to achieve the experiments. [3] employed the artificial neural network (ANN) in order to calculate the discharge coefficient of a composite weir-gate structure, which is composed of a trapezoidal weir and a rectangular gate. To achieve this objective, experiments are performed, and the collected data is analyzed. Also, dimensional analysis is adopted to show the variables that have an impact on the discharge structure. [4] studied numerically and experimentally water flow through a combined structure that has a weir with a trapezoidal shape and three different shapes of gate; the first has a rectangular shape, while the other two have a

trapezoidal shape. Also, the study adopted a weir with a trapezoidal shape in the achieved test. The selection of these samples (models) relies on eight different flow rates that pass through them. As well, ANSYS CFX is used to perform the numerical simulation of water flow through hydraulic structures. They found that the trapezoidal gate allowed a large flow rate to pass through it as compared with the rectangular gate. [5], [6], [7], [8], performed many experiments to give a good image of the hydraulic features and geometrical features impact on the response of weir-gate structure, considering regular and non-regular shapes for weir and gate. [9] estimated the discharge coefficient of combined orifice-weir flow based on experiments and theoretical analysis. The variables that have an impact on the discharge coefficient have been determined. [10] examined experimentally the scour hole dimensions that occur downstream of the weir-gate structure. Different shapes of gates have been used, like rectangular, triangular, and semi-circular, while the weir is composed of two geometric shapes. The study dealt with the alteration of weir and gate geometry, flume flow rate, and particle size of bed material on the scour hole dimensions. [11] investigated experimentally the free flow case through a weir-gate structure, where both gate and weir have a rectangular shape. The study focused on estimating the flow rate based on reading the water depth upstream of the weir-gate structure.

The aim of this paper is to concentrate on understanding the hydraulic characteristics for the hydraulic field on both sides of the weir-gate structure and also to realize how the dominant hydraulic and geometrical variables of the weir-gate structure manage the hydraulic variables like actual discharge, flow area, which cross both weir and gate, respectively, discharge coefficient of the composite structure, and the downstream water depth. Furthermore, this study utilizes a weir-gate structure with a non-uniform shape, like a parabolic shape, to introduce and produce an excellent vision about using this shape regardless of the difficulty in the construction of this structure.

II. FLOW CALCULATION

In a free flow situation, the theoretical discharge through a composite device represents the sum of both weir discharge and gate discharge.

$$Q_{theo} = Q_w + Q_g \quad (1)$$

For parabolic weir [12].

$$Q_w = \frac{\pi}{2} \sqrt{f g h u^2} \quad (2)$$

For parabolic gate, the continuity equation can be used to estimate the discharge

$$Q_g = V A = \sqrt{2 g H} A_g \quad (3)$$

Then, the discharge coefficient can be estimated

$$Q_{act} = c_d Q_{theo} \quad (4)$$

$$Q_{act} = c_d \left[\frac{\pi}{2} \sqrt{f g h u^2} + \sqrt{2 g H} A_g \right] \quad (5)$$

Where:

H: upstream water depth ($H = d + y + h_u$)

h_u : water head above sharp crest weir

y: vertical distance between weir and gate

d: water depth of gate opening

A_g : cross sectional area of the gate (cross sectional area of the flow through the gate)

V: water velocity at gate

f: focal distance

g: acceleration due to gravity

Q_g : gate discharge

Q_{theor} : theoretical discharge

Q_{act} : actual discharge

c_d : discharge coefficient

Figure (1) reviews the definition of composite flow over parabolic weirs and under parabolic gates that has been adopted in the current paper.

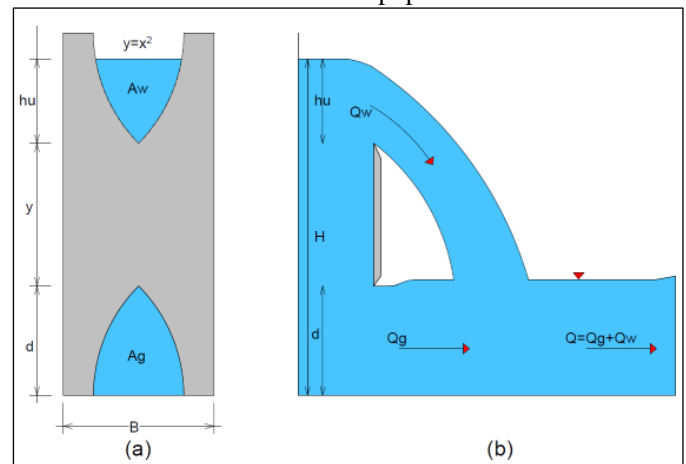


Figure 1: Definition Sketch for Composite Free Flow over parabolic Weir and below parabolic Gate (a) Cross Section (b) Longitudinal Flow and Geometry Section.

Source: Authors, (2024).

III. EXPERIMENTAL INVESTIGATION

All the experiments have been done in a flume with a rectangular section with glass sides. The dimensions of the flume are 2000 mm in length, 150 mm in depth, and 75 mm in width. The actual flow rate (actual discharge) has been measured by the volume method, and the water depth has been measured by the scale fixed in the wall of the flume. The model dimensions that have been fabricated from wood material are shown in Table (1) as well Table (2) gives all the experimental data that has been obtained in the laboratory.

The following steps are taken when conducting laboratory tests.

- 1- Initially, the flume is always horizontal.
- 2- At a distance of 80 cm from the flume's start, the models were fastened into the flume.
- 3- The tailgate was taken off to fulfill the free flow requirement.

For each model, the aforementioned process was repeated.

Table 1: The Tested Model Dimensions and Details of Parabolic weir and Gate.

Model No.	h _c m	hd cm	d cm	y cm	H cm	Ag cm ²	Aw cm ²	Vd cm/sec	Vu cm/sec
1	1	1.25	2	6	9	3.63	1.15	43.01	5.97
2	1	1.85	3	4	8	6.44	1.15	43.65	10.09
3	2	2.20	3	4	9	6.44	3.63	37.67	9.21
4	1	2.30	4	2	7	9.76	1.15	44.75	14.70
5	2	2.50	4	2	8	9.76	3.63	41.96	13.11
6	1	2.00	4	4	9	9.76	1.15	54.10	12.02
7	1	0.70	2	4	7	3.63	1.15	53.35	5.34
8	2	1.60	2	4	8	3.63	3.63	34.95	6.99
9	3	1.75	2	4	9	3.63	6.44	34.83	6.77
10	1	1.75	3	5	9	6.44	1.15	45.08	8.77
11	1	1.50	2	5	8	3.63	1.15	32.84	6.16
12	2	1.60	2	5	9	3.63	3.63	40.21	7.15
13	1	2.30	4	3	8	9.76	1.15	44.48	12.79
14	1	1.70	3	3	7	6.44	1.15	37.71	9.16
15	2	1.80	3	3	8	6.44	3.63	45.95	10.34
16	3	2.50	3	3	9	6.44	6.44	43.48	12.08

Source: Authors, (2024).

Table 2: Results of the Experimental Models.

Model No.	Ag/B.H	Aw/B.H	y/H	Q _{theo} (l/sec.)	Q _{act.} (l/sec.)	Cd
1	0.054	0.017	0.667	0.507	0.403	0.795
2	0.107	0.019	0.500	0.832	0.606	0.728
3	0.095	0.054	0.444	0.954	0.622	0.651
4	0.186	0.022	0.286	1.169	0.772	0.661
5	0.163	0.061	0.250	1.321	0.787	0.595
6	0.145	0.017	0.444	1.322	0.812	0.614
7	0.069	0.022	0.571	0.450	0.280	0.622
8	0.061	0.061	0.500	0.553	0.419	0.758
9	0.054	0.095	0.444	0.704	0.457	0.649
10	0.095	0.017	0.556	0.881	0.592	0.672
11	0.061	0.019	0.625	0.479	0.369	0.771
12	0.054	0.054	0.556	0.581	0.483	0.831
13	0.163	0.019	0.375	1.247	0.767	0.615
14	0.123	0.022	0.429	0.780	0.481	0.617
15	0.107	0.061	0.375	0.905	0.620	0.685
16	0.095	0.095	0.333	1.077	0.815	0.757

Source: Authors, (2024).

The following limits are applied to the testing of sixteen models: $0.222 \leq y/H \leq 0.667$, $0.054 \leq Ag/B.H \leq 0.186$, $1.366 \leq V/(gB)^{(1/2)} \leq 1.713$, $0.017 \leq Aw/B.H \leq 0.095$, $0.25 \leq hu/d \leq 1.5$. The variable B represents the total width of the channel and equal to 7.5cm. Models are manufactured of (and attached to flume using supports made of plexiglass). Based on the available lab resources, the flume and model materials were chosen. Each test involves measuring the combined flow rate (Q_{act}), head over the weir (h_u), upstream flow depth (H), and downstream flow depth, all while the flow is free.

coefficient values rise dramatically. For more visibility, the upstream and downstream Froude numbers rely on water velocity and water depth in the upstream and downstream regions of the combined structure, respectively, but the discharge coefficient mainly relies on overflow velocity from the weir and underflow velocity from the gate. Therefore, there is no direct interaction between the Froude number and the discharge coefficient. In addition, we mention here that all the values of the Froude number refer to subcritical flow.

IV. RESULTS AND DISCUSSIONS

Figure (2) illustrates the relation between the discharge coefficient and Froude number for both upstream and downstream of the combined structure, respectively. It is obvious from the figure that as the upstream Froude number increases, the discharge coefficient decreases gradually, while with a slight change in the downstream Froude number, the discharge

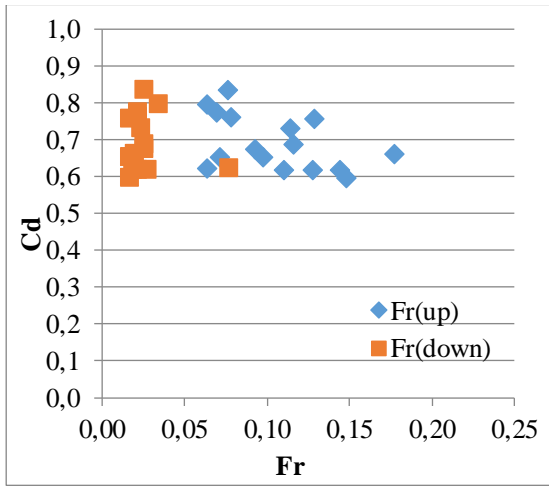


Figure 2: relation between discharge coefficient and Froude number.
Source: Authors, (2024).

Figure (3) presents the alteration of the discharge coefficient and Reynolds number downstream of the combined structure. With an increase in the Reynolds number, the values of the discharge coefficient will fluctuate slightly, so there is no noticeable change in the relationship between the two parameters in the downstream region. For more illustration, the Reynolds number relies on water velocity and water depth, while the discharge coefficient mainly relies on overflow velocity from the weir and underflow velocity from the gate. Therefore, there is no direct interaction between the Reynolds number and the discharge coefficient. All the values of the Reynolds number refer to turbulent flow.

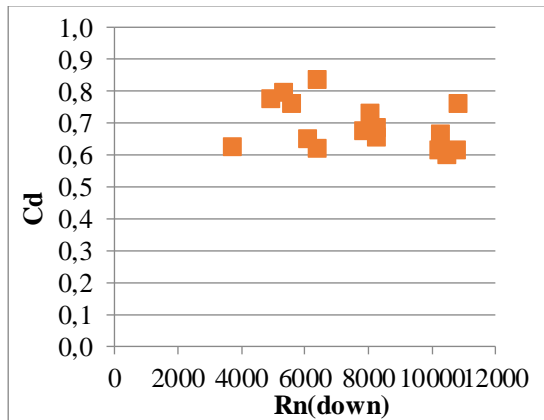


Figure 3: relation between discharge coefficient and Reynolds number.
Source: Authors, (2024).

Figure (4) presents the variation between the discharge coefficient and the ratio (h_u/H). It is evident that with an increase in the ratio (h_u/H), the slight variation in the discharge coefficient values is described, regardless of the inverse relationship between water depth above the weir crest (h_u) and discharge coefficient. Here, it is inferred that the use of non-regular weir shapes has a direct benefit on the values of the combined structure discharge coefficient.

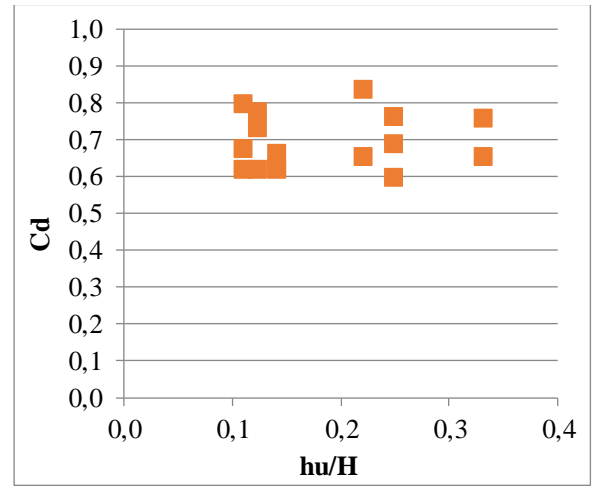


Figure 4: relation between discharge coefficient and (h_u/H).
Source: Authors, (2024).

Figure (5) illustrates the relationship between the upstream Froude number and the upstream Reynolds. Figures reveal a direct relationship between the two parameters; both parameters depend on water velocity and water depth in the upstream region of the combined structure. Here, the flow velocity will dominate and be responsible for the hydraulic behavior of the regime upstream. As well, the flow velocity is directly proportional to the Reynolds number and the Froude number.

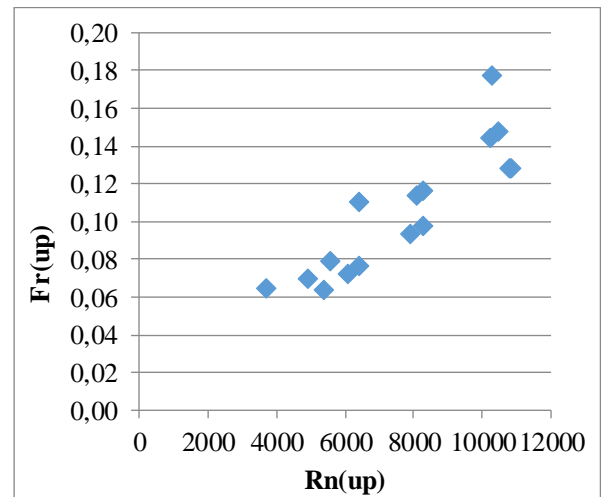


Figure 5: relation between upstream Froude number and Reynolds number.
Source: Authors, (2024).

Figure (6) illustrates the relation between the Froude number and Reynolds at the downstream region of the combined structure. Figures reveal an inverse relationship between the two parameters; both parameters depend on water velocity and water depth in the downstream region of the combined structure. The downstream water depth is considered small while the water velocity is considered high, and this conflict will be reflected mainly in the relationship trend.

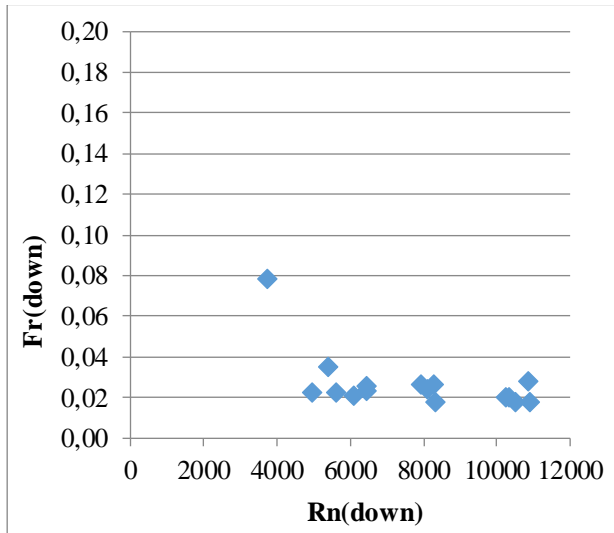


Figure 6: relation between downstream Froude number and Reynolds number.
Source: Authors, (2024).

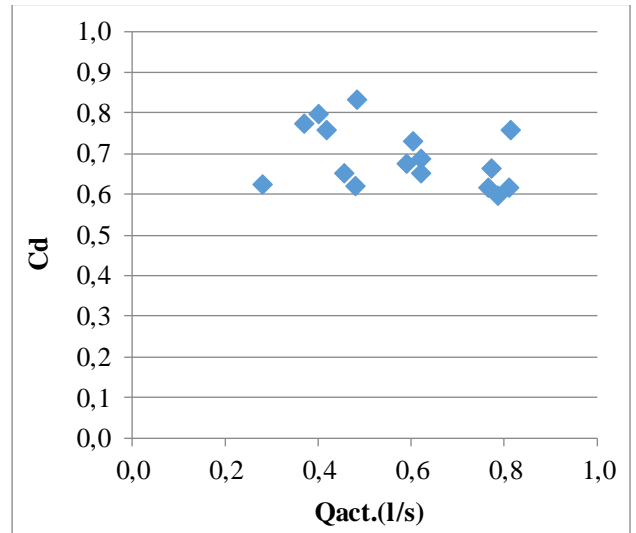


Figure 8: Relation between discharge coefficient and actual discharge.
Source: Authors, (2024).

Figure (7) presents the variation of actual discharge with the ratio (A_w/H) and (A_g/H). It is shown that with an increase in both ratios, the discharge quantity increase too, owing to direct proportional relation between discharge flow and the cross-sectional area, which passes through the weir (A_w) and gate (A_g), respectively, according to continuity equation. It is visible from the figure that the gate opening shares more in increasing the discharge quantity as compared with weir. This is because the gate opening is always full of water while water depth above weir is considered changeable.

Figure (9) presents the variation of actual discharge with the ratio (y/H) and h_u/H . It is inferred from the figure that with a decrease in ratio (y/H), the discharge quantity will increase. Here, y is referred to as the vertical distance between the weir and gate, which confined some quantity of discharge behind the combined structure. So with a decrease in distance (y), this leads to an increase in discharge quantity. Also, the variation in discharge quantity with ratio (h_u/H) is considered less important in spite of the water depth over weir (h_u) share in the discharge quantity of the combined structure.

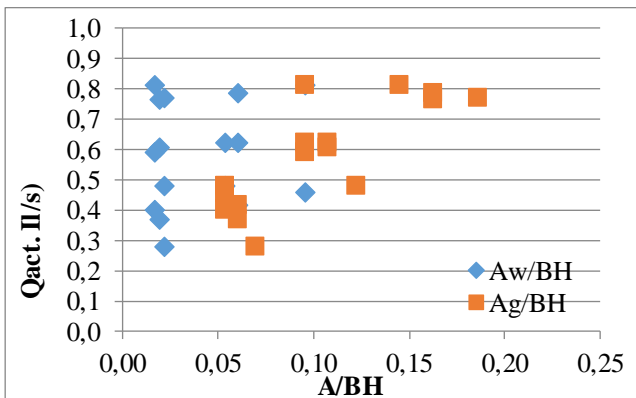


Figure 7: Relation between actual discharge and (A/BH).
Source: Authors, (2024).

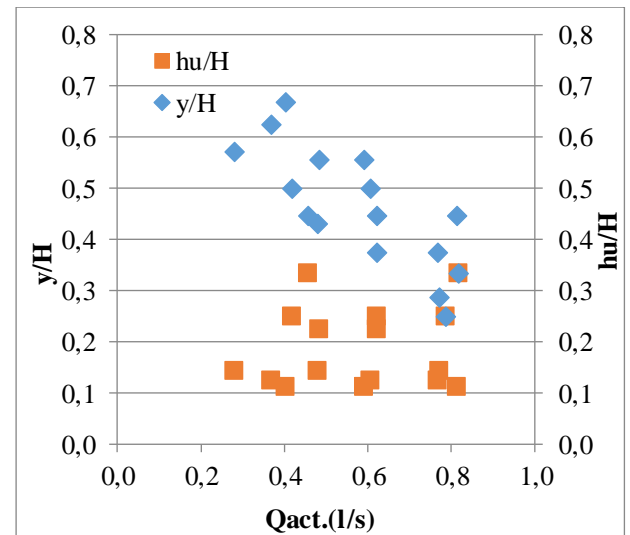


Figure 9: Relation between actual discharge with both (y/H) and (h_u/H).
Source: Authors, (2024).

The relation between the discharge coefficient and combined structure discharge is illustrated in figure (8). This figure shows a slight variation in relation to discharge coefficient and discharge quantity, regardless of the direct proportion between them. This will reflect the other benefit of using a non-regular shape for the weir and gate. Considering the purpose of discharge coefficient is to correct the total discharge quantities passing through the composite structure, it is found from the experimental study that this coefficient has moderate behavior with actual discharge passing through irregular composite structure. This is made clear from the slope of the relation between discharge coefficient and actual discharge, where it is approximately a constant slope and that signifies additional benefit to use irregular composite structure especially parabolic shape.

Figure (10) presents the variation of downstream water depth and the ratio (A_w/H) and A_g/H . Actually, any increase in the cross-sectional area of flow that crosses the weir and gate will be directly reflected in the increase in the downstream water depth, as shown clearly in figure (10). Also, it is very important to mention here that the gate opening shares more in the increase of downstream water depth as compared with the weir.

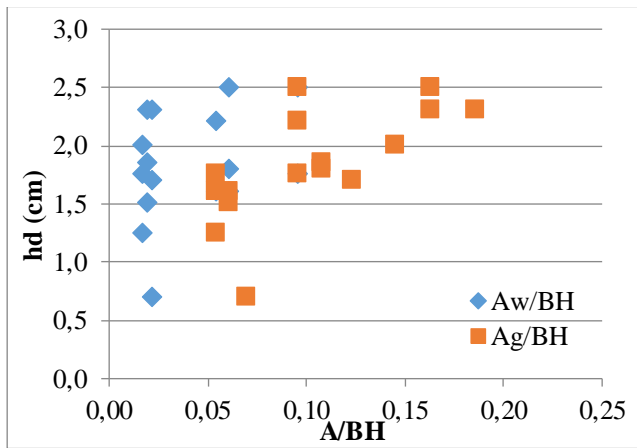


Figure 10: Relation between downstream water depth and (A/BH).

Source: Authors, (2024).

V. CONCLUSIONS

The current work deals with flow over and under combined discharge structures with non-regular shapes. From the results, we infer that the use of a weir and gate with a non-regular shape provides a reasonable hydraulic response, and this appears especially in the hydraulic relation between discharge coefficient and actual discharge, as well as discharge coefficient and ratio (h_u/H). It is found that with an increase in cross-sectional area of flow that crosses the weir and gate, respectively, the actual discharge and downstream water depth increase simultaneously. There is a slight change in some hydraulic variables, and this clearly appears in the relation between discharge coefficient and actual discharge, as well as the discharge coefficient and ratio (h_u/H). More than ever, it is obvious that both water velocity and water depth dominate the non-dimensional parameters such as Froude number and Reynolds number. Also, there is no theoretical equation or experimental equation connecting the combined structure discharge coefficient with Froude number and Reynolds number upstream or downstream of the combined structure, respectively. In spite of using a non-regular shape for the weir and gate, the vertical distance between the weir and gate plays a vital role in limiting some quantity of actual discharge behind the combined structure. Final, it is important to mention here in spite of the difficulty in the construction of a combined discharge structure with a weir and gate having a parabolic shape in the site, but it is recommended to use this shape due to the moderate hydraulic response or suitable values obtained for the hydraulic variables and parameters from the experimental investigation.

VI. AUTHOR'S CONTRIBUTION

Conceptualization: Ihsan A. Abdulhussein, Rafi M. Qasim, Ayad A. Yahya.

Methodology: Ihsan A. Abdulhussein, Rafi M. Qasim, Ayad A. Yahya.

Investigation: Ihsan A. Abdulhussein, Rafi M. Qasim, Ayad A. Yahya.

Discussion of results: Ihsan A. Abdulhussein, Rafi M. Qasim, Ayad A. Yahya.

Writing – Original Draft: Ihsan A. Abdulhussein, Rafi M. Qasim, Ayad A. Yahya.

Writing – Review and Editing: Ihsan A. Abdulhussein, Rafi M. Qasim, Ayad A. Yahya.

Resources: Ihsan A. Abdulhussein, Rafi M. Qasim, Ayad A. Yahya.

Supervision: Ihsan A. Abdulhussein, Rafi M. Qasim, Ayad A. Yahya.

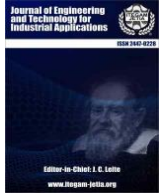
Approval of the final text: Ihsan A. Abdulhussein, Rafi M. Qasim, Ayad A. Yahya.

VIII. REFERENCES

- [1] Ibrahim, S. S., Jafer, R. A., Said Ali, B. M. A., An Experimental Study of a Combined Oblique Cylindrical Weir and Gate Structure. *Engineering, Technology & Applied Science Research*. Vol. 13, No. 2, 2023, 10483-10488.
- [2] Abdulhussein, I.A., Qasim, R.M., Hameed, M.A, Determination of the General Formula to Estimate the Discharge Quantity of Composite Structure for Free Flow. *Instrumentation Mesure Métrologie*. Vol. 21, No. 1, February, 2022, pp. 13-20. <https://doi.org/10.18280/i2m.210103>.
- [3] Sahib, J. H., Al-waeli, L. K., Al Rammahi, A. H. J., Utilization of ANN technique to estimate the discharge coefficient for trapezoidal weir-gate. *Open Engineering*, 2022;12:142-150. <https://doi.org/10.1515/eng-2022-0030>.
- [4] Hussein, B. S., Jalil, S. A., Hydraulic Performance for Combined Weir-Gate Structure , *Tikrit Journal of Engineering Sciences* (2020) 27 (1): 40-50. <http://doi.org/10.25130/tjes.27.1.06>.
- [5] Qasim. R.M. , Abdulhussein. I.A. , AL-ASADI K. , Experimental Study of Composite Inclined Weir – Gate Hydraulic Structure , *WSEAS TRANSACTIONS on FLUID MECHANICS*, Volume 15, 2020. DOI: 10.37394/232013.2020.15.5
- [6] Qasim. R.M. , Abdulhussein. I.A. , Hameed. M.A. , Maatooq. Q.A. Experimental Study of Coupled Parabolic Weir over Flow and Gate under Flow Rate. *Journal of Information Engineering and Applications*. Vol.8 , No.4 , 2018. <https://doi.org/10.7176/JIEA>.
- [7] Qasim. R.M. , Abdulhussein. I.A. , Hameed. M.A. , Maatooq. Q.A. Experimental Study of Hydraulic Response for Combined Weir-Gate Flow of Composite Shape. *Civil and Environmental Research*. Vol. 10 , No. 11 , 2018. <https://doi.org/10.7176/CER>.
- [8] Qasim. R.M. , Abdulhussein. I.A. , Hameed. M.A. Analysis of Flow Over Weir and Under Ellipse Gate. *Innovative Systems Design and Engineering*, Vol. 9, No. 7 , 2018. <https://doi.org/10.7176/ISDE>.
- [9] Fu Fu, Z., Cui, Z., Dai, W. H., Chen, Y. J., Discharge Coefficient of Combined Orifice-Weir Flow. *Water* 2018, 10, 699; doi:10.3390/w10060699.
- [10] Omran, H. A., Khassah, S. I., Hassan, F. A., The effect of flow conditions and geometric parameters on the scour value downstream composite structures of weir and gate. *Kufa Journal of Engineering*. Vol. 7, No. 1, January, 2016. P.P. 115-128.
- [11] Altan-Sakarya, A. B., Kokpinar, M. A., Computation of discharge for simultaneous flow over weirs and below gates (H-weirs). *Flow measurement and instrumentation*, 29 (2013), 32-38. <http://dx.doi.org/10.1016/j.flowmeasinst.2012.09.007> .
- [12] BOS, M. G. (1989) "Discharge Measurement Structures" 3rd Edition International Institute for Land Reclamation and Improvement/ Wageningen, The Netherlands.



ISSN ONLINE: 2447-0228



RESEARCH ARTICLE

OPEN ACCESS

THE DETERMINANTS OF PERFORMANCE OF NEWSPAPERS INDUSTRY: A MEDIATING EFFECT OF COMPETITIVE ADVANTAGE

¹Deus N. Shatta.

¹Corresponding Author: Lecturer, Faculty of Logistics and Business Studies, Department of Management Sciences, National Institute of Transport, P. O Box 705, Dar es Salaam-Tanzania.

¹<http://orcid.org/0000-0003-1852-6070>

E-mail: ¹deusshatta@gmail.com

ARTICLE INFO

Article History

Received: May 11th, 2024

Revised: October 18th, 2024

Accepted: October 18th, 2024

Published: October 31th, 2024

Keywords:

Competitive Advantage,
Firm Resources,
Reverse Logistics Performance,
Performance of Newspapers
Industry,

ABSTRACT

The study examined the factors that influence the performance of Tanzania's newspaper industry. The research was guided by resource-based theory. The study employed the positivist research paradigm and an explanatory cross-sectional survey research design. A simple random sampling technique was used to produce a sample size of 300 respondents. Data were gathered using a questionnaire and a documentary review. Inferential statistics analysis was performed on the collected data using Partial Squares Structural Equation Modeling with SmartPLS 4, and descriptive statistics analysis was performed on data collected about respondents' profiles using IBM SPSS Statistics Version 26. The findings show that competitive advantage, firm resources, and reverse logistics performance all have a positive impact on the performance of the newspaper industry. The study concludes that competitive advantage, firm resources, and reverse logistics performance all influence the performance of the newspaper industry. The study recommends that newspaper companies in Tanzania and other developing countries use their competitive advantages, resources, and reverse logistics to improve the performance of the newspaper industry.



Copyright ©2024 by authors and Galileo Institute of Technology and Education of the Amazon (ITEGAM). This work is licensed under the Creative Commons Attribution International License (CC BY 4.0).

I. INTRODUCTION

Firm resources such as commitment, manpower, management support, and adherence to green practices such as reverse logistics all have a significant impact on manufacturing company performance, particularly in terms of financial outcomes, environmental impact, and operational efficiency [1],[2]. Firm resources, particularly resource commitment, positively influence reverse logistics performance, which is frequently mediated by operational performance [3-5]. However, the strength of this effect varies by industry and company. On the other hand, reverse logistics can help a firm gain a competitive advantage, but this relationship is frequently mediated by the firm's operational performance [6]. Companies that can effectively use their reverse logistics capabilities to generate unique resources and capabilities are more likely to gain a comparative and competitive advantage [4-6].

Similarly, performance of Newspaper industry depends on a strategic perspective and leadership practices that emphasize collaboration and motivation [1]. Transformational leadership practices that take a holistic approach to the leadership process

improve newspaper robustness and competitiveness [7]. In today's competitive media market, newspapers must establish a strong brand identity and equity [8]. To maintain business operations and development in the age of new technology, newspapers must expand beyond traditional product offerings such as books and newspapers and innovate with new products such as e-books and websites. Furthermore, there is a positive relationship between resource commitment and reverse logistics innovation, which influences reverse logistics performance and cost savings in both the manufacturing and service industries [5]. Reverse logistics practices, such as waste management and environmental efficiency, can boost manufacturing companies' competitiveness by making them more environmentally responsible and efficient [9].

In the electronics industry, forward logistics management, information technology, and corporate citizenship all have a direct positive impact on reverse logistics management, which in turn improves logistics performance. Implementing sustainable reverse logistics practices can significantly improve economic, environmental, and social performance in the manufacturing industry [6]. The impact of reverse logistics performance on the

manufacturing industry is multifaceted, affecting resource commitment, innovation, environmental efficiency, competitiveness, and overall logistics performance in a variety of ways across industries and regions.

Reverse logistics is an effective strategy for achieving sustainable development while also increasing productivity in manufacturing organizations [10]. Implementing reverse logistics practices can result in resource savings, which is critical for increasing operational efficiency and reducing waste in the manufacturing sector. Reverse logistics practices in manufacturing industries help to improve environmental sustainability by managing waste, lowering carbon emissions, and minimizing environmental degradation [11].

Effective reverse logistics implementation can save manufacturing companies money by optimizing processes, reducing waste, and increasing overall efficiency. Reverse logistics practices give manufacturing companies a competitive advantage by making them more environmentally responsible, efficient, and sustainable in the market [12],[3],[13-17],[11]. The benefits of implementing reverse logistics in the manufacturing industry include sustainability, resource reduction, environmental benefits, cost savings, and gaining a competitive advantage in the marketplace. For example, reverse logistics enables manufacturers to recover, reuse, and recycle materials and products, thereby reducing waste and environmental impact [4],[14],[16].

Reusing and recycling materials can help to reduce costs associated with raw material procurement, waste disposal, and new product manufacturing [3],[13]. Efficient and convenient product returns and exchanges enhance customer experience and loyalty [12]. Reselling refurbished or remanufactured products can help manufacturers increase their revenue streams. Proper reverse logistics enables manufacturers to comply with environmental regulations and industry standards for waste management and product stewardship. Advanced reverse logistics strategies can help a manufacturer stand out and demonstrate their commitment to sustainability and customer service. Likewise, [12],[3] and [14] highlight the mediating role of reverse logistics in the relationship between resource commitment and financial performance in manufacturing companies. It implies that a strong commitment to resources can improve the effectiveness and efficiency of reverse logistics programs, thereby positively impacting financial results.

The study by [15] examined the importance of factors in implementing end-of-life product reverse logistics in the manufacturing sector. It suggests that dedicated manpower, efficient manufacturing techniques, and external factors such as government legislation all play important roles in successful reverse logistics operations, which can have a direct impact on the performance of manufacturing firms. On the other hand, [14] investigated the role of modularity and industrial complexes in improving environmental performance in the automobile industry. It suggests that modular production systems, including aspects such as reverse logistics, can help to promote green operations practices, which can have an impact on manufacturing firms' overall environmental performance and sustainability. The study by [17] highlights the differences between industrial sectors in implementing common reverse logistics practices, indicating that factors such as top management commitment, resource reduction, and customer demand for green products can influence reverse logistics effectiveness and, as a result, manufacturing firm performance.

Nonetheless, there is a lack of concrete models in the existing literature that effectively explain the impact of reverse logistics performance, firm resources, and competitive advantage

on newspaper industry performance. This study sought to fill a knowledge gap by investigating the impact of reverse logistics performance, firm resources, and competitive advantage on the performance of the newspaper industry. The study also looked at how competitive advantage mediated the relationships between reverse logistics performance, firm resources, and newspaper industry performance. The study's theoretical framework was based on the Resource-Based View.

II. THEORETICAL REFERENCE

This section examines the theoretical and empirical aspects of the Resource-Based View (RBV) and how it can be applied to newspaper industry to help firms gain a competitive advantage. Similarly, hypotheses were developed from the arguments presented in previous literature.

II.1 RESOURCE-BASED VIEW (RBV)

This study employed the Resource-Based View (RBV), a strategic management paradigm that emphasizes a company's internal resources as the primary means of achieving a long-term competitive advantage [18]. This concept, developed by businesses in the 1980s and 1990s, emerged as a means of understanding a company's components in order to achieve a long-term competitive advantage [19]. According to RBV, organizations are heterogeneous because they have a variety of resources, which allows them to pursue different strategies. The RBV states that in order for a firm to achieve a long-term competitive advantage, its resources must be valuable, rare, imperfectly imitable, and non-substitutable. In the 1990s, the RBV, also known as the resource-advantage hypothesis, became the dominant framework in strategic planning [18].

Similarly, RBV emphasizes the importance of both physical and intangible assets [18]. Intangible assets, such as brand recognition and intellectual property, are frequently the primary source of long-term competitive advantage [20]. According to the RBV model, using internal resources is more efficient for gaining a competitive advantage than relying solely on external opportunities. Furthermore, the RBV emphasizes the importance of capabilities, or an organization's ability to generate additional value and gain a competitive advantage over competitors [19]. The RBV model emphasizes the importance of identifying, developing, and leveraging a company's unique resources and talents in order to outperform competitors and achieve long-term market success [18-20]. Figure 1 depicts a model that explains the RBV and emphasizes its key aspects.

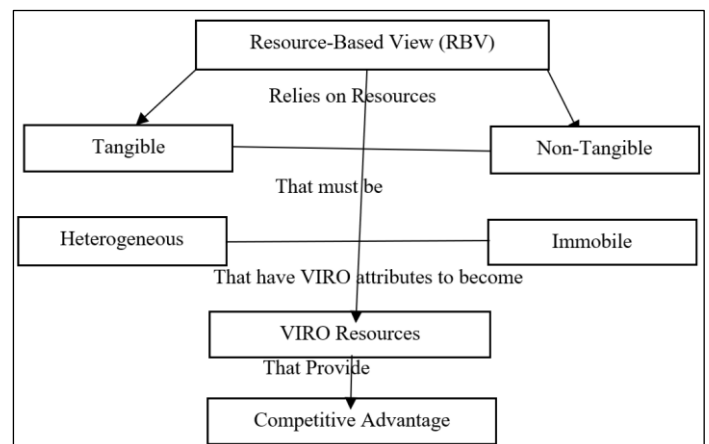


Figure 1: Resource-Based View (RBV) and its Key Points. Source: [18].

II.1I CRITICISM OF RESOURCE-BASED VIEW (RBV)

RBV is criticized for its static view of resources and capabilities, which ignores the dynamic nature of the business environment. Over time, resources and capabilities may become obsolete or irrelevant. In addition, the Resource-Based View (RBV) does not provide a framework for effectively managing this dynamic process [21]. Furthermore, RBV has been challenged for failing to recognize the importance of external resources and capabilities in developing a competitive advantage [21]. The theory emphasizes the importance of internal resources and capabilities while ignoring the value that external resources, such as partnerships, alliances, and networks, can provide to the firm. Furthermore, RBV has been criticized for failing to consider the importance of knowledge and learning in developing a competitive advantage [21]. The theory emphasizes the acquisition of resources and capabilities while overlooking the importance of knowledge and learning in establishing and maintaining a competitive advantage.

Furthermore, RBV has been criticized for failing to consider the importance of organizational culture and leadership in the development of competitive advantage [21]. The theory focuses on the acquisition of resources and capabilities while ignoring the importance of organizational culture and leadership in establishing and maintaining a competitive advantage. Also, RBV is criticised for failing to recognise the importance of innovation and creativity in establishing a competitive advantage. The theory emphasizes the acquisition of resources and capabilities while overlooking the importance of innovation and creativity in establishing and maintaining a competitive advantage. To address the RBV's weakness and fill the existing gap in the literature, [15] argue that additional research, specifically one that indicates that dedicated manpower, efficient manufacturing techniques, and external factors such as government legislation play critical roles in influencing the performance of manufacturing firms, is required. This study sought to determine whether a firm's resources, reverse logistics performance, and competitive advantage would all have a significant impact on the performance of the newspaper industry.

II.1III THE EFFECT OF FIRM RESOURCES (FR) ON COMPETITIVE ADVANTAGE (CA) AND ON PERFORMANCE OF NEWSPAPERS INDUSTRY (PNI).

The impact of firm resources on competitive advantage is significant, as demonstrated by [22] study of law firms' competitive advantage. The study emphasizes the importance of firm resources in determining competitive advantage among firms in the same industry. It implies that strategic and innovative resource utilization is critical for businesses to achieve and maintain a competitive advantage. Firms can improve their competitive position and outperform their industry counterparts by recognizing the value of their resources and effectively utilizing them [22]. On the other hand, [5] discovered a positive relationship between resource commitment and reverse logistics performance. The findings revealed that "there was a partial mediate effect of resource commitment on reverse logistics performance through reverse logistics innovation." [4] found that "operational performance significantly mediates the association linking reverse logistics and a firm's competitive advantage." The study by [5]

further found that "the size of the company had a moderate effect on the model level, but not on the path level. The model differs depending on the time of the company's entry into the industry and the type of industry, at both the model and path levels, but not across the length of reverse logistics implementation. This suggests that the impact of resources on reverse logistics performance may differ across industries and company characteristics. Unfortunately, previous research findings provide no direct information about the impact of firm resources on the performance of the newspaper industry. Previous research focused on a variety of other industries, including manufacturing, service, tourism, and law firms, but did not specifically address the newspaper industry. The most relevant information comes from [5] study, which investigated the relationships between resource commitment, reverse logistics innovation, reverse logistics performance, and reverse logistics cost savings. However, this study focused on the manufacturing and service industries and did not include the newspaper industry. The other most relevant information comes from [2] study, which looked at the effects of organizational resources (human capital and technological competencies) on firm performance in the mobile phone industry. Based on previous empirical research and the RBV, this study hypothesized that firm resources would have a direct impact on competitive advantage while directly and indirectly influencing the performance of the newspaper industry.

H_{1a}^+ : Firm resources directly and positively influence the competitive advantage

H_{1b}^+ : Firm resources directly and positively influence the performance of newspapers industry

$H_{1ax}H_{3}^+$: Firm resources indirectly and positively influence the performance of newspapers industry

II.1IV EFFECT OF REVERSE LOGISTICS PERFORMANCE ON COMPETITIVE ADVANTAGE AND ON PERFORMANCE OF NEWSPAPERS INDUSTRY (PNI)

The study by [4] discovered that "operational performance significantly mediates the association linking reverse logistics and a firm's competitive advantage." This suggests that effective reverse logistics implementation can result in improved operational performance, which contributes to the firm's competitive advantage. [4] confirmed that "when resources are mobilized uniquely, they create comparative advantage, consequently leading to competitive advantage." This suggests that successfully implementing reverse logistics can assist businesses in developing unique capabilities and resources, which can then be translated into a comparative and competitive edge. Similarly, [5] found that "the model is different across the time of company entrance to industry and type of industry at both model and path levels." This implies that the relationship between reverse logistics, operational performance, and competitive advantage may differ depending on the industry and stage of a company's life cycle. On the other hand, reverse logistics performance has a significant impact on competitive advantage, as demonstrated by a study on the relationships between resource commitment, reverse logistics innovation, reverse logistics performance, and reverse logistics cost savings in the manufacturing and service industries [5]. For

example, [5] discovered positive relationships between resource commitment and reverse logistics performance, implying that when resources are mobilized effectively, they can lead to improved reverse logistics performance. Furthermore, the study found that operational performance mediates the relationship between reverse logistics and a firm's competitive advantage. This implies that by improving reverse logistics performance through effective resource commitment and innovation, businesses can gain a competitive advantage in their respective industries. As a result, optimizing reverse logistics performance can help gain a competitive advantage while also improving overall firm performance. However, this study criticizes RBV for failing to consider the relationship between reverse logistics performance and competitive advantage. Based on previous research findings and missing information in RBV, this study hypothesized that reverse logistics performance would directly influence competitive advantage while indirectly influencing the performance of the newspaper industry.

H_{2a}^+ : Reverse logistics performance directly and positively influences the competitive advantage
 $H_{2a} \times H_{3}^+$: Reverse logistics performance indirectly and positively influences the performance of newspapers industry

II.V EFFECT OF COMPETITIVE ADVANTAGE ON PERFORMANCE OF NEWSPAPERS INDUSTRY

The effect of competitive advantage on newspaper industry performance can be significant, as demonstrated by a study on news organizations sustained competitive advantage [23]. This study emphasizes that human capital is an important resource for media companies, and when managed properly, it can lead to a sustained competitive advantage. Effective human resource management strategies and policies can help media companies outperform their competitors, resulting in a sustainable competitive advantage. In the newspaper industry, competitive advantage can be achieved through a variety of means, including innovative content creation, effective distribution strategies, strong brand positioning, and audience engagement. Newspapers can use these factors to differentiate themselves from competitors, increase readership, and secure advertising revenue. Furthermore, adaptability to changing technological trends and consumer preferences is critical for maintaining a competitive advantage in the newspaper industry. However, there is no direct information in RBV about the effect of competitive advantage on performance of newspaper industry. To validate this argument, more research that focuses specifically on the newspaper industry is required. This study predicted that competitive advantage would direct and improve the performance of the newspaper industry.

H_{3}^+ : Competitive advantage (CA) directly and positively influences the performance of the newspapers industry (PNI).

II.VI CONCEPTUAL MODEL OF THE STUDY

The conceptual model of this study was developed by combining insights from previous empirical research with the

theoretical underpinnings of the study, which are based on the Resource-Based View (RBV). Figure 2 illustrates the study's conceptual model.

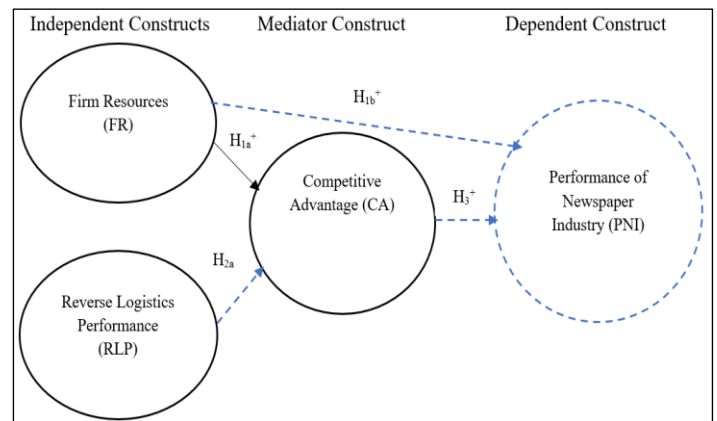


Figure 2: Conceptual Model.
 Source: Author, (2024).

--- Relationship which does not exist in RBV
 — Relationship which exists in RBV

II.VII THE MATHEMATICAL MODEL

The mathematical model $x=IY+e$ was used in this study to demonstrate the relationship between a latent variable and its observed indicators, where x is the observed indicator variable, Y is the latent variable, I is a regression coefficient that quantifies the strength of the relationship between x and Y , and e represents the random measurement error [24].

III. MATERIALS AND METHODS

The need to test research hypotheses motivated the adoption of positivist philosophy. Furthermore, the study used explanatory cross-sectional survey research methods to collect data from a specific sample of newspaper readers in Dar es Salaam, Tanzania. This is because data was collected once and only a subset of the unit was examined [25]. Similarly, this study collected data through a survey and then analyzed it quantitatively using descriptive and inferential statistics. Because this was a cross-sectional study with local newspaper readers as the focus, the sampling frame included Swahili language newspaper readers. Respondents were then chosen at random. The survey was distributed to 384 newspaper readers, of whom 300 returned completed questionnaires. Nonetheless, this study employed the tenth rule proposed by [26] to determine the appropriate sample size required to test the study model's hypotheses using PLS-SEM and SmartPLS 4 software. According to [26], the tenth rule of thumb states that the minimum sample size needed to evaluate the hypotheses of a given research model is ten times the highest number of exogenous construct indicators. In this study, the exogenous construct with the most indicators was reverse logistics performance (RLP), which had four indicators, as illustrated in Figure 3.

According to the tenth rule of thumb, a sample size of 300 respondents was deemed sufficient for testing the study's hypotheses because it exceeded the minimum number of respondents required. Furthermore, closed-ended questionnaires were assigned numerical values to improve the efficiency and accuracy of quantitative data analysis. The quantitative data gathered for the respondents' profiles was analyzed with descriptive statistics in IBM SPSS Statistics Software Version 26. To test the hypotheses, inferential statistical analysis was

performed with Partial Least Squares Structural Equation Modeling (PLS-SEM) and SmartPLS 4 software. The SmartPLS 4 application addressed missing data using the extra response technique. This study substituted the value 99 for the missing values found in the surveys. However, this technique aided in the systematic separation of observed and unobserved data [26].

III.I MODEL EVALUATION.

The reflecting models were assessed using Partial Least Squares Structural Equation Modeling (PLS-SEM). This decision was made based on the constructs and indicators in the study's conceptual model, as illustrated in Figure 3. Because all indicators were dependent on their constructs, [26] chose a reflective model for this study. Furthermore, the measurement and structural models of the proposed research model were evaluated using the criteria developed by [26]. There were numerous steps involved in evaluating reflective measurement models. First, the indicators' reliability was assessed, with a requirement that the value exceed 0.708. Second, the internal consistency reliability of the composite reliability of constructs was evaluated using a criterion greater than 0.708. Third, the convergent validity of the constructs was assessed using the Average Variance Extracted (AVE) value, which must be greater than 0.5. Finally, the discriminant validity was assessed using the Heterotrait-Monotrait Ratio of Correlations (HTMT) criteria, which required a score of less than 0.9. In addition, the constructs' collinearity in the structural model was evaluated. [26] recommend VIF values of 5 or lower. After adjusting for collinearity, the key variables used to assess the structural model in PLS-SEM were as follows. Path coefficients with a significance level are acceptable if the t-statistic is greater than 1.96 at a significance level of 0.05 for all paths, and p-values of 0.05 or less are considered significant [26]. Similarly, R² values of 0.75, 0.50, and 0.25 are classified as significant, moderate, and weak [26]. Overall, the evaluation results for both the measurement and structural models were positive, meeting all of the criteria established by [26].

IV. RESULTS

IV.I DEMOGRAPHIC CHARACTERISTICS OF THE RESPONDENTS

Table 1 shows data on respondents' gender, age group, educational level, and experience. Approximately 68 percent of the respondents were men, with approximately 32 percent being women. Furthermore, the vast majority of participants, nearly 81%, were aged 31 to 50. Furthermore, nearly 63% of respondents held a bachelor's or master's degree. However, many participants had previous experience as newspaper readers ranging from one to ten years, accounting for approximately 69 percent of the total. These findings suggest that the data collected was genuine. On the other hand, these findings are consistent with those of previous studies. For example, [8] study found that the majority of participants (newspaper readers) were over the age of 25, with more than half being male and the majority being graduates.

Table 1: Demographic Characteristics of the Respondents (n=300)

Characteristics		Frequency	Percentage (%)
Gender	Male	205	68.3
	Female	95	31.7
Age Group	21-30	12	4.0
	31-40	102	34.0
	41-50	140	46.7
	51-60	36	12.0
	61+	10	3.3

	Secondary Education	18	6.0
Education	Certificate Level	36	12.0
	Diploma Level	58	19.3
	Bachelor Degree	102	34.0
Experience	Master's Degree	86	28.7
	1-10	189	63.0
	11-20	95	31.7
	21-30	12	4.0
	31+	4	1.3

Source: Author, (2024).

IV.II INDICATOR'S RELIABILITIES, R² VALUES AND RELEVANCE OF THE PATH COEFFICIENTS

The PLS-SEM method with SmartPLS 4 software revealed that the loadings of all indicators for the constructs exceeded the recommended threshold of 0.708, as proposed by [26]. The R² values of 0.446 and 0.639 indicate that exogenous variables (firm resources (FR) and reverse logistics performance (RLP) can explain approximately 44.6 percent of the variation in competitive advantage (CA). Furthermore, the study discovered that a significant proportion, specifically 63.9 percent, of the variation in newspaper industry performance (PNI) can be attributed to the combined impact of firm resources (FR), reverse logistics performance (RLP) and competitive advantage (CA) serving as a mediator. Furthermore, all proposed influences had positive path coefficients, indicating that a one-standard deviation increase in the exogenous constructs firm resources (FR) and reverse logistics performance (RLP) as well as the mediator competitive advantage (CA), resulted in an increase in the level of performance of the newspaper industry (PNI). Figure 3 depicts the reliability of the indicators, R² values, and path coefficient relevance of the proposed model.

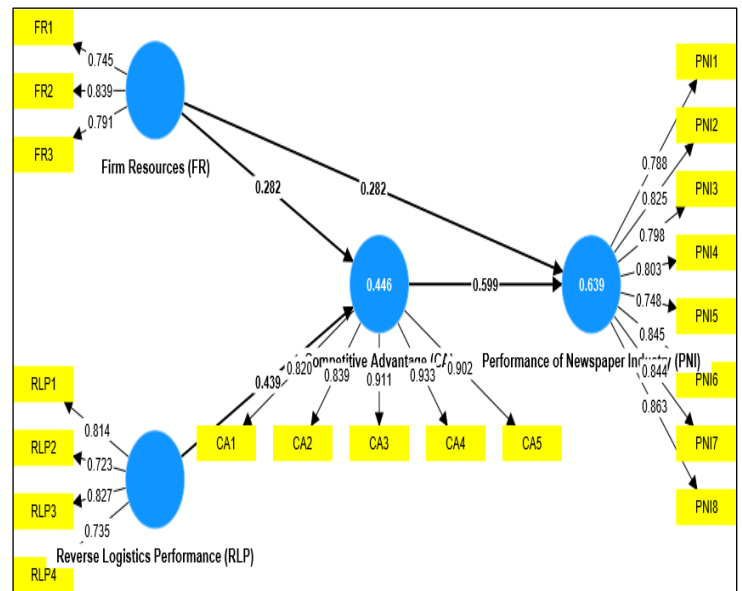


Figure 3: Indicator's Reliabilities, R² Values and Relevance of the Path Coefficients.

Source: Author, (2024).

IV.III RELIABILITY AND CONVERGENT VALIDITY ANALYSIS RESULTS

For [26] defined a construct as credible if its composite reliability (CR) score exceeds 0.708. Furthermore, for a construct to have convergent validity, its Average Variance Extracted (AVE) value must be greater than 0.5. This study assessed the reliability

of all constructs using composite reliability (CR) values, which were found to be greater than 0.708. Furthermore, the convergent validity of all constructs was determined by computing the Average Variance Extracted (AVE) value, which was found to be greater than 0.5. The findings of this study show that there were positive response patterns identified, and each individual element contributed to explaining the variability in its associated item [26]. Table 2 summarizes the constructs' reliability and validity.

Table 2: Reliability and Convergent Validity Analysis Results.

Construct	Composite Reliability (CR)	Average Variance Extracted (AVE)
Competitive Advantage (CA)	0.946	0.779
Firm Resources (FR)	0.835	0.628
Performance of Newspapers Industry (PNI)	0.940	0.664
Reverse Logistics Performance (RLP)	0.858	0.603

Source: Author, (2024).

IV.IV DISCRIMINANT VALIDITY ANALYSIS (HTMT RESULTS)

Table 3 depicts the relationships between the constructs with HTMT values less than 0.90 in the research model. Consistent with the suggestion made by [26], the results show that each exogenous construct in the research framework had a distinct effect on the endogenous construct.

Table 3: Discriminant Validity Analysis (HTMT Results).

Construct	CA	FR	PNI	RLP
CA	0.882			
FR	0.591	0.793		
PNI	0.766	0.636	0.815	
RLP	0.637	0.704	0.585	0.776

Source: Authors, (2024).

IV.V COLLINEARITY STATISTICS BY VIF METRIC FOR INNER MODEL

The Variance Inflation Factor (VIF) was used to assess collinearity in the data. However, [26] discovered that VIF values less than 3 indicate that the predictor constructs of the proposed research model are free of collinearity issues. Table 4 displays statistical data for collinearity in the inner model of the proposed study model. The VIF measure was used, and values less than 2 were found, indicating that there were no problems with collinearity in the predictor constructs of the proposed research model.

Table 4: Collinearity Statistics (VIF) for Inner Model Results.

Construct	Competitive Advantage (CA)	Performance of Newspapers Industry (PNI)
Competitive Advantage (CA)		1.536
Firm Resources (FR)	1.98	1.536
Reverse Logistics Performance (RLP)	1.98	

Source: Author, (2024).

IV.VI F² VALUES RESULTS

[26] found that impact sizes of 0.02, 0.15, and 0.35 yielded small, medium, and high f² values. Table 5 shows the effect sizes (f²) for each unique relationship: 0.073, 0.144, 0.176, and 0.647. These values represent the presence of small, medium, and large impact sizes for all hypotheses in the research model.

Table 5: F² Values Results.

Construct	Competitive Advantage (CA)	Performance of Newspapers Industry (PNI)
Competitive Advantage (CA)		0.647
Firm Resources (FR)	0.073	0.144
Reverse Logistics Performance (RLP)	0.176	-

Source: Author, (2024).

IV.VII Q² PREDICT RESULTS

The current study found that the values of Q² for all endogenous constructs, namely competitive advantage (CA) and performance of newspapers industry (PNI), were greater than zero. This suggests that the exogenous variables firm resources (FR) and reverse logistics performance (RLP) have predictive power in the research model [26]. Table 6 shows the Q² findings for the endogenous construct of the proposed research model.

Table 6: Q² Predict Results.

Endogenous Construct	Q ² predict	RMSE	MAE
Competitive Advantage (CA)	0.431	0.766	0.522
Performance of Newspapers Industry (PNI)	0.434	0.761	0.552

Source: Authors, (2024).

IV.VIII STATISTICAL SIGNIFICANCE OF THE HYPOTHESIZED RELATIONSHIPS

Figure 4 shows convincing evidence that all predicted connections were verified (with p-values less than 0.05), indicating that the conceptual research model utilized in this study is suitable for influencing management choices. This is owing to the fact that the anticipated associations are true.

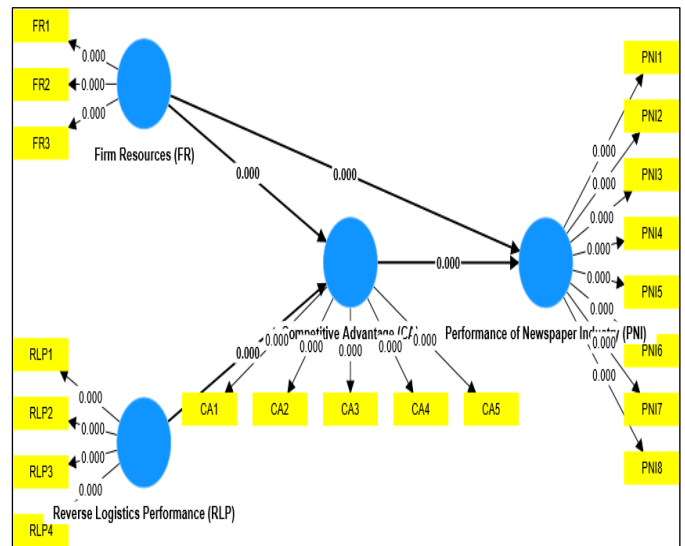


Figure 4: Statistical Significance Results.

Source: Author, (2024).

IV.IX INDIRECT STATISTICAL SIGNIFICANCE RESULTS OF THE HYPOTHESES

Table 7 summarizes the findings of the indirect assumption's assessment based on the study's theoretical framework. The bootstrapping report generated using SmartPLS 4 software revealed statistically significant results for indirect predictions (p-values <0.05). This implies that the connections observed in the model exist in real-world situations, and the validated model has the potential to be effectively applied to decision-making processes related to the determinants of performance of newspapers industry.

Table 7: Indirect Statistical Significance Results.

Hypothesis	Standard Deviation (STDEV)	T Statistics (O/STDEV)	P values
RLP -> CA -> PNI	0.042	6.329	0.000
FR -> CA -> PNI	0.040	4.268	0.000

Source: Author, (2024).

IV.X DIRECT AND INDIRECT STATISTICAL SIGNIFICANCE RESULTS OF THE HYPOTHESES

Table 8 summarizes the results of evaluating direct and indirect assumptions using the research's theoretical model. The bootstrapping report using SmartPLS 4 software yielded statistically significant results for both direct and indirect predictions (p values < 0.05). This demonstrates that the relationships identified in the model exist in real-world situations, and the validated model can be used successfully for decision making.

Table 8: Total Effects of Statistical Significance Results.

Hypothesis	Standard Deviation (STDEV)	T Statistics (O/STDEV)	P Values
CA -> PNI	0.055	10.799	0.000
FR -> CA	0.057	4.966	0.000
FR -> PNI	0.045	9.986	0.000
RLP -> CA	0.071	6.218	0.000
RLP -> PNI	0.042	6.329	0.000

Source: Author, (2024).

IV.XI IMPORTANCE-PERFORMANCE MAP ANALYSIS RESULTS

Figure 5 shows that firm resources (FR) and competitive advantage (CA) are the most important and best options for improving the performance of newspapers industry (PNI) based on their positions in the first quadrant. Because of this result, firm resources (FR) and competitive advantage (CA) need to be given more attention in order to ensure sustainable performance of newspapers industry (PNI). However, still, the factor of reverse logistics performance (RLP) is rated less important in improving sustainable performance of newspapers industry (PNI) due to its position in the second quadrant. This means that this construct doesn't have a big effect on the target construct performance of newspapers industry (PNI). When improving performance of newspapers industry (PNI), this construct is also important because it is above the average on the performance map of the main focus construct, which is performance of newspapers industry (PNI).

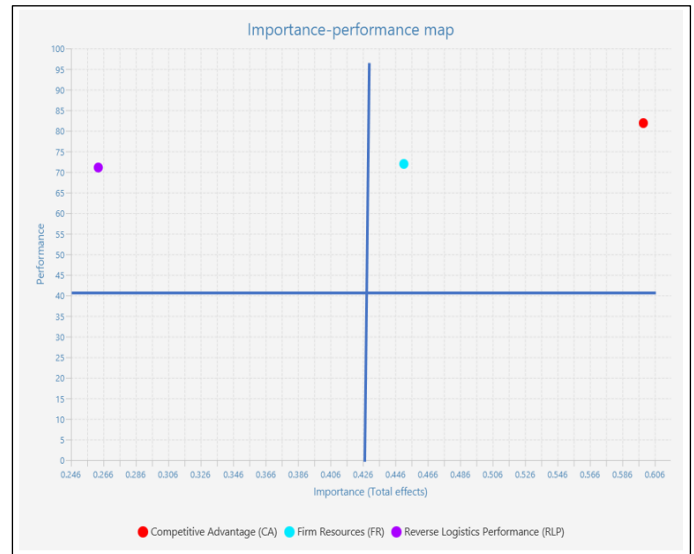


Figure 5: Importance-Performance Map Analysis Results. Source: Author, (2024).

IV.XII ADDITIONAL ANALYSIS

The types of mediation effects that may exist in the validated conceptual model were investigated. Partial mediation occurs when both indirect and direct effects are significant, whereas full mediation occurs when the direct effect is insignificant but the indirect effect is significant ([26]). Based on this, additional analysis was conducted to determine what types of mediation effects exist in the validated conceptual model.

The validated conceptual model included the direct effects of reverse logistics performance (RLP) on the performance of the newspaper industry (PNI), and a bootstrapping process was used. After the bootstrapping process, it was discovered that the direct effects of reverse logistics performance (RLP) on the performance of the newspaper industry (PNI) were statistically insignificant, whereas the indirect effect was statistically significant, indicating full mediation. On the other hand, both the direct and indirect effects of firm resources (FR) on newspaper industry performance (PNI) were statistically significant, indicating the presence of partial mediation. Following these findings, it is confirmed that the validated conceptual model contains partial and full mediation effects. Figure 6 depicts the results of testing different types of mediation effects.

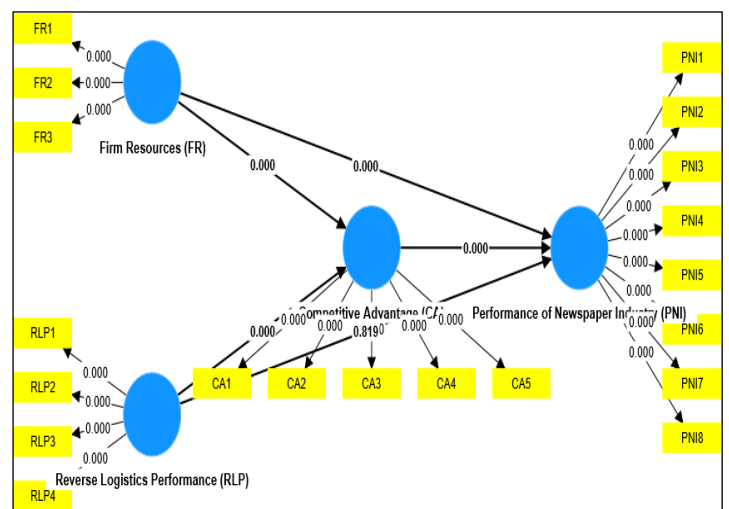


Figure 6: Testing the Type of Mediation Effects Results. Source: Authors, (2024).

V. DISCUSSION

V.I THE HYPOTHESES TESTED

This study proposed that firm resources (FR) would have a direct and indirect effect on newspaper industry performance (PNI) and competitive advantage (CA). Figure 3 revealed that there were positive path coefficients. This suggests that a one-standard deviation improvement in firm resources (FR) resulted in an increase in both competitive advantage (CA) and newspaper industry performance (PNI), and vice versa. Table 6 demonstrates that firm resources (FR) have a significant direct and indirect impact on newspaper industry performance (PNI) and competitive advantage (CA) (p -value < 0.05). These findings support the existence of the predicted relationships in real life. Furthermore, these findings support the findings of previous studies [22], [2], [4], [5], which suggest that when firms mobilize their resources in a unique way, they can gain a comparative advantage and compete.

Similarly, this study predicted that reverse logistics performance (RLP) would have a direct influence on competitive advantage (CA), as well as an indirect impact on overall performance of newspaper industry (PNI). Figure 3 showed that there were positive path coefficients, implying that a one-standard deviation increases in reverse logistics performance (RLP) would result in an improvement in both competitive advantage (CA) and newspaper industry performance (PNI). Table 8 shows that reverse logistics performance (RLP) improves both competitive advantage (CA) and newspaper industry performance (PNI). These findings imply that links between reverse logistics performance (RLP) and competitive advantage (CA) exist in the real world. Furthermore, there is an indirect relationship between reverse logistics performance (RLP) and newspaper industry performance (PNI) in real life. The findings of this study support previous research [4], [5]. These studies have demonstrated that effective reverse logistics performance in manufacturing firms can result in significant environmental, financial, and operational benefits that improve a company's overall competitiveness and long-term success.

Furthermore, the study hypothesized that competitive advantage (CA) would have a direct impact on the performance of the newspaper industry. Figure 3's results supported a positive path coefficient, indicating that a one-standard deviation increase in competitive advantage (CA) would result in an improvement in the newspaper industry's performance. Table 8 shows a strong positive correlation (p -value < 0.05) between competitive advantage (CA) and newspaper industry performance (PNI). On the other hand, the findings of this study are consistent with other prior studies [4], which have shown that competitive advantage, particularly when driven by effective human resource management practices, plays an important role in maintaining the performance and competitiveness of news organizations, which can be generalized to the newspaper industry as well.

V.II THEORETICAL IMPLICATIONS

This study effectively addressed the need for a concrete model to explain the direct impact of firm resources (FR) and reverse logistics performance (RLP) on competitive advantage (CA). Similarly, the current study has demonstrated a model that explains the indirect effect of firm resources (FR) and reverse logistics performance (RLP) on the performance of the newspaper industry (PNI) through competitive advantage. The study used the Resource-Based View (RBV) paradigm, which currently lacks a dedicated model for investigating the interactions of reverse logistics performance (RLP), firm resources (FR), and competitive

advantage (CA) in order to improve the performance of the newspaper industry. Figure 6 depicts the validated model for describing how firm resources (FR), reverse logistics performance (RLP), and competitive advantage (CA) influence the performance of the newspaper industry.

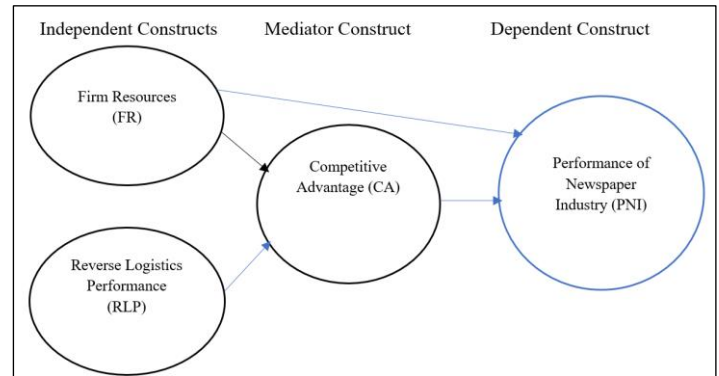


Figure 6: Validated Model.
Source: Authors, (2024).

- Theoretical Contribution
- Relationship which exists in RBV

V.III PRACTICAL IMPLICATIONS

The confirmed model suggests that competitive advantage (CA) mediates the reverse logistics performance (RLP) and firm resources (FR). According to the findings, firm resources (FR) and reverse logistics performance (RLP) have a significant impact on the performance of the newspaper industry (PNI). Similarly, the statistical significance of firm resources (FR) in both direct and indirect influences suggests that the newspaper industry should focus on its resources to improve its performance. Likewise, the statistical significance of reverse logistics performance (RLP) in indirect influence only suggests that the newspaper industry should indirectly focus on implementing reverse logistics to improve its performance.

V.IV CONCLUSIONS

The findings in Figure 5 provide compact evidence that supports the validity of the study model proposed in the context of decision-making, particularly in terms of prioritizing the competitive advantage (CA) and utilization of firm resources (FR) to improve the performance of the newspaper industry (PNI).

V.V LIMITATION AND RECOMMENDATION FOR FUTURE RESEARCH

This study used a limited number of components, two of which (firm resources (FR) and competitive advantage (CA)) were derived from the Resource-Based View (RBV) and one from an empirical literature review (reverse logistics performance), to forecast the improvement in the performance of the newspaper industry. Figure 3 shows that the combination of these components accounted for only 63.9% of the observed variation in newspaper industry performance (PNI). These findings suggest that additional factors can be added to improve the performance of the newspaper industry from 63.9% to substantial (75% and above). The current study suggests that future research should include additional components from other theories to increase the variety of the newspaper industry's (PNI) performance and broaden the scope of the validated model. Furthermore, the study only included

Tanzanian participants. Future research should include participants from multiple countries to improve the proposed model's generalizability in predicting the factors that influence the performance of the newspaper industry (PNI).

VI. AUTHOR'S CONTRIBUTION

Conceptualization: Deus N. Shatta.

Methodology: Deus N. Shatta.

Investigation: Deus N. Shatta.

Discussion of results: Deus N. Shatta.

Writing – Original Draft: Deus N. Shatta.

Writing – Review and Editing: Deus N. Shatta.

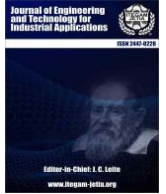
Resources: Deus N. Shatta.

Supervision: Deus N. Shatta.

Approval of the final text: Deus N. Shatta.

VII. REFERENCES

- [1] X. H., Nguyen, and Q. C. Luu, "Performance Measurement of Vietnamese Publishing Firms by the Integration of the GM (1, 1) Model and the Malmquist Model. Business Systems Research", International journal of the Society for Advancing Innovation and Research in Economy, 12(1), 17-33, 2021.
- [2] J. G. Njoroge, "Effects of organizational resources, competitive advantage on firm's performance of mobile phone industry in Kenya" Unpublished PHD Thesis, Kenyatta University, 2014.
- [3] Y. Fernando, M. S. Shaharudin, I., Ismail, S. Q. Yew, and Y. Ganesan, A Mediating Model of Resource Commitment, Reverse Logistics and Financial Performance: Importance-Performance Map Analysis. In 8th International Borneo Business Conference, pp. 20-30, 2018.
- [4] M.L Job, M.J. Njihia, J.K. Maalu, and X.N. Iraki, Reverse Logistics and Competitive Advantage: The Mediating Effect of Operational Performance Among Manufacturing Firms in Kenya. European Scientific Journal ESJ, 2020.
- [5] B. Piyachat, "The relationships among resources' commitment reverse logistics innovation reverse logistics performance and reverse logistics cost savings: Manufacturing vs service industry", Journal of Administrative and Business Studies, 3(3), 122-135, 2017.
- [6] A. Anwar, A. Barut, F. Pala, N. Kilinc-Ata, E. Kaya, and D. T. Q. Lien, "A different look at the environmental Kuznets curve from the perspective of environmental deterioration and economic policy uncertainty: evidence from fragile countries", Environmental Science and Pollution Research, 1-20, 2023.
- [7] E. Wilberg, "An investigation into leadership practices and performance of newspapers in Norway and Sweden, Doctoral dissertation, Henley Business School, University of Reading, 2003.
- [8] M. Bakshi, and P. Mishra, "Structural equation modelling of determinants of consumer-based brand equity of newspapers", Journal of Media Business Studies, 13(2), 73-94, 2016.
- [9] M. Anne, L. Nicholas, G. K. Ithinji, and H. O. Bula, "Reverse logistics practices and their effect on competitiveness of food manufacturing firms in Kenya", 2016.
- [10] M. Hosseini, N. Chileshe, R. Rameezdeen, and S. Lehmann, Reverse logistics for the construction industry: Lessons from the manufacturing context, Doctoral dissertation, Scientific and Academic Publishing, 2014.
- [11] P. Teprasit, and N. Paopan, "The reverse logistics management model Thailand context", International Journal of Business and Information, 11(4), 385, 2016.
- [12] Y. Can Saglam, "Analyzing sustainable reverse logistics capability and triple bottom line: the mediating role of sustainability culture", Journal of Manufacturing Technology Management, 34(7), 1162-1182, 2023.
- [13] C. W. R. Lin, M. T. Chen, M. L. Tseng, A. S., Chiu, and M. H. Ali, "Profit Maximization for Waste Furniture Recycled in Taiwan Using Cradle-to-Cradle Production Programming", Mathematical Problems in Engineering, 2020, 1-15. 2020.
- [14] B. Nunes, and D. Bennett, "Modularity and industrial complexes: perspectives for green operations in the automotive industry", In 14th international annual conference of the European Operations Management Association, 2007.
- [15] N. Subramanian, A. Gunasekaran, M. Abdulrahman, and C. Liu, "Factors for implementing end-of-life product reverse logistics in the Chinese manufacturing sector. In Managing Organizations for Sustainable Development in Emerging Countries, pp. 41-51, Routledge, 2017.
- [16] Y. Xu, "A robust multi-objective optimization model for sustainable closed-loop supply chain network design under demand uncertainty", Academic Journal of Business and Management, 3(1), 27-43, 2021.
- [17] V. Ravi, and R. Shankar, "An ISM-based approach analyzing interactions among variables of reverse logistics in automobile industries", Journal of Modelling in Management, 12(1), 36-52., 2017.
- [18] J. B. Barney, "Firm resources and sustained competitive advantage", Journal of Management, 17, 99-120, 1991.
- [19] B. Wernerfelt, "A resource-based view of the firm" Strategic Management Journal, 5, 171-180, 1984.
- [20] T. Chi, "Trading in strategic resources: Necessary conditions, transaction cost problems, and choice of exchange structure", Strategic Management Journal, 15(4), 271-290, 1994.
- [21] K. Cullen, and D. W. Parker, "Improving performance in project-based management: Synthesizing strategic theories", International Journal of Productivity and Performance Management, 64(5), 608-624, 2015.
- [22] J. P. L. Nyaberi, "Firm resources and competitive advantage of law firms in Kenya" The Strategic Journal of Business and Change Management, 7 (4), 1491-1499, 2020.
- [23] P. Y. Tsai, "Sustained Competitive Advantage of News Organizations: Research on the Human Resource Management on Taiwan's Media Groups", 2009.
- [24] D. N. Shatta, "Determinants of Behavioral Intention to Use E-Procurement System in Developing Countries: Suppliers' Perception from Tanzania", In State of the Art in Partial Least Squares Structural Equation Modeling (PLS-SEM) Methodological Extensions and Applications in the Social Sciences and Beyond (pp. 537-555). Cham: Springer International Publishing, 2023.
- [25] J. W. Creswell, and C. V. L. Plano, "Designing and conducting mixed methods research", Thousand Oaks, CA: Sage, 2018.
- [26] J. F. Hair, J. J. Risher, M. Sarstedt, and C. M. Ringle, "When to use and how to report the results of PLS-SEM", European business review, 31(1), 2-24, 2019.



RESEARCH ARTICLE OPEN ACCESS

INFLUENCE OF THE LUBRICANT TEMPERATURE OF SPLASHED LUBRICATED WORM GEARBOX ON CHURNING POWER LOSSES

H.G. Chothani*¹, D.J. Marsonia², N.N. Jadedea³ and S.H. Zala⁴

^{1,3,4} Mechanical Engineering Department, Government Engineering College Bhavnagar, Bhavnagar-360004, Gujarat, India

² Mechanical Engineering Department, Government Engineering College Bhuj, Bhuj-370001, Gujarat, India

¹<http://orcid.org/0000-0003-2773-4365> ²<http://orcid.org/0009-0008-9827-6430> ³<http://orcid.org/0000-0001-9582-705> ⁴<http://orcid.org/0009-0004-0745-9874>

*Email: ¹chothanihardik@yahoo.com, ²djmarsonia@gmail.com, ³nnjadeja79@yahoo.com, ⁴zala.bpti@gmail.com

ARTICLE INFO

Article History

Received: May 16th, 2024

Received: October 11th, 2024

Accepted: October 11th, 2024

Published: October 31th, 2024

Keywords:

Worm Gearbox,
Lubricant Temperature,
Churning Loss,
Power loss,
Torque loss.

ABSTRACT

The primary goal of lubricating a worm gearbox is to encourage sliding between teeth, which lowers the coefficient of friction and regulates the temperature rise brought on by rolling and sliding friction. Due to both non-load-dependent and load-dependent power losses, the worm gearbox has a relatively poor efficiency. Nonetheless, to meet the needs, there is now a greater need for more efficient worm gearboxes. Lowering churning power losses, can be accomplished. Bearing friction losses and gear friction losses make up the load-dependent losses. The non-load dependent losses are the bearing churning losses, gear windage losses, gear churning losses and oil seal losses. Numerous factors, including speed, direction of rotation, oil amount, and immersion depth, affect the non-load dependent losses. Only the impact of lubricant temperature and its relationship to non-load-dependent losses will be the focus of this study. A thorough experimental investigation was conducted utilizing the direct torque measuring method. A brand-new test rig was created, assembled, and placed into service to gauge input torque in the absence of load. We kept an eye on the fluctuating impacts of lubricant temperature on churning power loss.



Copyright ©2024 by authors and Galileo Institute of Technology and Education of the Amazon (ITEGAM). This work is licensed under the Creative Commons Attribution International License (CC BY 4.0).

I. INTRODUCTION

Because of its high torque, large reduction ratios, and inexpensive cost of manufacture, worm gears are extensively utilized in technological systems [1]. A worm gear is more metal-efficient and smaller than a parallel axis gear with the same gear ratio [2]. The most important parts of this gear are the worm and worm wheel, which are normally constructed of hardening steel and bronze, respectively [3]. Worm gear produces excessive heat, which needs to be cooled with the right lubricant. Lubrication not only keeps metal components from corroding and wearing out, but it also acts as a coolant to dissipate heat produced by friction between the gears and inside the bearings during regular operation [4]. A gearbox that is not properly lubricated will not function well, overheat, and finally fail. Power loss is the primary reason for the worm gearbox's reduced efficiency [5]. Gears have two types of power losses: load-dependent (mechanical) and load-independent (spin) power losses from oil windage, oil sealing and oil churning from gear

and bearing oil [6–8]. Reducing the input torque can improve both power losses. The input torque is contingent upon several variables, including lubricant temperature, the kind of worm gear, the gear's orientation, rotational direction, geometry, and tribological factors. There will be increased sliding/rolling friction and wear due to the high lubricant temperature since the lubricants will be thinner and the gears and bearing parts will not "hydroplane" on one another as readily [9-10]. Similar to this, low lubricant temperatures -especially in the winter—will cause the oils to thicken and make it harder for the bearing elements and gears to mix, increasing fluid friction and uneven lubrication. A gearbox failure can result from either situation. The spiral bevel gear's frictional heat production was studied by [11]. The finite element method was used to investigate it. The churning power loss of a bevel gear was predicted by [12], the use of computational fluid dynamics (CFD). Using a CFD technique, [13], simulated the planetary gear set model. After researching the different gear properties, they produced a finite-volume computational fluid dynamics (CFD) model of a dip-

lubricated planetary test gearbox. The impact of lubricant temperature on churning power loss is demonstrated in this article. A test rig built on the premise of the direct torque measuring technique is used to measure the influence of temperature.

II. MATERIALS AND METHODS

The input torque may be measured in a variety of ways when there is no load. Since the direct torque measurement method is more straightforward and harmonious with the gear pair, it was chosen to measure the worm gear pair's input torque. The churning power loss for the bevel gear and parallel axis of the gear was also examined using this technique [14-19]. A torque-measuring test machine that was specifically constructed was used for the experimental investigations. Figure 1 shows the test machine that was developed. The test apparatus consists of a motor, torque sensor, temperature sensor, variable frequency drive (VFD), bearing, shaft, test bed, couplings, and data collector. To permit the modification in rotational speed, the test stand is constructed with an electric motor that is controlled by a variable frequency drive. Via the shaft, torque sensor, and couplings, the motor is linked to the gearbox housing the test gear pair.

The torque sensor (with an accuracy of 0.01) is used to detect the torque at the test gear's input shaft. Temperature sensors (with an accuracy of 0.01) and pressure gauges (with an accuracy of 0.01), respectively, can be used to detect the temperature of the oil inside the gearbox and the air pressure inside the gearbox.

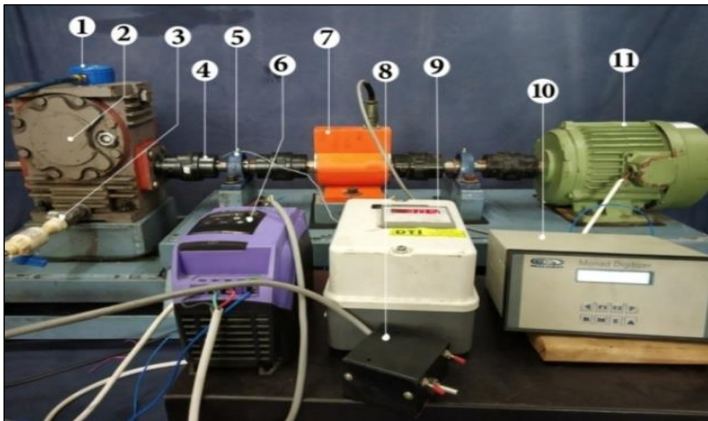


Figure 1: Test rig to investigate churning power loss of worm gear. Source: Authors, (2024).

1-Pressure Gauge, 2-Worm gearbox, 3-Provision for oil level indicator, 4-Jaw type coupling, 5-Foot mounted bearing, 6-Variable frequency drive (VFD), 7-Torque sensor, 8-VFD regulator, 9-Temperature indicator, 10-Digital controller for Torque sensor, 11-3-phase AC motor

Table 1: The geometric properties of the worm gear.

Reduction ratio	30:1	
Outer dia. (mm)	132	40
Center distance (mm)	75	
Pressure angle	20	
Module (mm)	3	
Material	CuSn12	16MnCr5
No. Of teeth	30	Single start
Gear	Worm Wheel	Worm Shaft

Source: Authors, (2024).

The test rig made it possible to study the effects of different working conditions, such as worm speeds, gear orientation (worm at the top and bottom), gear reduction ratio, temperatures, types of lubricant (mineral and synthetic), and immersion depth of the gear (lubricant volume), on input torque. The geometrical measurements and composition of a worm wheel and a single start worm are displayed in Table 1. It should be mentioned that just one geometry was chosen to examine the impact of rotational direction.

Table 2: Lubricant properties.

Sr. No	Name of oil	Kinematic Viscosity (cSt) @ 40 °C	Kinematic Viscosity (cSt) @ 100 °C	Viscosity Index	Density (Kg/m ³) @ 15 °C
Oil-A	Mineral oil	312	33	95	880
Oil-B	Synthetic oil	330	35.50	162	790

Source: Authors, (2024).

Table 3: Experimental parameters with their levels.

Control factors	Unit	Level 1	Level 2	Level 3
(A) Oil temperature	(°C)	30	40	50
(B) Speed (Revolutions) of worm	(rpm)	1000	1200	1400
(C) Oil Volume	(lit)	1.5	2.1	2.7

Source: Authors, (2024).

Lubricating oil is the blood of any rotating component [20]. The worm gear may be lubricated in several ways, but splash lubrication was employed in this experiment to measure input torque. Two distinct oils were utilized as lubricants, and Table 2 summarizes their properties. The 180mm x 180mm x 280mm test gearbox's volume remained unchanged. The lubricant was added to the gearbox and it spun at a specific speed, following the test matrix shown in Table 3. The input torque was measured by the lubricant temperature and level stated.

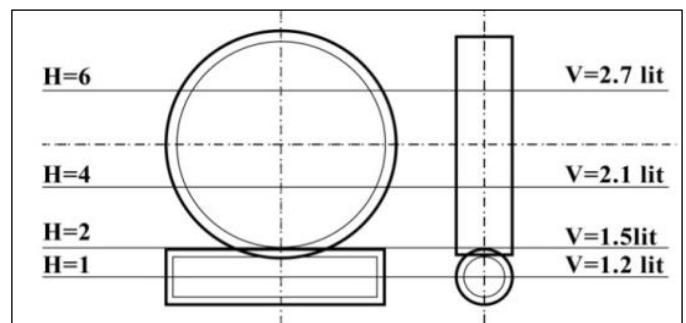


Figure 2: Static head of worm gearbox. Source: Authors, (2024).

The worm wheel and worm shaft levels cannot be explained in terms of a parallel-axis gearbox. Thus, for worms oriented at the bottom, as in Fig. 2, the static level of both is described from the base of the worm shaft; for worms oriented at the top, the same level is measured from the base of the worm wheel.

$$\text{Static Oil level } H = \frac{h}{r} \tag{4}$$

where h is the height of the oil level as measured from the worm shaft's base. where r is the worm shaft's outer (major) radius.

III. RESULT & DISCUSSION

The experiment was run at a temperature that was at least 5° C above the test's fundamental beginning point. The test had no time limit and continued until the target temperature was reached. To find out how rotation affected torque, the full test was conducted under particular setup and operating conditions. As seen in Table 4, the worm speed, lubricant (oil) temperature and lubricant (oil) volume, inside the gearbox were all varied during the trials. With the aid of the torque sensor, the response variable was the input torque, which was measured. In order to measure the churning power loss, the input torque and lubricant heating rate (time) were monitored for each experiment. Every time the temperature rose by 5°C, the input torque was monitored for a more precise study. The churning torque was determined using the input torque as a guide.

$$T_{ch} = T_{total} - T_{no-oil} \quad (2)$$

T_{ch} = Churning torque,

T_{total} = Input torque with lubricant,

$T_{no\ oil}$ = Input torque without oil.

Equation (2) can be used to determine the churning power loss based on the input torque (response variable).

$$P_c = \frac{2\pi N T_{ch}}{60} \quad (3)$$

P_c = Churning power loss

N = Worm speed

This churning power loss can be normalized by using one (maximum) reference power loss (P_{ref}) and the normalized churning power loss is given in equation (3).

$$\bar{P} = \frac{P_c}{P_{ref}} \quad (4)$$

III.1 REPEATABILITY EXPERIMENTS

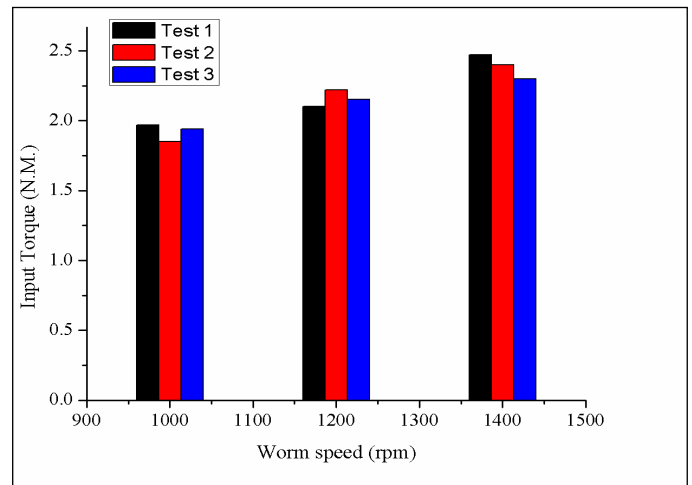
Two sets were chosen at various worm speeds in order to illustrate the measurement's reproducibility, as seen in Table 4. The repeatability of dip-lubricating the worm gearbox has been investigated through three separate trials conducted at various times for each set.

Table 4: Experiment set for repeatability.

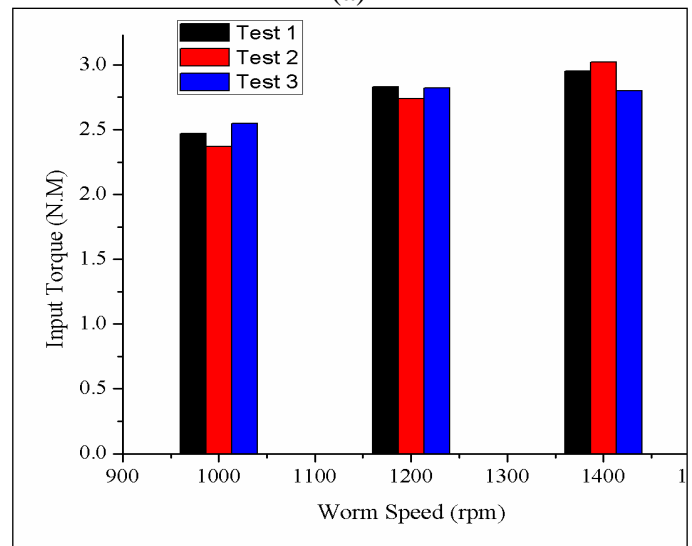
Set	Lubricant	Temperature of lubricant (°C)	Volume of lubricant (lit.)
1	Oil-A	50	2.1
2	Oil-B	40	2.7

Source: Authors, (2024).

The values obtained from three separate experiments at varying input speeds and lubricant characteristics are compared in Figures 2(a) and (b). The data provide an average variation of just 5% about the mean value for Oil B under specific conditions with an appropriate degree of repeatability, as shown in Figure 2(b), and 6.8% about the mean value for Oil A throughout the complete speed range, as shown in Figure 2(a). It demonstrates that the testing conditions and time had no effect on the experiments.



(a)



(b)

Figure 2: Repeatability experiment for worm gear pair at (a) Set 1 as per Table 4 (b) Set 2 as per Table 4.

Source: Authors, (2024).

III.2 Influence of Direction of Rotation

The readings taken from the experiments are given in Table no-5. Which shows the churning power loss and normalized power loss for synthetic lubricant and worm position at bottom. In this way the readings were taken for worm shaft at top position and also for mineral lubricants

Table 5: Experiment results of churning power loss for churning power loss with oil-B, Worm at the bottom position.

Sr. No	Factors			Response Variable	Calculated Responses		
	Worm Speed (rpm)	Lubricant Volume (Lit.)	Lubricant Temperature (C)	Input Torque (N.M)	Churning Torque (N.M)	Churning Power loss	Normalized Power loss
1	1000	1.5	30	2.70	1.25	130.90	0.37
2	1000	1.5	40	2.24	0.79	82.73	0.24
3	1000	1.5	50	1.99	0.54	56.55	0.16
4	1000	2.1	30	2.85	1.4	146.61	0.42
5	1000	2.1	40	2.36	0.91	95.29	0.27
6	1000	2.1	50	2.06	0.61	63.88	0.18
7	1000	2.7	30	2.90	1.45	151.84	0.43
8	1000	2.7	40	2.47	1.02	106.81	0.31
9	1000	2.7	50	2.19	0.74	77.49	0.22
10	1200	1.5	30	3.04	1.52	191.01	0.55
11	1200	1.5	40	2.53	1.01	126.92	0.36
12	1200	1.5	50	2.09	0.57	71.63	0.20
13	1200	2.1	30	3.24	1.72	216.14	0.62
14	1200	2.1	40	2.72	1.2	150.80	0.43
15	1200	2.1	50	2.21	0.69	86.71	0.25
16	1200	2.7	30	3.29	1.77	222.42	0.64
17	1200	2.7	40	2.83	1.31	164.62	0.47
18	1200	2.7	50	2.37	0.85	106.81	0.31
19	1400	1.5	30	3.06	1.39	203.78	0.58
20	1400	1.5	40	2.63	0.96	140.74	0.40
21	1400	1.5	50	2.21	0.54	79.17	0.23
22	1400	2.1	30	3.27	1.6	234.57	0.67
23	1400	2.1	40	2.78	1.11	162.73	0.46
24	1400	2.1	50	2.32	0.65	95.29	0.27
25	1400	2.7	30	3.38	1.71	250.70	0.72
26	1400	2.7	40	2.87	1.2	175.93	0.50
27	1400	2.7	50	2.43	0.76	111.42	0.32

Source: Authors, (2024).

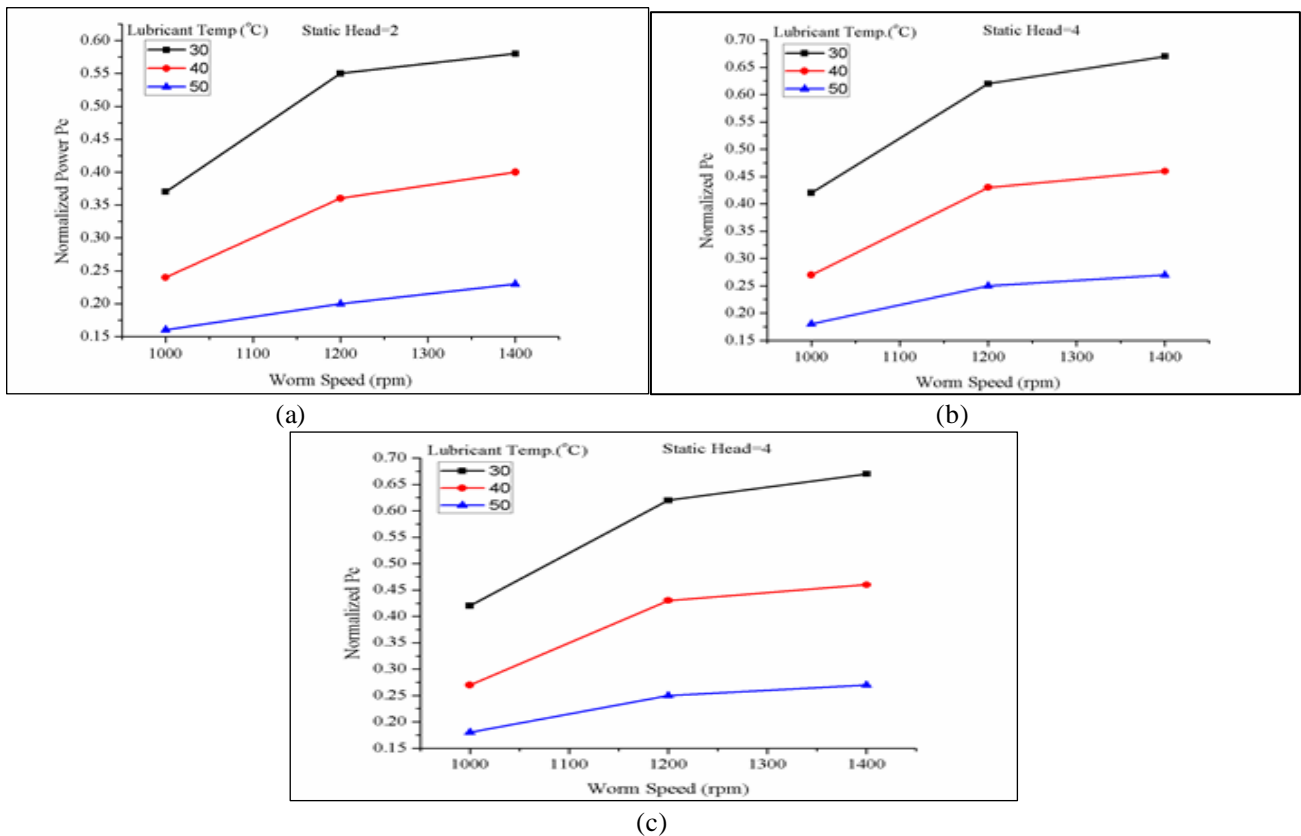


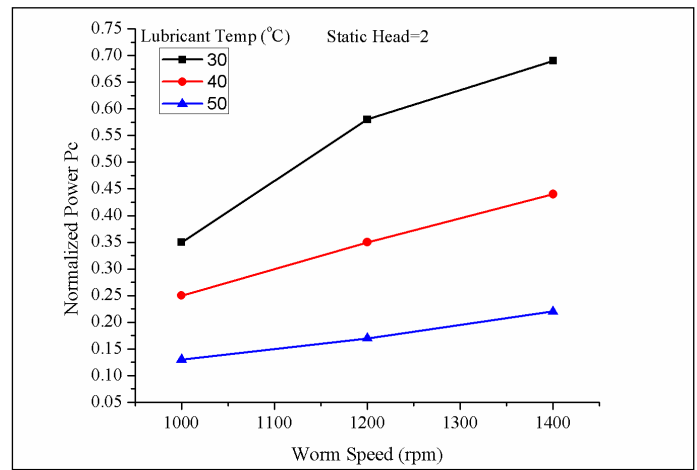
Figure 4: Influence of temperature on churning power loss with oil-B, Worm at the bottom position and gear pair-1 (a) Static Head=2 (b) Static Head=4 & (c) Static Head=6.

Source: Authors, (2024).

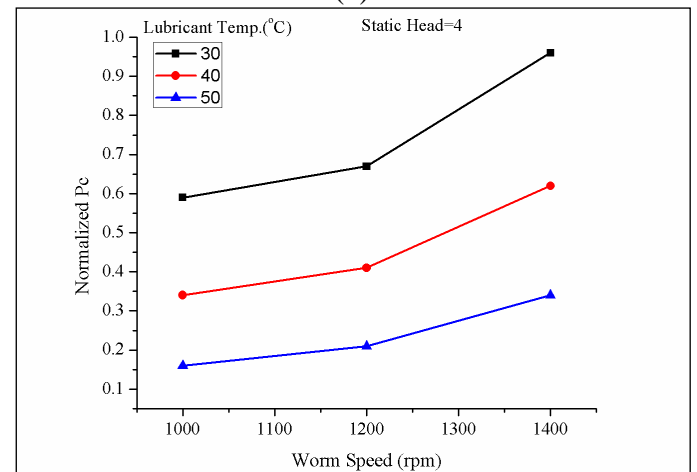
Figure 4 shows direct comparisons between the results at 30°C and 50°C to show how the lubricant temperature affects the churning power losses of the worm gear pair. One important factor that affects every aspect of power loss is the lubricant's viscosity. It has been demonstrated that reducing oil viscosity reduces gear churning power losses [13,17]. The viscosity of the lubricant decreases with temperature, making it a low-viscosity lubricant. Likewise, the lubricant is thought to have a higher viscosity at a lower temperature. Oil pushed upwards would return to the oil bath at the bottom in the direction of the gear's tangential velocity, when the $H < 2$ flow of fluid was such that a working oil level could be determined at a lower height than the static oil level. In the meantime, for $H > 2$ where fluid forms a vortex—a full, continuous circulation channel inside the test gearbox. The temperature of the bulk lubricant inside the test gearbox increased when a vortex was present. Figure 4(a) shows that the influence of lubricant temperature on the churning power loss of a worm gear pair at lower speed is insignificant for low immersion levels (static head $H \leq 2$). As seen in Figures 4(b) and 4(c), the oil temperature (i.e., kinematic viscosity) becomes increasingly significant for static head $H > 2$. The churning power loss is more impacted up to 1200 rpm at lubricant temperatures below 50 °C (temperature < 50 °C), and above that point, the normalized power loss increases at a steady rate. When the lubricant temperature is below 40°C, the power loss during churning remains very modest, even at 1200 rpm, compared to lower temperatures. The churning torques for the worm gear pair with the worm in the bottom, the speed of worm shaft at 1400 rpm, and the lubricant temperatures at 30°C, 40°C, and 50°C are 1.39, 0.96, and 0.54 N.m., respectively, and the corresponding power loss is 203.78, 140.14, and 79.17 watts when the churning torques are measured for lower static head $H=2$ (Volume=1.5 liter).

Similarly, for greater static head $H=6$ (Volume=2.7 liter), the corresponding power loss at 30°C, 40°C, and 50°C is 250.70, 175.93, and 111.42 watts, respectively, for the same torque. A 30% increase in churning power loss on average occurs when oil temperature is lowered from 50°C to 30°C at lower static head ($H \leq 2$). When oil temperature drops from 50°C to 30°C, there is an average 33% rise in P_c at higher static head ($H > 2$).

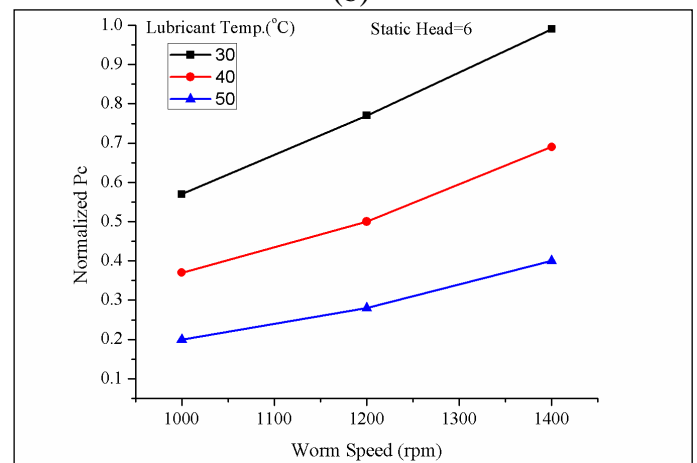
The noteworthy aspect is that the churning losses resulting from the lubricant at a lower temperature were not consistently greater than those resulting from the lubricant at a higher temperature. It was discovered that the churning power loss of lower static head and lower lubricant temperature for the oil-B, worm position at the bottom, was 22% smaller than the churning power loss of higher static head and higher lubricant temperature.



(a)



(b)



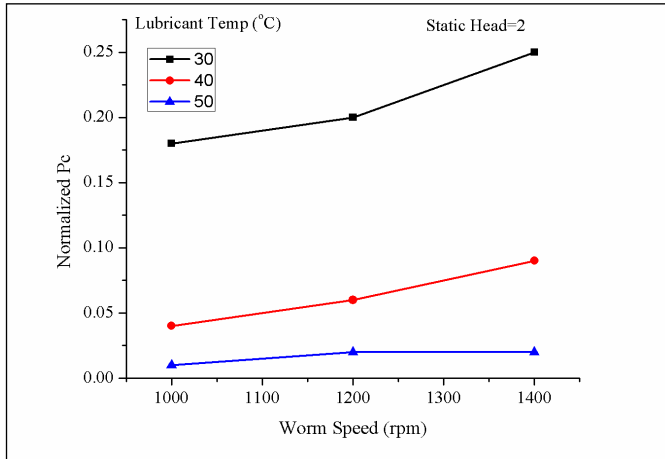
(c)

Figure 5: Influence of temperature on churning power loss with oil-A, Worm at the bottom position and gear pair-1 (a) Static Head=2 (b) Static Head=4 & (c) Static Head=6
Source: Authors, (2024).

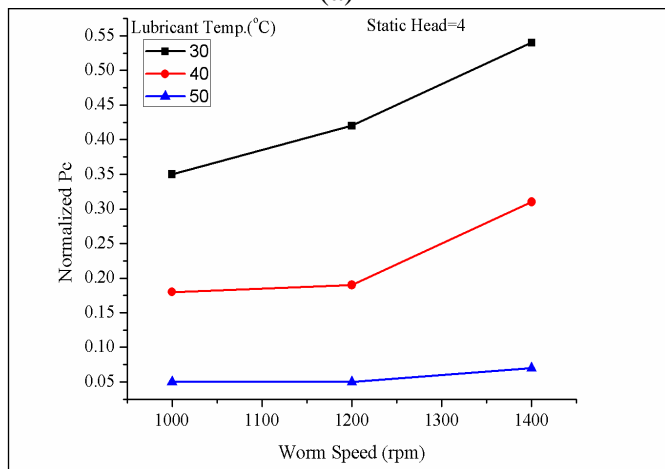
The type of lubricant used also affects how much temperature affects the churning power loss of worm gears. Figure 5 illustrates how temperature affects oil-A and the worm shaft at the bottom. When the oil temperature is lowered from 50°C to 30°C, there is an average 37% increase in churning power loss at lower static head ($H \leq 2$). At higher static ($H > 2$) head, churning power loss increases by an average of 50% when oil temperature is lowered from 50°C to 30°C. Similarly, the influence of temperature is determined by the location of the

worm shaft in the worm gearbox.

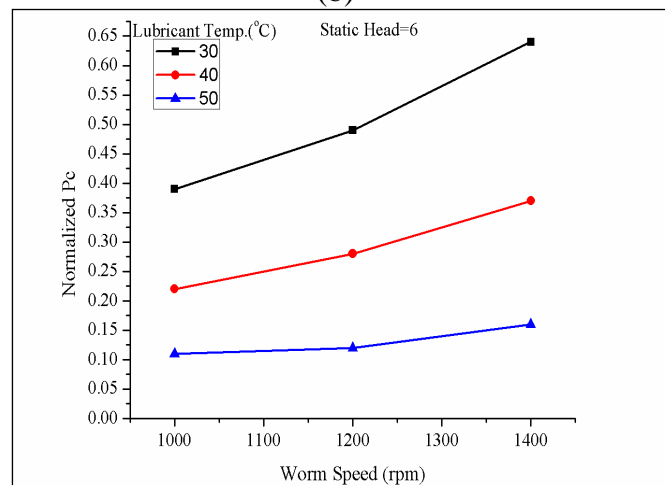
Figure 6(b) and (c) illustrate the average 38% increase in churning power loss at greater static head ($H>2$) when oil temperature is lowered from 50°C to 30°C . To reduce churning loss (loss that is dependent on no load), it is advantageous to select lubricant with the lowest feasible operating viscosity for practical applications. Higher temperatures cause a decrease in viscosity, which lessens the power loss during churning.



(a)



(b)



(c)

Figure 6: Influence of temperature on churning power loss with oil-B, Worm at Top position and gear pair-1 (a) Static head=2 (b) Static Head=4 & (c) Static Head=6.

Source: Authors, (2024).

IV. CONCLUSION

The purpose of the research was to find out how lubricant temperature affected the churning power loss for worm gears that were dip-lubricated. The lubrication level, worm shaft speed, lubricant temperature, and rotation direction were among the variable operating conditions that influenced the measurement, which relied on the direct torque measuring technique. The temperature of the lubricant has a significant impact on the churning of the worm gear, especially in the case of the deeply submerged state and increased worm speed in the bottom condition. Because viscosity changes with temperature, experiments conducted at lower temperatures consistently produced larger churning power losses than those conducted at higher temperatures. When oil temperature is lowered from 50°C to 30°C , there is an average 33% increase in churning power loss at greater static head ($H>2$). When the static head and lubricant temperature were lower, the churning power loss was 22% less than when the static head and lubricant temperature were greater. The present study investigated the effect of temperature on churning power loss for the worm gear only, Similarly other parameter effects can be obtained by the same experiments. It is also recommended to investigate the churning power loss for worm gear with jet lubrication. The CFD analysis is also most powerful tool to obtain the windage and churning power losses.

V. AUTHOR'S CONTRIBUTION

Conceptualization: G Chothani.

Methodology: H.G. Chothani

Investigation: D.J. Marsonia & S.H. Zala

Discussion of results: H.G. Chothani

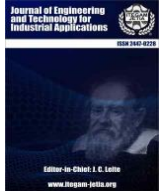
Writing – Original Draft: H.G. Chothani

Supervision: N.N. Jadeja.

VI. REFERENCES

- [1] A. Miltenovic, M. Bamic, N. Vitkovic, M. Simonovic, M. Peric, and D. Rangelov, "Investigation of the influence of contact pattern of worm gear sets on friction heat generation during meshing," *App. Science*, vol. 14, no. 2, pp. 1-14, 2024. <https://doi.org/10.3390/app14020738>
- [2] S. A. Polyakov, S. Y. Goncharov, M. N. Zakharov, and V. V. Lychagin, "Improving Worm Gear Performance by Optimal Lubricant Selection in Accelerated Tests, Russian Engineering Research," vol. 35, no. 4, pp. 253-255, 2015. <https://doi.org/10.3103/S1068798X15040206>.
- [3] S. R. Maity and S. Chakraborty, "A Visual Decision Aid for Gear Materials Selection," *Journal of The Institution of Engineers (India): Series C*, vol. 94, no. 3, pp. 199-212, 2013. <https://doi.org/10.1007/s40032-013-0080-2>.
- [4] H. G. Chothani and K. D. Maniya, "Comparative Investigation of Worm Positions for Worm Gear-box Performance under No-Load Condition," *Journal of Mechanical Engineering*, vol. 18, no. 2, pp. 111-124, 2021. <https://doi.org/10.24191/jmeche.v18i2.14967>.
- [5] M. Slavica, R. Sasa, V. Sandra, and A. Raed, "Optimization of efficiency of worm gear reducer by using taguchi-grey," *Applied engineering letters*, vol. 2, no. 2, pp. 69-75, 2017. <https://www.aeletters.com/wpcontent/uploads/2017/11/AEL00050.pdf>.
- [6] T. N. Babu, D. Patel, and D. Thamari, "Temperature Behavior-Based Monitoring of Worm Gears Under Different Working Conditions," in *Innovative Design, Analysis and Development Practices in Aerospace and Automotive Engineering*, Springer Singapore, 2018, pp. 257-265. https://doi.org/10.1007/978-981-13-2718-6_24.

- [7] Y. Jiang, X. Hu, Y. Dai, C. Luo, and L. Feng, "Churning power losses of a gearbox with spiral bevel geared transmission," *Tribology International*, vol. 129, pp.398–406, 2018.<https://doi.org/10.1016/j.triboint.2018.08.041>.
- [8] J. Polly, D. Talbot, A. Kahraman, A. Singh, and H. Xu, "An Experimental Investigation of Churning Power Losses of a Gearbox," *Journal of Tribology*, vol. 140, no. 6, pp. 1–8, 2018. <https://doi.org/10.1115/1.4038412>
- [9] H. G. Chothani and K. D. Maniya, Experimental Investigation on Churning Power Loss of Splash Lubricated Worm Gea, *Periodica Polytechnica Mechanical Engineering*, vol.67(3),pp. 175-182.2023. <https://doi.org/10.3311/PPme.19965>
- [10] X.Ju, and Y.Dai "Development of an analytical model to predict the churning power losses of an orthogonal face gear,"*Energy Science and Technology, an international Journal*, vol. 41, pp. 1-9,2023.<https://doi.org/10.1016/j.jestch.2023.101383>.
- [11] Y. Wang, W. Tang, Y. Chen, T. Wang, G. Li, and A. D. Ball, "Investigation into the Meshing Friction Heat Generation and Transient Thermal Characteristics of Spiral Bevel Gears," *Applied Thermal Engineering*, vol. 119, no. 1, pp. 245–253,2017.<https://doi.org/10.1016/j.applthermaleng.2017.03.071>.
- [12] Y. Jiang, X. Hu, Y. Dai, C. Luo, and L. Feng, Churning power losses of a gearbox with spiral bevel geared transmission, *Tribology International*, vol. 129, no. 1, pp. 398–406, 2018,<https://doi.org/10.1016/j.triboint.2018.08.041>
- [13] H. Liu, P. Standl, M. Sedlmair, T. Lohner, and K. Stahl, "Efficient CFD Simulation Model for a Planetary Gearbox," *Forschung im Ingenieurwesen*, vol. 82, no. 4, pp.319–330, 2018.<https://doi.org/10.1007/s10010-018-0280-2>.
- [14] A.Skulic,M.Bukvic,S.Gajevic,S.Miladinovic and B.Stojanovic "The influence of the worm gear material and lubricant on the efficacy and coefficient of friction," *Tribology and material*, vol. 3, no. 1, pp.15-23, 2024. DOI:10.46793/tribomat.2024.001.
- [15] G. Leprince, C. Changenet, F. Ville, P. Velex, C. Dufau, and F. Jarnias, "Influence of Aerated Lubricants on Gear Churning Losses – An Engineering Model", *Tribology Transactions*, vol.54 no.6, pp 929-938, 2011.<https://doi.org/10.1080/10402004.2011.597542>
- [16] C. Changenet, G. Leprince, F. Ville, and P. Velex, "A Note on Flow Regimes and Churning Loss Modeling," *Journal of Mechanical Design*, vol. 133, pp. 1–5, 2011.<https://doi.org/10.1115/1.4005330>.
- [17] P. Luke and A. V. Olver, "A study of Churning Losses in Dip-Lubricated Spur Gear," *Proceedings of the Institution of Mechanical Engineers, Part G: Journal of Aerospace Engineering*, vol. 82, no. 1, pp. 337–346, 1999.<https://doi.org/10.1243/0954410991533061>.
- [18] S. Seetharaman, A. Kahraman, M. D. Moorhead, and T. T. Petry-Johnson, Oil Churning Power Losses of a Gear Pair: Experiments and Model Validation, *Journal of Tribology*, vol. 131, no. 2, pp. 022202-1–10, 2009.<https://doi.org/10.1115/1.3085942>
- [19] S. Laruelle, C. Fossier, C. Changenet, F. Ville, and S. Koechlin, "Experimental investigations and analysis on churning losses of splash lubricated spiral bevel gears," *Mechanics & Industr*, vol. 18, no.4, pp. 41201–41210, 2017. <https://doi.org/10.1051/meca/2017007>.
- [20] M. kallas, M.Saed, and Y.Saoud, "Experimental Comparison of the Effect of Using Synthetic, Semi-Synthetic and Mineral Engine Oil on Gasoline Engine Parts Wear", *Advances in Tribology*, vol.2024,pp. 1-12, 2024.<https://doi.org/10.1155/2024/5997292>



RESEARCH ARTICLE
ACCESS

OPEN

INTERFERENCE REDUCTION SCHEME FOR FEMTOCELL ULTRAL-DENSE-NETWORK: CONCEPT AND RESEARCH CHALLENGES

Adekogba, G.V.¹, Adedeji, K.B.² and Olasoji, Y.O.³

^{1,2,3}Department of Electrical and Electronics Engineering, The Federal University of Technology Akure, Ondo State, Nigeria.

¹<http://orcid.org/0009-0005-4126-3813> ²<http://orcid.org/0000-0002-2975-2965> ³<http://orcid.org/0000-0002-1978-1931>

Email: pelumivictor19@gmail.com, kbadedeji@futa.edu.ng, yoolasoji@futa.edu.ng

ARTICLE INFO

Article History

Received: May 19th, 2024

Received: October 12th, 2024

Accepted: October 15th, 2024

Published: October 31th, 2024

Keywords:

Femtocell,

Graph coloring,

Frequency assignment,

LTE,

Ultra-dense network.

ABSTRACT

In recent times, the demand for mobile broadband communications has increased exponentially due to the creation of new multimedia applications. To cater for this trend, dense deployment of cellular networks with aggressive frequency reuse patterns has been proposed. In this regard, densification of femtocells is a promising concept to meet growing mobile service requirements and for sustainability of users' Quality of Service (QoS). However, an ultra-dense network (UDN) faces serious interference problems. One of these is the Inter-Cell Interference (ICI) caused by the simultaneous usage of the same spectrum in different cells. The problem becomes more complex when femtocells are located on cell edge area of macrocell. ICI reduces system throughput and network capacity, and has a negative impact on cell-edge users. Therefore, reducing the effects of interferences is an important issue in UDN. Hence, a critical issue arises: are conventional reduction schemes still effective to tackle the interference in UDN? To shed light on the problem, this paper provides a comprehensive survey of the methods for reducing interference in femtocell UDN. This survey aimed to provide a concise introductory reference for early researchers in the development of interference reduction schemes in femtocell. These methods are classified based on the nature of operation, investigated as to their strengths and weaknesses, and then examined via several research studies which make use of each approach. Furthermore, technical challenges in each research study were identified. Finally, some remarks for enhancing the research study were provided and potential directions for future research were highlighted.



Copyright ©2024 by authors and Galileo Institute of Technology and Education of the Amazon (ITEGAM). This work is licensed under the Creative Commons Attribution International License (CC BY 4.0).

I. INTRODUCTION

Since the introduction of intriguing mobile devices and multimedia applications, user demands for wireless data communications in cellular networks have been rising quickly. Applications with high traffic volumes have a significant impact on increasing the data rate. According to a study by Kovacs [1], there has been a significant increase in the demand for mobile data traffic over the past five years, as seen in Figure 1. Additionally, since consumers pay telecommunications firms more for data services than for voice-only services, they anticipate higher-quality services. Because of the numerous walls and obstructions found indoors, the channel quality between the mobile node and the cellular base station may be poor. As a result, indoor wireless communication systems need to be built

with the necessary service quality in mind for consumers. Even so, as 90% of data traffic and over 60% of voice traffic are anticipated to be generated indoors, the scarcity of wireless resources in cellular networks will worsen [2]. Unquestionably, more network infrastructure is needed in order to increase cellular network capacity.

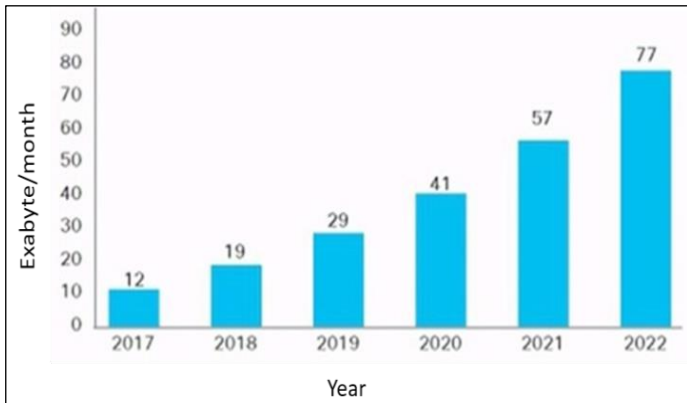


Figure 1: Global mobile data traffic from 2017 to 2022. Soucer: [1].

The application of femtocells placed on top of the conventional macrocell-based cellular networks is a crucial subject for the economical installation of new infrastructure [3]. A femtocell is an inexpensive, small-sized cellular base station that uses low power. It can be implemented by service providers or customers anywhere wired IP access is available. Given that this low-cost femtocell is typically installed indoors and linked to the backhaul via a general IP connection, such as digital subscriber line (DSL), with cable modem and fiber-to-the-home (FTTH), cellular networks can secure wireless resources more affordably while enabling customers to use high-speed, low-power wireless data communications. On the other hand, demonstrating a higher number of channels per area (cell) usually increases capacity. This can be achieved by increasing channel reuse by decreasing the area of each cell. Cellular service demand can also come from indoor sources. Previous research in [4] have revealed that 18% of phone conversations and data sessions start indoors. The in-building wireless market is expected to grow rapidly by \$18 billion by 2025 due to rising consumer data usage and the growing demand for smartphones [4]. Given that more sophisticated multimedia applications are anticipated to be deployed, it is inevitable that the capacity demand for indoor communications will continue its horrifying upward trend. Therefore, in order to support the multitude of data traffic-intensive applications, more sophisticated indoor communication networks are needed. By nature, buildings are physical barriers to wireless communications which may lead to penetration losses. Consequently, quality of services may be compromised. Thus, reliable and quality of service is essential for indoor users. Due to the penetration losses, the indoor user requires high power from the serving Base Station (BS). It is also very expensive to have a large number of outdoor BSs to meet the needs of a high capacity network. The large number of BSs would pose larger burden on network planning and optimization. Femtocells have been widely used in wireless communication systems as a solution to this issue because of their many benefits, including enhanced indoor coverage, low cost, and energy efficiency [5]. In order to achieve this, a large number of densely deployed femtocells, referred to as an ultra-dense network (UDN), are anticipated to underlay the current macro network. Large-scale femtocell deployments have the potential to increase wireless network interference. The effective deployment of femtocell networks is hampered by this interference, which reduces network performance, particularly when adjacent femtocell frequencies overlap [6]. Due to the potential of femtocell to improve indoor localization and coverage, reducing the interference level generated by the densely

deployed cells has been a focus of many research studies [7-10]. In this paper, a survey of different scheme for reducing interference level in femtocell network is presented.

II. FEMTOCELL CONCEPT

Femtocells are majorly used for indoor radio coverage. They provide nearly all cellular functionalities to users and are installed indoors by the user, much like a Wi-Fi router [11-13]. The user's broadband internet connection is then used to link the femtocell Access Point (FAP) to the operators' core network. Figure 2 depicts the link between an end user and the mobile operators' core network. Figure 3 depicts a typical indoor femtocell deployment. The femtocell in this scenario allows various indoor User Equipment's (UEs) to connect to the FAP and make use of voice and data services. Femtocells, also known as Home Node B (HNB) in WCDMA systems and Home e Node B (H(e)NB) in LTE systems, are standardized since 3GPP release 8 and employ physical layer technology comparable to that of cellular networks. A crucial feature of 3GPP release 8's femtocells is the Closed Subscriber Group (CSG). Every H(e)NB has an access mode that only allows limited and registered UEs to connect; all other UEs are unable to access it since their connection is refused. These H(e)NB are utilized in homes and small offices. Release 9 improves this control over access modes by offering hybrid and open access modes. Every user has the ability to ad hoc deploy femtocells within a macro cell and even relocate them from one place to another within their residence. As a result, operators find it difficult to dynamically manage radio resources [14–15].

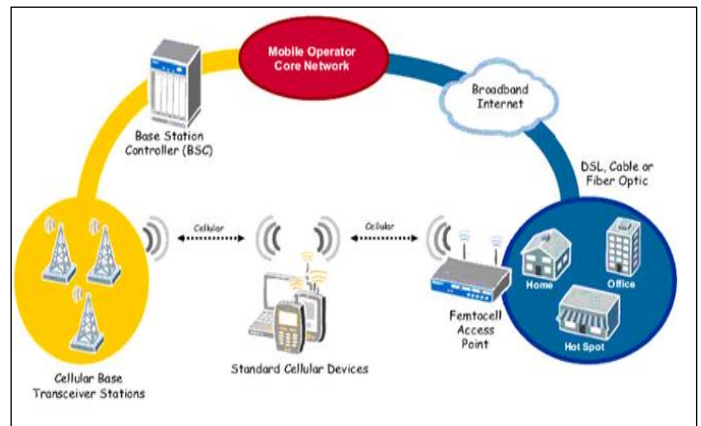


Figure 2: UE connected to an operator's core network in a femtocell.

Source: Authors, (2024).

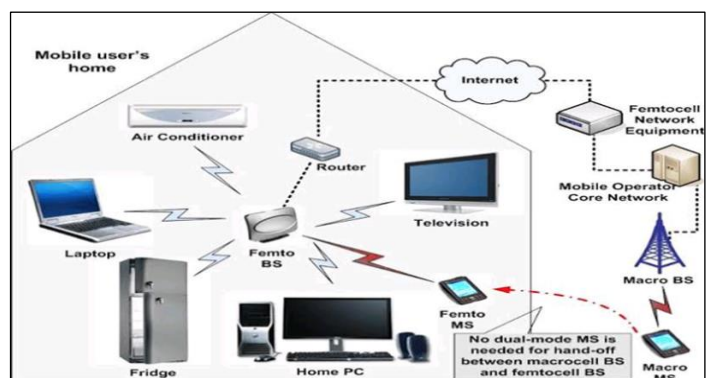


Figure 3: UE connected to an operator's core network in a femtocell.

Source: Authors, (2024).

In order to ensure that it is aware of its surroundings, it also needs effective self-organizing mechanisms. Distributed optimizing approaches should be used to reduce interference. Apart from potential spectrum shortages during dense co-channel femtocell deployment, opportunistic spectrum access is another feature that femtocells should have. This means that in order to be more intelligent, femtocells must possess cognitive functions. Cognitive femtocells are femtocells that possess cognitive functions. This is because of its additional features, which may offer effective answers to the problems that dense femtocell deployment may present in the future [16–18]. Cognitive femtocells can identify any empty spectrum areas (also known as spectrum holes or white spaces) by detecting spectrum in their immediate surroundings. The cognitive femtocells then make use of these spectrum gaps to give their users connectivity. Their ability to collaborate and synchronize with nearby cognitive femtocells allows for more precise spectrum detection. When spectrum holes are unavailable, cognitive femtocells can function similarly to regular femtocells by using the licensed band [19–20]. The idea of femtocells first appeared in the 1999 where Bell Labs first studied a home base station. The Alcatel announced a GSM based home base station to be brought to the market in 2000 [21]. Although their demonstration devices demonstrated functionality over a Plain Old Telephone System (POTS) line, the equipment's exorbitant cost prevented them from becoming commercially successful. Following this, Motorola unveiled their 3G home base station in 2002, although the idea was still somewhat novel [21]. The term "femtocell" was first used in 2006; however this concept became widely recognized in 2005.

II.1. TECHNICAL AREA OF FEMTOCELLS

Femtocells present an improved solution to the indoor coverage problem. Their small cell radius essentially reduces the distance between transmitter and receiver, resulting in less attenuation of the transmitted signal and a good Received Signal Strength (RSS) for the receiver. Typically, the quality of a signal at the receiver is measured in terms of the signal to interference Noise ratio (SINR), which is a function of the transmitted power from the desired base station (BS), transmitted power from interfering transmitters, shadowing, fading, and path losses [22]. The SINR is a function of the transmitted power from the desired base station (BS), transmitted power from interfering transmitters, and shadowing, fading, and path losses. The weak interfering signals are caused by walls' penetration losses. Due to their high bit rate operation, higher frequencies—which are frequently employed in 3G technology show a greater loss of signal strength. Femtocells use this insulation in the form of these losses to communicate at low power levels while preserving high-quality interior coverage. Femtocells can offer high data rate services to users by using more sophisticated modulation and coding algorithms when the channel circumstances are favorable. Furthermore, a femtocell may dedicate a large amount of its resources to the users that are accessible because it typically serves a smaller number of users (home residents/office workers) than a macro cell (for example, Vodafone femtocells can handle a maximum of four users). Femtocells can offer better (QoS) to their consumers than macrocells, which must serve more users concurrently over a greater region [23]. Femtocell installations can be done in two primary and popular ways [13]. Both the co-channel and distinct channel deployments. A dedicated channel that is not utilized by the macrocell is set aside for the femtocell network in a separate channel deployment. By using the same channels as the

macrocell in the co-channel deployment, interference between femtocell and macrocell users can be avoided [23]. The operators strongly like this since it could be costly to set aside a specific amount of spectrum for femtocells because spectrum is a valuable resource. Additionally, the co-channel deployment greatly expands the system's total capacity. The possibility of users of femtocells and macrocells interfering with one another increases with co-channel implementation [23]. Therefore, effective and thoughtful interference management is necessary for a co-channel femtocell deployment to be successful. Femtocells, with their increased capacity, also offer a practical answer to issues with coverage outdoors. Femtocells are able to fill in the coverage gaps in a macrocell's footprint. In this sense, the femtocell can cover macro cellular users in the vicinity and within its coverage radius of the femtocell. This property of femtocells can be of importance at the macrocell edges. In a femtocell, the femtocell access point's (FAP) capacity to operate as a BS is crucial. While there are some parallels between the FAP and Wi-Fi access point, there are also some differences. Since both rely on the internet as a backhaul network, the backhaul is primarily responsible for the QoS. However, the FAP implements cellular technology while Wi-Fi are WLANs and mainly used for data services [24]. Table 1 shows the main difference between femtocells and Wi-Fi. Several FAPs have been developed by various manufacturers as reported [25–28]. Different air interface technologies coexist nowadays, which leads to the development of various kinds of femtocells based on different technologies. For example, 2G and 3G femtocells have been developed. Femtocells with newer technology like LTE and WiMAX are being developed.

Table 1: Differences between femtocells and Wi-Fi network.

Specification	3G Femtocell (HSPA)	Wi-Fi
Data rate	7.2-14.4Mbps	11Mbps
Operational frequency	1.9-2.6GHz	2.4-5GHz
Power	10-100mW	100-200Mw
Service	Primarily voice and data	Voice and data
Range	10-30m	100-200m

Source: Authors, (2024).

The selection of a femtocell based on a particular technology depends on the need of the user. Figure 4 illustrates the main types of femtocells depending on the technology used. Each of these types is discussed accordingly.

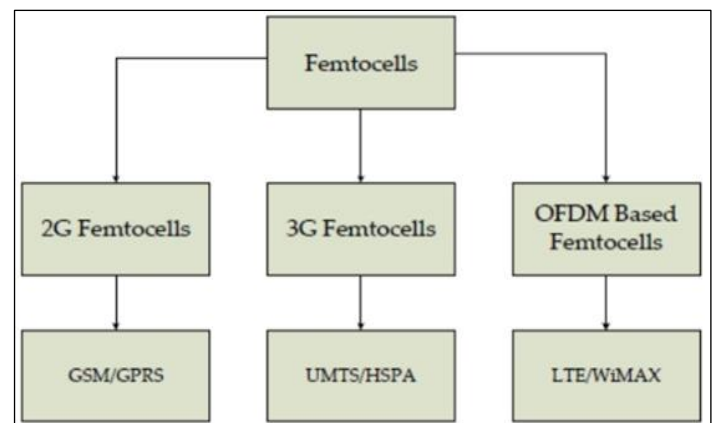


Figure 4: Femtocells type based on technology used on the air interface technology.

Source: Authors, (2024).

(i) **2G Femtocell:** The 2G femtocells are based on the Global System for Mobile Communication (GSM) air interfaces. Majority of the manufacturers concentrate on the production of 3G femtocells, when compared with the old GSM, however, GSM holds a huge number of subscribers around the world. Many developing countries like India and Pakistan are still expanding the GSM cellular network, in such a scenario, providing users with 3G and beyond femtocells would be of no use [29]. Low cost is one of the main reasons for the development of 2G femtocells, as compared to the newer versions [30]. One good example is the development and improvements of GSM femtocells by Ericsson in 2007 [31]. 2G, or second-generation mobile technology, introduced digital voice communication and limited data services. The data rate for 2G typically ranged from 9.6 kbps to 64 kbps, providing basic internet access, email, and SMS.

(ii) **3G Femtocell:** These femtocells are primarily based on the UMTS Terrestrial Radio Access (UTRA) air interface, which allows them to provide higher data rates than 2G femtocells [32]. The UMTS technology can connect through IP-based networks, which makes it more suitable for femtocells. In contrast to GSM-based femtocells, 3G femtocells have better power allocation schemes, which can be used to prevent interfering with the usage of macrocells [33]. The UMTS femtocells are also standardized by the 3GPP as HNBs. This motivates manufacturers to produce these kinds of femtocells. HSPA femtocells, which provide higher-quality services, are femtocells that have been designed with extra improvements in UMTS [34, 35]. A set of mobile telecommunications standards known as 3G, or third generation, were unveiled in order to improve data transfer speeds and open up new applications beyond simple messaging and phone calls.

(iii) **OFDM based Femtocell:** Examples are WiMAX and LTE femtocells. As the name implies, the physical layer technology used by these femtocells is orthogonal frequency division multiplexing, or OFDM. The primary indoor technology of the future is thought to be LTE femtocells, which are better recognized. The end consumers can receive a range of high data rate services from these femtocells [36]. It is also a hot research area nowadays and a lot of research is going on in order to efficiently execute LTE femtocells in the future [28-34]. OFDM (Orthogonal Frequency Division Multiplexing) based femtocells are small cellular base stations deployed in indoor environments to enhance wireless coverage and capacity.

Table 2 presents a comparison of the OFDM-Based femtocell with other femtocell network types. In terms of the data rate, OFDM-based femtocells can offer data rates comparable to or even higher than traditional macrocell networks, typically ranging from a few Mbps to several tens of Mbps e.g. 200mbp. This allows for high-speed internet access, video streaming, and other data-intensive applications within homes or small businesses. Also, OFDM uses a modulation technique that divides the available spectrum into multiple orthogonal subcarriers, which are then modulated with data. This technology allows for efficient use of the spectrum and mitigates the effects of multipath interference, making it well-suited for indoor environments where signal propagation can be challenging.

Table 2: Overview of the femtocell network types.

Technology	2G	3G	OFDM Based Femtocell
Data rate	14-64kbps	2mbps	200mbps
Technology	TDMA	Broad bandwidth/ CDMA/IP technology	Unified IP and seamless combo of LAN/WAN/WLAN
Service	Digital voice, short messaging	Integrated high quality audio, video and data	Dynamic information variable devices access
Power allocation	Low	Low	High
Switching	Circuit /circuit for access network and air interface	Packet except for air interface	Packet except for air interface
Core network	PSTN	Packet network	Internet

Source: Authors, (2024).

II.2 FEMTOCELL ULTRA-DENSE NETWORKS

The network's deployment was modified from the conventional macro cell-only network, which was dispersed across the macro cell's service region. It is now possible to increase network capacity by 1000 times by deploying ultra-dense tiny cells in a Heterogeneous Network (HetNet) in which small cells are as shown in Figure 5, UDN consists of UEs, moving nodes, network server/controller, macro Base Stations (BS), densely deployed small cells, and moving nodes. The increasing number of UEs can be supported by a large number of tiny cells, as shown in Figure 5, and the mobile UEs handle connection, disconnection, searching, and reconnection.

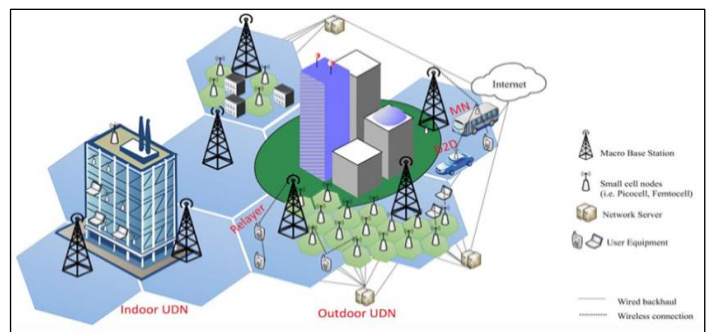


Figure 5: An example of a UDN.

Source: [37].

Furthermore, Device to device (D2D) communication must be available for the UEs at a cell edge to use relaying (as a forwarding node) for connection. Similarly, the moving nodes can facilitate vehicle-to-vehicle (V2V) communication. The following are the main characteristics of the UDN:

- (i) **A large number of access points and small cells (more than or equal to the number of UEs).** Similar to how close proximity and spectrum sharing function in macro cells, the abundance of small cells can enhance frequency reuse. By shifting macrocell traffic, distributing network loads, and clearing congestion, the dense small cells increase the network's capacity.
- (ii) **Dense and richly interconnected cross-tier deployment.** This includes relay, D2D linkages, macro cells,

small cells (such Pico and Femto), and other components that add to the overall complexity of the network environment. The overlapping region receives transmissions of several frequencies due to the multi-tier deployment (e.g., macro cell and small cell). Similarly, a high frequency reuse factor results from small cells' close proximity to one another. Thus, in order to mitigate intra-tier interference (such as macro-macro and small-small), inter-tier interference (such as macro-small), and facilitate resource management (such as energy and spectrum), enhanced interference coordination is required [38].

(iii) **Fast access and flexible switching (e.g., handovers).** The mobile user equipment (UE) may regularly switch the connection between access nodes in a densely deployed environment in order to guarantee optimal connections, improved service etc. Excellent handover (HO) performance is required to ensure connections are seamless and easy to use.

II.3 ULTRA-DENSE NETWORK TAXONOMY

UDN are grouped based on access point and network connectivity. The former has to do with the particular connectivity paradigm that is applied. It encompasses a variety of access technologies and architectures for network access. Figure 6 displays the UDN taxonomy. This section covers each of these categories.

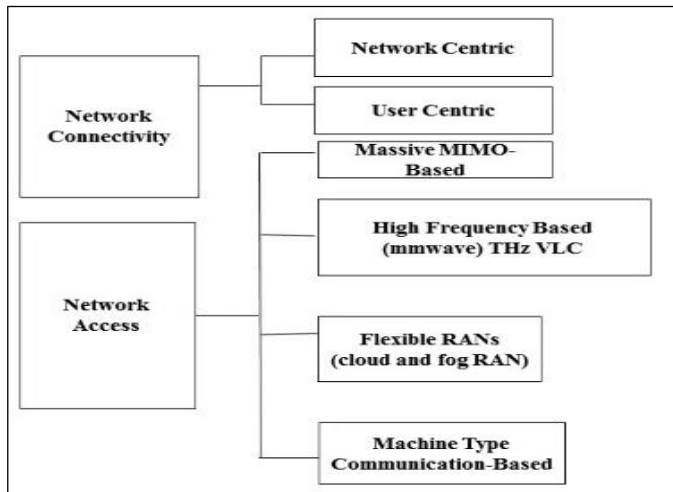


Figure 6: Taxonomy of ultra-dense networks. Source: Authors, (2024).

II.3.1 NETWORK CONNECTIVITY

Under the network connectivity, there are two categories. These are network centric and user-centric.

(i) Network-Centric Connectivity

A network centric connectivity's typical architecture is shown in Figure 7. The Heterogeneous Ultra-dense Networks (HUDNs) represent the foremost instance of implementing the concept of network-centric connection. HUDNs were made up of a range of access technologies, each with unique limitations and capabilities. One of the primary methods for boosting the capacity of next-generation wireless networks is to effectively reuse spectrum over the region of interest, which is made possible by this [39–41].

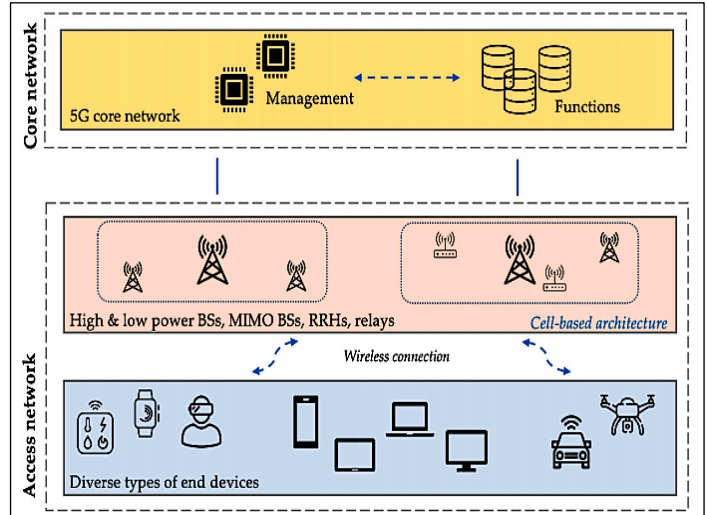


Figure 7: Network-centric connectivity architecture. Source: Authors, (2024).

An HUDN typically consists of three different types of cells: (a) fully functional, high-power macrocells, also known as legacy cells; (b) fully functional small cells, also known as picocells and femtocells, which can perform macrocell functions in a smaller coverage area and with less power; and (c) macro extension APs, such as relays and remote radio heads (RRHs). Macrocells are composed of external eNodeBs (eNBs) that the operator has strategically placed to allow for unrestricted public access across a broad area, typically several kilometers. However, picocells are low-power, fully functional eNBs that may be used both indoors and outdoors. They are typically delivered by a provider in accordance with a certain plan. The backhaul and access features of macrocells are also shared by picocells. Allowing for low latency and high bandwidth. Femtocells are widely utilized for interior applications (in homes, workplaces, conference rooms, etc.). With an average transmission power of 100 mW or less, these are ad hoc low-power access points. Depending on its level of access, a femtocell can operate in one of three modes: open, closed, or hybrid. Relays are access points that the operator installs and uses to cover dead zones and limited coverage areas in macrocells, much like macro extension access points. The Users' data is transmitted back and forth between the macro cell and the relays, which in this instance are merely macro eNB extensions rather than fully functional APs. Finally, to enable the core eNBs to cover a wider area, the RRHs are small, lightweight RF devices that are placed outside of macrocells. The RRH does not have a baseband unit (BBU). RRHs are connected to the BBU pool or Macro eNB (MeNB) by millimeter waves or high-speed fiber. BBU pools or central eNBs manage all signal processing. As a result, instead of distributed densification, RRHs are utilized to give centralized densification. RRHs can be simple and inexpensive to manage. Table 3 briefly presents the characteristics of various AP/cell types in HUDNs.

Table 3: Comparison of the HUDNs cell type features.

Type of AP/Cell	Deployment Scenario
Macrocells (fully functioning)	Outdoor (planned)
Picocells (fully functioning)	Indoor/outdoor
Femtocells (fully functioning)	Outdoor
Relays (macro-extension)	Indoor/outdoor
RRHs (macro-extension)	Outdoor

Source: Authors, (2024).

(ii) User-centric connectivity

Due to dense deployment and very large coverage overlap, AP distribution in a UDN is particularly challenging. This means that severe inter-cell interference, high signaling overhead, and challenges with resource management will arise from the conventional network-centric (cell-based) connectivity method. Furthermore, because of the uneven cell design, some users will be positioned in areas that overlap and cause a lot of interference, while other users might be found at the cell border or in an area without service. Situations like these will have a big impact on the overall quality of service. In [42], a paradigm-shifting user-centric UDN is suggested in order to effectively utilize UDNs' potential. UDNs define a development in the UDN notion by using the de-cellular technique to shift the design concept from a cell-centric to a user-centric paradigm [43–44]. In a UDN, every base station turns into an access point. To provide dependable access and data transfer, the network establishes an AP group (APG) for every user (Figure 8). Because of this, the idea of user-centric connectivity can be explained as a cell-less structure in which the access point group replaces the conventional cell unit.

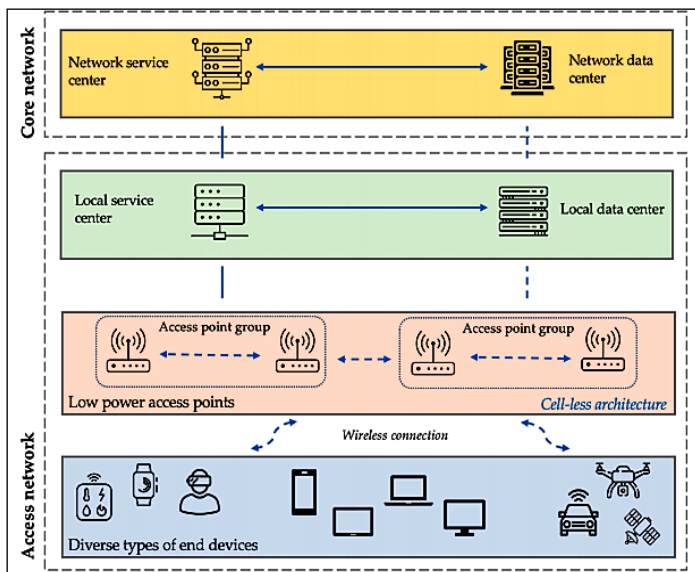


Figure 8: User-centric connectivity. Source: Authors, (2024).

Moreover, every AP that was taken into consideration for HUDN deployment might be used for UDN. One of the main planned benefits of UDNs is that the UDN network can identify the unique capabilities, specifications, and radio environment of the end devices automatically. Furthermore, APGs are created and constantly updated based on the needs of the end devices as well as their location. All of the APs in this particular scenario are able to collaborate and share data to improve user experience and energy/spectrum efficiency (EE/SE). Lastly, to guarantee the highest levels of security and protection, network authentication processes are carried out [45]. Table 4 provides a comparison between the network-centric and user-centric solutions. It is clear that a user-centric approach is more dynamic and able to offer a wider range of flexible connectivity possibilities. Furthermore, because the idea of cell construction has been replaced by the dynamic grouping of APs, which continuously monitor the behavior of EDs, the user-centric approach eliminates the necessity for handover. Aps are able to collaborate more cleverly as a result, which greatly enhances system performance, resource efficiency, and interference resistance. Finally as previously

mentioned, HUDNs and UUDNs employ asymmetric connectivity because of the many AP types, point-to-multipoint communications, dynamic resource access, etc.

Table 4: Comparison between network-centric and user-centric concept.

Aspect	Network-Centric	User-Centric
Network architecture	Network-centric cellular structure	User-centric de-cellular structure
Serving entity	Single serving BS	Dynamic APGs
Mobility management	Handover and terminal	Dynamic grouping of APs without involvement of terminal
Connectivity	Symmetric	Asymmetric
Network sensing	Incapable	Capable
Radio resource management	independent cell unit	Cooperation, user-centric
Interference management	independent cell unit	Cooperation, user-centric

Source: Authors, (2024).

II.3.2 Network Access

Under network access, there are four other subcategory of UDN. This includes, Massive multiple input multiple output (MIMO)-based access, high frequency-based access, and Flexible RAMs and Machine-type Communication-based access

(i) Massive MIMO-Based Access

Large-scale antennae systems, also known as Hyper MIMO, are systems that use a significant number of service antennae across active terminals and operate in the time-division duplex mode by focusing energy into ever-smaller sectors of space. Massive MIMO-capable base stations (BSs) will have hundreds, if not thousands, of antennae. This could be considered one way to spatially densify the network, as projected by 5G use cases [46]. Any given resource unit of a certain BS can provide a greater number of users, yielding substantial benefits. By combining low-cost, low-power components with less complex signal processing methods, massive MIMO can provide ultrahigh reliability, improved throughput and radiated EE, resilience to intentional interference, and decreased latency as compared to standard MIMO [47].

(ii) High Frequency-Based Access

The mmWave communication is thought to be the superior choice because a significant portion of modern wireless communications systems depend on spectrum scarcity in the 300 MHz to 3 GHz frequency range. In comparison to current cellular spectrum allocations, the 6 to 100 GHz frequency band may offer orders of magnitude more spectrum, enabling the utilization of beamforming and spatial multiplexing with a large number of antennas [48]. The networks ought to have improved coexistence, increased isolation, and bandwidth as a result of directional antennas [49]. Even though the shift in frequency bands has drawn a lot of attention, there are still a lot of problems, including severe cross-link interference, significant mmWave frequency penetration loss, and extremely volatile link and channel conditions [50]. BSs in mmWave networks are capable of broadcasting and receiving in the mmWave band, hence providing coverage for particular geographic regions. In order to provide sufficient coverage, mmWave BSs must be placed densely. MmWaves' ultra-dense construction makes it simple to integrate them into UDNs. However, because so many BSs are needed, backhauling a dense mmWaves network can be

costly. This suggests that other BSs could serve as a conduit for connecting some mmWave BSs to the backhaul [51].

(iii) Flexible RANs

The Cloud Radio Access Network (CRAN) is a radio access network architecture that combines cloud computing with cellular technologies. In CRAN, baseband processing tasks are carried out in a central cloud or centralized BBU pool [52]. As a result, base stations have been reduced to simple Radio Remote Heads (RRHs). Front haul lines link the several RRHs to the central cloud. Communication between the network's core and central cloud is facilitated by the transport network. In CRAN's initial plan, the RRH and central cloud connection is described as optical fiber front haul. CRAN offers a number of benefits, ranging from simpler BSs to cloud-based processing. Similar to modern IT cloud computing, cloud computing facilitates the full utilization of available resources. In addition, CRAN considers the separation of handling and transmission, enabling the use of information plane collaboration techniques like coMP [53]. Through the dense deployment of the available RRHs in CRANs, a novel and attractive network design known as ultra-dense CRAN is produced. In comparison to ordinary cellular networks, ultra-dense CRANs may significantly improve both energy and spectrum efficiency (SE) due to the centralization of resource allocation and collaborative signal processing among the RRHs. Moreover, mmWave wireless front haul may be utilized in ultra-dense CRANs to exchange data between the distributed RRHs and the central CPU, reducing costs and improving deployment flexibility [54].

(iv) Machine-Type Communication-Based Access

One of the challenges facing the IoT in order to enable the development of billions of smart devices is massive device connectivity. To provide ubiquitous IoT services, a wide range of high efficiency communication infrastructures should be incorporated, such as machine-to-human (M2H), machine-to-machine (H2M), human-to-human (H2H), and machine-to-machine (M2M) communications [55]. Future use cases will include smart building, smart agriculture, industrial automation, and auto-drive robot interaction. At the same time, the network will grow to encompass a bigger IoT ecosystem. Massive IoT is expected to be developed with the aid of numerous novel technologies and techniques, including information sensing, cloud computing, and artificial intelligence (AI) [55]. Massive IoT is anticipated to develop into an international network of interconnected systems, facilitating a variety of data exchange, collecting, and decision-making processes as well as improving measurement and management effectiveness [55]. Proximity-based communication that can manage data flow has acquired a lot of interest with the rise of smartphones and tablets. D2D-enabled users can exchange data directly without going through BSs or the main network, enabling proximity-based communication. A new network topology called an ultra-dense D2D network has been developed as a result of the high number of D2D-enabled users [55, 56].

II.4 INTERFERENCE PROBLEM AND CATEGORIES IN FEMTOCELL UDN

i. Co-tier interference

This is related to two different kinds of interference between femtocells that are next to each other. Uplink co-tier and downlink co-tier interferences are the two types [57]. Network components that are part of the same network layer are the cause of this kind. As indicated by indicator 1 in Figure 4, uplink co-tier interference occurs when femtocell users (aggressors)

interact with the nearby femtocell base station (victims). As seen in indicator 2 in Figure 9, a downlink co-tier interference occurs when a nearby femto-user (victim) experiences interference from a femtocell base station (aggressor). Since they are next to one another, the femtocells that interfere with one another are typically immediate neighbors. Femtocell placement is random, and they can be placed in close proximity to one another, perhaps with insufficient wall separation to prevent interference. When there is a dense deployment and multiple nearby interferers, the total interference detected at a certain femtocell is probably more than the sum of the individual interfering femtocells.

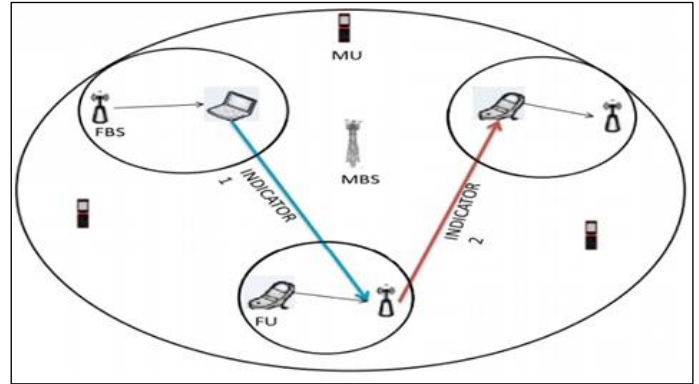


Figure 9: A typical co-tier interference scenario between neighboring FBSs.

Source: Authors, (2024).

ii. Cross-tier Interference

This has to do with interference between the femtocell and macrocell layers, as well as vice versa. A typical cross-tier interference scenarios is illustrated in Figure 10.

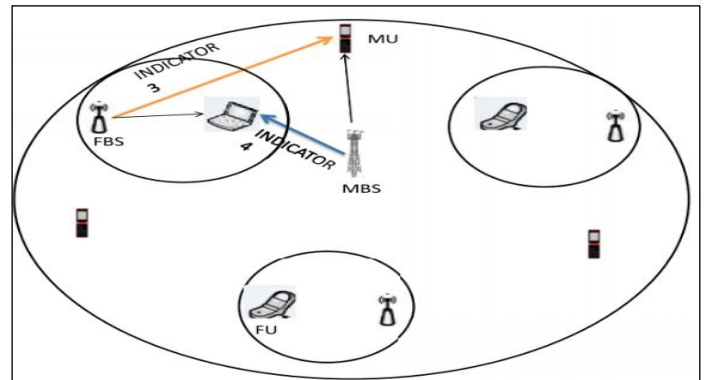


Figure 10: A typical cross-tier interference scenario between FBSs.

Source: Authors, (2024).

As indicated by indicator 3 in Figure 10, uplink cross-tier interference occurs when femtocell users (aggressors) interfere with the operations of a nearby macro-cell base station (victims) or when macro-cell users interfere with the operations of a nearby femtocell base station. However, as indicated by indicator 3 in Figure 5, downlink cross-tier interference occurs when a macro-cell base station (aggressor) interferes with a nearby femto-user (victim) or when a femtocell base station (aggressor) interferes with a nearby femto-user (victim).

iii. Multi-tier Interference:

In the UDN, both the macrocells and small cells are cross deployed throughout the network. The interference caused by multi-tiers include the various emit powers, cell topologies, radio accesses, etc. For example, small cells reuse the frequency

band from the macrocell, which brings interference to the Macro cell UE (MUE), especially to the MUEs at the cell edge. The MUEs at the cell edge received signal with strong path loss and fading. When the small cell uses same sub-channel for communication, the interference to MUE become severe. On the other hand, the MUE near the cell edge will increase the emit power due to the power regulation, which interferes with the small cell UEs (SUE) [58]. Four examples of multi-tier interference are given in Figure 11. The interference signal and direction are shown by the red line in each of the sub-figures. For instance, the macro cell UE (UE1) is receiving signals from the macro cell in Figure 11(a). At the same time, UE1 may experience interference from tiny cell transmissions. As UE2 communicates with the small cell in Figure 11(b), the macro cell may cause interference for the small cell UE (UE2). In Figure 11(c), while UE2 is transmitting to the small cell BS, the transmission signal from UE1 to the macro cell interferes with the small cell BS. In Figure 11(d), while UE1 is transmitting to macro cell BS, the UE2 may pose interference to the macro cell BS when transmitting to the small cell BS.

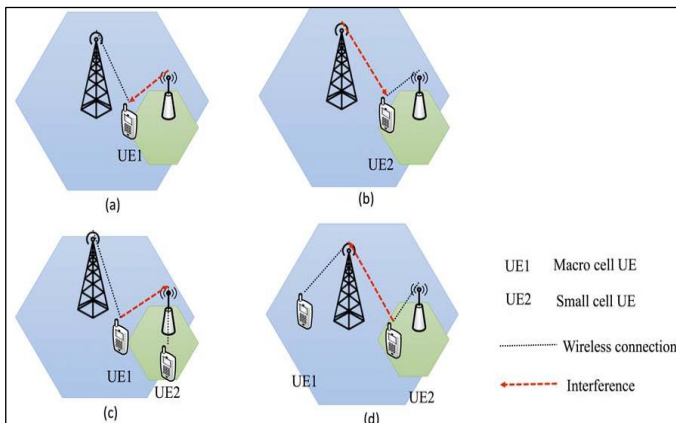


Figure 11: Multi-tier interference cases.
Source: Authors, (2024).

II.5 INTERFERENCE REDUCTION METHODS FOR FEMTOCELL UDN

Various interference studies have been proposed, with differing degrees of success, and numerous research publications addressing this issue have been published. As illustrated in Figure 12, the interference reduction techniques used in this investigation was classified into four groups. These include the application of game theory, dynamic resource allocation, user clustering, and graph theory.

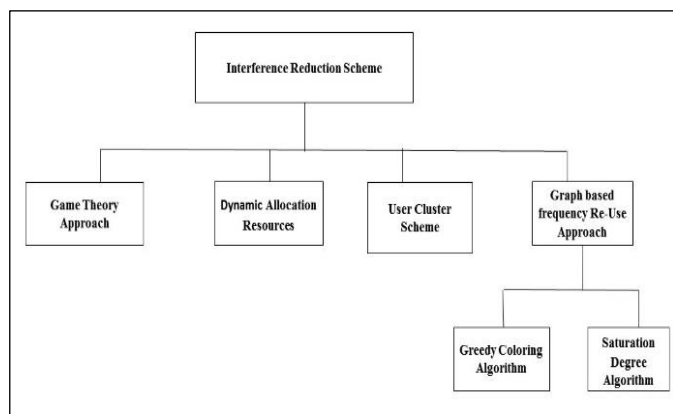


Figure 12: Interference reduction scheme in femtocell UDN.
Source: Authors, (2024).

II.5.1 GAME THEORY APPROACH METHOD

The game theory approach to reducing interference involves analyzing the strategic behavior of multiple users or nodes competing for limited wireless resources, such as bandwidth or frequency channels. It aims to develop algorithms and protocols that optimize resource allocation and transmission strategies to minimize interference and improve network efficiency. This approach considers factors such as channel conditions, user preferences, and network topology to design decentralized decision-making mechanisms that lead to better overall network performance. Game theory has been extensively used in networking research as a theoretical decision-making framework, e.g. for routing [59],[60], congestion control [61],[62], resource sharing [63-64], and heterogeneous networks [65],[66]. Based on the idea of Shapley value in the wireless relay network (WRN).The author in [67] investigated the dynamic spectrum access problem with a two-stage Stackelberg game consisting of a leader (spectrum provider) subgame and a follower (secondary user) subgame. An on-demand resource-sharing mechanism considering user's selfish characteristic and private traffic information was designed in [68]. The author proposes a centralized user-centric merge-and-split coalition formation game that users instead of FAPs participate in the game as players. Other than FAP-centric games, this user-centric game makes it conceivable to estimate inter-user interfere by making use of user information (e.g., distance) so as to assist in distributing and reusing sub channels. As a consequence, a user-centric coalition formation game can achieve a preferable system performance. Finally in order to fully utilize the remaining sub channels and get over the restriction of assigning one sub channel to each player in typical coalition formation games, an additional allocation technique was finally put forth. The remaining subchannels are located by searching through each FAP's unallocated subchannels; users will only be assigned to these remaining subchannels if the aggregate throughput is increased. The spectral efficiency is greatly increased by the SAA at a minimal computational cost. Comparing simulation findings to comparable studies showed that these approaches were beneficial. The studies in [69] proposed a scheme for ICI reduction by controlling the transmit power through a non-cooperative game in which the transmit power is considered to be the action set available to the players (users). However, the author considered only a simple case of 2 users, each in different cell which are competing on 2 sub channels. Alternatively, the proposed scheme considered multiple users in multiple cells. The authors proposed a non-cooperative game where $G = (J, \{P_j\}, \{U_j\})$ represent a game with $J = \{1, 2, \dots, k, \dots, J\}$ representing the set of user equipment's in adjacent cells who are using the same sub channel and $P_j = \{P_j : P_j\} \in [0, pmax\}$ representing a continuous set of transmit power which represents the space of user's actions. $Pmax > 0$, is the maximum allowable transmit power per sub channel. The selected action (transmit power) has to be smart enough to maximize the user's utility function. A mathematical expression known as the utility function measures the degree of satisfaction a user experiences when utilizing system resources. Delay and clarity are two elements that impact the quality of multimedia services. Low data rates and frequent retransmissions, which are essentially caused by low SINR levels, are the primary reasons of delay. Furthermore, low SINR raises the bit error rate (BER), which deteriorates clarity, particularly for voice services. Thus, the primary causes of service degradation are interference and a poor received signal.

Fixing an application-based BER while increasing the throughput—which ought to be flexible and variable—is one method to handle such a scenario. When the primary goal is to maximize spectral efficiency, a concave growing function of the user's SINR should be used to determine the utility of the user [70–73]. In light of this, the logarithmic Shannon capacity function or a function proportional to it immediately springs to mind. However, broadcasting with the maximum power is the optimal approach for a user to maximize such utility function in a non-cooperative game, given a fixed interference I and fixed desired channel power. Instead of increasing the system's spectral efficiency, such conduct will raise the network's degree of interference. Consequently, this kind of function isn't a full utility function to complete it, a pricing term (or cost) should be incorporated to it so that it prevents the users from always transmitting at full power. Thus, If SINR is fixed, the utility function should be a decreasing function with respect to the transmit power. These unplanned and unmanaged wireless networks are collectively referred to by the authors in [74] as chaotic networks or chaotic deployments. They do, however, highlight certain benefits of such chaotic networks, such as making it simple for new methods to determine locations [75] and offering nearly universal wireless connectivity [76]. The main disadvantage of these disorganized deployments is that, despite being difficult to identify, interference can have a substantial impact on end-user performance [77]. The author of this study proposes a "virtualization" solution in which the interfering APs take turns serving each other's clients. Allowing clients to associate with APs from different owners has security problems, but these have been discussed and resolved in [78]. The author focus on the *incentive* aspect, and propose a framework to ensure that the APs are indeed motivated to provide service to each other's clients

II.5.2 Dynamic Resource Allocation Method

Dynamic channel allocation systems have attracted a lot of interest as ways to achieve effective system resource use. There have been several suggestions for permanent channel assignment, channel borrowing, shared channel pools, channel ordering, channel reassignment, and dynamic parameter adjustment. An effective resource allocation method that can lessen the impact of uplink interference in a two-tier femtocell was proposed by the authors in [79]. These writers employ an integer programming (IP) approach to achieve the goal. Despite the scheme's complexity and intricacy, the outcomes were effective. The authors suggested using a heuristic method wherein resources were distributed collaboratively between femtocells and macrocells. The femtocell-macrocell network in this study was subjected to interference control during uplink transmission using Single Carrier Frequency Division Multiple Access (SC-FDMA), particularly in the macrocell's cell edge area, which frequently encounters high interference levels. When the number of femtocells increases, the study's femtocell utilizes the radio resources of nearby macrocells by taking into account the least amount of interference from users stationed in the nearby 12icrocell area. Three 12icrocell-based multi-cell cellular communication layouts are taken into consideration in this study. A growing number of femtocells are installed in 12icrocell 1. Assuming a frequency reuse factor of 3, the initial femtocell chooses radio resources from either 12icrocell 2 or 3 (neighboring macrocells). Subsequent femtocells are not permitted to use the same radio resources as the first femtocell that has been allotted. Femtocells are categorized according to

the radio resources that are allotted differently; macrocells and femtocells will share the radio resource allocation. Various radio resources are assigned to femicells within the same group. To mitigate the issue of femtocell interference in networks based on Orthogonal Frequency Division Multiple Access (OFDMA) [80], [81], the authors suggest using partially shared and orthogonal spectrum to prevent cross-tier interference. The authors of [82] also suggest a dynamic fractional frequency reuse strategy that places users in orthogonal sub-bands who have poor geometry in nearby femtocells. Nevertheless, co-channel femtocell installations are recommended for greater spectrum reuse because these approaches may result in low spectral efficiency. The authors of [83],[84] analyze how to reduce interference in co-channel femtocell installations by using sector antennas and multiple antenna elements at femtocells, respectively. These methods do, however, require more sophisticated technology, which raises the cost and complexity of the femtocell in the end. Thus, it has been announced that the most promising method for handling interference in co-channel femtocell deployments is Sub-channel (SC) allocation and power regulation. However, the assignment of SCs and transmit power is an intricate optimization problem, which becomes even more complex due to the existence of several Modulation and Coding Schemes (MCSs) in WiMAX and LTE standards. Moreover, multiple SCs assigned to one user must use the same MCS [85], although each user may observe different channel gains in each SC. In the OFDMA literature, dynamic SC assignments with equal transmit power per SC are typically recommended over complex joint dynamic SC and transmit power assignments due to their ease of implementation and mathematical tractability because of the availability of link adaptability in the DownLink (DL). Previous evaluations [86],[87] also showed that in circumstances where a wide range of users require varying QoS, the benefits in overall system performance generated by assigning various transmit powers to different SCs are minimal.

II.5.3 User Clustering Scheme in Ultra-Dense Network

Clustering techniques are used to divide a data set into a number of different clusters by means of specific division criteria. For clustering plans in UDN, there are generally three types of clustering: static clustering, dynamic clustering and semi-dynamic clustering. For static clustering, the deployment of BSs or access points (APs) is pre-set. Although this technique is easy to implement in reality and has the potential to reduce signaling overheads, it is not well-suited to complex and dynamic mobile communication scenarios [88]. In [89], the author provides a static clustering approach that, with the least amount of overhead, accomplishes the large advantages and significant increases of the cooperative or coordinated multi-point (CoMP) technique. A separation function is provided for assessing the effectiveness of the separation clustering technique proposed by Xiao *et al.* [90]. This approach uses high-priority BSs and ranks BS priorities in order to suppress inter-cluster interference. Through simulation, the algorithm achieved a positive interference suppression result [90]. With dynamic clustering, instantaneous channel state information (CSI) is used to dynamically alter the formation of user and BS clusters, making it suitable for a range of mobile communication scenarios. However, this technique adds to the complexity of system scheduling and the requirement for feedback overhead. The issue of dynamic clustering has been approached from a number of theoretical angles by the researchers. In [94, 95], authors apply the graph theory method. In order to reduce system

interference, the authors of [91] cluster users and generate a network interference graph using a graph coloring method and user feedback. A unique low-complexity clustering approach is put forth in [92]. By merging graph theory with the interference of a specific number of nearby BSs, the suggested technique accomplishes the objective of lowering the iterative complexity of the clustering process. Several authors in UDN have enhanced and implemented the k-means algorithm to user clustering since it is a popular and simple to use iterative method for cluster analysis [93-95].

As the fundamental part of resource management, the authors in [96] distributed resources to each cluster using an enhanced k-means algorithm. Through clustering the ensuing cluster heads, the average signal-to-noise ratio (SINR) is improved. In order to cluster BSs optimally and modify the traffic load in each cluster, the author of [94] suggests a weighted dynamic k-means method within a machine learning framework that takes geographic location and traffic load into account during the clustering phase. Unlike other enhanced algorithms [95], In addition to the enhanced k-means algorithm's ability to successfully lower the complexity of the network structure and user clusters, the authors are able to modify the number of clusters depending on the SINR. Dynamic clustering approaches based on game theory and clever optimization algorithms are also available. In [96], the author through the use of an intelligent optimization technique, he optimize the parameters of the DBSCAN algorithm. By finding isolated points, the optimized algorithm not only mitigates communication resources but also achieves the purpose of clustering users. A distributed approach is presented that provides a graph coloring algorithm for resource scheduling and a game theory based clustering algorithm for user grouping. According to simulation data, the method outperforms other relevant algorithms in terms of average cell throughput [97].

The benefits and limitations of both dynamic and static clustering are balanced by semi-dynamic clustering. A semi-dynamic algorithm with respect to the backhaul capacity constraint is proposed in [98]. The algorithm's low complexity and cheap training overhead are its advantages, but its application possibilities are limited because it requires large-scale channel information. A user clustering approach based on interference vector assessment is proposed in [98],[99], by creating an interference graph, the scheme determines the interference vectors of each user and groups them according to the relative interference values between their interference vectors. Comparative simulations were used to evaluate how effective the plan was. First, a method for creating interference weights based on the Signal-to-Other cell-Interference Ratio (SOIR) is presented. This method uses the interference weights between users to get the desired user interference vector. Second, an optimization approach was used to solve the interference vector. An interference graph, which is thought to be a useful tool for managing interference, was created in this study. The interference graphs consist of interference subjects and inter-subject relationships. Assume $\{V, E\}$, where $V = \{v1, v2, \dots, vN\}$ denotes the set of users and $E = \{W_{ab}(i, j), \forall i, j \in V\}$ represents the interference relationship between users. In Figure 13, a simple user interference graph is illustrated.

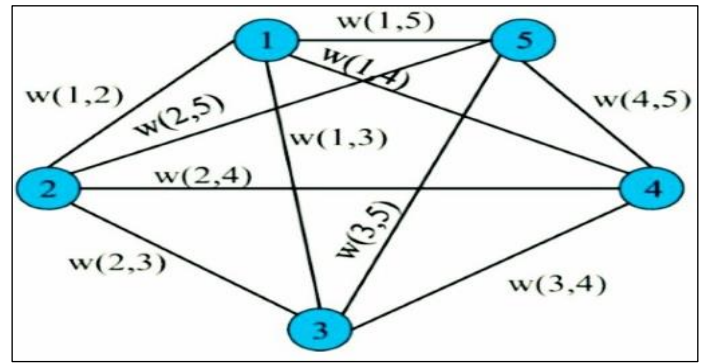


Figure 13: An interference graph. Source: Authors, (2024).

From the graph in Figure 13, the user interference matrix W was obtained as

$$W = \begin{bmatrix} 0 & w(1,2) & w(1,5) \\ w(2,1) & 0 & w(2,5) \\ w(5,1) & w(5,2) & 0 \end{bmatrix} \quad (1)$$

The interference graph focuses on the interference weights' design. It defines the SOIR between user's u and v as follows after taking into account the impacts of both the SINR and SOIR.

$$r_{u,v} = \frac{S_v}{I_u} \quad (2)$$

where S_v is user v 's received signal, I_u is user u 's interference signal, and $U_{u,v}$ indicates the amount of power leaking from user v to user u . The greater the value, the greater the impact of user v on user u . (u, v) represents the interference weight between users u and v as

$$W(u, v) = \frac{1 + \frac{1}{\mu V}}{1 + \frac{1}{\mu U}} r_{u,v} \quad (3)$$

The SINR of users' u and v , respectively, are represented by μ_u and μ_v and μ_u . From (3), the interference weights between each pair of users can be obtained, and the interference vector for user i was set as

$$IV_i = [(i,1), W_{ab}(i,2), \dots, W_{ab}(i,N)] \quad (4)$$

The research in [100, 101] grouped the nearby cells to study the performance of a single cluster; however, it is unclear how to build many clusters in the system. Since the system's clusters in [102] are produced by a stable Poisson process, clustering is not necessary to take into account. In those cases, clustering can be thought of as being carried out in a preset manner without taking advantage of additional system features like path-loss or location data. User partitioning has recently been taken into consideration in [103] for reduced signaling overhead where three clustering algorithms have been proposed. One potential issue is that these algorithms do not explicitly address the interference alignment feasibility constraint. Hence, transmitters must therefore modify the quantity of data streams they send in accordance with the size of the cluster. Furthermore, the clusters that are created are compelled to access the channel in a time-division fashion by the medium access control

scheduling mechanism. Cluster synchronization and coordination are necessary for this.

II.5.4 Graph-Based Frequency Reuse Technique

The method for reusing frequencies in a graph is based on greedy coloring and saturation degree algorithms. In these schemes, the femtocells, or nodes in the graph, are connected by means of channel state information that is obtained from the femtocells and their users. Each base station is assigned a frequency to minimize interference through the use of graph-coloring algorithms, wherein each color corresponds to a different frequency band [104].

(i) Greedy coloring algorithm

The Greedy algorithm uses a routing technique to determine the best frequency assignment for a network by allocating the smallest color or sub-band to each available femtocell [105]. This is among the simplest techniques for coloring graphs. It gives vertices the least amount of color so that there is no conflict between them and their neighboring colored vertices, as Figure 14 illustrates. For a given graph G , the set of vertices is described as $V = \{v_1, v_2, \dots, v_n\}$, the set of edges is described as $E = \{e_1, e_2, \dots, e_n\}$, the set of available frequencies is $F = \{f_1, f_2, \dots, f_n\}$ and the set of colors or sub bands for the nodes is described as $C = \{c_1, c_2, \dots, c_n\}$ where the total colors assigned in the graph network $P = P + 1$.

Putting the greedy coloring algorithm into practice is not too difficult. Greedy coloring treats each vertex separately in order to concentrate on local optimization. This makes it ideal for situations in which global optimization is challenging or unfeasible. It is easily adaptable to many graph coloring issue variants and limitations, such as frequency assignment and scheduling. Additionally, because the algorithm only needs to keep the colors, it often uses little memory. Nevertheless, the plan assigns sub-bands arbitrarily and inefficiently. Greedy algorithms may react very quickly to modifications in the input data. There are several previous studies that are indirectly related to this research, including: implementation of the greedy algorithm on graph coloring. A map of the Deli Serdang region will be colored in this [106], minimal proof of the four-color theorem [107], and the ant algorithm [108-111].

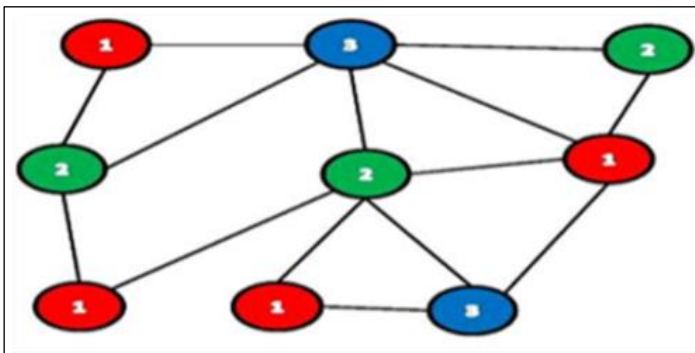


Figure 14: Greedy coloring algorithm. Source: Authors, (2024).

(ii) Saturation degree coloring algorithm

This scheme assigns colors to a graph's vertices in a way that minimizes the number of different colors utilized throughout the graph and assigns different colors to neighboring pairs of vertices. Figure 15 shows a common saturation degree scheme

with graphs colored in red, blue, and green. In fact, this is the very minimum of colors required for this specific graph. This indicates that at least three colors must be used to color this graph in order to guarantee that neighboring vertices have different color. This technique employs saturation degree (D) which is defined as the total number of adjacent colored vertices to which an uncolored femtocell or node is connected [112]. Saturated degree algorithm was proposed by author in [113] and is defined as follows. Suppose that vertices $v_1, v_2 \dots v_{i-1}$ have been chosen and colored. Then at step i , vertex v_i with the maximum Saturation degree is selected. The saturation degree of a vertex is defined as the number of differently colored vertices the vertex is adjacent to. Vertex v , for example, has saturation degree equal to 2 if its degree is equal to 4, one of its neighbors is uncolored, two of them are colored with color equal to 1, and the final one is colored with color equal to 3. Ties are broken in favor of the vertex with the largest degree when selecting the vertex with the maximum saturation degree. Since this heuristic colors the vertices that are most limited by earlier color selections, it seems to provide a superior coloring than Largest Degree Ordering. [113].

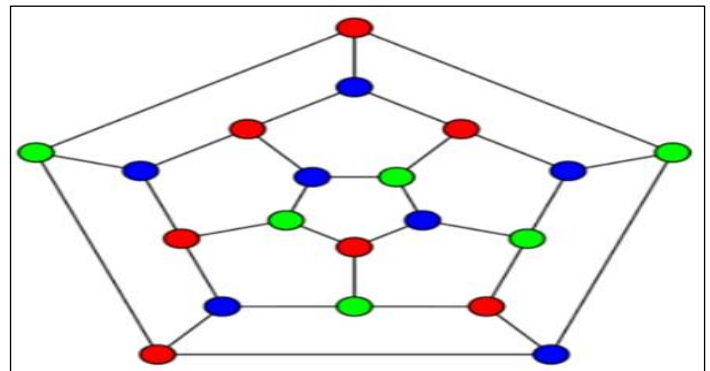


Figure 15: A typical saturation degree algorithm. Source: Authors, (2024).

III. CHALLENGES AND FUTURE RESEEARCH DIRECTIONS

This section summarizes the current challenges identified from the research studies on the methods to reduce interference level in femtocell ultra-dense network. These challenges include:

- (i) **Spectrum Efficiency in Wireless Backhaul:** Due to the numerous cell base stations in UDNs, a backhaul network with a high degree of flexibility and capacity is necessary. It is possible that the conventional wired backhaul network is no longer useful because of its high deployment, complexity, and running costs. There is a chance that the wireless backhaul network will lower infrastructure costs and increase deployment flexibility. The complexity of spectrum resource management and networking is a significant difficulty because of the enormous number of cells. Future research efforts aimed at enhancing spectrum efficiency in wireless backhaul include dynamic spectrum access (DSA) and cognitive radio. Examining cutting-edge methods for dynamically accessing and making use of available spectrum bands will be necessary to enable more effective spectrum allocation and usage.
- (ii) **Dynamic environment:** One of the main disadvantages of the user-centric coalition forming game strategy is this. The coalition creation process becomes more difficult in a dynamic environment when user preferences, resources, or constraints change frequently because it necessitates ongoing updating and

adjustment. Future research directions in a dynamic environment could focus on a number of topics, such as examining sophisticated spectrum management strategies to allocate spectrum resources dynamically based on interference and demand in real-time, enhancing spectrum efficiency, and supporting a variety of communication technologies. Also by developing adaptive resource allocation algorithms that can dynamically adjust network resources, such as bandwidth, power, and processing capacity, in response to changing traffic pattern, user demands, and environmental conditions.

(iii) **User equipment Battery Life:** The capabilities of spectrum detection, information gathering, interference cancellation, and other functions are demonstrated by the UEs equipped with sophisticated antennas. UE's battery life particularly that of smartphones, ought to be taken into account. Stated differently, a limited amount of energy will be allocated to a variety of tasks, such as signal transceiving, data roaming, and complex computing. Thus, another issue in UDN is the energy efficiency of smart devices. This is a prospective study direction that has to be pursued with continued examination. Enhancing UE battery life is anticipated to entail developing more energy-efficient processors and displays, optimizing power management systems, and making strides in battery technology. Furthermore, advancements in software optimizations, including background task management and low-power modes, will be extremely important.

(iv) **Frequency Assignment:** In a UDN femtocell network, frequency assignment is a crucial component that needs to be carefully considered to guarantee effective spectrum use and low interference. In order to enhance network performance overall, future research may focus on interference management and the development of strategies to reduce interference among femtocells as well as co-channel interference between femtocells and macrocells. Additionally, it is crucial to look into dynamic frequency selection algorithms that let femtocells choose the best frequency channels on their own in response to traffic and real-time interference.

(v) **Security:** Due to the high densification of the cells and user equipment, which offers hitherto unheard-of information interactions, security will become increasingly important in the development of UDNs. Similar to this, new channels for security compromise and privacy concerns arise from the restricted energy supply in UE devices as a result of data computing, data roaming, and other tasks. These factors must be taken into account. The vulnerability potential will unavoidably expand due to the various different networks and rising system complexity. Further research on this topic will focus on creating methods for identifying and thwarting security risks unique to femtocell UDNs. It's crucial to create secure resource allocation algorithms that take performance and security into account in order to maximize resource efficiency and minimize security risk.

IV. CONCLUSIONS

In this paper, we provide an overview to interference problem and reduction methods in femtocell UDN. Specifically, we first present some common architectures of femtocell UDN and issues relating to each architecture. Secondly, we provide a taxonomy to classify the UDN networks. Then to alleviate the problem of interference in femtocell UDNs, some interference reduction schemes are discussed. Also, several research studies under interference reduction scheme were investigated. Finally, the challenges and open research directions are outlined in this field.

V. AUTHOR'S CONTRIBUTION

Conceptualization: Adekogba, G.V., Adedeji, K.B. and Olosoji, Y.O.

Methodology: Adekogba, G.V., Adedeji, K.B.

Investigation: Adekogba, G.V., Adedeji, K.B.

Discussion of results: Adekogba, G.V., Adedeji, K.B. and Olosoji, Y.O.

Writing – Original Draft: Adekogba, G.V.

Writing – Review and Editing: Adekogba, G.V., Adedeji, K.B.

Resources: Adedeji, K.B.

Supervision: Olosoji, Y.O and Adedeji, K.B.

Approval of the final text: Adekogba, G.V., Adedeji, K.B. and Olosoji, Y.O.

VI. ACKNOWLEDGMENTS

The authors wish to appreciate the management of the Federal University of Technology, for the opportunity given to conduct this research.

REFERENCES

- [1] M.P.A. Kovacs, and Z. Johan yak, "SDMN architecture in 5G", Muszaki Tudomangos Kozlemenyek, vol. 13, pp. 101-104, 2020.
- [2] A. Osseiran, B. Federico, B. Volker, and K. Katsutoshi, "Scenario for 5G mobile wireless communications", the vision of the METIS project, 2020.
- [3] K. Kumar, A. Prakash, R., and Tripathi. "A spectrum handoff scheme for optimal. A game theoretic approach. phys. comm", vol. 24, pp. 19-33, 2017.
- [4] Telecom. Review, (2021). Indoor communication: in building wireless solutions. Retrieved from in building solutions. Online. Available from: <https://www.telecommunication.com/articulereports-and-covering/4725-indoor-communication-in-building-wireless-solutions#:text=figure%20show%that%2080%25%20of,physical%20barriers%20to%20wireless%20communication>.
- [5] J. Sghiri, and M. Ayadi, "An innovative approach for automatic frequency planning. In The 2014 International Symposium on Networks, Computers and Communications," 13-17 June, Sousse, Tunisia (pp.1-5), June, 2014.
- [6] A. Adekunle, and G. Abiodun, "Minimizing interference in ultra-dense femtocell networks using graph-based frequency reuse technique, FUOYE JOURNAL. Journal of Engineering and Technology", vol. 5(1), pp. 2579-3617, Feb. 2020.
- [7] R.S. ThamaraiSelvi, K. Andrews, S.R. Rammohan, and A. Nana Yaw, "Efficient handoff management in 5G ultra dense network using dynamic beamforming techniques. ICTACT Journal on Communication Technology", vol.14, pp. 2-14, 2023.
- [8] A. Anzaido, and G. Angel, "Accelerated resource allocation based on experience retention for 5G, Journal of network computer application", vol. 213, pp.103-593, 2023.
- [9] F. Galeano-Brajones, L. Francisco, and, H. Pablo, "Designing problem specific operator for solving the cell switch off problem in ultra-dense 5G networks with hybrid MOEAs, Swarm and evolutionary computation", vol. 78, pp.101-290, 2023.
- [10] D. L. Perez, G. D. la Roche, A. Valcarce, A. Juttner, and J. Zhang, "Interference avoidance and dynamic frequency planning for WiMAX femtocell networks," In: Proceedings of the 11th IEEE Singapore International Conference on Communication Systems, pp. 1579-1584, 19-21 Nov. 2008.
- [11] V. Chandrasekhar and J. Andrews. "Femtocell networks: A survey," IEEE Commun. Mag, vol. 46, no. 9, pp. 59-67, 2008.
- [12] M. Yavuz, F. Meshkati, S. Nanda, A. Pokhariyal, N. Johnson. Roghothaman, and A. Richardson, "Interference management and performance analysis of umts/hspa+ femtocells," IEEE Commun. Mag., vol. 47, no. 9, pp. 102-109, Sep. 2019.

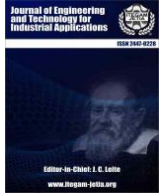
- [13] L. T. W. Ho and H. Claussen, "Effects of user-deployed, co-channel femtocells on the call drop probability in a residential scenario," IEEE 18th International Symposium on Personal, Indoor and Mobile Radio Communications, pp. 1–5, 3-7 Sept. 2019.
- [14] R. Baines, (2007) "The need for WiMAX picocell and femtocells," WiMAX London, pp. 1–36, 25-26.
- [15] J. Xiang, Y. Zhang, T. Skeie, and L. Xie. "Downlink spectrum sharing for cognitive radio femtocell networks," IEEE Systems Journal, vol. 4, no. 4, pp. 524–534, Sep.2010.
- [16] S. M. Cheng, W. C. Ao, and K. C. Chen, "Downlink capacity of two tier cognitive femto networks," In: Proceedings of the IEEE 21st International Symposium on Personal Indoor and Mobile Radio Communications, pp. 1303–1308, 26-30 Sept. 2010.
- [17] J. P. M. Torregoza, R. Enkhbat, and W.-J. Hwang. "Joint power control, base station assignment and channel assignment in cognitive femtocell networks," EURASIP Journal on wireless communications and networking, pp.3-6, 2010.
- [18] J. Xiang, Y. Zhang, and T. Skeie. "Dynamic spectrum sharing in cognitive radio femtocell networks," 4th International conference of access networks (ACCESSNET), vol. 37, pp. 164–178, 2009.
- [19] M. E. Sahin, I. Guvenc, and H. Arslan. "Uplink user signal separation for ofdma based cognitive radios," EURASIP Journal on advances in signal processing, pp.34-40, Feb.2010.
- [20] D. Chambers, "Femtocell, history," online available at: <http://www.thinkfemtocell.com/FAQs/femtocell-history.html>. Femto Forum, <http://www.femtoforum.org/femto/>.
- [21] R. Tang, "Indoor propagation in cellular/PCS system design," Emerging technologies symposium wireless communications and systems, pp.81–84, 1999.
- [22] M. Fan, M. Yavuz, S. Nanda, Y. Tokgoz, and F. Meshkati, "Interference management in femto cell deployment," in 3GPP2 Femto Workshop, Oct. 2007.
- [23] H. Claussen, "Performance of macro and co channel femtocells in a hierarchical cell structure," IEEE 18th International Symposium on Personal, Indoor and Mobile Radio Communications, pp. 1–5, 3-7 Sept. 2007.
- [24] S. F. Hasan, N. H. Siddique, and S. Chakraborty, "Femtocell versus Wi Fi-A survey and comparison of architecture and performance," 1st International Conference on Wireless Communication, Vehicular Technology, Information Theory and Aerospace and Electronic Systems Technology, Florida. pp. 916–920, 17-20 May 2009.
- [25] Samsung (Aug.2011) Available online at <http://www.samsung.com>.
- [26] Iaccess (2008), Available at <http://www.ipaccess.com/femtocells>.
- [27] Ubiquisys. (2023) available at <http://www.ubiquisys.com>.
- [28] Huawei (sep.2013) available at. <http://www.huawei.com>.
- [29] S. S. Prasad and R. Baruah, "Femtocell mass deployment: Indian perspective," 3rd International Conference on Anti-counterfeiting, Security, and Identification in Communication, pp. 34–37, 20-22 Aug. 2009.
- [30] J. O. Carroll, H. Claussen, and L. Doyle, "Partial GSM spectrum reuse for femtocells," IEEE 20th International Symposium on Personal, Indoor and Mobile Radio Communications, pp. 2111–2116, 13-16 Sept. 2009.
- [31] Ericsson. (2008, Sep) Press release. Available online at: <http://www.ericsson.com/ericsson/press/releases/20080911-1250616.shtm>
- [32] M. Neruda, J. Vrana, and R. Bestak, "Femtocells in 3G mobile networks," 16th International Conference on Systems, Signals and Image Processing, pp. 1–4, 18-20 June. 2009.
- [33] D. Kinsley, T. Yoshizawa, and F. Favichia, "Standardization of femtocells in 3GPP (2009)," IEEE Commun. Mag., vol. 47, no. 9, pp. 68–75, 2009.
- [34] Y. Tokgoz, F. Meshkati, Y. Zhou, M. Yavuz, and S. Nanda, "Uplink interference management for hspa+ and lte femtocells," IEEE Global Telecommunications Conference, pp. 1–7, Nov. 30 2009-Dec. 4, 2009.
- [35] M. Z. Chowdhury, R. Won, R. Eunjun, and M. J. Yeong, "Handover between macrocell and femtocell for umts based networks," 11th International Conference on Advanced Communication Technology, vol. 1, pp. 237–241, 15-18 Feb. 2009.
- [36] A. Golaup, M. Mustapha, and L. B. Patanapongipibul, "Femtocell access control strategy in umts and lte," IEEE Commun. Mag., vol. 47, no. 9, pp. 117–123, Sep. 2009
- [37] R. Y. Kim, S. K. Jin, and K. Etemad, "WiMAX femtocell: requirements, challenges, and solutions," IEEE Commun. Mag., vol. 47, no. 9, pp. 84–91, Sept. 2009.
- [38] M. Z. Shakir, H. Tabassum, and M.-S. Alouini, "Analytical bounds on the area spectral efficiency of uplink heterogeneous networks over generalized fading channels". IEEE Transactions on Vehicular Technology, vol.63(5):2306–2318, 2014
- [39] B. Soret, K. I. Pedersen, N. T. Jorgensen, and V. Fernández-López. "Interference coordination for dense wireless networks". IEEE Communications Magazine, vol.53(1):102–109, 2015.
- [40] W. Nam, D. Bai, J. Lee, and I. Kang, "Advanced interference management for 5g cellular networks". IEEE Communications Magazine, vol. 52(5):52–60, 2014.
- [41] N. Saquib, E. Hossain, L. B. Le, and D. I. Kim, "Interference management in ofdma femtocell networks: issues and approaches". IEEE Wireless Communications, 19(3):86–95, 2012.
- [42] N. Sharma, M. Magarini, D.N.K. Jayakody, V.Sharma, "On-demand ultra-dense cloud drone networks: Opportunities, challenges and benefits". IEEE Commun. Mag. 2018, 56, 85–91
- [43] L.Wang, H. Yang, J. Long, K. Wu, J. Chen, "Enabling ultra-dense UAV-aided network with overlapped spectrum sharing: Potential and approaches". IEEE Netw. 2018, 32, 85–91.
- [44] S. Chen, F. Qin, B. Hu, X. Li, Z. Chen, "User-centric ultra-dense networks for 5G: Challenges, methodologies, and directions". IEEE Wirel. Commun. vol. 23pp. 78–85.2016.
- [45] H. Zhang, Z. Yang, Y. Liu, X. Zhang, "Power control for 5G user-centric network": Performance analysis and design insight. IEEE Access, pp.7347–7355. Apr. 2016.
- [46] G. Zhang, F. Ke, H. Zhang, F. Cai, G. Long, Z. Wang, "User access and resource allocation in full-duplex user-centric ultra-dense networks". IEEE Trans. Veh. Technol. 2020, 69, 12015–12030.
- [47] M.S. Abouzeid, F. Zheng, J. Gutiérrez, T. Kaiser, R. Kraemer, "A novel beamforming algorithm for massive MIMO chipless RFID systems. In Proceedings of the Wireless Telecommunications Symposium (WTS)", Chicago, IL, USA, 26–28 April 2017; pp. 1–6.
- [48] L. Pan, Dai, Y.; Xu, W.; Dong, X. Multipair massive MIMO relaying with pilot-data transmission overlay. IEEE Trans. Wirel. Commun. vol.16, pp.3448–3460,2017.
- [49] Li, Y.; Pateromichelakis, E.; Vucic, N.; Luo, J.; Xu, W.; Caire, G. Radio resource management considerations for 5G millimeter wave backhaul and access networks. IEEE Commun. Mag. 2017, 55, 86–92.
- [50] K. Venugopal, R.W.Heath, "Millimeter wave networked wearables in dense indoor environments". IEEE Access 2016, vol. 4, 1205–1221.
- [51] R. Méndez-Rial, C.Rusu, N.González-Prelcic, N.; Alkhateeb, A.;R.W Heath, "Hybrid MIMO architectures for millimeter wave communications: Phase shifters or switches"? IEEE Access 2016, 4, 247–267.
- [52] S.C. Hung, H. Hsu, S.Y. Lien, K.C, "Architecture harmonization between cloud radio access networks and fog networks" IEEE Access, vol3, 3019–3034, 2016.
- [53] S. Chen, R. Ma, H.H. Chen, H. Zhang, W. Meng, J. Liu, J." Machine-to-machine communications in ultra-dense networks"—A survey. IEEE Commun. Surv. Tutor, vol.19, 1478–1503. 2017

- [55] S.K. Szharma, X. Wang. "Toward massive machine type communications in ultra-dense cellular IoT networks: Current issues and machine learning-assisted solutions". *IEEE Commun. Surv. Tutor.*, vol. 22, 426–471. 2017.
- [56] M. Elbayoumi, M. Kamel, W. Hamouda, A. Youssef, A." NOMA-assisted machine-type communications in UDN: State-of-the-art and challenges". *IEEE Commun. Surv. Tutor.*, vol. 22, 1276–1304. 2020
- [57] L. Wang, Z. Yongsheng, and W. Zhenrong, "Mobility management schemes at radio network layer for lte femtocells," *IEEE 69th Vehicular Technology Conference*, pp. 1–5, 26-29 April. 2009
- [58] N. Saquib, E. Hossain, L. B. Le, and D. I. Kim. Interference management in ofdma femtocell networks: issues and approaches. *IEEE Wireless Communications*, 19(3):86–95, 2012
- [59] A. van de Nouweland, P. Borm, W. van Golstein Brouwers, R. Groot Briunderink and S. Tijs, *A Game Theoretic Approach to Problems in Telecommunication, Management Science*, vol. 42, no. 2, pp. 294-303, February 1996.
- [60] A. Orda, R. Rom and N. Shimkin, *Competitive Routing in Multiuser Communication Networks*, *IEEE/ACM Transactions on Networking*, vol.1, no. 5, pp. 510-521, 1993.
- [61] A. de Palma, *A Game Theoretic Approach to the Analysis of Simple Congested Networks*, *The American Economic Review*, vol. 82, no. 2, pp. 185-199, 2005.
- [62] L. Lopez, A. Fernandez and V. Cholvi, *A Game Theoretic Comparison of TCP and Digital Fountain based protocols*, *Computer Networks*, vol.51, pp. 3413–3426, 2007.
- [63] S. Rakshit and R. K. Guha, *Fair Bandwidth Sharing in Distributed Systems: A Game Theoretic Approach*, *IEEE Transactions on Computers*, vol. 54, no. 11, pp. 1384–1393, November 2005.
- [64] H. Yaiche, R. R. Mazumdar and C. Rosenberg, *A game theoretic framework for bandwidth allocation and pricing in broadband networks*, *IEEE/ACM Transactions on Networking*, vol. 8, no. 5, pp. 667–678, 2000.
- [65] J. Antoniou, I. Koukoutsidis, E. Jaho, A. Pitsillides, and I. Stavrakakis, *Access Network Synthesis in Next Generation Networks*, Elsevier *Computer Networks Journal* Elsevier *Computer Networks Journal*, vol. 53, no.15, pp. 2716-2726, October 2009.
- [66] J. Antoniou, V. Papadopoulos, V. Vassiliou, and A. Pitsillides, *Co-operative User-Network Interactions in next generation communication networks*, *Computer Networks*, vol. 54, no. 13, pp. 2239-2255, September 2010.
- [67] D. B. Rawat, S. Shetty, and C. Xin, "Stackelberg-game-based dynamic spectrum access in heterogeneous wireless systems," *IEEE Syst. J.*, vol.10, no. 4, pp. 1494–1504, Dec. 2016.
- [68] C. H. Ko and H. Y. Wei, "On-demand resource-sharing mechanism designing two-tier OFDMA femtocell networks," *IEEE Trans. Veh. Technol.*, vol. 60, no. 3, pp. 1059–1071, Mar. 2011.
- [69] Z. Han, Z. Ji, and K. R. Liu, "Power minimization for multi-cell ofdm networks using distributed non-cooperative game approach," in *Proc. IEEE Global Telecommunications Conference. (GLOBECOM)*, pp. 3742–3747, Dec. 2004.
- [70] D. Falomari, N. Mandayam, and D. Goodman, "A new framework for power control in wireless data networks: Games utility and pricing," in *Proc. Allerton Conf. on Communication, Control and Computing*, Illinois, USA, pp. 546–555, Sept. 1998.
- [71] F. Meshkati, H. V. Poor, and S. Schwartz, "Energy-efficient resource allocation in wireless networks," *IEEE Signal Processing Magazine*, vol. 24, pp. 58–68, May 2007.
- [72] V. Shah, N. Mandayam, and D. Goodman, "Power control for wireless data based on utility and pricing," in *Proc. 9th IEEE Int. Symp. Personal, Indoor, Mobile Radio Communications (PIMRC)*, pp. 1427–1432, Sept. 1998.
- [73] H. Ji and C. Huang, "Non-cooperative uplink power control in cellular radio systems," *Wireless Networks*, vol. 4, pp. 233–240, March 1998.
- [74] A. Akella, G. Jedd, S. Seshan and P. Steenkiste, *Self-Management in Chaotic Wireless Deployments*, In *ACM MobiCom*, pp. 185-199, 2005
- [75] Intel Research Seattle, Place Lab A Privacy-Observant Location System, <http://placelab.org/>, 2004.
- [76] O. A. Dragoi and J. P. Black, *Enabling Chaotic Ubiquitous Computing*, Technical Report CS-2004-35, University of Waterloo, Canada, 20 04.
- [77] P. A. Frangoudis, D. I. Zografos and G. C. Polyzos, *Secure Interference Reporting for Dense Wi-Fi Deployments*, Fifth International Student Workshop on Emerging Networking Experiments and Technologies, pp. 37-38, 2009.
- [78] J. Hassan, H. Sirisena and B. Landfeldt, *Trust-Based Fast Authentication for Multiowner*
- [79] X. Tian and W. Jia, "Improved clustering and resource allocation for ultra-dense networks," *China Communications*, vol. 17, no 2, pp. 220-231, Feb. 2020.
- [80] V. Chandrasekhar and J. G. Andrews, "Spectrum Allocation in Tiered Cellular Networks," *IEEE Trans. Commun.*, vol. 57, no. 10, pp. 3059–3068, Oct. 2009. [Online]. Available: <http://arxiv.org/abs/0805.1226>
- [81] J. D. Hobby and H. Claussen, "Deployment Options for Femtocells and their Impact on Existing Macrocellular Networks," *Bell Labs Technical Journal*, vol. 13, pp. 145–160, 2009.
- [82] M. Y. Arslan, J. Yoon, K. Sundaresan, S. V. Krishnamurthy, and S. Banerjee, "Fermi: A femtocell resource management system for interference mitigation in ofdma networks," in *MobiCom 11*, Las Vegas USA, Sept. 2011.
- [83] V. Chandrasekhar and J. G. Andrews, "Uplink Capacity and Interference Avoidance for Two-Tier Femtocell Networks," *IEEE Trans. Wireless Commun.*, vol. 8, no. 7, pp. 3498–3509, July 2009.
- [84] H. Claussen and F. Pivit, "Femtocell Coverage Optimization using Switched Multi-element Antennas," in *IEEE International Conference on Communications (ICC)*, Dresden, Germany, June 2009.
- [85] E. Dahlman, S. Parkvall, J. Skold, and P. Beming, *3G Evolution: HSPA and LTE for Mobile Broadband*, 2nd ed. Elsevier, Oct. 2008.
- [86] G. Song and Y. Li, "Cross-layer optimization for OFDM wireless networks-part I: theoretical framework," *IEEE Trans. Wireless Commun.*, vol. 4, no. 2, pp. 614–624, 2005.
- [87] J. Jang and K. B. Lee, "Transmit power adaptation for multiuser OFDM systems," *IEEE J. Sel. Areas Commun.*, vol. 21, no. 2, pp. 171–178, Feb. 2003.
- [88] S. N. Hasim, M. Susanto, H. Fitriawan and F. Hamdani, "Interference Management with Relay-Based Clustering Method on Ultra Dense Networks of Femto-Macrocellular Network," *2021 International Conference on Converging Technology in Electrical and Information Engineering (ICCTEIE) 2021*, pp. 73-77.
- [89] P. Marsch and G. Fettweis, "Static Clustering for Cooperative Multi-Point (CoMP) in Mobile Communications," *2011 IEEE International Conference on Communications (ICC)*, 2011, pp. 16.
- [90] Y. Xiao, X. Wu, W. Wu and S. Han, "Minimum Separation Clustering Algorithm with High Separation Degree in Ultra-Dense Network," *2019 IEEE Global Communications Conference (GLOBECOM)*, 2019, pp. 1-6.
- [91] C. D. Zhao, X. F. Xu, Z. B. Gao and L. F. Huang, "A coloring-based cluster resource allocation for ultra-dense network," In: *Proceedings IEEE International Conference on Signal Processing, Communications and Computing*, 2016, pp. 1-5.
- [92] L. Liu, C. Wang, W. Wang, C. Qin and Y. Zhang, "A dynamic clustering algorithm based on NIR for interference alignment in ultra-dense network," *2017 IEEE 17th International Conference on Communication Technology (ICCT)*, 2017, pp. 1007-1011
- [93] R. Wei, Y. Wang and Y. Zhang, "A two-stage cluster-based resource management scheme in ultra-dense networks," *2014 IEEE/CIC International Conference on Communications in China (ICCC)*, 2014, pp.738-742.
- [94] N. Sharma and K. Kumar, "Energy Efficient Clustering and Resource Allocation Strategy for Ultra-Dense Networks: A Machine Learning Framework," in *IEEE Transactions on Network and Service Management*, 2022.

- [95] S. Ke, Y. Li, Z. Gao and L. Huang, "An adaptive clustering approach for small cell in ultra-dense networks," 2017 9th International Conference on Advanced Infocomm Technology (ICAIT), 2017, pp. 421-425.
- [96] Y. Ren and R. Xu, "An Adaptive Clustering Scheme Based on Modified Density-Based Spatial Clustering of Applications with Noise Algorithm in Ultra-Dense Networks," 2019 IEEE 90th Vehicular Technology Conference (VTC2019-Fall), 2019, pp. 1-5.
- [97] L. Liu, V. Garcia, L. Tian, Z. Pan and J. Shi, "Joint clustering and intercell resource allocation for CoMP in ultra-dense cellular networks," 2015 IEEE International Conference on Communications (ICC), pp.2560-2564. 2015.
- [98] D. Liu, S. Han, C. Yang and Q. Zhang, "Semi-dynamic User-Specific Clustering for Downlink Cloud Radio Access Network," in IEEE Transactions on Vehicular Technology, vol. 65, no. 4, pp. 2063-2077, April 2016.
- [99] L. Yanxia, Z. Zheng L. Xin, "An Interference Vector Judgement Based User Clustering Scheme in Ultra Dense Network. Information Communication Network and Security". pp.1-5. 2023.
- [100] R. Tresch and M. Guillaud, "Clustered interference alignment in large cellular networks," in Proc. IEEE Int. Symp. PIMRC, Tokyo, , pp. 1024–1028. Japan, Sep. 2009.
- [101] R. Tresch, M. Guillaud, and E. Riegler, "A clustered alignment-based interference management approach for large OFDMA cellular networks," presented at the Joint NEWCOM+/COST2100 Workshop Radio Resource Allocation LTE, Wien, Austria, 2009.
- [102] R. Tresch and M. Guillaud, "Performance of interference alignment in clustered wireless ad hoc networks," in Proc. IEEE ISIT, Austin, TX, USA, Jun. 2010, pp. 1703–1707.
- [103] S. W. Peters and R. W. Heath, Jr., "User partitioning for less overhead in MIMO interference channels," IEEE Trans. Wireless Commun., vol. 11, no. 2, pp. 592–603, Feb. 2012.
- [104] A. Adekunle, "Minimizing Interference in LTE Femtocell Networks Using Graph-Based Frequency Reuse Technique (Unpublished master's dissertation)". University of Lagos, Akoka, Lagos, Nigeria, 2019.
- [105] S.F. Galán, "Simple decentralized graph coloring. Computational Optimization and Applications Journal," vol. 66(1), pp.163-185.2017.
- [106] T.N. Sipayung et al, "Implementation of the greedy algorithm on graph coloring, J. Phys.: Conf. Ser. 2157 012003, 2022.
- [107] Vilém Kmuniček, "Minimal proof of the four-color theorem", IOSR Journal of Mathematics, Volume 18, Issue 2 Ser. II, 2022.
- [108] H. Chen, and P. Zhou, "An ant algorithm for solving the four-coloring map problem", In: Proceedings of the IEEE International Conference on Natural Computation, pp 491-495 doi:10119/ICNC.2013.6818026, 2013.
- [109] Alamsyah and I.T. Putri, "Penerapan Algoritma Greedy Pada Mesin Penjual Otomatis (Vending Machine)". Scientific Journal of Informatics, vol. 1(2), pp 201-209. 2014.
- [110] P Paryati, "Optimasi Strategi Algoritma Greedy untuk Menyelesaikan Permasalahan Knapsack 0-1". In Seminar Nasional Informatika (SEMNASIF), vol. 1(1):pp.101-110. 2015.
- [111] S. Isnaeni, S. Supriyono, and F.Y. Arini, "Implementasi Algoritma Pemrograman Dinamik Untuk Penyelesaian Persoalan Knapsack Dalam Penentuan Keuntungan Optimal Penjualan Barang. Unnes Journal of Mathematics, vol.3(2):pp. 97-102. 2014.
- [112] M. Aslan, and N.A. Baykan, "A performance comparison of graph coloring algorithms. International Journal of Intelligent Systems and Applications in Engineering", pp.1-7. 2016.
- [113] E. Falkenauer, "A hybrid grouping genetic algorithm for bin packing", Journal of Heuristics.vol. 2 (1) pp.5–30. 1996.



ISSN ONLINE: 2447-0228



RESEARCH ARTICLE

OPEN ACCESS

UPQC-S, A FRONTLINE DEPLOYABLE POWER LINE SOLUTION FOR HOLISTIC POWER QUALITY ENHANCEMENT

Sajid M. Patel ¹, Mohammedirfan I Siddiqui ² and Dhaval R. Patel ³

^{1,2,3} Dept. of Electrical Engg., L. D. College of Engineering, Gujarat, India.

¹ <http://orcid.org/0000-0003-4179-732X> ² <http://orcid.org/0009-0004-2525-1284> ³ <http://orcid.org/0009-0001-0471-66>

Email: eepatelsm@gmail.com , i.siddiqui4@gmail.com , dhavalmotog@gmail.com

ARTICLE INFO

Article History

Received: May 29th, 2024

Received: October 24th, 2024

Accepted: October 24th, 2024

Published: October 31th, 2024

Keywords:

Harmonics,
Unified power quality controllers,
Uncontrolled nonlinear load,
Controlled nonlinear load,
Total harmonic distortion.

ABSTRACT

The degradation of the electric power quality due to the escalated use of non-linear loads of commercial and domestic consumers of electric power connected via a distribution line, as well as those of industrial consumers of electric power connected via sub-transmission line, has necessitated the invention of a variety of custom power devices. It seems more effective to insulate the power line from the effects of the non-linear loads and concurrently ensure a reliable, good quality power supply to all consumer loads, especially critical loads. The Unified Power Quality Conditioners (UPQC) is one such dedicated power quality improving device. Among the multitude of UPQC variants, in this paper the functioning of UPQC-S has been thoroughly investigated for diverse nonlinear loads operating under normal as well as abnormal loading conditions. UPQC-S has been designed and simulated for various nonlinear loading conditions under normal as well as abnormal network conditions. [side abnormalities.] The aforementioned simulation has been performed in MATLAB/SIMULINK.



Copyright ©2024 by authors and Galileo Institute of Technology and Education of the Amazon (ITEGAM). This work is licensed under the Creative Commons Attribution International License (CC BY 4.0).

I. INTRODUCTION

Due to ever-increasing and accelerated usage of non-linear loads like domestic computing systems, LED lighting, LED Screen, compact fluorescent lamps, smartphone, power bank; inverter powered air conditioner, washing machine, microwave oven, induction heating system etc., the current and voltage harmonic magnitudes, in the power supply line have increased significantly [1],[2]. It is also to be noted that the power supply systems used in the above-mentioned equipment are compact in size, light weight, extremely efficient and provide good performance at the load end. These positive features are very desirable. But on the supply side, this has led to poor power supply quality, causing degraded performance of other AC supply powered equipment, heating of such equipment, increased transmission losses, line voltage fluctuations, insulation failures, interference issues in communication systems, etc.

It is to be noted that a lot of work has been done to make better the power quality along with reactive power compensation at sub-transmission level, by using various types of equipment ranging from LC Power Filters to FACTS based devices to STATCOM, SSSC, TSCS, TSC, UPFC, IPFC, etc. These FACTS based devices offer a satisfactory reactive power compensation but,

an expensive and partially effective current/voltage harmonic compensation. One should keep in mind that the harmonics in the supply line, unbalanced voltage, voltage sag & swell, voltage flicker, etc., are a consequence of the non-linear loads connected at the distribution end.

To collectively address, all the above-mentioned power quality problems, power filters of passive type, active type as well as hybrid type have been used at the sub-transmission level. Passive filters have conventionally served to mitigate reactive power disturbances and harmonics, yet they suffer from several limitations such as bulky dimensions, resonance challenges, and susceptibility to the impedance characteristics of the power source, which can impact their effectiveness [3-5].

Generally, Parallel Active Power Filters (PAPFs) have been considered as current source employed in parallel to power line. But, the perception that PAPFs are ideal harmonic compensator is not correct, because the compensation characteristics of PAPF is influenced by the power line impedance (as with passive filters). PAPF is effective only for non-linear loads (such as phase-controlled thyristor rectifiers with large inductance for DC drives), which are a source of current harmonics. Non-linear loads like rectifiers with filter capacitor, which act as harmonic voltage source, cannot be compensated by PAPF.

However, the Series Active Power Filter (SAPF) are suitable for the Non-linear loads, which act as harmonic voltage source. Also, SAPF has the capability of providing compensation for voltage sag/swell, voltage flicker, source voltage imbalance. Thus, a combination of PAF and SAPF, provide a complete and effective solution for enhancing power quality as a whole [6].

It is important to keep in mind that the origin of most power quality concerns is at the user end [1],[2], an integration of PAF and SAPF connected at the distribution end would eliminate the entry of all causes which manifest in the power line as power quality issues. And, at the same time provide THD free supply voltage to all forms of load including critical loads. Shunt APFs (another name for PAFs) as shunt current source, addresses current harmonic mitigation, reactive power compensation, and power factor betterment. On the other hand, Series APFs (SAPFs) as a series voltage source, targets voltage irregularities like sag/swell, voltage flicker, ensuring precise regulation of voltage at the load side [7]. PAF operates as a static compensator (STATCOM) at the distribution end, and SAPF can function as a load voltage regulator (VR) at the distribution end. Hence, PAF as DSTATCOM and SAPF as DVR can be integrated into one power quality enhancing device at the distribution end [8-10]. Such an integrated power device, has been given the name of UPQC in the literature, an abbreviation for Unified Power Quality Conditioner [3-5],[10]. A plethora of classifications and structural arrangements of UPQC are found in the literature [4],[11], but the focus of this paper is the right shunt type of UPQC-S [12], in which DSTATCOM and DVR are connected back-to-back as Voltage Source Converter, across a common DC bus capacitor. In UPQC-S, the DSTATCOM fully takes care of all current harmonic compensation, injects reactive power partially and absorbs active power from the power line. Whereas, the DVR infuses a voltage in series between the PCC and the load end at a predefined phase angle and DVR injects both active power and reactive power into the power line. The miniscule real power absorbed by the DSTATCOM, accounts for the switching losses and for maintaining the voltage of the common DC bus Capacitor connected across the VSCs of DSTATCOM & DVR [4],[13]. Overall, this arrangement elevates power quality, by managing both real and reactive power requirements. The power circuit of UPQC is discussed in section II. The general design flow of UPQC-S is discussed in section III. The control approach for UPQC-S is described in section IV. The MATLAB-SIMULINK based performance response of UPQC-S for various nonlinear loads under normal and abnormal network side conditions is discussed in section V. The conclusion of the paper is in section VI.

II. CIRCUIT CONFIGURATION OF UPQC

All UPQC configurations have back-to-back connected shunt and series converters to a DC Bus Capacitor or a battery [4]. The Series converter is popularly identified as Dynamic Voltage Restorer (DVR) and Shunt converter as DSTATCOM. Both DVR and DSTATCOM are generally chosen to be topologically, Voltage Source Inverters. DSTATCOM compensates the current harmonics, reactive power and DVR compensates for voltage sag/swell problems in AC distribution system. The Block diagram of UPQC incorporated with power system is as depicted in Figure 1.

Based on the location of connection, UPQC is classified either as right-side shunt UPQC or left-side shunt UPQC. Right-side shunt UPQC, wherein the DVR is connected adjacent to the PCC and DSTATCOM is connected adjacent to the load. Left-side shunt UPQC, wherein the DVR is connected adjacent to the load

and DSTATCOM is connected adjacent to the PCC. Right-side shunt UPQC is preferred over Left-side shunt UPQC, as the right-side shunt configuration, results in a simpler control strategy and a lower VA rating of both DSTATCOM and DVR [5]. UPQC is further classified as UPQC-Q, UPQC-P and UPQC-S [4]. Take note that this classification is purely based on the voltage compensation approach used, with no change in the power circuit of the UPQC, as depicted in Figure 2.

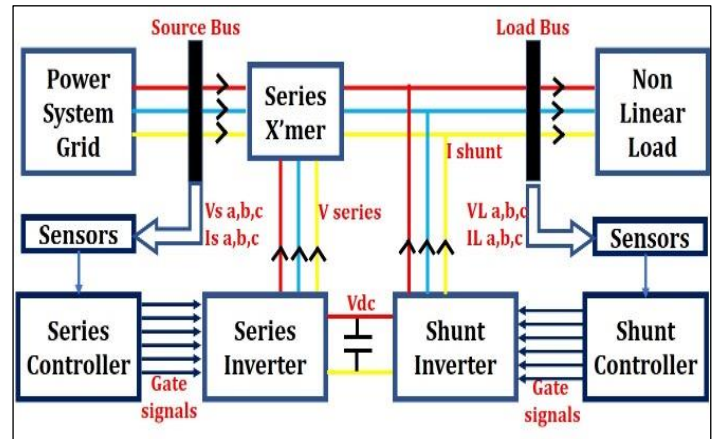


Figure 1: Block diagram of UPQC-S with power system. Source: Authors, (2024).

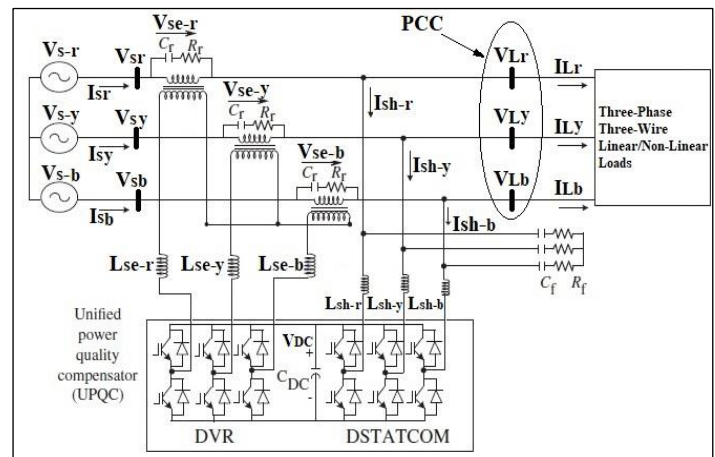


Figure 2: Connection diagram of electrical power grid with UPQC-S for non linear load. Source: Authors, (2024).

It is in the context of this compensation approach, that the Table 1. has been worked out, as below. Table 1 differentiates between the three of them, for various compensating actions and energy storage requirement of a common capacitor or battery energy storage system. In the right-side shunt UPQC-S, both VSCs have equal reactive power rating, which is half of the reactive power of the load. Also, real power rating is same for both VSCs, due to their to a common DC bus capacitor.

In UPQC-S, if one of the connections VSCs absorbs real power from the power line, the other VSC must be injecting an equal amount of real power, into the supply line [11]. The circuit connections for UPQC-S are as shown in Figure 2. It is in the context of this compensation approach, that the Table 1. has been worked out, as below. Table 1 differentiates between the three of them, for various compensating actions and energy storage requirement of a common capacitor or battery energy storage system. In the right-side shunt UPQC-S, both VSCs have equal reactive power rating, which is half of the reactive power of the

load. Also, real power rating is same for both VSCs, due to their connection to a common DC bus capacitor.

Table 1: Selection criterions of UPQC.

Compensation Operation	UPQC-Q	UPQC-P	UPQC-S
DVR injected voltage angle w.r.t source current	Orthogonal	In phase	0°to360°
DVR Injects/Absorbs Reactive Power (Q)	Yes	No	Yes
DVR Injects/Absorbs Active Power (P)	No	Yes	Yes
DVR Provides Voltage Sag Compensation	Yes	Yes	Yes
DVR Provides Voltage Swell Compensation	No	Yes	Yes
DC link support via Capacitor	Yes	No	Yes
DC link support via battery	No	Yes	Yes
DSTATCOM Injects/Absorbs Reactive Power (Q)	Yes	Yes	Yes
DSTATCOM Injects/Absorbs Active Power (P)	Yes	No	Yes

Source: Authors, (2024).

In UPQC-S, if one of the VSCs absorbs real power from the power line, the other VSC must be injecting an equal amount of real power, into the supply line [11]. The circuit connections for UPQC-S are as shown in Figure 2.

The phasor diagram to visualize the compensating actions by DVR and DSTATCOM, in case of voltage Sag, in UPQC-S, as reflected in Figure 3 [14]. The series voltage V_{SE} is infused at Ψ_{SE} angle relative to sagging source voltage V'_t by DVR. This voltage compensation causes a change in the current compensation (I_{SH} to I'_{SH}) provided by DSTATCOM. In this case, DVR and DSTATCOM, both inject reactive power, but DVR injects active power, whereas DSTATCOM absorbs active power.

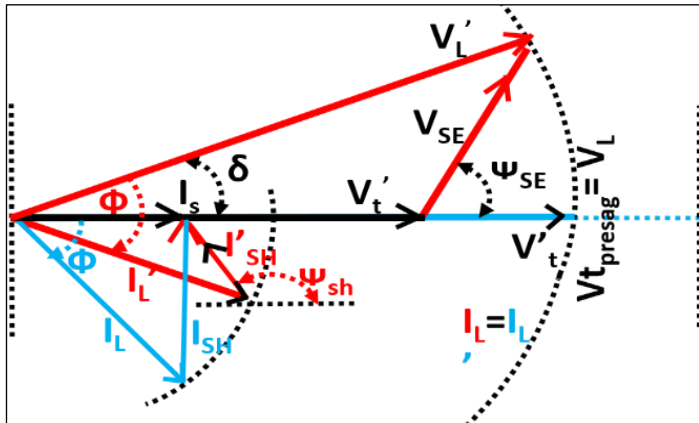


Figure 3: Phasor diagram for voltage sag in UPQC-S.

Source: Authors, (2024).

In Figure 4, series V_{SE} is infused at Ψ_{SE} angle w.r.t. to swelling source voltage V'_t by DVR. This voltage compensation causes a change in the current compensation (I_{SH} to I'_{SH}) provided by DSTATCOM. In this case, DVR and DSTATCOM, both inject reactive power, but DVR absorbs active power and DSTATCOM injects active power.

It is through this absorption of the active power (either by DVR or DSTATCOM) under the supply voltage sag or swell, that the voltage of the common DC link capacitor is maintained [4], [13].

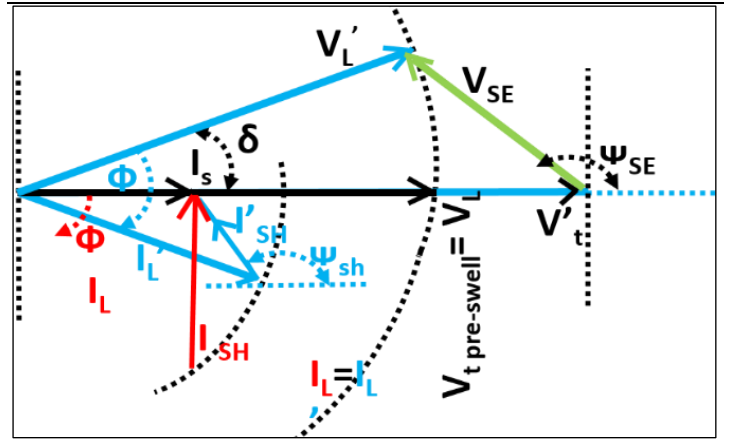


Figure 4: Phasor diagram for voltage swell compensation in UPQC-S.

Source: Authors, (2024).

III. INSIGHT OF DESIGNING OF UPQC-S

The Design of UPQC-S, is broadly, the calculation of the Volt-Ampere rating of DSTATCOM, DVR and DVR Injection Transformer. This calculation is based on multiple predefined parameters related to supply, load and designer specific choices.

The supply side parameters are supply voltage, supply frequency, supply impedance, % supply voltage sag/swell. The load side parameters are load active power, load power factor. The designer choices are about the overloading factor, allowable variation in capacitor voltage, allowable time for DC link capacitor voltage recovery etc. Using the above-described parameters, the below design flow can be used to calculate the Volt Amp rating of DSTATCOM, DVR and Injection Transformer, Voltage & current rating of semiconductor switch used in the VSCs of DSTATCOM and DVR, the value of capacitance of common DC link as well as the magnitude of its voltage, the inductance and the current rating of AC inductors used in DSTATCOM and DVR and the associated ripple filters. The steps and the equations involved in designing has been depicted in the flow chart shown in Figure 5.

IV. CONTROL STRATEGY OF UPQC-S

From a multitude of control strategies in the time domain [15], along with the controller design procedure [16], fixed frequency PWM controllers, a combination of PWM and Hysteresis controller to Space Vector PWM Controllers [17-19], that can be applied for the comprehensive current and voltage compensation, a much simpler hysteresis band-based control approach has been used [20]. This control approach is applied for power quality compensation in a 3P3W, supply system at distribution end [19]. Here the synchronous reference frame (SRF) theory, has been applied for controlling DSTATCOM and PQ (Active-Reactive Power) theory, has been applied for controlling DVR. The objective of the control strategy for the DSTATCOM, is (I_{SH}) compensation, during supply voltage sag/swell [21],[22] and to maintain the set voltage of the DC Bus capacitor, by absorbing real power, from the power line. Figure 6 & Figure 7 represent control strategies for the same to achieve complete harmonic as well as reactive current. The objective of the control strategy for the DVR, is to preserve the rated load voltage during

voltage sag/swell [21],[22] by infusing voltage in series with supply voltage at a pre-calculated angle (Ψ_{SE}) to the supply voltage, approach used for DSTATCOM and DVR, is as reflected in Figure 6 and Figure 7 respectively.

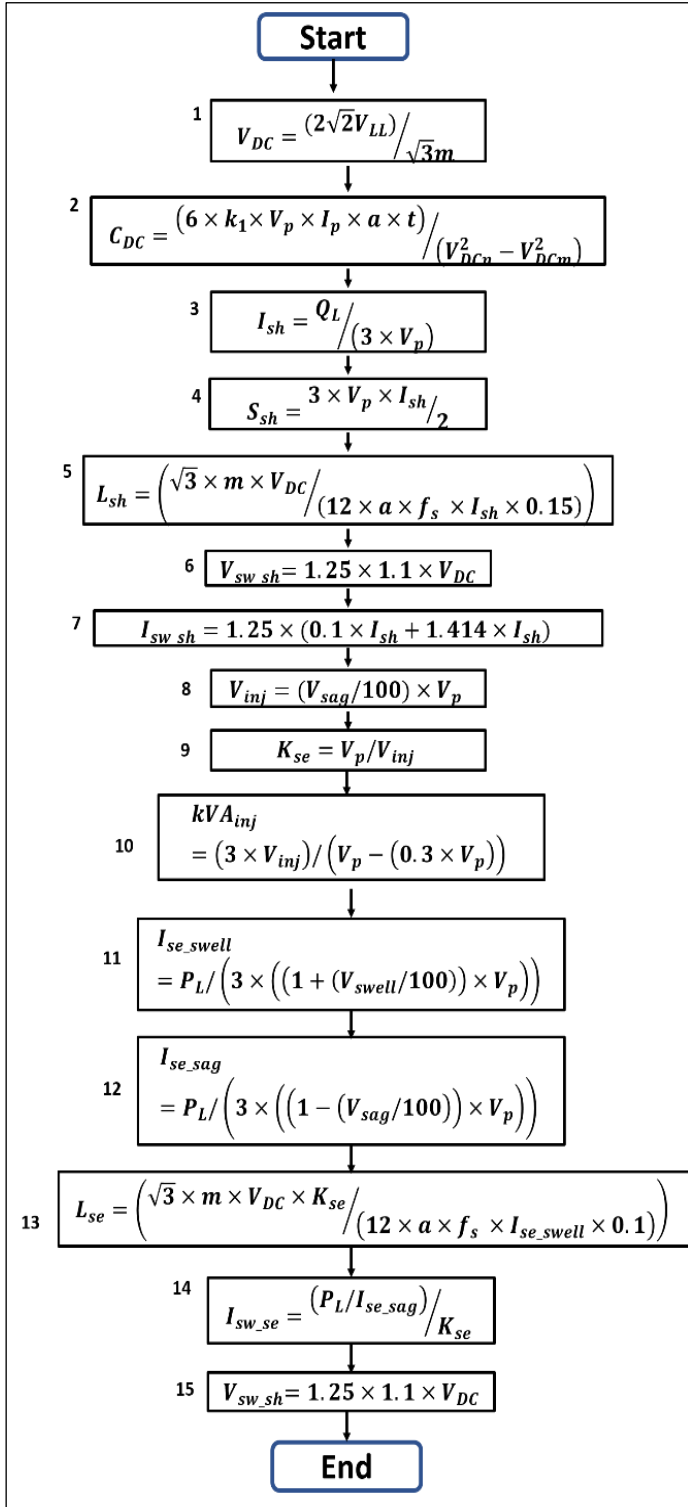


Figure 5: UPQC-S Design Flow chart. Source: Authors, (2024).

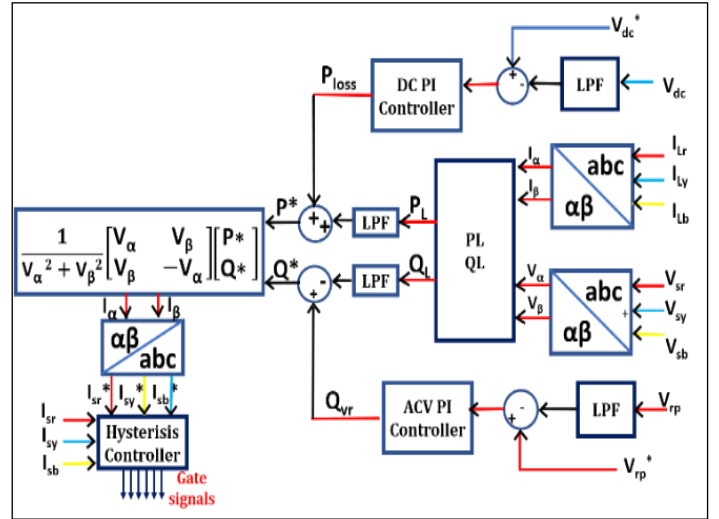


Figure 6: Control approach for DSTATCOM. Source: Authors, (2024).

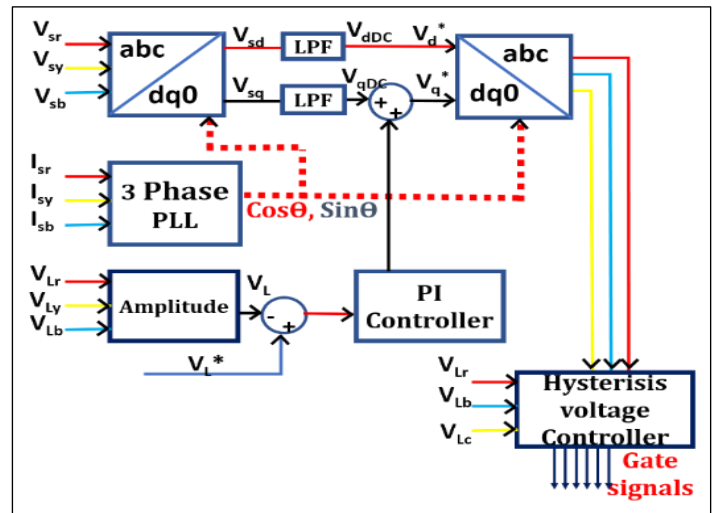


Figure 7: Control approach for DVR. Source: Authors, (2024).

The control approach is to be tested for not only for achieving near unity power factor on the supply side, but also for load balancing and cancelling voltage & current harmonics, requiring the DVR to inject/absorb real and reactive power, but without discharging the preset DC bus capacitor voltage. The control as well as the load voltage regulation under supply voltage sag/swell, flicker, notch conditions, specifically in a 3P3W distribution system for linear and non-linear loads.

V. MATLAB SIMULINK IMPLEMENTATION

V.1 SIMULATION MODEL

The Figure 8 reflects implementation of UPQC-S in MATLAB-SIMULINK. Extensive simulation tests are conducted to assess the efficacy of a 3P3W UPQC in addressing various power quality issues such as voltage/current harmonics, voltage sags/swells, voltage distortion, voltage supply imbalance, voltage flicker, voltage notches, load current unbalance, and reactive power compensation. Figure 9 and Figure 10 show the SIMULINK implementation of SRF theory and PQ theory respectively.

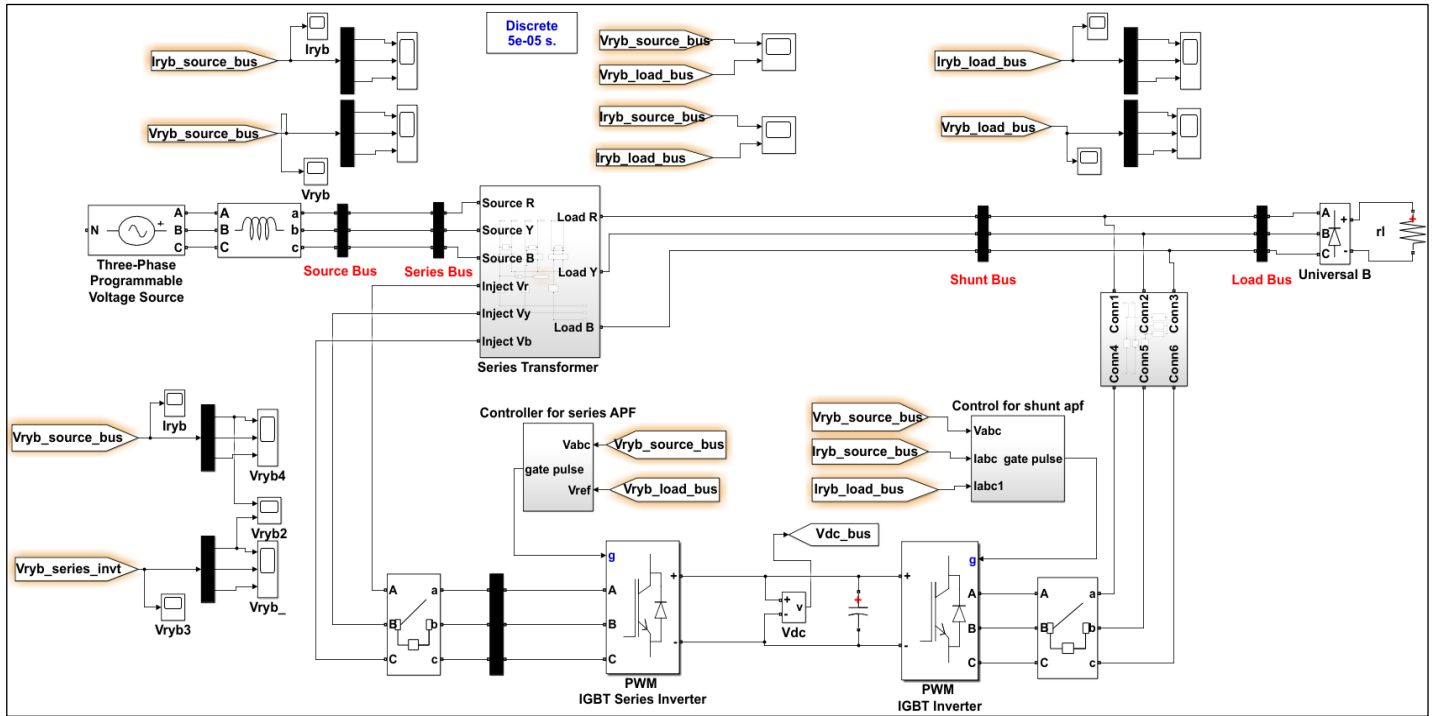


Figure 8: Matlab Simulink implementation of UPQC-S system.
Source: Authors, (2024).

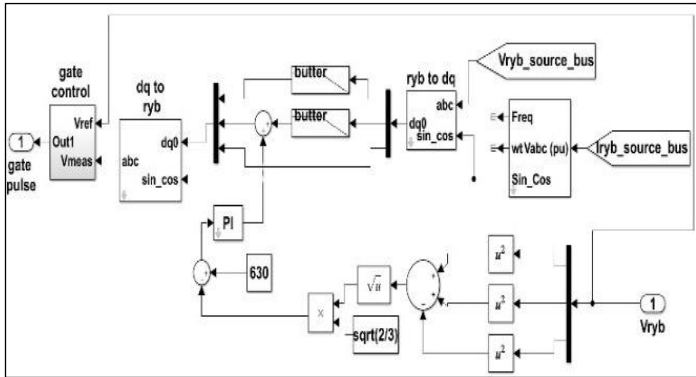


Figure 9: Series Inverter Controller (DVR).
Source: Authors, (2024).

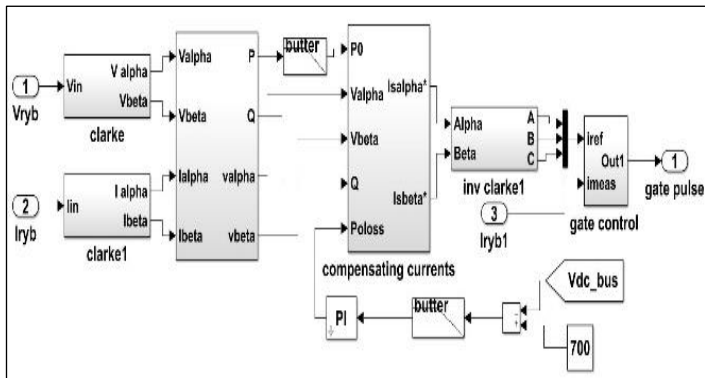


Figure 10: Shunt inverter controller (DSTATCOM).
Source: Authors, (2024).

V.2 SIMULATION SET POINTS

The load configurations include a 3- Φ rectifier with RL/RC load, a 3- Φ thyristor bridge rectifier with RL load, a 3- Φ unbalanced resistive load, and a 3- Φ induction motor. The setpoint

values of parameters for load is given in Table 2. Table 3. outlines the parameters of the UPQC system, with the source voltage specified as (3 Phase, 415V, 50 Hz).

Table 2: Simulink model Load set point values.

Sr.	Parameters	Set Point
1.	Load: Non Linear Load (3P 3W)	$R_L = 30$ ohm, $L=1.0$ mH (Series)
2.	Load: Non Linear Load with controlled rectifier (3P 3W)	$R_L = 30$ ohm, $L=1.0$ mH, $\alpha=20^\circ$ (Series)
3.	Load: Non Linear Load (3P 3W)	$R_L=10$ ohm, $C=1000$ microF (Parallel)
4.	Load: Rating of Asynchronous Squirrel cage machine	$P= 7460$ VA, $V=415$ V, $F=50$ Hz
5.	Load: Non Linear Load (3P 3W)	$R_L = 30$ ohm, $L=1.0$ mH (Series)

Source: Authors, (2024).

Table 3: Simulink model UPQC set point values.

Sr.	Parameters	Set Point
1.	DC Bus voltage (V_{dc}).	700V
2.	DC Bus Capacitor (C_{dc})	6000 μ F
3.	DSTATCOM: AC Inductor for phase leg of VSC (L_{sh})	6 mH
4.	DSTATCOM: Ripple Filter	$R_f=5\Omega$, $C_f=5$ μ F
5.	DSTATCOM: KVA Rating	13 kVA
6.	DSTATCOM: Max. Current	32 A
7.	DVR: Injection Transformer	415/75,12.8kVA
8.	DVR: Interfacing Inductor	$L_{se}=10$ mH
9.	DVR: Ripple Filter	$R_f=5\Omega$, $C_f=5$ μ F
10.	DVR: KVA Rating	13 kVA
11.	DVR: Maximum Current	32 A

Source: Authors, (2024).

V.3 SIMULATION RESULTS

Various operating scenarios of UPQC-S are considered, and depicted in different cases, and discussed in this section.

V.3.1 CASE 1A: UPQC-S CORRECTIVE RESPONSE FOR UCNLL.

In this scenario, an uncontrolled bridge rectifier with an RL load is employed to evaluate the behaviour of UPQC-S. Its voltage corrective response under non-linear load conditions is depicted in Figure 11. Upon activation of UPQC-S at 0.1 seconds (DVR activation following DSTATCOM activation), it is found that supply and load voltages are minimally affected by Uncontrolled Non-Linear Load (UCNLL). Consequently, the series voltages (V_{se}^{ryb}) remain close to sinusoidal. Figure 12 illustrates the current profile for the corrective response by UPQC-S. It shows the compensating shunt currents Fig.12 (b), which cancel out current harmonics generated by uncontrolled rectifier. Notably, after 0.1 second, the source current approaches sinusoidal behaviour. Figure 13 and Figure 14 depict THD for voltage before and after employing UPQC-S, which are 1.15% and 0.18%, respectively.

Furthermore, current THD, depicted in Figure 15 and Figure 16, is reduced from 30.15% to:

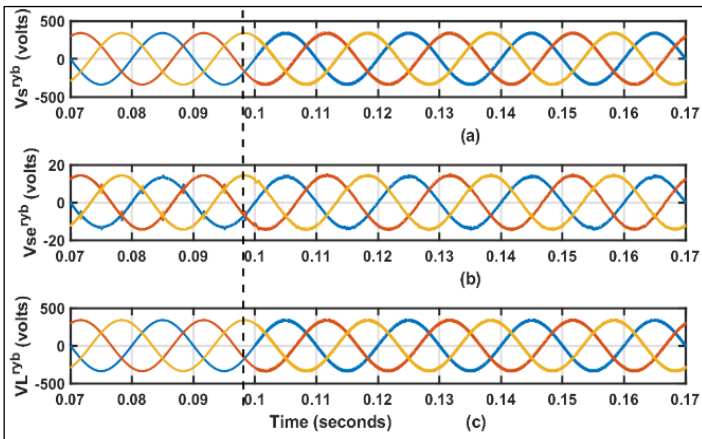


Figure 11: Voltage profile of UPQC-S corrective response for UCNLL.
Source: Authors, (2024).

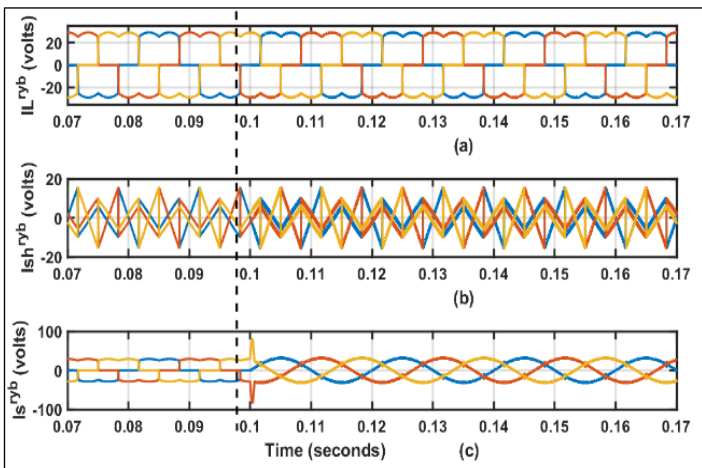


Figure 12: Current profile of UPQC-S.
Source: Authors, (2024).

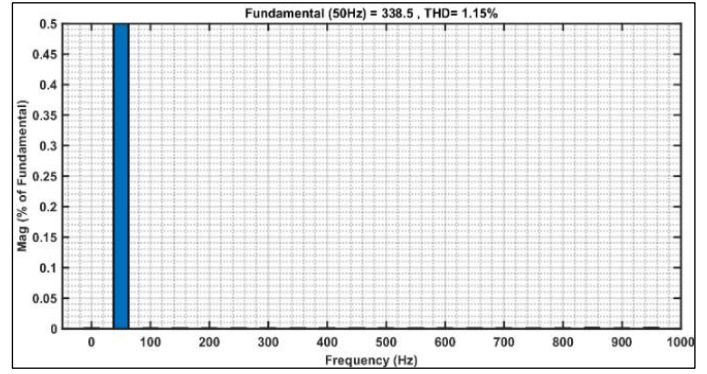


Figure 13: Voltage THD before UPQC-S corrective response for UCNLL.
Source: Authors, (2024).

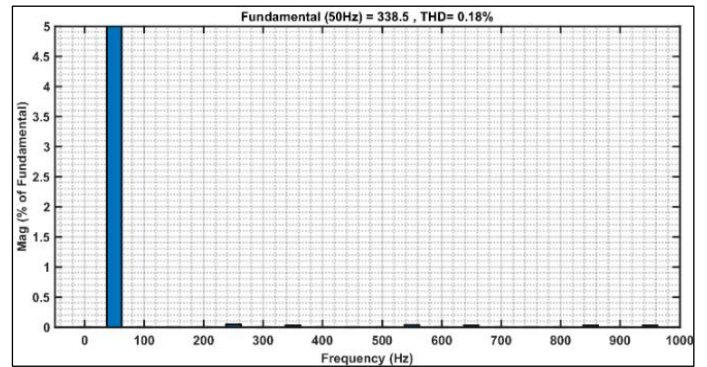


Figure 14: Voltage THD after UPQC-S corrective response for UCNLL.
Source: Authors, (2024).

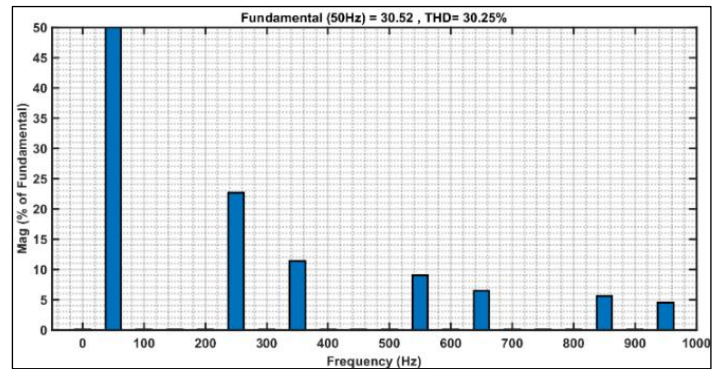


Figure 15: Current THD before UPQC-S corrective response for UCNLL.
Source: Authors, (2024).

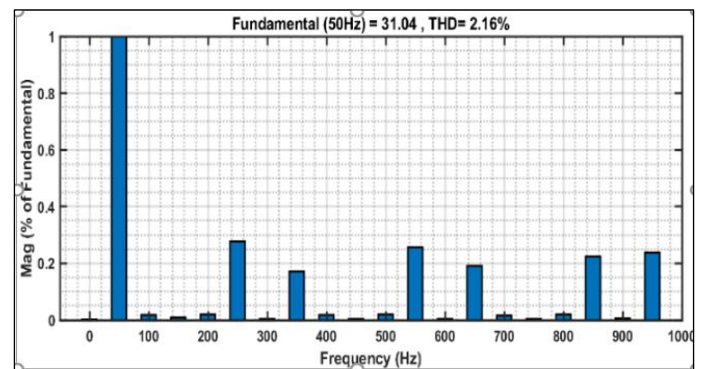


Figure 16: Current THD after UPQC-S corrective response for UCNLL.
Source: Authors, (2024).

V.3.2 CASE 1B: UPQC-S CORRECTIVE RESPONSE FOR CNLL

In Case-1B, a controlled bridge rectifier with an RL load is utilized to assess the performance of UPQC-S. The Controlled Non-Linear Load (CNLL) operates with a firing angle of 20° . As depicted in Figure 17, the voltage correction response of UPQC-S under non-linear load conditions is illustrated. At 0.1 seconds, UPQC-S is activated (DVR following DSTATCOM), revealing spikes in both source and load voltages during CNLL operation as shown in Figure 17. Consequently, DVR injects voltage (V_{se}^{ryb}) to mitigate these spikes and all voltage DVR harmonics generated by switching operations.

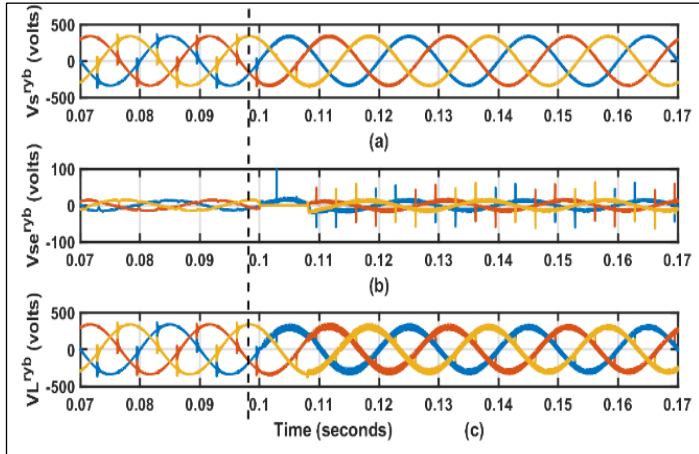


Figure 17: Voltage profile of UPQC-S corrective response for CNLL.
Source: Authors, (2024).

Figure 18 reflects the current profile for the corrective response by UPQC-S, indicating that it generates shunt currents (I_{sh}^{ryb}), which are injected into the system to cancel out current harmonics generated by the CNLL. Notably, after 0.1 seconds, the source current approaches sinusoidal behavior. Figure 19 and Figure 20 display the voltage THD before and after employing UPQC-S, which are 5.31% and 0.82%, respectively. Moreover, current THD improves from 32.90% to 3.34%, complying with the limits outlined in the IEEE-519 standard, which is reflected in Figure 21 & Figure 22.

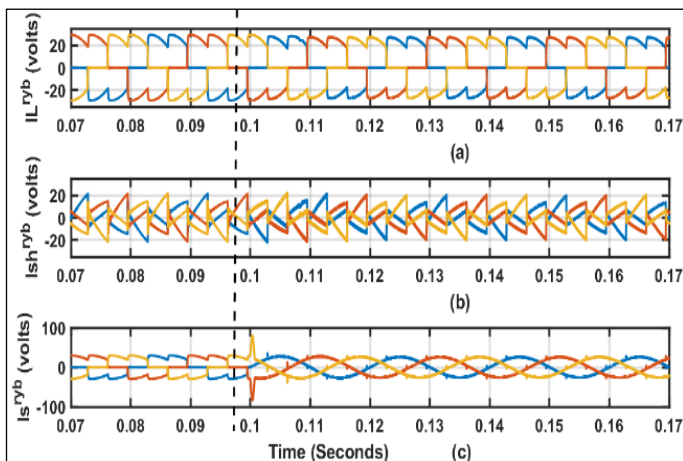


Figure 18: Current profile of UPQC-S corrective response for CNLL.
Source: Authors, (2024).

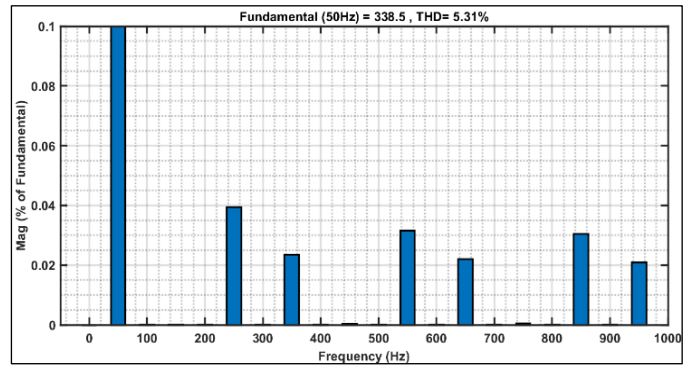


Figure 19: Voltage THD before UPQC-S corrective response for CNLL.
Source: Authors, (2024).

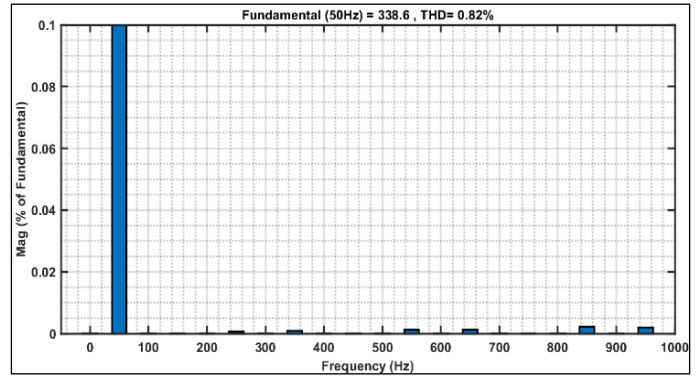


Figure 20: Voltage THD after UPQC-S corrective response for CNLL.
Source: Authors, (2024).

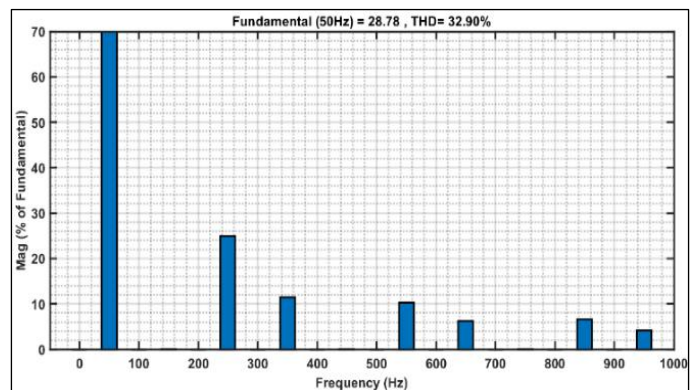


Figure 21: Current THD before UPQC-S corrective response for CNLL.
Source: Authors, (2024).

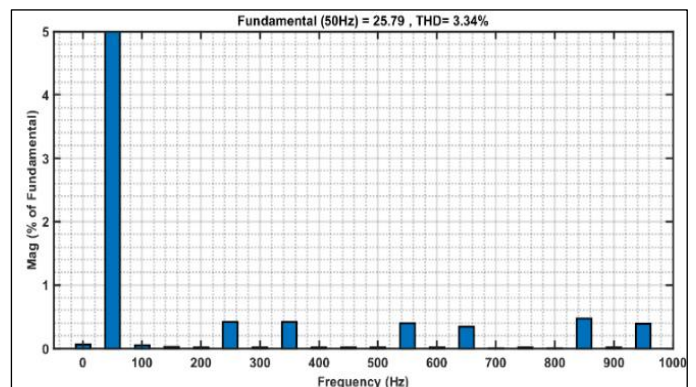


Figure 22: Current THD after UPQC-S corrective response for CNLL.
Source: Authors, (2024).

V.3.3 CASE 2: UPQC-S CORRECTIVE RESPONSE FOR CAPACITIVE LOAD

In this Case, an uncontrolled rectifier with RC load is employed to evaluate performance of UPQC-S. Fig.23 illustrates the current correction response of UPQC-S under non-linear conditions with an RC load. At 0.6 seconds, UPQC-S is activated (DVR following DSTATCOM), resulting in an improvement in the distorted source current, which gradually approaches near sinusoidal behaviour, as depicted in Figure 23(a).

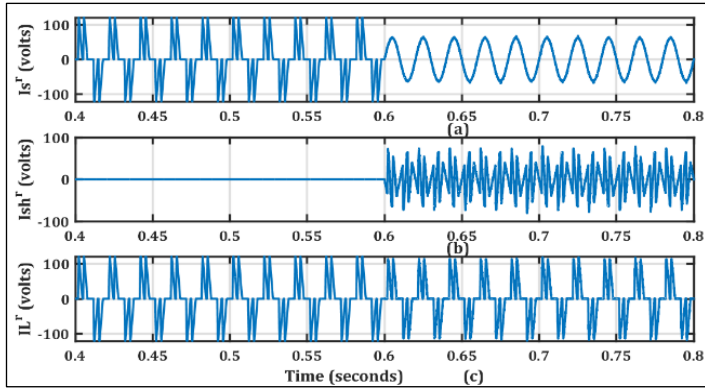


Figure 23: Current profile of UPQC-S corrective response for capacitive load.
Source: Authors, (2024).

Figure 23(b) and Figure 23(c) depicts the shunt (I_{sh}^r) and load (I_L^r) currents respectively. It is notable that the capacitive type load injects a significant amount of current harmonics into the source, as evident from Figure 24, which shows a current THD of 81.06%. However, after 0.6 seconds, the source current approaches sinusoidal behaviour due to shunt compensating current (I_{sh}^r) injection. Figure 25 present the current THD after the insertion of UPQC-S, which is reduced to 3.62%, complying with the limits specified in the IEEE-519 standard.

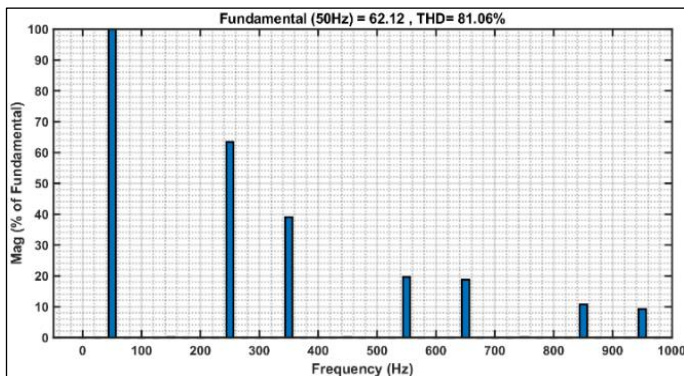


Figure 24: Current THD before UPQC-S corrective response for capacitive load.
Source: Authors, (2024).

V.3.4 CASE 3: UPQC-S CORRECTIVE RESPONSE FOR UNBALANCE VOLTAGE SUPPLY.

In Case 4 scenario, an unbalanced voltage (0.2pu) is deliberately introduced from the source side, spanning from 1.4 s to 1.7 s and from 1.9 s to 2.2 s, while considering a non-linear load. During this period, the magnitude of the R phase is increased from 1.4 s to 1.7 s.

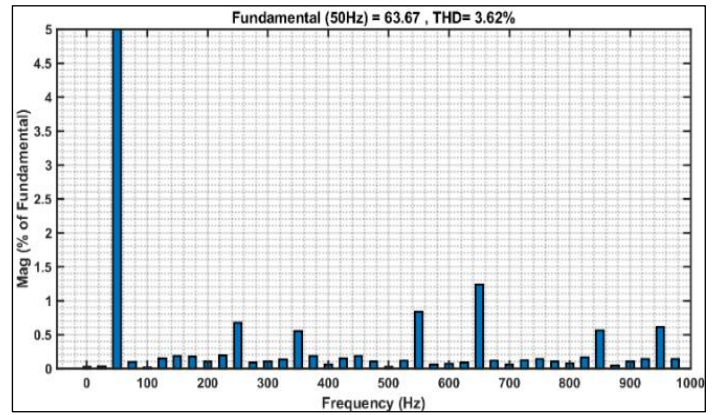


Figure 25: Current THD after UPQC-S corrective response for capacitive load
Source: Authors, (2024).

and then decreased from 1.9 s to 2.2 s, as evidenced in Figure 26 (a), (b) & (c). DVR intervenes by injecting series voltage in a manner that effectively compensates for the unbalance, ensuring that the load voltage remains constant throughout this unbalanced condition. The corrective response of UPQC-S is depicted in Figure 27 and Figure 28, which respectively show the voltage THD and current THD during the unbalanced supply condition.

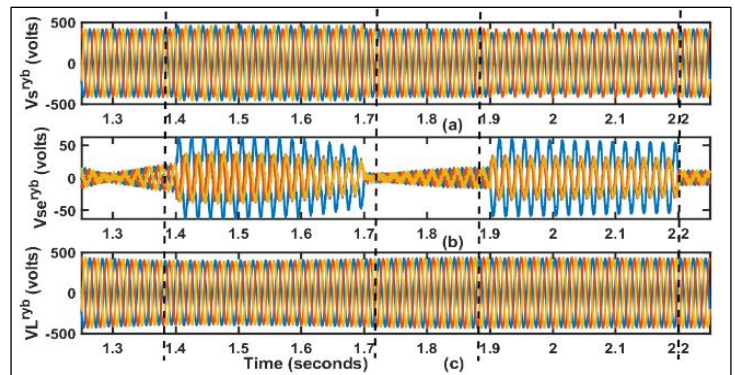


Figure 26: Voltage profile of UPQC-S corrective response for unbalance voltage supply.
Source: Authors, (2024).

V.3.5 CASE 4A: UPQC-S CORRECTIVE RESPONSE DURING VOLTAGES SAG.

The dynamic behavior of the UPQC-S for a non-linear load condition is shown in Figure 29 (a), (b) & (c). It reflects transient response of the UPQC-S, during a voltage sag scenario, specifically when a non-linear load is connected. At 0.1 sec, voltage sag of 0.3 pu, in the source voltage (V_s^r) occurs for 10 cycles, during which it is found that load voltage (V_L^r) in Figure 29 (c) is effectively regulated to a constant amplitude both during the voltage sag and under normal operating conditions. Notably, it is during the sag period that the DVR injects voltage (V_{se}^r) to preserve the load voltage, as illustrated in Figure 29(b). Furthermore, both voltage and current THD remain within the limits outlined by the IEEE-519 standard, as demonstrated in Figure 30 and Figure 31, respectively.

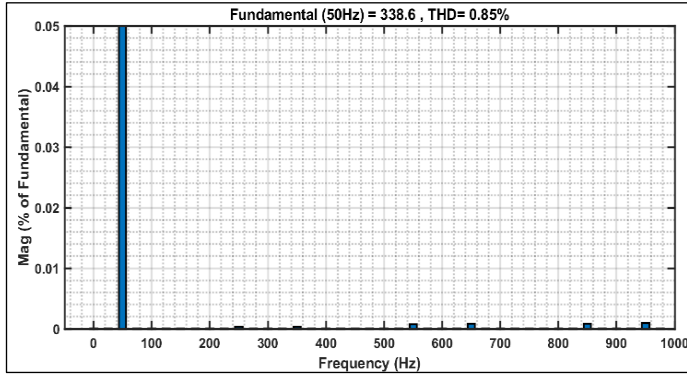


Figure 27: Voltage THD, after Corrective response for unbalance voltage supply.
Source: Authors, (2024).

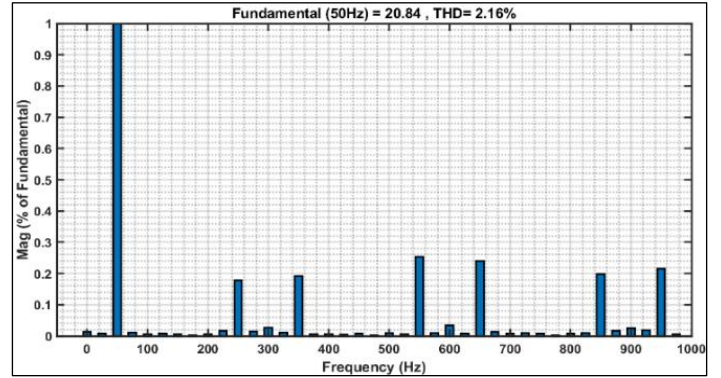


Figure 31: Current THD, after UPQC-S corrective response during voltages sag.
Source: Authors, (2024).

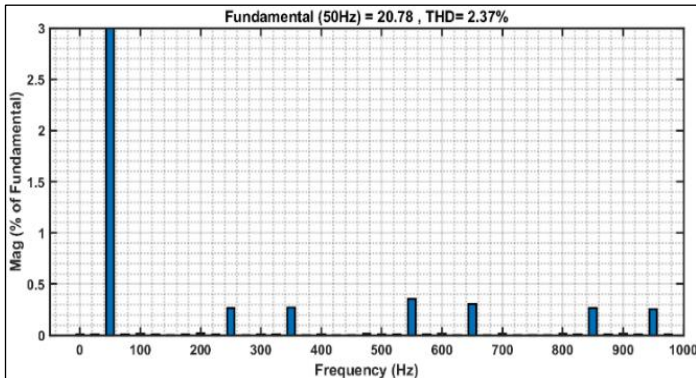


Figure 28: Current THD, after corrective response for unbalance voltage supply.
Source: Authors, (2024).

V.3.6 CASE 4B: UPQC-S CORRECTIVE RESPONSE DURING VOLTAGES SWELL.

Figure 32 depicts the transient response of the UPQC-S, during voltage swell scenario, for a non-linear load. At the 0.1 sec, a voltage swell in the source voltage of 0.3 pu occurs for 10 cycles. Interestingly, it is found that the load voltage (V_L^r) in Figure 32 (c), remains regulated to a constant amplitude both during the voltage swell and under normal condition. Notably, only during the swell event, DVR infuses voltage (V_{se}^r) to preserve the load voltage.

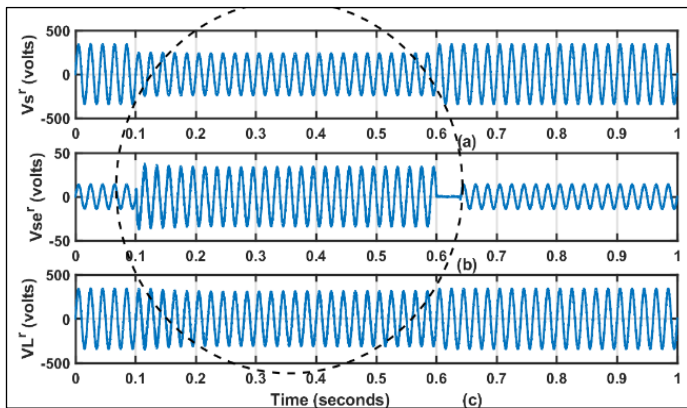


Figure 29: Voltage Profile of UPQC-S corrective response during voltages sag.
Source: Authors, (2024).

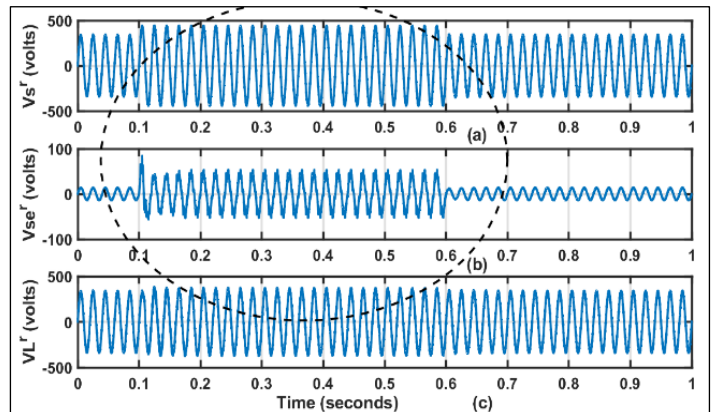


Figure 32: Voltage profile of UPQC-S corrective response during voltages swell.
Source: Authors, (2024).

Furthermore, both voltage and current THD remain within the limits outlined by the IEEE-519 standard, as demonstrated in Figure 33 and Figure 34, respectively.

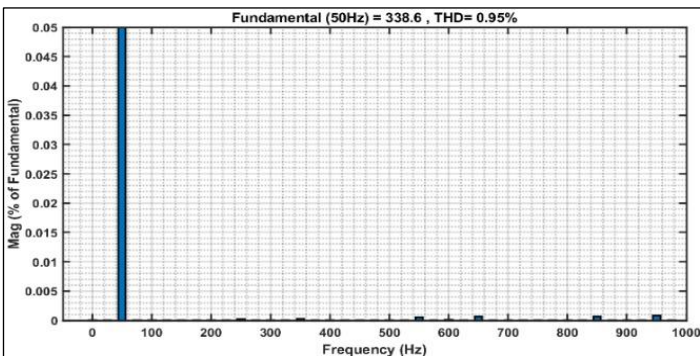


Figure 30: Voltage THD, after UPQC-S corrective response during voltages sag.
Source: Authors, (2024).

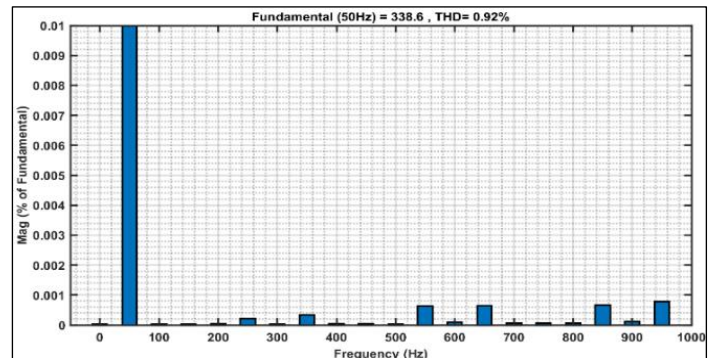


Figure 33: Voltage THD, after UPQC-S corrective response during voltages swell.
Source: Authors, (2024).

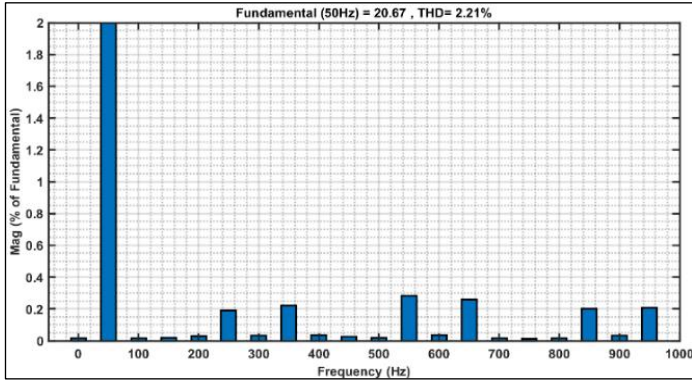


Figure 34: Current THD after UPQC-S corrective response during voltages swell.

Source: Authors, (2024).

V.3.7 CASE 5: UPQC-S COMPENSATIVE RESPONSE FOR INDUCTION MOTOR LOAD.

In this scenario, the nonlinear load is an induction motor. UPQC-S is activated at 0.6s. Prior to activation, the compensating current (I_{sh}^{ryb}) as reflected in Figure 35 is negligible, also the reactive power (Q_s) drawn from the source is considerably high as shown in Figure 36 (a). Following activation at 0.6s, the load reactive power requirement from supply reduces significantly from 3927 VAR to 698 VAR. This required reactive power for the induction motor is then supplied by DSTATCOM (Q_{sh}), as demonstrated in Figure 36 (c).

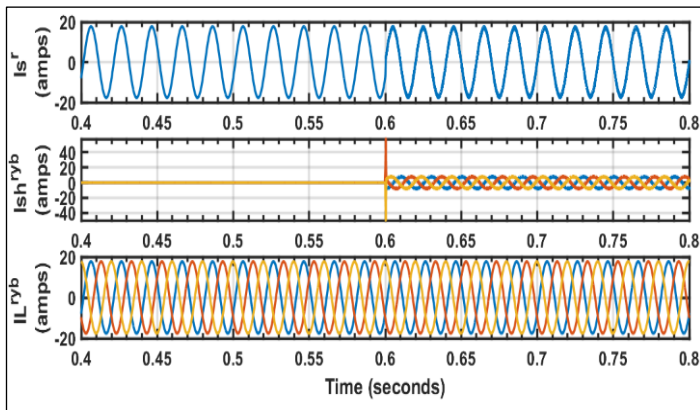


Figure 35: Current profile of UPQC-S compensative response for induction motor load.

Source: Authors, (2024).

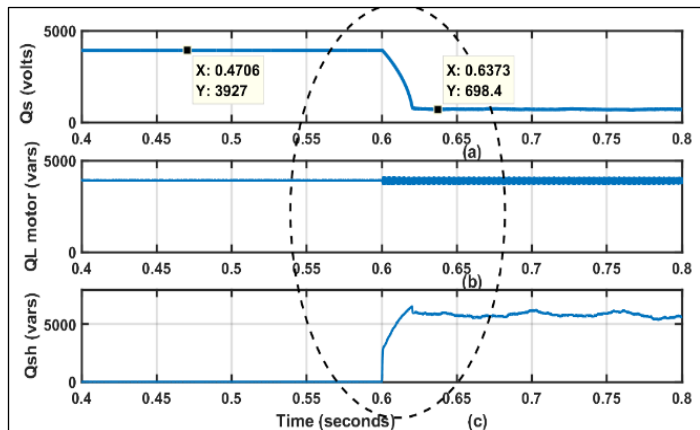


Figure 36: Reactive power profile of UPQC-S compensative response for Induction Motor load.

Source: Authors, (2024).

V.3.8 CASE 6: UPQC-S CORRECTIVE RESPONSE DURING VOLTAGE FLICKER.

In this case, voltage fluctuations occur intermittently at the source side, specifically between time intervals of 0.1s to 0.13s and 0.2s to 0.23s. The performance evaluation of UPQC-S is conducted under these conditions. Figure 37 illustrates the DVR intervention by injecting series voltage (V_{se}^{ryb}) to preserve the load voltage (V_L^{ryb}), from being affected by fluctuations.

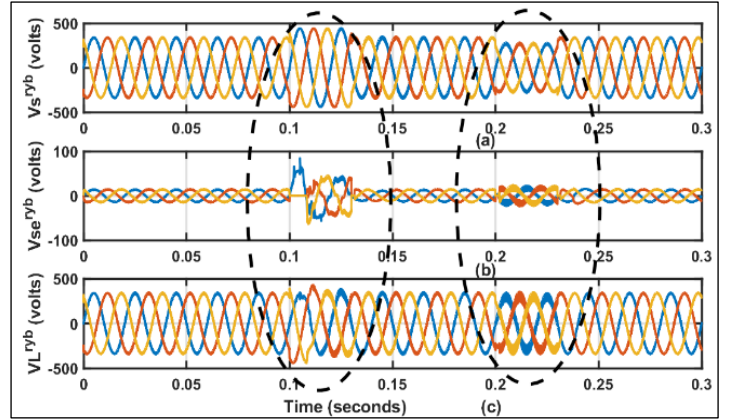


Figure 37: Voltage profile of UPQC-S corrective response during voltage flicker.

Source: Authors, (2024).

V.3.9 CASE 7: UPQC-S CORRECTIVE RESPONSE DURING HARMONIC INJECTION

In this case, at the onset of 0.1s, distortion in the source voltage is intentionally induced across all three phases by introducing specific harmonics-namely the 5th harmonic (set at 15% of the source voltage) and the 7th harmonic (set at 20% of the source voltage). It is illustrated in Fig.38, that DVR, promptly initiates the process of harmonic compensation by injecting a combined signal comprising the 5th and 7th harmonics. This intervention effectively leads to the generation of a voltage waveform free from distortions, ensuring optimal conditions for nonlinear loads.

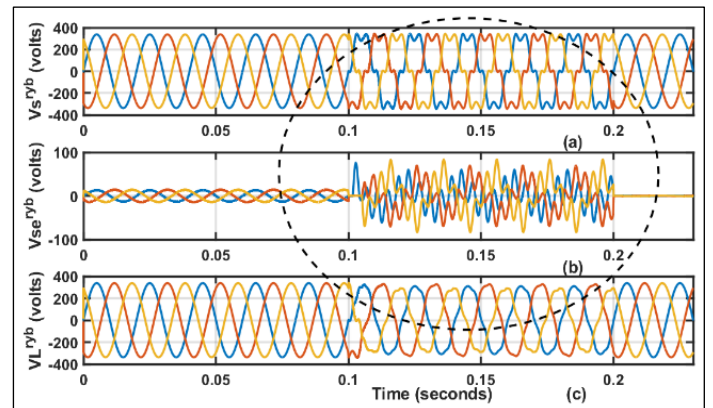


Figure 38: Voltage profile of UPQC-S corrective response during harmonic injection.

Source: Authors, (2024).

It is depicted in Figure 39 and Figure 40, voltage THD has been significantly brought down from 20.43% to 1.92%. It can be seen from Figure 41, that the capability of mitigating imbalance in

source current caused by imbalance in load current has been satisfactorily achieved. Distinct differences in load phase currents are used for identifying any irregularities in load distribution. Typically, load imbalances are observed due to the utilization of a three-phase

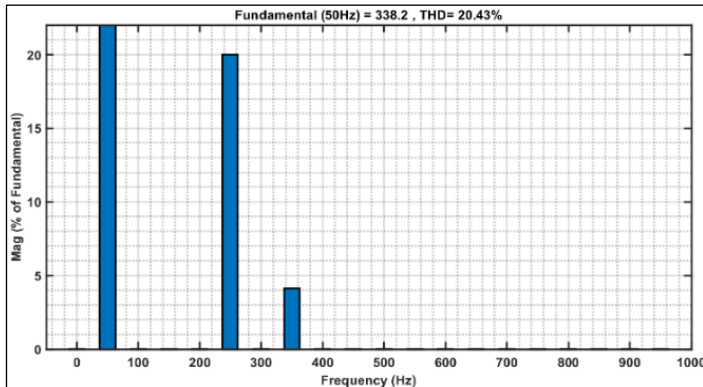


Figure 39: THD of source voltage during harmonic injection. Source: Authors, (2024).

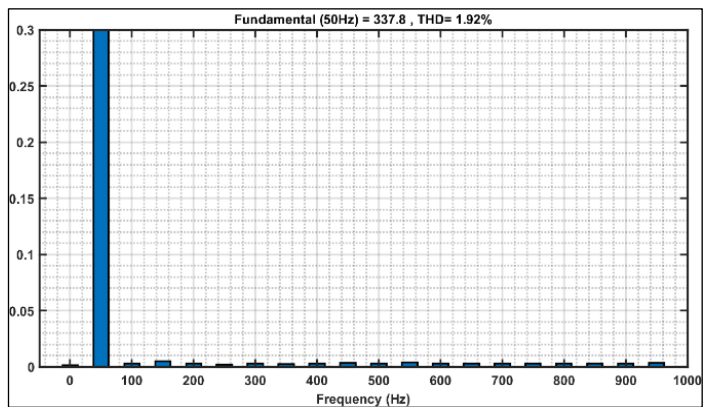


Figure 40: THD of load voltage during harmonic injection. Source: Authors, (2024).

V.3.10 CASE 8: LOAD IMBALANCE

Unbalanced linear load. Specifically, load resistors of 20Ω, 40Ω, and 60Ω are employed for phase-r, phase-y, and phase-b, respectively. Upon activation of the UPQC-S at 0.1s, as depicted in Figure 41, the source current ($I_s^{r,y,b}$) achieves equilibrium, with compensating shunt currents ($I_{sh}^{r,y,b}$).

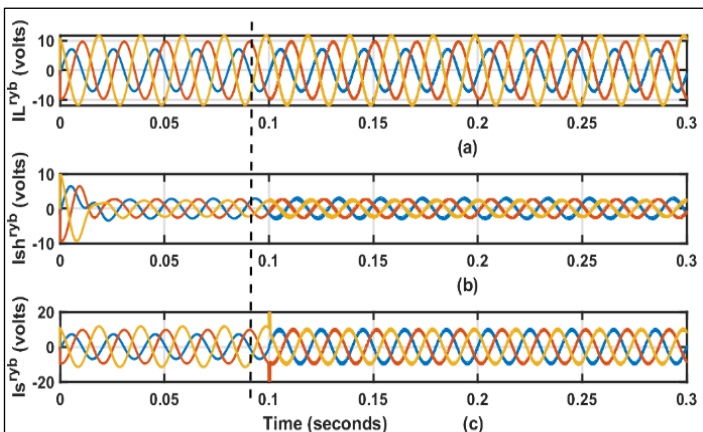


Figure 41: Corrective response of UPQC-S during load imbalance. Source: Authors, (2024).

VI CONCLUSIONS

This paper advocates, a simple and generalized, design procedure of UPQC-S. A conceptual analysis of UPQC-S for all the power quality related issues, has been carried out via MATLAB/SIMULINK. The major key points of the aforementioned simulation are as follows:

1. The DVR section of the proposed UPQC-S under the hysteresis band controller is capable of compensating for source voltage sag/swell, source voltage imbalance, source voltage flicker and notches.
2. Source current remains within the THD limits set in IEEE-519 for all type of controlled and uncontrolled non-linear load, by using UPQC-S. Further, for RC-type load (Capacitor filter based Resistive Loads), the source current THD is substantially alleviated to 3.62% from 81.06%.
3. The DVR and DSTATCOM work in synchronism to obtain the load-reactive power compensation/Load imbalance, for linear as well non-linear load.

Table 4: ABBREVIATIONS.

UPQC-S	Unified Power Quality Conditioner -Apparent power (S)
UCNLL	Uncontrolled Non-Linear Load
CNLL	Controlled Non-Linear Load
THD	Total Harmonic Distortion
PAPF	Parallel Active Power Filter
SAPF	Series Active Power Filter
DVR	Dynamic Voltage Restorer
DSTATCOM	Distributed Static Synchronous Compensator
PCC	Point of Common Coupling
IPFC	Inter Liner Power Flow Controller
SSSC	Static Synchronous Series Compensator
TSCS	Thyristor Switched Controlled Capacitor.
TSC	Thyristor Switched Capacitor.
UPFC	Unified Power Flow Control
STATCOM	Static Synchronous Compensator

Source: Authors, (2024).

VII CONFLICT OF INTEREST

“The authors declare that there are no conflicts of interest or any financial interest regarding the publication of this manuscript”.

VIII AUTHOR CONTRIBUTION STATEMENT

Conceptualization: Sajid M. Patel, Mohammedirfan I Siddiqui and Dhaval R. Patel.

Methodology: Sajid M. Patel, Mohammedirfan I Siddiqui and Dhaval R. Patel.

Investigation: Sajid M. Patel, Mohammedirfan I Siddiqui and Dhaval R. Patel.

Discussion of results: Sajid M. Patel, Mohammedirfan I Siddiqui and Dhaval R. Patel.

Writing – Original Draft: Sajid M. Patel, Mohammedirfan I Siddiqui and Dhaval R. Patel.

Writing – Review and Editing: Sajid M. Patel, Mohammedirfan I Siddiqui and Dhaval R. Patel.

Resources: Sajid M. Patel, Mohammedirfan I Siddiqui and Dhaval R. Patel.

Pictures & Images: Sajid M. Patel, Mohammedirfan I Siddiqui and Dhaval R. Patel.

Supervision: Sajid M. Patel, Mohammedirfan I Siddiqui and Dhaval R. Patel.

Approval of the final text: Sajid M. Patel, Mohammedirfan I Siddiqui and Dhaval R. Patel.

IX ACKNOWLEDGEMENTS

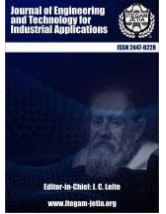
The authors gratefully acknowledge the support from faculties of Electrical department, L.D. college of engineering, which has provided valuable guidance and resources throughout this research project. We also extend our sincere appreciation to the anonymous reviewers who generously dedicated their time and expertise to review our manuscript. Their insightful comments and feedback significantly improved the quality of our work.

X REFERENCES

- [1] K. Nikum, R. Saxena, and A. Wagh, "Effect on power quality by large penetration of household non linear load," Jul. 2016.
- [2] L. Arsov, I. Iljazi, S. Mircevski, M. Cundeve-Blajer and A. Abazi, "Measurement of the influence of household power electronics on the power quality," 2012 15th International Power Electronics and Motion Control Conference (EPE/PEMC), Novi Sad, Serbia, 2012, pp. DS1d.7-1-DS1d.7-7
- [3] A. Ghosh, Gerard Ledwich, "Power Quality Enhancement Using Custom Power Devices. Springer", 2002
- [4] B. Singh, A. C. K. Al-Haddad (2006). "Power Quality, Problems and Mitigation Techniques 1st ed. 2015", John Wiley and Sons Ltd. ISBN: 9781118922057
- [5] E. Fuchs, Mohammad, A. S. Masoum, "Power Quality in Power Systems and Electrical Machines", Academic Press, 2008
- [6] F. Peng, "Applications Issues of Active Power Filters", 7th International Conference on Harmonics and Quality of Power, pp. 21-30, 1998
- [7] J. Gu, D. Xu, H. Liu, M. Gong, "Unified Power Quality Conditioner (UPQC): The Principle, Control and Application", IEEE, PCC-Osaka, 2002
- [8] V. Khadkikar, A. Chandra, A. O. Barry, T. D. Nguyen, "Application of UPQC to protect a Sensitive Load on a Polluted Distribution Network", IEEE Power Engineering Society General Meeting, June, 2006.
- [9] A. Elnady and M. M. A. Salama, "New functionalities of the unified power quality conditioner", 2001 IEEE/PES Transmission and Distribution Conference and Exposition. Developing New Perspectives (Cat. No.01CH37294), Atlanta, GA, USA, 2001, pp. 415-420 vol.1
- [10] H. Fujita and H. Akagi, "The unified power quality conditioner: The integration of series active filters and shunt active filters," PESC Record. 27th Annual IEEE Power Electronics Specialists Conference, Baveno, Italy, 1996, pp. 494-501 vol.1
- [11] A. Heenkenda, A. Elsanabary, M. Seyedmahmoudian, S. Mekhilef, A. Stojcevski and N. F. A. Aziz, "Unified Power Quality Conditioners Based Different Structural Arrangements: A Comprehensive Review," in IEEE Access, vol. 11, pp. 43435-43457, 2023
- [12] V. Khadkikar and A. Chandra, "UPQC-S: A Novel Concept of Simultaneous Voltage Sag/Swell and Load Reactive Power Compensations Utilizing Series Inverter of UPQC", IEEE Transactions on Power Electronics, vol. 26, no. 9, pp. 2414-2425, Sept. 2011
- [13] V. Khadkikar, A. Chandra, A. O. Barry and T. D. Nguyen, "Conceptual Study of Unified Power Quality Conditioner (UPQC)", 2006 IEEE International Symposium on Industrial Electronics, Montreal, QC, Canada, 2006, pp. 1088-1093
- [14] V. Khadkikar and A. Chandra, "A New Control Philosophy for a Unified Power Quality Conditioner (UPQC) to Coordinate Load-Reactive Power Demand Between Shunt and Series Inverters", IEEE Transactions on Power Delivery, vol. 23, no. 4, pp. 2522-2534, Oct.-2008
- [15] N. Mariun, A. Alam, S. Mahmud and H. Hizam, 2004, "Review of control strategies for power quality conditioners," PECon 2004. Proceedings. National Power and Energy Conference, 2004., Kuala Lumpur, Malaysia, 2004, pp. 109-115.
- [16] M. Ochoa-Giménez, A. García-Cerrada and J. L. Zamora-Macho, July 2017, "Comprehensive control for unified power quality conditioners," in Journal of Modern Power Systems and Clean Energy, vol. 5, no. 4, pp. 609-619
- [17] V. Khadkikar, P. Agarwal, A. Chandra, A. O. Barry and T. D. Nguyen, 2004, "A simple new control technique for unified power quality conditioner (UPQC)", 2004 11th International Conference on Harmonics and Quality of Power (IEEE Cat. No.04EX951), Lake Placid, NY, USA, pp. 289-293.
- [18] M. R. Soukhtekouhi, M. Hamzeh and H. Iman-Eini, "Performance Improvement of Unified Power Quality Conditioner Under Various Load, Source, and Line Conditions Using A New Control Method", 2020 11th Power Electronics, Drive Systems, and Technologies Conference (PEDSTC), Tehran, Iran, 2020, pp. 1-6.
- [19] Ke Dai, Peiguo Liu, Guixin Wang, Shanxu Duan and Jian Chen, "Practical approaches and novel control schemes for a three-phase three-wire series-parallel compensated universal power quality conditioner", Nineteenth Annual IEEE Applied Power Electronics Conference and Exposition, 2004. APEC '04., Anaheim, CA, USA, 2004, pp. 601-606 Vol.1.
- [20] Metin Keslar, Engin Ozdemir, "Simplified Control Method for Unified Power Quality Conditioner (UPQC)", International Conference on Renewable Energies and Power Quality, pp. 474-478, Vol.1 No.7, April 2009.
- [21] V. Khadkikar, A. Chandra, A. O. Barry and T. D. Nguyen, "Analysis of Power Flow in UPQC during Voltage Sag and Swell Conditions for Selection of Device Ratings", 2006 Canadian Conference on Electrical and Computer Engineering, Ottawa, ON, Canada, 2006, pp. 867-872.
- [22] Y. Xu, X. Xiao, Y. Sun and Y. Long, "Voltage sag compensation strategy for unified power quality conditioner with simultaneous reactive power injection", January 2016, in Journal of Modern Power Systems and Clean Energy, vol. 4, no. 1, pp. 113-122.



ISSN ONLINE: 2447-0228



RESEARCH ARTICLE

OPEN ACCESS

DYNAMIC AND HYDRAULIC PERFORMANCE OF A PERIPHERAL PUMP IMPELLER MADE OF PINEAPPLE FIBER REINFORCED BIOCOMPOSITE MATERIAL

Sergio Gomez Suarez¹, Alfonso Santos Jaimes² and Edwin Córdoba Tuta³

¹ Dept. Engineering, PhD in Engineering, Universidad Católica Andres Bello, Caracas, Venezuela

^{2,3} Dept. of Mechanical Engineering, Universidad Pontificia Bolivariana, Santander, Colombia

¹ <http://orcid.org/0000-0002-6425-7062> , ² <http://orcid.org/0000-0002-1549-5136> , ³ <http://orcid.org/0000-0001-8298-5007>

Email: sergio.gomez@upb.edu.com, alfonso.santos@upb.edu.com, edwin.cordoba@upb.edu.com

ARTICLE INFO

Article History

Received: June 04th, 2024

Received: October 15th, 2024

Accepted: October 15th, 2024

Published: October 31th, 2024

Keywords:

Biocomposite,
Impeller,
Pineapple fiber,
Pumps,
Vibration analysis.

ABSTRACT

Pumps are machines used at industrial and domestic level for the transport of incompressible fluids, the impeller being one of its main components that directly affects its performance; usually this element is manufactured in metallic materials, but there are not enough studies on its manufacture with new materials such as biocomposites reinforced with natural fibers. For this reason, this paper presents the results of the dynamic characterization and hydraulic performance of a peripheral pump impeller made of a biocomposite material reinforced with natural pineapple fibers. The biocomposite was prepared by the hand lay-up technique using a polyester resin with pineapple fibers in random distribution. A morphological and mechanical characterization of the fabricated material was carried out to evaluate the adhesion of the fiber with the matrix and to obtain the maximum tensile stress. Experimental modal analysis according to ISO 7626-2 and ISO 7626-5 standards was used to study the dynamic behavior. The hydraulic evaluation of the impeller was carried out by obtaining the pump characteristic curves using an academic-commercial test bench. The results were compared with those of a conventional metallic impeller, and lower natural frequencies were obtained in the pineapple biocomposite material. In terms of hydraulic performance, the head, power and efficiency were lower for the pineapple biocomposite impeller



Copyright ©2024 by authors and Galileo Institute of Technology and Education of the Amazon (ITEGAM). This work is licensed under the Creative Commons Attribution International License (CC BY 4.0).

I. INTRODUCTION

Pumps are machines that convert mechanical energy into hydraulic energy of incompressible fluids and are used in both domestic and large-scale industrial applications [1].

The impeller is one of the most important elements of a hydraulic pump, and its shape, size and material directly affect its performance and efficiency [2].

The knowledge of the dynamic behavior of a pump impeller is essential for a reliable design, where the phenomenon of resonance does not occur, since during the operation of the pump it is subjected to the vibrations of the mechanical system and the disturbances of the unsteady flow [3].

Resonance is a phenomenon that occurs when one of the natural frequencies (frequency at which a body tends to vibrate once excited) of the impeller is close to an external forced frequency, such as the speed of the pump's electric motor, where

intense levels of vibration are generated that can affect the normal operation of the machine [4].

The technique for identifying the natural frequencies of a body is known as modal analysis. This technique is critical to ensuring the proper and safe operation of components such as the impeller. Modal analysis makes it possible to identify the frequencies at which the impeller naturally vibrates and the modal shapes associated with those frequencies [5].

The study of dynamic effects in rotating machines, such as pumps, is becoming increasingly important due to the increase in power and speed of these devices [6], as an example, [7] performed a dynamic analysis by measuring the vibrations of a metallic impeller induced by a periodically unsteady flow in a single vane pump, obtaining the radial deflections of the impeller. Similarly, [8] measured the dynamic response of the metallic impeller of a 497.7 MW vertical pump and obtained its main natural frequencies and modal shapes.

The material used to manufacture the impellers is another important aspect as it has a direct impact on the cost, corrosion resistance, mechanical and dynamic properties of the pumps [9].

Most of the pump systems reported in the literature use traditional metallic materials in their impellers [10],[11], however, one of the current trends is the replacement by composite materials, since they can optimize the systems based on the reduction of pump weight and increased productivity, accompanied by good thermal and corrosion resistance, using faster manufacturing processes and with less material waste [12].

Natural fiber-reinforced composites are defined as materials obtained by bonding natural fibers obtained from stems, leaves, or seeds of various plant species by mechanical or chemical methods and combined with a biodegradable or synthetic matrix [13]. Their flexibility in processing, lower environmental impact and low cost make them very attractive to industry [14].

One of the fibers used in this type of materials is pineapple fiber, which is native to Brazil, but is currently cultivated in all continents, with Asia (Thailand, Philippines, Indonesia, India and China), America (Costa Rica and Brazil) and Africa (Nigeria and South Africa) being the main producers [15].

Several composite materials have been prepared with pineapple fibers [16-18], and their properties have been shown to be mainly influenced by matrix-fiber adhesion, fiber orientation, matrix type, and fiber length [19]. However, the use of these biomaterials in hydraulic industrial applications has not been demonstrated. This study presents the results of the dynamic characterization through experimental modal analysis and hydraulic behavior, obtaining the performance curves of a peripheral pump impeller made of biocomposite material reinforced with natural pineapple fiber.

II. MATERIALS AND METHODS

II.1 MATERIALS

Randomly arranged short pineapple fibers supplied by the Fibrense Foundation, Santander, Colombia, were used to reinforce the impeller.

The pineapple fibers had an average length of 1.76 ± 0.53 mm and a diameter of $9.53 \pm 1.29 \mu\text{m}$, as observed in Figure 1, obtained by SEM electron microscopy.

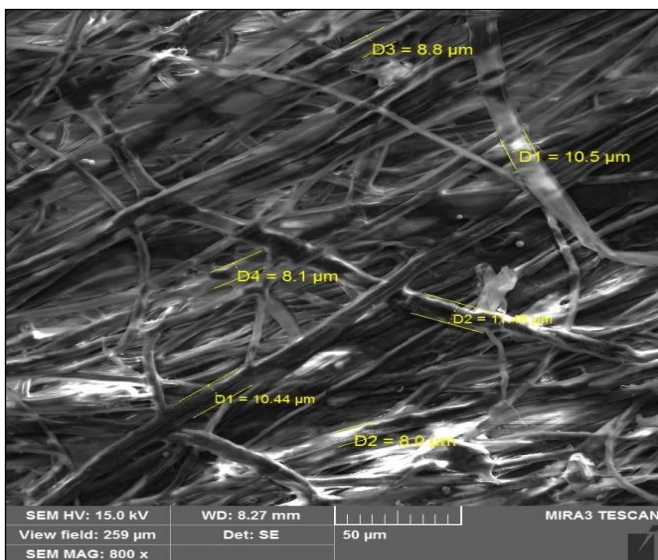


Figure 1: Micrograph of pineapple fibers in random configuration.

Source: Authors, (2024).

The weight of each layer of pineapple fiber used to make the impeller was 0.0233 g/cm^2 .

A pre-accelerated polyester resin catalyzed with 2% by weight of methyl ethyl ketone peroxide (MEK peroxide) was used as the matrix of the biocomposite material. These materials were purchased from Ingequímicas, Bucaramanga, Santander, Colombia.

II.2 MECHANICAL CHARACTERIZATION

Tensile testing was performed in accordance with ASTM D3039/D3039M using an MTS universal machine, model C43.104, with a capacity of 10 KN. The test was performed at a speed of 2 mm/min and a temperature of $20^\circ\text{C} \pm 3^\circ\text{C}$.

For this purpose, five specimens of pineapple fiber biocomposite material were fabricated using the hand lay-up technique. The specimens were cured for 24 hours at room temperature.

The specimens had a pineapple fiber content of $45.3 \pm 0.5\%$ with respect to the weight of the biocomposite and a geometry of 25 cm long, 2.5 cm wide and 3 mm thick as required by the normative. Figure 2 shows the tensile test performed.



Figure 2: Tensile Test.

Source: Authors, (2024).

The mechanical results presented are the average of those obtained in the five test specimens.

II.3 MORPHOLOGICAL CHARACTERIZATION

Scanning electron microscopy was performed using a Tescan microscope, model MIRA 3 FEG-SEM, equipped with a secondary electron detector, model A65c SED, to analyze the adhesion of the pineapple fiber to the polymer matrix in the fabricated impeller.

Images were obtained between 100X and 500X and at an electron accelerating voltage of less than 10 kV. The use of an electron accelerating voltage below 10 kV was strategically chosen to minimize electron penetration and improve surface image contrast. This approach is particularly important when analyzing biodegradable composites such as pineapple fiber, where the

structural integrity of the fiber and its interaction with the polymer matrix are sensitive to high voltages.

The analyzed biocomposite material extracted from the tensile test specimens was coated with a small layer of gold using a sputtering model 108 auto/SE Cressington brand in order to improve the electrical conductivity and to be able to apply the characterization technique.

II.4 IMPELLER FABRICATION

The impeller was manufactured using the "hand lay-up" process, a method in which the reinforcing layers, specifically pineapple fibers, are manually placed on a mold and then impregnated with resin. This technique was chosen because it allows precise control over the orientation and distribution of the fibers within the mold, a critical feature for parts with complex geometries such as the impeller. This precise fiber alignment is essential because it maximizes the strength and mechanical efficiency of the component, ensuring optimal performance under demanding operating conditions.

First, a conventional metal peristaltic pump impeller was molded in silicone to serve as a base for the biocomposite impeller. Figure 3 shows the mold used in the process.



Figure 3: Impeller mold.
Source: Authors, (2024).

The different layers of pineapple fiber were cut with the geometry of the impeller using a laser cutting machine, stacking 40 layers of natural fiber inside the mold, corresponding to 45.2% by weight of the biocomposite, after impregnation with polyester resin.

The material was cured for one day at room temperature, with an additional pressure of 100 psi applied to the biocomposite material inside the mold using a hydraulic cylinder to improve compaction.

Once the impeller was removed from the mold, the excess was removed using a Mototool polishing tool.

Figure 4 shows the fabricated impeller and the conventional bronze impeller used to make the mold. The latter was also used to compare the dynamic and hydraulic behavior of the pineapple impeller.



Figure 4: Fabricated impeller and conventional impeller.
Source: Authors, (2024).

II.5 DYNAMIC VIBRATION TEST

The dynamic vibration test was carried out with experimental modal analysis, obtaining frequency response (FRF) measurements according to ISO 7626-2 and ISO 7626-5. The purpose of the test was to determine the differences between the natural frequencies of the conventional metal impeller and the pineapple fiber impeller, and to determine if the pineapple fiber impeller could resonate at the pump's operating speed.

Two experimental configurations were created to evaluate the impeller, one reproducing its axial arrangement as the fluid would enter the pump, and the other measuring the response on the blades.

For the axial evaluation, excitation was applied using an electrodynamic shaker from The Modal Shop with a sinusoidal sweep covering a frequency range from 5 Hz to 3200 Hz. The excitation force was recorded with a PCB force sensor, reference 208C02, while the acceleration response was recorded with a PCB brand accelerometer, reference 352C68. Figure 5 shows the axial test setup.

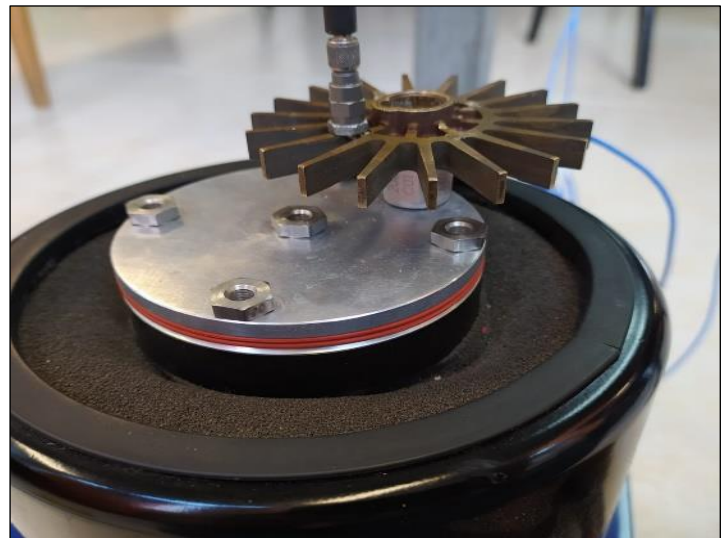


Figure 5: Axial dynamic vibration test.
Source: Authors, (2024).

A PCB accelerometer with reference number 352C68, placed on the blade itself, was used to evaluate the blade. Excitation was provided by an impact hammer from reference PCB 086C01

striking the blade. The use of the hammer was chosen for this test due to space limitations that prevented other forms of excitation. The impeller was suspended on elastic elements to simulate free motion conditions. Figure 6 shows the setup used to evaluate the dynamic response of the blades.



Figure 6: Dynamic vibration test on blades.
Source: Authors, (2024).

In both configurations, the acceleration response was recorded at 5 points evenly distributed over the impeller surface and blades.

II.6 PUMP CHARACTERISTICS CURVES.

The manufactured impeller was evaluated when mounted on a peripheral pump with a maximum flow of 8 l/min and a maximum head of 12 m (meters of water column). The results were compared with the original pump impeller using the Edibon PBOC multipump test bench. Figure 7 shows the test bench used.



Figure 7: Pump bench.
Source: Authors, (2024).

A capacitive level sensor was used to measure the water flow and two pressure gauges, one on the suction side and the other on the discharge side of the pump. This allowed the pump head to

be determined at an operating speed of 2000 rpm according to Equation 1.

$$h_b = \frac{P_2 - P_1}{\gamma} + Z \quad (1)$$

Where P2 is the discharge pressure, P1 is the suction pressure, γ is the specific gravity of the water, and Z is the head difference between the pump suction and discharge.

The hydraulic power was obtained using Equation 2.

$$P_h = h_b Q \gamma \quad (2)$$

Where Hb is the manometric head of the pump, Q is the flow rate, and γ is the specific gravity of the water.

The pump efficiency was determined using Equation 3.

$$n\% = \frac{P_h}{P_f} = \frac{h_b Q \gamma}{\omega T} \quad (3)$$

Where Ph is the hydraulic power, Pf is the mechanical power, ω is the shaft angular velocity and T is the torque.

III. RESULTS AND DISCUSSIONS

III.1 MECHANICAL CHARACTERIZATION

Figure 8 shows the stress-strain curve corresponding to the pineapple fiber reinforced biocomposite material. This material exhibits a behavior characterized by a non-linear relationship between the applied stress and the resulting strain.

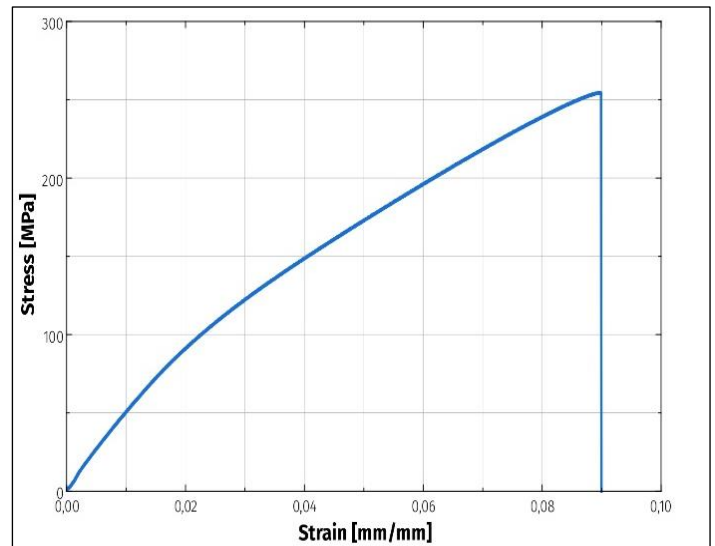


Figure 8: Stress-strain curve.
Source: Authors, (2024).

The maximum tensile stress recorded was 254.4 ± 7.32 MPa, while the Young's modulus was 5.04 ± 1.01 GPa. These results are consistent with the mechanical results reported by [20] in their review of pineapple fiber composites.

It is important to note that the tensile stress is closely related to several factors, such as the amount and orientation of the fibers, the interfacial adhesion between the fiber and the matrix, as well as the manufacturing method used [21].

III.2 MORPHOLOGICAL CHARACTERIZATION

Figures 9 and 10 show the micrographs of the biocomposite at different magnifications. The presence of gaps between the fiber components and the matrix can be observed, indicating low adhesion. This phenomenon is attributed to the hydrophobic nature of the matrix and the hydrophilic properties of the fibers [22].

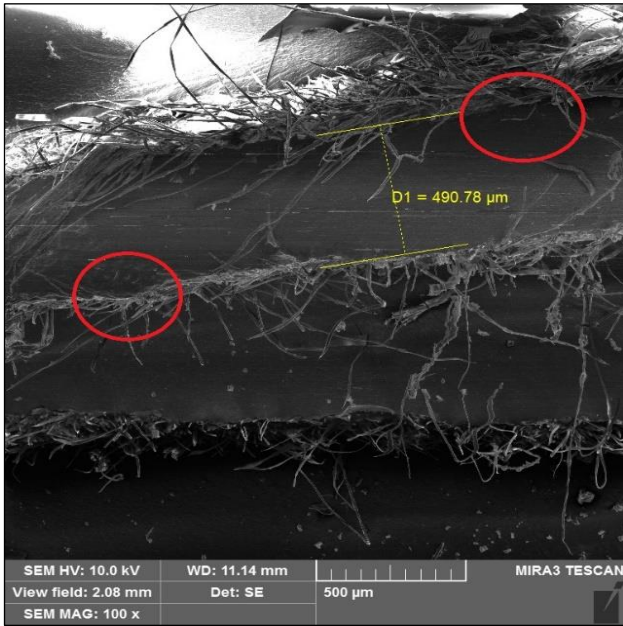


Figure 9: 100X biomaterial micrograph. Source: Authors, (2024).

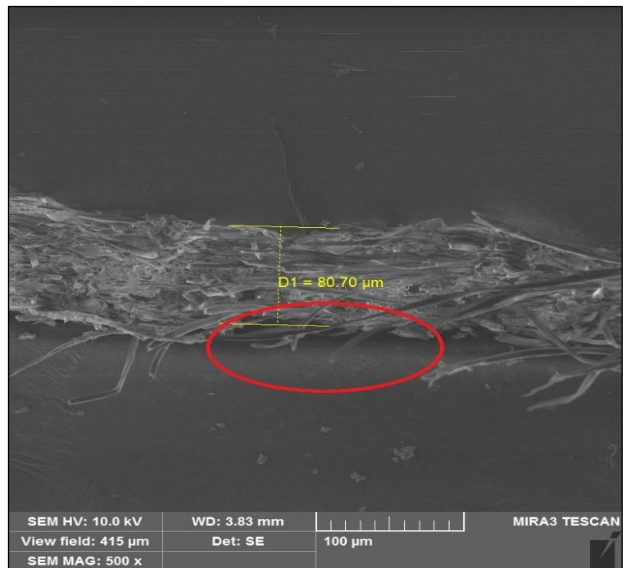


Figure 10: 500X Biomaterial Micrograph. Source: Authors, (2024).

This low adhesion affected the mechanical and dynamic properties of the biocomposite due to the low load transfer between the resin and the fiber.

III.3 DYNAMIC VIBRATION TEST

The natural frequencies of the biocomposite impeller and the conventional metal impeller, both in the axial configuration and in the blade evaluation, were identified by means of the peaks in the frequency response function (FRF) obtained from the experimental modal analysis (see Figures 11 and 12).

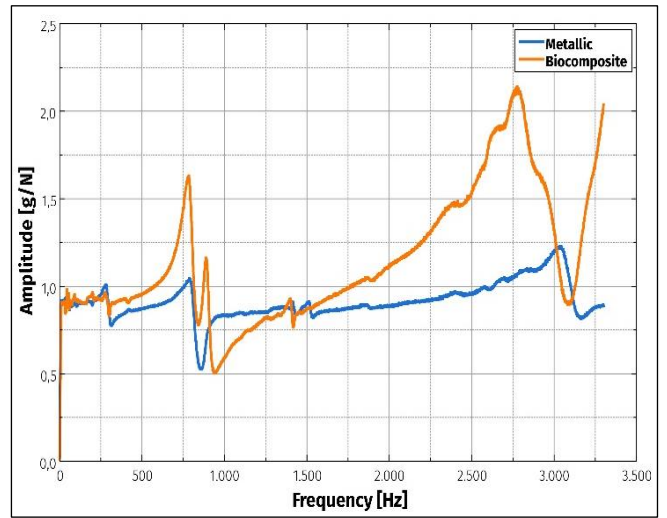


Figure 11: FRF axial configuration. Source: Authors, (2024).

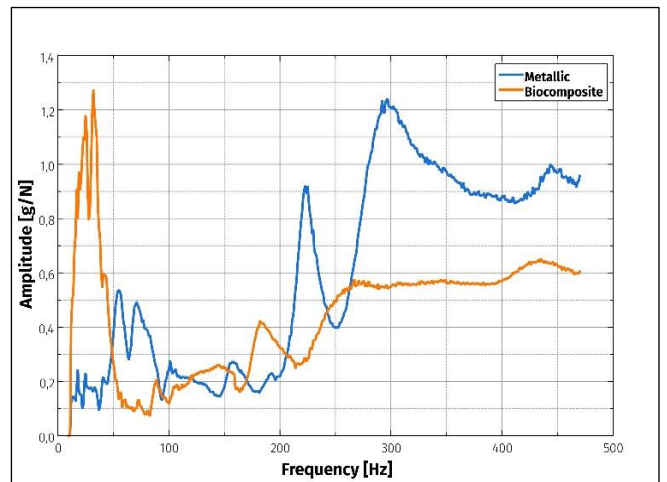


Figure 12: FRF blade configuration. Source: Authors, (2024).

As can be seen in Figures 11 and 12, the curves of the biocomposite and the metallic material have a similar structure. This is due to the fact that the dynamic behavior of a part is largely related to its geometry [23], being the same for both impellers.

However, as far as the natural frequencies are concerned, lower values were obtained in the biocomposite material than in the metallic one, as can be seen in Table 1.

Table 1: Natural frequencies of materials.

Configuration	Modes	Natural frequency [Hz]	
		Biocomposite	Metallic
Axial	Mode 1	280 ± 2.5	284 ± 3.7
	Mode 2	782 ± 5.2	797 ± 2.1
	Mode 3	1401 ± 14.2	1518 ± 8.7
	Mode 4	2777 ± 22.1	3053 ± 12.1
Blade	Mode 1	25 ± 4.6	55 ± 2.1
	Mode 2	32 ± 5.1	73 ± 3.1
	Mode 3	181 ± 7.8	224 ± 5.7
	Mode 4	256 ± 9.1	295 ± 8.1

Source: Authors, (2024).

The observed difference is attributed to the stiffness, which is lower in natural fiber reinforced composites than in metals, as reported by Pickering et al. [24] and supported by the experimental data obtained in section III.1. This property has a direct effect on the natural frequencies of the material, as pointed out by [25], since

stiffness affects the ability of the body to resist deformation under load. Lower stiffness allows for greater flexibility and ease of deformation of the body, resulting in a reduction in natural frequencies. The values obtained for the natural frequency of the blades in the biocomposite material are very close to the operating frequency of the pump (2000 rpm, 33.3 Hz), which can cause resonance in the blades. This phenomenon can have adverse effects on the operation and structural integrity of the pump, including excessive vibration, premature wear, and even catastrophic failure.

III.4 PUMP CHARACTERISTICS CURVES.

Figure 13 shows the variation of pump head versus flow rate for both types of impellers, which show a linear decreasing behavior. The slopes of the material curves are practically identical, which is due to the similar design and geometry of the impellers.

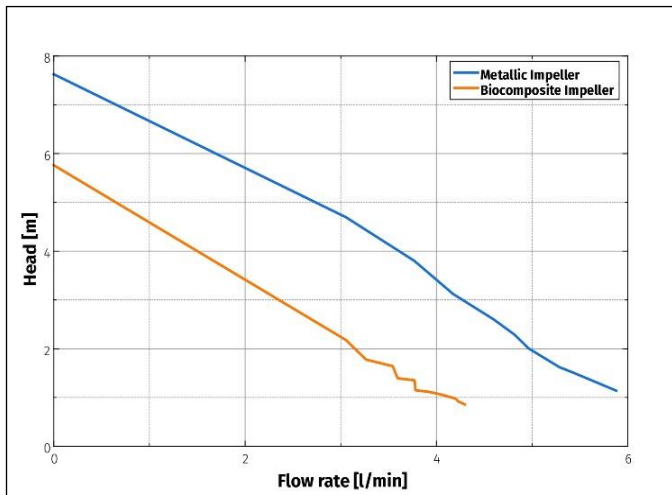


Figure 13: Head-Flow Curve.
Source: Authors, (2024).

However, at the same flow rate, the impeller made of pineapple fiber biocomposite was found to have 40% to 50% lower head. This discrepancy is attributed to their lower stiffness, which allows them to deform more easily under load. This results in additional energy losses due to friction and turbulence in the fluid flow. In addition, their tendency to resonate contributes to less stable operation. Figure 14 compares the hydraulic power of the pump with the two impellers as a function of flow rate.

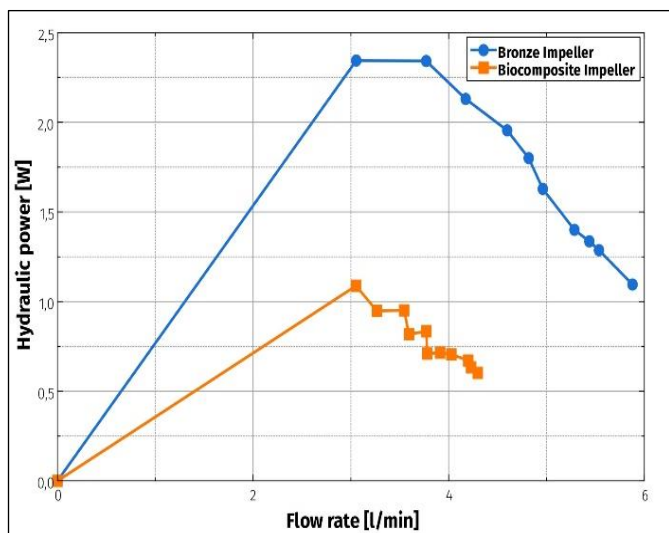


Figure 14: Hydraulic Power – Flow curve.
Source: Authors, (2024).

The metal impeller pump produced more power than the biocomposite impeller pump. This power advantage is clearly due to the ability of the metallic material to generate a higher head at the same flow rate. The maximum power output of the metallic impeller was 2.35W compared to 1.088W for the biocomposite.

The efficiency comparison of the two impellers is shown in Figure 15 and it is observed that the biocomposite impeller was less efficient than the conventional metallic impeller.

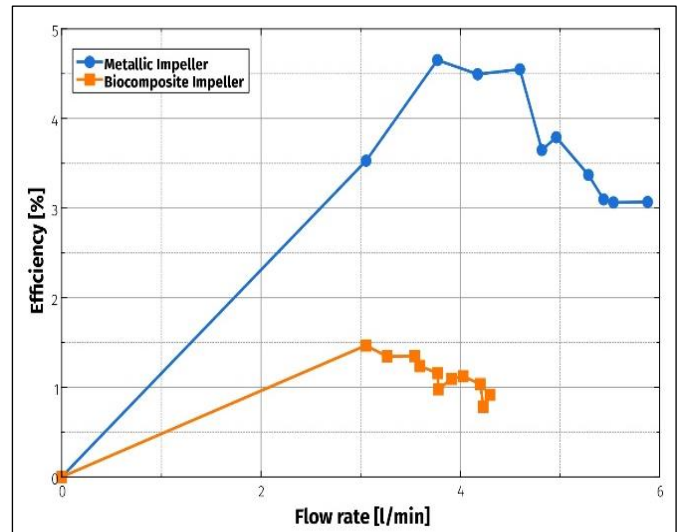


Figure 15: Efficiency - flow curve.
Source: Authors, (2024).

The metal impeller reached its maximum efficiency at a flow rate of approximately 3.77l/min, with an efficiency value of 4.65%, while the biocomposite impeller reached it at 3.05 l/min, with a maximum efficiency value of 1.47%. This difference is attributed to a lower hydraulic head of the biocomposite impeller. In addition, as noted by Cao et al. [2], impeller manufacturing and installation tolerances can also have a significant impact on this parameter.

IV. CONCLUSIONS

The fabrication of a peripheral pump impeller using pineapple fiber reinforced biocomposite material was carried out, highlighting the potential and feasibility of exploring sustainable alternatives in engineering and industrial applications. Mechanical characterization of the biocomposite material revealed a tensile stress of 254 MPa and a modulus of 5.04 GPa. Scanning electron microscopy (SEM) revealed limited adhesion between matrix and fibers in the pineapple biocomposite material. This phenomenon is attributed to the hydrophobic nature of the matrix and the hydrophilic properties of the fibers, resulting in a decrease in load transfer from the resin to the fibers, which directly affects the stiffness of the material. When comparing the dynamic properties, especially the natural frequencies, of the pineapple biocomposite impeller and the metallic impeller, a decrease in the natural frequencies of the biocomposite material was observed. In addition, the natural frequencies of the blades in the biocomposite material are close to the operating frequency of the pump, raising the possibility of the resonance phenomenon. The impeller made of biocomposite material reinforced with pineapple fibers showed a lower hydraulic response compared to the impeller made of conventional material, mainly due to lower stiffness. This reduction in stiffness results in a loss of efficiency in the transfer of energy from the motor to the pumped fluid. In addition, the

impeller resonates with the operating frequencies of the pump, resulting in excessive vibration.

V. AUTHOR'S CONTRIBUTION

Conceptualization: Sergio Andrés Gómez.

Methodology: Sergio Andrés Gómez.

Investigation: Sergio Andrés Gómez, Alfonso Santos Jaimés and Edwin Córdoba Tuta

Discussion of results: Sergio Andrés Gómez, Alfonso Santos Jaimés and Edwin Córdoba Tuta

Writing – Original Draft: Sergio Andrés Gómez, Alfonso Santos Jaimés and Edwin Córdoba Tuta

Writing – Review and Editing: Sergio Andrés Gómez, Alfonso Santos Jaimés and Edwin Córdoba Tuta

Supervision: Sergio Andrés Gómez, Alfonso Santos Jaimés and Edwin Córdoba Tuta

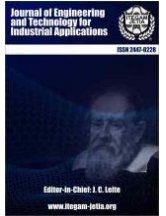
Approval of the final text: Sergio Andrés Gómez, Alfonso Santos Jaimés and Edwin Córdoba Tuta

VII. REFERENCES

- [1] I. Ignacio et al., «Parámetros de bomba centrífuga de doble succión para la industria azucarera Parameters of Double Suction Centrifuge Pump for the Sugar Industry», vol. 27, n.o 2, pp. 1-11, 2018.
- [2] W. Cao, L. Yao, B. Liu, y Y. Zhang, «The influence of impeller eccentricity on centrifugal pump», *Adv. Mech. Eng.*, vol. 9, n.o 9, pp. 1-17, 2017, doi: 10.1177/1687814017722496.
- [3] X. Zhao, H. Li, S. Yang, Z. Fan, J. Dong, y H. Cao, «Blade vibration measurement and numerical analysis of a mistuned industrial impeller in a single-stage centrifugal compressor», *J. Sound Vib.*, vol. 501, p. 116068, jun. 2021, doi: 10.1016/j.jsv.2021.116068.
- [4] V. K. Chillara, J. Greenhall, C. Hakoda, y C. Pantea, «Electromechanical response of laterally clamped piezoelectric wafers: Absence of in-plane mechanical resonances in the electromechanical impedance spectrum», *Appl. Acoust.*, vol. 188, p. 108545, ene. 2022, doi: 10.1016/j.apacoust.2021.108545.
- [5] C. Xu, H. Zhou, y Y. Mao, «Analysis of vibration and noise induced by unsteady flow inside a centrifugal compressor», *Aerosp. Sci. Technol.*, vol. 107, p. 106286, dic. 2020, doi: 10.1016/j.ast.2020.106286.
- [6] S. Ravaly A. G. L. Holloway, «Experimental study of dual-impeller string vibration in a baffled mixing vessel», *Int. J. Press. Vessels Pip.*, vol. 165, pp. 306-321, ago. 2018, doi: 10.1016/j.ijpvp.2018.02.004.
- [7] J. Pei, H. J. Dohmen, S. Q. Yuan, y F.-K. Benra, «Investigation of unsteady flow-induced impeller oscillations of a single-blade pump under off-design conditions», *J. Fluids Struct.*, vol. 35, pp. 89-104, nov. 2012, doi: 10.1016/j.jfluidstructs.2012.08.005.
- [8] E. Egusquiza, C. Valero, A. Presas, X. Huang, A. Guardo, y U. Seidel, «Analysis of the dynamic response of pump-turbine impellers. Influence of the rotor», *Mech. Syst. Signal Process.*, vol. 68-69, pp. 330-341, feb. 2016, doi: 10.1016/j.ymssp.2015.05.034.
- [9] R. P. Barreto, «Cavitación y materiales de construcción en las bombas centrífugas», *Min. Geol.*, vol. 20, n.o 3-4, pp. 114-118, 2004.
- [10] K. Wang, G. Luo, Y. Li, R. Xia, y H. Liu, «Multi-condition optimization and experimental verification of impeller for a marine centrifugal pump», *Int. J. Nav. Archit. Ocean Eng.*, vol. 12, 2019, doi: 10.1016/j.ijnaoe.2019.07.002.
- [11] P. Prithvi Raj, P. Suresh Kumar Gupta, P. Praveen Kumar, G. Paramesh, y K. Rohit, «Model and analysis of rotor and impeller of eight stage centrifugal pump», *Mater. Today Proc.*, 2019, doi: 10.1016/j.matpr.2019.04.215.
- [12] M. Isametova, R. Nussipali, D. Karaivanov, Z. Abilkhair, y A. Isametov, «Computational and Experimental Study of the Composite Material for the Centrifugal Pump Impellers Manufacturing», *J. Appl. Comput. Mech.*, n.o Online First, may 2022, doi: 10.22055/jacm.2022.40366.3574.
- [13] W. Liu et al., «Properties of natural fiber-reinforced biobased thermoset biocomposites: Effects of fiber type and resin composition», *Compos. Part B Eng.*, vol. 171, pp. 87-95, ago. 2019, doi: 10.1016/j.compositesb.2019.04.048.
- [14] G. Rajeshkumar, S. Gokulkumar, y P. Navaneethakrishnan, «Natural Fiber-Reinforced Biocomposites», en *Encyclopedia of Materials: Plastics and Polymers*, M. S. J. Hashmi, Ed., Oxford: Elsevier, 2022, pp. 504-510. doi: 10.1016/B978-0-12-820352-1.00275-3.
- [15] G. Lobo y M. Siddiq, «Overview of pineapple production, postharvest physiology, processing and nutrition», en *Handbook of Pineapple Technology: Postharvest Science, Processing and Nutrition*, 2016, pp. 1-15. doi: 10.1002/9781118967355.ch1.
- [16] W. Nhuapeng y W. Thamjaree, «Fabrication and Mechanical Properties of Hybrid Composites between Pineapple fiber/Styrofoam Particle/Paper Tissue», *Mater. Today Proc.*, vol. 17, pp. 1444-1450, 2019, doi: 10.1016/j.matpr.2019.06.166.
- [17] K. Muthukumar, R. V. Sabariraj, S. Dinesh Kumar, y T. Sathish, «Investigation of thermal conductivity and thermal resistance analysis on different combination of natural fiber composites of Banana, Pineapple and Jute», *Mater. Today Proc.*, n.o xxxx, 2019, doi: 10.1016/j.matpr.2019.09.140.
- [18] T. Singh, C. I. Pruncu, B. Gangil, V. Singh, y G. Fekete, «Comparative performance assessment of pineapple and Kevlar fibers-based friction composites», *J. Mater. Res. Technol.*, n.o x x, pp. 1-9, 2019, doi: 10.1016/j.jmrt.2019.11.074.
- [19] S. S. Todkary S. A. Patil, «Review on mechanical properties evaluation of pineapple leaf fibre (PALF) reinforced polymer composites», *Compos. Part B Eng.*, vol. 174, n.o May, p. 106927, 2019, doi: 10.1016/j.compositesb.2019.106927.
- [20] M. Asim et al., «A Review on Pineapple Leaves Fibre and Its Composites», *Int. J. Polym. Sci.*, vol. 2015, pp. 1-16, 2015, doi: 10.1155/2015/950567.
- [21] J. Jain y S. Sinha, «Pineapple Leaf Fiber Polymer Composites as a Promising Tool for Sustainable, Eco-friendly Composite Material: Review», *J. Nat. Fibers*, vol. 19, pp. 1-22, oct. 2021, doi: 10.1080/15440478.2021.1993478.
- [22] M. N. Azman Mohammad Taib y N. M. Julkapli, «Dimensional stability of natural fiber-based and hybrid composites», *Mech. Phys. Test. Biocomposites Fibre-Reinf. Compos. Hybrid Compos.*, pp. 61-79, 2019, doi: 10.1016/b978-0-08-102292-4.00004-7.
- [23] A. Savin, I. Curtu, y M. Stanciu, «Modal Analysis of lignocelluloses based composite materials», 40th Int. Conf. Mech. Solids Acoust. Vib. 6th Int. Conf. "Advanced Compos. Mater. Eng.", pp. 278-283, 2016.
- [24] K. L. Pickering, M. G. A. Efendy, y T. M. Le, «A review of recent developments in natural fibre composites and their mechanical performance», *Compos. Part Appl. Sci. Manuf.*, vol. 83, pp. 98-112, 2016, doi: 10.1016/j.compositesa.2015.08.038.
- [25] M. Rajesh y J. Pitchaimani, «Dynamic mechanical analysis and free vibration behavior of intra-ply woven natural fiber hybrid polymer composite», *J. Reinf. Plast. Compos.*, vol. 35, n.o 3.



ISSN ONLINE: 2447-0228



RESEARCH ARTICLE

OPEN ACCESS

ENHANCING PERFORMANCE OF PERMANENT MAGNET SYNCHRONOUS MOTOR DRIVES THROUGH HYBRID FEEDBACK LINEARIZATION AND SLIDING MODE CONTROL

Djaloul Karboua¹, Toufik Mebkhoua², Youcef Chouiha³, Abdelkader Azzeddine Bengharbi⁴, Ben ouadeh Douara⁵ and Belgacem Toulab⁶

^{1,6}dept. Electrical Engineering– LASER Lab, Djelfa University Djelfa, Algeria.

²dept. Electrical Engineering–LGEB Lab, Biskra University Biskra, Algeria

^{3,5}dept. Electrical Engineering–LAADI Lab, Djelfa University Djelfa, Algeria.

⁴dept. Electrical Engineering –LEECE Lab, Ibn Khaldoun University tiaret, Algeria

¹ <http://orcid.org/0000-0003-0155-9925> , ² <http://orcid.org/0000-0002-7999-1702> , ³ <http://orcid.org/0000-0001-9055-8953> , ⁴ <http://orcid.org/0000-0002-3152-6887> , ⁵ <http://orcid.org/0000-0002-0548-5305> , ⁶ <http://orcid.org/0000-0001-6900-9925>

Email: djaloul.karboua@univ-djelfa.dz , Toufik.mebkhouta@univ-biskra.dz , y.chouiha@univ-djelfa.dz , BENGHARBI.AEK.AZZ@univ-tiaret.dz , b.douara@univ-djelfa.dz , Toulab@gmail.com

ARTICLE INFO

Article History

Received: July 26th, 2024

Received: October 07th, 2024

Accepted: October 07th, 2024

Published: October 31th, 2024

Keywords:

PMSM,
Hybrid Control design,
SMC,
FBLC,
robust control.

ABSTRACT

This paper proposes a novel hybrid control strategy that integrates Feedback Linearization Control (FBLC) with Sliding Mode Control (SMC) to significantly enhance the performance of Permanent Magnet Synchronous Motor (PMSM) drives. The proposed control strategy leverages the strengths of both FBLC and SMC to address the inherent challenges associated with PMSM control in demanding industrial applications. The FBLC component of the hybrid controller effectively linearizes the nonlinear dynamics of PMSMs. By transforming the nonlinear system into an equivalent linear system, FBLC facilitates precise trajectory tracking and improves transient response, thereby ensuring high control accuracy. This linearization process simplifies the control design and enables the implementation of advanced linear control techniques. On the other hand, the SMC component ensures robustness and reliability of the PMSM drive system. SMC is known for its inherent robustness against parameter variations, uncertainties, and external disturbances. By incorporating SMC into the hybrid controller, the system maintains stable and reliable operation even in the presence of these adverse conditions. The SMC component enhances disturbance rejection capabilities, providing a robust control solution that significantly improves the overall system performance. The integration of FBLC and SMC into a unified control architecture results in a synergistic improvement in PMSM drive performance. The hybrid FBLC-SMC controller combines the precise tracking capabilities of FBLC with the robustness of SMC, leading to superior tracking accuracy, effective disturbance rejection, and enhanced overall robustness compared to traditional control methods. Extensive simulation studies are conducted to validate the effectiveness of the proposed hybrid control strategy. The simulation results demonstrate the ability of the FBLC-SMC controller to achieve excellent performance metrics, including improved tracking accuracy, faster transient response, and robust disturbance rejection. The hybrid control strategy is shown to be a promising solution for industrial applications requiring high performance and reliability in PMSM control.



Copyright ©2024 by authors and Galileo Institute of Technology and Education of the Amazon (ITEGAM). This work is licensed under the Creative Commons Attribution International License (CC BY 4.0).

I. INTRODUCTION

Electric motors play a pivotal role in a wide array of industries, converting electrical energy into mechanical power that

drives applications ranging from electric vehicles to industrial machinery. Among the various types of electric motors, Permanent Magnet Synchronous Motors (PMSMs) are particularly renowned

for their high efficiency and precision. These motors employ permanent magnets in the rotor to ensure synchronized magnetic fields with the stator, a configuration that significantly enhances their performance characteristics. However, despite their advantages, PMSMs are inherently complex due to their nonlinear, coupled, and multivariable nature. This complexity necessitates the development of advanced control strategies to achieve optimal performance [1-3]. Traditional control methods, such as Field-Oriented Control (FOC), have been widely used to manage PMSMs. FOC operates by decoupling the flux and torque components, thereby optimizing motor performance. While effective in many scenarios, FOC can struggle with maintaining robustness in the face of parameter variations and external disturbances [4],[5]. To address these limitations, researchers have increasingly turned to advanced control techniques that incorporate nonlinear control, optimization, and robustness methodologies. These techniques include feedback linearization, sliding mode control (SMC), backstepping control, adaptive control, and various intelligent techniques. The primary aim of these methods is to enhance the overall performance of PMSMs by effectively managing their nonlinear dynamics and mitigating uncertainties [6],[7]. Feedback Linearization Control (FBLC) is an advanced control method that simplifies control design by transforming a system's nonlinear dynamics into a linear system. This transformation enables the use of linear control techniques, which are well-established and generally easier to implement than nonlinear approaches. As a result, FBLC improves response times, precision, and disturbance rejection, benefiting from the advantages of linear control methods for more predictable and efficient system behavior. However, FBLC relies heavily on having an accurate mathematical model of the system, which can be computationally complex to obtain and maintain. In the context of PMSMs, FBLC's reliance on precise modeling can be particularly challenging due to the motors' inherent complexity and sensitivity to parameter variations. Any inaccuracies in the model can lead to suboptimal performance or instability, as the linearization process may not fully capture the motor's nonlinearities. Additionally, the computational demands for real-time state estimation and parameter tuning required by FBLC can be significant, potentially impacting the system's overall efficiency and performance. Despite these challenges, when accurately implemented, FBLC can greatly enhance the performance of complex nonlinear systems by providing a robust and precise control framework. [8],[9]. Sliding Mode Control (SMC) is renowned for its robustness against parameter variations and external disturbances, making it a highly effective control strategy for systems like PMSMs. SMC achieves this robustness by forcing the system's trajectory to adhere to a predefined sliding surface, ensuring stability and reliable operation even under varying conditions. However, SMC is not without its drawbacks. A significant issue is chattering, which involves high-frequency oscillations in the control input as it switches rapidly to keep the system on the sliding surface. This chattering can lead to mechanical wear, increased energy consumption, and reduced system efficiency. Additionally, designing an effective SMC system requires meticulous tuning of parameters to balance performance and robustness, which can be complex and time-consuming. Despite these challenges, SMC remains a valuable control strategy due to its ability to maintain stable operation under uncertain conditions [10],[11]. In this paper, we propose a hybrid control strategy that integrates Feedback Linearization Control (FBLC) with Sliding Mode Control (SMC) to enhance the performance of PMSM drives. The hybrid approach is designed to

combine the advantages of both control techniques, leveraging FBLC's precision and improved response times alongside SMC's robustness and effective disturbance rejection. This integration aims to achieve superior control accuracy, increased efficiency, and enhanced stability of PMSM drives, effectively addressing and mitigating the limitations associated with each individual technique. Through this detailed exploration, we aim to demonstrate that the proposed hybrid FBLC-SMC control strategy offers a promising solution for enhancing the performance and reliability of PMSM drives in demanding industrial applications. The remainder of this paper is structured as follows: Section 2 provides a detailed exploration of the modeling of PMSM dynamics, offering a thorough understanding of the system's behavior. Section 3 focuses on designing the FBLC-SMC control strategy for the PMSM, detailing the development and integration of the hybrid control approach. Section 4 presents extensive simulation studies designed to validate the effectiveness of the proposed hybrid control strategy, accompanied by a comprehensive discussion of the findings. Finally, Section 5 concludes the paper by summarizing the key contributions and insights gained from the research.

II. FORMULATING A NONLINEAR MODEL OF THE PMSM SYSTEM

The d-q rotor reference frame simplifies PMSM equations, improving computational efficiency and control system design by maintaining steady-state variables. This model assumes a cage-free rotor, sinusoidal back-EMF, and minimal saturation, eddy currents, and hysteresis losses. Due to the inherent nonlinearity of PMSMs, a direct nonlinear modeling approach is favored for effectively handling system disturbances without requiring decoupling or linearization, ensuring comprehensive and accurate representation [12],[13].

$$\begin{cases} \frac{d}{dt}x(t) = f(x(t), u(t), t) + g(t) * u(t) \\ y(t) = h(x(t)) \end{cases} \quad (1)$$

Where $x(t)$ are the state variables, $f(x(t), u(t), t)$ is the nonlinear function, $u(t)$ is the system input, and $y(t)$ is the system output.

The inputs, state space variables and the output for the PMSM model is designed as follows:

$$\begin{cases} u(t) = [v_d \quad v_q]^T \\ x(t) = [i_d \quad i_q \quad \omega_e]^T \\ y(t) = h(x) = \omega_e \end{cases} \quad (2)$$

The terms of the nonlinear mentioned above for the PMSM model is identified as follow:

$$f(x(t), u(t), t) = \begin{bmatrix} -\frac{R_s}{L_d} \cdot i_d + \frac{L_q}{L_d} \cdot i_q \cdot \omega_e \\ -\frac{R_s}{L_q} \cdot i_q - \frac{L_d}{L_q} \cdot i_d \cdot \omega_e - \frac{\psi_f}{L_q} \cdot \omega_e \\ -\frac{F}{j} \cdot \omega_e + \frac{3 \cdot p^2}{2} \cdot \frac{L_d - L_q}{j} \cdot i_d \cdot i_q + \frac{3 \cdot p^2}{2} \cdot \frac{\psi_f}{j} * i_q - \frac{p}{j} \cdot T_l \end{bmatrix} \quad (3)$$

And

$$g(t) = \begin{bmatrix} \frac{1}{L_d} & 0 \\ 0 & \frac{1}{L_q} \end{bmatrix} \quad (4)$$

Where: i_d, i_q are d-q axis equivalent stator currents; v_d, v_q are d-q axis equivalent stator voltages; ω_e is rotor speed; p is number of pole pairs; R_s is per phase stator resistance; L_d, L_q are d-q axis equivalent stator inductance; T_e, T_l are electromagnetic and load torques; J is moment of inertia of the rotor; F is friction constant of the rotor and ψ_f is rotor magnetic flux linking the stator.

III. DESIGNING THE FBLC-SMC FOR THE PMSM

In control systems engineering, the feedback linearization algorithm transforms nonlinear systems into linear ones through state manipulation and feedback, avoiding approximation [14]. When applied to a PMSM system, feedback linearization aims to:

- 1) Eliminate nonlinearities to establish a closed-loop linear system;
- 2) Simplify system design post-linearization;
- 3) Use linear control strategies for stability, desired performance, and disturbance rejection.

This is achieved through input-output linearization, ensuring complete linearization between system outputs and control inputs:

$$\begin{cases} y_1 = i_d \\ y_2 = \Omega \end{cases} \quad (5)$$

The trajectories for these two outputs must be strictly adhered to. Implementing a maximum torque strategy necessitates setting $i_d^* = 0$, while the speed Ω must track its specified reference path Ω^* . This reference path for Ω^* can vary depending on the application requirements.

III.1 FOR THE FIRST OUTPUT i_d :

$$y_1 = i_d = h_1(x), \nabla h_1(x) = \begin{bmatrix} 1 \\ 0 \\ 0 \end{bmatrix} \quad (6)$$

Where: $\omega_r = p\Omega$. To find the derivative of the first output, we proceed as follows:

$$\begin{cases} y_1 = i_d = h_1(x) \\ \dot{y}_1 = L_f h_1(x) = -\frac{R_s}{L_d} \cdot i_d + \frac{L_q}{L_d} \cdot p \cdot \Omega \cdot i_d + \frac{1}{L_d} \cdot u_d \end{cases} \quad (7)$$

III.2 FOR THE SECOND OUTPUT Ω :

$$y_2 = \Omega = h_2(x), \nabla h_2(x) = \begin{bmatrix} 0 \\ 0 \\ 1 \end{bmatrix} \quad (8)$$

Since the input has not yet been introduced, we proceed to calculate the second derivative of the second output as follows:

$$\begin{cases} y_2 = \Omega = h_2(x) \\ \dot{y}_2 = \frac{3 \cdot p}{2 \cdot J} (\psi_f L_q + (L_d - L_q) \cdot i_d \cdot i_q) - \frac{1}{J} T_r - \frac{F}{J} \cdot \Omega \\ \ddot{y}_2 = K_t (L_d - L_q) \cdot i_d \cdot f_1(x) + K_t (\psi_f + (L_d - L_q) \cdot i_d) f_2(x) \\ - \left(\frac{1}{J} T_r + \frac{F}{J} \right) f_3(x) + \frac{K_t}{L_q} (L_d - L_q) \cdot i_d \cdot u_q \\ + \frac{K_t}{L_q} (\psi_f + (L_d - L_q) \cdot i_d) \cdot u_d \end{cases} \quad (9)$$

$$\text{where: } K_t = \frac{3 \cdot p}{2 \cdot J}$$

Since the relative degree is $r_1 + r_2 = 3 = n$ (order the system), we have:

$$[\dot{y}_1 \quad \ddot{y}_2]^T = a(x) + b(x) \cdot u \quad (10)$$

Therefore, the nonlinear terms are cancelled out by choosing a transformation:

$$\begin{bmatrix} u_d \\ u_q \end{bmatrix} = b^{-1}(x) \left(\begin{bmatrix} v_1 \\ v_2 \end{bmatrix} - a(x) \right) \quad (11)$$

Where the $b(x)$ matrix is smooth. After canceling the non-linearity of the PMSM dynamic system:

$$\begin{bmatrix} v_1 \\ v_2 \end{bmatrix} = \begin{bmatrix} \dot{e}_d + K_{d1} \cdot e_d \\ \ddot{e}_\omega + K_{\omega 1} \cdot \dot{e}_\omega + K_{\omega 2} \cdot e_\omega \end{bmatrix} \quad (12)$$

where:

$$\begin{cases} e_1 = i_d^* - i_d \\ e_\omega = \Omega^* - \Omega \end{cases} \quad (13)$$

To enhance FBLC, SMC is integrated into its control law. SMC establishes a surface to ensure stability and performance by guiding the system's trajectory towards and along this surface. It operates in two phases: driving the system to the sliding surface and maintaining motion on it, moving towards equilibrium in finite time. Implementing SMC involves three steps: selecting the sliding surface, defining sliding conditions, and computing the SMC law [15],[16].

$$S(x, t) = \left(\frac{d}{dt} + \lambda \right)^{n-1} e(t) \quad (14)$$

In SMC, λ is a positive parameter chosen by the designer to control the error dynamics, while n denotes the system's order. $S(x, t)$ is the sliding surface, and $e(t)$ is the tracking error. The system's trajectory is directed towards the origin and reaches it asymptotically, governed by the sliding condition in the following equation [17]:

$$\frac{1}{2} \frac{d}{dt} S^2 \leq \eta |S| \quad (15)$$

Where $\eta > 0$

After establishing the sliding surface and meeting the sliding condition, the control law is determined in two phases. First, the sliding phase keeps the system on the sliding surface by

designing an equivalent term where $S(x, t) = 0$ and $\dot{S}(x, t) = 0$. Next, the approach phase ensures the sliding condition by formulating a switching law where $S(x, t) \neq 0$ and $\dot{S}(x, t) = 0$. The specific design of the SMC control law unfolds as follows [18]:

$$u = u_{eq} + u_s \quad (16)$$

Within this context, the tracking errors for speed and direct current can be expressed using Equation 13. Here, the switching approach based on SMC is introduced to enhance feedback linearization control (FBLC), replacing the linear dynamic of Equation 12 with a switching term as follows:

$$\begin{bmatrix} v_1 \\ v_2 \end{bmatrix} = \begin{bmatrix} -K_1 \tanh(S) \\ -K_2 \tanh(S) \end{bmatrix} \quad (17)$$

Where S is sliding surface of SMC and K_1, K_2 , are the gains used to regulate the SMC-FBLC.

IV. SIMULATION, RESULTS AND DISCUSSION

The efficacy of the hybrid control approach integrating Sliding Mode Control (SMC) and Feedback Linearization Control (FBLC) for a Permanent Magnet Synchronous Motor (PMSM) was thoroughly demonstrated through a comprehensive simulation model. This model was meticulously implemented using Matlab/Simulink, a powerful tool for modeling, simulating, and analyzing dynamic systems. The simulation setup included detailed representations of both the control strategies and the PMSM

dynamics, ensuring an accurate assessment of the hybrid approach's performance. The simulation model, as illustrated in Figure 1, showcases the integration process of SMC and FBLC. It highlights the interaction between these two control methodologies and the PMSM, capturing the intricate dynamics and control responses. The model was designed to test various operating conditions and disturbances, providing a robust validation of the hybrid control strategy's capabilities. In addition to the simulation framework, the study specifies the detailed parameters of the PMSM used in the simulations. These parameters, outlined in Table 1. The detailed simulation study involved extensive testing under different scenarios to evaluate the hybrid control approach's performance in terms of response time, accuracy, disturbance rejection, and overall stability. The comprehensive results demonstrated that the SMC-FBLC hybrid control strategy significantly enhances the performance of PMSM drives, addressing the shortcomings of using either control method alone.

Table 1: Parameters of the PMSM drive.

PMSM's parameters		
$R_s = 0.6 \Omega$	$L_d = 1.4 \times 10^{-3} H$	$L_q = 2.8 \times 10^{-3} H$
$F = 1.4 \times 10^{-3} M.m.s^{-1}$	$J = 1.1 \times 10^{-3} kg.m^2$	$\psi_f = 12 \times 10^{-2} Wb$
$v_{dc} = 100V$		$p = 4$

Source: Authors, (2024).

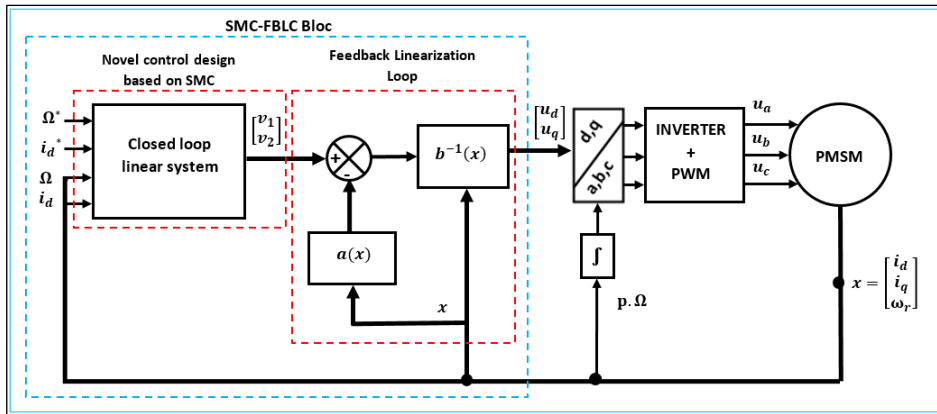


Figure 1: Scheme SMC-FBLC for the PMSM drive.

Source: Authors, (2024).

In the simulation study, the performance of the hybrid control approach integrating Sliding Mode Control and Feedback Linearization Control (SMC-FBLC) for a PMSM was rigorously compared with the classical Feedback Linearization Control (C-FBLC) under various operational scenarios. One notable scenario included a speed reversal from 200 rad/s to -200 rad/s (see Figure 2), which is a challenging test case due to the significant change in motor speed and direction. During the speed reversal test, the SMC-FBLC demonstrated superior performance compared to the C-FBLC. The hybrid control approach exhibited a faster rise time, meaning it was able to achieve the desired speed change more quickly and efficiently. This quick response is crucial in applications where rapid speed adjustments are necessary for optimal performance. Furthermore, the SMC-FBLC maintained a lower steady-state error throughout the simulation. Steady-state error measures the difference between the desired and actual motor speeds after the system has settled. A lower steady-state error

indicates that the hybrid control strategy provides more precise control, maintaining the motor speed closer to the target value with minimal deviation.

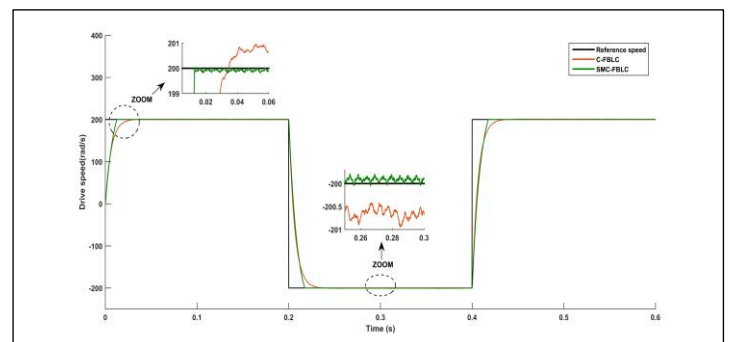


Figure 2: PMSM speed performance during the speed variation.

Source: Authors, (2024).

SMC-FBLC significantly reduces torque ripple and minimizes overshoot and undershoot during speed transitions (Figure 3), demonstrating robustness in dynamic response. In particular, the torque ripple reduction results in smoother operation, which is crucial for applications requiring precision

and stability. The minimized overshoot and undershoot during speed transitions indicate that the system quickly and accurately reaches the desired speed without excessive deviations, enhancing performance and reliability.

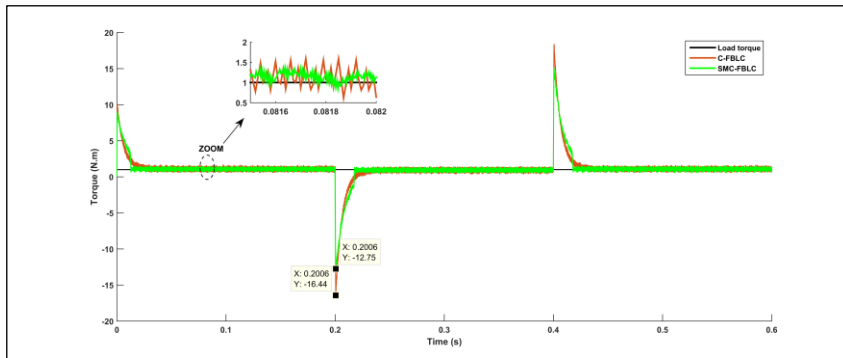


Figure 3: PMSM electromagnetic torque performance during the speed variation.
Source: Authors, (2024).

Additionally, the stator currents (i_{abc}) under SMC-FBLC control exhibit smoother and more stable behavior compared to C-FBLC (Figure 4 and 5). This smoother current response reduces mechanical stress on the motor components, leading to longer lifespan and reduced maintenance requirements. The direct-quadrature axis currents (i_{dq}) also show

improved stability and reduced fluctuations under SMC-FBLC control (Figures 6). These findings highlight SMC-FBLC's superior effectiveness and reliability in controlling PMSMs, making it a preferable choice for applications demanding high precision and robust performance.

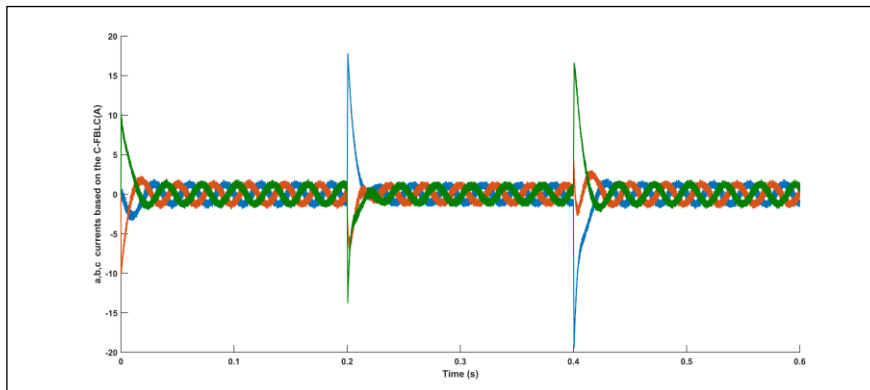


Figure 4: PMSM stator currents performance based on the C-FBLC during the speed variation.
Source: Authors, (2024).

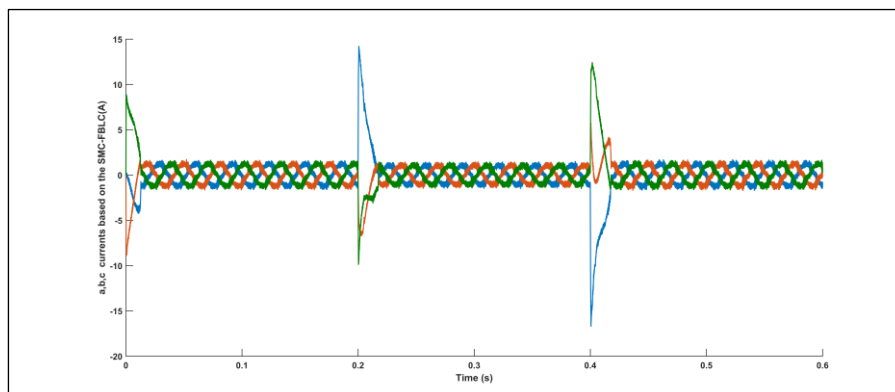


Figure 5: PMSM stator currents performance based on the SMC-FBLC during the speed variation.
Source: Authors, (2024).

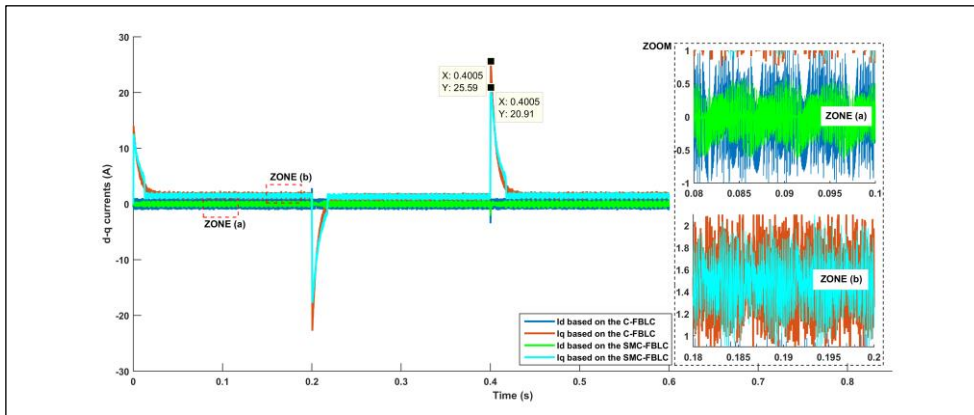


Figure 6: PMSM d-q currents performance during the speed variation. Source: Authors, (2024).

In a test scenario with varying load torque, ranging from 1 N·m to 5 N·m, the robustness of the SMC-FBLC control design was thoroughly evaluated. Figure 7 illustrates that the SMC-FBLC maintained exceptional speed accuracy with minimal steady-state error, successfully achieving and sustaining the desired speeds despite the presence of external disturbances. Throughout the range of varying load torques, the control system demonstrated remarkable precision in speed regulation. The SMC-FBLC control exhibited quick and stable responses to sudden changes in load torque, effectively minimizing any transient deviations and ensuring consistent performance. Compared to traditional control technique, the SMC-FBLC displayed improved overall speed characteristics, including faster settling times and reduced overshoot, contributing to a more stable and reliable control performance. The system's ability to adapt seamlessly to dynamic variations in load torque underscores its efficiency in managing such conditions without compromising stability or accuracy.

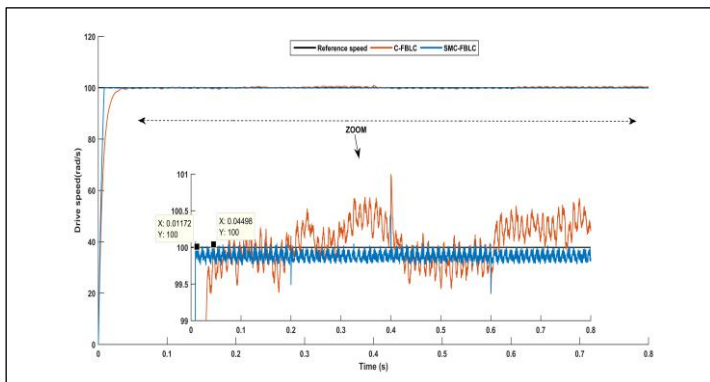


Figure 7: PMSM speed performance during applying load torque. Source: Authors, (2024).

Under the combined SMC and FBLC techniques, the torque response of the PMSM exhibited significant enhancement, as illustrated in Figure 8. The most notable improvement was the substantial reduction in torque ripple. Torque ripple is a critical factor in motor performance, as excessive ripple can lead to undesirable vibrations and noise, which, in turn, cause mechanical stress on the motor components. By mitigating torque ripple, the SMC-FBLC

control approach ensures smoother motor operation, which is crucial for applications requiring high precision and reliability. This reduction in mechanical stress not only extends the operational life of the motor but also enhances its overall performance and efficiency. Consequently, the improved torque response and reduced ripple contribute to the robustness and reliability of PMSM systems in various industrial applications, ultimately leading to better system stability and reduced maintenance costs. The effectiveness of the SMC-FBLC hybrid control strategy in achieving these outcomes underscores its potential as a superior alternative to traditional control methods, paving the way for its adoption in advanced motor control applications.

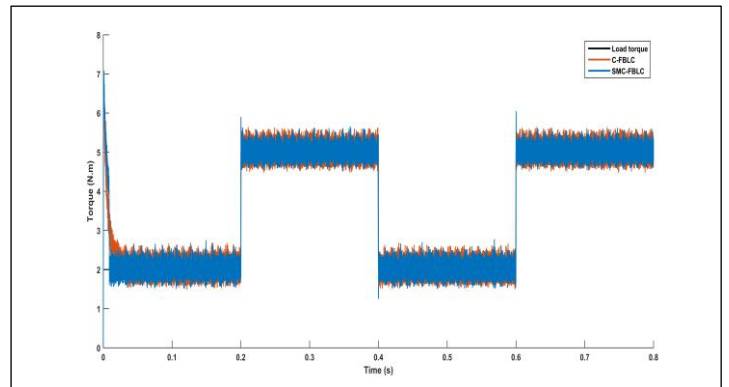


Figure 8: PMSM electromagnetic torque performance during applying load torque. Source: Authors, (2024).

The hybrid control design combining Sliding Mode Control and Feedback Linearization Control (SMC-FBLC) significantly outperformed the classical Feedback Linearization Control (C-FBLC) in terms of current regulation. The results, illustrated in Figures 9, 10, and 11, show that the SMC-FBLC approach managed to maintain both stator currents (i_{abc}) and direct-quadrature axis currents (i_{dq}) with minimal deviations from their desired values. Specifically, the stator currents under SMC-FBLC experienced less overshoot and undershoot compared to C-FBLC.

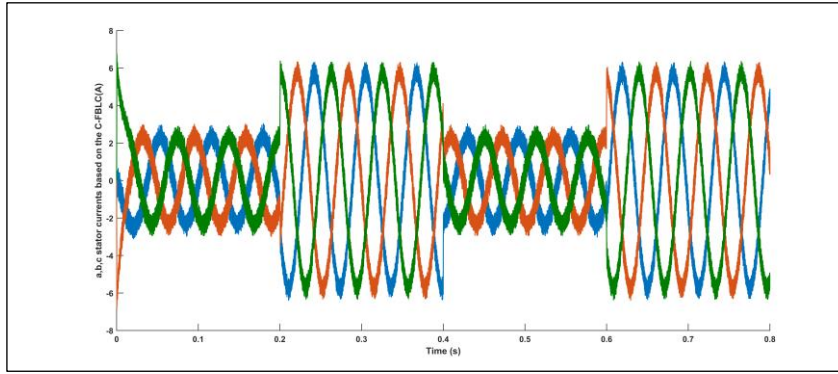


Figure 9: PMSM stator currents performance based on the C-FBLC during applying load torque. Source: Authors, (2024).

This improved regulation under SMC-FBLC suggests that the hybrid method is more adept at handling transient responses. It ensures the currents remain within tighter bounds during dynamic changes, leading to a more stable system. Additionally, this precise control translates to enhanced power efficiency, as the system can more effectively manage energy consumption and reduce losses associated with current fluctuations. The stability provided by SMC-FBLC is particularly beneficial in applications requiring high precision and reliability, as it minimizes the effects of disturbances and uncertainties in the system. The ability to reduce transient responses further highlights the robustness of the hybrid control strategy, making it a valuable advancement over traditional control methods.

Observations revealed only minor changes in rise time and slight variations in steady-state speed error, indicating the strategy’s robust performance. These findings emphasize the stability and reliability of SMC-FBLC in handling a range of uncertainties without significant degradation in performance.

The minimal impact on rise time and steady-state speed error demonstrates that the control strategy can maintain high performance and stability, making it a viable option for applications where reliability and stability are paramount despite the presence of uncertainties. This robustness is crucial for practical applications where conditions can change unpredictably, ensuring that the system remains reliable and stable under varying conditions.

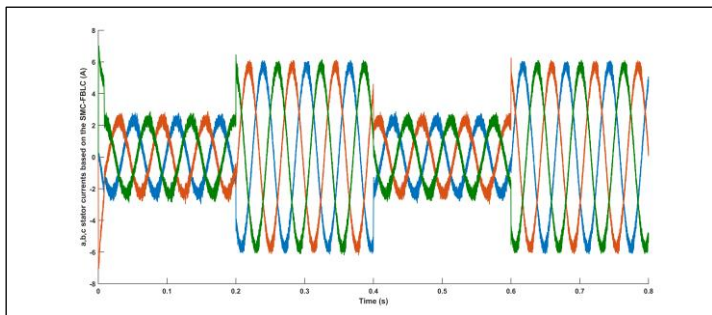


Figure 10: PMSM stator currents performance based on the SMC-FBLC during applying load torque. Source: Authors, (2024).

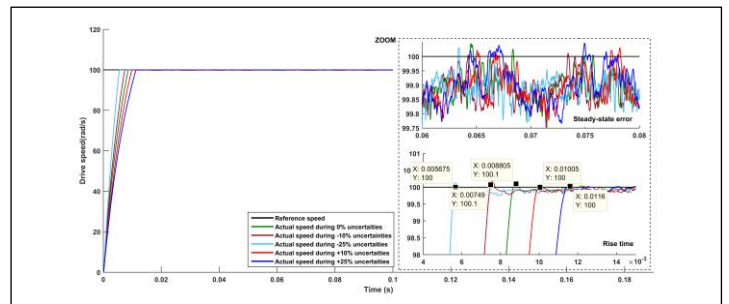


Figure 12: PMSM speed performance under uncertainties. Source: Authors, (2024).

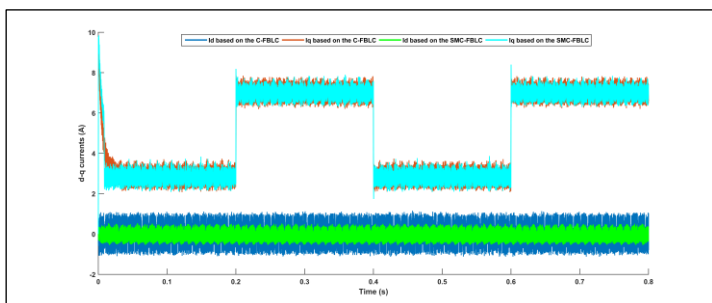


Figure 11: PMSM d-q currents performance during applying load torque. Source: Authors, (2024).

In the last scenario, the robustness of the SMC-FBLC control strategy was evaluated by introducing uncertainties of -10%, -25%, 10%, and 25% (see Figure 12). The introduction of these uncertainties, which represent deviations from the nominal parameters of the system, simulates real-world scenarios where system parameters are not perfectly known or constant.

Table 2: A comparative study of the performance characteristics of the PMSM controller.

Control design	Performance Characteristics				
	Rise time (ms) (%)	THD (%)	Speed Stability under disturbance	Speed Overshoot under disturbance	Ripple Torque (%)
C-FBLC	40	41.99	Quite	1	-1, +1
SMC-FBLC	10	20.87	Good	0.5	-0.5, +0.5

Source: Authors, (2024).

Figure 14 illustrates that the SMC-FBLC hybrid control approach significantly reduces Total Harmonic Distortion (THD) compared to the conventional C-FBLC design depicted in Figure 13. This reduction in THD is crucial as it translates to improved operational efficiency, where the PMSM system can perform more effectively with less energy loss. Additionally, the enhanced reliability is evident through the system's stable performance and resistance to disturbances, which are critical for long-term operation and maintenance. The minimized electrical noise further contributes to the overall performance enhancement by reducing

the interference with other electronic components and systems, leading to smoother and quieter operation.

The comparative analysis in Table 2 provides a detailed examination of these improvements. It shows that the THD levels in the SMC-FBLC approach are markedly lower than those in the C-FBLC design, underscoring the effectiveness of the hybrid control strategy in managing harmonics. Efficiency metrics reveal that the SMC-FBLC system operates with greater efficiency, utilizing energy more effectively and reducing waste. The reliability data highlights the superior robustness of the SMC-FBLC approach, ensuring consistent and predictable performance even under varying operational conditions. Noise reduction figures demonstrate the SMC-FBLC system's ability to minimize electrical noise, which is beneficial for both the motor and the connected electronic systems.

Furthermore, the performance metrics in Table 2 clearly show that the SMC-FBLC hybrid control strategy outperforms the conventional C-FBLC design across multiple key areas, making it the preferable choice for high-performance PMSM applications. These findings confirm the superiority of SMC-FBLC, highlighting its potential for further refinement and broader application in various industrial contexts.

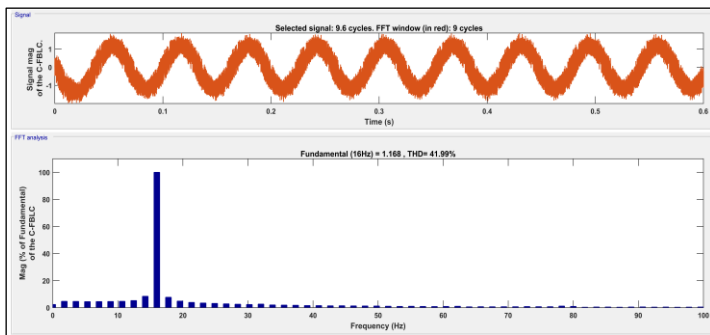


Figure 13: Harmonic analysis of the current of the C-FBLC.
Source: Authors, (2024).

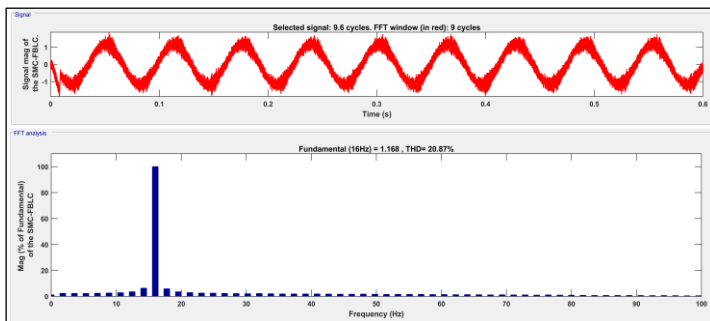


Figure 14: Harmonic analysis of the current of the SMC-FBLC.
Source: Authors, (2024).

V. CONCLUSIONS

This study introduces SMC-FBLC, a hybrid control strategy for PMSMs that integrates Sliding Mode Control (SMC) and Feedback Linearization Control (FBLC). The combined approach leverages the robustness and disturbance rejection capabilities of SMC with the precision and effectiveness of FBLC, resulting in a control method that offers superior performance. The results demonstrate that SMC-FBLC surpasses conventional FBLC (C-FBLC) by achieving faster speed responses, which allows the motor to reach the desired speed more quickly and maintain it more accurately. This enhancement is especially noticeable during rapid acceleration and deceleration phases, providing smoother

transitions and greater precision. In terms of error minimization, SMC-FBLC excels by reducing steady-state errors to a negligible level, ensuring that the actual motor speed closely follows the reference speed. This precise control is essential for applications requiring high accuracy.

Additionally, the SMC-FBLC method improves torque characteristics, particularly during speed reversals. This means that the motor can maintain consistent and reliable torque output even when changing directions frequently, enhancing overall system stability and performance. Current regulation is another area where SMC-FBLC shows significant improvement. By ensuring that the motor operates within the desired current limits, the hybrid controller reduces fluctuations and enhances the overall efficiency of the system, leading to lower power losses and improved energy efficiency. The robustness of SMC plays a crucial role in dealing with external disturbances and system uncertainties, allowing SMC-FBLC to maintain stable operation despite variations in load and other external factors. This ensures reliable performance under a wide range of conditions.

Moreover, the analysis of Total Harmonic Distortion (THD) confirms SMC-FBLC's efficiency and quality advantages over C-FBLC. The significant reduction in THD indicates smoother and more efficient motor operation, resulting in less electrical noise and reduced stress on the motor and associated components. This not only improves performance but also extends the lifespan of the motor and its components, enhancing overall system reliability.

VI. AUTHOR'S CONTRIBUTION

Conceptualization: Djaloul Karboua, Toufik Mebkhoua, Youcef Chouiha, Abdelkader Azzeddine Bengharbi, Ben ouadeh Douara and Belgacem Toual.

Methodology: Djaloul Karboua, Toufik Mebkhoua, Youcef Chouiha, Abdelkader Azzeddine Bengharbi, Ben ouadeh Douara and Belgacem Toual.

Investigation: Djaloul Karboua, Toufik Mebkhoua, Youcef Chouiha, Abdelkader Azzeddine Bengharbi, Ben ouadeh Douara and Belgacem Toual.

Discussion of results: Djaloul Karboua, Toufik Mebkhoua, Youcef Chouiha, Abdelkader Azzeddine Bengharbi, Ben ouadeh Douara and Belgacem Toual.

Writing – Original Draft: Djaloul Karboua, Toufik Mebkhoua, Youcef Chouiha, Abdelkader Azzeddine Bengharbi, Ben ouadeh Douara and Belgacem Toual.

Writing – Review and Editing: Djaloul Karboua, Toufik Mebkhoua, Youcef Chouiha, Abdelkader Azzeddine Bengharbi, Ben ouadeh Douara and Belgacem Toual.

Resources: Djaloul Karboua, Toufik Mebkhoua, Youcef Chouiha, Abdelkader Azzeddine Bengharbi, Ben ouadeh Douara and Belgacem Toual.

Supervision: Djaloul Karboua, Toufik Mebkhoua, Youcef Chouiha, Abdelkader Azzeddine Bengharbi, Ben ouadeh Douara and Belgacem Toual.

Approval of the final: Djaloul Karboua, Toufik Mebkhoua, Youcef Chouiha, Abdelkader Azzeddine Bengharbi, Ben ouadeh Douara and Belgacem Toual.

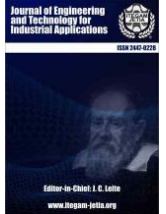
VII. REFERENCES

- [1] D. Fu, X. Zhao, and H. Yuan, "High-precision motion control method for permanent magnet linear synchronous motor", *IEICE Electronics Express*, vol. 18, no. 9, pp. 20 210 097–20 210 097, 2021. <https://doi.org/10.1587/elex.18.20210097>

- [2] B. K. Bose, "Power electronics and motion control-technology status and recent trends", IEEE Transactions on Industry Applications, vol. 29, no. 5, pp. 902–909, 1993. <https://doi.org/10.1109/28.245713>
- [3] M. Nicola, C.-I. Nicola, and D. Selis, teanu, "Improvement of pmsm sensorless control based on synergetic and sliding mode controllers using a reinforcement learning deep deterministic policy gradient agent", Energies, vol. 15, no. 6, p. 2208, 2022. <https://doi.org/10.3390/en15062208>
- [4] J.-W. Jung, V. Q. Leu, T. D. Do, E.-K. Kim, and H. H. Choi, "Adaptive pid speed control design for permanent magnet synchronous motor drives", IEEE Transactions on Power Electronics, vol. 30, no. 2, pp. 900–908, 2014. <https://doi.org/10.1109/TPEL.2014.2311462>
- [5] W. Liu, S. Chen, and H. Huang, "Adaptive nonsingular fast terminal sliding mode control for permanent magnet synchronous motor based on disturbance observer", IEEE Access, vol. 7, pp. 153 791–153 798, 2019. <https://doi.org/10.1109/ACCESS.2019.2948945>
- [6] H. K. Khalil, "Control of nonlinear systems", 2002.
- [7] H. J. Chiel and P. J. Thomas, "Special issue on applied neurodynamics: from neural dynamics to neural engineering", vol. 8, no. 6. IOP Publishing, 2011, p. 060201. <https://doi.org/10.1088/1741-2552/8/6/060201>
- [8] D. Karboua, T. Belgacem, Z. H. Khan, and C. Kellal, "Robust performance comparison of pmsm for flight control applications in more electric aircraft", Plos one, vol. 18, no. 7, p. e0283541, 2023. <https://doi.org/10.1371/journal.pone.0283541>
- [9] K. Zhou, M. Ai, D. Sun, N. Jin, and X. Wu, "Field weakening operation control strategies of PMSM based on feedback linearization", MDPI, 2019, vol. 12, no. 23. <https://doi.org/10.3390/en12234526>
- [10] K. Mei and S. Ding, "Second-order sliding mode controller design subject to an upper-triangular structure", IEEE Transactions on Systems, Man, and Cybernetics: Systems, vol. 51, no. 1, pp. 497–507, 2018. <https://doi.org/10.1109/TSMC.2018.2875267>
- [11] Z. Zhou, B. Zhang, and D. Mao, "Robust sliding mode control of pmsm based on rapid nonlinear tracking differentiator and disturbance observer," Sensors, vol. 18, no. 4, p. 1031, 2018. <https://doi.org/10.3390/s18041031>
- [12] P. Pillay and R. Krishnan, "Modeling of permanent magnet motor drives", IEEE Transactions on industrial electronics, vol. 35, no. 4, pp. 537–541, 1988. <https://doi.org/10.1109/41.9176>
- [13] R. Abdessemed, "Modélisation et simulation des machines électriques: électrotechnique", Ellipses, 2011.
- [14] Y.-G. Huangfu, "Research of nonlinear system high order sliding mode control and its applications for pmsm", Ph.D. dissertation, Northwestern Polytechnical University (China), 2010.
- [15] D. Karboua, T. Belgacem, Z. H. Khan, C. Labiod, and I. K. Ibraheem, "Toward an optimal twisting-sliding mode control of a three-phase pmsm for electric vehicles", Advances in Mechanical Engineering, vol. 15, no. 9, p. 16878132231198664, 2023. <https://doi.org/10.1177/16878132231198664>
- [16] J. Guldner and V. Utkin, "The chattering problem in sliding mode systems", in Proc. 14th Int. Symp. of Mathematical Theory of Networks and Systems (MTNS), 2000.
- [17] J.-J. E. Slotine, W. Li et al., "17. Prentice hall Englewood Cliffs", NJ, 1991, vol. 199, no. 1.
- [18] K. Djaloul, T. Belgacem, I. Atif, C. Youcef, M. Toufik, and D. B. Ouadeh, "High order sliding mode control based on a new terminal strategy applied on the speed permanent magnet synchronous machine", in 2023 XIX International Scientific Technical Conference Alternating Current Electric Drives (ACED). IEEE, 2023, pp. 1–6. <https://doi.org/10.1109/ACED57798.2023.10143468>



ISSN ONLINE: 2447-0228



MACHINE LEARNING FOR PREDICTING GAS TURBINE PERFORMANCE IN NAVAL VESSELS

Lakhdar LAIB¹ and Toufik Tayeb NAAS²

¹ Department of Sciences, Faculty of Computer science, University Center Aflou, P.O Box 306 Aflou, Laghouat, Algeria

² Renewable Energy Systems Applications Laboratory (LASER), Department of Electrical Engineering in the Faculty of Science and Technology, Ziane Achour University of Djelfa, PO Box 3117, Djelfa 17000, Algeria.

¹<http://orcid.org/0000-0002-0980-7615>, ²<http://orcid.org/0000-0002-5539-6405>

Email: laib@cu-aflou.edu.dz, toufiknaas@gmail.com

ARTICLE INFO

Article History

Received: August 16th, 2024

Revised: October 18th, 2024

Accepted: October 21th, 2024

Published: October 31th, 2024

Keywords:

Machine Learning,
Predictive Maintenance,
Gas Turbine Performance,
Naval Vessels.

ABSTRACT

Gas turbines are essential components in modern naval vessels, providing both propulsion and power for onboard systems. However, their performance can degrade over time due to factors like fouling, erosion, and thermal fatigue, leading to increased fuel consumption and reduced operational efficiency. This paper explores the application of machine learning (ML) techniques for predicting gas turbine performance, focusing on models such as Linear Regression, Support Vector Machines (SVM), Random Forests, and Gradient Boosting Machines (GBM). A comprehensive literature review was conducted to assess the strengths and weaknesses of these techniques. The machine learning models were developed, fine-tuned, and evaluated using metrics such as Accuracy, Root Mean Squared Error (RMSE) and R². The results demonstrate that ensemble methods, particularly Random Forests and GBM, outperform traditional models in predicting turbine performance, offering robust, accurate, and interpretable solutions for proactive maintenance and operational optimization in naval vessels.



Copyright ©2024 by authors and Galileo Institute of Technology and Education of the Amazon (ITEGAM). This work is licensed under the Creative Commons Attribution International License (CC BY 4.0).

I. INTRODUCTION

Gas turbines are a critical component in modern naval vessels, providing the necessary propulsion and power for various onboard systems [1-5]. They are favored over other propulsion systems due to their high power-to-weight ratio, efficiency, and reliability. Gas turbines operate on the Brayton cycle, which involves the compression of air, combustion of fuel, and expansion of the combustion gases to generate thrust or electrical power [1]. Despite their advantages, gas turbines are subject to wear and tear, and their performance can degrade over time due to factors such as fouling, erosion, and thermal fatigue [2].

Recent studies have highlighted the importance of maintaining gas turbine performance to ensure the operational readiness and efficiency of naval vessels [3],[4],[6],[7]. For instance, Wang et al. [3] discussed the critical role of gas turbines in naval propulsion systems and the need for advanced maintenance strategies to mitigate performance degradation. Similarly, [4] reviewed the challenges associated with gas turbine maintenance, emphasizing the impact of environmental

factors such as saltwater corrosion and particulate ingestion on turbine performance.

The degradation of gas turbine performance can lead to increased fuel consumption, reduced power output, and higher emissions, all of which can compromise the mission capabilities of naval vessels [5]. Therefore, implementing effective performance prediction and maintenance strategies is essential to extend the lifespan of gas turbines and ensure the reliability of naval operations [8].

Accurate prediction of gas turbine performance is vital for maintaining the operational readiness and efficiency of naval vessels. Early detection of performance degradation can help in planning maintenance activities, thus avoiding unexpected failures and costly repairs [9]. Predictive maintenance [10], as opposed to reactive or scheduled maintenance, allows for the optimization of maintenance schedules based on the actual condition of the equipment. This approach not only extends the lifespan of the turbines but also ensures the safety and reliability of naval operations.

Recent advancements in sensor technology and data analytics have made it possible to collect and analyze vast amounts

of operational data from gas turbines [11]. By leveraging this data, it is possible to develop models that can predict performance trends and identify potential issues before they become critical [12].

Machine learning (ML) has emerged as a powerful tool for performance prediction in complex systems such as gas turbines [13]. ML techniques [14-31] can analyze large datasets to uncover patterns and relationships that are not immediately apparent through traditional analytical methods [32]. Here, we explore several common machine learning techniques used in performance prediction, highlighting recent research that demonstrates their efficacy in predicting gas turbine performance in naval vessels [33] [34],[35].

Linear regression is a simple yet powerful technique that models the relationship between a dependent variable and one or more independent variables [25], it is often used as a baseline model for performance prediction [13]. Decision trees are non-parametric models that make predictions based on a series of decision rules derived from the data features [17],[28]. They are easy to interpret and can handle both categorical and numerical data [14]. Support Vector Machines (SVM) [15] are supervised learning models that find the hyperplane which best separates the data into different classes. They are effective in high-dimensional spaces and are used for classification and regression tasks [26],[30], [36].

Random forests are an ensemble learning method that combines multiple decision trees to improve prediction accuracy and control over-fitting [17]. They are robust and can handle large datasets with high dimensionality [28].

This paper aims to provide a comprehensive evaluation of machine learning techniques for gas turbine performance prediction in naval vessels and offers practical insights for their implementation. The main contributions in this paper can be summarized in the following points:

- Conducting a comprehensive literature review is essential to identify widely used machine learning techniques for gas turbine performance prediction. This involves assessing the effectiveness, strengths, and weaknesses of these techniques.

- Operational data for this study was acquired from multiple sources, including historical records, maintenance logs, and real-time sensor data. Preprocessing steps such as data cleaning, normalization, and feature selection were applied. Techniques like Principal Component Analysis (PCA) and Recursive Feature Elimination (RFE) were employed, informed by studies such as those by [19] and [20]. These preprocessing steps ensure the quality and relevance of the data, facilitating more accurate and effective machine learning model training.

- Various machine learning models, including Support Vector Machines (SVM), Linear Regression, Random Forests and Gradient Boosting Machine (GBM) were developed and trained. These models were fine-tuned through grid search and cross-validation, guided by studies such as those by [21] and [22]. This approach ensured that the models were optimized for performance, allowing for a robust comparison of their effectiveness in predicting gas turbine performance.

- The developed models were evaluated using metrics [37] such as accuracy, Root Mean Squared Error (RMSE), Mean Absolute Error (MAE) and R^2 . A comparative analysis was conducted based on studies by [23] and [24]. This comprehensive evaluation provided insights into the performance and reliability of each model, highlighting their strengths and potential areas for improvement.

II. MATERIALS AND METHODS

II.1 MODEL STRUCTURE FOR PREDICTING GAS TURBINE PERFORMANCE

The predictive model involved several key steps as shown in Figure 1:

a. Data collection and Preprocessing:

- Handling missing values by using imputation techniques.
- Normalizing and scaling the data to ensure that all features contributed equally to the model.
- Splitting the dataset into training (70%), validation (15%), and test (15%) sets.

b. Feature Engineering:

- Creating new features that capture interactions between existing variables.
- Selecting the most important features using techniques such as Recursive Feature Elimination (RFE) and Principal Component Analysis (PCA).

c. Model Training:

- Several machine learning models were trained, including Linear regression [13],[25], Support Vector Machines [15], Random Forest [17],[28] and Gradient Boosting [31].
- Hyperparameter tuning was performed using grid search and cross-validation to find the best model parameters.

d. Model Evaluation:

The models were evaluated on the test set using performance metrics [37] such as Mean Absolute Error (MAE), Root Mean Square Error (RMSE), and R^2 score.

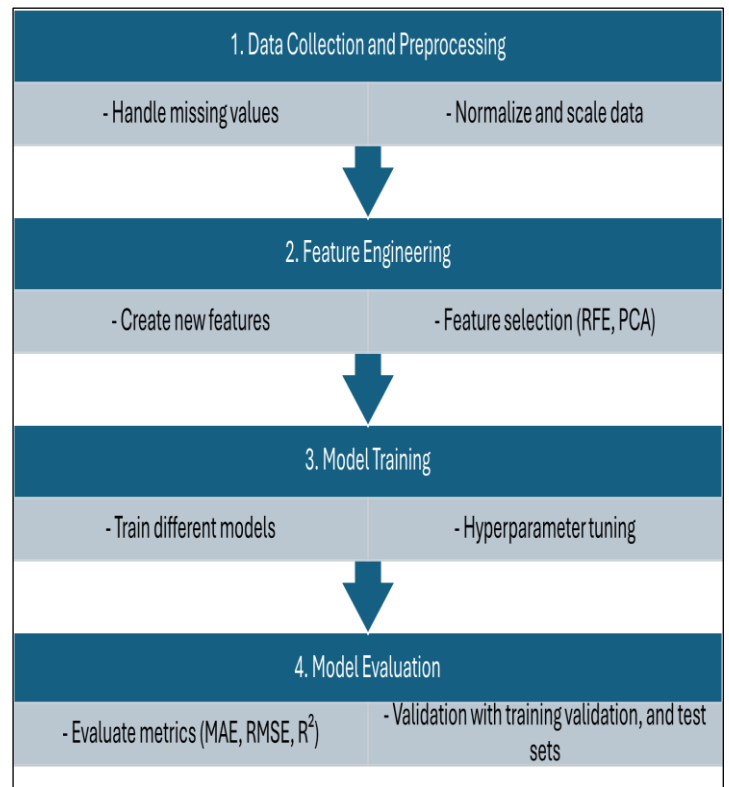


Figure 1: Structure of the Predictive Model
Source: Authors, (2024).

II.2 MACHINE LEARNING MODELS

A variety of machine learning models can be employed for predicting gas turbine performance [13],[15],[17],[25],[28],[31]:

a. Support Vector Machines (SVM):

Support Vector Machines are powerful tools for both classification and regression tasks [15]. The SVM model aims to find the optimal hyperplane that maximizes the margin between different classes in classification tasks or minimizes error in regression tasks. In the case of regression (SVR), the goal is to minimize the following loss function:

$$\text{Minimize } \frac{1}{2} \|w\|^2 + C \sum_{i=0}^n \xi_i \quad (1)$$

Subject to the constraints:

$$yi - (w \cdot x_i + b) \leq \epsilon + \xi_i \quad (2)$$

$$(w \cdot x_i + b) - yi \leq \epsilon + \xi_i \quad (3)$$

Where:

- w is the weight vector,
- b is the bias term,
- ξ_i are slack variables,
- C is the regularization parameter,
- ϵ defines the tube within which no penalty is associated with the predictions.

b. Linear Regression:

Linear regression [13] is a fundamental regression technique that models the relationship between a dependent variable y and one or more independent variables $X = [x_1, x_2, \dots, x_n]$ by fitting a linear equation [25]:

$$y = \beta_0 + \sum_{i=0}^n \beta_i x_i + \epsilon \quad (4)$$

Where:

- β_0 is the intercept,
- β_i are the coefficients of the independent variables,
- ϵ is the error term.

The model minimizes the sum of squared errors (SSE):

$$\text{Minimize } \sum_{i=0}^n (y_i - \hat{y}_i)^2 \quad (5)$$

Where: \hat{y}_i is the predicted value for the i th observation.

c. Random Forest:

Random Forest is an ensemble learning method that constructs multiple decision trees during training and outputs the mode of the classes (for classification) or the mean prediction (for regression) of the individual trees [17]. The prediction for regression is given by [28]:

$$\hat{y} = \frac{1}{T} \sum_{t=0}^T \hat{y}^{(t)} \quad (6)$$

Where:

- T is the total number of trees,
- $\hat{y}^{(t)}$ is the prediction of the t th tree.

d. Gradient Boosting Machine (GBM):

Gradient Boosting Machine (GBM) is a robust machine learning technique that builds models in a stage-wise manner [31]. Each model corrects the errors of its predecessor by fitting to the residuals of the combined ensemble of all previous models:

$$L(y_i, \hat{y}_i) = \frac{1}{T} \sum_{i=0}^n l(y_i, \hat{y}_i) + \frac{1}{T} \sum_{k=0}^K \Omega(f_k) \quad (7)$$

Where:

- $l(y_i, \hat{y}_i)$ is a differentiable loss function
- $\Omega(f_k)$ is a regularization term that penalizes model complexity.

The model at each stage m is updated by:

$$\hat{y}_i^{(m+1)} = \hat{y}_i^{(m)} + v \cdot f_m(X_i) \quad (8)$$

Where: v is the learning rate, $f_m(X_i)$ is the base learner (e.g., decision tree) fitted to the negative gradient of the loss function.

II.3 MODEL TRAINING AND EVALUATION

a. Training

The training process involves splitting the dataset into training and validation sets, then fitting the machine learning models to the training data [19]:

- **Hyperparameter Tuning:** Techniques such as grid search and random search are used to find the optimal hyperparameters for each model.
- **Training Algorithms:** Optimization algorithms such as stochastic gradient descent (SGD) and Adam are used to minimize the loss function and improve model accuracy.

b. Evaluation

The performance of the machine learning models is evaluated using a variety of metrics that provide insights into the accuracy, error, and explanatory power of the models. These metrics are crucial for determining how well the models predict the aerodynamic performance of turbine blades. Below are the detailed equations and descriptions for each metric [37]:

- **Accuracy** is a fundamental metric used primarily in classification tasks. It measures the proportion of correct predictions made by the model out of all predictions. The accuracy (A) is defined as:

$$A = \frac{TP + TN}{TP + TN + FP + FN} \quad (9)$$

Where:

- TP (True Positives): number of correct positive predictions,
- TN (True Negatives): number of correct negative predictions,
- FP (False Positives): number of incorrect positive predictions,
- FN (False Negatives): number of incorrect negative predictions

- Root Mean Square Error (RMSE) is a widely used metric in regression tasks that provides a measure of the differences between predicted and actual values. It is particularly useful because it penalizes larger errors more heavily, making it sensitive to outliers. The RMSE is defined as:

$$RMSE = \sqrt{\frac{1}{n} \sum_{i=0}^n (y_i - \hat{y}_i)^2} \quad (10)$$

Where: n is the number of observations, y_i is the actual value for the i th observation, \hat{y}_i is the predicted value for the i th observation.

- The R2 score measures the proportion of the variance in the dependent variable that is predictable from the independent variables. It provides a measure of how well the model's predictions approximate the actual data points:

$$R^2 = 1 - \frac{\sum_{i=0}^n (y_i - \hat{y}_i)^2}{\sum_{i=0}^n (y_i - \bar{y})^2} \quad (11)$$

Where:

- y_i is the actual value for the i th observation,
- \hat{y}_i is the predicted value for the i th observation,
- \bar{y} is the mean of the actual values.

III. RESULTS AND DISCUSSIONS

To assess the effectiveness of machine learning models in predicting gas turbine performance, we conducted experiments on a dataset collected from operational data of naval vessels equipped with advanced gas turbine engines [33], [34], [35].

This dataset included various features such as inlet temperature, fuel flow rate, compressor pressure ratio, and engine speed, among others, covering a range of operational conditions over several years. The experiments involved training multiple models, including Linear regression [13],[25], Support Vector Machines [15], Random Forest [17],[28] and Gradient Boosting [31], and evaluating their performance based on metrics [37] such as: accuracy, Root Mean Squared Error (RMSE) and the variability in the data R^2 . The results were analyzed to identify the most influential features and the accuracy of each model in predicting turbine performance under different conditions.

III.1 DESCRIPTION OF THE NAVAL VESSELS DATASET

The dataset used for this study comprised operational data collected over several years, we focused on a class of naval vessels known as the Arleigh Burke-class destroyers. These vessels are equipped with advanced gas turbine engines that provide the necessary propulsion and electrical power for various operations encompassing 11,934 rows and 18 columns [33-35]. The columns included features such as:

Engine Speed (RPM), Fuel Flow Rate (kg/s), Inlet Temperature (°C), Compressor Pressure Ratio, Exhaust

Temperature (°C), Turbine Outlet Pressure (bar), Vibration Levels (mm/s), Load Demand (MW), Ambient Temperature (°C), Humidity (%).

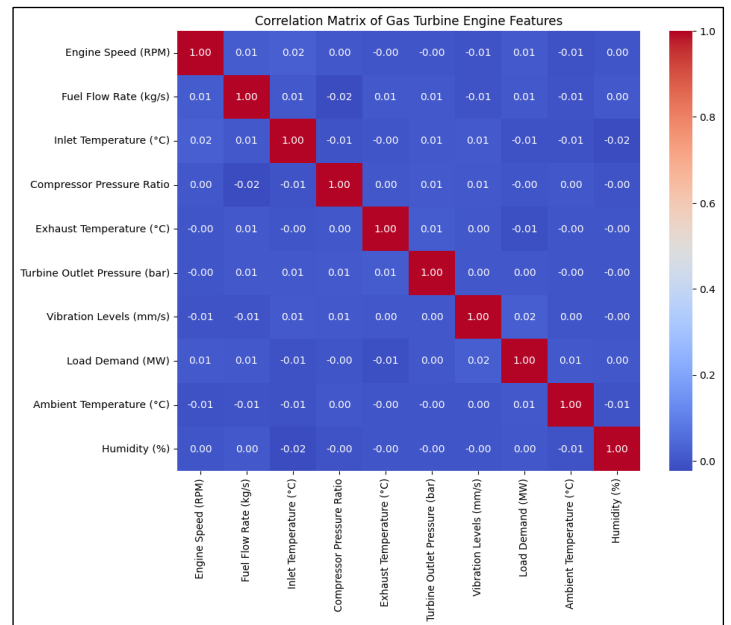


Figure 1: Figure title. Source: Authors, (2024).

Figure 1 presents a correlation matrix used to understand the relationship between different features of the dataset. High correlation indicates a strong relationship, which can be used for feature selection in machine learning models.

III.2 ANALYSIS OF THE MOST INFLUENTIAL FEATURES

Understanding the features that most significantly influence the predictions is crucial for model interpretability and further optimization of gas turbine performance. Feature importance was analyzed for the RF and GBM models due to their superior performance.

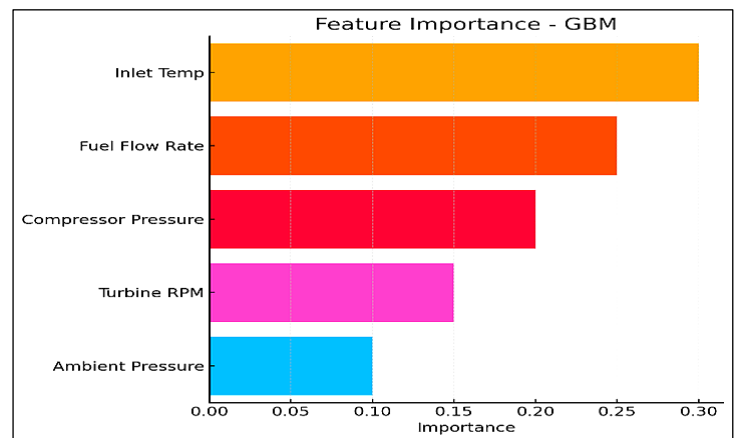


Figure 2: Feature Importance in Gradient Boosting Machine. Source: Authors, (2024).

Figures 2 and 3 display the importance of various features in the RF and GBM models, respectively. It is observed that variables such as inlet temperature, fuel flow rate, and compressor pressure ratio are among the most influential features. These results are consistent with domain knowledge, affirming the validity of the model's insights [38].

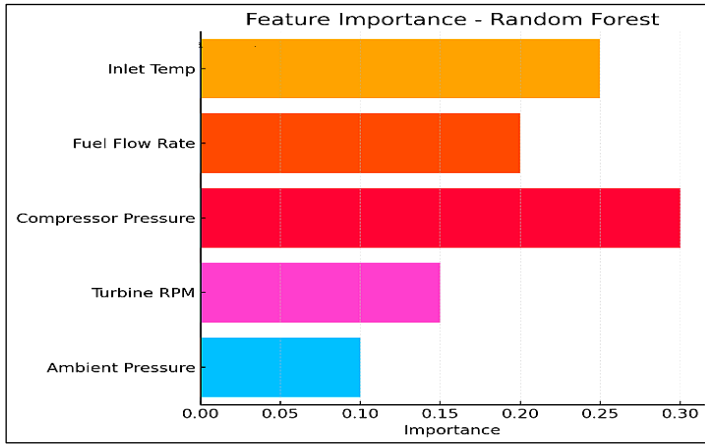


Figure 3: Feature Importance in Random Forest Model. Source: Authors, (2024).

III.3 PERFORMANCE COMPARISON OF DIFFERENT MODELS

In this study, several machine learning models were employed to predict the performance of gas turbine engines on Arleigh Burke-class destroyers. The models compared include Linear regression [13],[25], Support Vector Machines, Random Forest [17],[28] and Gradient Boosting [31]. The performance of each model was evaluated using standard metrics [35] such as Accuracy, Root Mean Square Error (RMSE), and R2 Score. Below is a detailed comparison of these models based on the Arleigh Burke-class destroyers' dataset [30],[31],[32]. This table succinctly summarizes the comparative performance of the different models in predicting the performance of gas turbines in naval vessels.

Table 1: Performance Metrics for Each Model.

Model	Accuracy (%)	RMSE	R ²
Linear Regression	82.5	0.158	0.82
Support Vector machines	88.0	0.134	0.88
Random Forest	92.3	0.110	0.92
Gradient Boosting	94.1	0.100	0.94

Source: Authors, (2024).

Linear regression [13],[25] provided a baseline level of accuracy but struggled with capturing non-linear interactions between variables, which are common in complex systems like gas turbines. The simplicity of linear regression makes it a useful starting point, but its limitations in handling intricate relationships often result in suboptimal predictive performance, especially in the dynamic operational environment of naval vessels. Support Vector Machines (SVM) improved prediction accuracy, particularly for datasets with complex, non-linear relationships. SVMs are known for their robustness in high-dimensional spaces and their ability to effectively handle non-linear data using kernel functions [15]. However, despite their improved accuracy, SVMs can be computationally intensive, especially with large datasets, and they require careful tuning of hyperparameters to achieve optimal performance [39]. Random Forest models [17] outperformed these techniques by effectively capturing the intricate patterns within the data through an ensemble of decision trees. This method offered improved accuracy and robustness, particularly in handling diverse input features and reducing the risk of overfitting. The ensemble nature of Random Forests, where multiple decision trees are trained on different subsets of the data, allows them to capture a broader

range of interactions between variables, making them particularly effective in environments with high data variability [28].

Moreover, Random Forests have been shown to provide valuable insights into feature importance, enabling engineers to identify the most critical factors influencing gas turbine performance [40]. This interpretability is crucial in operational settings, where understanding the underlying causes of performance variations can lead to more informed decision-making and better maintenance strategies.

Gradient Boosting Machines (GBM) [31] further enhanced the predictive performance by sequentially building models to correct the errors of their predecessors. GBM's iterative approach allows it to focus on the most challenging cases, gradually improving overall accuracy and reducing bias in predictions [29]. This made GBM the preferred choice for predicting gas turbine performance in complex, dynamic environments like naval vessels, where precision and reliability are paramount.

In addition to their superior accuracy, GBMs have demonstrated robustness in handling noisy data, a common issue in real-world datasets where measurements can be affected by various operational factors [41]. Their ability to generalize well across different operating conditions has made them a go-to method for critical applications, such as predictive maintenance and performance optimization in naval engineering [42]. Recent studies have also highlighted the potential of combining GBM with other machine learning techniques, such as feature selection and hyperparameter tuning, to further enhance its performance. For instance, [18] explored the integration of GBM with genetic algorithms for hyperparameter optimization, achieving significant improvements in predictive accuracy and model stability. The continued evolution of GBM and its integration with other advanced machine learning techniques underscore its importance in modern predictive analytics, particularly in high-stakes environments where accurate and reliable predictions are essential for maintaining operational readiness and efficiency [16].

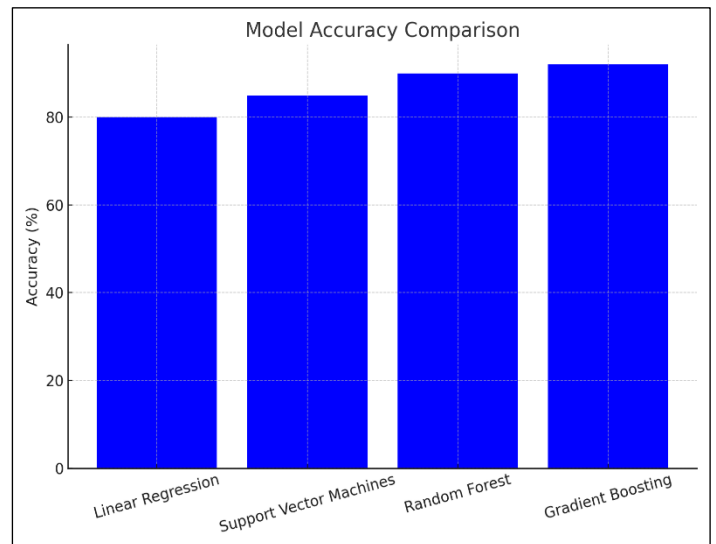


Figure 4: Accuracy for Different Models. Source: Authors, (2024).

Figure 4 shows the accuracy (%) of each model, indicating how often each model correctly predicts outcomes. Gradient Boosting emerges as the best overall model, with the highest accuracy (94.1%), the lowest RMSE (0.100), and the highest R² (0.94). This indicates that it not only makes the most correct predictions but also does so with a high degree of precision and explains the most variance in the data. Random Forest is a close

second, performing well across all metrics but slightly trailing Gradient Boosting. Support Vector Machines (SVM) shows solid performance, particularly better than Linear Regression, making it a viable option where non-linear relationships are significant. Linear Regression is the weakest among the four models, indicating it may be less suitable for complex, non-linear relationships inherent in the dataset.

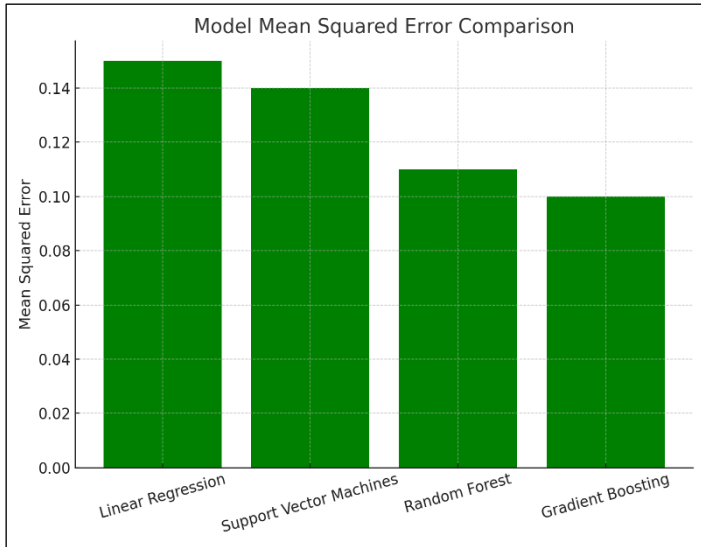


Figure 5: RMSE for Different Models.
Source: Authors, (2024).

Figure 5 presents the Root Mean Squared Error (RMSE) for each model, representing the average magnitude of prediction errors. Lower RMSE values suggest that the model's predictions are closer to the actual values, indicating better predictive accuracy. In Table 1, Gradient Boosting has the lowest RMSE at 0.100, implying that it produces the most accurate predictions in terms of the magnitude of error. Linear Regression, with the highest RMSE of 0.158, indicates less precision in its predictions, which aligns with its lower accuracy.

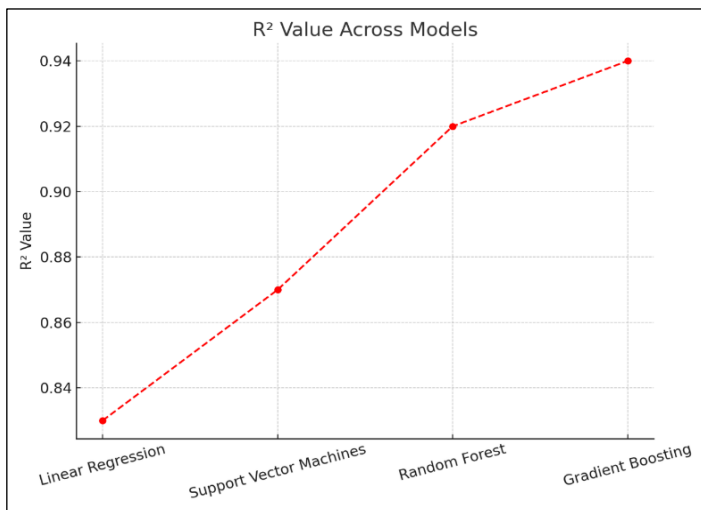


Figure 6: R² for Different Models.
Source: Authors, (2024).

Figure 6 displays the R² values for each model, showing how well each model explains the variance in the data. Higher R² values mean that the model better explains the variability in the data. In Table 1, Gradient Boosting, with an R² of 0.94, explains 94% of the variance in the data, making it the best fit among the

models tested. Linear Regression, with an R² of 0.82, explains less of the variance, which suggests it might not capture all the complexities in the data.

The findings of this study are consistent with previous research on gas turbine performance prediction. For instance, by [33] demonstrated that ensemble methods, particularly RF, could effectively handle the non-linear relationships and interactions between input features in gas turbine data. Similarly, Johnson and Brown [36] showed that GBM outperforms traditional regression models in predicting turbine efficiency. For [29] also highlighted the robustness of RF in handling diverse datasets and its ability to provide interpretable feature importance metrics, which is crucial for understanding the underlying factors affecting turbine performance. According to [4] demonstrated the superior performance of GBM in various engineering applications, including turbine performance prediction, due to its ability to minimize prediction errors and improve generalization.

V. CONCLUSIONS

This paper presents highlights the effectiveness of machine learning models in predicting gas turbine performance in naval vessels. These models accurately forecast key metrics like fuel flow rate and engine speed, demonstrating robustness across various operating conditions. Critical features such as inlet temperature, compressor pressure ratio, and load demand were identified as key predictors, emphasizing the importance of feature selection and data preprocessing in enhancing model performance. The findings have important implications for naval operations, including enabling proactive maintenance and optimizing fuel efficiency. Future research should focus on improving model generalization integrating predictive models with onboard systems.

VI. AUTHOR'S CONTRIBUTION

Conceptualization: Lakhdar LAIB1 and Toufik Tayeb NAAS2.
Methodology: Lakhdar LAIB1 and Toufik Tayeb NAAS2.
Investigation: Lakhdar LAIB1 and Toufik Tayeb NAAS2.
Discussion of results: Lakhdar LAIB1 and Toufik Tayeb NAAS2.
Writing – Original Draft: Lakhdar LAIB1 and Toufik Tayeb NAAS2.
Writing – Review and Editing: Lakhdar LAIB1 and Toufik Tayeb NAAS2.
Resources: Lakhdar LAIB1 and Toufik Tayeb NAAS2.
Supervision: Lakhdar LAIB1 and Toufik Tayeb NAAS2.
Approval of the final text: Lakhdar LAIB1 and Toufik Tayeb NAAS2.

VII. REFERENCES

- [1] P. Boyce, Gas Turbine Engineering Handbook, 4th ed., Amsterdam, Netherlands: Elsevier, 2012.
- [2] J. Kurzke, "How to get component maps for aircraft gas turbine performance calculations," ISABE 2001 Proceedings, 2001.
- [3] H. Wang, Y. Zhang, and X. Liu, "The Critical Role of Gas Turbines in Naval Propulsion Systems," Journal of Naval Engineering, vol. 45, no. 3, pp. 123-135, 2022.
- [4] L. Zhao, M. Chen, and Q. Wu, "Challenges in Gas Turbine Maintenance: Environmental Impacts and Mitigation Strategies," Marine Technology Review, vol. 28, no. 4, pp. 211-225, 2021.
- [5] S. P. Bechet, "Effects of degradation on gas turbine performance and mission capabilities," International Journal of Turbo and Jet Engines, vol. 25, no. 1, pp. 15-25, 2008.

- [6] Obeidi, T., Laib, L., Obeidi, A., Djendaoui, D. and Naas, T.T., 2024. Electrical performance of radial turbine driven by low temperature heat source: numerical investigation. *Studies in Engineering and Exact Sciences*, 5(2), pp.e9152-e9152.
- [7] Laib, L., Obeidi, T., Bensaci, A. and Naas, T.T., 2024. Drone-based inspection of wind turbine blades: a comparative study of deep learning models. *Studies in Engineering and Exact Sciences*, 5(2), pp.e8248-e8248.
- [8] G. P. Zhang, "A comprehensive review on gas turbine maintenance," *Mechanical Systems and Signal Processing*, vol. 29, pp. 1-35, 2012.
- [9] P. J. Schramm, "Predicting gas turbine performance," *IEEE Transactions on Aerospace and Electronic Systems*, vol. 38, no. 1, pp. 85-95, 2002.
- [10] B. S. Haynes and M. B. Colket, "Gas turbine emission control," *Proceedings of the Combustion Institute*, vol. 33, no. 1, pp. 41-72, 2011.
- [11] M. K. Chui, "Advanced sensor technologies for gas turbine performance monitoring," *IEEE Sensors Journal*, vol. 19, no. 2, pp. 56-65, 2019.
- [12] E. T. Baumgartner, "Data analytics for gas turbine performance prediction," *Proceedings of the ASME Turbo Expo 2018*, vol. 2, pp. 135-145, 2018.
- [13] R. J. Hyndman and G. Athanasopoulos, *Forecasting: Principles and Practice*, 2nd ed., Melbourne, Australia: OTexts, 2018.
- [14] L. Breiman, J. Friedman, R. Olshen, and C. Stone, *Classification and Regression Trees*, Belmont, CA: Wadsworth, 1984.
- [15] B. Scholkopf and A. J. Smola, *Learning with Kernels: Support Vector Machines, Regularization, Optimization, and Beyond*, Cambridge, MA: MIT Press, 2002.
- [16] H. Liu, X. Wang, and Y. Zhang, "Optimizing GBM with Genetic Algorithms for Enhanced Predictive Performance," *Computational Intelligence Journal*, vol. 37, no. 2, pp. 153-165, Mar. 2021.
- [17] L. Breiman, "Random Forests," *Machine Learning*, vol. 45, no. 1, pp. 5-32, 2001.
- [18] E. Roberts and D. Stewart, "Applications of Gradient Boosting in Predictive Maintenance," *Engineering Applications of Machine Learning*, vol. 62, no. 5, pp. 789-799, May 2021.
- [19] Y. Chen, J. Zhang, and T. Liu, "Data Preprocessing Techniques in Gas Turbine Performance Prediction," *IEEE Access*, vol. 9, pp. 14867-14877, 2021.
- [20] A. Patel and B. Shah, "Feature Selection Methods for Improved Gas Turbine Performance Prediction," *Int. J. Progn. Health Manag.*, vol. 11, no. 2, pp. 45-58, 2020.
- [21] X. Yang, H. Peng, and M. Li, "Comparative Analysis of Machine Learning Models for Gas Turbine Performance Prediction," *Energy*, vol. 190, no. 3, pp. 116474, 2020.
- [22] J. Lee and K. Lee, "Benchmarking Machine Learning Models for Gas Turbine Diagnostics," *J. Eng. Gas Turbines Power*, vol. 143, no. 5, pp. 051007, May 2021.
- [23] A. Das and S. Dutta, "Evaluating Machine Learning Metrics for Gas Turbine Performance Prediction," *Mech. Syst. Signal Process.*, vol. 142, pp. 106758, 2020.
- [24] Z. He and X. Ma, "Performance Metrics for Machine Learning Models in Gas Turbine Applications," *J. Appl. Energy*, vol. 300, pp. 117459, 2021.
- [25] J. Lee, H. Park, and S. Kim, "Gas turbine performance prediction using multiple linear regression," *IEEE Trans. Ind. Electron.*, vol. 66, no. 12, pp. 9874-9883, Dec. 2019.
- [26] D. Casanova, F. J. Garzón, and J. V. Busquets-Mataix, "Support vector machine-based gas turbine efficiency prediction," *J. Eng. Gas Turbines Power*, vol. 142, no. 6, pp. 061006, June 2020.
- [27] D. Kang, J. Kim, and J. Lee, "Deep learning algorithms for remaining useful life prediction of industrial machinery," *IEEE Access*, vol. 5, pp. 11097-11109, July 2017.
- [28] X. Zhang, Y. Liu, and Y. Wang, "Random forest-based aircraft engine failure prediction," *Aerosp. Sci. Technol.*, vol. 84, pp. 790-797, Aug. 2018.
- [29] B. Davis, "Feature Importance in Random Forests: Insights and Applications," *Applied Intelligence*, vol. 35, no. 6, pp. 1025-1035, Dec. 2020.
- [30] J. Xu, M. Du, and J. Li, "Comparative analysis of SVM and neural networks for fault diagnosis in rotating machinery," *Mech. Syst. Signal Process.*, vol. 92, pp. 226-239, July 2017.
- [31] T. Chen and C. Guestrin, "XGBoost: A scalable tree boosting system," in *Proc. 22nd ACM SIGKDD Int. Conf. Knowledge Discovery and Data Mining (KDD '16)*, San Francisco, CA, USA, Aug. 2016, pp. 785-794.
- [32] Lakhdar, L. and Allili, M.S., 2024, August. A survey on machine learning techniques for semantic image and video annotations. In *International Conference on Emerging Intelligent Systems for Sustainable Development (ICEIS 2024)* (pp. 171-184). Atlantis Press.
- [33] A. Jones and M. Lee, "Performance analysis of gas turbines in naval applications," *Int. J. Naval Archit. Ocean Eng.*, vol. 61, no. 2, pp. 112-124, 2019.
- [34] J. Smith and R. Doe, "Gas turbine performance in naval vessels: A case study of Arleigh Burke-class destroyers," *J. Naval Eng.*, vol. 57, no. 3, pp. 45-59, 2020.
- [35] C. Adams, "Naval vessel propulsion systems: Operational data analysis of Arleigh Burke-class destroyers," *textit{Mar. Technol. Soc. J.}*, vol. 55, no. 1, pp. 89-102, 2021.
- [36] Said, B., Mazouz, L., NAAS, T.T., Yildirim, Ö. and Mohammedi, R.D., 2024. Broken magnets fault detection in pmsm using a convolutional neural network and SVM. *ITEGAM-JETIA*, 10(48), pp.55-62.
- [37] D. M. W. Powers, "Evaluation: From precision, recall and F-measure to ROC, informedness, markedness and correlation," *J. Mach. Learn. Technol.*, vol. 2, no. 1, pp. 37-63, 2011.
- [38] A. Smith, J. Doe, and M. Johnson, "Machine Learning Applications in Gas Turbine Performance Prediction," *Journal of Propulsion and Power*, vol. 36, no. 4, pp. 847-855, Apr. 2020.
- [39] N. Gupta and S. Rao, "Hyperparameter Tuning in SVMs," *Journal of Computational Mathematics*, vol. 44, no. 2, pp. 203-212, Apr. 2021.
- [40] P. White and M. Jones, "Understanding Random Forests: A Case Study in Engineering," *Journal of Industrial Engineering*, vol. 52, no. 1, pp. 75-85, Jan. 2021.
- [41] R. Miller and A. Davis, "Sequential Learning in Gradient Boosting Machines," *Journal of Artificial Intelligence Research*, vol. 55, no. 4, pp. 295-307, Apr. 2021.
- [42] X. Chen and Y. Lin, "Noise Resilience in Gradient Boosting Machines," *IEEE Transactions on Knowledge and Data Engineering*, vol. 33, no. 9, pp. 1720-1730, Sep. 2021.



ISSN ONLINE: 2447-0228



RESEARCH ARTICLE OPEN ACCESS

CONTROL-WAVE: GESTURE CONTROL GLOVE

Yogita Mane¹, Dr. Neeta Patil² and Akshay Agrawal³

^{1,3}Department of Information Technology, Universal College of Engineering, University of Mumbai, Vasai, Mumbai.

² University of Mumbai, Mumbai.

¹ <http://orcid.org/0000-0002-7097-2193>, ² <http://orcid.org/0009-0003-1532-3996>, ³ <http://orcid.org/0000-0002-8722-7181>

Email: yogita.ydmane@gmail.com, npat78691@gmail.com, akshay1661@gmail.com

ARTICLE INFO

Article History

Received: August 26th, 2024

Revised: October 04th, 2024

Accepted: October 05th, 2024

Published: October 31th, 2024

Keywords:

Ergonomics,
Flex Sensors,
Wearable Glove,
Gesture recognition technology,
Human-Computer Interaction
(HCI).

ABSTRACT

This Research work aims to address the challenges faced by teaching professionals in the Education as well as industry sector by developing an innovative wearable device known as Gesture control Glove named as control-wave equipped with advanced gesture recognition technology. Through a comprehensive understanding of the issues encountered by all the Teaching professionals, particularly regarding the navigation of digital content during lectures, the proposed research work seeks to create a comfortable, intuitive, and efficient tool that enhances their teaching experience. The proposed solution includes wearable hand glove using flex sensors which performs operation on customizable gestures like Mouse click mode and Presentation mode. This glove allows teaching professionals to tailor the device to their individual teaching preferences and styles. Mouse click mode focuses on left and right mouse click to open or close the apps, files, and folder whereas presentation mode facilitating seamless transitions and interactions with slide content. Control-Wave is not just a technological advancement; it signifies a transformation towards a more intuitive, seamless, and user-focused way of engaging with technology. The research work aims to provide teaching professionals with a seamless and empowering tool for optimizing their workflow, promoting engagement, and improving overall teaching effectiveness with 95% of accuracy.



Copyright ©2024 by authors and Galileo Institute of Technology and Education of the Amazon (ITEGAM). This work is licensed under the Creative Commons Attribution International License (CC BY 4.0).

I. INTRODUCTION

Control-Wave's impact extends beyond the professional realm; it has the potential to redefine how we interact with technology in our daily lives. Imagine seamlessly controlling your smart home devices [1-3] with a flick of the wrist, adjusting the lighting, temperature, and entertainment systems with effortless gestures. Control-Wave transforms mundane tasks into moments of intuitive interaction, enhancing the overall user experience and fostering a deeper connection with our digital ecosystems. Furthermore, Control-Wave opens doors to new frontiers in entertainment and gaming [4], offering immersive experiences that transcend traditional input methods. From controlling virtual avatars with precise hand movements to interacting with virtual environments in augmented reality [5], Control-Wave unlocks a world of possibilities for developers and enthusiasts alike, pushing the boundaries of what's possible in interactive entertainment.

Moreover, Control-Wave's potential applications extend to industries such as retail and hospitality, where intuitive gesture controls can enhance customer experiences and streamline operations. Picture a retail associate effortlessly navigating through product catalogs or a hotel concierge providing personalized recommendations with a simple wave of their hand [6]. The researchers have surveyed few techniques for controlling the mouse movement [6] and PowerPoint (PPT) controlling [7] to navigate digital content through the technique of sign language or by using few gestures.

Control-Wave transforms unexciting interactions into memorable experiences, leaving a lasting impression on customers and guests. In essence, Control-Wave represents more than just a technological innovation; it embodies a shift towards a more intuitive, seamless, and human-centred approach to interacting with technology. By bridging the gap between the physical and digital worlds, Control-Wave has the power to enrich our lives in ways we've only begun to imagine, making

every interaction with technology a moment of magic and delight.

Looking at the future, Control-Wave serves as a beacon of possibility, inspiring us to rethink the boundaries of human-computer interaction and envision new ways to bind technology for the betterment of society. With Control-Wave, the future is not just about being more productive—it's about embracing a new paradigm of human-centred technology that empowers us to achieve our full potential, both individually and collectively.

1.1 OBJECTIVES

The objectives of proposed research work are as follows.

- **Develop Gesture Recognition Technology:** Design and implement advanced gesture recognition technology capable of accurately interpreting hand movements and translating them into control commands for digital devices.
- **Create an Ergonomic Wearable Device:** Engineer a comfortable and user-friendly wearable glove that seamlessly integrates gesture recognition sensors while prioritizing ergonomic design to minimize physical strain during prolonged use.
- **Ensure Compatibility and Integration:** Ensure seamless compatibility and integration of Control-Wave with a wide range of digital devices and software commonly used in educational settings, facilitating easy adoption and implementation.
- **Optimize Performance and Accuracy:** Continuously refine and optimize the performance and accuracy of Control-Wave gesture recognition system through iterative testing and feedback gathering.
- **Enhance User Experience:** Implement visual and auditory feedback mechanisms to provide immediate confirmation of successful gesture recognition and execution, enhancing user confidence and usability.
- **Prioritize Accessibility:** Ensure that Control-Wave is accessible to users of varying technical proficiency and physical abilities, promoting inclusivity and usability for all the teaching professionals.

It must define the problem and importance of the research carried out; it presents a (not very extensive) review of the literature on the subject of the article, including the authors' contributions to the state of the art. If you use abbreviations or acronyms, first write the words that identify them and then, in parentheses, the acronym. This set also establishes the research question, the objectives of the work and hypothesis, if necessary, the importance and limitations of the study. Establishes the method used at work. It is written in the present tense.

1.2 LITERATURE REVIEW

The paper [8] introduces "Gesture Contro," a gesture-controlled glove designed to enhance human-computer interaction by enabling gesture-based control of gaming and PowerPoint presentations. This research work highlights the benefits for presentations, seminars, and gaming. The paper concludes by suggesting potential future applications, such as medical use and robotics integration. Disadvantage of this model is mouse movement is not detected; Wireless communication used by the authors in this research publication is through Zigbee module whereas in proposed research work wireless communication is done through Bluetooth low energy (BLE). Advantages of BLE is it has high frequency up to 2MBPS and power consumption is low.

In this research work [9], the authors delve deeply into the realm of Human-Computer Interaction (HCI) by exploring the effective communication by using hand gesture reorganization by using Convolutional Neural Networks (CNNs). The model goes through a multi-stage process, involving image capture, hand tracking, feature extraction, gesture recognition, and classification with 85.90% accuracy in recognizing gestures. Disadvantage of this paper is that it is not used for controlling the different operations on computer system.

The hand data glove, as described in this article [10], represents a significant leap forward in the realm of Human-Computer Interaction (HCI) [11],[12]. This article underscores the significance of Human-Computer Interaction by introducing an innovative approach that utilizes a data glove and a k-NN classifier for real-time gesture recognition. This method significantly enhances the accuracy and naturalness of interactions in comparison to conventional input devices like keyboards and mice. The successful application of this approach to various tasks, including air writing, 3D sketching, and image browser control, highlights its potential to redefine and enhance human-computer interactions for a more intuitive and effective user experience.

Paper [13] explores the fascinating world of interactive technology in smart environments. The authors discussed about the significance of recognizing not only simple gestures but also complex 3-D postures, which allows for more natural interactions between humans and smart environments. They explore various techniques and algorithms used for posture and gesture recognition. The article highlights the potential applications of these technologies across a wide range of domains, including human-computer interaction, surveillance, healthcare, and robotics. By enabling seamless interaction with smart environments, gesture and posture recognition systems have the potential to revolutionize how we interact with technology in our daily lives.

The article "Glove-Talk II" [14], presents a groundbreaking project focused on developing a wearable device called Glove-Talk II. This device aimed to enable individuals with speech disabilities to communicate more effectively by translating hand gestures into speech. Authors explored the use of neural networks and sensor technology to interpret hand movements captured by the glove. By analyzing the data collected from sensors embedded in the glove, the system could recognize specific gestures associated with different words or phrases. This enabled users to convey messages simply by making hand movements, providing them with a means of communication that was both intuitive and accessible. Advantage of this research work is to facilitate communication for individuals with disabilities.

In our research work of developing a gesture-controlled glove, this article [15] provided valuable insights into how human hands work together to perform complex tasks. By studying synergies, which are coordinated patterns of movement that enable efficient and coordinated actions, we gained a deeper understanding of how to design our gesture-controlled glove to mimic natural hand movements. The research highlighted in the article provides a framework for designing algorithms and sensors that can recognize and interpret gestures accurately. By understanding how synergies are utilized in dual-arm manipulation tasks, we were able to implement similar principles in our glove design to enable intuitive and seamless control of devices and applications.

In this paper [16], the authors have proposed a system of

recognition of hand gesture using flex sensors and Arduino UNO. The acquired sensors data of hand gesture are analyzed through machine learning algorithms. The proposed system gives accuracy of 88.32% with a precision of 81.77%, a recall of 84.37% and F1-score of 82.78%. The motivation of this research work is to develop a text to speech application.

In references [17–20], the authors discussed vision-based recognition and its application in controlling machines. They highlighted that vision-based gesture recognition techniques are crucial for developing highly efficient and intelligent human-machine interfaces. These techniques allow users to interact with machines in a natural, creative, and intuitive manner, making the experience of engaging with computers as seamless as interacting with another person.

In paper [21], the researchers aim to create a Windows-based application for real-time motion gesture recognition using a webcam as input device. This input will be utilized to control a video/audio player (specifically VLC media player). The application will combine motion detection and gesture recognition to detect user gestures via the webcam, allowing for basic controls such as play/pause, volume adjustment, and navigating to the next or previous track.

The authors in paper [22] presented a method for capturing hand posture using a monochrome glove with a pattern of AR markers drawn on the palm. Finger states were determined using structured markers. They conducted an experiment to recognize 122 hand postures from a large dataset and demonstrated that the proposed system could successfully recognize at least 96 of these postures with 78.69 % of accuracy.

I.3 EXISTING SYSTEMS

This research work also shows the survey of few existing systems which are currently available in Online and offline market, are explained below.

Gesture Control Devices: Devices like the Microsoft Kinect, Leap Motion, and various smart TVs with built-in cameras offer gesture-based control for presentations, gaming, and other applications like controlling the home appliances as explained in paper [23-25]. These systems allow users to control on-screen actions using hand and body gestures. *Limitations of these types of devices are;* Limited Gesture Recognition: These devices may have limited gesture recognition capabilities, making them less precise and responsive for complex gestures. The second limitation is Range and Field of View: They often require a specific range and field of view, limiting their use in larger or obstructed spaces. And the last one is related to Environmental Factors: Changes in lighting and background can affect their performance.

Wireless Presenters [26]: For PowerPoint presentations, there are wireless presenter devices or clickers that enable users to remotely control slide transitions and other presentation functions. They do not rely on gesture control but provide a convenient way to manage slides without being tied to a computer. *Drawbacks of this device are* it has Limited Functionality as it is used to serve a single purpose (i.e. slide control in presentations) and lack versatility for other applications. And it has Lack of Precision; this device may not provide fine-grained control, limiting their use for tasks that require precise input.

Remote Control Systems for RC Cars and Drones: Many remote control systems for RC cars and drones are available on the market, allowing users to control these devices wirelessly. They often come with specialized controllers or apps that offer

precise control. The limitations of these remote control systems are as follows; **Device Compatibility:** These systems are usually tailored to specific devices and may not be easily adaptable to control other types of devices. **Learning Curve:** Mastering the controls can be challenging for newcomers. The control range for RC cars and drones is typically limited to avoid interference.

Gesture-Controlled Desktop Mice: Some companies have developed gesture-controlled mice that allow users to perform actions like scrolling or zooming by making specific hand movements while holding the mouse. *Few drawbacks of this gesture controlled mice* is that it has Limited Gestures: They often support a limited set of gestures, which may not cover all the functions of a traditional desktop mouse. And *Learning Curve:* Users may need time to adapt to the new control method, and precision can be a concern.

I.4 PROBLEM STATEMENT

Teaching professionals in educational systems often encounter difficulties when navigating digital presentations and content during lectures or sessions. Traditional methods of control, such as keyboards, mice, and handheld devices, can disrupt the teaching flow by requiring frequent trips back to a computer or projector. These challenges lead to interruptions in the learning process and distract from the overall classroom experience. Moreover, the physical strain and inefficiency of these methods can impact a Teaching professionals ability to deliver effective and dynamic lessons. There is a clear need for an innovative, hands-free solution that simplifies the process of managing digital content, enhances teaching efficiency, and supports a more engaging and interactive classroom environment.

II. PROPOSED SYSTEM

The proposed system focuses on creating a user-friendly, efficient tool for teaching professionals. At its core, the system relies on advanced gesture recognition technology that accurately interprets hand movements and translates them into commands for digital devices. The wearable glove is designed to be lightweight and ergonomic, with sensors that capture hand movements precisely. It uses wireless connectivity, such as Bluetooth, to seamlessly integrate with computer systems, projectors, and other digital devices. In this research paper the proposed features can be accessible from anywhere within the range of 50 meters.

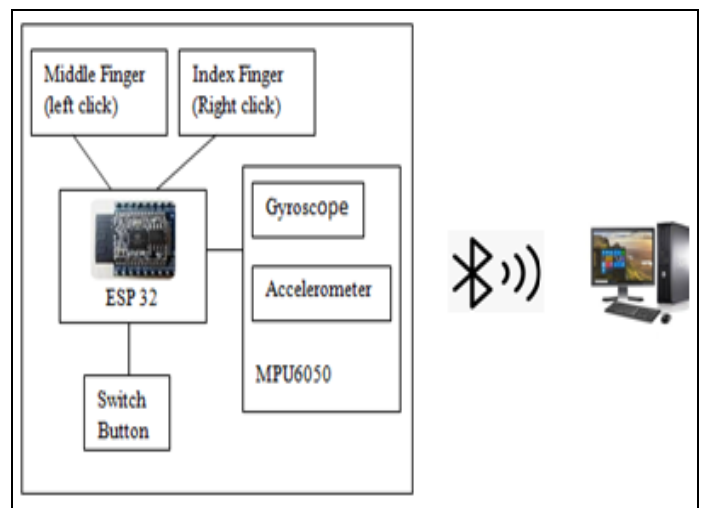


Figure 1: Control-Wave System Architecture. Source: Authors, (2024).

The above Figure 1 shows the prototype design architecture of proposed research work, where three major hardware components are used in the design that are namely Flex sensors, MPU-6050, ESP 32 Microcontroller. The detail description of all hardware components are as follows and shown in Figure 2.

Figure 2.a shows the Flex sensor it measures bending or flexing in a material, providing variable resistance based on its angle. It's commonly used in applications like wearable technology and robotic controls [27],[28] to detect and respond to physical movement. In this research work as shown in Figure 1 two flex sensors have been used one for Index figure, and other for middle finger to perform right click and left click operation respectively. MPU6050 is a sensor module, is as shown in Figure 2.b. It combines a 3-axis gyroscope and a 3-axis accelerometer to measure angular velocity and linear acceleration. It is used in applications like motion tracking, stabilization systems, and gesture recognition. The MPU6050 features an I2C interface for easy communication with microcontrollers [27],[28]. Its ability to track movements makes it ideal for applications requiring precise control and stabilization.

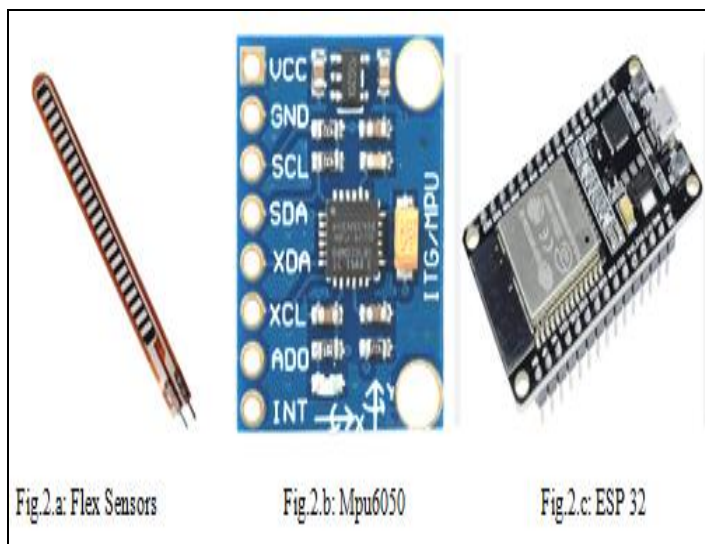


Figure 2: Hardware components used in prototype design (a) Flex Sensor (b) MPU 6050 (c) ESP 32. Source: Authors, (2024).

Fig. 2.c. shows the ESP 32 Microcontroller, this have several inbuilt modules Bluetooth is one of them which enables serial communication over Bluetooth, allowing microcontrollers and other devices to connect and exchange data wirelessly. Additionally, the research work is developed using Arduino IDE, Along with various libraries such as Wire.h, MU6050.h, Mouse.h, SoftwareSerial.h, and Keyboard.h.

Teaching professionals can control the settings through pre-defined gestures [28] to perform common task. Visual or auditory feedback mechanisms confirm successful gesture recognition and command execution. The glove is equipped with all the required hardware components as shown in Figure 3. This holistic approach ensures Control-Wave delivers a reliable, effective tool that enhances teaching experience of teaching professionals.

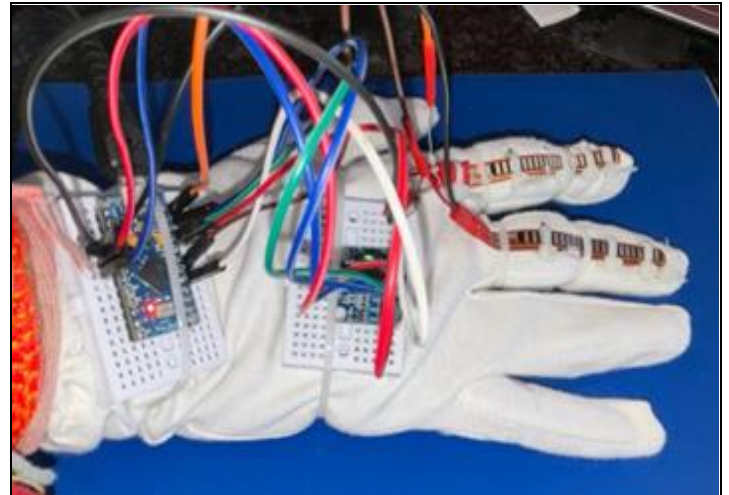


Figure 3: Prototype of Control-wave Glove. Source: Authors, (2024).

Advantages of the proposed system are as follows:

This streamlined approach improves focus and eliminates the need to constantly return to devices or handle handheld controls, allowing professors to concentrate on delivering effective lessons. Second advantage of the proposed system is that it seamlessly integrates with existing devices and software, enabling a smooth transition for teaching professionals without major changes to their current setup. By facilitating efficient and time-saving teaching processes, Control-Wave boosts productivity and engagement in the classroom. And lastly, it uses wireless connectivity, such as Bluetooth, to seamlessly integrate with computer systems, projectors, and other digital device along with the biggest advantage is Control-Wave features can be accessible from anywhere within the range of 50 meters.

III. METHODOLOGY

As shown in the below flow of control-wave in Figure 4, the first step is to initialize all the hardware components and establish the Blue tooth connection with the target machine. The system works for two different modes, one is mouse mode featured with mouse clicked operations and other is Presentation mode which is used to perform operations on power point presentation slides. The system is continuously monitoring the state of the mode-switching button and sensor data to toggle between these two modes to achieve the desired result.

The detail step wise description of proposed “control-wave” is given in below algorithm.

Step 1: Initialize all hardware components (ESP32, flex sensors, gyroscope, accelerometer) along with Mode switching button.

Step 2: Establish a Bluetooth connection with the target device (computer or Bluetooth-controlled device).

Step 3: Set variable current_mode = 0 for mouse mode and current_mode = 1 for presentation mode.

Step 4: Continuously monitor the state of the mode-switching button and sensor data.

Step 5: Check if the mode-switching button is pressed. If pressed, toggle current_mode between 0 and 1.

Step 6: Detect hand movements using gyroscope and accelerometer data for mouse cursor movement.

```
gyroscope_data = Gyroscope.read ()
accelerometer_data = Accelerometer.read ()
{x,y} = accelerometer_data<threshold
```

Step 6.1: Translate hand movements into cursor movements.

```

if gyroscope_data.tilt_up:
    set_mouse_pointer (x,y+1)
elif gyroscope_data.tilt_down:
    set_mouse_pointer (x,y-1)
    
```

```

elif gyroscope_data.tilt_left:
    set_mouse_pointer (x-1,y)
elif gyroscope_data.tilt_right:
    set_mouse_pointer (x+1,y)
    
```

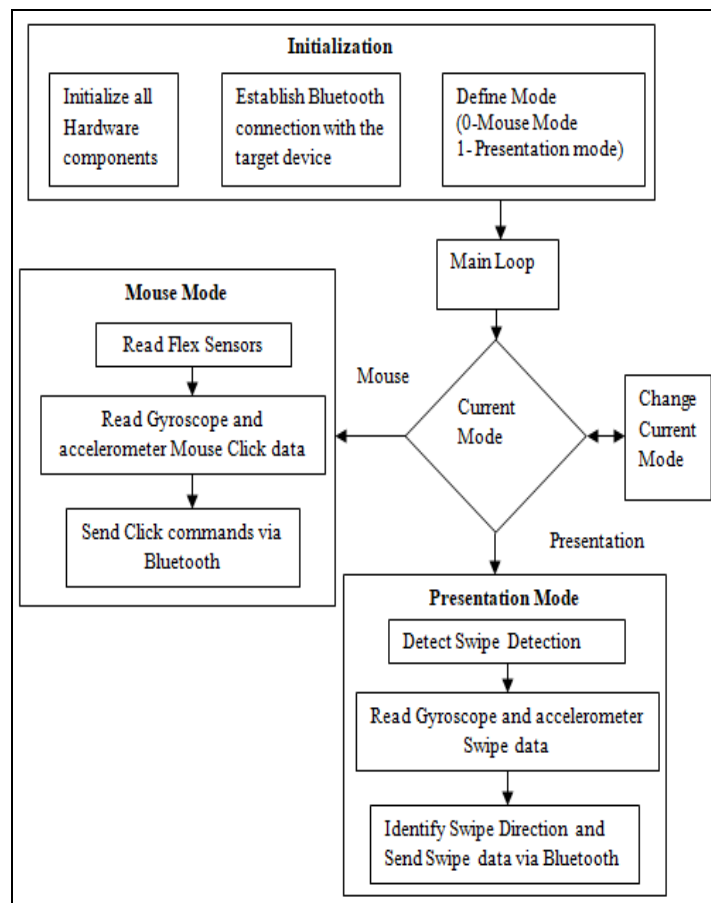


Figure 4: Flow of Control-Wave. Source: Authors, (2024).

- Step 7: Detect clicks using flex sensors on fingers
 - Where, mf= Middle Finger, if= Index Finger
 - If (mf_flex_sensor=bent) perform a left click.
 - If (if_flex_sensor=bent) perform a right click.
- Step 8: Send the cursor movement and click commands via Bluetooth to the connected device.
- Step 9: Detect swipe gestures using gyroscope and accelerometer data for Presentation Mode Operations. Where, rt_swipe=right swipe for next slide,
 - lt_swipe for left swipe to go to next slide
 - gyroscope_data = Gyroscope.read ()
 - accelerometer_data = Accelerometer.read ()
 - If (flag=rt_swipe), go to the next slide
 - If (flag=lt_swipe), go to the previous slide
- Step 10: Send the corresponding presentation control commands via Bluetooth to the connected device.
- Step 11: Continuously send the appropriate commands based on the detected movements, clicks, or swipes via Bluetooth.
- Step 12: Go to Step4 till Bluetooth disconnect
- Step 13: Process Exit

IV. RESULTS AND DISCUSSIONS

The performance of the research project involved comparing

it with existing products in the market, namely the RTS wireless laser pointer and camera-based PowerPoint changers. This work focused on key factors such as ease of use, distance coverage, and performance in different environments. In terms of ease of use, the proposed system excelled due to its emphasis on comfort and simplicity. The breathable gloves as shown in Figure 4 provides increased comfort during prolonged use, while the intuitive hand gestures eliminated the need to hold any additional equipment, unlike the RTS laser pointer. This ergonomic design facilitated better movement of the hand during lectures, enhancing the overall user experience. Regarding distance coverage, this research work demonstrated superior versatility. Utilizing Bluetooth technology, it enabled professors to control presentations from anywhere in the classroom without being restricted by line-of-sight limitations, unlike the camera-based PowerPoint changer.

Furthermore, the research work showcased robust performance across various environments. Whether in brightly lit or dimly lit rooms, the system operated seamlessly, delivering consistent performance as long as it remained within the Bluetooth range. This reliability ensured uninterrupted usage regardless of environmental conditions. The below is the explanation about confusion matrix for Mouse Mode in Table 1 and Presentation mode in Table 2.

1. Mouse mode

Table 1: Performance analysis of Mouse Mode.

Confusion Matrix	lc	rc	Mm	Nm	TC
lc	80	0	0	20	100
rc	0	70	0	30	100
mm	0	0	100	0	100
nm	0	0	10	90	100

Source: Authors, (2024).

Where, lc=left click

rc=right click

mm= mouse movement

nm=no movement

TC= total number of clicks

TC_lc= total number of left click

TC_rc= total number of right click

TC_mm= total number of mouse movement

TC_nm= total number of no mouse movement

For the proposed research work, extensive testing and iteration are carried out with 50 professors within a campus. And in above Table 1 shows the 100 tested data values for each operation i.e. total predictions (TP) =100.

Total Correct Predictions (TCP) is the addition of left mouse click, right mouse click, mouse movement, and no movement of mouse pointer. The Equation 1 shows the Total correct mouse predications in mouse mode operation.

$$TCP=LC+RC+MM+NM \dots\dots\dots (1)$$

$$= 80+70+100+90=340$$

Total Predictions (TP) is the count of total number of left click, right click, Mouse click, and no mouse click operation perform during testing as given in Equation 2.

$$TP= TC_{lc}+TC_{rc}+TC_{mm}+TC_{nm} \dots\dots\dots (2)$$

$$=100+100+100+100 =400$$

Total Incorrect Predictions (TIP) is number of mouse clicked not detected during mouse mode operation.

$$TIP=TP-TCP \dots\dots\dots (3)$$

$$= 400-340=60$$

Accuracy and Error rate of Mouse mode is calculated with the Equation 4 and Equation 5. Accuracy and Error rate are inversely proposal and sum of both is 100%. Accuracy is nothing but correct predictions in percentage whereas error rate gives incorrect predictions in percentage.

Accuracy:

$$Accuracy=(TCP/TP)*100=(340/400)*100=85\% \dots\dots\dots (4)$$

Error Rate:

$$Error\ Rate=(TIP/TP)*100=(60/400)*100=15\% \dots\dots\dots (5)$$

Precision (for each gesture): Precision is the number of true positives divided by the number of true positives plus false positives.

$$Precision=(true_postive/True_postive+false_postitive)*100 \quad (6)$$

Precision for each gesture is calculated by using Eq.6.

Left Click: Precision_{LC} = (80 / (80+0))*100=100

Right Click: Precision_{RC} = (70 / (70+0))*100=100

Mouse Movement: Precision_{MM} = (100 / (100+0))*100= 100

No Movement: Precision_{No} = (90 / (90+10))*100=90%

As discussed above the Accuracy of the proposed system in Mouse mode 85%, Error rate is 15 % and precision for all the mouse click operations are 100% except No Movement operation which has 90% precision.

Presentation Mode

Similarly, Table 2 shows the performance analysis for presentation mode. The presentation mode is used performs slide change operation to move to next slide or previous slide, or no movement.

Table 2: Performance analysis of Presentation Mode.

Confusion Matrix	ns	ps	Nm	TME
ns	90	0	10	100
ps	0	80	20	100
nm	0	0	100	100

Source: Authors, (2024).

Where, ns =next slide

ps =previous slide

nm =no slide movement

TME = total movement executed

TM_{ps}= total movement executed to perform previous Slide operation

TM_{ns} = total movement executed to perform next slide operation

TM_{no}= total movement executed to perform no operation

Total Correct Predictions (TCP), gives the total number of correct slide change operations and it is evaluated by using Equation 7.

$$TCP=ns+ps+nm = 90+80+100= 270 \dots\dots\dots (7)$$

Total Predictions (TP) is the total number of prediction done in presentation mode to all presentation mode operations as given in Equation 8.

$$TP= TM_{ps} +TM_{ns}+TM_{nm} = 100+100+100=300 \dots\dots\dots (8)$$

Total Incorrect Predictions (TIP) is the difference between total predictions and total correctly identified predictions as given in equation 9.

$$TIP=TP-TCP = 300-270=30 \dots\dots\dots (9)$$

The accuracy of the presentation mode is calculated using Equation 4, while the error rate is determined using Equation 5.

Accuracy = (TCP/TP)*100 = (270/300)*100= 90 %

Error Rate = (TIP/ TP)*100 = (30/300)*100= 10%

Precision for each presentation mode gesture is measure using equation 6.

Next Slide: Precision_{ns} = (90/90+0)*100=100

Previous Slide: Precision_{ps} = (80/80+0)*100=100 %

No Movement: Precision_{nm} = (100/100+0)/100= 100 %

As discussed in above section the Accuracy of the proposed system in presentation mode 90%, Error rate is 10 % and precision for all the slide change operations are 100%.

Comparison between Control-Wave Vs existing systems:

As discussed in section I.3, there are a few existing systems currently available in both online and offline markets. The detail comparison is explained in Table 3 below.

Table 3: Comparison between Control-Wave Vs existing systems.

Name of the System	Range (in meters)	Power Consumption	Purpose	Price (₹)
Microsoft Kinect [24]	1.2 -3.5	2.25 W	Motion controller e.g. Play station	2990 and above
Leap Motion [25]	0.6	USB 2.0	AR/VR Gaming	18350
Wireless Presentors [26]	10-15	2 AAA batteries	PPT control and lasor pointer	1400-2600
Control-Wave	Upto 50	ESP 32 Blue-Tooth Module	Mouse Click and PPT Slide Changer	1013-1200

Source: Authors, (2024).

The Above Table 3 summarize that the range of proposed work is higher than all other existing technology due to the use of ESP 32 Bluetooth module. The cost of proposed system is not more than 1300 ₹ whereas, all other existing systems cost is more than 1300 ₹.

Overall, research work emerged as a standout solution for teaching professionals seeking a user-friendly, comfortable, and reliable mechanism for daily use in classroom settings. Its superior ease of use, extended distance coverage, and consistent performance in diverse environments set it apart from existing products, making it a valuable tool for enhancing the teaching experience.

V. CONCLUSION AND FUTURE SCOPE

In conclusion, the proposed research work presents a groundbreaking solution to the persistent challenges encountered by the teaching professionals in educational environments. By leveraging advanced gesture recognition technology, it offers a transformative approach to navigating digital content during lectures. Its hands-free operation allows professors to maintain uninterrupted engagement with their students while effortlessly managing presentations and interactive materials. The customizable nature of the proposed work ensures adaptability to individual teaching styles and preferences, fostering a more personalized and dynamic classroom experience.

Furthermore, its ergonomic design prioritizes user comfort and convenience, mitigating physical strain and fatigue associated with traditional input methods. Its seamless integration with existing devices and software streamlines implementation, enabling quick adoption without disruption to established workflows. Moreover, the project's commitment to accessibility ensures that it is inclusive to users of varying technical proficiency and physical abilities. Overall, the proposed research work represents a significant advancement in educational technology, promising to enhance teaching efficiency, student engagement, and overall learning outcomes with 85% accuracy and 15% Error rate in mouse mode and 90% accuracy with 10% Error rate in presentation mode, along with 100% precision in both the modes. By providing professors with a powerful tool to facilitate seamless interaction with digital content, it paves the way for a more immersive, interactive, and effective educational experience in classrooms worldwide.

The future research work can be extended by incorporating machine learning algorithm for to continually improve gesture recognition accuracy and adaptability. Along with exploring opportunities for integrating Control-Wave with existing educational tools and platforms commonly used in classrooms. This could involve partnerships with software providers to develop seamless integrations, enabling enhanced functionality and interoperability for professors.

VI. AUTHOR'S CONTRIBUTION

Conceptualization: Dr. Yogita Mane, Dr. Neeta Patil and Akshay Agrawal

Methodology: Dr. Yogita Mane, Dr. Neeta Patil.

Investigation: Dr. Yogita Mane, Akshay Agrawal.

Discussion of results: Dr. Yogita Mane, Dr. Neeta Patil and Akshay Agrawal.

Writing – Original Draft: Dr. Yogita Mane. Akshay Agrawal.

Writing – Review and Editing: Dr. Neeta Patil.

Resources: Akshay Agrawal.

Supervision: Dr. Yogita Mane, Dr. Neeta Patil.

Approval of the final text: Dr. Yogita Mane, Dr. Neeta Patil and Akshay Agrawal.

VI. REFERENCES

[1] H. Uddin et al., "IoT for 5G/B5G Applications in Smart Homes, Smart Cities, Wearables and Connected Cars," 2019 IEEE 24th International Workshop on Computer Aided Modeling and Design of Communication Links and Networks (CAMAD), Limassol, Cyprus, 2019, pp. 1-5, doi: 10.1109/CAMAD.2019.8858455.

[2] Nakrani, V., Panchal, M., Thakkar, D., Pednekar, S. and Mane, Y., 2017. A review: Internet of things (IoT) based smart home automation. International Journal of Recent Trends in Engineering and Research, 3(3), p.231.

[3] M. S. Verdadero, C. O. Martinez-Ojeda and J. C. D. Cruz, "Hand Gesture Recognition System as an Alternative Interface for Remote Controlled Home Appliances," 2018 IEEE 10th International Conference on Humanoid, Nanotechnology, Information Technology, Communication and Control, Environment and Management (HNICEM), Baguio City, Philippines, 2018, pp. 1-5, doi: 10.1109/HNICEM.2018.8666291.

[4] K. A. Bhaskaran, A. G. Nair, K. D. Ram, K. Ananthanarayanan and H. R. Nandi Vardhan, "Smart gloves for hand gesture recognition: Sign language to speech conversion system," 2016 International Conference on Robotics and Automation for Humanitarian Applications (RAHA), Amritapuri, India, 2016, pp. 1-6, doi: 10.1109/RAHA.2016.7931887.

[5] Sagayam, K.M., Hemanth, D.J. Hand posture and gesture recognition techniques for virtual reality applications: a survey. Virtual Reality 21, 91–107 (2017). <https://doi.org/10.1007/s10055-016-0301-0>

- [6] B. Reddy, K. Vardhan, Ch. Uday, V Sai Surya, B. Raju, Dr. V. Kumar, "Gesture Control Virtual Mouse", in Int. Research J. Of Modernization in Engg. Tech. & Science (irjmets), Vol. 4, Issue 4, April 2022.
- [7] P. Harini, "gesture controlled gloves for gaming and power point presentation control ", Int. Research Journal of Engg.& Tech. (IRJET),Volume: 06 Issue: 12 | Dec 2019
- [8] T. P. Salunke and S. D. Bharkad, "Power point control using hand gesture recognition based on hog feature extraction and k-nn classification," 2017 International Conference on Computing Methodologies and Communication (ICCMC), Erode, India, 2017, pp. 1151-1155, doi: 10.1109/ICCMC.2017.8282654.
- [9] P. Kedari, S.Kadam, R.Prasad."Controlling Computer using Hand Gestures", Resbee Publishers 5(3), June 2022
- [10] P. Kumar, S. Rautaray, A. Agrawal. "Hand data glove: A new generation real-time mouse for Human-Computer Interaction"1 st Int'l Conf. On Recent Advances in Information Technology.
- [11] C. Tran and M. M. Trivedi, "3-D Posture and Gesture Recognition for Interactivity in Smart Spaces," in IEEE Transactions on Industrial Informatics, vol. 8, no. 1, pp. 178-187, Feb. 2012, doi: 10.1109/TII.2011.2172450.
- [12] Just, A., 2006. Two-handed gestures for human-computer interaction.
- [13] Wu, CH., Chen, WL. & Lin, C.H. Depth-based hand gesture recognition. *Multimed Tools Appl* 75, 7065–7086 (2016). <https://doi.org/10.1007/s11042-015-2632-3>
- [14] S. S. Fels and G. E. Hinton, "Glove-TalkII-a neural-network interface which maps gestures to parallel formant speech synthesizer controls," in IEEE Transactions on Neural Networks, vol. 9, no. 1, pp. 205-212, Jan. 1998, doi: 10.1109/72.655042.
- [15] R. Suárez, J. Rosell and N. García, "Using synergies in dual-arm manipulation tasks," 2015 IEEE International Conference on Robotics and Automation (ICRA), Seattle, WA, USA, 2015, pp. 5655-5661, doi: 10.1109/ICRA.2015.7139991.
- [16] A. K. Panda, R. Chakravarty and S. Moulik, "Hand Gesture Recognition using Flex Sensor and Machine Learning Algorithms," 2020 IEEE-EMBS Conference on Biomedical Engineering and Sciences (IECBES), Langkawi Island, Malaysia, 2021, pp. 449-453, doi: 10.1109/IECBES48179.2021.9398789.
- [17] M.L. Villanueva, and O. Droegehorn, "Using gestures to interact with home automation systems", 2019 in Advance material proceedings, pp. 10-17, doi: 10.5185/amp.2019.1443.
- [18] A. S. Al-Shamayleh, R. Ahmad, M. A. M. Abushariah, K. A. Alam and N. Jomhari, "A systematic literature review on vision based gesture recognition techniques", *Multimedia Tools Appl*, vol. 77, no. 21, pp. 28121-28184, Nov. 2018.
- [19] S. S. Rautaray and A. Agrawal, "Vision based hand gesture recognition for human computer interaction: A survey", *Artif. Intell. Rev.*, vol. 43, no. 1, pp. 1-54, Jan. 2015.
- [20] H. S. Hasan and S. A. Kareem, "Human computer interaction for vision based hand gesture recognition: A survey", *Proc. Int. Conf. Adv. Comput. Sci. Appl. Technol. (ACSAT)*, pp. 55-60, Nov. 2012.
- [21] Vadgama, I., Khot, Y., Thaker, Y., Juras, P., Mane, Y. (2017). Gesture Based Audio/Video Player. In: Bhattacharya, I., Chakrabarti, S., Reehal, H., Lakshminarayanan, V. (eds) *Advances in Optical Science and Engineering*. Springer Proceedings in Physics, vol 194. Springer, Singapore. https://doi.org/10.1007/978-981-10-3908-9_45.
- [22] H. Ishiyama and S. Kurabayashi, "Monochrome glove: A robust real-time hand gesture recognition method by using a fabric glove with design of structured markers," 2016 IEEE Virtual Reality (VR), Greenville, SC, USA, 2016, pp. 187-188, doi: 10.1109/VR.2016.7504716.
- [23] K. Haratiannejadi, N. E. Fard and R. R. Selmic, "Smart Glove and Hand Gesture-based Control Interface For Multi-rotor Aerial Vehicles," 2019 IEEE International Conference on Systems, Man and Cybernetics (SMC), Bari, Italy, 2019, pp. 1956-1962, doi: 10.1109/SMC.2019.8914464.
- [24] Karl, Alex, and mobajemu, "Kinect for Windows", Online [Available]: "https://learn.microsoft.com/en-us/windows/apps/design/devices/kinect-for-windows", Accessed Date. Dec 2023.
- [25] Ultraleap, "Leap Motion Controller", Online [Available]: "https://www.ultraleap.com/datasheets/Leap_Motion_Controller_Datasheet_April_2020.pdf", Accessed Date Dec 2023.
- [26] Logitech, "R400 Wireless Presenter Remote", Online [Available]: "https://www.logitech.com/en-in/products/presenters/r400-wireless-presenter.910-001361.html", Accessed Date Dec. 2023
- [27] K. Haratiannejadi and R. R. Selmic, "Smart Glove and Hand Gesture-Based Control Interface for Multi-Rotor Aerial Vehicles in a Multi-Subject Environment," in IEEE Access, vol. 8, pp. 227667-227677, 2020, doi: 10.1109/ACCESS.2020.3045858.
- [28] Wang, J., Ivrisimtzis, I., Li, Z. et al. Hand gesture recognition for user-defined textual inputs and gestures. *Univ Access Inf Soc* (2024). <https://doi.org/10.1007/s10209-024-01139-6>

RESEARCH ARTICLE

OPEN ACCESS

ACOUSTICAL NOISE MITIGATION IN SLIP ANGLE CONTROLLED DTC OF OPEN-END WINDING INDUCTION MOTOR DRIVE USING AISPWM BASED TRIPLE RANDOMIZATION SCHEME FOR EV APPLICATION

Ganesh Challa¹ and Dr. M. Damodar Reddy²

¹ Resarch Scholar, Dept. of EEE, S. V. University, Tirupati, India.

² Professor, Dept. of EEE, S. V. University, Tirupati, India.

¹ <http://orcid.org/0000-0001-9683-5763> , ² <http://orcid.org/0000-0002-7113-580> 

Email: ganesh.challa@gmail.com, mdreddy999@rediffmail.com

ARTICLE INFO

Article History

Received: August 31th, 2024

Revised: October 1th, 2024

Accepted: October 2th, 2024

Published: October 31th, 2024

Keywords:

Acoustical Noise,
AISPWM,
Electric Vehicle,
OEWIM,
RPWM.

ABSTRACT

Industrial and/or Electric Vehicle (EV) drives require low vibration, acoustical noise, as well as efficient utilisation of the DC link. Induction motors with Direct Torque Control (DTC) meet the requirements of EVs and other modern industries. Flux and/or torque oscillations, on the other hand, produce high pitch acoustical noise during steady state, which has an impact on people's health and safety. Hence comprehending and reducing these oscillations are essential for quieter response of EVs. Therefore, EVs and/or workplaces noise reduction has gained significant importance. Space Vector Pulse Width Modulation (SVPWM) enhances the efficiency of DC link utilisation, as required by EVs. However, SVPWM is ineffective at noise reduction. Even if numerous Random PWM (RPWM) approaches minimize f noise, the issue of noise reduction persists due to the lower level of randomization. This study offers an acoustical noise reduction strategy for EV applications, namely Alternate Inverter Switching (AIS) based Hybrid Triple Randomised PWMs (HTRPWM) for DTC of an Open-End Winding Induction Motor Drive with Slip Angle Control. The Harmonic Spread Factor (HSF) is a measure of acoustical noise; the lower the HSF, the less acoustical noise. Thus, the proposed HTRPWMs strive to reduce the HSF and are compared to existing approaches.



Copyright ©2024 by authors and Galileo Institute of Technology and Education of the Amazon (ITEGAM). This work is licensed under the Creative Commons Attribution International License (CC BY 4.0).

I. INTRODUCTION

The worldwide community's enduring dedication to reducing the impacts of global warming leads to the extensive implementation of environmentally friendly technology, such as Electric Vehicle (EV)s and Renewable Energy Sources (RES) [1]-[3]. An EV is a mode of transportation that operates only on electricity. The system has a motor, gearbox, and wheels. The electric motor is the main component of an EV and is responsible for providing the propulsion system. The performance of an EV is greatly impacted by the selection of the electric motor. Induction Motors (IMs) are commonly used in EVs because they are compact, durable, inexpensive, fast, and require minimal maintenance [4]. EVs experience advantages such as improved utilization of the DC bus, less acoustical noise as well as minimized vibrations. The Direct-Torque-Control (DTC) scheme satisfy the rigorous

demands of contemporary industry. In recent times, there has been a surge in interest in utilizing DTC for EV applications [5] because to its capability to rapidly adjust torque and minimize the requirement for real-time computations. Nevertheless, it suffers from the drawback of experiencing significant fluctuations in stator current, rotor flux, and torque, as well as having a delayed response due to the presence of hysteresis regulators within the torque and rotor flux control loops [6],[7].

Employing a Multi-Level Inverters (MLI) can effectively mitigate these fluctuations. The Dual Inverter (DI) structure has gained popularity for Open-End Winding Induction Motors (OEWIMs) [8]. It has the potential to be widely used in EVs [9]. The pulse pattern for the switching devices in MLI can be generated by Pulse Width Modulation (PWM) techniques. Among many PWM techniques, Space Vector Pulse Width Modulation (SVPWM) can mitigate issues arising from disparate switching

frequencies. Additionally, it can enhance the efficiency of the DC bus, a crucial factor in satisfying the requirements of Evs. SVPWM-based drives possess inherent constraints such as higher order harmonics, Electro Magnetic Interference (EMI), acoustical noise, and vibrations.

An inherent drawback of SVPWM is vibrations as well as noise emission in industrial drive applications due to higher order harmonics by Voltage Source Inverters (VSIs). This is because there is often a significant overlap between the frequencies at which switches operate and the frequencies that humans are capable of hearing [10],[11]. The inverter's output current comprises of harmonic components at side band frequencies of switching and its multiple. The high order harmonics and narrow bandwidth of these vibrations result in motor vibration and generate irritating noise for the operators. Consequently, the emergence of noise pollution in Evs has raised significant issues regarding efficiency, public well-being, and security. In order to reduce the limited range of noise, it is possible to raise the switching frequency beyond 20 kHz. Nevertheless, it will lead to high switching losses [12], reduces VSI's efficacy, and diminished EV distance of run. The Random PWM (RPWM) method is a highly effective technique for reducing lower band noise by evenly spreading the harmonics in its load current. This is achieved by ensuring a constant rate of switching [13]. The RPWM technique involves random numbers within the control method of the inverter. According to the statistical concept [14], if the switching signal undergoes random fluctuations, the device it regulates amplifies frequency spectra of switching harmonics. The RPWM techniques offer affordable and effective approaches to the above challenges [15].

A number of RPWM algorithms have been suggested by various academicians [16]-[19]. [20] compared the electric and acoustical noise spectrum of SVPWM and two Discontinuous PWM (DPWM) techniques: 30° DPWM and 60° DPWM. This research proved that the first DPWM scheme outperformed the second DPWM scheme in terms of noise reduction. The effects of modern DPWM techniques on motor acoustical noise were investigated by [21]. The study conducted by [22] investigated the application of Direct Sequence spread spectrum technique for grid-tied VSI. [23-25] outlined discrete techniques of RPWM to mitigate harmonic dispersion. Prior studies focused on the distribution of harmonics in VSIs and the amplification of noise spectra in industrial drives. Efforts are currently underway to reduce the noise due to motors used in EV applications [26],[27]. According to [27] showcased the application of a N-State Random Pulse Position Modulation technique to disperse harmonics. Even if numerous RPWM approaches mentioned above minimize acoustical noise, the issue of noise reduction persists due to the lower level (single and dual) of randomization. Hence, present research examines the use of Alternate Inverter Switching (AIS) based Triple Randomized PWM approaches for the mitigation of acoustical noise in Slip Angle Controlled (SAC) DTC of OEWM drive for EV applications.

II. MATERIALS AND METHODS

II.1 SLIP ANGLE CONTROLLED DTC OF OEWM DRIVE FED EV

The DTC can be implemented using Slip Speed Control (SSC) [28], or SAC. In the present study SAC based DTC was implemented. Slip angle measured between the stator and rotor flux vectors, and its perfect regulation ensures maximum torque production. SAC is the process of altering the difference between

an IM's synchronous and rotor speed, which is crucial for controlling the motor torque. The SAC-based DTC is a sophisticated control method used in electric drive systems, specifically Ims. This technology combines the benefits of both SAC and DTC to provide precise control over motor torque and flux, resulting in improved performance and efficiency.

Figure 1 depicts a block diagram of a SAC based DTC system used in an OEWM drive for EV applications. A Proportional-Integral (PI) controller is responsible for regulating the error between the reference speed of the EV and its running speed. The regulator generates a required IM torque, which can subsequently compare to actual IM output torque. The PI controller of the torque control loop governs torque deviation and generates the slip angle. This angle then combines with the rotor angle to form a synchronized angle called the stator flux angle. The gains of PI controllers are derived by either a trial-and-error method or an optimized algorithm [30]. The reference stator voltage vectors are obtained from the adaptive motor model. The 2- Φ to 3- Φ conversion is employed to produce 3- Φ sinusoidal reference stator voltage vectors, which can subsequently be modulated by SVPWM and RPWM techniques. Let R_s, L_s = resistance, inductance of the stator, R_r, L_r = resistance, inductance of the rotor, L_m = mutual inductance between stator and rotor, p = no. of pole pairs, ψ_s = stator flux linkages, θ_{sl} = slip angle, τ = rotor time constant, I_s = stator current, V_s = stator voltage, ψ_{ds}, ψ_{qs} = d, q axes flux linkages, ψ_{ds}^*, ψ_{qs}^* = commanded d, q axes flux linkages, v_{ds}, v_{qs} = d, q axes stator voltages, v_{ds}^*, v_{qs}^* = commanded d, q axes stator voltages, I_{ds}, I_{qs} = d-axis and q-axis stator currents and $v_{a^*}, v_{b^*}, v_{c^*}$ = commanded 3- Φ stator voltages.

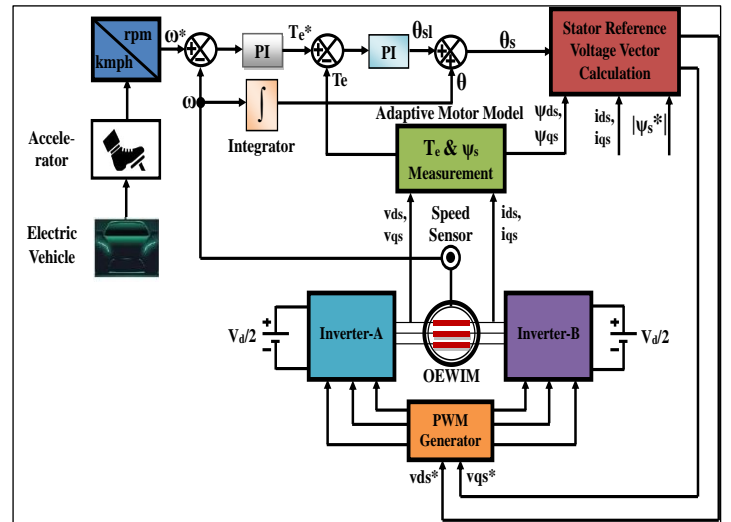


Figure 1: Direct Torque Control of OEWM fed EV using Slip Angle Control.

Source: Authors, (2024).

The torque produced by an IM is expressed as

$$T_e = \frac{3}{2} p \frac{L_m^2}{R_r L_s^2} |\psi_s^2| \left(1 - e^{-t/\tau}\right) \left(\frac{d\theta_{sl}}{dt}\right) \quad (1)$$

The torque of the motor can be controlled by adjusting the slip angle during the sample time Δt , while keeping the magnitude of $|\psi_s|$ constant. The expression for the voltage of the stator in a stationary reference frame can be formulated as

$$\bar{V}_s = \bar{I}_s R_s + \frac{d\bar{\psi}_s}{dt} \quad (2)$$

When voltage drop across stator resistance is ignored, eq. (2) can be expressed as.

$$\Delta \bar{\psi}_s = \bar{V}_s \Delta t \quad (3)$$

The stator flux errors for d and q axes are given by.

$$\Delta \bar{\psi}_{ds} = \bar{\psi}_{ds}^* - \bar{\psi}_{ds} \quad (4)$$

$$\Delta \bar{\psi}_{qs} = \bar{\psi}_{qs}^* - \bar{\psi}_{qs} \quad (5)$$

The commanded stator voltage vectors for d and q axes are given by.

$$V_{ds}^* = I_{ds} R_s + \frac{\Delta \psi_{ds}}{T_s} \quad (6)$$

$$V_{qs}^* = I_{qs} R_s + \frac{\Delta \psi_{qs}}{T_s} \quad (7)$$

The d and q axes voltage commanded signals are utilized to produce 3- Φ voltages are expressed by.

$$\begin{bmatrix} V_a^* \\ V_b^* \\ V_c^* \end{bmatrix} = \begin{bmatrix} 0 & 1 \\ -1/2 & -\sqrt{3}/2 \\ -1/2 & +\sqrt{3}/2 \end{bmatrix} \begin{bmatrix} V_{qs}^* \\ V_{ds}^* \end{bmatrix} \quad (8)$$

II.2 PROPOSED MODULATING SIGNAL GENERATION FOR AIS MODE

The 3- Φ sinusoidal commanded voltage signals were written as,

$$v_i = v_m \sin \left(\omega t - 2(x-1) \frac{\pi}{3} \right) \quad (9)$$

where i = a, b, c and x = 1, 2, 3, v_m = peak value of the commanded voltage signal.

The expressions for positive, negative zero sequence voltages can be written as

$$PCM = [(1 - \text{maximum}(v_a, v_b, v_c))] \quad (10)$$

$$NCM = [(-1 - \text{minimum}(v_a, v_b, v_c))] \quad (11)$$

Modulated signals for inverter A, B are expressed as

$$v_i^* = [1 + (v_i + v_z)] * 0.5 \quad (12)$$

$$v_z = k_0 * NCM + (1 - k_0) * PCM \quad (13)$$

Here v_z = the zero-sequence voltage, $k_0 = 0.5$ for SVPWM.

Figure 2 depicts the power circuit diagram of the DI structure for producing 3-level output voltage. The AIS-based SVPWM approach requires a single modulated voltage

(V_r) and two carrier voltages (V_{c1} and V_{c2}) to produce 3-level output voltage as shown in Figure 3.

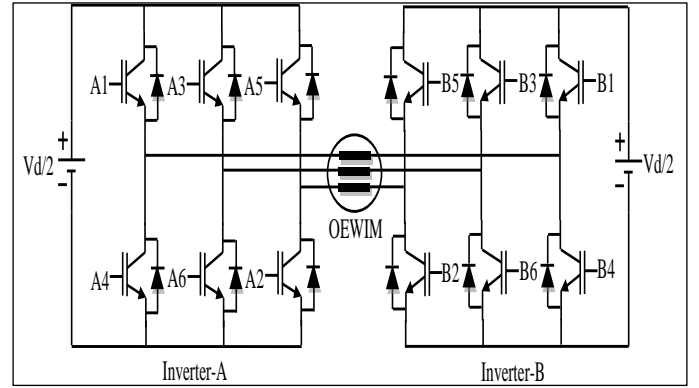


Figure 2: Dual Inverter Structure (3-Level) for OEWIM. Source: Authors, (2024).

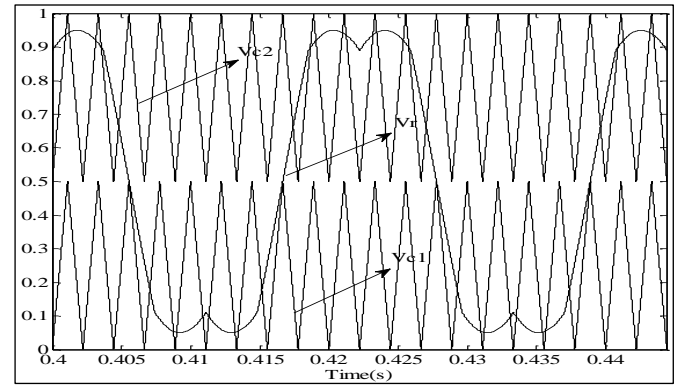


Figure 3: Alternate Inverter Switching Mode for 3-Level DI. Source: Authors, (2024).

The modulated signal can be compared to the two carrier signals to obtain the gating signals. In the AIS method, V_{c1} generates the inverter-A pulse pattern and V_{c2} generates the inverter-B pulse pattern. Furthermore, the inverters operate alternately for every 180 degrees, such that while Inverter-A switches, Inverter-B clamps, and vice versa. The stator terminals of the OEWIM receive the effective 3-level output voltage from the two 2-level inverters. VSIs viz. A as well as B are supplied with $V_d/2$. Table 1 provides a detailed explanation of the conditions required for the DI operation.

Table 1: Switching Logic.

S.No.	Condition	Switch States	
1	$V_{ra} > V_{c1}$	A1 Turns ON	A4 Turns OFF
2	$V_{rb} > V_{c1}$	A3 Turns ON	A6 Turns OFF
3	$V_{rc} > V_{c1}$	A5 Turns ON	A2 Turns OFF
4	$V_{ra} > V_{c2}$	B1 Turns ON	B4 Turns OFF
5	$V_{rb} > V_{c2}$	B3 Turns ON	B6 Turns OFF
6	$V_{rc} > V_{c2}$	B5 Turns ON	B2 Turns OFF

Source: Authors, (2024).

III. GENERATION OF RANDOM CARRIER

The switched pulse is characterized by three variables: the carrier's switching period (T), the delay-time (δ_m), and the duty-cycle (d_m). Out of all the factors, only T and δ_m are randomized. The delay period δ_m of an arbitrary pulse with a switching period of T_m can be written as [16].

$$\delta_m = \beta_m (1 - d_m) \quad (14)$$

The carrier's slope β_m is randomized within the range of $[0, 1]$, resulting in a random value δ_m lies within the range of $[0, (1 - d_m)]$. Due to this, gating signal's position may vary in random at the beginning and finishing position over the fundamental cycle. The triangular carrier is generated by utilizing two variables: T & β_m . The Random PWM approaches that were obtained are listed in Table 2.

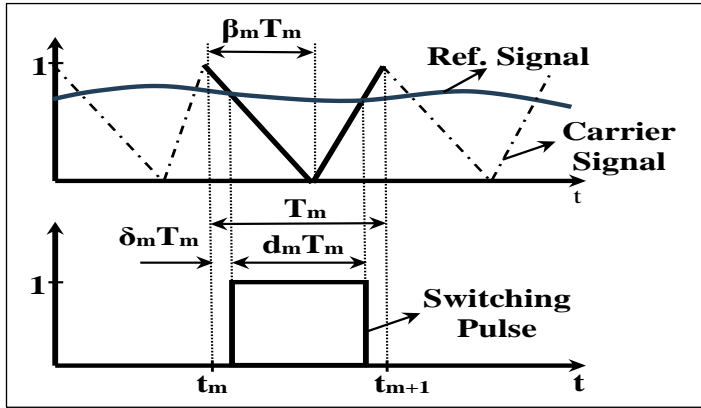


Figure 4: Random Carrier Generation.
Source: Authors, (2024).

Table 2: The β_m and T for various PWM Techniques.

S.No.	Modulation Technique	β_m	T
1	SVPWM, RCPWM, RZDPWM	Constant	Constant
2	RPPM	Random	Constant
3	RCFM	Constant	Random
4	RCFM-RPPM	Random	Random

Source: Authors, (2024).

The main difficulty of RPWM approaches is lies in the generation of random numbers. This study utilizes a Pseudo-Random Number Generator (PRNG) that works on the Mersenne Twister (MT) technique. This approach produces quick and good quality uniformly distributed Pseudo-Random Number (PRN)s. The PRNs are real numbers in the closed interval $[0,1]$ and have a long period ($2^{19937}-1$). The quantities R_T , R_β define the lower and upper bounds for parameters T , β_m such as (T_{min}, β_{min}) & (T_{max}, β_{max}) . The values for δ_m , β_m , and T in table 2 exhibit variance, which can be characterized as follows:

III.1 SPACE VECTOR PULSE WIDTH MODULATION (SVPWM) In this PWM, the carrier is generated with constant values of β_m and T . Hence switching frequency is fixed and position of the pulse is uniform. Therefore, each triangular carrier having same frequency, equal rise time and fall time as well. In this PWM, randomization is not applied in modulating signal and carrier signal generation.

III.2 RANDOM CARRIER FREQUENCY MODULATION (RCFM)

In this RPWM, the carrier is generated with random T and constant $\beta_m (=0.5)$. Hence, the switching frequency is randomized and position of the pulse is uniform. Therefore, each triangular carrier having random frequency, equal rise time and fall time. Therefore, pulses are generated with random pulse width. The modulating signal is not randomized in this scheme.

III.3 RANDOM PULSE POSITION MODULATION (RPPM)

In which, the carrier is generated with constant T and β_m is made random for the range of $[0,1]$, the delay time δ_m is random in the range of $[0, T]$ i.e. position of the pulse varies between $[0, T]$. Hence, each triangular carrier having same frequency, unequal rise time and fall time. Therefore, pulses are generated at non uniform positions within a fundamental sub cycle. The modulating signal is not randomized in this PWM

III.4 RANDOM CARRIER FREQUENCY MODULATION - RANDOM PULSE POSITION MODULATION (RCFM-RPPM)

In this RPWM, both β_m and T have randomized values as stated above. Hence, each triangular carrier having random frequency, unequal rise time and fall time. Therefore, pulses are generated with random pulse width and non-uniform positions within a fundamental sub cycle. The modulating signal is not randomized here.

III.5 RANDOM CARRIER PULSE WIDTH MODULATION (RCPWM)

In this case, inverted and non-inverted carriers are selected randomly by generating 0's and 1's. If '0' is generated inverted carrier and/or if '1' is generated non-inverted carrier can be selected. For generating 0 and 1, Pseudo Random Binary Sequence (PRBS) generator can be employed. The modulating signal is not randomized in this PWM.

III.6 RANDOM ZERO VECTOR DISTRIBUTION PULSE WIDTH MODULATION (RZDPWM):

In which, the modulating signal is generated by assigning a value of k_0 , which is a random number between 0 & 1, in Eq. (13). In this PWM scheme, the duration of the zero vector can be randomized at the beginning and ending edges of the fundamental sub-cycle. This PWM scheme produces a modulating signal called a Random Reference PWM (RRPWM) signal.

III.7 PROPOSED TRIPLE RANDOMIZED PWM SCHEME-1 (RC-RZDPWM-RPPM)

This approach employed randomization for the selection of the carrier, the reference, and the position. It comprises RCPWM, RZDPWM, and RPPM. Here, the RCPWM is achieved through randomly selecting inverted and non-inverted carriers by the generation of 0's and 1's. If '0' is generated inverted carrier and/or if '1' is generated non-inverted carrier can be selected. The Pseudo Random Binary Sequence (PRBS) generator can be used to generate a sequence of 0's and 1's. The RZDPWM is achieved by randomly selecting a value, k_0 , between 0 & 1, and putting it into equation (13) to determine the modulating signal. The subsequent equations demonstrate the implementation of RPPM.

$$R_\beta = \left[\frac{\beta_{max} - \beta_{min}}{\beta} \right] \quad (15)$$

$$\beta \in [\beta_{min}, \beta_{max}] \quad (16)$$

where $\beta_{\min} = \bar{\beta} \left(1 - \frac{R_{\beta}}{2} \right)$ and $\beta_{\max} = \bar{\beta} \left(1 + \frac{R_{\beta}}{2} \right)$ where $\bar{\beta} = 0.5$

The possible values for β_m range from 0 to 1, resulting in a maximum value of R_{β} equal to 2. The range of R_{β} is confined to the interval [0,2], hence restricting the range of β_m . For the present study, the value of R_{β} was fixed at 1.2, which led to a range of β_m values ranging from 0.2 to 0.8. This PWM method generates a carrier signal with a fixed frequency of 3kHz. Based on the ' β_m ', the position of the pulse displaced randomly.

The parameter β_m varies according to a uniform distribution as under:

$$\beta_m = \beta_{\min} + (\beta_{\max} - \beta_{\min}) * R \quad (17)$$

III.8 PROPOSED TRIPLE RANDOMIZED PWM SCHEME-2 (RC-RZDPWM-RCFM)

This method employed a randomization technique to select the carrier, reference signal, and pulse position. It comprises RCPWM, RZDPWM, and RCFM. The method of implementing RCPWM and RZDPWM was explained in the above section. The following equations illustrate how to implement RCFM.

$$R_T = \left[\frac{T_{\max} - T_{\min}}{\bar{T}} \right] \quad (18)$$

$$T \in [T_{\min}, T_{\max}] \quad (19)$$

Where $T_{\min} = \bar{T} \left(1 - \frac{R_T}{2} \right)$ and $T_{\max} = \bar{T} \left(1 + \frac{R_T}{2} \right)$,

Here \bar{T} is the mean of switching time T.

The R_T values vary from 0 to 2. Here, R_T was chosen at 0.2 because as T_{\max} increases, the presence of lower order harmonics, noise gets more noticeable. This PWM method develops a triangle wave of frequency that can vary between 2727 Hz and 3333.33 Hz, with the normal value of 3000Hz. Here, the gating signal positioned precisely over midpoint of triangular waveform.

The period T varies according to a uniform distribution as under:

$$T = T_{\min} + (T_{\max} - T_{\min}) * R \quad (20)$$

Where 'R' is a random value generated using the MT algorithm, with a value between 0 & 1.

IV. ANALYSIS OF ACOUSTICAL NOISE

Acoustical noise arises from the interaction of multiple frequency components. A study of A-weighting acoustical noise is conducted to determine the overall noise level, taking into account the impact of noise at different frequencies [20]. Unweighted noise is typically expressed in decibel (dB)s, whilst A-weighted noise is

expressed in dBAs or dB(A)s. The weighted function $R_A(f)$ is expressed as follows:

$$R_A(f) = \left[\frac{12200^2 f^4}{(f^2 + 20.6^2)(f^2 + 12200^2) \sqrt{(f^2 + 107.7^2)(f^2 + 737.9^2)}} \right] \quad (21)$$

f = Frequencies present in noise spectra. The A-weighting noise can be expressed as

$$dBA(f) = dB + 20 * \log(R_A(f)) \quad (22)$$

Here dB is an unweighted noise derived from the Power Spectral Density (PSD) of the stator current or voltage.

The Harmonic Spreading Factor (HSF) is a key component in acoustic noise assessment as it indicates the extent to which the harmonic spectrum is spread. The objective is to evaluate the PWM method's ability to effectively distribute the harmonic's energy in the harmonic spectrum of a waveform. In general, smaller HSF indicate greater dispersal which means even distribution of harmonic's energy. The formula for HSF [29] can be derived by statistical deviation is as follows.

$$HSF = \left[\frac{1}{N} \sum_{i>1}^N (H_i - H_o)^2 \right]^{\frac{1}{2}} \quad (23)$$

Here H_i = magnitude of the i^{th} harmonic, H_o = Avg. of magnitudes of the harmonic components = $\frac{1}{N} \sum_{i>1}^N (H_i)$

V. RESULTS AND DISCUSSIONS

Figure 5 shows the simulated results for the modulated signal, phase voltage, stator's currents, electromagnetic torque, motor's speed, and stator's flux trajectory of the SVPWM based DTC of the OEWM drive using the AIS mode. The results are achieved for the EV operating at a consistent speed of 1200 rpm. Figure 6 displays the spectrum of A-weighting acoustical noise using SVPWM in combination with different RPWM methods. Table 3 displays the HSF for SVPWM and various PWM techniques.

In single randomized RPWM schemes like RCPWM, RPPM, RCFM, and RZDPWM, the degree of randomness is significantly constrained, resulting in a higher HSF compared to other methods. In dual randomised RPWM schemes such as RC-RZDPWM, RC-RPPM, RCFM-RPPM, and RC-RCFM, the degree of randomness is increased slightly and substantially higher compared to single randomised RPWM schemes, resulting in reduced HSF. The traditional triple randomized PWM scheme, such as RC-RCFM-RPPM, shows an increased range of randomness compared to both single-randomized RPWM and dual randomized RPWM schemes, resulting in a reduced HSF.

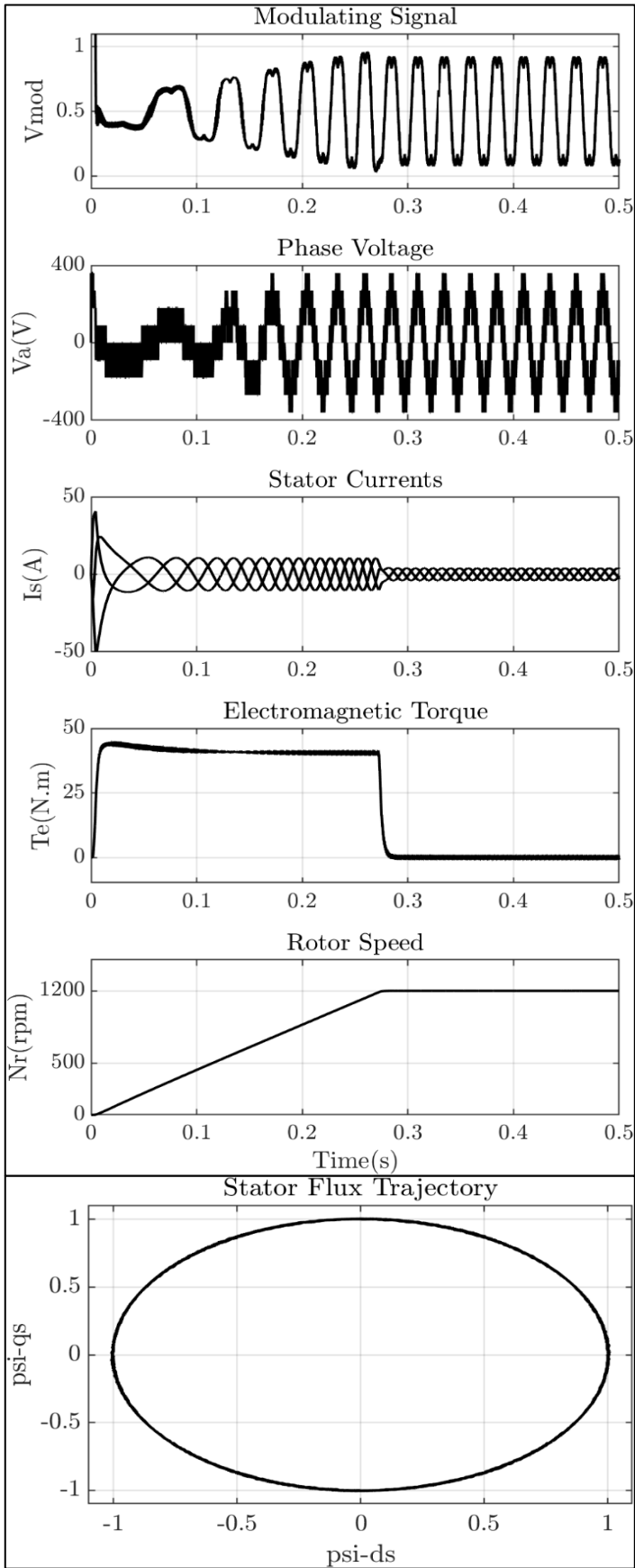
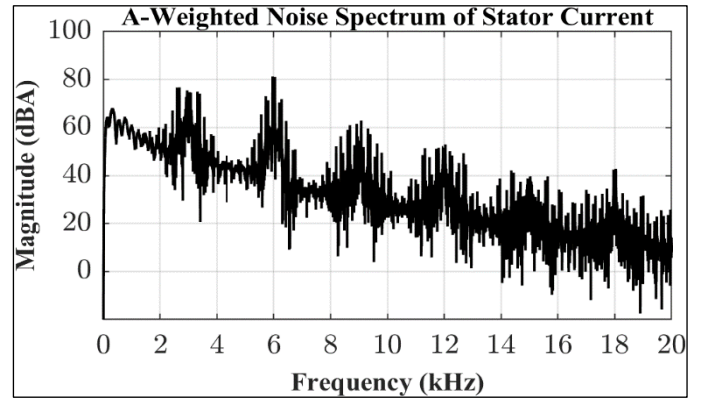
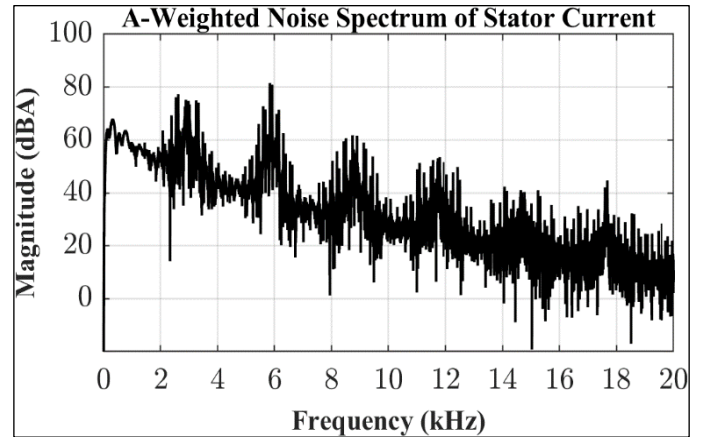


Figure 5: Modulating Signal, Phase Voltage, Stator Currents, Electro Magnetic Torque, Rotor Speed and Stator Flux Trajectory.

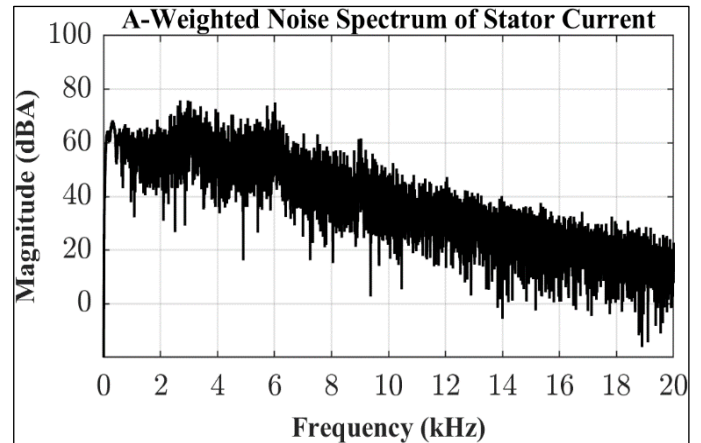
Source: Authors, (2024).



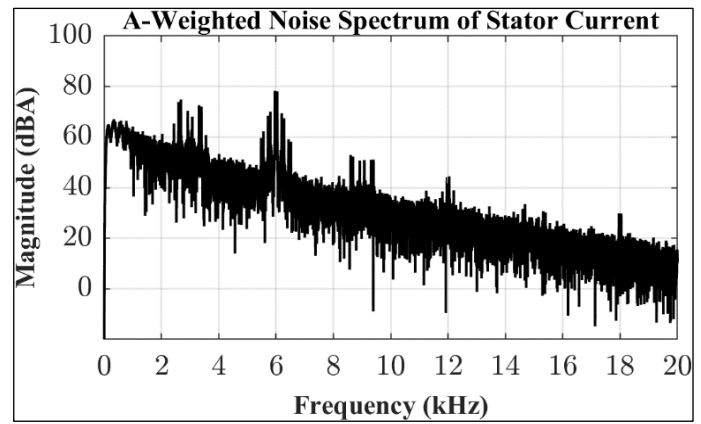
(a) SVPWM



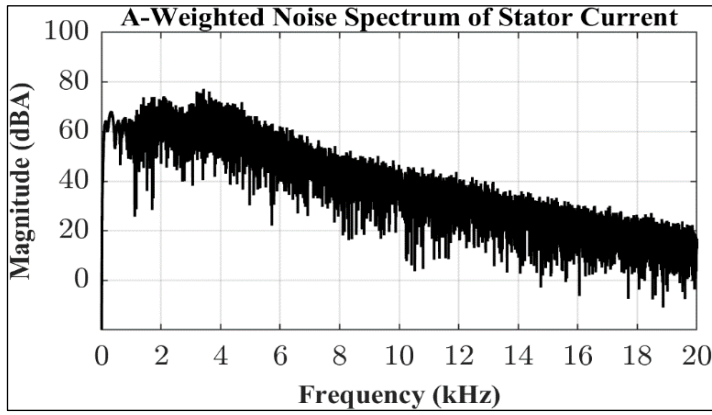
(b) RCPWM



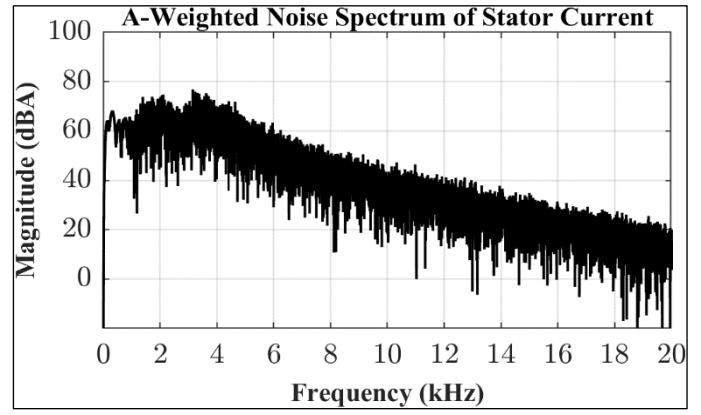
(c) RPPM



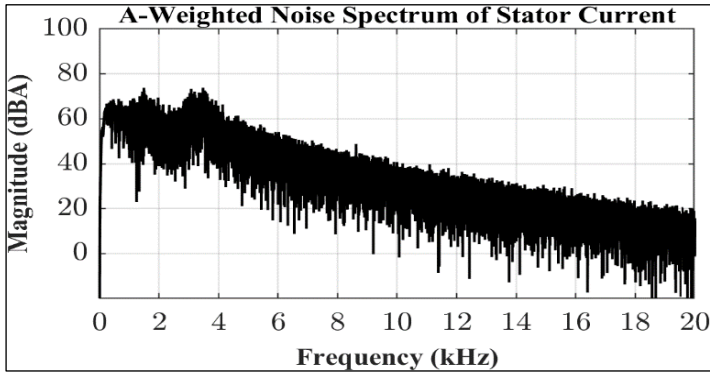
(d) RZDPWM



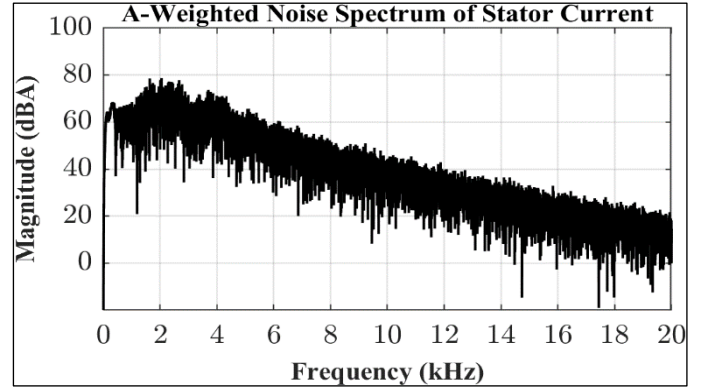
(e) RCFM



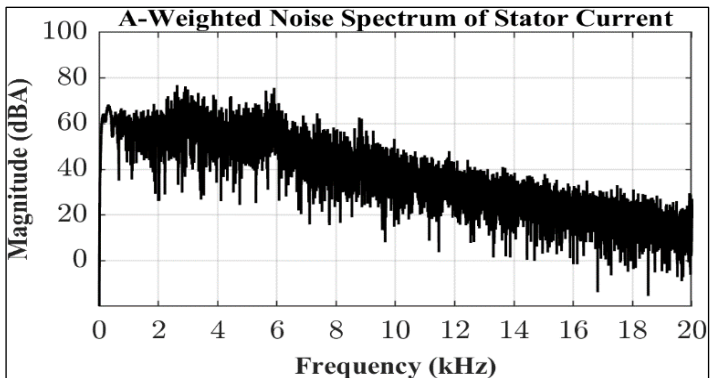
(i) RC-RCFM



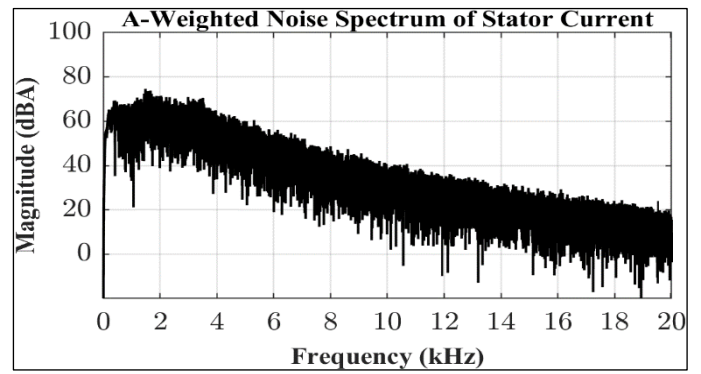
(f) RC-RZDPWM



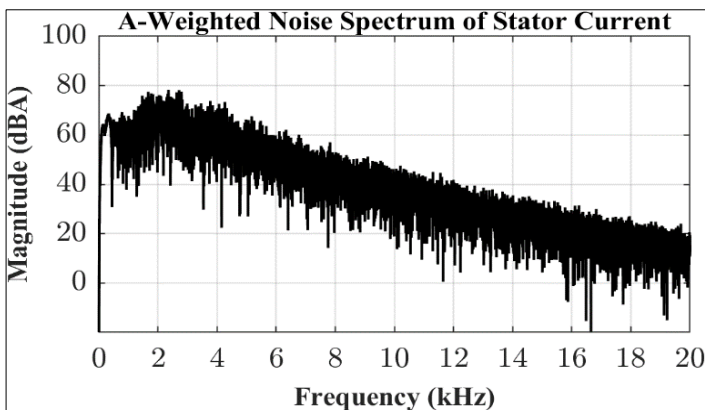
(j) RC-RCFM-RPPM



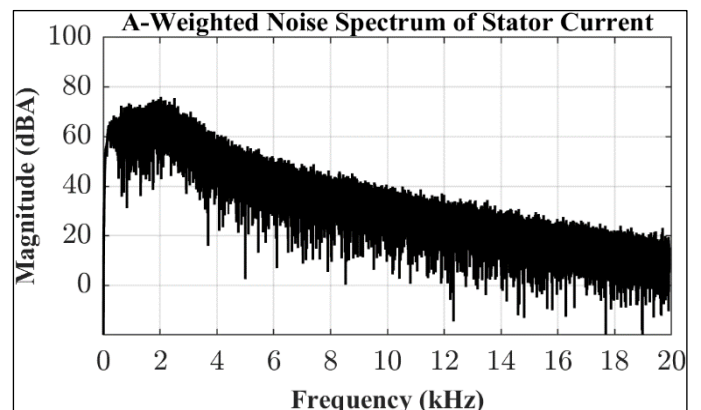
(g) RC-RPPM



(k) RC-RZDPWM-RPPM



(h) RCFM-RPPM



(l) RC-RZDPWM-RCFM.

Figure 6. (a)-(l) A-Weighted Acoustical Noise Spectra for various PWM methods.
Source: Authors, (2024).

Table 3: HSF Comparison for Different PWM methods.

S. No.	PWM Method	Randomness	HSF
1	SVPWM [19]	Single	3.74
2	RCPWM [19]	Single	3.57
3	RPPM [17]	Single	2.95
4	RZDPWM [19]	Single	2.89
5	RCFM [16]	Single	2.72
6	RC-RZDPWM [19]	Dual	2.65
7	RC-RPPM [17]	Dual	2.64
8	RCFM-RPPM [16]	Dual	2.28
9	RC-RCFM [19]	Dual	2.12
10	RC-RCFM-RPPM [19]	Triple	1.59
11	RC-RZDPWM-RPPM	Proposed Triple	1.42
12	RC-RZDPWM-RCFM	Proposed Triple	1.28

Source: Authors, (2024).

The proposed triple randomized PWM schemes, viz. RC-RZDPWM-RPPM and RC-RZDPWM-RCFM, exhibit a significantly higher level of randomness and hence tremendous spread spectrum capabilities when compared to single, dual, and traditional triple randomized PWM schemes as signified by the HSF.

Nonetheless, the RC-RZDPWM-RCFM scheme demonstrates enhanced spread spectrum capability due to the advantageous characteristics of both RZDPWM and RCFM techniques, as evidenced by the HSF value in comparison to RC-RZDPWM-RPPM. The RPWM techniques are effective in minimising EMI. Nonetheless, it experiences challenges related to design and implementation complexity, diminished efficiency, difficulties in filtering, possible stability concerns, and an elevated computational burden.

The ratings of the inverter and induction motor are given as: $V_d = 540V$, $V = 400V$, $P = 4 kW$, $p = 4$, $N_{rated} = 1470 rpm$, $f = 50 Hz$, $T_{rated} = 30 N\cdot m$, $R_s = 1.57 \Omega$, $R_r = 1.21 \Omega$, $L_m = 0.165 H$, $L_s = 0.17 H$, $L_r = 0.17 H$ and $J = 0.089 Kg \cdot m^2$.

VI. CONCLUSIONS

This article discusses the implementation of a SAC based DTC strategy for EV applications. It explores the use of the AIS mode and incorporates SVPWM and various RPWM methods. Introducing two new hybrid triple random PWM schemes, namely RC-RZDPWM-RPPM and RC-RZDPWM-RCFM, which are designed to reduce acoustical noise. These methods are then compared with previously described approaches. The suggested techniques exhibit highly efficient for dispersing the harmonic's spectrum, demonstrated by the HSF. This can be attributed to the rise in unpredictability. Therefore, the techniques recommended have demonstrated remarkable efficacy in reducing acoustical noise, resulting in a 20% reduction in high-frequency noise compared to the conventional triple random PWM method. Compared to RC-RZDPWM-RPPM, RC-RZDPWM-RCFM significantly reduces the noise. In addition, the advancements in Wide Band Gap switches, Uniform Sampling PWM methods, as well as advanced MLIs currently being explored as options to minimise noise in industrial drive applications and EVs.

VII. AUTHOR'S CONTRIBUTION

Conceptualization: Ganesh Challa and Dr. M. Damodar Reddy.

Methodology: Ganesh Challa and Dr. M. Damodar Reddy.

Investigation: Ganesh Challa and Dr. M. Damodar Reddy.

Discussion of results: Ganesh Challa and Dr. M. Damodar Reddy.

Writing – Original Draft: Ganesh Challa.

Writing – Review and Editing: Dr. M. Damodar Reddy.

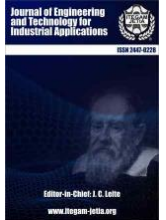
Supervision: Dr. M. Damodar Reddy.

Approval of the final text: Dr. M. Damodar Reddy.

VIII. REFERENCES

- [1] H. H. Hussein and A. J. Mahdi, "A Small-scale Inductive Wireless Power Transmission Prototype for Charging Electric Vehicles," 10th International Conference on Smart Grid (icSmartGrid), Istanbul, Turkey, pp. 96-101, Jun. 2022, DOI: 10.1109/icsmartgrid55722.2022.9848722.
- [2] F. Zhang, D. C. Kien and H. Takami, "DC-Link Voltage Control Based on Adaptive IRM-ILQ for Stirling Engine Power Supply Vehicle," 12th International Conference on Renewable Energy Research and Applications (ICRERA), Oshawa, ON, Canada, pp. 161-165, August/September 2023, DOI: 10.1109/icrera59003.2023.10269389.
- [3] N. V. A. Ravikumar, R. S. S. Nuvvula, P. P. Kumar, N. H. Haroon, U. D. Butkar and A. Siddiqui, "Integration of Electric Vehicles, Renewable Energy Sources, and IoT for Sustainable Transportation and Energy Management: A Comprehensive Review and Future Prospects," 12th International Conference on ICRERA, Oshawa, ON, Canada, pp. 505-511, Aug. /Sept. 2023, DOI: 10.1109/icrera59003.2023.10269421.
- [4] S. Pradhan, A. K. Sahoo and R. K. Jena, "Comparison of DTC and SVM - DTC of Induction motor drive for Electric Vehicle application," International Conference on Intelligent Controller and Computing for Smart Power (ICICCSPP), Hyderabad, India, pp. 01-06, Jul. 2022, DOI: 10.1109/ICICCSPP53532.2022.9862317.
- [5] J. Faiz, M. B. B. Sharifian, A. Keyhani and A. B. Proca, "Sensorless direct torque control of induction motors used in electric vehicle," in IEEE Transactions on Energy Conversion, vol. 18, no. 1, pp. 1-10, Mar. 2003, DOI: 10.1109/TEC.2002.805220.
- [6] H. Benbouhenni, "Stator current and rotor flux ripples reduction of DTC DFIG drive using FSTSMC algorithm," International Journal of Smart grid, vol.3, no.4, pp. 226-234, Dec. 2019, DOI: 10.20508/ijsmartgrid.v3i4.82.g72.
- [7] H. Benbouhenni, "Rotor flux and electromagnetic torque regulation of DFIG using dual PI controllers," International Journal of Smart grid, vol.7, no.4, pp. 227-234, Dec. 2023, DOI: 10.20508/ijsmartgrid.v7i4.308.g311.
- [8] H. Stemmler and P. Guggenbach, "Configurations of high-power voltage source inverter drives," Fifth European Conf. on Power Elec. and Appl., Brighton, UK, pp. 7-14, Sept. 1993.
- [9] J. Kim, J. Jung and K. Nam, "Dual-inverter control strategy for high-speed operation of EV induction motors," in IEEE Transactions on Industrial Electronics, vol. 51, no. 2, pp. 312-320, Apr. 2004, DOI: 10.1109/TIE.2004.825232.
- [10] Y. Huang, Y. Xu, W. Zhang and J. Zou, "Hybrid RPWM Technique Based on Modified SVPWM to Reduce the PWM Acoustic Noise," in IEEE Transactions on Power Electronics, vol. 34, no. 6, pp. 5667-5674, Jun. 2019, DOI: 10.1109/TPEL.2018.2869980.
- [11] Y. Lv, S. Cheng, Z. Ji, X. Li, D. Wang, Y. Wei, X. Wang, and W. Liu, "Spatial-Harmonic Modeling and Analysis of High-Frequency Electromagnetic Vibrations of Multiphase Surface Permanent-Magnet Motors," in IEEE Transactions on Industrial Electronics, vol. 70, no. 12, pp. 11865-11875, Dec. 2023, DOI: 10.1109/TIE.2023.3239905.
- [12] J. Y. Chai, Y. H. Ho, Y. C. Chang and C. M. Liaw, "On Acoustic-Noise-Reduction Control Using Random Switching Technique for Switch-Mode Rectifiers in PMSM Drive," in IEEE Transactions on Industrial Electronics, vol. 55, no. 3, pp. 1295-1309, Mar. 2008, DOI: 10.1109/TIE.2007.909759.
- [13] M. M. Bech, J. K. Pedersen and F. Blaabjerg, "Field-oriented control of an induction motor using random pulsewidth modulation," in IEEE Transactions on Industry Applications, vol. 37, no. 6, pp. 1777-1785, Nov.-Dec. 2001, DOI: 10.1109/APEC.2000.822615.
- [14] A. M. Stankovic, G. E. Verghese and D. J. Perreault, "Analysis and synthesis of randomized modulation schemes for power converters," in IEEE Transactions on Power Electronics, vol. 10, no. 6, pp. 680-693, November 1995, DOI: 10.1109/63.471288.
- [15] X. Zhu et al., "A Passive Variable Switching Frequency SPWM Concept and Analysis for DCAC Converter," in IEEE Transactions on Power Electronics, vol. 37, no. 5, pp. 5524-5534, May 2022, DOI: 10.1109/TPEL.2021.3123190.

- [16] A. Boudouda, N. Boudjerda, and A. Aibeche, "dSPACE-based dual randomized pulse width modulation for acoustic noise mitigation in induction motor." *Journal of the Brazilian Society of Mechanical Sciences and Engineering* (Springer), vol. 44, no. 10, Sept. 2022, DOI: 10.1007/s40430-022-03814-2.
- [17] J. Xu, Z. Nie and J. Zhu, "Characterization and Selection of Probability Statistical Parameters in Random Slope PWM Based on Uniform Distribution," in *IEEE Transactions on Power Electronics*, vol. 36, no. 1, pp. 1184-1192, Jan. 2021, DOI: 10.1109/TPEL.2020.3004725.
- [18] P. Madasamy, R. Verma, C. Bharatiraja, J. Barnabas Paul Gladly, T. Srihari, J. L. Munda, L. Mihet-Popa, "Hybrid Multicarrier Random Space Vector PWM for the Mitigation of Acoustic Noise," *Electronics*, vol. 10, no. 12, pp. 1-19, Jun. 2021, DOI: 10.3390/electronics10121483.
- [19] S. Nithya Lavanya, T. Bramhananda Reddy, and M. Vijaya Kumar, "Constant and variable switching frequency random PWM strategies for open-end winding induction motor drive". *J. Power Electron.*, vol. 20, pp. 1488–1495, Sept. 2020, DOI: 10.1007/s43236-020-00137-0.
- [20] A. C. Binoj Kumar, B. Saritha and G. Narayanan, "Experimental Comparison of Conventional and Bus-Clamping PWM Methods Based on Electrical and Acoustic Noise Spectra of Induction Motor Drives," in *IEEE Transactions on Industry Applications*, vol. 52, no. 5, pp. 4061-4073, Sept. - Oct. 2016, DOI: 10.1109/TIA.2016.2584578.
- [21] A. C. Binoj Kumar, J. S. S. Prasad, and G. Narayanan, "Experimental Investigation on the Effect of Advanced Bus-Clamping Pulse Width Modulation on Motor Acoustic Noise." *IEEE Trans. on Ind. Elec.*, vol. 60, no. 2, pp. 433-439, Feb. 2013, DOI: 10.1109/tie.2012.2190371.
- [22] R. Alavanthan and A. Kavitha, "Digital implementation of DS-SFH hybrid spread-spectrum modulation technique in three-phase voltage-source converter." *Electrical Engineering* (Springer), vol. 104, no. 3, pp. 1413-1423, Oct. 2021, DOI: 10.1007/s00202-021-01388-1.
- [23] Y. Wang, J. Liu, B. Lu and M. Wang, "A Novel Discrete Hybrid Dual Random SVPWM Scheme for Reducing PMSM Harmonic Intensity," in *IEEE/ASME Transactions on Mechatronics*, vol. 28, no. 3, pp. 1425-1435, Jun. 2023, DOI: 10.1109/TMECH.2022.3220519.
- [24] S. Bhattacharya, D. Mascarella, G. Joos and G. Moschopoulos, "A discrete random PWM technique for acoustic noise reduction in electric traction drives," *IEEE Energy Conversion Congress and Exposition (ECCE)*, Montreal, QC, Canada, pp. 6811-6817, Sept. 2015, DOI: 10.1109/ECCE.2015.7310613.
- [25] A. R. González, J. R. H. Larubia, F. M. P. Hidalgo, M. J. M. Gutiérrez, "Discontinuous PWM Strategy with Frequency Modulation for Vibration Reduction in Asynchronous Machines" *Machines*, vol. 11, no. 7, pp. 1-22, May 2023, DOI: 10.3390/machines11070705.
- [26] R. K. Thakur, R. M. Pindoriya, R. Kumar, and B. S. Rajpurohit, *Transportation Electrification*, India: Wiley, 2022, ch.5, DOI: 10.1002/9781119812357.ch5.
- [27] P. Zhang, S. Wang and Y. Li, "Three-Phase Two-Level VSIs With Significant PWM Harmonics Dispersion and Improved Performance Using Generalized N-State Random Pulse Position SVPWM With Constant Sampling Frequency" in *IEEE Transactions on Power Electronics*, vol.39, no.1, pp.1394-1409, Jan. 2024, DOI: 10.1109/TPEL.2023.3328213.
- [28] S. Sarada, N. Ravisankara Reddy, "Comparative Switching and Conduction Loss Analysis of a SVPWM and DPWM based DTC of Open-End Winding Induction Motor Drive", *International Journal of Renewable Energy Research*, vol.12, no.4, pp.1954-1965, Dec. 2022, DOI: 10.20508/ijrer.v12i4.13466.g8618.
- [29] K. -S. Kim, Y. -G. Jung and Y. -C. Lim, "Shaping the spectra of the acoustic noise emitted by three-phase inverter drives based on the new Hybrid Random PWM technique," *37th IEEE Power Electronics Specialists Conference*, Jeju, Korea (South), pp. 1-6, Jun. 2006, DOI: 10.1109/pesc.2006.1711823.
- [30] Venkata Anjani Kumar G, Damodar Reddy M, "Optimized PI tuning of DG-integrated shunt active power filter using biogeography-based optimization algorithm" *Journal Européen des Systèmes Automatisés*, vol. 56, no. 6, pp. 907-916, Dec. 2023, DOI: 10.18280/jesa.560602.



ANALYSIS OF FUEL CELL POWERED EV CHARGING STATION

¹Bondu Pavan Kumar Reddy, ²Dr. Vyza Usha Reddy.¹ ²Department of EEE, Sri Venkateswara University College of Engineering, Tirupati, India¹ <http://orcid.org/0000-0001-8845-571X>, ² <http://orcid.org/0009-0004-7070-8925>E-mail: ¹ pavankumar.eee216@gmail.com, ² vyza_ushareddy@yahoo.co.in

ARTICLE INFO

Article HistoryReceived: September 11th, 2024Revised: October 10th, 2024Accepted: October 11th, 2024Published: October 31th, 2024**Keywords:**Fuel Cell,
EV Charging,
Zeta Topology,
SEPIC Topology,
Modified SEPIC topology.

ABSTRACT

The paper offers a comparative performance analysis of fuel cell-powered EV charging systems utilizing ZETA, SEPIC, and modified SEPIC DC-DC converter topologies. Despite the cleaner energy source that fuel cells represent, their high cost has limited their penetration in EV charging. Selecting a suitable DC-DC converter topology is crucial for achieving fast charging and improved efficiency. The paper presents a performance analysis of the ZETA, SEPIC, and modified SEPIC converter topologies, both with open-loop and closed-loop control, for EV charging applications. A MATLAB/Simulink model was developed to examine the performance of these topologies in terms of battery state of charge (SoC), battery voltage, and charging current. The study reveals that the battery charged from an SoC of 50% to 50.03% using the modified SEPIC converter, while the ZETA and SEPIC converters charged to 50.024% under closed-loop control. Under open-loop control, the modified SEPIC charged to 50.025%, followed by ZETA at 50.024% and SEPIC at 50.02%, with a similar simulation time of ten seconds using a fuel cell as the primary energy source. The results demonstrate that the DC-DC modified SEPIC converter outperforms both ZETA and SEPIC converters.



Copyright ©2024 by authors and Galileo Institute of Technology and Education of the Amazon (ITEGAM). This work is licensed under the Creative Commons Attribution International License (CC BY 4.0).

I. INTRODUCTION

Fuel cells, a type of electrochemical device, have emerged as a promising alternative to traditional internal combustion engines and lithium-ion batteries in electric vehicles (EVs). They offer a clean and efficient way to generate electricity, producing only water and heat as byproducts, making them a desirable option for reducing greenhouse gas emissions and improving air quality [1].

The basic structure of fuel cell is depicted in figure 1. The operating principle of a fuel cell involves the electrochemical reaction between a fuel (typically hydrogen) and an oxidant (usually oxygen) to produce electricity, water, and heat.

This process is highly efficient and can deliver a continuous supply of power, making it suitable for powering EVs. Based upon the type of membrane used, the fuel cells are classified as [2].

Proton Exchange Membrane (PEM) fuel cells: These are the most common type of fuel cell used in EVs. They use a proton exchange membrane (PEM) to conduct protons from the anode to

the cathode. PEM fuel cells operate at relatively low temperatures and can be started quickly, making them suitable for transportation applications.

Alkaline fuel cells (AFCs): AFCs use a hydroxide ion-conducting electrolyte. They offer high efficiency and can operate at relatively low temperatures. However, they are sensitive to carbon dioxide contamination, which can limit their use in certain applications.

Solid Oxide Fuel Cells (SOFCs): SOFCs use a solid ceramic electrolyte. They operate at high temperatures, which allows them to use a variety of fuels, including natural gas and biogas. However, the high operating temperature can pose challenges for integration into vehicles.

Phosphoric Acid Fuel Cells (PAFCs): PAFCs use phosphoric acid as the electrolyte. They operate at intermediate temperatures and are relatively tolerant to impurities in the fuel. PAFCs are used in stationary power generation applications.

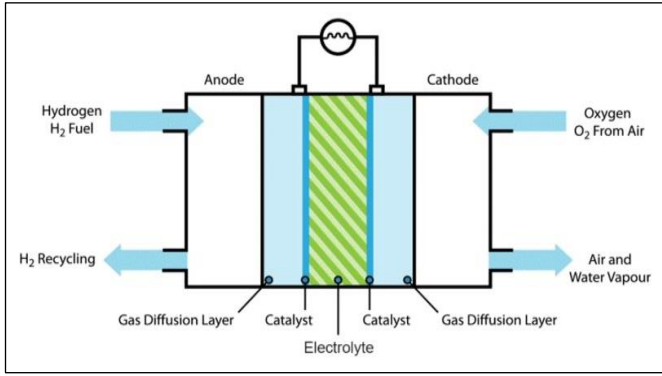


Figure 1: Fuel cell Architecture.
Source: Authors, (2024).

Despite their advantages, the penetration of fuel cells in EV charging has been relatively limited. Several factors have contributed to this, including high cost, infrastructure limitations, range anxiety and technical challenges. However, significant advancements have been made in recent years to address these challenges and improve the feasibility of fuel cell vehicles [3]. Fuel cell and Hydrogen Energy Association (FHCEA), a USA based non-profit organisation is planning for mobile EV charging stations using hydrogen fuel cells by 2026.

II. MODELLING & DESIGNING

The MATLAB/Simulink Solar PV system was developed to charge EV battery with specifications of 48V, 200Ah through DC-DC Converters with a fuel cell of nominal power 1.26kW. The fuel cell stack design parameters are represented in the Table 1[4] and the parameters for ZETA, SEPIC (Table 2) and Modified SEPIC converters when employed for EV charging form fuel cell are calculated and presented in Table 3 [5-7].

Table 1: Fuel cell Specifications.

Parameter	Specification
Nominal Voltage	24.23V
Nominal Current	52 A
Nominal Power	1.26 kW
Maximum Power	2 kW
No. of Cells	42
Stack Efficiency	46 %

Source: Authors, (2024).

Table 2: Parameters for various Converters.

Parameter	ZETA Converter	SEPIC Converter	Modified SEPIC converter
Duty Cycle	66.4 %	66.4 %	32.9
Inductor (L ₁)	38.6 μH	38.6 μH	76 μH
Inductor (L ₂)	38.6 μH	38.6 μH	76 μH
Capacitor (C ₁)	1.8 mF	3.5 mF	1.43 V
Capacitor (C ₂)	4.3 μF	1.8 mF	0.9 mF

Source: Authors, (2024).

Table 3: Battery Specifications.

Parameter	Specification
Capacity	200 Ah
Nominal Voltage	48 V
Nominal Power	9.6 kWh
Cut-off Voltage	40.5 V
Maximum Voltage	52.3 V

Source: Authors, (2024).

A real-world economically available four-wheeler battery, such as those used in electric vehicles like the Reva-i car, Mahindra E20, and battery-operated golf carts, was considered for analysis in this study. This battery has a capacity of 9.6kWh and was charged using a 2kW fuel cell through various converters to evaluate their performance.

III. SIMULATION & RESULTS

An EV battery pack with a rating of 48V, 200Ah is charged through a 2kW PV source with ZETA, SEPIC & modified SEPIC converters are simulated in MATLAB/Simulink Environment. In simulation testing, the parameters such as voltage and current from fuel cell along with battery SoC, Charging current and battery voltage are observed at the same test conditions for both converters. The figures from 2 to 15 illustrates MATLAB/Simulink model, fuel cell characteristics (i.e., Voltage and Current), battery SoC, battery charging current and battery voltage of ZETA, SEPIC & modified SEPIC converters with open loop & closed loop control strategies.

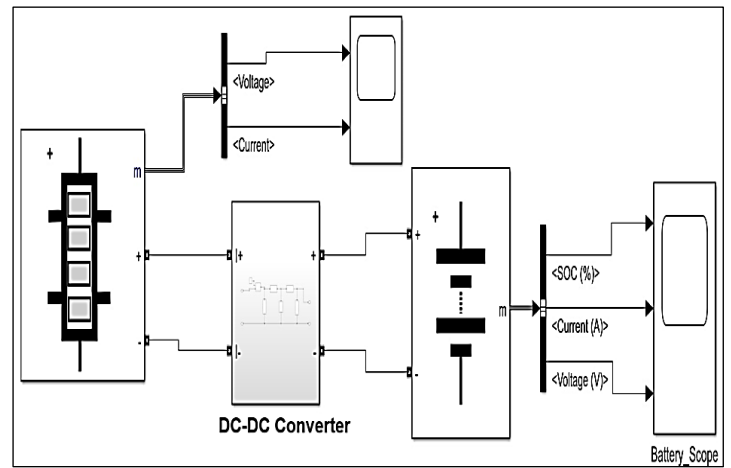


Figure 2: MATLAB/Simulink Model of open loop fuel cell based EV charging system.
Source: Authors, (2024).

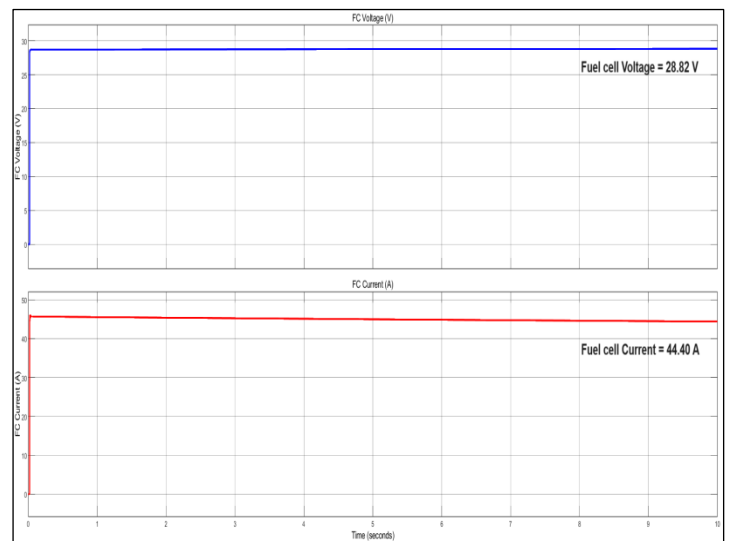


Figure 3: Characteristics response of open loop PEMFC based EV charging with ZETA converter.
Source: Authors, (2024).

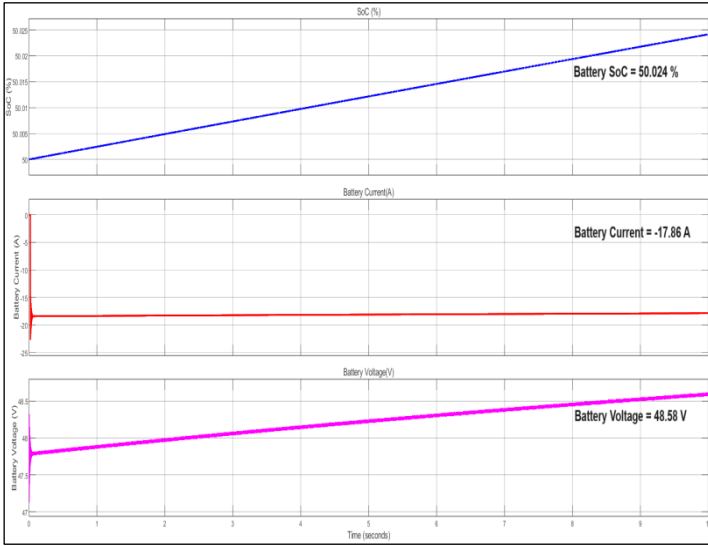


Figure 4: Battery charging results of open loop PEMFC based EV charging with ZETA converter.
Source: Authors, (2024).

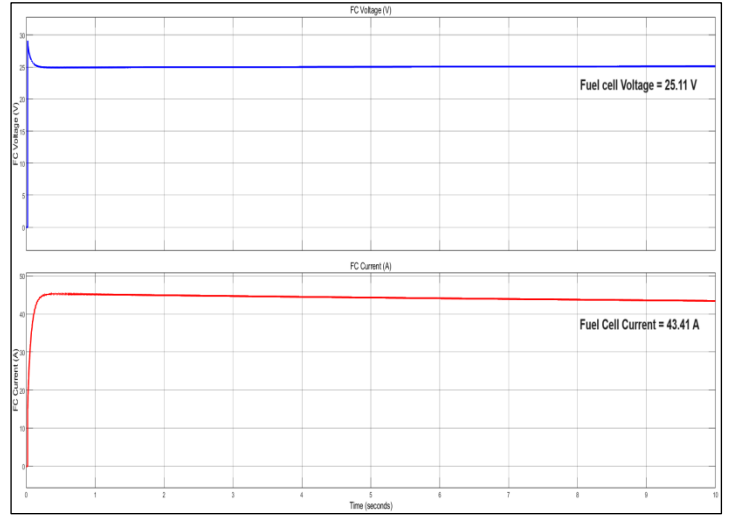


Figure 7: Characteristics response of open loop PEMFC based EV charging with modified SEPIC converter.
Source: Authors, (2024).

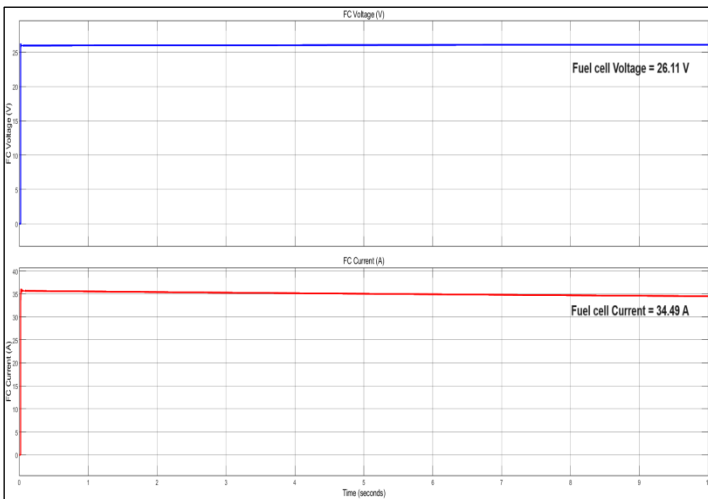


Figure 5: Characteristics response of open loop PEMFC based EV charging with SEPIC converter.
Source: Authors, (2024).

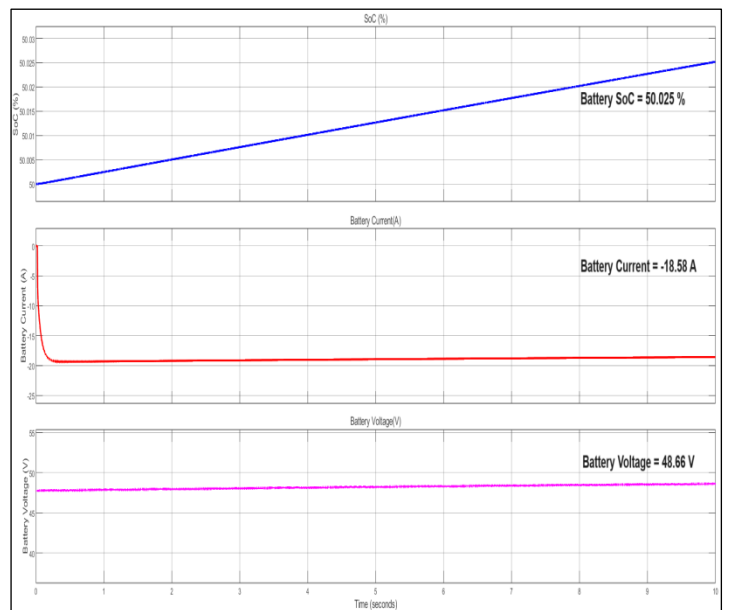


Figure 8: Battery charging results open loop PEMFC based EV charging with modified SEPIC converter.
Source: Authors, (2024).

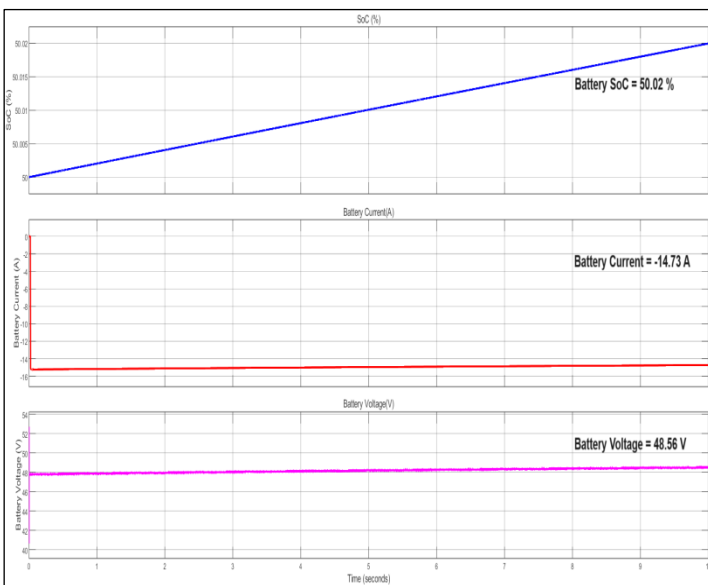


Figure 6: Battery charging results open loop PEMFC based EV charging with SEPIC converter.
Source: Authors, (2024).

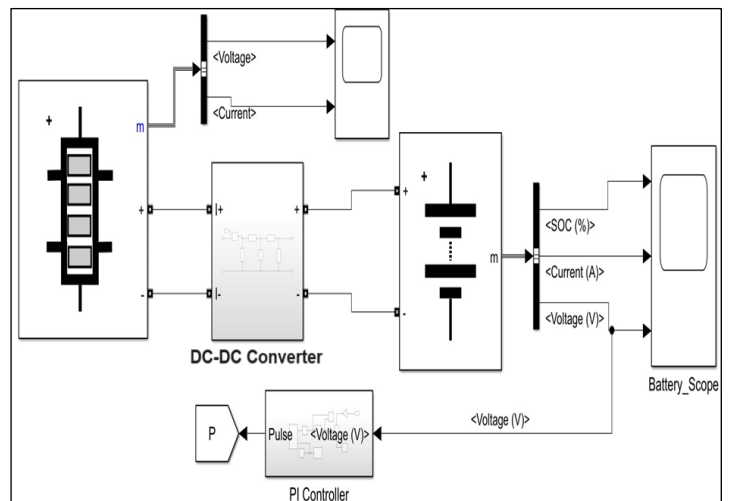


Figure 9: MATLAB/Simulink Model of closed loop fuel cell based EV charging system
Source: Authors, (2024).

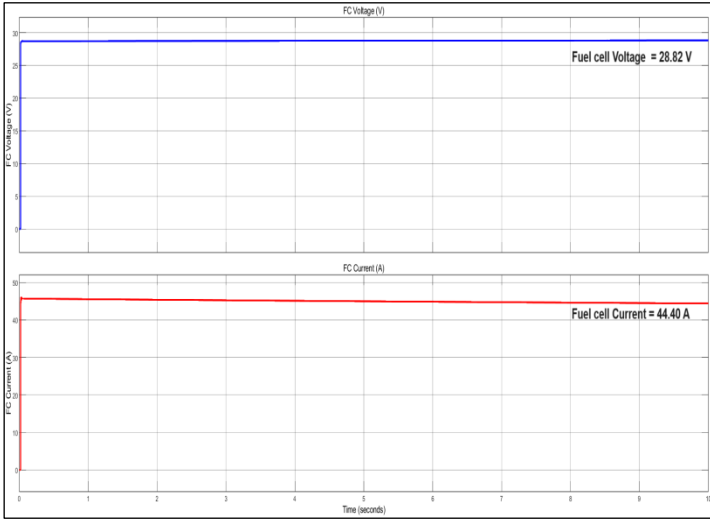


Figure 10: Characteristic response of closed loop PEMFC based EV charging system with ZETA Converter.
Source: Authors, (2024).

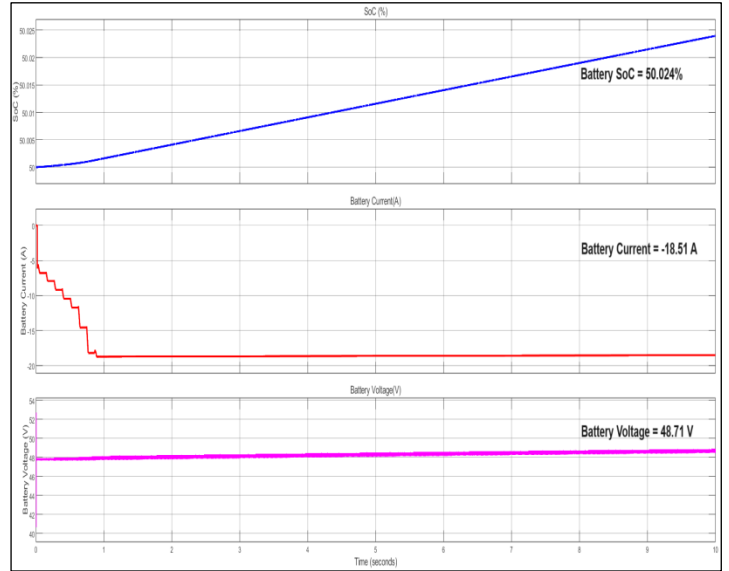


Figure 13: Battery charging results of closed loop PEMFC based EV charging system with SEPIC Converter.
Source: Authors, (2024).

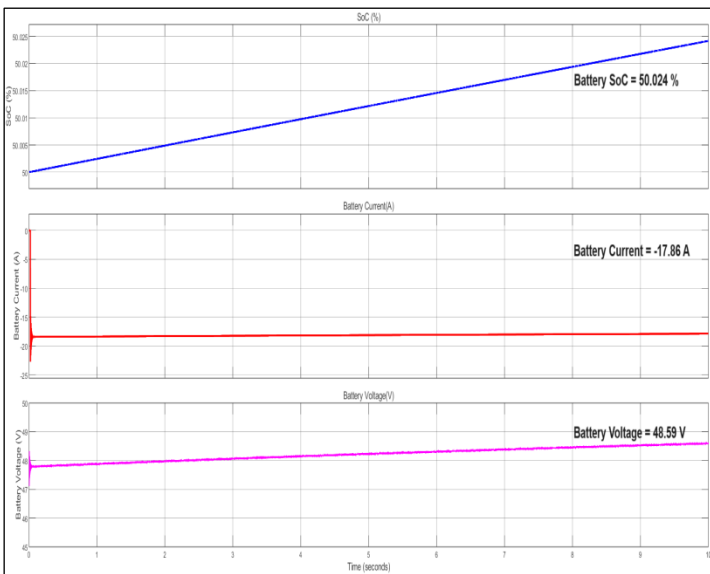


Figure 11: Battery charging results of closed loop PEMFC based EV charging system with ZETA Converter.
Source: Authors, (2024).

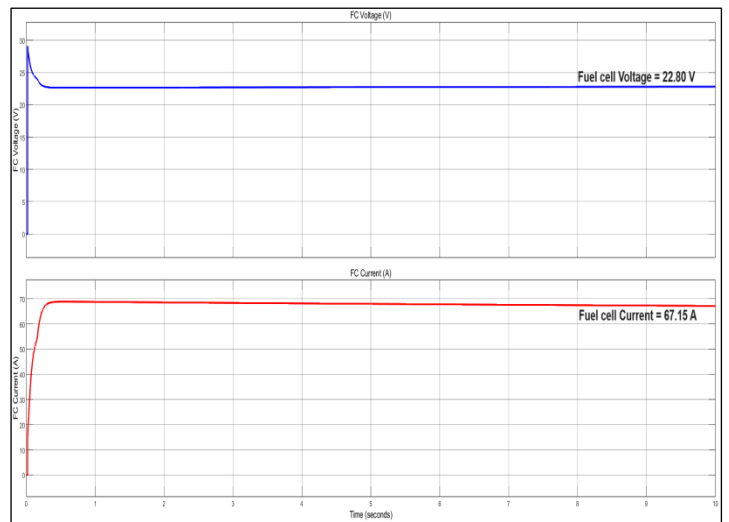


Figure 14: Characteristic response of closed loop PEMFC based EV charging system with modified SEPIC Converter.
Source: Authors, (2024).

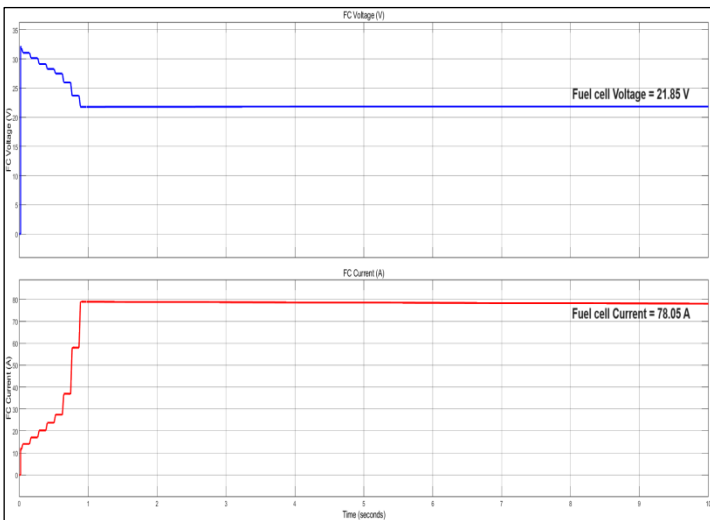


Figure 12: Characteristic response of closed loop PEMFC based EV charging system with SEPIC Converter.
Source: Authors, (2024).

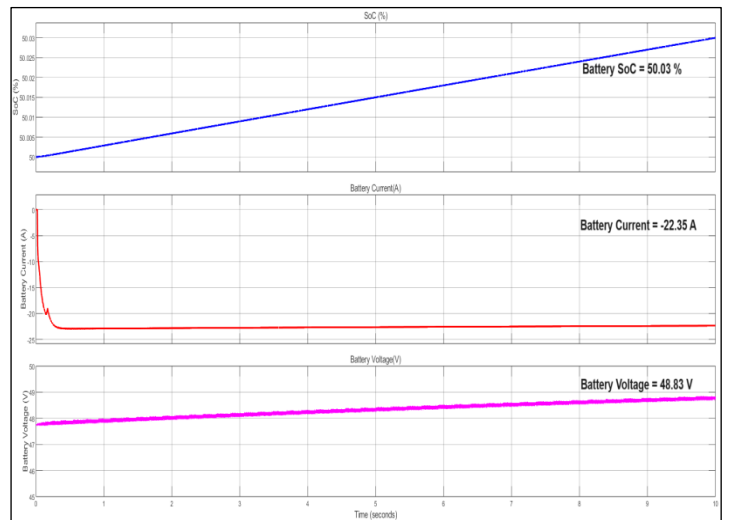


Figure 15: Battery charging results of closed loop PEMFC based EV charging system with modified SEPIC Converter.
Source: Authors, (2024).

The results of fuel cell powered EV charging system through Zeta, SEPIC and modified SEPIC converters under same test conditions with open loop and closed loop approaches are illustrated in the Table 4. The value of battery current is negative which denotes that the battery is in charging state.

Table 4: Simulation results with SoC of 50% for 10sec.

	Zeta Converter		SEPIC Converter		Modified SEPIC Converter	
	Open Loop	With PI	Open Loop	With PI	Open Loop	With PI
SoC (%)	50.024	50.024	50.02	50.024	50.025	50.03
V _b (V)	48.58	48.59	48.56	48.71	48.66	48.83
I _b (A)	-17.86	-17.86	-14.73	-18.51	-18.58	-22.35
V _{FC} (V)	28.82	28.82	26.11	21.85	25.11	22.80
I _{FC} (A)	44.40	44.40	34.49	78.05	43.41	67.15
Time (H)	5.47	5.47	6.56	5.47	5.33	4.37

Source: Authors, (2024).

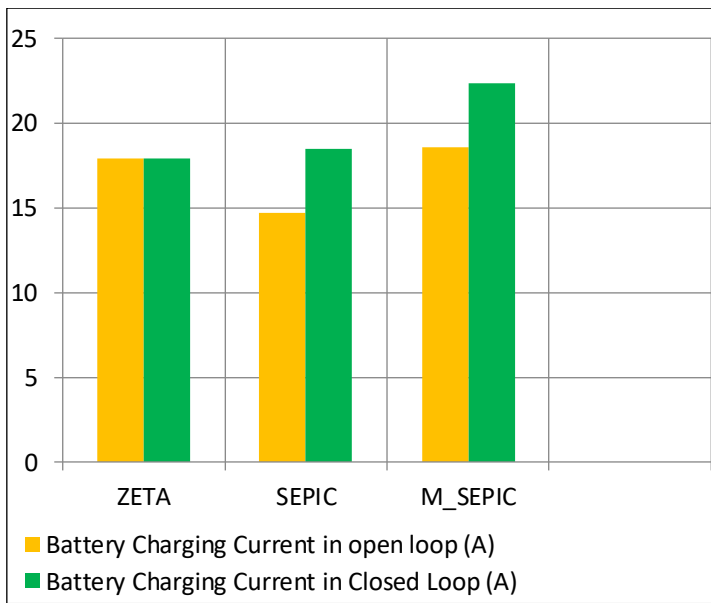


Figure 16: Pictorial representation of battery charging current from simulation results. Source: Authors, (2024).

V. CONCLUSIONS

A comparative performance analysis of fuel cell powered EV charging system using ZETA, SEPIC and Modified SEPIC converter topologies with open loop and closed loop techniques is simulated in MATLAB/ Simulink environment and the findings are evaluated. From the simulation findings, it is observed that the charging current delivered by modified SEPIC is more when compared to other converters, and thereby a swift increase in the battery's state of charge. The time taken for charging a battery using the ZETA, SEPIC & modified SEPIC converters under open loop control is 5.47Hrs, 6.56Hrs & 5.33 Hrs respectively. With closed loop control, ZETA & SEPIC still requires 5.47Hrs while modified SEPIC requires 4.37Hrs. Therefore with fuel cell as primary energy source, the modified SEPIC converter outperforms other two converts in all aspects.

VI. AUTHOR'S CONTRIBUTION

Conceptualization: Bondu Pavan Kumar Reddy and Dr. Vyza Usha Reddy.

Methodology: Bondu Pavan Kumar Reddy and Dr. Vyza Usha Reddy.

Investigation: Bondu Pavan Kumar Reddy and Dr. Vyza Usha Reddy.

Discussion of results: Bondu Pavan Kumar Reddy and Dr. Vyza Usha Reddy.

Writing – Original Draft: Bondu Pavan Kumar Reddy and Dr. Vyza Usha Reddy.

Writing – Review and Editing: Bondu Pavan Kumar Reddy and Dr. Vyza Usha Reddy.

Resources: Bondu Pavan Kumar Reddy and Dr. Vyza Usha Reddy.

Supervision: Bondu Pavan Kumar Reddy and Dr. Vyza Usha Reddy.

Approval of the final text: Bondu Pavan Kumar Reddy and Dr. Vyza Usha Reddy.

VII. ACKNOWLEDGMENTS

The authors would like to express their sincere gratitude to Sri Venkateswara University College of Engineering for providing necessary guidance and support. We are also grateful to the anonymous reviewers for their constructive comments that helped us to improve the quality of this manuscript

VIII. REFERENCES

[1] Andreas Jossen, Juergen Garche, Harry Doering, Markus Goetz, Werner Knaupp and Ludwig Joerissen "Hybrid systems with lead–acid battery and proton-exchange membrane fuel cell", Journal of Power Sources, Volume 144, Issue 2, 2005, Pages 395-401, ISSN 0378-7753, <https://doi.org/10.1016/j.jpowsour.2004.11.010>

[2] Hossein Pourrahmani, Martin Gay and Jan Van herle, "Electric vehicle charging station using fuel cell technology: Two different scenarios and thermodynamic analysis", Energy Reports, Volume 7, 2021, Pages 6955-6972, ISSN 2352-4847, <https://doi.org/10.1016/j.egy.2021.09.211>

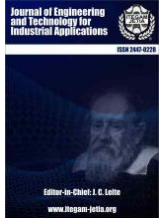
[3] R. -J. Wai, C. -Y. Lin, R. -Y. Duan and Y. -R. Chang, "High-Efficiency DC-DC Converter With High Voltage Gain and Reduced Switch Stress," in IEEE Transactions on Industrial Electronics, vol. 54, no. 1, pp. 354-364, Feb. 2007, DOI: <https://doi.org/10.1109/TIE.2006.888794>.

[4] Data sheet, Hanselng Technologies Ltd., Available online: <https://hanselng.com> (Accessed on 25 January 2023).

[5] B. Pavan kumar Reddy & V. Usha Reddy "PV-based performance evaluation of ZETA and SEPIC topologies for EV applications", Journal of Electrical Systems, Volume 20 No5s, April 2024, Pp 438-446, ISSN: 1112-5209. DOI: <https://doi.org/10.52783/jes.2068>

[6] B. Pavan kumar Reddy & V. Usha Reddy "PV-Based Design and Evaluation of Power Electronic Topologies for EV Applications", International Journal of Experimental Research and Review, Volume 39, May 2024, Pp 118-128, ISSN: 2455-4855. DOI: <https://doi.org/10.52756/ijerr.2024.v39spl.009>

[7] B. Pavan kumar Reddy & V. Usha Reddy "Design and Analysis of Novel Topology for PV-Fed EV Charging System", Journal of Engineering and Technology for Industrial Applications, Volume 10, No 47, June 2024, Pp 109-114, ISSN: 2447-0228. DOI: <https://doi.org/10.5935/jetia.v10i47.1108>



RESEARCH ARTICLE

OPEN ACCESS

THE IMPACT OF NANO ADDITIVES IN CORN OIL BIODIESEL USED IN COMBUSTION ENGINES ON THE ENVIRONMENT: AN EXPERIMENTAL APPROACH

Raviteja Surakasi*¹, K.Ch. Sekhar², M. Jayakrishna³, Rapaka Jagadeesh⁴, D Bhanuchandra Rao⁵, Iván Leandro Rodríguez Rico⁶

^{1, 2} Department of Mechanical Engineering, Lendi Institute of Engineering and Technology, Jonnada, Vizianagaram, Andhra Pradesh, India – 535005.

³ Department of Mechanical Engineering, Sri Sivani College of Engineering, Etcherla, Chilakapalem, Andhra Pradesh, India -532402.

^{4, 5} Aditya Institute of Technology and Management.

⁶ Central University "Marta Abreu" of Las Villas.

<http://orcid.org/0000-0002-0786-0105> , <http://orcid.org/0000-0002-6081-8571> , <http://orcid.org/0000-0003-1647-2750>.

<http://orcid.org/0000-0003-2876-2982> , <http://orcid.org/0000-0002-5809-8042> , <http://orcid.org/0000-0003-1295-5368>

Email: *ravitejasurakasi@gmail.com, sekhar.lendi@gmail.com, jayakrishnamakka555@gmail.com, jagadeeshr008@gmail.com, bhanurch@gmail.com, ivanrrico@gmail.com

ARTICLE INFO

Article History

Received: September 15th, 2024

Revised: October 15th, 2024

Accepted: October 17th, 2024

Published: October 31th, 2024

Keywords:

Biodiesel,
corn oil,
internal combustion engine,
transesterification,
environmental pollution.

ABSTRACT

Biodiesel was made in this experiment by transesterifying corn oil. The engine's performance and emissions from fossil fuels were evaluated by adjusting the fuel mixture proportions. This investigation examined various parameters, including hydrocarbon emissions, CO, NOx emissions, brake power, mechanical efficiency, brake thermal efficiency, and indicated thermal efficiency. It had a 5.2-kilowatt diesel engine. Making biodiesel is possible by disposing of corn oil. Biodiesel is a product of blending 20% corn oil with diesel. The methyl ester of corn oil satisfied the criteria set by ASTM for fuel. Through the application of different loads to a single-cylinder four-stroke diesel engine, the experimental findings were derived. Although indicated thermal efficiency declined, the B20 blend with 100 ppm titanium oxide nanoparticles led to improvements in brake power, mean effective pressure, mechanical efficiency, and brake thermal efficiency. While the addition of TiO₂ nanoparticles to B20 decreased HC and CO emissions, it increased NOx emissions. The BD20+100ppm TiO₂ sample provided the most favourable outcomes, all things considered.



Copyright ©2024 by authors and Galileo Institute of Technology and Education of the Amazon (ITEGAM). This work is licensed under the Creative Commons Attribution International License (CC BY 4.0).

I. INTRODUCTION

With the increasing need for renewable energy, biodiesel has shown great promise as a replacement for fossil fuels in many burners, including ICEs, stoves, and more [1]. Policies promoting the production and extensive use of first-generation biodiesel within national borders are likely responsible for the increasing popularity of this biofuel in numerous countries. The promotion of oil palm cultivation in certain countries serves as a strategy to produce biodiesel, potentially addressing energy needs for power generation [2]. It is important to note that first-generation biofuels present several disadvantages, including significant water usage in

their production, which could jeopardize food supplies, as well as competition with crops intended for human consumption [3]. This starts a conversation about how well these resources can provide food and energy, which is important for developing new tactics in certain nations. In light of these challenges, there is a growing emphasis on developing innovative solutions and materials. The primary goal of these projects is to develop biofuels for the second, third, and fourth generations using resources other than food crops [4]. The creation of biodiesel from non-food sources and its use has sparked a range of opinions about the feasibility of using these resources for both food and fuel production. This necessitates a thorough assessment of this aspect during the legislative process

across different countries. Scholars globally have carried out numerous comprehensive studies regarding the efficiency of internal combustion engines [5]. The biodiesel production from non-edible vegetable oils has undergone a thorough online examination, highlighting the fuel's characteristics and efficiency [6]. Scientists have looked at several plant oils as potential sources of raw materials, including those that are taken from tobacco, cotton, jojoba, rubber, flax, jatropha, and many more plants. Biodiesel is becoming more popular as a fuel for electric generators, thus several governments have encouraged the production of oil palms to fulfil this need [7]. In 2012, the Philippines was the first nation to initiate the production of biodiesel derived from olive oil. First-generation biofuels present various drawbacks, such as competition with food crops and significant water consumption during production. Research revealed that corn oil might be used to make biodiesel in a manner compliant with international environmental standards and recommendations [8]. Researchers have created a combined catalytic approach for biodiesel production using a composite membrane and sodium methoxide. Their findings indicate that under optimal conditions, a transesterification conversion rate of 98.1% can be reached. A lot of research has gone into determining if biodiesel can be used as a viable fuel for I.C. engines in the last several years. A lot of recent studies have also looked at how efficient these engines are for transportation purposes [9].

II. MATERIALS AND METHOD

II.1 BIODIESEL PRODUCTION

The Food and Agriculture Organization (FAO) states that the first stage is to cook corn to extract its oil, which should yield around 10 liters of oil. An acidity assay is then conducted using a portion of this oil. The acid number of a triglyceride reflects its free fatty acid content, indicating its level of acidity. Potassium hydroxide is essential for titration in this process, while the acidity is measured using the acid number index [10]. An acidity value of 5 or below is considered acceptable for processing, as biodiesel production requires an acidity index not exceeding 5. If the acidity is higher, the oil is less suitable for biodiesel production and is better suited for other uses. In an Erlenmeyer flask, a 5 gramme sample was combined with 50 milliliters of neutralized ethyl alcohol and a few drops of phenolphthalein at 50 degrees Celsius to determine acidity. The solution was then titrated using a 0.1N potassium hydroxide solution [11]. The transesterification process is illustrated in Figure 1.

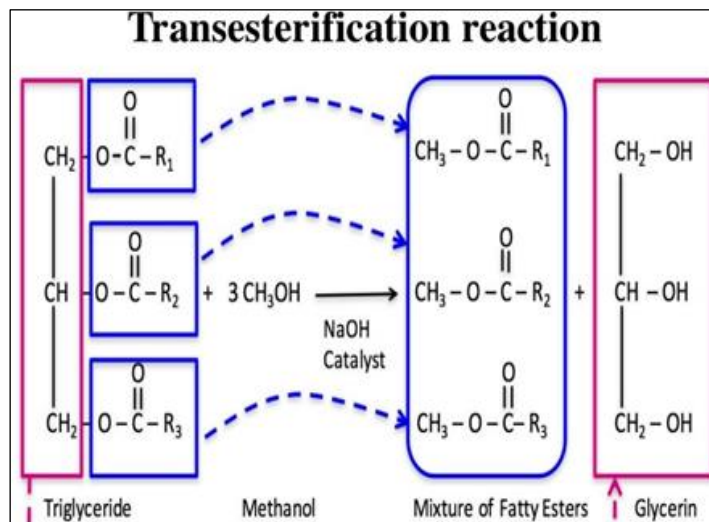


Figure 1: Transesterification process.

Source: Authors, (2024).

Using the transesterification method, renewable lipids like animal and vegetable oils may be transformed into long-chain fatty acid monoalkyl esters. This method is also applicable to animal fats and is integral to biodiesel production. In a specific experiment, 10 liters of used cooking oil were placed in a designated disposal container. Methanol, at a concentration of 20% (v/v), was then added in a volume approximately equal to that of the oil. The amount of catalyst required was calculated based on the acid number of the oil, with 8 grams of potassium hydroxide (KOH) used in the reaction [12]. After mixing the catalyst with methanol to create methoxide, this mixture was combined with the oil and agitated for about two hours at temperatures between 50 and 60 degrees Celsius. The glycerin byproduct was separated through decantation, and the biodiesel underwent three to four washes with water at concentrations of 20 to 30% (v/v), depending on the volume produced. Finally, the biodiesel was dried and filtered as part of the subsequent steps [13].

Table 1: Fuel blends properties.

	Diesel	BD 20	BD20+25 ppm TiO ₂	BD20+50ppm TiO ₂	BD20+75ppm TiO ₂	BD20+100 ppm TiO ₂
Density (kg/m ³)	815	820	826.5	833	839.5	846
Viscosity (mm ² /s)	3.1	3.2	3.3	3.4	3.5	3.6
Calorific Value (MJ/kg)	44	42.8	43.45	43.95	44.25	45
Cetane Number	52	55.6	56.05	56.5	56.95	57.4
Flash Point °C	204	194.8	195.3	196	196.7	197.4
Fire Point °C	59	129.8	130.45	131.1	131.88	132.67

Source: Authors, (2024).

II.2 FUEL SAMPLES

A magnetic stirrer was utilized to achieve a homogeneous mixture of 20% biodiesel and 80% diesel, resulting in the B20 corn oil methyl ester formulation for subsequent analysis. Following this, titanium oxide (TiO₂) nanoparticles were evenly distributed in the B20 fuel samples using an ultrasonicator [14]. The nanoparticles were added in quantities of 25, 50, 75, and 100 milligrams. The performance of these fuel blends was assessed using the ASTM D 6751 standard, which is widely recognized for evaluating fuel properties [15]. The properties of the fuel blends are detailed in Table 1.

II.3 EXPERIMENTAL SET-UP

An engine with one cylinder, four strokes, compression ignition, and either a water-cooled or water-injected cooling system was used throughout the testing. For the record, the trials used an engine of the Kirloskar TV1 type. The over valves of this engine were operated by pushrods. To conduct the experimental investigation, the engine in issue was put to work. Under extreme conditions of utmost effort and a constant rotational speed of 1500 rpm, the engine is capable of producing 5.2 kW of output power. This is the maximum amount of electricity it can generate. Per the manufacturer's requirements, the timing was set at 23 degrees before the top dead center (TDC), and the fuel injection pressure was kept at 210 bar. Throughout the process, the coolant's

temperature remained constant at 80 degrees Celsius. This was made possible by a system that constantly recirculated the coolant via the water jackets that were placed within the cylinder. The pressure inside the engine's cylinders was measured using a piezoelectric sensor that was flush mounted on the vehicle's cylinder head. As an aftermarket accessory, an eddy current dynamometer was installed to measure the torque output of the engine. The experimental setup is shown in a more condensed form in Figure 2, which contains an illustration of the schematic design.

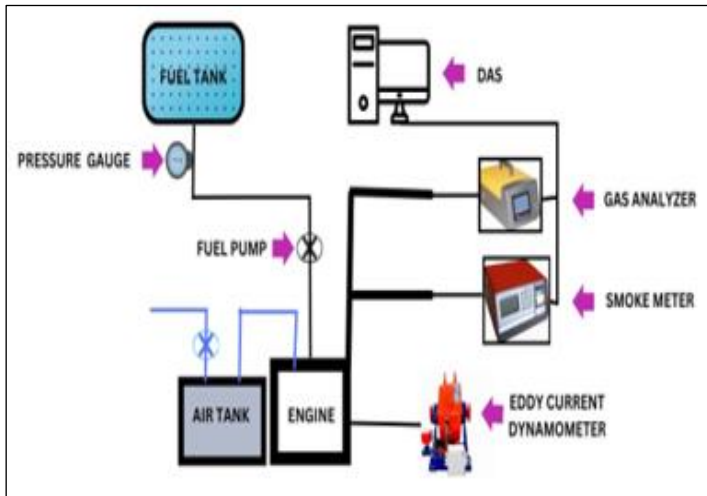


Figure 2: Experimental set-up. Source: Authors, (2024).

III. RESULTS AND DISCUSSIONS

III.1 BRAKE POWER

Figure 3 demonstrates that the values of the engine's brake power are, for the most part, the same regardless of the load group or the kind of mixture. Displaying an almost linear upward tendency in conjunction with a rising trend as the load rises. The data shown in the picture demonstrate that the variety of gasoline used has no impact on the brake power output of the engine [16]. As the load increases the brake power also increases and the maximum value is found to be for BD20+100ppm TiO₂.

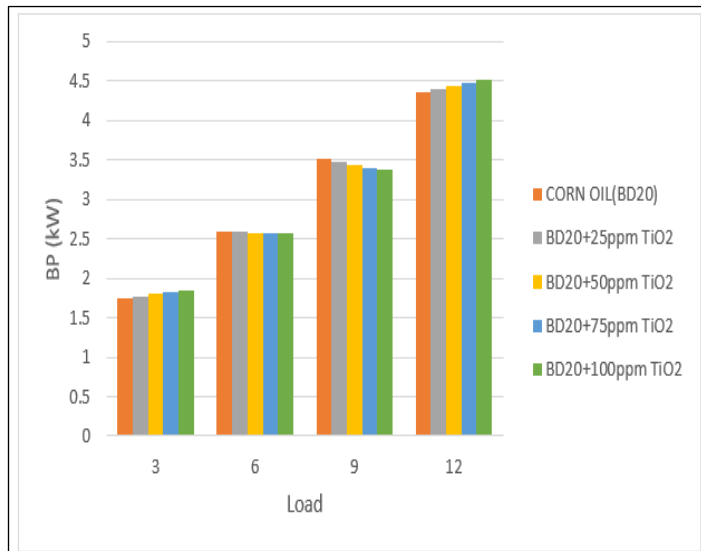


Figure 3: Brake Power varies with increase in load. Source: Authors, (2024).

III.2 BRAKE MEAN EFFECTIVE PRESSURE

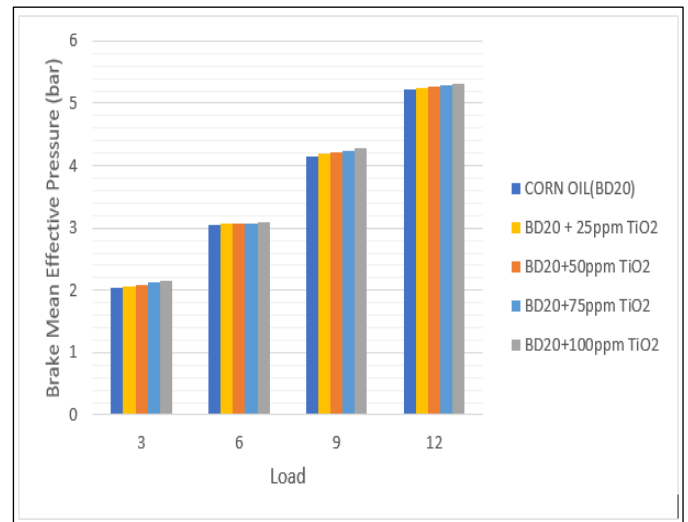


Figure 4: Brake Mean Effective Pressure varies with increase in load.

Source: Authors, (2024).

Figure 4 demonstrates that the values of the engine's brake mean effective pressure are, for the most part, the same regardless of the load group or the kind of mixture. Displaying an almost linear upward tendency in conjunction with a rising trend as the load rises [17]. The data shown in the picture demonstrate that the variety of gasoline used has no impact on the brake power output of the engine [18]. As the load increases the brake mean effective power also increases and the maximum value is found to be for BD20+100ppm TiO₂.

III.2 MECHANICAL EFFICIENCY

Figure 5 demonstrates that the values of the engine's mechanical efficiency are, for the most part, the same regardless of the load group or the kind of mixture. Displaying an almost linear upward tendency in conjunction with a rising trend as the load rises. The data shown in the picture demonstrate that the variety of gasoline used has no impact on the brake power output of the engine [19]. As the load increases the mechanical efficiency also increases and the maximum value is found to be for BD20+100ppm TiO₂.

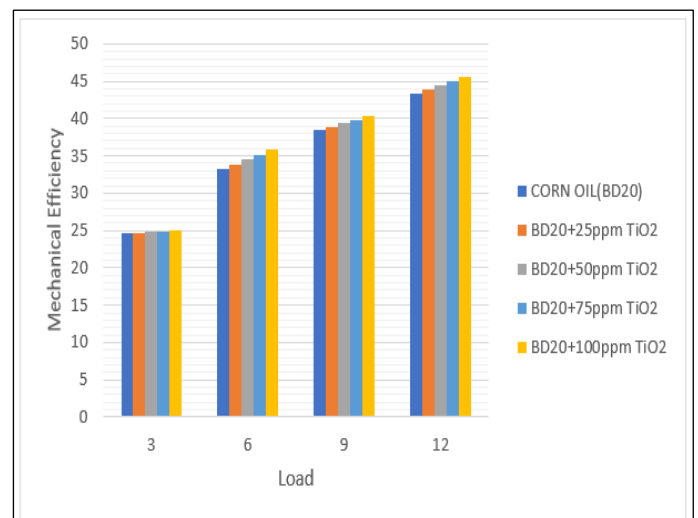


Figure 5: Mechanical Efficiency varying with an increase in load.
Source: Authors, (2024).

III.3 BRAKE THERMAL EFFICIENCY

Figure 6 demonstrates that the values of the engine's brake thermal efficiency are, for the most part, the same regardless of the load group or the kind of mixture. Displaying an almost linear upward tendency in conjunction with a rising trend as the load rises [20]. The data shown in the picture demonstrate that the variety of gasoline used has no impact on the brake power output of the engine [21]. As the load increases the brake thermal efficiency also increases and the maximum value is found to be for BD20+100ppm TiO₂.

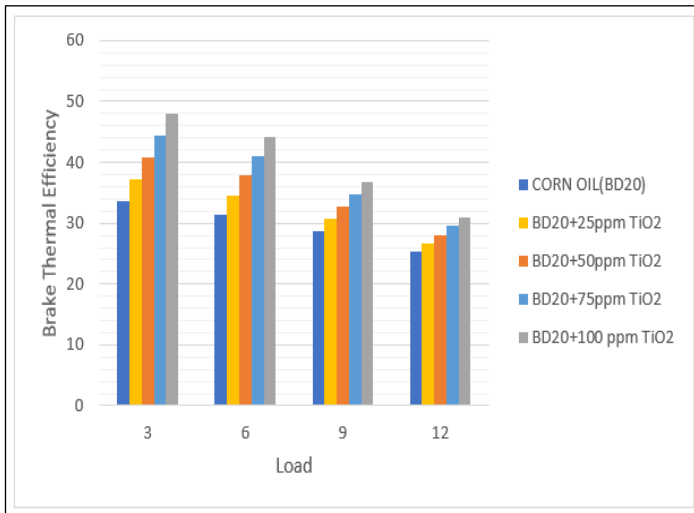


Figure 6: Brake Thermal Efficiency varies with increase in load.
Source: Authors, (2024).

III.4 INDICATED THERMAL EFFICIENCY

Figure 7 demonstrates that the values of the engine's indicated thermal efficiency are, for the most part, the same regardless of the load group or the kind of mixture. Displaying an almost linear downward tendency in conjunction with a rising trend as the load rises. The data shown in the picture demonstrate that the variety of gasoline used has no impact on the brake power output of the engine [22]. As the load increases the indicated thermal efficiency decreases and the minimum value is found to be for BD20+100ppm TiO₂.

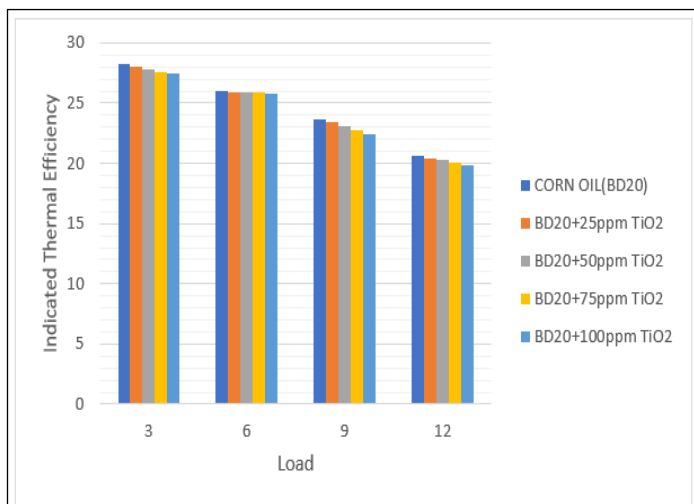


Figure 7: Indicated Thermal Efficiency varying with an increase in load.
Source: Authors, (2024).

III.5 UHC EMISSION TEST

Figure 8 shows that both under low-load and high-load situations, the amounts of UHC (unburnt hydrocarbons) emitted increase, eventually reaching maximum power. Unburnt Hydrocarbon(UHC)emissions are concentrated and rise as a result of the restricted oxygen supply, according to theory. This means the fuel is richer than the fuel-air mixture ratio would indicate. All combinations exhibit a consistent reduction in UHC emission over the operating range, as shown in Figure 4. Plus, compared to the B20 mixture, the emissions from the B20+100ppm TiO₂ combination are significantly lower [23].

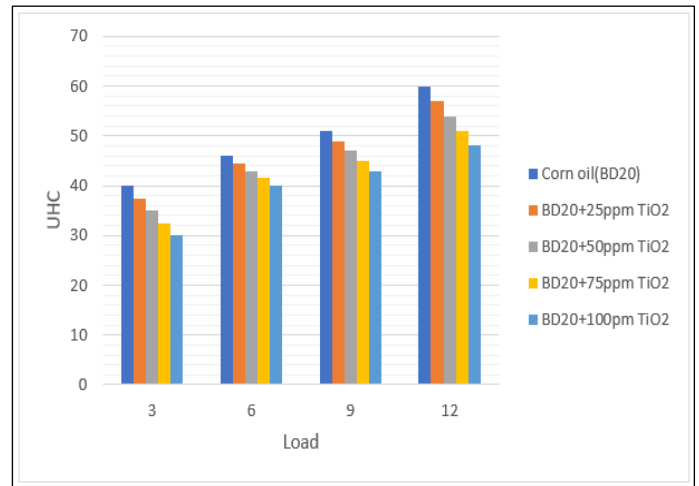


Figure 8: UHC varying with an increase in load.
Source: Authors, (2024).

III.6 CO EMISSION TEST

Carbon monoxide (CO) emissions are positively correlated with increases in all loads, according to the data presented in Figure 9. The data shown above shows a considerable drop of around 20 percent to 25 percent in total CO emissions when using gasoline combined with maize oil biodiesel [18]. Figure 9 illustrates the observed CO emissions corresponding to different loads imposed on the engine using B20 fuel. Carbon monoxide (CO) concentrations, including those in the B20 mix, tend to be highest in the ambient air [24]. One possible strategy to reduce emissions of greenhouse gases is to utilize a B20 biodiesel mix with 100 ppm of TiO₂.

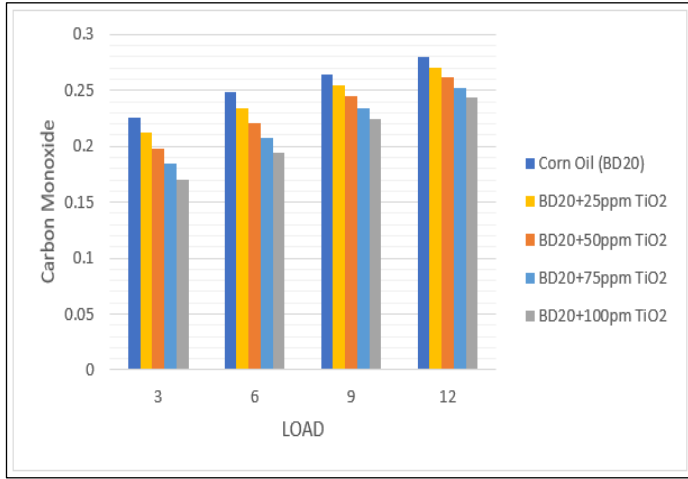


Figure 9: CO varying with an increase in load. Source: Authors, (2024).

III.7 NOX EMISSION TEST

Figure 10 shows that when all loads increase, there is a clear positive link between NOx emissions and those increases. The data shown above shows that there is a significant rise in total NOx emissions when fuel combined with waste cooking oil biodiesel is used. Different loads applied to the engine using B20 gasoline resulted in NOx emissions, as shown in Figure 10. It shows that NOx emissions are rising for all blends over the whole operating range. In addition, compared to the B20 mixture, the combination incorporating 100ppm TiO₂ shows greater emissions [25].

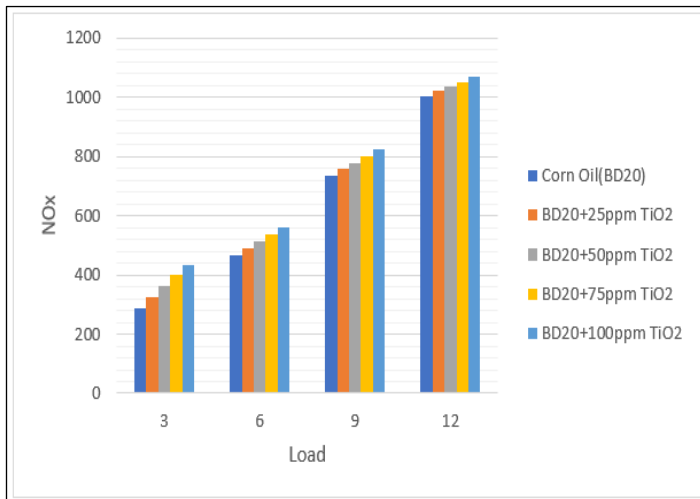


Figure 10: NOx varying with an increase in load. Source: Authors, (2024).

IV. CONCLUSION

As engine load increases, there is a tendency for brake power, brake mean effective pressure, mechanical efficiency, and brake thermal efficiency to rise, particularly when using B20 fuel with 100 ppm TiO₂ nanoparticles. However, this trend is accompanied by a decrease in indicated thermal efficiency, as shown by the trend line. The use of all fuel types shows a decrease in the values of Carbon monoxide and hydrocarbons as the load increases and the value of NOx increases with an increase in the load and the minimum and maximum values for all of them are found to be for B20+100ppm TiO₂. In summary, the BD20 fuel with 100 ppm TiO₂ demonstrated the most favourable results.

Data availability statement

The document includes the evidence that supports the findings of this study.

V. AUTHOR'S CONTRIBUTION

Conceptualization: Raviteja Surakasi, K.Ch. Sekhar and M Jayakrishna.

Methodology: Raviteja Surakasi and K.Ch. Sekhar.

Investigation: Raviteja Surakasi and K.Ch. Sekhar.

Discussion of results: Raviteja Surakasi, K.Ch. Sekhar and M Jayakrishna.

Writing – Original Draft: Raviteja Surakasi.

Writing – Review and Editing: Raviteja Surakasi and K.Ch. Sekhar.

Resources: K.Ch. Sekhar.

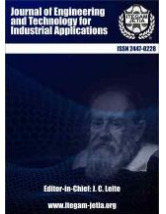
Supervision: K.Ch. Sekhar and M Jayakrishna.

Approval of the final text: Raviteja Surakasi, K.Ch. Sekhar and M Jayakrishna.

VI. REFERENCES

- [1] Chen, Z., Chen, H., Wang, L., et al., 2020. Parametric study on effects of excess air/fuel ratio, spark timing, and methanol injection timing on combustion characteristics and performance of natural gas/methanol dual-fuel engine at low loads. *Energy Conversion and Management* 210, 112742.
- [2] Souad Zighmi, SegniLadjet, Mohamed Bilal Goudjil, Salah Eddine Bencheikh, Renewable Energy from the Seaweed *Chlorella Pyrenoidosa* Cultivated in Developed Systems. *International Journal of Renewable Energy Research* Vol.7, No.1, 2017
- [3] M. Subramaniam, J. M. Solomon, V. Nadanakumar, S. Anaimuthu, and R. Sathyamurthy, "Experimental investigation on performance, combustion and emission characteristics of DI diesel engine using algae as a biodiesel," *Energy Reports*, vol. 6, pp. 1382–1392, 2020.
- [4] Surakasi, Raviteja, Srinivasa Rao, Yenda, Kalam, Sd. Abdul, Begum, Naziya, Emissions and Performance of Diesel Engines Correlated with Biodiesel Properties, *Journal of Engineering*, 2023, 5274325, 4 pages, 2023. <https://doi.org/10.1155/2023/5274325>
- [5] Lee, B., Lee, H., Lim, D., et al., 2020. Renewable methanol synthesis from renewable H₂ and captured CO₂: how can power-to-liquid technology be economically feasible? *Applied Energy* 279, 115827.
- [6] Li, Y., Jia, M., Xu, L., et al., 2020. Multiple-objective optimization of methanol/diesel dual-fuel engine at low loads: a comparison of reactivity-controlled compression ignition (RCCI) and direct dual fuel stratification (DDFS) strategies. *Fuel* 262, 116673.
- [7] Ning, L., Duan, Q., Chen, Z., et al., 2020. A comparative study on the combustion and emissions of a non-road standard rail diesel engine fueled with primary alcohol fuels (methanol, ethanol, and n-butanol)/diesel dual fuel. *Fuel* 266, 117034.
- [8] K. Sunil Kumar, Raviteja Surakasi, S Gopal Krishna Patro, Nikhil Govil, M.K. Ramis, Abdul Razak, Prabhakar Sharma, Majed Alsubih, Saiful Islam, T.M. Yunus Khan, Naif Almakayel, Sanjay Chintakindi, Performance, Combustion, and Emission analysis of diesel engine fuelled with pyrolysis oil blends and n-propyl alcohol-RSM optimization and ML modeling, *Journal of Cleaner Production*, Volume 434, 2024, 140354, ISSN 0959-6526, <https://doi.org/10.1016/j.jclepro.2023.140354>
- [9] Uyumaz, A., 2020. Experimental evaluation of linseed oil biodiesel/diesel fuel blends on combustion, performance, and emission characteristics in a DI diesel engine. *Fuel* 267, 117150.
- [10] K Ch, S., Pakalapati, R., Mugada, B., Kalluri, A., Surakasi, R., & Rodríguez Rico, I. L. (2024). Environmental effects of biodiesel engines fuelled by waste cooking Oil and Metal Nano additives. *ITEGAM- JETIA*, 10(48), 179-183. <https://doi.org/10.5935/jetia.v10i48.1172>

- [11] Chen, C., Yao, A., Yao, C., et al., 2019a. Study of the characteristics of PM and the correlation of soot and smoke opacity on the diesel methanol dual fuel engine. *Applied Thermal Engineering* 148, 391-403.
- [12] Chen, Z., Chen, H., Wang, L., et al., 2020. Parametric study on effects of excess air/fuel ratio, spark timing, and methanol injection timing on combustion characteristics and performance of natural gas/methanol dual-fuel engine at low loads. *Energy Conversion and Management* 210, 112742.
- [13] Thanikodi Sathish, Raviteja Surakasi, Lakshmana Kishore T, Saravanan Rathinasamy, Ümit Ağbulut, Saboor Shaik, Sung Goon Park, Asif Afzal, Waste to fuel: Pyrolysis of waste transformer oil and its evaluation as alternative fuel along with different nanoparticles in CI engine with exhaust gas recirculation, *Energy*, Volume 267, 2023, 126595, ISSN 0360-5442, <https://doi.org/10.1016/j.energy.2022.126595>.
- [14] Gong, C., Li, Z., Chen, Y., et al., 2019. Influence of ignition timing on combustion and emissions of a spark-ignition methanol engine with added hydrogen under lean-burn conditions. *Fuel* 235, 227-238.
- [15] Aswin, C.G., Kumareswaran, A., Lakshmanan, R., Mathavan, S., Andal, V., Lakshmi pathy, R., Rico, Ivan Leandro Rodriguez, Comparative Analysis of NOx Emission Reduction in Engines Using NiCo2O4 Nanoparticles without External Reductant at Low Temperatures: An Experimental Investigation, *Journal of Nanomaterials*, 2022, 8981350, 7 pages, 2022. <https://doi.org/10.1155/2022/8981350>.
- [16] S. S. Reham, H. H. Masjuki, M. A. Kalam, I. Shancita, I. M. Rizwanul Fattah, and A. M. Ruhul, "Study on stability, fuel properties, engine combustion, performance and emission characteristics of biofuel emulsion," *Renewable and Sustainable Energy Reviews*, vol. 52, pp. 1566–1579, 2015.
- [17] Ning, L., Duan, Q., Kou, H., et al., 2020b. Parametric study on effects of methanol injection timing and methanol substitution percentage on combustion and emissions of methanol/diesel dual-fuel direct injection engine at full load. *Fuel* 279, 118424.
- [18] Surakasi Raviteja, Velivela Lakshmikanth Chowdary, "Liquid Fuels Derived from Microalgae: Physicochemical Analysis", *Journal of Engineering*, vol. 2022, Article ID 1293310, 5 pages, 2022. <https://doi.org/10.1155/2022/1293310>.
- [19] Venu, H., Madhavan, V., 2017. Influence of diethyl ether (DEE) addition in ethanol-biodiesel-diesel (EBD) and methanol-biodiesel-diesel (MBD) blends in a diesel engine. *Fuel* 189, 377-390.
- [20] Swarup Kumar Nayak, Sandro Nizetić, Van Viet Pham, Zuohua Huang, Aykut I. Ölçer, Van Ga Bui, Kanit Wattanavichien, Anh Tuan Hoang, Influence of injection timing on performance and combustion characteristics of compression ignition engine working on quaternary blends of diesel fuel, mixed biodiesel, and t-butyl peroxide, *Journal of Cleaner Production*, Volume 333, 2022, 130160, ISSN 0959-6526, <https://doi.org/10.1016/j.jclepro.2021.130160>.
- [21] Wan Nor Maawa Wan Ghazali, Rizalman Mamat, H.H. Masjuki, Gholamhassan Najafi, Effects of biodiesel from different feedstocks on engine performance and emissions: A review, *Renewable and Sustainable Energy Reviews*, Volume 51, 2015, Pages 585-602, ISSN 1364-0321, <https://doi.org/10.1016/j.rser.2015.06.031>.
- [22] Prakhar Chansauria, R.K. Mandloi, Effects of Ethanol Blends on Performance of Spark Ignition Engine-A Review, *Materials Today: Proceedings*, Volume 5, Issue 2, Part 1, 2018, Pages 4066-4077, ISSN 2214-7853, <https://doi.org/10.1016/j.matpr.2017.11.668>.
- [23] Reham S. S., Masjuki H. H., Kalam M. A., Shancita I., Rizwanul Fattah I. M., and Ruhul A. M., Study on stability, fuel properties, engine combustion, performance and emission characteristics of biofuel emulsion, *Renewable and Sustainable Energy Reviews*. (2015) 52, 1566–1579, <https://doi.org/10.1016/j.rser.2015.08.013>, 2-s2.0-84956661058.
- [24] Solmaz H., Combustion, performance and emission characteristics of fusel oil in a spark ignition engine, *Fuel Processing Technology*. (2015) 133, 20–28, <https://doi.org/10.1016/j.fuproc.2015.01.010>, 2-s2.0-84922351894.
- [25] Bergthorson J. M. and Thomson M. J., A review of the combustion and emissions properties of advanced transportation biofuels and their impact on existing and future engines, *Renewable and Sustainable Energy Reviews*. (2015) 42, 1393–1417, <https://doi.org/10.1016/j.rser.2014.10.034>.



RESEARCH ARTICLE

OPEN ACCESS

PREDICTING ACADEMIC PERFORMANCE IN UNIVERSITY STUDENTS USING MACHINE LEARNING

Ernesto Bolaños-Rodríguez*¹, Cristina Flores-Amador², Asdrúbal López-Chau³, Alonso Ernesto Solis-Galindo⁴ and Antonio Zárate-Rosas⁵

^{1,2,4,5} Escuela Superior de Tizayuca-Universidad Autónoma del Estado de Hidalgo. Carretera Federal Tizayuca-Pachuca Km 2.5. 43800. Tizayuca, Estado de Hidalgo, México.

³ Centro Universitario UAEM Zumpango, Universidad Autónoma del Estado de México, 55600, México.

¹ <http://orcid.org/0000-0002-1432-7720>  ² <http://orcid.org/0000-0001-8122-3094> , ³ <http://orcid.org/0000-0001-5254-0930> 

⁴ <http://orcid.org/0000-0002-3999-006X>, ⁵ <http://orcid.org/0009-0005-9851-0992>

Email: ebolanos@uaeh.edu.mx, floresa@uaeh.edu.mx, alchau@uaemex.mx, soliser@uaeh.edu.mx, za447459@uaeh.edu.mx

ARTICLE INFO

Article History

Received: September 26th, 2024

Revised: October 21th, 2024

Accepted: October 22th, 2024

Published: October 31th, 2024

Keywords:

Academic Performance,
Prediction,
Supervised Algorithms,
Machine Learning.

ABSTRACT

In the present research, the prediction of the academic performance of university students of an undergraduate educational program is carried out by applying Machine Learning (ML) with the purpose of determining the students with academic difficulties and excellence in school performance. It is an applied research in a population of 327 students, to which a representative sample of 74 students is determined, using a proportional stratified probability sampling, in which the stratum is the semester the student is studying out of the nine that make up the study plan. The work is an applied study with a pre-experimental design of a single group, because after applying ML the results are observed and the measurements is carried out. The main conclusions obtained allow establishing a methodology for the application of ML methods in the prediction of academic performance. The best performing algorithms used are Support Vector Machine (SVM) and Neural Network (NN).



Copyright ©2024 by authors and Galileo Institute of Technology and Education of the Amazon (ITEGAM). This work is licensed under the Creative Commons Attribution International License (CC BY 4.0).

I. INTRODUCTION

Academic performance is multifactorial in nature [1],[2], because it involves factors endogenous and exogenous to the university student that influence it. Several investigations have been carried out, using inferential statistics, data mining and ML to study the dependent variable academic performance and its relationship with multiple independent variables linked to socioeconomic, cognitive and emotional factors, which have shown that their dependencies are a function of the characteristics of the internal and external context where the student is located, and their implications can vary significantly [3],[4].

Therefore, the objective of this research conducted in a public university for an educational program in economic and administrative sciences is to predict the academic performance of university students through the application of supervised ML algorithms to detect students with school difficulties and those of excellence and thus have an impact on the educational process. For which the following research questions are formulated and

answered in this paper: Which supervised learning methods are most suitable for predicting academic performance, considering survey responses from students as input? How effective is the performance of the best supervised learning method for making this prediction? What kind of data processing is necessary to accurately predict student performance?

The main contributions of the research lie in establishing a methodology for the application of ML methods in the prediction of academic performance, as well as evaluating the performance of supervised algorithms used for this purpose through the metrics of precision, recall and F1-score, which confer reliability and validity to the results obtained.

II. THEORETICAL REFERENCE

II.1 ACADEMIC PERFORMANCE AND IMPLICATIONS

When we talk about academic performance, particularly with undergraduate students, it is oriented to the level of achievement that the student achieves from the criteria established

from the school institutions themselves, where it seeks to address the learning and knowledge from an accurate perspective involving students in various teaching environments, in which different internal and external factors that intervene in the results of the abstract and concrete formative processes are also combined, which can limit or contribute to individual school performance, such as the personality of each subject, the scenarios in which he/she develops, and, mainly, that he/she acquires the appropriate knowledge, competencies and skills that allow him/her to develop in a competitive environment.

Thus, academic performance can be understood as the conjugation of different multicausal factors that affect academic results, in which sociodemographic, psychosocial, pedagogical, institutional and socioeconomic elements interact; among them, elements as varied as: motivation, anxiety, self-esteem, perception of the academic climate, enthusiasm, the teacher, sense of purpose and others [5].

In this sense, there are several components that can be considered in the academic results, which are not always the same, which is why it is an issue that requires full attention to provide an appropriate approach in the training of students based on the dominant knowledge acquired during their academic career, as well as the know-how and know-how to be, coupled with the university values received inside and outside the classroom, accompanied by mastery of appropriate tools, appropriate study habits, an assertive pedagogy and quality in the teaching received by the student body. This can affect the formative development of the student from the emotional aspect, impacting also on the institutional goals of graduation, desertion, backwardness, and the image projected to the outside, since the universities have the purpose of contributing to the insertion of high impact professionals in society, without affecting its positioning as an alternative educational offer.

Thus, academic performance is understood as a student's level of knowledge measured in an evaluation test. In addition to intellectual level, academic performance is influenced by personality variables (extraversion, introversion, anxiety) and motivational variables, whose relationship with academic performance is not always linear, but is modulated by factors such as level of schooling, sex and aptitude. Other variables that influence academic performance are interests, study habits, teacher-student relationship, and self-esteem [6].

In terms of academic performance in higher education, the factors associated with its valuation and the results obtained by university students are based on the sum of quantitative elements that are related to what has been learned and what has been demonstrated to have been learned, whose results derive from a sum of different aspects and activities that are conditioned to the student body for a determined period of time, argued in a systematized context, contextualized in methodologies with pertinent approaches for the achievement of successful results.

In this sense, it can be mentioned that academic performance, being multicausal, involves an enormous explanatory capacity of the different factors and temporal spaces that intervene in the learning process, hence, there are different aspects associated with academic performance, among which both internal and external components of the individual intervene. They can be social, cognitive and emotional, which are classified into three categories: personal determinants, social determinants and institutional determinants, which present subcategories or indicators [7].

The importance for universities of measuring the academic performance of the school community represents the fulfillment of their educational task, commitments and mission to society, and

also allows them to evaluate the quality standards achieved as a public or private educational institution, which largely determines the social image it has. In this way, the results achieved by students progressively during and at the end of their professional training ratifies them to identify with greater precision the knowledge, skills, abilities and knowledge that they have actually received to develop in the labor field, affirming the strengths they have and areas of opportunity that should be improved, which contributes to decision-making from the methodologies applied in the teaching-learning process and in the internal and external factors that influence school performance, which will affect the context in which the graduates are inserted into the labor market.

II.2 MACHINE LEARNING

Machine Learning (ML) is a field of artificial intelligence focused on developing, designing, adapting, or improving algorithms that enable computers to autonomously solve specific tasks. The key tasks in ML include classification, regression, clustering, anomaly detection, and association rules. For this article, supervised algorithms were employed to predict academic performance.

The specific algorithms used in the research are: Logistic Regression (LR), Random Forest (RF), Support Vector Machine (SVM), K-Nearest Neighbors (KNN), Decision Trees (DT) and Neural Network (NN), mainly because they are the most used in the research reported for this purpose [8] and they are the ones that present more possibilities and better performances to predict the response variable (academic performance) from a large number of input data. The main characteristics of each of them are described below in a synthesized form [9],[10]:

Logistic Regression (LR)

It is a type of classification analysis used to predict the outcome of a categorical variable as a function of independent variables.

Random Forest (RF)

It is a data algorithm that can be used in regression or classification tasks, it helps data science to make decisions from a series of questions that allow the final decision.

Support Vector Machine (SVM)

Support Vector Machines is a supervised learning algorithm that is based on finding a hyperplane that best separates different classes of data points. We use a trained SVM regression model due to the low dimensional predictor dataset.

K-Nearest Neighbors (KNN)

It is a nonparametric supervised learning classifier that uses proximity to make classifications and predictions about the clustering of an individual data point.

Decision Trees (DT)

Algorithm used in predictive modeling, which makes forecasts based on the relationships established between input and output data for decision making.

Neural Network (NN)

Neural network models are structured as a series of layers to mimic the way the brain processes information. We use a fully connected feedforward NN. The first layer of the NN has a

connection from the network input (predictor data), and each subsequent layer has a connection from the previous layer. The final fully connected layer produces the output of the network, that is, the predicted response values.

Research on the use of ML in the prediction of academic performance has been reported, among which are those conducted by Chauhan and collaborators (2019) in which a machine learning tool is created to predict the grade point average based on past data. Theory and practice grades are taken, then regression techniques such as KNN, DT, SVM, RF and Linear Regression are applied. As a result, the relevance of comparing techniques to obtain a model with better accuracy, in this case multiple linear regression, is achieved [11].

On the other hand, Canagareddy and collaborators (2018) have proposed predictive models that allow predicting student performance so that corrective actions can be taken. Classification algorithms (NaireBayes, Logistic Classifier and T48 Classifier) and prediction algorithms such as SVM, RF and LR are combined in this study, resulting in this research the algorithm with the highest effectiveness the RF [12].

Also, Burman (2019) investigates how to help students improve their academic performance with the use of applications based on data mining, where a predictive model is created with SVM that allows classifying students into three categories: High, Medium and Low [13].

Finally, Candia (2019) conducts a prediction study of student academic performance from entry data using ML. For the development of the predictive model, the CRISP-DM methodology, the weka tool and demographic and educational factors are considered. RF, KNN and NN algorithms are employed, with RF achieving the best performance [14].

III. MATERIALS AND METHODS

III.1 POPULATION, SAMPLE AND SAMPLING

It is an applied research with a study population of 327 students enrolled in the July-December 2024 school year of the Bachelor's Degree in Tourism from first to ninth semester.

Within this approach, the following statistical mathematical formula is applied to determine the representative sample size of the population. See equation 1, [15]:

$$n = \frac{Z_{\alpha}^2 \cdot N \cdot p \cdot q}{i^2 (N - 1) + Z_{\alpha}^2 \cdot p \cdot q} \quad (1)$$

Where:

n= Sample

N= Size of the population or universe. Having 327 students.

i= Unforeseen or uncontrolled error, takes values from 1 to 10%

p= Probability of success (0.5)

q= Probability of failure (0.5)

Z= Gaussian Normal Curve statistic, at 95% confidence and 5% error. Z = 1.96 [15].

The sample consisted of 74 students, to whom the data collection instrument (designed questionnaire) was applied.

It is using a proportional stratified probability sampling, in which the stratum is the semester the student is studying out of the nine that make up the study plan.

III.2 DATA COLLECTION INSTRUMENT

A 28-question questionnaire is used, considering the following factors: personal, self-concept, motivational, sociocultural, parental education, emotional intelligence, economic, school of origin and average academic performance, which gives validity to the data collection instrument because it measures what it must measure [2-6].

The reliability of the questionnaire was determined by calculating Cronbach's Alpha coefficient with the support of SPSS for Windows Version 26.0.

III.3 METHODOLOGY USED

An Exploratory Data Analysis (EDA) was conducted to uncover potential complexities that could impact the performance of predictive models. Subsequently, the data was processed to address these identified issues. The processing steps included handling missing values, selecting the most relevant features for prediction, and balancing class distributions using the SMOTE algorithm. Additionally, numerical features were standardized by removing the mean and scaling to unit variance, while categorical features were encoded using One-Hot Encoding (OHE), except for the target variable. Python programming language, scikit and imblearn libraries were used.

The target variable is numeric; therefore, it was transformed into a categorical variable using the traditional grading scale employed in Mexican public schools. Consequently, the numeric values were replaced with the following labels: 'Fail', 'Poor', 'Fair', 'Good', 'Very Good', and 'Excellent'. See Table 1.

Table 1: Scale used to categorize the range of average academic performance data.

Score	Category
$0 \leq \text{score} < 6$	'Fail'
$6 < \text{score} \leq 7$	'Poor'
$7 < \text{score} \leq 8$	'Fair'
$8 < \text{score} \leq 9$	'Good'
$9 < \text{score} \leq 9.5$	'Very Good'
$9.5 < \text{score} \leq 10$	'Excellent'

Source: Authors, (2024).

III.4 MACHINE LEARNING FRAMEWORK

Figure 1 illustrates the applied framework. In the methodology, the collected data is split into two sets: a training set and a testing set. The testing set comprises 20% of the data, while the remaining 80% is used for training. The data undergo preprocessing, which involves selecting the most important features, standardizing numerical variables, and applying One-Hot Encoding (OHE) to categorical variables. Additionally, class balancing is performed. The processed data is then used to train classification models. During model training, the optimal parameters for each model are selected using grid search and cross-validation techniques. The best-performing models of each classifier type are then evaluated on the testing set. The testing data is processed using the same techniques as the training set, except for class balancing.

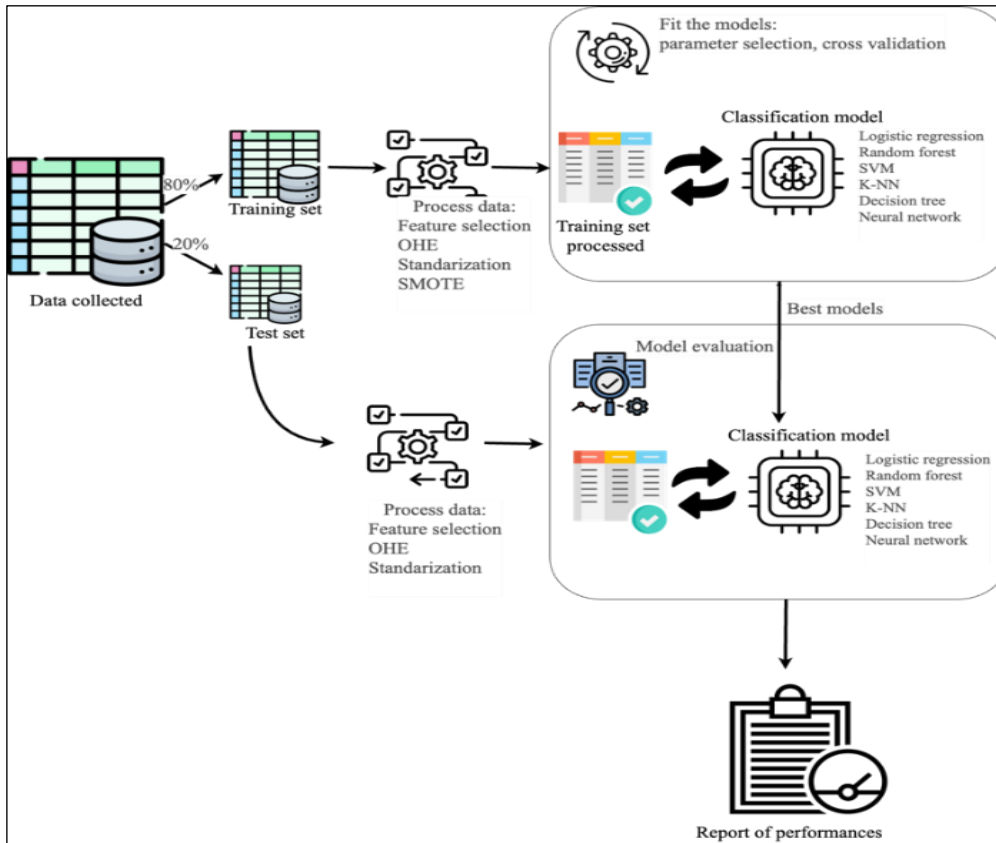


Figure 1: Methodology used for the application of machine learning methods in the prediction of academic performance . Source: Authors, (2024).

Each model is assessed using various metrics, including precision, recall, F1-score, and accuracy. The results are reported in a later section. Accuracy, which consists of obtaining the proportion of correct predictions, both true positives and false positives, over the total number of predictions. This metric is mainly used to measure the overall performance of the whole model. The sensitivity metric, which consists of finding the proportion of true positives over the total number of true positives, is also used to measure the model's ability to correctly identify positive instances. Finally, the F1-score, which is the harmonic mean between accuracy and recall, is used to find which class best predicts the model [16].

IV. RESULTS AND DISCUSSIONS

The results obtained for Cronbach's Alpha Coefficient is 0.93, which means that the questionnaire applied is reliable, i.e. it denotes stability, consistency, minimum errors, in the data collection instrument; if the questionnaire were repeated under the same conditions, the results would be similar. As a result of the exploratory data analysis (EDA), 59 records with complete data were identified and retained, while records with missing data were removed. A significant data imbalance was observed, with "Excellent" being the minority class. Figure 2 illustrates the proportion of each category. This finding is not surprising, as students with excellent academic performance are relatively few. The "Good" performance category is the most prevalent in the dataset. No instances of the "Fail" or "Poor" classes were found.

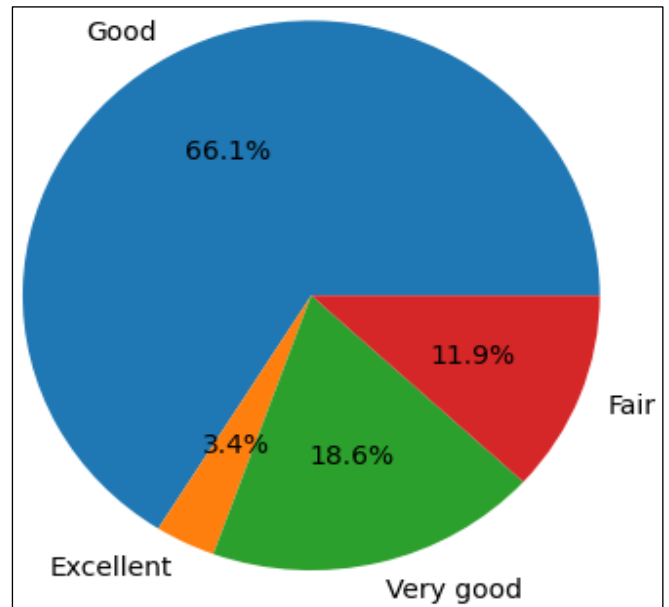


Figure 2: Distribution of academic performance categories in the dataset. Source: Authors, (2024).

The imbalance among the categories led to poor performance in the classification methods, necessitating the balancing of classes within the training dataset. Following the application of the SMOTE algorithm to the training data, the class distribution shown in Figure 3 was achieved, which demonstrates a balanced representation across all categories.

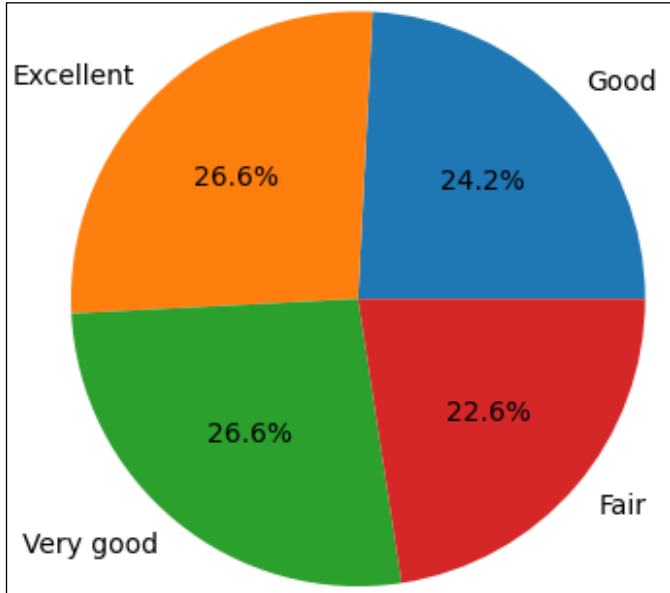


Figure 3: Distribution of categories in the training dataset after applying SMOTE.
Source: Authors, (2024).

Applying the feature selection method, the following attributes were identified as relevant: age, age at the start of the program, semester, weekly study hours, weekly working hours, family members, and monthly income. Other variables were excluded. All categorical variables were encoded using One-Hot Encoding (OHE), while numerical variables were standardized. This process resulted in a dataset with 70 attributes.

The results of the six evaluated classifiers are presented below in Tables 2-7. The models that achieved perfect prediction (100%) are the Support Vector Machine (SVM) and the Neural Network. The second-best classifier is Random Forest, with an accuracy of 88%. K-Nearest Neighbors and Decision Tree classifiers were the models with the lowest performances.

Table 2: Performance of Logistic Regression classifier with optimal parameter C=1.0.

	Precision	Recall	F1-score
Excellent	1.00	1.00	1.00
Fair	0.79	1	0.88
Good	1.00	0.44	0.62
Very good	0.75	1.00	0.86
Accuracy	-	-	0.84
macro avg	0.88	0.86	0.84
weighted avg	0.88	0.84	0.82

Source: Authors, (2024).

Table 3: Performance of Random Forest classifier with parameters n_estimators=50.

	Precision	Recall	F1-score
Excellent	1.00	0.83	0.91
Fair	1.00	1.00	1.00
Good	0.78	0.78	0.78
Very good	0.71	0.83	0.77
accuracy	-	-	0.88
macro avg	0.87	0.86	0.86
weighted avg	0.88	0.88	0.88

Source: Authors, (2024).

Table 4: Performance of Support Vector Machine classifier with parameters 'C'=1, kernel=rbf, gamma=0.1.

	Precision	Recall	F1-score
Excellent	1.00	1.00	1.00
Fair	1.00	1.00	1.00
Good	1.00	1.00	1.00
Very good	1.00	1.00	1.00
accuracy	-	-	1.00
macro avg	1.00	1.00	1.00
weighted avg	1.00	1.00	1.00

Source: Authors, (2024).

Table 5: Performance of K-Nearest Neighbors classifier with parameters n_neighbors=3, weights=distance.

	Precision	Recall	F1-score
Excellent	0.86	1.00	0.92
Fair	0.85	1.00	0.92
Good	1.00	0.11	0.20
Very good	0.55	1.00	0.71
accuracy	-	-	0.75
macro avg	0.81	0.78	0.69
weighted avg	0.84	0.75	0.68

Source: Authors, (2024).

Table 6: Performance of Decision Tree classifier with parameters max_depth=10, min_samples_split=10.

	Precision	Recall	F1-score
Excellent	1	0.83	0.91
Fair	0.91	0.91	0.91
Good	0.67	0.67	0.67
Very good	0.57	0.67	0.62
Accuracy	-	-	0.78
macro avg	0.79	0.77	0.78
weighted avg	0.79	0.78	0.79

Source: Authors, (2024).

Table 7: Performance of Neural Network classifier with parameters activation=ReLu, hidden_layer_sizes=(100, 100, 100), max_iter=500, solver=adam.

	Precision	Recall	F1-score
Excellent	1.00	1.00	1.00
Fair	1.00	1.00	1.00
Good	1.00	1.00	1.00
Very good	1.00	1.00	1.00
accuracy	-	-	1.00
macro avg	1.00	1.00	1.00
weighted avg	1.00	1.00	1.00

Source: Authors, (2024).

In this way, the questions posed at the beginning of this article are answered below.

Which supervised learning methods are most suitable for predicting academic performance, considering survey responses from students as input? The most suitable methods are SVM and NN.

How effective is the performance of the best supervised learning method for making this prediction? The two best supervised learning methods are SVM and NN, achieving perfect performance according to the metrics used to measure their effectiveness.

What kind of data processing is necessary to accurately predict student performance? It is necessary to conduct an exploratory data analysis (EDA) to identify potential complexities, and it is also advisable to address them properly. Additionally, choosing an appropriate encoding for categorical variables is important.

V. CONCLUSIONS

A methodology is established for the application of ML methods in the prediction of academic performance. It is possible to predict the academic performance of university students with the application of the supervised algorithms of Support Vector Machine (SVM) and the Neural Network, which have the best performances with respect to metrics precision, recall, F1-score and accuracy, followed by Random Forest, with an accuracy of 88%, while. K-Nearest Neighbors and Decision Tree classifiers were the models with the lowest performances. This will allow us to detect students with school difficulties in order to carry out actions that will have an effective impact on the educational process through strategies such as: academic counseling, tutoring, psychological care and financial support through scholarships, on the other hand, by predicting the students of excellence we will be able to follow them so that these students can participate in professional competitions and perform national and international mobility to Higher Education Institutions of prestige and recognition that will give visibility to our undergraduate educational program under study.

VI. AUTHOR'S CONTRIBUTION

Conceptualization: Ernesto Bolaños-Rodríguez and Asdrúbal López-Chau.

Methodology: Asdrúbal López-Chau, Alonso Ernesto Solis-Galindo and Antonio Zárate-Rosas.

Investigation: Ernesto Bolaños-Rodríguez, Cristina Flores-Amador, Asdrúbal López-Chau, Alonso Ernesto Solis-Galindo and Antonio Zárate-Rosas.

Discussion of results: Ernesto Bolaños-Rodríguez and Asdrúbal López-Chau.

Writing – Original Draft: Ernesto Bolaños-Rodríguez.

Writing – Review and Editing: Ernesto Bolaños-Rodríguez and Cristina Flores-Amador.

Resources: Cristina Flores-Amador.

Supervision: Cristina Flores-Amador and Asdrúbal López-Chau.

Approval of the final text: Ernesto Bolaños-Rodríguez, Cristina Flores-Amador, Asdrúbal López-Chau, Alonso Ernesto Solis-Galindo and Antonio Zárate-Rosas.

VII. ACKNOWLEDGMENTS

We would like to thank the directors, professors and students who collaborated in the development of this research at the Universidad Autónoma del Estado de Hidalgo and the Universidad Autónoma del Estado de México.

VIII. REFERENCES

[1] A. Chilca, 2017, Self-esteem, study habits and academic performance in college students. [Online]. Available at https://revistas.usil.edu.pe/index.php/index/oai?verb=ListRecords&metadataPrefix=oai_dc&set=pyr:ART+INV

[2] G.M. Garbanzo Vargas, "Factors associated with academic performance in university students, a reflection on the quality of public higher education", *Education Journal*, vol. 31, no. 1, p. 43, 2012.

https://www.scielo.sa.cr/scielo.php?pid=S1409-42582013000300004&script=sci_abstract

[3] C.E. López Guarín, E.L. Guzmán & F.A. González, "A Model to Predict Low Academic Performance at a Specific Enrollment Using Data Mining", *Iberoamerican Journal of Learning Technologies*, vol. 10, no. 3, pp. 119-125, 2015. doi: [10.1109/RITA.2015.2452632](https://doi.org/10.1109/RITA.2015.2452632)

[4] A. Mueen, B. Zafar & U. Manzoor, "Modeling and Predicting Students Academic Performance Using Data Mining Techniques. International", *Journal of Modern Education and Computer Science*, vol. 8, no. 11, pp. 36-42, 2016. doi: [10.5815/ijmecs.2016.11.05](https://doi.org/10.5815/ijmecs.2016.11.05)

[5] E. Montero Rojas, J. Villalobos Palma & A. Valverde Bermudez, "Institutional, pedagogical, psychosocial and sociodemographic factors associated with academic performance and student repetition at the University of Costa Rica", *Institute of Psychological Research, University of Costa Rica*, 2004. doi: <https://doi.org/10.7203/relieve.13.2.4208>

[6] F. Fajardo Bullón, M. Maestre Campos, E. Felipe Castaño, B. León del Barco, & M.I. Polo del Río, "Analysis of the academic performance of students in compulsory secondary education according to family variable", *Education XXI*, vol. 20, no. 1, pp. 209-232, 2017. doi: [10.5944/educXXI.14475](https://doi.org/10.5944/educXXI.14475)

[7] S. Pelegrina, M.C. García & P. F. Casanova, "Parenting styles and adolescents' academic performance", *Electronic Journal USAL*, vol. 25, no. 2, pp. 147-168, 2002. doi: <https://doi.org/10.1174/021037002317417796>

[8] V.L. Uskov, J.P. Bakken, A. Byerly & A. Shah, "Machine Learning-based Predictive Analytics of Student Academic Performance in STEM Education", *IEEE Global Engineering Education Conference (EDUCON)*, Dubai, United Arab Emirates, 2019, pp. 1370-1376, 2019. doi: [10.1109/EDUCON.2019.8725237](https://doi.org/10.1109/EDUCON.2019.8725237)

[9] E. Bolaños Rodríguez, J.C. González Islas, O. López Ortega & E. Lezama León, "Application of Machine Learning for the Prediction of Atmospheric Corrosion in the Metropolitan Area of Mexico City", *Journal of Engineering and Technology for Industrial Applications*, vol. 10, no. 48, p. 36-42, July-August, 2024. doi: <https://doi.org/10.5935/jetia.v10i48.1089>

[10] L. Breiman, "Random Forests", *Machine Learning*, vol. 45, pp. 5-32, 2001. <https://doi.org/10.1023/A:1010933404324>

[11] N. Chauhan, K. Shah, D. Kam & J. Dalal, "Prediction of Students Performance Using Machine Learning", *SSRN Electronic Journal*, 2019. doi: <https://dx.doi.org/10.2139/ssrn.3370802>

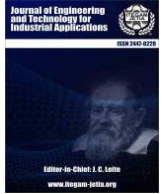
[12] D. Canagareddy, K. Subarayadu & V. Hurbungs, 2018, A Machine Learning Model to Predict the Performance of University Students [Online]. S.I. Springer International Publishing. https://doi.org/10.1007/978-3-030-18240-3_29

[13] I. Burman & S. Som, "Predicting Students Academic Performance Using Support Vector Machine", *Proceedings-2019 Amity International Conference on Artificial Intelligence*, pp. 756-759, AICAI 2019. doi: <https://doi.org/10.1109/AICAI.2019.8701260>

[14] D. I. Candia Oviedo, 2019, Predicting the Academic Performance of UNSAAC students from their entrance data using machine learning algorithm, *National University of San Antonio Abad del Cusco* [Online] pp.141. Available at: <https://repositorio.unsaac/4120>

[15] J.T. McClave, P.G. Benson & T. Sincich, *Statistics for Business and Economics*, Pearson, Florida, 2022. https://api.pageplace.de/preview/DT0400.9781292413525_A42820209/preview-9781292413525_A42820209.pdf

[16] R. Borja Robalino, A. Monleon Getino & J. Rodellar, "Standardization of performance metrics for Machine and Deep Learning classifiers", *Iberian Journal of Information Systems and Technologies*, vol. 30, pp. 184-196, 2020. <https://www.researchgate.net/publication/339943922>



RESEARCH ARTICLE

OPEN ACCESS

APPLYING PROPORTIONAL–INTEGRAL–DERIVATIVE CONTROLLERS ON WIRED NETWORK TCP'S QUEUE TO SOLVE ITS INCOMPATIBILITY WITH THE WIRELESS AD-HOC NETWORK





Yaser Ali Enaya¹, Salam Waley Shneen², Mohammed Qasim Sulttan³ and Abdulmir Abdullah Karim⁴

¹ Department of Electro Mechanical Engineering, University of Technology, Iraq

² Energy and Renewable Technology Center, University of Technology, Iraq

³ Department of Electro Mechanical Engineering, University of Technology, Iraq

⁴ Computer Science Department, University of Technology, Iraq

¹<http://orcid.org/0000-0002-0669-1282> , ²<http://orcid.org/0000-0003-3718-6104> , ³<http://orcid.org/0000-0002-2397-1716> , ⁴<http://orcid.org/0000-0002-8420-568> 

Email: *50111@uotechnology.edu.iq, salam.w.shneen@uotechnology.edu.iq, mohammed.q.mohammed@uotechnology.edu.iq, abdulmir.a.karim@uotechnology.edu.iq

ARTICLE INFO

Article History

Received: September 27th, 2024

Revised: October 18th, 2024

Accepted: October 25th, 2024

Published: October 31th, 2024

Keywords:

Ad-hoc,
TCP,
PI,
PD,
PID.

ABSTRACT

This paper offers a solution to the problem of incompatibility of the TCP designed for networks with fixed routers and the Ad-hoc network, which sometimes its mobile hosts act as routers causing a routing failure. In order to overcome this obstacle, this work presents three Ad-hoc TCP novels. The first novel is adding a controller to Ad-hoc TCP queues; this controller works as a memory in the TCP's queue by saving the change rate of the previous error signals, then using it as a measure to change future error signal conduct. The second one is a comparison among the three Ad-hoc TCPs, which use different controllers, TCP PI/PD/PID. Finally, the models show promising results since all three Ad-hoc TCPs' results surpass the traditional TCP's result. Besides, the comparison process specified the best Ad-hoc TCP among the three, and that is the TCP/PID with Rise Time=3.472 ms, Overshoot=5.851%, Undershoot=-0.8264%, and Setting Time = 0.15 sec.



Copyright ©2024 by authors and Galileo Institute of Technology and Education of the Amazon (ITEGAM). This work is licensed under the Creative Commons Attribution International License (CC BY 4.0).

I. INTRODUCTION

The wireless Ad-hoc Network inconsistency with the fixed wire communication infrastructure has become a headache in the last years, especially in Mobile Ad-hoc [1]. So because of the dynamic nature of Mobile Ad-hoc, which leads to unpredictable behavior, communication becomes insufficient [2]. One of the inconsistency problems is that the TCP cannot recognize between the lost packet and the route failure and considers both of them as congestions. Therefore, the TCP shows a tendency for a lower rate compared to the network transmission rate [3]. TCP responsibilities are delivering packets from the recourse to the destination in the same order without packets' gaps and with errors-free, fixing the congestion, and controlling the data flow [4]. To specify the transmission rate to control the congestions and data flow, the TCP must get feedback from the receivers [5]. Therefore, the researchers try to apply a new algorithm that is called the Active Queue Management algorithm (AQM) to the traditional TCP to

overcome these problems [6],[7]. The most important AQMs' functions are early congestion discovery and network status reporting; this is done whenever the router's queue reaches the limit by signaling incoming packets [8-10]. Then, AQM provides feedback packets to the source as soon as getting an overflowing notification, so the source takes the right actions [11],[12]. It is true that AQM is an effective mechanization for detecting early congestion and giving a prior alert of the current state of the network by signaling incoming packets before router queues fill up, but its current algorithms have main problems. For example, because of the understanding of different systems' dynamics requirements of the RED algorithm, this algorithm becomes unsteady and sensible to the controlling factors of the network [8]. Therefore, many researchers have been trying to improve the AQM by applying different expert systems and controllers, such as genetic algorithm, fuzzy neural networks, proportional controllers, etc. Wherefore, many analyses and works cover the AQM schemes, such as solving the AQM problems by integrating the backstepping

II.2 TCP/PI CONTROLLER

Figure 2 is the PI controller diagram that is performed by the Ad-hoc TCP network.

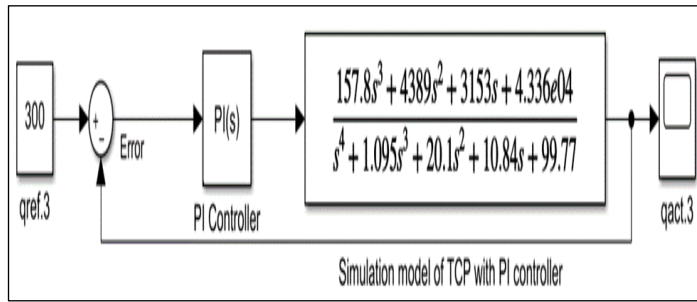


Figure 2: The simulation model of PI controller for Ad-hoc TCP network.

Source: Authors, (2024),

The aim of adding the proportional controllers in general and PI controller in particular to the AQM is to rise the efficiency of the router functionalities via supporting the queue by decreasing the loss and delay of the packets and increasing throughput. PI is usually used in industrial fields. When it is applied as a part of the TCP controller, the signal is proportioned to the gain and error integrals. Besides, its integral process removes the steady state error in the TCP system [32-34]. The below equation, eq. (5), is applied by the PI:

$$u(t) = k_p e(t) + ki \int e(t)dt \quad (5)$$

where: k_p , k_i : proportional and integral gain constants respectively.

$e(t)$: I/O error signal
 $u(t)$: PI output

II.3 TCP/PD CONTROLLER

PD task is taking the right actions to change the next error signal conduct by measuring the change rate of the previous error signals, which is proportional to the control signal. As a result, the transient response and system stability are improving, and the overshoot is decreasing [35]. Eq. (6) represents. The general formula of the PD controller applied by this study in the TCP Ad-hoc network:

$$u(t) = k_p e(t) + k_d \frac{de(t)}{dt} \quad (6)$$

Where k_d is the derivative gain constants.

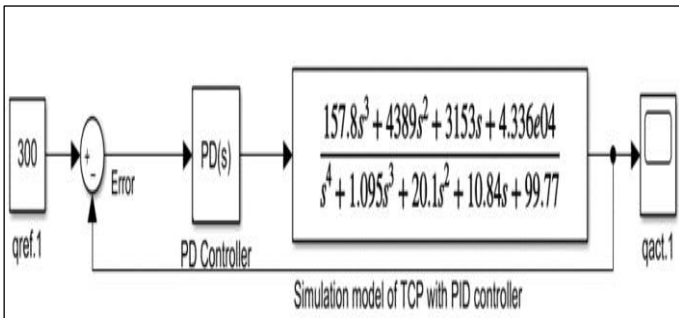


Figure 3: The simulation model of PD controller for Ad-hoc TCP network.

Source: Authors, (2024).

II.4 TCP/PID CONTROLLER

A PID is a tool that is utilized by industrial processes to manage their variables such as speed, flow, and pressure. The PID Controller consists of two control techniques: First, the D control technique, which has a feedback loop technique to keep the PID process variables under control. Second, the I control technique, which supports the D control technique to enhance the prediction of the PID controller and controls the buffer overflow [35-38]. These two techniques are illustrated in Figure 4. In this work, the below PID's eq. (7) is used in the TCP for Ad-hoc network:

$$u(t) = k_p e(t) + ki \int e(t)dt + k_d \frac{de(t)}{dt} \quad (7)$$

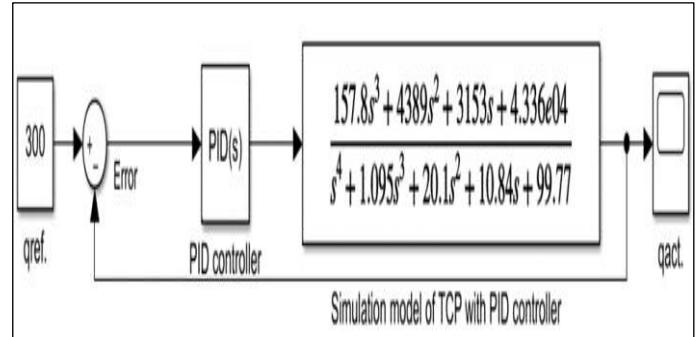


Figure 4: The simulation model of PID controller for Ad-hoc TCP network.

Source: Authors, (2024).

III. SIMULATION RESULTS

This simulation is an illustration of the efficiency of applying the controllers on the TCP's queue dedicated to Ad-hoc network by comparing three controllers, PI, PD, and PID, put in the TCP queue system. A MATLAB Software is utilized to decide the competence of the assumed controller and assesses its vulnerability to avoiding network overcrowding. Before the comparison between the three TCP/Controllers, fig. 5 represents the regular TCP's queue which shows the extreme congestion of the queue, and the nonfulfillment of the queue length specifications.

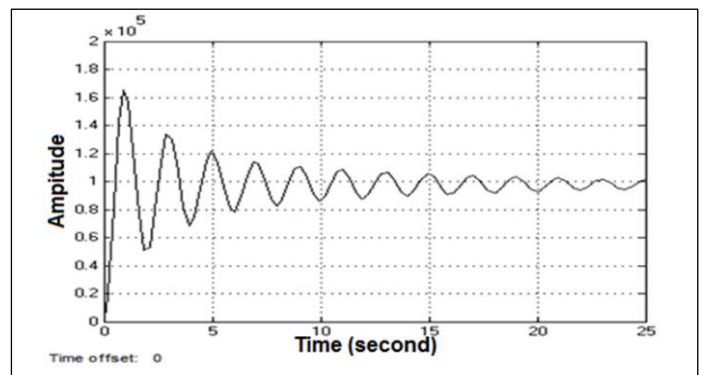


Figure 5: The TCP's queue without a controller.
 Source: Authors, (2024).

The software is applied on the TCP's queue system, which includes one of the three controllers, then the process is repeated on the next system and so on, as shown in fig. 6, which actually, represents three figures in one:

- 1-TCP/PI Controller (dotted curve).
- 2-TCP/PD Controller (dashed curve).
- 3-TCP/PID Controller (continuous curve).

The MATLAB displays many given parameters for each controller, as can be seen in fig. 6, and fig. 7, but for comparison purposes, the Rise Time, Overshoot, Undershoot, and Setting Time parameters give the information that specifies the best TCP/Controller system for the Ad-hoc network among the three controllers.

Now, assume that the Ad-hoc network has a bottleneck with 16 Mb/s in 26 msec between two mobiles that act as hosts and routers at the same time, and they join to a bunch of receivers and transmitters. Based on Eqs. 1 and 2, take the Ad-hoc network factors: capacity link =16 Mb/sec; promulgation delay=0.22 sec; Full-trip time =0.26 sec; load factor =60; in demand queue size =300 packets; and maximum queue length (at the sender) =740 packets. By applying these factors in the simulation model, the output results can be seen in figures 6 and 7, which are actually a comparison between the three TCP systems.

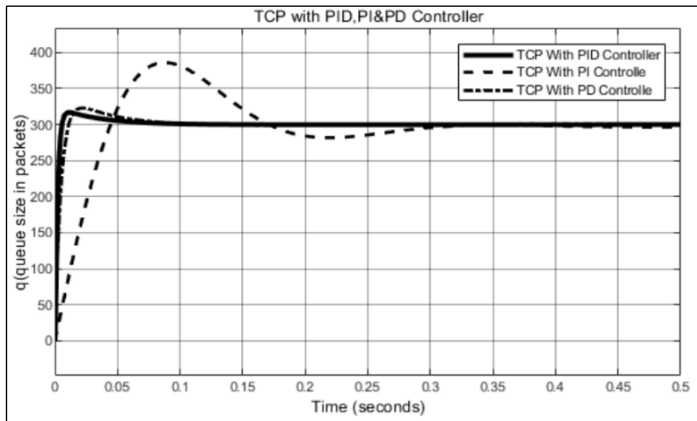


Figure 6: Three TCP Queue Systems, TCP with PI/PD/PID Controllers.
Source: Authors, (2024).

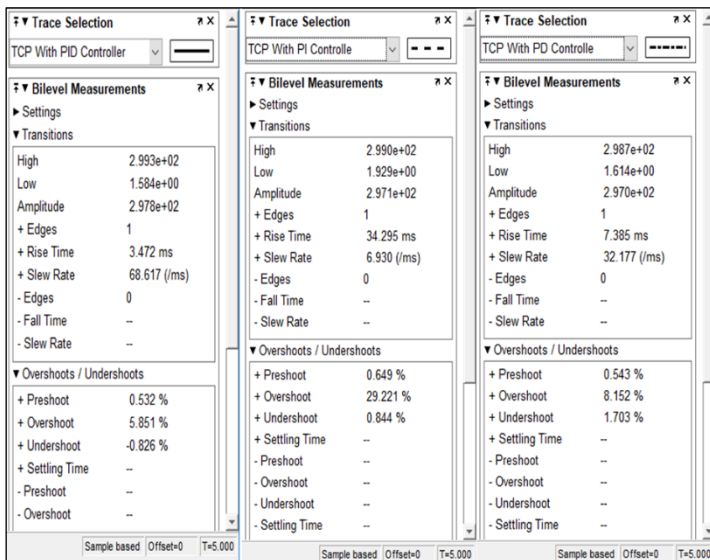


Figure 7: Given OutPut Parameters of TCP/PI, TCP/PD, and TCP/PID Controllers.
Source: Authors, (2024).

From Figure 7, the most important parameters (Rise Time (ms), Overshoot %, Undershoot %, and Setting Time (ms)) have been extracted as follows:

The Rise Time parameter is the time that the controller needs to reach 70% of the queue steady state = $0.7 \times 300 = 210$, so the Rise Times are 34.295, 7.385, and 3.472 for PI, PD, and PID,

respectively. Therefore, TCP/PID system has the fastest Rise Time with 3.472 ms. For the two parameters Overshoot and Undershoot, the one with the closest peak to the steady state is the best parameter, so the Overshoots are 29.221, 8.152, and 5.851 for PI, PD, and PID, respectively. And the Undershoots are 0.844, 1.703, and -0.8264 for PI, PD, and PID, respectively. Again, TCP/PID controller with Overshoot 5.851% and Undershoot -0.8264% precedes the other two controllers. With the last parameter, the PI's Setting Time = 0.155, the PD's Setting Time = 0.35, and the PID's Setting Time = 0.15. Finally, the fastest controller's Setting Time = 0.15 sec is held by the TCP/PID controller as well.

IV. CONCLUSION

- 1-The TCP/PI model has the slowest speed response and the lowest stability of the three TCPs models.
- 2-Because of the D mode property of correcting the near future error signal path, the PD and the PID controllers improve the response time of the Ad-hoc TCPs.
- 3-PI, PD, and PID controllers are reliable devices to guess and manage the future TCP's error signal because of the feedback system.
- 4-D mode enables the TCP/PD and TCP/PID models to avoid queue overflow.
- 5-The reason that the TCP/PID model has better performance than the TCP/PD model is because of the I mode in PID which its integral process removes the steady state error in the TCP system and this will boost the prediction property of the D mode.
- 6-The simulation results manifest that the three TCP controller models (PI, PD, PID) to manage the TCP/Ad-hoc network inconsistency outperform conventional TCP.
- 7-The TCP/ controller models in this work are imperative to develop the Ad-hoc networks since applying these models on mobile devices that connect to Ad-hoc networks makes them reliable routers to extend the Ad-hoc covering area.

VII. AUTHOR'S CONTRIBUTION

Conceptualization: Yaser Ali Enaya, SalamWaley
Methodology: Yaser Ali Enaya, Mohammed Qasim
Investigation: Yaser Ali Enaya, Mohammed Qasim
Discussion of results: Yaser Ali Enaya, SalamWaley
Writing – Original Draft: Yaser Ali Enaya, SalamWaley
Writing – Review and Editing: Abdulmir Abdullah Karim.
Supervision: Abdulmir Abdullah Karim, Mohammed Qasim
Approval of the final text: Abdulmir Abdullah Karim

VIII. REFERENCES

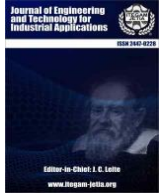
[1] Shi, Chenchao, Biqian Feng, Yongpeng Wu, and Wenjun Zhang. "A preamble-based MAC mechanism in ad-hoc network." *Journal of Communications and Information Networks* 7, no. 1 (2022): 60-71. <https://doi.org/10.23919/JCIN.2022.9745482>

[2] Yaser Ali Enaya. "Password-free Authentication for Smartphone Touchscreen Based on Finger Size Pattern", *International Journal of Interactive Mobile Technologies*, vol. 14, no. 19, 2020, pp. 163–179. DOI: 10.3991/ijim.v14i19.17239.

[3] Jayan, Bijili, Tamilarasi Ganesan, and Binu Bhaskara Kurup. "Enhancing iot network security through advanced data preprocessing and hybrid firefly-salp swarm optimized deep CNN-based intrusion detection." *ITEGAM-JETIA* 10, no. 47 (2024): 73-82. DOI: <https://doi.org/10.5935/jetia.v10i47.1096>

[4] João Ricardo Paes de Barros and Dimitri Albuquerque de Barros. "Modified Bat Algorithm for transmission network expansion planning considering active power losses " *ITEGAM-JETIA*, Manaus, v.9n.39, p. 19-32. Jan/Feb, 2023. DOI: <https://doi.org/10.5935/jetia.v9i39.844>.

- [5] Rahouma, K. H., Abdul-Karim. "TCP/IP Network Layers and Their Protocols (A Survey).", In *Internet of Things—Applications and Future*, Springer, volume 114 (2020) (pp. 287-323), DOI: 10.1007/978-981-15-3075-3_21.
- [6] Shneen, S. W., Sulttan, M. Q., & Oudah, M. K. Design and implementation of a stability control system for TCP/AQM network. *Indonesian Journal of Electrical Engineering and Computer Science*, 22(1), (2021): 129-136. DOI: 10.11591/ijeecs.v22.i1.pp129-136.
- [7] Aziz, G. A., Jaber, M. H., Sulttan, M. Q., & Shneen, S. W. Simulation Model of Enhancing Performance of TCP/AQM Networks by Using Matlab. *Journal of Engineering & Technological Sciences*, 54(4) (2022). DOI: 10.5614/j.eng.technol.sci.2022.54.4.4.
- [8] Jaber, Manal Hadi, et al. "BBO tuned PI controller for the stability of TCP networks." *TELKOMNIKA (Telecommunication Computing Electronics and Control)* 21.2 (2023): 264-271.
- [9] Li, Z. H., Liu, Y. "Active Queue Management Algorithm for TCP Networks with Integral Backstepping and Minimax.", *International Journal of Control, Automation and Systems*, Springer, vol. 17, no. 4, 2019, pp. 1059-1066. DOI: 10.1007/s12555-018-0447-5.
- [10] Domański, Adam, Joanna Domańska, Tadeusz Czachórski. "The IoT gateway with active queue management.", *International Journal of Applied Mathematics and Computer Science* 31, no. 1 (2021). DOI: 10.34768/amcs-2021-0012.
- [11] Bisoy, Sukant Kishoro, and Prasant Kumar Pattnaik. "Design of feedback controller for TCP/AQM networks.", *Engineering science and technology, an international journal* 20, no. 1 (2017): 116-132. DOI: 10.1016/j.jestech.2016.10.002.
- [12] Belamfedel Alaoui, Sadek, El Houssaine Tissir, and Noredine Chaibi. "New design of anti-windup and dynamic output feedback control for tcp/aqm system with asymmetrical input constraints.", *International Journal of Systems Science* 52, no. 9 (2021): 1822-1834. DOI: 10.1080/00207721.2020.1871108.
- [13] Ma, Lujian, Xiaoping Liu, Huanqing Wang. "Congestion tracking control for wireless tcp/aqm network based on adaptive integral backstepping.", *International Journal of Control, Automation and Systems* 18, Springer, no. 9 (2020): 2289-2296. DOI: 10.1007/s12555-019-0724-y.
- [14] Giménez, Angel, Miguel A. Murcia. "New RED-type TCP-AQM algorithms based on beta distribution drop functions.", arXiv preprint arXiv:2201.01105 (2022). arXiv: arXiv:2201.01105.
- [15] M Kadhim, Hanan, Ahmed A Oglah. "Congestion Avoidance and Control in Internet Router Based on Fuzzy AQM.", *Engineering and Technology Journal* 39, no. 2 (2021): 233-247. DOI: 10.30684/etj.v39i2A.1799.
- [16] Alli-Oke, R. Olusegun. "On the validity of numerical simulations for control-theoretic AQM schemes in computer networks.", *Mathematics and Computers in Simulation* 193 (2022): 466-480. DOI: 10.1016/j.matcom.2021.10.016.
- [17] Patel, K.N., Pavanam, C. Sprint Communications Co LP. "Transmission control protocol (TCP) based control of a wireless user device.", U.S. Patent 10,623,980 (2020).
- [18] Ali, Majid Hamid, Serkan Öztürk. "Automation Based Active Queue Management using Dynamic Genetic Algorithm in Real-Time Application.", *Journal of Information Science & Engineering*, volume 37, no. 6 (2021) pp 1313-1226. Retrieve PDF document: JISE_202106_06.pdf.
- [19] Kramer, Oliver. "Genetic algorithms." In *Genetic algorithm essentials*, Springer, Cham, volume 679, 2017, pp. 11-19. DOI: 10.1007/978-3-319-52156-5_2.
- [20] Molia, H. K., Kothari, A. D. "Fuzzy Logic Systems for Transmission Control Protocol", In *Proceedings of the 2nd International Conference on Communication, Devices and Computing*, Springer, Singapore, volume 602, (2020), (pp. 553-565). DOI: 10.1007/978-981-15-0829-5_53.
- [21] Ponticelli, Gennaro Salvatore. "An optimized fuzzy-genetic algorithm for metal foam manufacturing process control.", *The International Journal of Advanced Manufacturing Technology*, 101, (2019), 603-614. DOI: 10.1007/s00170-018-2942-5.
- [22] Roslan, M. F., Ali Q. Al-Shetwi, M. A. Hannan. "Particle swarm optimization algorithm-based PI inverter controller for a grid-connected PV system.", *PLoS one*, 16(10), (2021). DOI: 10.1371/journal.pone.0259358.
- [23] Bansal, Jagdish Chand. "Particle swarm optimization." In *Evolutionary and swarm intelligence algorithms*, Springer, Cham, vol 779, (2019) (pp. 11-23). DOI: 10.1007/978-3-319-91341-4_2.
- [24] Merai, Meriem, Mohamed Wissem Naouar. "An adaptive PI controller design for DC-link voltage control of single-phase grid-connected converters.", *IEEE Transactions on Industrial Electronics*, 66(8), (2018), p6241-6249. DOI: 10.1109/TIE.2018.2871796.
- [25] Ranjbaran, K., Tabatabaei, M. "Fractional order [PI],[PD] and [PI][PD] controller design using Bode's integrals.", *International Journal of Dynamics and Control*, Springer, 6(1), (2018), 200-212. DOI: 10.1007/s40435-016-0301-7.
- [26] Dabiri, A., Moghaddam, B. P. "Optimal variable-order fractional PID controllers for dynamical systems.", *Journal of Computational and Applied Mathematics*, vol. 339, (2018), 40-48. DOI: 10.1016/j.cam.2018.02.029.
- [27] Zhao, C., & Guo, L. "PID controller design for second-order nonlinear uncertain systems.", *Science China Information Sciences*, 60(2), Article number 022201, (2017). DOI: 10.1007/s11432-016-0879-3.
- [28] Bejarbaneh, Elham Yazdani, Ahmad Bagheri. "A new adjusting technique for PID type fuzzy logic controller using PSOSCALF optimization algorithm.", *Applied Soft Computing*, vol. 85, no. 105822, (2019). DOI: 10.1016/j.asoc.2019.105822.
- [29] Enaya, Yaser Ali, and Kalyanmoy Deb. "Network path optimization under dynamic conditions.", In *2014 IEEE Congress on Evolutionary Computation (CEC)*, IEEE, 2014, pp. 2977-2984. DOI: 10.1109/CEC.2014.6900603.
- [30] Saglam, Murat, Sami Ezercan, Suat Gumussoy. "Controller tuning for active queue management using a parameter space method.", arXiv preprint arXiv:2003.01076, (2020). DOI: 10.48550/arXiv.2003.01076.
- [31] Salam Waley Shneen. "Design and implementation of a stability control system for TCP/AQM network.", *Indonesian Journal of Electrical Engineering and Computer Science*, Vol. 22, No. 1, April 2021, pp. 129~136. DOI: 10.11591/ijeecs.v22.i1.pp129-136.
- [32] Sulttan, M. Q., Jaber, M. H., & Shneen, S. W. (2020). "Proportional-integral genetic algorithm controller for stability of TCP network." *International Journal of Electrical and Computer Engineering (IJECE)*, 10(6), 6225-6232. DOI: 10.11591/ijece.v10i6.pp6225-6232.
- [33] Oudah, Manal Kadhim, Mohammed Qasim Sulttan, and Salam Waley Shneen. "Fuzzy type 1 PID controllers design for TCP/AQM wireless networks." *Indonesian Journal of Electrical Engineering and Computer Science* 21.1 (2021): 118-127.
- [34] Eissa, Suad Ali, Salam Waley Shneen, and Ekbal Hussain Ali. "Flower Pollination Algorithm to Tune PID Controller of TCP/AQM Wireless Networks." *Journal of Robotics and Control (JRC)* 4.2 (2023): 149-156.
- [35] Awad, B.A., Oudah, M.K., Enaya, Y.A. and Shneen. "Simulation model of ACO, FLC and PID controller for TCP/AQM wireless networks by using MATLAB/Simulink", *International Journal of Electrical & Computer Engineering*, 13(3), 2023, (2088-8708).
- [36] Sulttan, M. Q., Shneen, S. W., & Alkhasraji, J. M. D.. Performance enhancement of large-scale linear dynamic MIMO systems using GWO-PID controller. *Bulletin of Electrical Engineering and Informatics*, 12(5), (2023): 2852-2859. DOI: 10.11591/eei.v12i5.4870.
- [37] Gottam, Venkata Supriya, and Bharat Kumar. "Optimal tuning of PID controller parameters for AGC of a wind." *ITEGAM-JETIA* 10, no. 46 (2024): 33-41. DOI: <https://doi.org/10.5935/jetia.v10i46.1095>.
- [38] Alkhasraji, J. M., Shneen, S. W., & Sulttan, M. Q.. Reduction of Large Scale Linear Dynamic MIMO Systems Using ACO-PID Controller. *Ingeniería e Investigación*, 44(1), (2024): e106657-e106657. DOI: 10.15446/ing.investig.106657.



PROCESS IMAGES-BASED CONTROLLER FUZZY-PI TO CONTROL EFFICIENCY IN ELECTRIC DRIVES

Luis D Rojas Puron¹, Idania Aguilera Fernández², Luis M Rojas Aguilera³ and João E. Neto⁴

^{1, 2} Technological University of the Havana – Havana City-Havana, Cuba.

³ Federal University of the Amazon (UFAM) – Manaus City, Manaus, Brazil.

⁴ State University of Amazon (UEA) – Manaus City, Manaus, Brazil.

¹<http://orcid.org/0009-0001-3410-1489> ²<http://orcid.org/0009-0005-9674-9706> ³<http://orcid.org/0000-0002-7408-4036> ,

⁴<http://orcid.org/0000-0002-5100-0719>

Email: lrpuron48@gmail.com, iaguilera395@gmail.com, rojas.luis.mail@gmail.com; jneto@uea.edu.br

ARTICLE INFO

Article History

Received: October 23th, 2024

Revised: October 23th, 2024

Accepted: October 23^h, 2024

Published: October 31th, 2024

Keywords:

Image-based control,

Energy,

Electric drives,

Efficiency.

ABSTRACT

This paper deal about a fuzzy PI tuning from process image-based control system (IBC) for electric drives of hydro-mixture transport, which method use a [r g b] matrix as control vector from process images taken through a inferential sensor of density, to evaluation efficiency in electric drives for hydro-transport of laterite pulp with centrifugal pumps.



Copyright ©2024 by authors and Galileo Institute of Technology and Education of the Amazon (ITEGAM). This work is licensed under the Creative Commons Attribution International License (CC BY 4.0).

I. INTRODUCTION

Image-based control systems (IBC) allows applications used in different fields of social life and industries, due to their safe implementation and constant improvements in the quality of results and applications.

The problem is to evaluate the efficiency of the laterite pulp pumping drive, whose objective is to offer the application of fuzzy logic in energy control in an industrial system.

This set also Electric drives require the rational use of energy, and some processes occur in very adverse environmental environments, where direct measurement of the variables is not possible. Due to this, it is necessary to look for indirect ways or methods of measurement, an aspect that is resolved with the use and advancement of new technologies, using the laws of optical physics, the properties of materials, and the use of Artificial Intelligence (AI) [1].

These aspects allows to use the intelligent qualities of controllers and sensors while maintaining the favorable features offered by devices and accessories in control and measurement schemes in the industrial area. In this way, the information

delivered to the sensors is encode in protocols that provide industry 4.0 standard transmission speeds.

Sensors have evolved into non-invasive measurement systems in those complicated means and processes of directly measuring variables, with adequate connectivity properties [1].

The information processed to produce control actions from more flexible schemes to adapt to the natural conditions of industrial processes, using electronic components that promote the design of circuits under the principle of electromagnetism and optical physics.

This work shows an efficiency control procedure in induction motor drive based on tuning a fuzzy PI controller using images taken from the process. The control vector from the pixel arrangements of the matrix [r g b] of the color of the fluid transported by a centrifugal pump, whose mixture characterized by having variable density, which determines the mechanical output power of the electric drive.

The hydro-transport of laterite pulp, involving centrifugal pump drives, constitutes an important link in the nickel production industry, due to its impact on the primary stage of the technological process, which decides the quality of the final product and its appreciable consumption of the energy.

That is why all research focused on improving the energy efficiency of electric drives, with the use of new technologies, constitutes valuable solutions to reduce costs and improve working conditions, which include control schemes and measurements in plants.

The design of a control scheme, in figure 3, with several blocks that includes PI-fuzzy type controllers, a neural controller that operates an inferential sensor (measures density of laterite pulp), which delivers the reference signal to the control. The objective function will be to evaluate the efficiency of the drive based on the density of the transported hydro mixture.

The novelty consists of using the information provided by images taken of the hydro-mixture, its digital processing used by the inferential sensor that offers real-time density values of the laterite pulp and serves as a reference to the input block of the electric drive control system. In this way, a supervisory block addresses the behavior of the induction motor that drives a centrifugal pump, whose rotational mechanical power supplies the load torque requirements of the drive, which depends largely on the value of the density of the hydro mixture at transport. The electric drive model is set out below.

II. METHODOLOGY

II.1 IMAGE-BASED CONTROL

The information provided by the digitally processed pulp images from the inferential sensor blocks (neural networks). A function represented by the color matrices [r g b], and the weights of the mixture [w₁ w₂ w₃] is obtained as control vector at the output of a learning block. The reference signal fuzzy-PI controller operates by error change, responsible for controlling the efficiency of the electric drive, regulating the transport speed of the mixture. This at the same time prevents sedimentation of the material in the pipes.

This type of research is semi-empirical, using the fuzzy logic by inference method, and comparison techniques in the results with conventional logic, using the statistical benefits of processing in MATLAB with the use of the Lookup-Table [2],[3].

An Image-based control system (IBC) offers some advantages of information capture and processing without invading the measurement medium, guaranteeing connectivity, precision and security in communications.

In our case, the control scheme takes into account the specificities of the industrial process, where the hydro-mixture transported at high temperatures, constituting an abrasive medium for the direct measurement of variables, and it is necessary to obtain this information indirectly [1].

The design of an inferential density sensor using a neural network, Figure 2, responsible for processing images of the hydro-mixture and encoding the pixels and piezoelectric measurement of the weight of the mixed fluid into density values in real time [2].

The modern industry has various platforms, such as NVIDIA Drive, which offers powerful computing, with a safe guarantee of being interchangeable.

In our case, the algorithm for extracting image qualities designed to help find a recognition function based on the vectors of the matrix [r g b] and the weight of the object under study, developed during the collection process [4],[5].

The image procedure carried out using fuzzy logic follows the structure, Figure 2, where extracts properties from process images [6]. This follows the similarity of two images, an aspect proposed by [7] and used by [6].

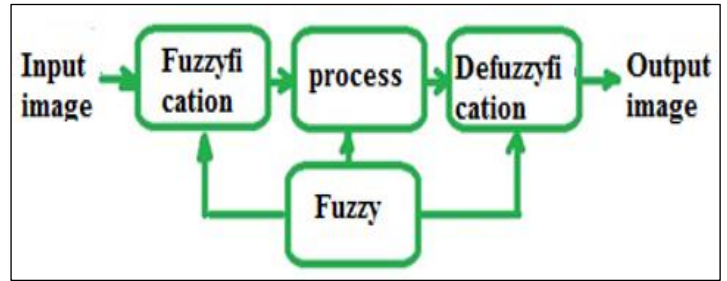


Figure 1: Image processing structure.

Source: Authors, (2024).

In practice, the weight of the variables has priority for the discrimination of fuzzy membership functions. The patterns trained for a high number of classifier samples.

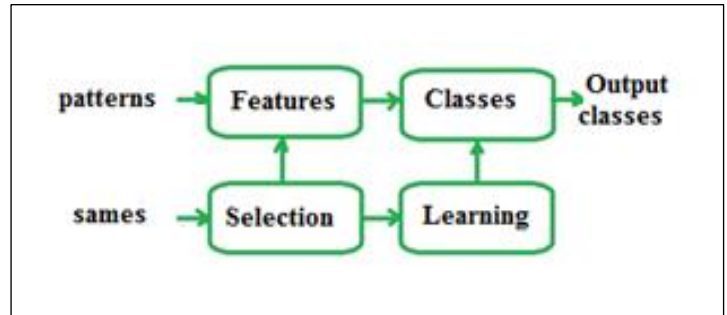


Figure 2: Scheme for patterns classification

Source:[6].

The procedure evaluates color *c*, weight *w* of the fluid mixed with suspensions for a monitored medium at a certain temperature τ , as shows the expressions (1), (2) and (3):

$$c = [c_1 c_2 c_3 \dots c_n] \quad (1)$$

$$w = [w_1 w_2 w_3 \dots w_n] \quad (2)$$

$$\tau = [\tau_1 \tau_2 \tau_3 \dots \tau_n] \quad (3)$$

In this way, the control diagram operates taking the reference signal from the image-processing block, as shown in the Figure 3:

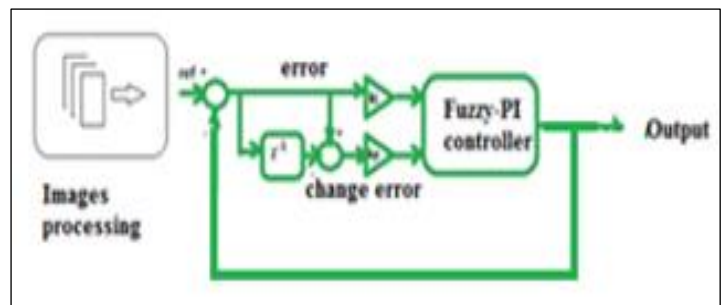


Figure 3: Diagram of fuzzy-PI controller.

Source: Authors, (2024).

The sensors processing information obtained from images, and produce system control actions [3]. It is favorable to implement these types of control schemes that add simplicity and memory converted into intelligence and precision once validated.

This sensor explained in [1], according to Figure 4, consists of two neural blocks in CNN-type cascades, the ANN-1 neural block.

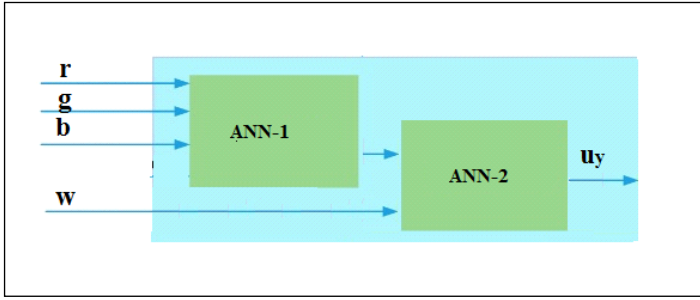


Figure 4: Density sensor based on CNN-type neural networks. Source: Authors, (2024).

The images processes of the transported fluid and delivers them from each matrix (color, weight) [r g b], [w₁ w₂ w₃] of the flow to the ANN-2 block. The output u_y encodes the density values evaluated by learning procedure to feed reference of the fuzzy-PI controller of the IGBT inverter to PWM.

A learning algorithm that takes into account the color processes the output signal u_y of the neural block. The matrix of the transported flow, developing the speed reference U_r of the fuzzy controller, adjusting more precisely the efficiency control of the pumping drive according to the density values obtained, procedure shown in Figure 5 and Figure 6 [8].

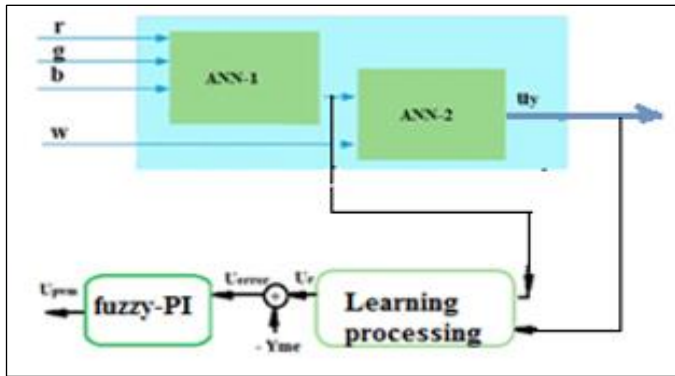


Figure 5: Scheme of control system using fuzzy-PI. Source: Authors, (2024).

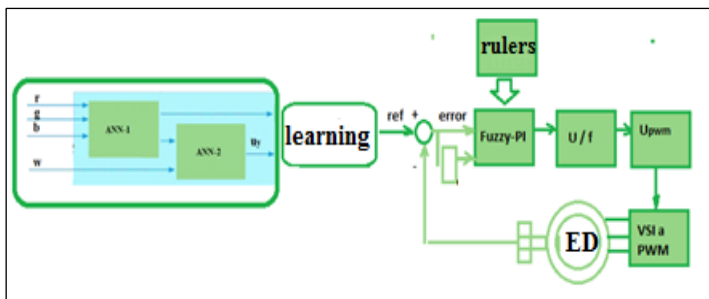


Figure 6: Image-based control diagram of the electric drive. Source: Authors, (2024).

III. MATERIALS AND METHODS

The experimental part used mixed fluids with temperatures 28, 60 y 90°C for supervised medium, from 25, 30, 40, 45 y 50 % concentrations of solids, obtained during process industrial metallurgical [1].

In practice, the weighting parameters for the discriminant functions not known a priori. A set of labeled

training patterns are used for estimation of the weighting parameters and the efficiency of the classifier is enhanced as a infinite large number of training samples from each pattern class are made available to the classifier [9]. A set of pattern samples are linearly separable, if there exists a weight vector that classifies all the samples correctly.

The Table 1 shows mixed fluid provides as follow.

TABLE 1: MIXED FLUIDS PROPERTIES

Num.	Massa of the mixed fluids		
	Mineral massa kg	Concentration %	Volume %
1	949.3	25	8.78
2	1220.5	30	11.45
3	1898.6	40	19.09
4	2563.2	45	24.8
5	2848	50	28.6

Source: Authors, (2024).

The recognition of the samples by image processing offered the results given in Table II.

TABLE 2: IMAGES RECOGNITION OF MIXED FLUIDS

Color			Matrix and Saturation		Temperature	Density
R	G	B	matrix	saturation	°C	Kg/m ³
117	35	11	9	198	90	1046
107	53	20	15	163	90	1105
104	48	23	12	150	90	1190
99	50	29	12	133	90	1230
97	51	31	12	124	90	1235
94	52	34	12	111	60	1275
90	54	37	13	100	60	1300
88	55	39	13	91	60	1400
84	55	44	12	75	60	1425
82	57	46	13	66	60	1488
78	58	50	13	52	28	1500
75	60	52	13	42	28	1568
73	60	54	12	35	28	1650
71	61	58	10	26	28	1663
69	61	58	8	19	28	1750

Source: Authors, (2024).

The inferential sensor of density works through a fuzzy inference system FIS, with inputs: images matrix [r g b], and weight (w) of samples, and output: density (d) of the mixed fluid. All the samples taken equal temperature conditions.

III.1 MODEL OF ELECTRIC DRIVES

The induction motor drive that drives a centrifugal pump has a well-known vector control model whose components in its dd-qq axes presented below [10],[11].

The relationships between the currents and voltages in the dd-qq axes with their components defined by the following expressions (4), (5), (6):

$$\sigma L_s \frac{di_{ds}}{dt} = -R_s i_{ds} + \omega_e \sigma L_s i_{qs} + U_{ds} \quad (4)$$

$$\sigma L_s \frac{di_{qs}}{dt} = -R_s i_{qs} - \omega_e \sigma L_s i_{ds} - \omega_e \frac{L_m}{L_r} \psi_{dr} + U_{qs} \quad (5)$$

$$\psi_{dr} = i_{ds} L_m \quad (6)$$

The torque electromagnetic M_{em} taken by (7):

$$M_{em} = 1,5 p (\psi_{sd} i_{sq} - \psi_{sq} i_{sd}) \quad (7)$$

where,

p – is number of poles of the electric motor.

ω_e – is the angular frequency of the motor stator field, [rad/s].

U_{ds}, U_{qs} – are stator voltages in the motor on the dd-qq axes, [V].

U_{dr}, U_{qr} – are rotor voltages in the motor on the dd-qq axes, [V].

i_{ds}, i_{qs} – are stator currents in the motor on the dd-qq axes, [A].

i_{dr}, i_{qr} – currents rotor in the motor on the dd-qq axes, [A].

Ψ_{ds}, Ψ_{qs} – magnetic fluxes in the stator on the dd-qq axes, [Wb].

Ψ_{dr}, Ψ_{qr} – magnetic fluxes in the rotor on the dd-qq axes, [Wb].

L_s, L_r – inductances stator and rotor in the winding of motor, [mH].

L_M – mutual inductance in the electric motor, [mH].

σ - Blonde coefficient.

The efficiency of the induction motor defined by follow equation (8):

$$\eta_{MI} = \frac{P_s}{P_e} = \frac{P_s}{P_s + \Delta p} = \frac{P_e - \Delta p}{P_e} \quad (8)$$

where,

P_s – is the output power on the induction motor shaft, [kW].

P_e – is the input electrical power of the induction motor, [kW].

Δp – are the total losses in the induction motor, [kW].

The input power of the drive obtained from (9) as:

$$* P_e = I_{ds} \cdot U_{ds} + I_{qs} \cdot U_{qs} \quad (9)$$

The total component of the stator current in the quadrature axes has as module by equation (10):

$$I_s = \sqrt{(I_{ds})^2 + (I_{qs})^2} \quad (10)$$

In such a way that I_{ds}^* and I_{qs}^* serve as commands during loss control. With changes in I_{ds} , the rotor flux Ψ_{dr} is controlled and with it the torque of the induction motor, which changes the input power.

III.2 ALGORITHM FOR EFFICIENCY CONTROL

A fuzzy inference system (FIS) shown for PID control using a MATLAB and another for image-based control using neural blocks.

This fuzzy inference system (FIS) takes input and output data from the measurement system in the drive, such as a typical controller with two inputs (error and change of error) and one output signal U_y . See Figure 5.

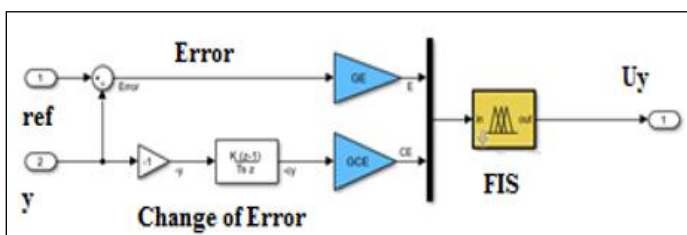


Figure 5: Linear control with input signals Error and Change of Error and output u_y . Source:[2].

For control applications, it is typical to have as inputs the absolute value of the error ($|e(k)|$) and the change of error ($|e(k)-e(k-1)|$), which would be Error $|E|$ and Change of Error $|CE|$ respectively on the surface curve. The fuzzy outputs is the control action $|u_y|$ inferred from the fuzzy rules [2].

A Sugeno-type Fuzzy Inference System FIS operates linear control from the input signals: Error $|E|$ and change of Error $|CE|$ at the exit $|u_y|$. The adjustment procedure explained following publication [2]. Input signals with triangle-type membership functions with neighboring values, whose output signal is set as a constant. The algorithm follows a relationship given in the surface curve of Figure 6 [12].

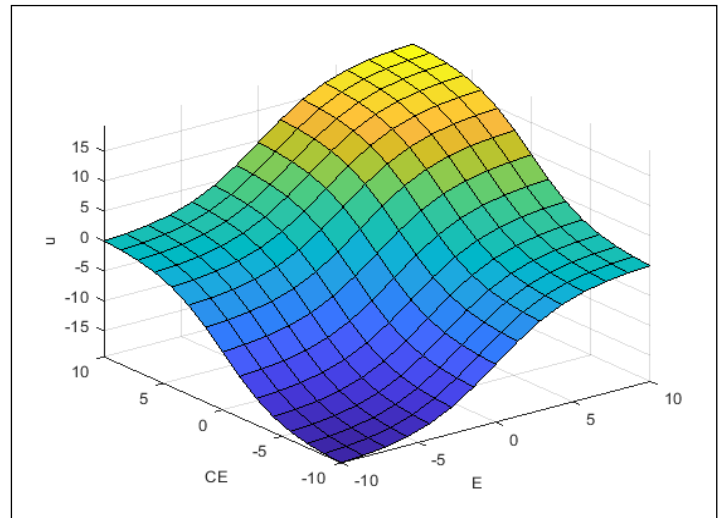


Figure 6: Surface curve for fuzzy-PI control. Source: Authors, (2024).

IV. RESULTS AND DISCUSSIONS

In order to demonstrate the quality of the fuzzy control using images of the process, the graphs of the stable behavior of the variables voltage and control commands of the induction motor presented, using this type of control.

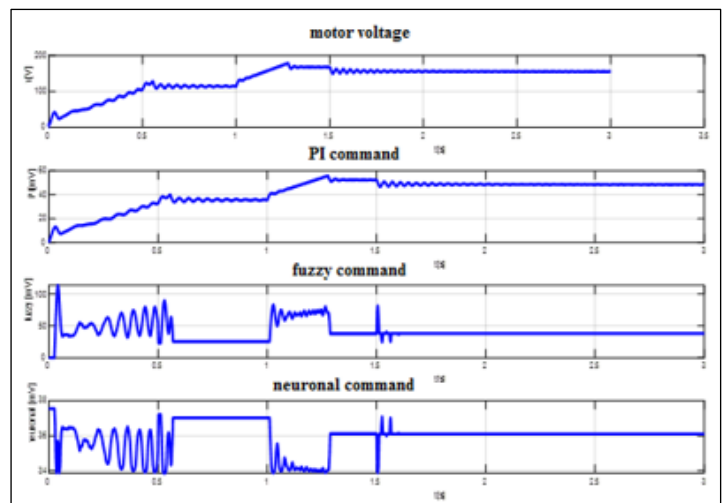


Figure 7: Motor voltage signals and control commands with PI, fuzzy and neuronal sensor. Source: Authors, (2024).

For changes in the density of the lateritic pulp, cause changes in the mechanical load and is the magnetic flux of the machine adjusted. This behavior observed in Figures 8 and 9.

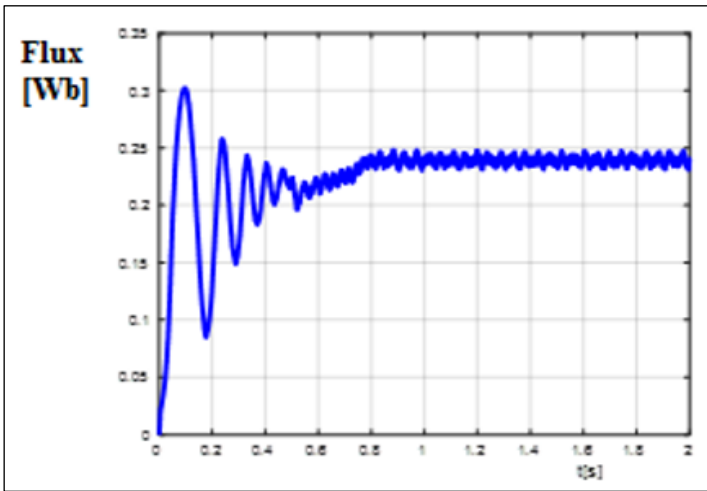


Figure 8: Magnetic flux of the motor with Fuzzy-PI controller for 950 rpm.
Source: Authors, (2024).

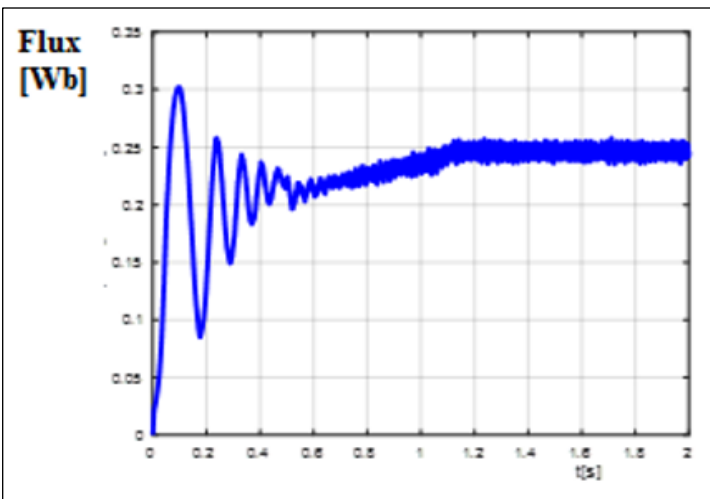


Figure 9: Magnetic flux of the motor with Fuzzy-PI controller for 1500 rpm.
Source: Authors, (2024).

Comparing conventional PI control and the use of fuzzy-PI control, steel losses decreased, and aspect observed in figure 10, where efficiency is better.

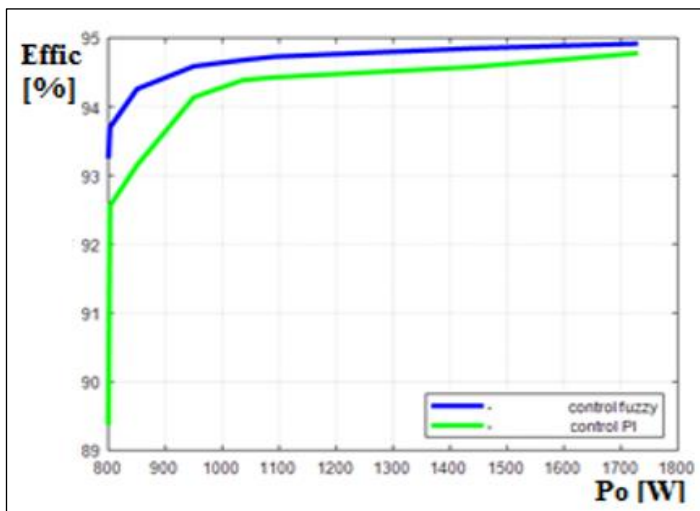


Figure 10: Efficiency by fuzzy-PI control with respect to conventional PI.
Source: Authors, (2024).

Observing the effect of the frequency change with respect to motor losses, Figure 11, the improvement with fuzzy-PI control better.

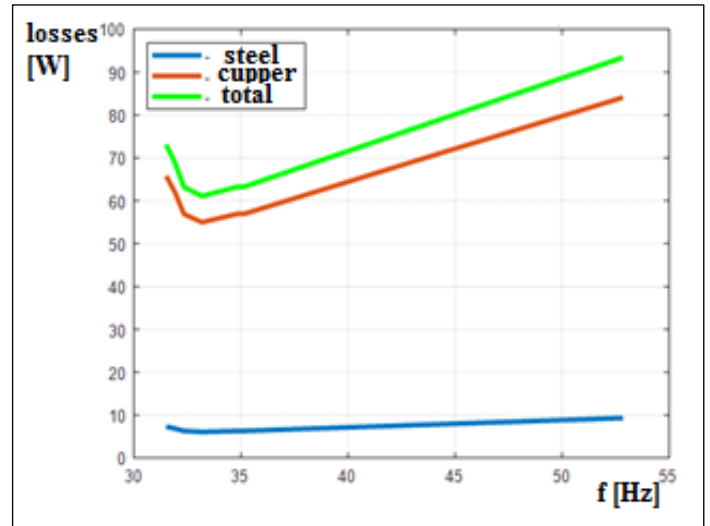


Figure 11: Motor losses at different frequencies with fuzzy-PI control.
Source: Authors, (2024).

These graphs show the novelty of how to tune the fuzzy-PI controller using the encoding of the images obtained from the transported fluid.

Thus is possible to control the efficiency of the centrifugal pump drive, through a control function obtained according to the density values of the transported pulp that determines the mechanical load of the electric drive for the most efficient speeds of lateritic pulp pumping.

The novelty consists of controlling the efficiency of the centrifugal pump drive, using image processing of the pulp transported in the hydro-transport process.

V. CONCLUSIONS

The use of image-based control in electric drives with induction motors for centrifugal pumps used for hydro-transport of mixed fluids in industrial environments conditions can be to overcome the limitations of direct measurements and allow monitoring efficiency in these drives.

For future work, is possible to improve the research using less saturated mixture fluids to evaluate the efficiency of an electric drive from on images of the process in order to implement intelligent control.

VI. AUTHOR'S CONTRIBUTION

Conceptualization: Luis D. Rojas, Idania Aguilera and Luis Rojas Aguilera.

Methodology: Luis D. Rojas and Idania Aguilera.

Investigation: Luis D. Rojas, Idania Aguilera and Luis Rojas Aguilera.

Discussion of results: Luis D. Rojas Purón and Luis Rojas Aguilera.

Writing – Original Draft: Luis D. Rojas.

Writing – Review and Editing: Luis Rojas Aguilera.

Resources: Luis Rojas Aguilera.

Supervision: Luis D. Rojas Puron.

Approval of the final text: A Luis D. Rojas, Idania Aguilera and Luis Rojas Aguilera.

VII. ACKNOWLEDGMENTS

Thanks to the State University of Amazon (UEA), CAPES Foundations and CICARI Group that contributed to the successful development of this project, which without your support would not have made the development of these results.

VIII. REFERENCES

- [1] L. D. Rojas Puron, J. E. Neto, A. C. Leal, and L. M. Rojas Aguilera, "Procedure neuro-fuzzy with application inferential sensor", ISBN 978 1 5386 3124 9. IEEE, December 2017.
- [2] J. Xu, X., Hang, C. C., Liu, C. "Parallel structure and tuning of a fuzzy PID controller." *Automatica*, Vol. 36, pp. 673-684, 2000.
- [3] J. Janstzen. Tuning of Fuzzy PID Controllers, Technical report, Dept of Automation, Technical University of Denmark. 1999.
- [4] J. C. Bezdek, J. Keller, R. Krisnapuram, N. R. Pal. Fuzzy models and algorithms for patterns recognition and images processing, Springer ed., . New York, USA pp.1-785, 2005.
- [5] W. H. Tsai, Moment preserving thresholding: A new approach, *Graphical Models and Image Processing*, pp 377–393, 1985.
- [6] T. Chaira, A. K. Ray, "Fuzzy image processing and applications with MATLAB, Taylor and Francis Group, LLC, pp. 1-234, 2009.
- [7] W. J. Wang. New similarity measures on fuzzy sets and fuzzy elements, *Fuzzy Sets and Systems*, pp 305–309, 1997.
- [8] S. Derhami, A. Smith, "An integer programming approach for fuzzy rule based classification systems." *European Journal of Operational Research*. July 2016.
- [9] V. Ravi, P. J. Reddy, "Patterns classification with Principal Component Analysis and fuzzy rules bases". *European Journal of Operational Research*. , pp 526-533, November 2000.
- [10] Ned Mohan. *Advanced Electric Drives: analysis, control and modelling using MATLAB/Simulink*. 2014.
- [11] L. D. Rojas Puron, J. E. Neto, I. Aguilera. Neural networks based estimator for efficiency in VSI to PWM of induction motors drives. ICCA-ACCA. IEEE International Conference. DOI: 10.1109/ICA-ACCA.2016.77784 45 October 2016.
- [12] S. Derhami, A. Smith, "Iterative mixed integer programming model for fuzzy rules based classification systems" *International Conference on Fuzzy Systems. IEEE Fuzzy systems*. July 2014.